JAEA-Review
2013-039

研究炉（JRR-3 及び JRR-4）利用における研究成果集（平成２０年度）

Activity Report on the Utilization of Research Reactors (JRR-3 and JRR-4) (Japanese Fiscal Year, 2008)

（編）研究炉利用課

(Ed.) Research Reactor Utilization Section

東海研究開発センター
原子力科学研究所
研究炉加速器管理部

Department of Research Reactor and Tandem Accelerator
Nuclear Science Research Institute
Tokai Research and Development Center

February 2014

Japan Atomic Energy Agency

日本原子力研究開発機構

JAEA-Review

独立行政法人日本原子力研究開発機構　研究技術情報部　研究技術情報課
〒319-1195　茨城県那珂郡東海村白方白根 2 番地 4
電話 029-282-6387, Fax 029-282-5920, E-mail:ird-support@jaea.go.jp

2-4 Shirakata Shirane, Tokai-mura, Naka-gun, Ibaraki-ken 319-1195 Japan
Tel +81-29-282-6387, Fax +81-29-282-5920, E-mail:ird-support@jaea.go.jp

JAEA-Review 2013-039

研究炉（JRR-3及びJRR-4）利用における研究成果集（平成２０年度）

日本原子力研究開発機構 東海研究開発センター 原子力科学研究所
研究炉加速器管理部
（編）研究炉利用課

（2013年 9月 24日受理）

JRR-3は、中性子散乱、即発ガンマ線分析、中性子ラジオグラフィなどの実験利用、及び、放射化分析、原子炉燃料材料、ラジオアイソトープ製造、フィッションートラック年代測定の照射利用など、様々な目的に利用されている。

JRR-4については、医療照射（Boron Neutron Capture Therapy：BNCT)、即発ガンマ線分析、放射線測定器の感度試験、原子炉研修運転実習等の実験利用、及び、放射化分析、ラジオアイソトープ製造、フィッショントラック年代測定のための照射利用など、様々な目的に利用されている。

平成20年度、研究炉JRR-3は7サイクルの運転（1サイクル：26日連続運転）の施設共用運転を行なった。研究炉 JRR-4は反射体要素の吊り手溶接部に割れが発見され、取り替え用反射体要素の製作及び交換が必要となったため、運転は行われなかった。

本報告書は、平成２０年度に実施した施設利用成果の提出を研究炉の利用者（原子力機構外を含む）から受け、中性子散乱11分野（構造、磁性、超伝導など)、中性子ラジオグラフィ、放射化分析、その他、の分野別についてその研究成果を取りまとめたものである。

原子力科学研究所：〒319-1195　茨城県那珂郡東海村白方白根2-4

JAEA-Review 2013-039

Activity Report on the Utilization of Research Reactors (JRR-3 and JRR-4)
(Japanese Fiscal Year, 2008)

(Ed.) Research Reactor Utilization Section

Department of Research Reactor and Tandem Accelerator
Nuclear Science Research Institute
Tokai Research and Development Center
Japan Atomic Energy Agency
Tokai-mura, Naka-gun, Ibaraki-ken

(Received September 24, 2013)

JRR-3 is used for the purposes below;

- Experimental studies such as neutron scattering, prompt gamma-ray analyses, neutron radiography
- Irradiation for activation analyses, radioisotope (RI) productions, fission tracks
- Irradiation test of reactor materials

etc.

JRR-4 is used for the purposes below;

- Medical irradiation (Boron Neutron Capture Therapy : BNCT)
- Prompt gamma-ray analyses
- Sensitivity measurement of radiation detectors
- Experiment and practice in the nuclear reactor training
- Irradiation for activation analyses, RI productions, fission tracks

etc.

In the fiscal year 2008, the research reactor JRR-3 was operated for 7 cycles (cycle operation : 26days/cycle) for utilization sharing of facility.

The research reactor JRR-4 was not operated in 2008. Because a crack was found on the weld of the aluminum cladding of a graphite reflector element. JRR-4 has remained shutdown until the reflector elements were replaced.

The volume contains 250activity reports, which are categorized into the fields of neutron scattering (11 subcategories), neutron radiography, neutron activation analyses, and others submitted by the users in JAEA and other Organizations.

Keywords: JRR-3, JRR-4, Research Reactor, Neutron Scattering, Neutron Radiography, Neutron Activation Analysis, Neutron Beam, Irradiation

目　　次

Contents

はじめに

平成２０年度には、ＪＲＲ－３において７サイクルの共同利用運転が行われ、これに伴いさまざまな利用が行われた。ＪＲＲ－４については取り替え用反射体要素の製作及び交換が必要となったため、運転は行われなかった。

本報告書は、利用者（原子力機構外利用者を含む）から当該利用の成果の提出を受け、取りまとめたものである。

提出して頂いた成果の件数は、中性子散乱２２３件、中性子ラジオグラフィ５件、放射化分析２１件、その他１件で合計２５０件であった。なお、本報告書の一部は、貴重な研究成果を公開する機会を広げるため、下記報告書の中から転載させて頂いたものである。

最後に、原稿を提出して頂いた利用者の皆様のご協力に感謝するとともに、今後も研究炉が有効に利用され、種々の研究がさらに進展されることを期待します。

研究炉利用課長
笹島　文雄

---

1)標　　題　：ACTIVITY REPORT ON NEUTRON SCATTERING
RESEARCH issued by ISSP-NSL,University of Tokyo,Vol.16
（東京大学物性研究所発行）
編　　者　：東京大学物性研究所
発 行 年　：２００９年

2)標　　題　：原子力機構施設利用総合共同研究成果報告集（平成２０年度）
編　　者　：東京大学大学院工学系研究科原子力専攻共同利用管理本部
発 行 年　：２００９年

This is a blank page.

研究成果一覧

Research Reports

1.　中性子散乱　1）構造・励磁

1. Neutron Scattering　1）Structure・Excitation

This is a blank page.

1-1-1

Phonon Dispersion Relations of $LaAlO_3$-$SrTiO_3$

H. Yamauchi, T. Shimada[1], K. Ichikawa[1], J. Breeze[2] and N. McN Alford[2]

Quantum Beam Science Directorate, Japan Atomic Energy Agency, Tokai, Ibaraki 319-1195
[1]*Advanced Electronics Research Laboratory, Hitachi Metals, Ltd., Kumagaya, Saitama 360-0843*
[2]*London South Bank University, London SE1 0AA, UK*

The $SrTiO_3$ doped $LaAlO_3$ (LAO-STO) has the pseudo-cubic perovskite structure. It has been expected to apply single crystal LAO-STO in dielectric resonators and electromagnetic filters because of extremely low dielectric loss at microwave communications frequencies$^{1)}$. However, it is known that its loss is strongly depend on whether the incident direction of electromagnetic wave is along [1 0 0] or [1 1 0]$^{2)}$. Predicting the dielectric loss in applicative materials at microwave frequency band has generally turned out to be highly problematic, though it is valuable for material developers to possess the means of the preliminary prediction. Spark *et al.* proposed that two-phonon absorption process between transverse acoustic (TA) and optic (TO) modes at the Brillouin zone (BZ) boundary is mainly important for dielectric loss in the microwave region$^{3,4)}$.

In order to collect the fundamental phonon dispersion data, we therefore carried out inelastic neutron scattering experiments at room temperature using the triple-axis spectrometer TAS-1. The single crystal sample of 1.5 mol% $SrTiO_3$ doped $LaAlO_3$ was used for experiments. Measurements were performed in the constant-Q mode with incident neutron energies of 14.7 – 41.0 meV. The scattering was carried out in a net plane of $(h\,k\,k)$.

Figure 1 shows the dispersion curves for phonons with wave vectors along [1 0 0] and [1 1 0] directions. The markers denote the experimental data. The calculated dispersion curves of $LaAlO_3$ with cubic symmetry are also shown as reference by the dashed lines. The open circles and triangles correspond to TA and TO phonon modes, respectively. The closed circles stand for longitudinal acoustic modes. The experimental results are largely consistent with the calculated dispersion except for the TO mode and a part of the TA modes in $\boldsymbol{q} \parallel [1\,1\,0]$. The energy gap between the TA and TO modes at the BZ boundary is 18.3 meV in $\boldsymbol{q} \parallel [1\,0\,0]$ and 13.7 meV in $\boldsymbol{q} \parallel [1\,1\,0]$. Comparing theoretical prediction of losses with direct measurements is not straightforward because theories assume perfect (defect- and impurity-free) single crystals. Theories, however, have prospects of providing a lower limit for the intrinsic dielectric loss. In the future, we will examine the availability of the theoretical method for predicting dielectric loss in LAO-STO as a candidate of the applicative materials.

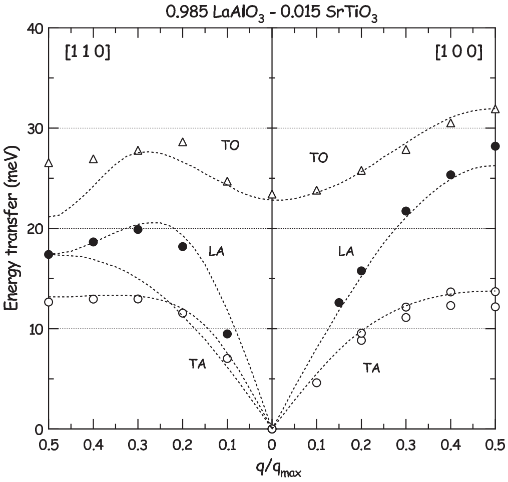

Figure 1: Phonon dispersion curves for $0.985\,LaAlO_3$ - $0.015\,SrTiO_3$. The dashed lines represent the calculation of phonon dispersion relation in $LaAlO_3$.

References

1) T. Shimada *et al.*, J. Eur. Ceram. Soc. 26, 2017 (2006).
2) T. Shimada *et al.*, J. Eur. Ceram. Soc. 25, 2901 (2005).
3) M. Spark *et al.*, Phys. Rev. B 26, 6987 (1982).
4) X. Aupi *et al.*, J. Appl. Phys. 95, 2639 (2004).

原子炉：JRR-3　装置：TAS-1(2G)　分野：中性子散乱（構造）

1-1-2

Crystal Structure and Nuclear Density Distribution of $LiCo_{1/3}Ni_{1/3}Mn_{1/3}O_2$ Analyzed by Applying Rietveld/Maximum Entropy Method

N. Igawa, T. Taguchi, H. Fukazawa, H. Yamauchi, and W. Utsumi

Quantum Beam Science Directorate, JAEA, Tokai, Ibaraki 319-1195

$LiCo_{1/3}Ni_{1/3}Mn_{1/3}O_2$ is one of the candidate materials for cathode of next generation Li ion batteries. In general, the crystal structure and Li diffusion pathway are the keys to increase efficiency for the battery. Recently maximum entropy method (MEM) combined with neutron powder diffraction has been extensively used to investigate the crystal structures of ionic conductors, because MEM is effective for revealing static and dynamic disorder in crystals. In this study, we analyzed the nuclear density (scattering length density) distribution of $LiCo_{1/3}Ni_{1/3}Mn_{1/3}O_2$ by Rietveld and MEM analysis of neutron powder diffraction data to estimate the Li diffusing pathway.

The sample was prepared by a solid state reaction method. We used ^{7}Li enriched LiOH as a starting material to suppress the adsorption of neutron beam. Neutron powder diffraction measurements were carried out at room temperature using the HRPD. A neutron wavelength of 0.1823 nm was used. Crystal structure was determined from the diffraction pattern by the Rietveld method using the program“ RIETAN-FP ”.[1] After the Rietveld analysis, the scattering density distribution map was estimated by applying the maximum entropy method analysis using the program “ PRIMA ”.[2]

Figure 1 shows a result of Rietveld refinement. All peaks were from the sample and no reflections of impurities were observed. The R_{wp}, R_B and S are 4.28 %, 1.66 % and 1.19. $LiCo_{1/3}Ni_{1/3}Mn_{1/3}O_2$ has a hexagonal structure with the space group R-3m. Lattice parameters were refined to be a = 2.8643(2) Å, c = 14.2460(6) Å. Though Li mainly occupies 3a site, Co, Ni and Mn occupy 3b site, and O 6c site, approximately 4 % of Li and Ni atoms substitute from their original sites (3a and 3b) to 3b and 3a sites.

Figure 2 shows the scattering length density distribution maps of $LiCo_{1/3}Ni_{1/3}Mn_{1/3}O_2$ drawn with the absolute values of isosurface level, a)1.0 fm/Å^3 and b)0.05 fm/Å^3. While the scattering length density distributions of Co, Mn, Ni, and O atoms were localized at their sites, those of Li atoms at z=0, 1/3 and 2/3 widely spread on the planes parallel to (0001) plane.

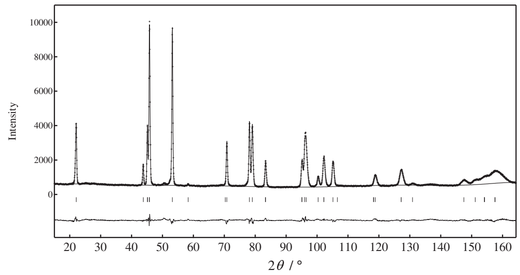

Figure 1: The result of the Rietveld analysis of $LiCo_{1/3}Ni_{1/3}Mn_{1/3}O_2$.

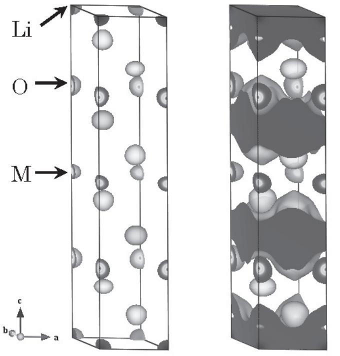

a)1.0 fm/Å^3 b) 0.05 fm/Å^3

Figure 2: Scattering length density distribution maps.

References

1) F. Izumi et al.:“Solid State Phenom.”, 130:15(2007).
2) F. Izumi et al.:“Recent Research Development in Physics II”, 3, 699(2002).

原子炉：JRR-3　　装置：HRPD(1G)　　分野：中性子散乱（構造）

1-1-3

Neutron Powder Diffraction Study of Water-Dissolved $Ba_2In_2O_5$

T. Nagasaki[1], S. Shiotani[2], M. Yoshino[2], K. Iwasaki[2],
N. Igawa[3], H. Fukazawa[3], H. Yamauchi[3] and W. Utsumi[3]

[1]*EcoTopia Science Institute, Nagoya University, Nagoya 464-8603*
[2]*Department of Materials, Physics and Energy Engineering, Graduate School of Engineering, Nagoya University, Nagoya 464-8603*
[3]*Quantum Beam Science Directorate, JAEA, Tokai, Ibaraki 319-1195*

In our previous studies [1,2], we carried out neutron powder diffraction experiments on $BaSn_{0.5}In_{0.5}O_{2.75}$, a proton conducting oxide with perovskite structure, with and without dissolved H_2O/D_2O. Analyzing the data by the Rietveld method and the maximum entropy method (MEM), we found that the deuterium atoms in $BaSn_{0.5}In_{0.5}O_{2.75+\alpha}$were located at the $48n$ site close to the $12h$ site of the cubic perovskite structure (space group $Pm\bar{3}m$).

In the present study, we have carried out similar experiments on another proton conducting oxide $Ba_2In_2O_5$, which has perovskite-derivative (brownmillerite) structure. Because of its lower symmetry, $Ba_2In_2O_5$ has various interstitial sites, some of which must be more stable than others for hydrogen.

Figure 1(a) shows the diffraction pattern of (dry) $Ba_2In_2O_5$ at 8 K. Although it was well fitted by the orthorhombic (Imma) structure model [3], there remained a few small peaks that could not be assigned. In fact, these extra peaks were also seen in the reported diffraction patterns [3,4]. Because they disappeared after water uptake [4], they are unlikely to be caused by impurities.

Figure 1(b) and (c) show the diffraction patterns for $Ba_2In_2O_6H_2$ and $Ba_2In_2O_6D_2$ at 8 K, respectively. While the Rietveld fitting based on the tetragonal (P4/mbm) structure model [5,6] gives a reasonable fit for the protonated material, it gives a poor fit for the deuterated material. Provided that the isotope effect in the crystal structure is negligible, this result suggests that the actual atomic arrangement especially of hydrogen is different from that in the structure model. Accordingly we have tested larger unit cells with lower symmetry, but not yet obtained satisfactory fits to the observed patterns. Further study is needed.

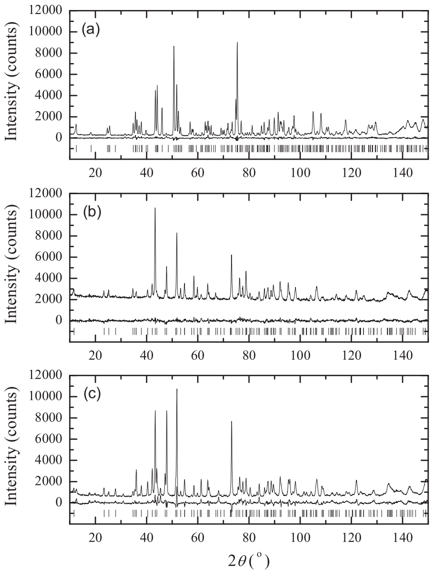

Figure 1: Neutron powder diffraction patterns at 8 K of (a)$Ba_2In_2O_5$, (b)$Ba_2In_2O_6H_2$, and (c)$Ba_2In_2O_6D_2$, together with the results of Rietveld fitting (difference plots) using RIETAN-FP.

References

1) T. Ito, T. Nagasaki et al. :"Solid State Ionics", 178, pp. 607-613 (2007).
2) T. Nagasaki et al. :"J. Solid State Chem.", in press (2009).
3) P. Berastegui et al. :"J. Solid State Chem.", 164, pp. 119-130 (2002).
4) T. Yildirim et al. :"Solid State Ionics", 145, pp. 429-435 (2001).
5) V. Jayaraman et al. :"Solid State Ionics", 170, pp. 25-32 (2004).
6) J.-R. Martinez et al. :"J. Solid State Chem.", 180, pp. 3388-3392 (2007).

原子炉：JRR-3　　装置：HRPD(1G)　　分野：中性子散乱（構造）

1-1-4

Structure of Ice XI and a New Form, Ice XV

H. Fukazawa
Quantum Beam Science Directorate, JAEA, Tokai, Ibaraki 319-1195

Ice is the major solid component in the universe. By infrared space observatory (ISO), ice has been founded in many locations from interstellar clouds to planets, their satellites and Kuiper belt objects. The infrared spectra have a strong peak at around 3.08 micro meter, which assigned to OH stretching vibration in crystal ice. The observed crystal ice in space is generally cooled below 80 K. According to the third low of thermodynamics and Pauling's ice rules, the hydrogen in crystal ice should be ordered at very low temperature. Thus frigid ice in space may be not ice Ih but hydrogen-ordered ice. The ordered ice is named ice XI (eleven). A hypothesis that ice XI exists in the Universe is reported [1-7].

We measured neutron powder diffraction (NPD) and infrared (IR) absorption spectra of doped ice samples with impurities, in order to understand the properties of ice in space. NPD shows that the hydrogen is ordered in ice and the resulting solid becomes ferroelectric ice XI (eleven). The ferroelectric ice is stable in wide range of temperature and pressure. IR spectra of ice XI have sharp peaks in librational and OH stretching modes.

Ferroelectric high-pressure ice, named ice XV, has long been predicted to exist above 0.7 GPa and below 160 K. We made ice XV at 1 GPa and 70 K on the HRPD using a high-pressure cell (McWhan type cell of alumina powder developed by Prof. Onodera) and top loading cryostat. In this march we have obtained the diffraction profile of ice XV at 1 GPa, which has a new peak (2.37 angstrom) from hydrogen-ordered structure. The profile is consistent with a ferroelectric structure.

Our preliminary study suggests that a new ice XV is also ferroelectric. Thus large quantities of ferroelectric ice should exist on icy bodies in outer solar system. The properties of ferroelectric ice are of interest in space because of long-range electrostatic force. The ferroelectricity becomes very important feature for planetary formation and material (including life origin material) evolution in space. A plan (ISO by a space telescope) to prove this hypothesis is proposed [8].

References

1) H. Fukazawa, et al. :"Astrophys. J. Lett.", 652, pp. L57-L60 (2006).
2) H. Fukazawa, et al. :"Physica B", 385-386, pp. 113-115 (2006).
3) H. Fukazawa :"JAEA RD Review", p. 43 (2007).
4) H. Fukazawa :"Planetary People", 16, pp. 7-12 (2007).
5) H. Fukazawa :"Hamon (The Japanese Society for Nuetron Science)", 18, pp. 97-102 (2007).
6) H. Fukazawa :"J. Crystallog. Soc. Jpn", 51, pp. 84-85 (2009).
7) H. Fukazawa et al. :"Nucl. Instrum. Methods Phys. Res. A", 600, pp. 279-281 (2009).
8) M. Arakawa, et al. :"Astrophys. J.", in press.

原子炉：JRR-3　　装置：HRPD(1G)　　分野：中性子散乱（構造）

1-1-5

Correlation Effects among Thermal Displacements of Atoms in KBr

T. Sakuma, Xianglian, N. Shimizu, J. Yokokawa, H. Takahashi[1] and N. Igawa[2]

Institute of Applied Beam Science, Ibaraki University, Mito 310-8512
[1]*Institute of Applied Beam Science, Ibaraki University, Hitachi 316-8511*
[2]*Japan Atomic Energy Agency, Tokai 319-1195*

Correlation effects among thermal displacements of atoms are important to realize the thermal properties of materials$^{1)}$. The oscillatory diffuse scattering intensities were observed from ordered crystals at room temperature due to the correlation effects among thermal displacements of atoms$^{2)}$. The values of correlation effects decrease rapidly with the increase of inter-atomic distance.

The correlation effects among thermal displacements of atoms are also obtained by EXAFS analysis. The value of the correlation effects of 1st nearest neighboring atoms in KBr was very small compared to other ionic crystals. We discuss the inter-atomic distance and temperature dependence of correlation effects in KBr by neutron diffraction method.

Neutron diffraction measurements were performed on powder KBr at 7 and 295 K by HRPD. Powder samples were set in a vanadium container of 10 mm in diameter. Incident neutron wavelength was 1.823 Å. The scattering data were collected in the range of scattering angle from 10° to 160° with step angle 0.05°. The observed diffuse neutron scattering intensities of KBr are shown by solid lines (295K) and broken lines (7K) in Fig. 1.

The diffuse neutron scattering profile of KBr at room temperature was explained by the correlation effects among thermal displacements of atoms up to third neighboring atoms. The value of correlation effects among 1st nearest neighboring atoms in KBr (0.68) by diffuse neutron scattering measurement is greater than that (0.4) by EXAFS measurement. When we calculate the diffuse scattering intensity with the value 0.4, the oscillatory feature of the calculated intensity is very weak compared with that of the observed neutron diffuse scattering intensity.

The force constant is related to correlation effects and Debye-Waller temperature parameters. The phonon dispersion relation is calculated by the force constants among atoms. The force constant of first nearest neighboring atoms is obtained by EXAFS measurement, whereas the force constants of first, second and third nearest neighboring atoms are obtained by the analysis of diffuse scattering. Therefore we would estimate the phonon dispersion relation from the analysis of diffuse scattering intensity by X-ray and neutron diffraction measurements with a high accuracy than the method of EXAFS measurement. The derivation of phonon dispersion relation from the correlation effects is in progress.

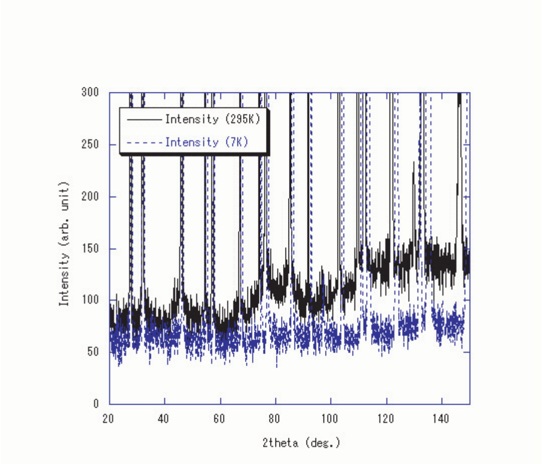

Figure 1: Neutron scattering intensities of powder KBr.

References

1) T. Sakuma:“J. Phys. Soc. Jpn.”, 62, pp. 4150-4151 (1993).
2) T. Sakuma *et al.*:“Solid State Ionics”, 176, pp. 2689-2693 (2005).

原子炉：JRR-3　　装置：HRPD(1G)　　分野：中性子散乱（構造）

1-1-6

Effect of Consolidation Condition on Nano-Size Oxide Particle Dispersion in 9Cr-ODS Steel

S. Ohtsuka[1], J. Suzuki[2], T. Kaito[1],M. Inoue[1], S. Kim[1], S. Obara[1] and T. Asayama[1]

[1] *Core and Structural Materials Group, Advanced Nuclear System R&D directorate*
[2] *Materials and Life Science Division, J-Parc Center*

The 9Cr-oxide dispersion strengthened ferritic (9Cr-ODS) steel is a primary candidate for fuel cladding tube of advanced fast breeder reactor. In the development of this material, nano-structure control is a critical technique to produce uniform and high population oxide particle dispersion that stabilizes microstructure even under high-temperature and high dose neutron irradiation environment of reactor core. In this research, effect of consolidation temperature on the nano-size particle dispersion in 9Cr-ODS steel was investigated using SANS-J-II in JRR-3.

Mixture of 9Cr-ferritic alloy powder and yttria (Y_2O_3) powder was mechanically alloyed (MA) in argon gas atmosphere. The MA powder was consolidated by hot isostatic pressing (HIP) with two conditions, i.e. 1233K for 4h at 98MPa and 1423K for 4h at 98MPa. The chemical composition was controlled to be 9mass%Cr-0.13C-2W-0.2Ti-0.35Y_2O_3. Nano-structure characterization was performed using small angle neutron scattering (SANS) and direct observation using transmission electron microscope (TEM). The number density of nano-size oxide particles was quantitatively evaluated by SANS profile analysis, where scattering length density of $Y_2Ti_2O_7$ was adopted. Vickers hardness tests were conducted at 1kgf.

As shown in Fig.1, the nano-particle number density qualitatively appears to be somewhat higher in the 1233K-HIPed steel than in the 1423K HIPed one. The SANS analysis results is displayed in Fig.2(a), which clearly indicates that the nano-particle number density of the 1233K-HIPed steel is higher than the 1423K HIPed one; the HIP consolidation temperature is a critical parameter dominating nano-particle dispersion condition. In Fig.2(b), Vickers hardness was plotted against the square root of nano-particles number density(Np) multiplied by the particle diameter(d), which is known to be proportional to oxide dispersion strengthening. The nanometer scale SANS analysis results are well consistent with macroscopic Vickers hardness. Optimization of 9Cr-ODS consolidation process is now under way based on SANS results of the consolidated steels at various fabrication conditions.

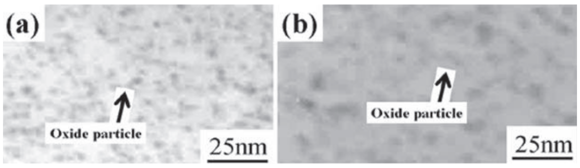

Figure 1: TEM observation results of (a)1233K HIPed steel and (b)1423K HIPed steel.

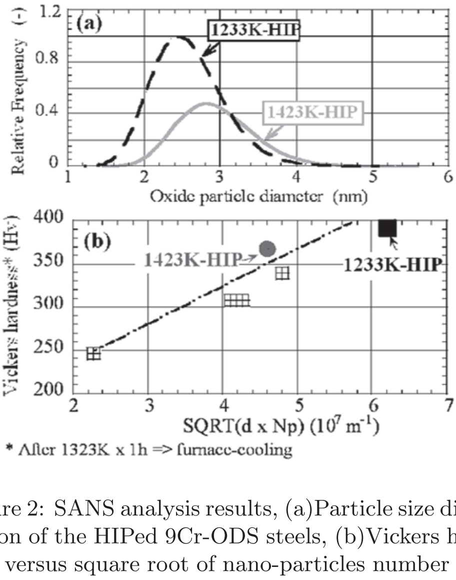

* After 1323K x 1h => furnace-cooling

Figure 2: SANS analysis results, (a)Particle size distribution of the HIPed 9Cr-ODS steels, (b)Vickers hardness versus square root of nano-particles number density multiplied by the particle diameter.

原子炉：JRR-3　　装置：SANS-J(C3-2)　　分野：中性子散乱（構造）

1-1-7

Nano-structure analysis of high Cr steel for long life FBR structural material

S. Obara[1], J. Suzuki[2], T. Wakai[1], S. Ohtsuka[1], M. Inoue[1] and T. Asayama[1]

[1] *Core and Structural Materials Group, Advanced Nuclear System RD Directorate*
[2] *Materials and Life Science Division, J-Parc Center*

For the commercialization of fast breeder reactor (FBR), it is essential to reduce construction cost by employing high chromium (Cr) steels as main structural materials. The conventional high Cr steels which have been developed as the materials for thermal power boilers have both excellent high temperature strength and thermal properties, such as thermal conductivity and thermal expansion rate. Generally, high temperature strength of the high Cr steels is achieved by several strengthening mechanisms. Precipitation strengthening mechanism by fine precipitations, such as V(C,N), Nb(C,N) and $Cr_{23}C_6$, is the most important one. In this study, in order to estimate the precipitation strengthening effect in high Cr steel, the size distribution and number density of fine precipitations were estimated using transmission electron microscope (TEM) and small angle neutron scattering (SANS) analyzer. In addition, the relationship between high temperature properties and number density of fine precipitations was evaluated based on the mechanical test results and microstructural observations.

In order to estimate the size distribution and number density of fine precipitations, V and Nb added high Cr steel was prepared. Chemical compositions of the steel are 0.1C-10Cr-1.2Mo-0.12V-0.03Nb-0.05N-Fe (mass%). The steel were normalized at three different temperatures, namely 1060˚C, 1100˚C and 1150˚C for 1 hour, and then tempered at 760˚C for 1 hour. The TEM observation was performed using extracted replicas specimen. The SANS analyses were performed in the q range of 0.01〜1 (nm^{-1}) using SANS-J-II in JRR-3, and the nuclear scattering information was obtained by applying one-directional magnetic field of 1 (Tesla) to the specimens.

The shape, distribution and chemical compositions of fine precipitations were investigated using TEM observations. Then, the size distribution and number density of fine precipitations were obtained from the measured SANS profiles and TEM observations. The influence of normalizing temperature on the size distribution of fine precipitations obtained from SANS analyses is shown in Figure 1. The mean diameter of fine precipitations decreased with increase of normalizing temperature, and the number density became lager with increase of normalizing temperature. Figure 2 shows the relationship between high temperature strength and normalizing temperature. Both 0.2% proof stress and ultimate tensile strength increased with increase of normalizing temperature. Number density of fine precipitations also described in Figure 2, there is a good correlation between high temperature strength and number density of fine precipitations. These results show that SANS analyses and TEM observations can evaluate size distribution and number density of fine precipitations which correlated with high temperature strength of high Cr steel.

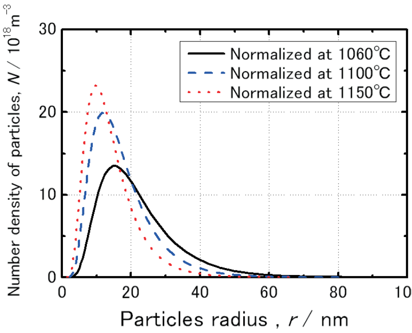

Figure 1: Influence of normalizing temperature on size distribution of fine precipitations in high Cr steel.

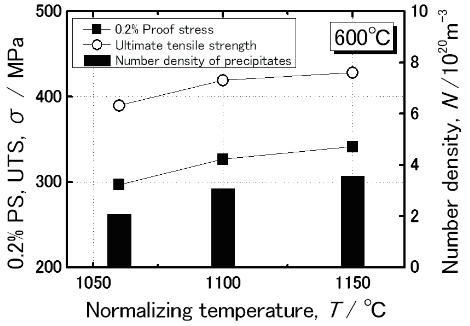

Figure 2: High temperature strength and number density of fine precipitations versus normalizing temperature.

原子炉：JRR-3　　装置：SANS-J(C3-2)　　分野：中性子散乱（構造）

1-1-8

Development of High Pressure Device for Neutron Powder Diffraction − Feasibility Test using Lanthanum Hydride −

W. Utsumi, T. Hattori, A. Machida[1] and N. Igawa

Quantum Beam Science Directorate, JAEA, Tokai, Ibaraki 319-1195
[1]*Quantum Beam Science Directorate, JAEA, Sayo, Hyogo 679-5148*

In situ powder diffraction with x-rays or neutrons is an indispensable technique to investigate the structure of materials under high pressure. For neutron diffraction, various high-pressure experiments have previously been conducted at nuclear reactors and with pulsed neutron sources. Further rapid progress is expected owing to the opening of J-PARC. Development of high pressure device suitable for neutron diffraction has been made using the High Resolution Powder Diffractometer (HRPD) at JRR-3.

A Paris-Edinburgh press was mounted on the rotation stage of HRPD. A pair of toroidal anvils made of tungsten carbide (WC) was used for the pressure generation. Diffraction profiles of Lanthanum hydride (LaH_x) powder (initial size: 5mm in diameter and 2.5mm in height) placed in the high pressure cell were observed at 3.5 GPa (applied load: 37 ton). Lanthanum hydride has been studied intensively because it exhibits metal-insulator transition upon hydrogenation and various phase transition occurs under high pressure. Incident and diffracted neutron beams (wavelength:1.823 °A) pass through the anvil gap which is perpendicular to the compression axis. The exposure time was 37 hours.

Figure 1 shows the diffraction profiles at 3.5 GPa. Nine peaks of LaH_x were clearly observed together with those from WC anvils. Although there are still many problems to be solved such as reduction of background and precise intensity measurements, feasibility of neutron powder diffraction under high pressure was confirmed. Using this high pressure device, the first high experiment was carried out at J-PARC (BL19), and the diffraction profiles of standard sample (Pb) were successfully obtained.

References

1) W.Utsumi, H.Kagi, K.Komatsu, H.Arima, T.Nagai, T.Okuchi, T.Kamiyama, Y.Uwatoko, M.Matsubayashi and T.Yagi, Nucl.Instr.Meth.Phys.Res.A 600, 50 (2009).

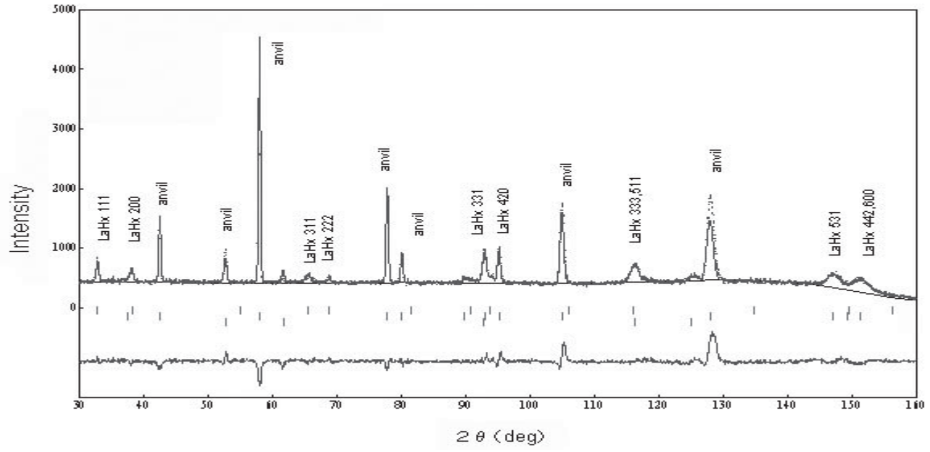

Figure 1: Diffraction profiles of LaHx at 3.5 GPa.

原子炉：JRR-3　装置：HRPD(1G)　分野：中性子散乱（構造）

1-1-9

Study of Mesoscale Spatial Distribution of Electron Spins in High Crystallinity Polyethylene Doped with TEMPO Using Time-Resolved Dynamic Nuclear Polarization and Small-Angle Neutron Scattering Methods

T. Kumada, Y. Noda, S. Koizumi, T. Hashimoto

Advanced Science Research Center, JAEA, Tokai, Ibaraki 319-1195

We studied the mesoscale spatial distribution of the electron spins in the high-crystalline polyethylene (PE) doped with TEMPO radicals by means of combined time-resolved dynamic nuclear polarization (DNP) and small-angle neutron scattering (SANS). DNP results from transferring spin polarization from electrons to nuclei, thereby aligning the nuclear spins to the extent that the electron spins are aligned. Proton spins at the neighbor of the electron spins are dynamically polarized by DNP. Since scattering length of a polarized neutron against a proton remarkably depends on relative direction of their spins, the scattered pattern of the polarized neutron reflects the spatial distribution of the proton polarization. The idea is that the spatial distribution of the electron spins can be determined by the SANS measurement of the distribution of the polarization generated by DNP.

We implemented the technique of double microwave-frequency DNP system and time-resolved SANS system. The DNP system enables to generate positive and negative proton polarization by switching the microwave (MW) frequency. The time-resolved SANS measures the spatial distribution of the polarization as a function of time after the switching of MW.

Figure 1 shows SANS profiles of the dynamically polarized PE. The scattering intensity at $q \leq 0.02$ $\mathring{A}$ measured 1 min after the stwiching of MW is larger than that measured ≥ 10 min after the switching and that of the unpolarized sample, whereas intensity of the peak at $q = 0.02$ $\mathring{A}^{-1}$ was much less changed.

High crystallinity PE has lamellar structure composed of crystalline (C) and amorphous (LA) phases, which generates the peak at $q = 0.02$ $\mathring{A}^{-1}$, whereas the regions other than the lamellar are amorphous (AA). It was found by electron spin resonance study that TEMPO is localized in the LA and AA regions but not in the C region. We speculate that the polarization at the AA region grew faster than that at the C and LA regions. The remarkable increase in the scattered intensity measured 1 min after the switching is expected to be due to the difference in polarization between the lamellar and the other regions. The small change in the peak intensity at $q = 0.02$ $\mathring{A}^{-1}$ suggests that the spin diffusion between C and LA is too fast to observe their difference in polarization within the time-scale of measurement.

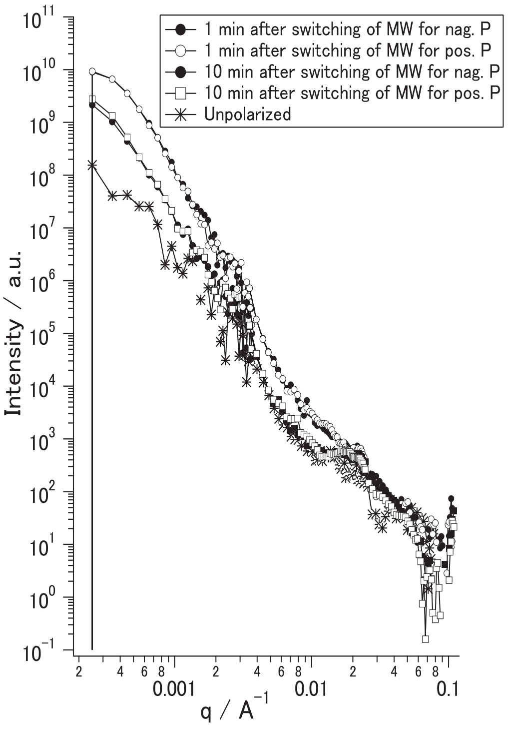

Figure 1: SANS profiles of dynamically polarized high crystallinity PE doped with TEMPO measured at 3.3 T and 1 K.

原子炉：JRR-3　　装置：SANS-J(C3-2)　　分野：中性子散乱（構造）

1-1-10

High Temperature Neutron Diffraction Study of (La0.5Sr0.5)CoO3-d Perovskite

K. Nomura (A), H. Kageyama (A), K. Kakinuma (B), T. Maekawa (C), S. Nakamura (C),H. Miyazaki (C), H. Imabayashi (C), T. Ito (C), and M. Yashima (D)
(A) AIST, (B) Yamanashi University, (C) New Cosmos Electric Co., Ltd., (D) Tokyo Institute of Technology

Recently, strontium-doped lanthanum cobaltate perovskites, (La1-xSrx)CoO3-d have been investigated as the cathode materials of solid oxide fuel cells, because of the high electronic and high oxide-ion conductivity [1]. However, the detailed crystal structures under cell operation conditions, i.e., at elevated temperatures under oxygen partial pressures, P(O2)<=0.21atm, have not been reported yet. In this study, we have measured high temperature neutron diffraction data of 50 mol% Sr-doped LaCoO3, (La0.5Sr0.5)CoO3-d (LSC), at elevated temperatures, 298<=T<=1273K, under 0.0002<=P(O2)<=0.21atm, to investigate the detailed crystal structures.

Neutron diffraction measurements were performed with a 150-detector system, HERMES [2], installed at the JRR-3M reactor in JAEA (Tokai). The neutron wave length was 1.8265(1)A and the diffraction data were collected in the 2θ range from 20 to 153 deg. in step interval of 2θ = 0.1 deg. A furnace with Pt-Rh heaters installed in a vacuum chamber was placed on the sample stage, and used for neutron-diffraction measurements at high temperatures under different P(O2) conditions. The diffraction data obtained were analyzed using the Rietveld program RIETAN-2000 [3]. The diffraction data of LSC could be indexed assuming a trigonal symmetry (R-3c, No.167) between 298 and 608K, or a cubic one (Pm-3m, No.221) between 723 and 1273K under P(O2) = 0.21atm. Almost all the diffraction peaks could be indexed as a tetragonal system (P4/mmm, No.123) at 1073K in P(O2) = 0.0002atm. Figure 1 shows the Rietveld refinement result of LSC measured at 1273K in P(O2) = 0.0004atm. Under this condition, almost all the diffraction peaks could be indexed as a cubic perovskite phase (Pm-3m, No.221) (In addition, trace amount of CoO phase was detected). The refined cell parameters of perovskite phase were as follows: Z = 1, a = 3.9395(3)A, α = 90 deg., V = 61.138(8)A^3. The reliability factors were Rwp = 5.81%, RI = 3.93%, RF = 2.14%, and Re = 2.12%. Goodness of fit (S = Rwp/Re) was 2.73.

References
[1] N. Minh, J. Am. Ceram. Soc., 76, 563 (1993).
[2] K. Ohoyama, T. Kanouchi, K. Nemoto, M. Ohashi, T. Kajitani, and Y. Yamaguchi, Jpn. J. Appl. Phys., 37, 3319 (1998).
[3] F. Izumi and T. Ikeda, Mater. Sci. Forum, 321-324, 198 (2000).

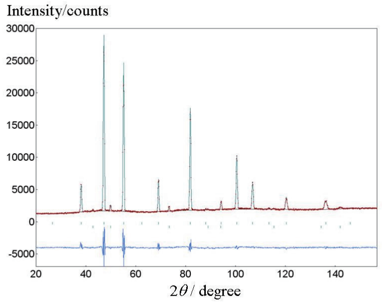

Fig. 1. Rietveld refinement result of (La0.5Sr0.5)CoO3-d at 1273K in P(O2) = 0.0004 atm.

1-1-11

Structural Disorder and Diffusional Pathway of Oxide Ions in a Doped Pr2NiO4-Based Mixed Conductor

Masatomo Yashima, †,* Makiko Enoki, ‡ Takahiro Wakita, † Roushown Ali, ¶, †
Yoshitaka Matsushita, ¶ Fujio Izumi, ¶ Tatsumi Ishihara ‡
† *Department of Materials Science and Engineering, Interdisciplinary Graduate School of Science and Engineering, Tokyo Institute of Technology, Nagatsuta-cho 4259, Midori-Ku, Yokohama, Kanagawa 226-8502, Japan,* ‡ *Department of Applied Chemistry, Faculty of Engineering, Kyushu University, Motooka 744, Nishi-Ku, Fukuoka, Fukuoka 819-0395, Japan, and* ¶ *Quantum Beam Center, National Institute for Materials Science, 1-1 Namiki, Tsukuba, Ibaraki 305-0044, Japan*

Mixed oxide-ionic and electronic conducting ceramics (MIECs) are attracting much interest as materials for oxygen separation membranes. Oxygen can permeate through MIECs membranes when a gradient of oxygen chemical potential exists. A2BO4-based oxides with K2NiF4-type structure have extensively been studied as new mixed ionic-electronic conductors, where A and B are cations. The development of improved MIECs requires a better understanding of the mechanism of ionic conduction, and crucial to this is a comprehensive knowledge of the crystal structure. It was speculated that the oxide ion conduction in the A2BO4-based oxides occurs by diffusion of excess oxide ions along the rock-salt-type AO layers. However, the diffusion path of oxide ion has not been determined yet. Pr2NiO4-based oxides have high oxygen permeability and high diffusivity of oxide ions. Here, we report for the first time the diffusion path of oxide ions in a K2NiF4-type mixed conductor (Pr0.9La0.1)2(Ni0.74Cu0.21Ga0.05)O4+d (PLNCG), through a high-temperature neutron powder diffraction study (M. Yashima, M. Enoki, T. Wakita, R. Ali, Y. Matsushita, F. Izumi and T. Ishihara, “ Structural Disorder and Diffusional Pathway of Oxide Ions in a Doped Pr2NiO4-Based Mixed Conductor ”, J. Am. Chem. Soc. (Communications), 139, [9] 2762-2763 (2008).). We chose this chemical composition, because it exhibits high oxygen permeability. The present result would give hints for the design of K2NiF4-type conductors.

A PLNCG sample was prepared by a solid-state reaction method at 1300 oC for 6 h in air. Neutron powder diffraction data of PLNCG were in situ measured at 606.6 oC and 1015.6 oC using a furnace and a 150 detector system HERMES at a neutron wavelength of 1.82646 . Neutron diffraction patterns at both temperatures indicated a K2NiF4-type structure with I4/mmm space group. Neutron-diffraction data were analyzed by a combination of Rietveld analysis, the maximum-entropy method (MEM), and MEM-based pattern fitting (MPF). A computer program RIETAN-2000 was utilized for the Rietveld analysis and MEM-based whole pattern fitting, and VESTA for visualization of nuclear density (scattering-length density) distribution. It is known that MPF makes it possible to determine nuclear densities in compounds containing disordered chemical species from neutron diffraction data.

Rietveld refinements of the neutron diffraction data of PLNCG at 606.6 oC and 1015.6 oC were successfully performed on the basis of the K2NiF4-type structure with I4/mmm space-group symmetry. It was found that PLNCG has a crystal structure consisting of (Ni,Cu,Ga)O6 octahedron and (Pr,La)-O layers. Refined occupancy factors indicated the excess oxygen of d = 0.0154(3) in (Pr0.9La0.1)2(Ni0.74Cu0.21Ga0.05)O4+d, which is ascribed to the interstitial O3 atom. The O3 atom is located at a 16n site, i.e., (x, 0, z) where x = 0.666(19) and z = 0.223(9) at 1015.6 oC. The oxy-

Activity Report on Neutron Scattering Research: Experimental Reports **16** (2009)
Report Number: 687

gen atom at the O2 site (4e; (0, 0, z); z = 0.1752(4) at 1015.6 oC) exhibits highly anisotropic thermal motion (U11 = U22 = 0.115(3) 2 and U33 = 0.021(3) 2), which leads to the migration of oxide ions to the nearest-neighbor interstitial O3 positions. The striking feature in the nuclear density distribution is the curved O2-O3 diffusion path. This feature is ascribed to the repulsion between (Pr,La) and O atoms. In fact, the distance between the (Pr,La) and O atoms are kept approximately constant along the diffusion paths. This fact suggests that the large-sized cations such as Pr and La ions at the A site in the A2BO4-type conductor are effective in improving the oxide-ionic conduction on the A-O layer. The conduction path is along the <100> directions near the O2 site and roughly along the <301> directions around the center of the paths. The nuclear-density distribution also shows the two-dimensional (2D) network of the O2-O3-O2 diffusion paths of oxide ions. The 2D feature is consistent with the anisotropic transport of oxide ions in La2NiO4+d. The nuclear density on the diffusion path at 1015.6 oC is larger than that at 606.6 oC, which is consistent with the improved oxygen permeability at higher temperatures.

1-1-11

1-1-12

Neutron diffraction study of Yb compounds

M.Kurisu, H.Murakami, G.Nakamoto, T.Tsutaoka(1) and Y.Andoh(2)
Japan Advanced Institute of Science and Technology, Ishikawa 923-1292, Japan
(1)Graduate School of Education, Hiroshima University, Hiroshima 739-8524, Japan
(2)Faculty of Regional Sciences, Tottori University, Tottori 680-8551, Japan

The interesting phenomenon of zero thermal expansion has been recently reported to occur in a wide temperature range from 100 to 300 K in YbGaGe compound [1]. The anomalous thermal expansion is caused by the decrease of Yb ion radius associated with valence fluctuation with increasing temperature. Because the temperature dependence of the effective magnetic moment calculated from the result of susceptibility measurement indicated that the valence of the Yb ion varies from 2+ to 3+. However, the experimental result was shown to suggest that the YbGaGe compound is diamagnetic [2]. Therefore, a correlation between valence fluctuation and zero thermal expansion has been doubted.

Furthermore, as for the thermal expansion anomaly that this compound showed, its sample dependence was large. A lot of questions do not yet reach solution about presence and cause of zero thermal expansion in the YbGaGe compound.

The purpose of this study is to examine the zero thermal expansion in the YbGaGe compound experimentally.

The single phase polycrystalline samples of YbGaGe compound was prepared by melting the constituent elements in a tetra-arc furnace under a Ti-gettered high-purity argon atmosphere. The measurement of thermal expansion of bulk samples was performed with differential transformer and strain gage methods. The powder neutron diffraction was carried out in the temperature range from 10 to 300 K at neutron beam-line T1-3 of JRR-3M at Tokai. Rietveld method was employed for the analysis. Heat capacity was measured with a PPMS.

The powder neutron diffraction pattern at 300 K is shown in Figure 1. The anisotropic thermal expansion was observed. The analysis is in progress.

References
[1] J. R. Salvador, F. Guo, T. Hogan and M. G. Kanatzidis: Nature 425(2003) 702.
[2] Y. Muro, T. Nakagawa, K. Umeo, M. Itoh, T. Suzuki and T. Takabatake: Journal of the Physical Sociey of Japan 73 (2004) 1450.

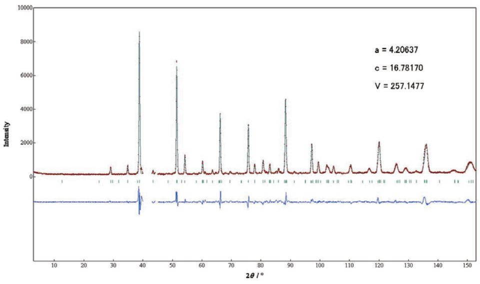

Fig. 1. The powder neutron diffraction pattern of YbGaGe at 300 K

1-1-13

Measurement of over dumped phonon on protonic conductor $K_3H(SeO_4)_2$

F. Shikanai[1], S. Itoh[2], K. Tomiyasu[3], N. Aso[4], T. J. Sato[4], S. Ikeda[2] and T. Kamiyama[2]
[1] *Univ. Tsukuba,* [2] *IMSS-NSL KEK,* [3]*IMR, Tohoku University,* [4]*ISSP-NSL Univ. Tokyo*

Protonic conductor $K_3H(SeO_4)_2$ undergoes first order phase transition at 390 K (T_C, 385 K on the cooling process), and shows high electric conductivity above T_C. We have measured the inelastic neutron scattering (INS) of the material, and observed a broad spectrum around 0 meV at zone boundary L-point above T_C. Intensity of the spectrum increases with decreasing the temperature, and the spectrum is considered to be caused by an over dumped phonon. However, quantitative nature of the spectrum was unclear because of the narrow shape of the spectrum less than the resolution. We, therefore, performed an energy scan from -0.2 meV to 0.2 meV under a possible high resolution within the scattering condition. The final momentum vector k_f was fixed at 1.39 $Å^{-1}$. The energy resolution was estimated as 88(3) μeV from the FWHM of incoherent scattering of hydrogen under a collimation of G-Be-20′-S-40′-Be-40′.

Figure 1 shows the temperature dependence of INS spectrum at L-point subtracted incoherent scattering which obtained at 0.7 2 0. The broad peak was observed only at L-point, therefore, the spectra are caused by an coherent scattering having the same symmetry of rotational SeO_4 tetrahedra. To analyze the data in Fig. 1, a equation formulated for neutron scattering cross section by over dumped phonon [1] was used. The equation was simplified as $AT\gamma\{(T-T_0+B\Delta q^2)(E^2+\gamma^2)\}^{-1}$ with the four parameters A, B, T_0 and γ. The results of fitting substituted $\Delta q = 0$ for the fitting function are illustrated as the plane in Fig 1. As shown in the figure, the data are good agreement with the calculated plane. The extrapolated Curie temperature T_0 was obtained as 368(2) K. The parameter γ was assumed as a linear function of T obtained from fitting at each temperature using a normal Lorentz function, as shown in the inset of Fig 1. The FWHM of the spectrum, 2γ, slightly depends on the temperature, and is obtained as 60(4) μeV and 70(6) μeV at 386 K and 435 K, respectively. This energy range corresponds to 14(1) GHz and 17(1) GHz, and gives the lifetime from $7.1(4) \times 10^{-11}$ s to $5.9(4) \times 10^{-11}$ s. Although it is expected that the lifetimes are little longer then this result because of the resolution, this time scale agrees with the stationary time of conduction proton, $9.0(8) \times 10^{-11}$ s at 388 K and $4.9(3) \times 10^{-11}$ s at 433 K, obtained from quasi elastic neutron scattering (QENS) [2]. It shows that proton conduction is simultaneous with the motion of rotational mode in phase I.

References

[1] Y. Yamada *et al.*: Phys. Rev. **177** (1969)848.
[2] F. Shikanai *et al.*: Ferroelectrics **347** (2007)74.

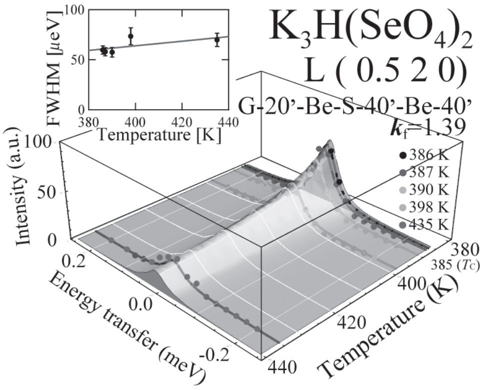

Fig. 1. Temperature dependence of INS spectra at L-point (subtracted incoherent scattering).

1-1-14

Phonon dispersion of off-stoichiometric Ni$_2$MnGa sigle crystal

K. Inoue^A, Y. Yamaguchi^B, H. Hiraka^B
^{A}*Advanced Research Institute for Science and Engineering, Waseda University,* ^{B}*IMR, Tohoku University*

Inelastic neutron scattering experiments were used to study an off-stoichiometric Heusler-type Ni$_{2.16}$Mn$_{0.78}$Ga$_{1.06}$ single crystal. A triple-axis neutron spectrometer, AKANE, was used. The alloy has a martensitic transformation temperature around room temperature (293 K) coincident with a Curie temperature. It is ferromagnetic in the martensitic phase and paramagnetic in the mother phase and is expected as a magnetic-field-induced shape memory alloy. With decreasing temperature the alloy transforms from a cubic structure to a metastable orthorhombic structure and finally to a stable tetragonal structure.$^{1)}$ Diffraction patterns of the cubic structure and of the orthorhombic structure projected on the reciprocal cubic c^*-plane are shown in Figs. 1(a) and (b). At 400 K the alloy shows a cubic structure and at 279K it shows an orthorhombic one. In the orthorhombic structure at 279 K, we see several elastic diffuse scatterings along the $\langle 110 \rangle$ and $\langle 100 \rangle$ directions of the orthorhombic c^*-plane and many weak satellite peaks on these diffuse scatterings. These diffuse scatterings and the satellite peaks appear to show that the lattice is modulated to various extent along $\langle 110 \rangle$ and $\langle 100 \rangle$ directions.

TA$_2$-phonon dispersions with $\langle 110 \rangle$ and $\langle 100 \rangle$ propagations in the cubic phase were measured at several temperatures. As shown in Figs. 1(c) or (d), the softening of the phonon is observed at q=0.3 or at q=0.23, respectively. The softening of the phonon with $\langle 110 \rangle$ propagation is explicitly temperature dependent. However, the temperature dependence of the softening of the phonon with $\langle 100 \rangle$ propagation is not clear. Near the position in the q-space corresponding to the softening of the TA$_2$-phonon dispersion, the elastic satellite peaks in the metastable orthorhombic structure appear. Thus, the softening of the TA$_2$-phonon in the mother phase appears to be a precursory phenomenon to the metastable martensitic structure.

1) K. Inoue, Y. Yamaguchi, H. Hiraka, *et. al.*: J. Phys. Soc. Jpn. **78** (2009) 034602.

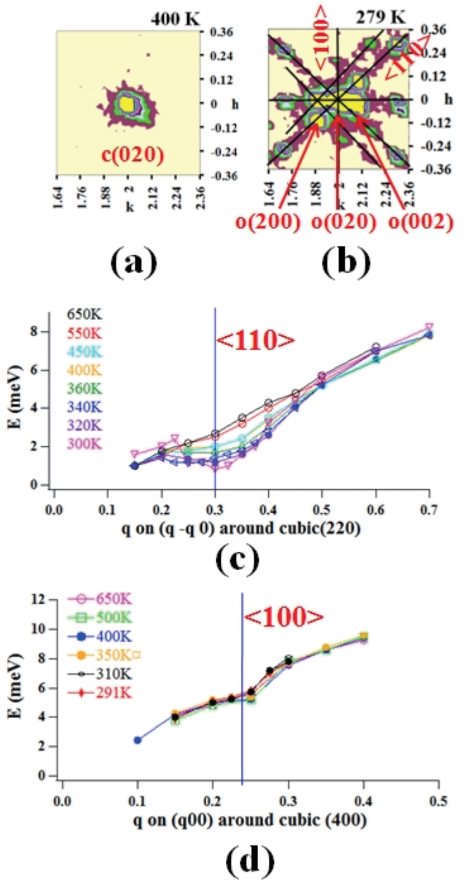

Fig. 1. (a), (b) Elastic q-mesh scans on the reciprocal lattice cubic c^*-plane at 400 and 279 K, (c), (d) TA$_2$-phonon dispersions with cubic $\langle 110 \rangle$ and $\langle 100 \rangle$ propagations.

1-1-15

Structure and Magnetism of Infinite Layer Iron Oxide with a Square-Planar Coordination

Tassel C., Tsujimoto Y., Kageyama H., Yoshimura K., Takano M., Nishi M., Ohoyama K.
Kyoto University, University of Tokyo, Tohoku University

The coordination geometries more usually exhibited by iron in oxides are octahedral and tetrahedral.1 However the use of calcium hydride as a low-temperature reductant, a technique recently introduced by Hayward, Rosseinsky and coworkers, has provided a way to circumvent this structural choice. For instance, Tsujimoto et al. have recently reported a new material, SrFeO2, in which a high-spin Fe2+ exhibits a square-planar coordination. This material is build from unprecedented FeO2 infinite layers in between which the Sr2+ cations reside (see Fig. 1(left)) and exhibits a number of surprising structural and physical properties. The study of the electronic structure of SrFeO2 has provided important clues to understand this situation. Later, this material was shown to be remarkably robust towards cation substitution and temperature6 opening the way towards possible applications. More recently the same technique was used to prepare a new spin-ladder iron oxide, Sr3Fe2O5, which again exhibits high-spin Fe2+ ions in a square-planar coordination.

The neutron diffraction study and the synchrotron X-ray diffraction revealed that CaFeO2 exhibit an unprecedented layered structure [1]. The new phase was obtained through a low-temperature reduction procedure using calcium hydride. The XAS spectra near the Fe-K edge for the whole solid solution (Sr1-xCax)FeO2 supports that iron is in a square-planar coordination for $0 < x < 0.8$ but clearly suggests a change of coordination for $x = 1$. The new structure contains infinite FeO2 layers in which the FeO4 units unprecedentedly distort from square-planar toward tetrahedra and rotate along the c axis (see Fig. 1(right)), in marked contrast to well-studied and accepted concept that octahedral rotation in perovskite oxides occurs but the octahedral shape is kept almost regular.

[1] T. Cedric et al., J. Am. Chem. Soc. 131, 221-229 (2008).

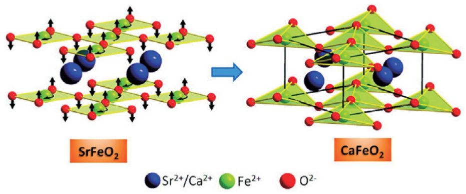

Fig. 1. Crystal structures of the ideal infinite structure SrFeO2 (left) and the distorted one CaFeO2 (right).

1-1-16

Observation of the spin gap in a two-dimensional quantum spin system (CuCl)Ca2Nb3O10

Tsujimoto Y., Kageyama H., Yoshimura K., Ajiro Y., Nishi M.
Department of Chemistry, Graduate School of Science, Kyoto University; Institute for Solid Staet Physics, University of Tokyo

Low-temperature syntheses may offer promising routes to innovate low-dimensional magnetic compounds, as metastable solids. Indeed, reacting a double-layered nonmagnetic Dion-Jacobson phase RbLaNb2O7 with CuX2 yields a perovskite/metal halide intergrowth structure (CuX)LaNb2O7 (X = Cl, Br), where the interlayer Rb+ ions are replaced by the [CuX]+ layer with an S = 1/2 square lattice. We have recently reported that the ground state of (CuCl)LaNb2O7 is described by the quantum spin liquid, where no long-range order exists down to 20 mK and the spin-singlet ground state is separated from the triplet excited states by a gap of 2.3 meV. On the other hand, (CuBr)LaNb2O7 has a spin order at 32 K, with a spin structure of the so-called collinear (pi, 0) type. We then explored the triple-layered system (CuX)A2B3O10 which is expected to have an enhanced two-dimensionality as the magnetic CuX layer in the triple-layered system is separeted by the perovskite slab as long as 16 angstrom, 1.5 times longer than the double-layered case. (CuBr)Sr2Nb3O10 showed a quantized magnetization plateau corresponding to the 1/3 of the fully saturated magnetization for Cu. The stability of the 1/3 plateau can be controlled by substituting A and B site with Ca, Ba, Pb, and with Ta, respectively.

In this study, we investigate a series of (CuCl)A2B3O10 compounds. From the magnetic susceptiblity and magnetization measurements, the spin singlet nature with a finite gap to the first excited triplet state is suggested in (CuCl)Ca2Nb3O10. It follows that this compound provides the good comparison to (CuCl)LaNb2O7. In order to directly probe the existence of the singlet-triplet excitations and to understand the spin-singlet formation mechanism, we performed the inelastic neutron scattering study using two spectrometers at JRR-3, 5G and C1-1.

As shown in Fig. 1, we successfully observed the singlet-triplet excitations at around 1.5 meV, obtained at C1-1. The obtained spin-gap value agrees well with the gap estimated from the magnetic susceptibility and specific heat measurements. The Q-dependence of this excitation shows a fast oscillation behavior, as in the case of (CuCl)LaNb2O7, and a simple dimer picture gives the dimer distance as long as 8 angstrom, which is physically unlikely.

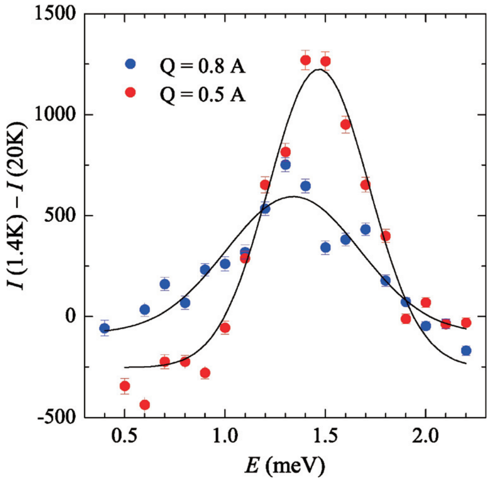

Fig. 1. Singlet-triplet excitations in (CuCl)Ca2Nb3O10

1-1-17

Behavior of Thermal Parameters and the Phase Transition in DKDP

H. Mashiyama^A, T. Miyoshi^A, T. Asahi^A, H. Kimura^B, Y. Noda^B
^{A}*Fac. Sci. Yamaguchi Univ.*, ^{B}*IMRAM Tohoku Univ.*

It has been considered that the tunneling character of proton is coupled with other heavy atoms to induce ferroelectricity below 123 K in KDP (KH_2PO_4). If protons are replaced by deuterons, the transition temperature elevates up to T_c = 213 K in DKDP. There remains a question whether heavy atoms are in disordered or displacive within anharmonic potentials above T_c. In order to elucidate this point, we have performed detailed structure analyses of DKDP above and below T_c.

Single crystals were grown by evaporation method from a heavy water solution of DKDP powder provided commercially. A rectangular prism of 2.8 × 2.6 × 2.5 mm^3 was cut from a transparent block of the crystal. Aluminum electrodes were attached on the *c*-planes to apply an electric field so that the crystal was single domain below T_c. Neutron diffractmeter FONDER was employed to collect diffracted intensity data. Measured temperatures were 10, 70, 120, 160, 190, 210, 223, 250 and 303 K. Every profiles of the reflection peaks were checked and programs DABEX and RADIEL were used to correct absorption and extinction effects. Crystal structures were refined by using the least squared-calculation program, SHELXL-97. Split atom method was employed to represent disordered character of deuteron above T_c. All data sets were successfully analyzed; the *R* factors were about 4 % with anisotropic thermal parameters.

The positional parameters are almost steady below T_c. Figure 1 (a) displays the temperature dependence of the dipole moment of the unit cell estimated by assigning simple ionic point charges to each atom. The values are almost in good agreement with the reported spontaneous polarization (Samara 1973). All the Debye-Waller factors (mean-squared displacement) U_{33} decrease monotonically with decreasing temperature as shown in Fig. 1 (b). They do not vanish even at 0 K, representing quantum zero-point vibration, whose magnitude is lower than the expected value from the room temperature phase (Nelmes *et al*. 1982).

Below T_c, the ordering of deuteron induces a distortion of PO_4^{3-} tetrahedron and a displacement of K^+ ion. The magnitudes of the thermal vibration of K and P changes little at T_c. If they are disordered units in the paraelectric phase, they should have greater thermal parameters. So it is hard to image a disordered P or K above T_c. The thermal parameter indicates that D is almost in the ground state below 100K. A comparison with KDP will be presented elsewhere.

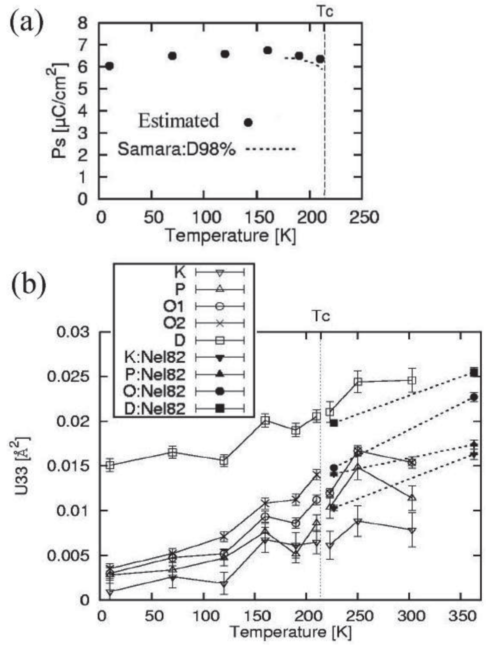

Fig. 1. Temperature dependence of (a) the estimated polarization with K^+, D^+, P^{5+} and O^{2-}, and (b) the Debye-Waller factor U_{33}.

1-1-18

Correlation between crystal defects and the diffuse scattering in relaxor ferroelectric $(Na_{0.5}Bi_{0.5})TiO_3$

M. Matsuura[1], K. Hirota[1], Y. Noguchi[2], and M. Miyayama[2]

[1] *Department of Earth and Space Science, Faculty of Science, Osaka University, Toyonaka, 560-0043.*

[2] *Institute of Industrial Science, The University of Tokyo, 4-6-1 Komaba, Meguro-ku, Tokyo 153-8505*

Relaxor ferroelectrics have attracted considerable attention since the discovery of giant piezoelectricity in relaxor-based single crystals. $(Na_{0.5}Bi_{0.5})TiO_3$ (NBT) forms perovskite structure with two different ions Na^+ and Bi^{3+} at the A-site of ABO_3. A key-concept to understand the relaxor behavior is polar nanoregion (PNR), a local nanometer-sized region with ferroelectric polarization and atomic shift. Such an atomic shift in PNR was observed for a typical relaxor such as PMN and PZN as characteristic diffuse scattering. In NBT, we have revealed anisotropic diffuse scattering which extends along ⟨110⟩-directions. Recently, Noguchi *et al.* succeeded in suppressing Bi-defects in NBT single crystal by high O_2-pressure, and found larger polarizations than those in the crystal grown in air.[1] The purpose of the present work is to compare the diffuse scattering in crystals grown in different O_2 pressure to clarify the correlation between the diffuse scattering and ferroelectric properties. Neutron scattering experiments were performed on the triple-axis spectrometers HQR installed at the JRR-3 Guidehall of JAEA.

Figure 1 shows profiles of $(h, 1, 0)$ scan measured at room temperature. At $T \sim 300$ K, large diffuse scattering appears around (110) and extends along ⟨110⟩-directions. In order to compare diffuse scattering quantitatively, scattering intensities are normalized by sample mass. Profiles consist of sharp peak of (110) Bragg reflection and broad peak of diffuse scattering. Apparently, the diffuse scattering for O_2-10 atm crystal is smaller than that for O_2-0.2 atm crystal. From previous measurement, we found that this anisotropic diffuse scattering shows large temperature dependence and appears strongly along transverse direction, which suggests close correlation between the diffuse scattering and ferroelectric fluctuations. Since number of Bi-defects is expected to be smaller in O_2-10 atm crystal than O_2-0.2 atm crystal, the current results indicate that the diffuse scattering, in other words, PNR are pinned ferroelectric fluctuations at crystal defects.

References

[1] Y. Noguchi *et al.*, Jpn. J. Appl. Phys. 47(9B), 7623 (2008).

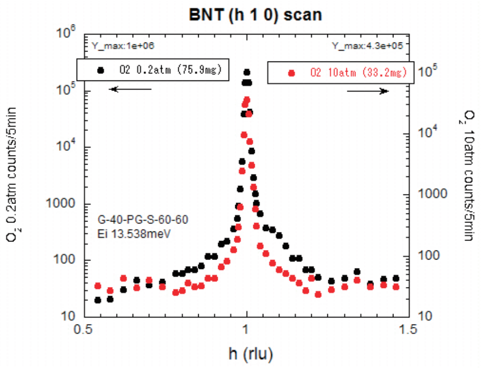

Fig. 1. Profiles of $(h, 1, 0)$ scan for NBT single crystals grown in air (black circles: O_2 0.2 atm) and high O_2 pressure (red circles: O_2 10 atm).

1-1-19

Temperature dependence of waterfall feature of phonons in $(Na_{0.5}Bi_{0.5})TiO_3$

M. Matsuura[1], K. Hirota[1], Y. Noguchi[2], and M. Miyayama[2]

[1] Department of Earth and Space Science, Faculty of Science, Osaka University, Toyonaka, 560-0043.

[2] Institute of Industrial Science, The University of Tokyo, 4-6-1 Komaba, Meguro-ku, Tokyo 153-8505

Relaxor ferroelectrics have attracted considerable attention since the discovery of giant piezoelectricity in relaxor-based single crystals. $(Na_{0.5}Bi_{0.5})TiO_3$ (NBT) forms perovskite structure with two different ions Na^+ and Bi^{3+} at the A site of ABO_3. Recently, NBT regains attention as promising applications to piezoelectric devices containing no toxic lead. Last year, we studied the lattice dynamics in NBT and clarified so-called waterfall feature, anomalous damping of transverse optic (TO) phonons for reduced wave vector less than $q_{wf} = 0.2\text{Å}^{-1}$, which was commonly observed in typical lead-containing relaxors as PMN[1] and PZN-8%PT[2]. For PMN, it has been shown that the recovery of TO mode occurs in ferroelectric phase and at very high temperatures[3]. The purpose of the present work is to study temperature dependence of waterfall feature in detail and to confirm recovery of TO mode. Neutron scattering experiments were performed on the triple-axis spectrometers PONTA installed at the JRR-3 Reactor hall of JAEA.

Figure 1 shows profiles of constant-E scan along transverse direction from (220). Inset shows the TA and TO dispersions at $T = 670$ K, where no propagating mode was observed for $q < 0.10$ rlu, and the TO branch drops like waterfall to the TA branch. Constant-E scan at $E = 11$ meV, represented as the red arrow in inset, crosses the waterfall TO branch and shows peak at $q = 0.16$ rlu at $T = 700$ K. With decreasing temperature, the peak shifts towards Γ-point, and eventually disappears at $T = 300$ K, which indicates disappearance of waterfall feature and recovery of TO mode at $T = 300$ K. Actually, we observed TO mode at $\omega = 15$ meV at Γ-point for $T = 300$ K (not shown). Hlinka *et al.* proposed that the waterfall feature is explained by coupled damped TA and TO modes[4]. The current result indicates that such coupling is universal in relaxors and plays an important role in formation of PNR.

References

[1] P. M. Gehring *et al.*, Phys. Rev. Lett. **87** 277601 (2000).

[2] P. M. Gehring *et al.*, Phys. Rev. Lett. **84** 5216 (2000).

[3] S. Wakimoto *et al.*, Phys. Rev. B., **65** 172105 (2002).

[4] J. Hlinka *et al.*, Phys. Rev. Lett., **91** 107602 (2003).

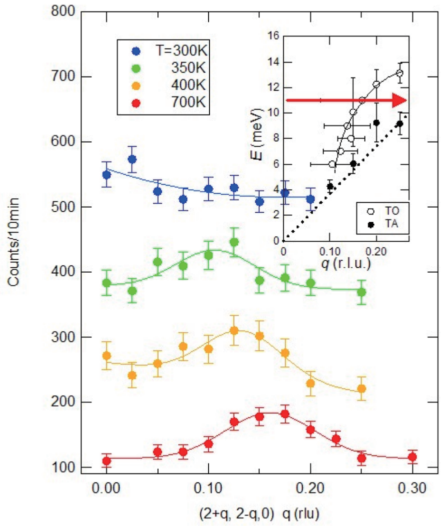

Fig. 1. Profiles of constant-E scan of $(2-q, 2+q, 0)$ with fixed energy transfer of 11 meV. The data at different temperatures are plotted with offsets.

1-1-20

Study of slow lattice dynamics in relaxor PMN-30%PT by neutron spin echo technique

M. Matsuura^1, H. Endo^2, and K. Hirota^1
^{1}*Department of Earth and Space Science, Faculty of Science, Osaka University, Toyonaka, 560-0043.*
^{2}*Institute for Solid State Physics, The University of Tokyo, 106-1 Shirakata, Tokai, 319-1106*

Relaxor ferroelectrics are characterized by a giant piezoelectricity associated with significant frequency dispersion. The variation of the diffuse maximum of the dielectric constant in wide frequency range gives evidence for an important role of slow dynamics. A key-concept to understand the relaxor behavior is slowly relaxing polar nanoregion (PNR), a local nanometer-sized region with ferroelectric polarization and atomic shift. Such an atomic shift in PNR was observed for a typical relaxor such as PMN and PZN as characteristic diffuse scattering. However, there is no decisive understanding of the microscopic mechanism of the PNR formation at present. In addition, recent neutron spin-echo measurement concluded that the diffuse scattering is purely elastic and is not related to polarization fluctuations[1]. The purpose of the present work is to reinvestigate the intrinsic energy width of the diffuse scattering and clarify its mechanism. Neutron spin-echo experiments were performed on the *i*NSE installed at the JRR-3 Guide-hall of the JAEA. The sample was a high-quality PMN-30%PT single crystal with a volume of 1cc grown at JFE Mineral. The data were taken with incident neutron energies of 3.38 meV which enables access to diffuse scattering near Q =(100) at $2\theta = 74.5$ degree.

Figure 1 shows the normalized intermediate scattering functions of the diffuse scattering at Q =(0.98, 0.02, 0) measured at various temperatures. Below $T = 400$ K, the normalized intermediate scattering functions $I(Q,t)/I(Q,0)$ do not decay, which is associated with the long-range ordered ferroelectric phase for $T < T_C = 400$ K. Note that the averaged $I(Q,t)/I(Q,0)$ are less than 1, indicating fast relaxations even in the ordered phase. At $T = 450$ K, $I(Q,t)/I(Q,0)$ is flat as $T \leq 400$ K, but it drops from 0.9 to 0.6, suggesting enhancement of fast relaxations above T_C. This is consistent with enhancement of meV-range broad quasielastic scattering at high temperatures[2]. Above $T = 500$ K, the $I(Q,t)/I(Q,0)$ has maximum at 0.5 ns. Assuming this peak is the first peak of oscillation, it corresponds to excitation of 4 μeV. This ultra-low energy mode may be related to the ferroelectric fluctuations in PNR. Further study is highly required to clarify the nature of this mode.

References

[1] S. Vakhrushev, A. Ivanov, and J. Kulda, Phys. Chem. Chem. Phys. **7** 2340 (2005).
[2] H. Hiraka *et al.*, Phys. Rev. B, **70** 184105 (2004).

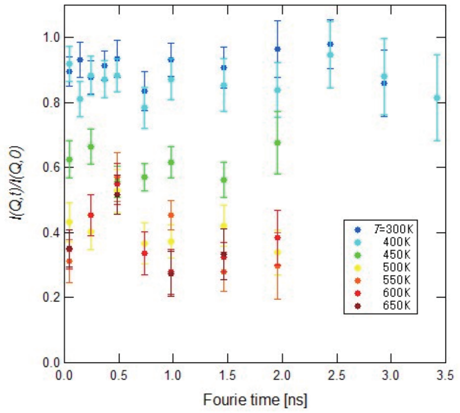

Fig. 1. Normalized intermediate scattering functions I(Q,t)/I(Q,0) of the diffuse scattering at (0.98, 0.02, 0).

1-1-21

Pseudospin-phonon coupling in Relaxor Ferroelectrics PMN-x%PT

M. Matsuura and K. Hirota
Department of Earth and Space Science, Faculty of Science, Osaka University, Toyonaka, 560-0043.

Relaxor ferroelectrics gain much attention due to their extreme piezoelectric responses over a wide temperature range. It is widely believed that polar nanoregion (PNR), a local nanometer-sized region with ferroelectric polarization and atomic shift, plays an important role in the relaxor behavior. Despite intense investigations, the microscopic mechanism of the formation of PNR remains unclear. The structural phase transition are usually divided in displacement or of order-disorder type. From neutron scattering, soft mode was reported, suggesting displacement behavior[1]. On the other hand, quasi-elastic scattering has also been reported, which indicates order-disorder mechanism. This coexistence reminds pseudospin-phonon coupled system which was studied thoretically by Y. Yamada *et al.*[2] and confirmed experimentally by Y. Noda[3]. The purpose of the present work is to clarify the nature of pseudospin-phonon coupling in relaxors. Neutron scattering experiments on typical relaxor ferroelectrics PMN-30%PT single crystal were performed on the triple-axis spectrometers HER installed at the JRR-3 Guide-hall of the JAEA.

Figure 1 shows the contour map of the phonon scattering intensity at $(1+q, 1-q, 0)$ measured at $T = 400$ K. At $T = 400$ K($\sim T_C$), the transverse acoustic (TA) mode below 2.5 meV is heavily overdamped, while the TA mode above 2.5 meV is underdamped. This overdamping starts from $T \sim 500$ K on cooling. In the pseudospin-phonon coupled system, phonon becomes overdamped on cooling to T_C when phonon frequency is comparable to the relaxation rate of spin-flipping. On the other hand, underdamped spectrum is expected for higher frequency phonon modes than the relaxation mode. Current result indicate that relaxors is the intermediate case between displacive and order-disorder type due to strong coupling between relaxations ($\Gamma \sim 2.5$ meV) of polarization in PNR and phonon modes.

References

[1] P. M. Gehring *et al.*, Phys. Rev. Lett., **87**, 277601 (2001).
[2] Y. Yamada *et al.*, J. Phys. Soc. Jpn, **36** 641 (1974).
[3] Y. Noda *et al.*, J. Phys. Soc. Jpn, **48** 1576 (1980).

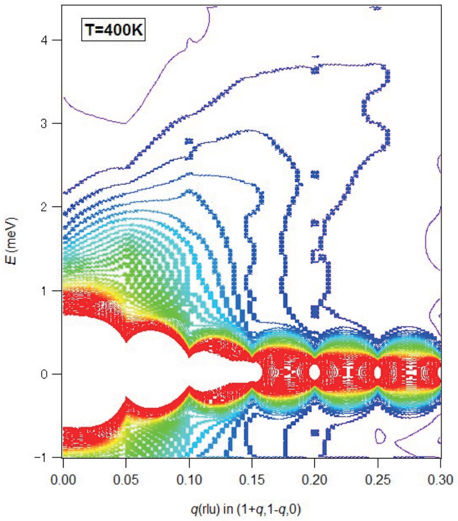

Fig. 1. The contour map of the phonon scattering intensity at $(1+q, 1-q, 0)$ as a function of q and energy measured at $T = 400$ K. The line of color shows intensity from 5 counts (blue) to 1000 counts (red).

1-1-22

Crystal structure analysis in pressure-induced commensurate magnetic phase of multiferroic $HoMn_2O_5$

H. Kimura[1], Y. Sakamoto[1], T. Yamazaki[1], Y. Noda[1], N. Aso[2], T. Fujiwara[3], K. Matsubayashi[4] and Y. Uwatoko[4]

[1]*IMRAM, Tohoku University*, [2]*Ryukyu University*, [3]*Department of Physics, Yamaguchi University*, [4]*ISSP, The university of Tokyo*

$HoMn_2O_5$ is well known as multiferroics showing colossal magnetoelectric effect. We have reported recently that hydrostatic pressure induces the incommensurate–commensurate magnetic phase transition[1], which leads to the induction of large electric polarization[2]. This indicates the strong relevance between the magnetic structure and ferroelectricity. It was thought that the minute change of bond lengths (or angles) between the magnetic manganese ions by applying pressure has much effect on the competing magnetic ground states in this magnetically frustrated system. In the present study we thus performed crystal structure analysis under pressure to elucidate what kind of magnetic interactions between manganese ions is essential for stabilizing the pressure induced magnetic phase.

Crystal structure analysis was carried out at FONDER. Hydrostatic pressure was applied up to $p = 1.39$ GPa, at which the magnetic structure is almost commensurate. Temperature was fixed at $T = 8$ K. Crystal structure was well solved with $R = 0.035$. Figure 1 shows two different bond lengths between Mn^{4+} and Mn^{4+} ions linked by oxygens as function of ionic radii of rare-earth ion. The interatomic bonds shown in Fig. 1(a) and in Fig. 1(b) contribute to the magnetic interactions of J_1 and J_2, respectively, of which paths are schematically shown in Fig. 1(c). This figure indicates that the length associated with J_1 decreases with decreasing the ionic radii. On the contrary, the length associated with J_2 is hardly affected by the size of the ionic radii. Furthermore in $HoMn_2O_5$, the bond length associated with J_1 significantly shortens with applying pressure while that associated with J_2 doesn't change at all, indicating that magnetic interaction J_1 highly contributes to stabilizing the commensurate magnetic phase.

References

[1] H. Kimura *et al.*: JPSJ **77** (2008) 063704.
[2] C. R. Cruz *et al.*: PRB **76** (2007) 174106.

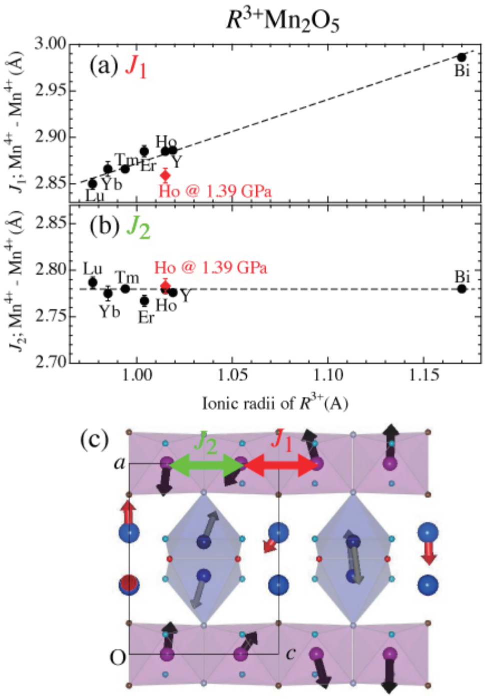

Fig. 1. (a), (b) Two different bond distances between Mn^{4+} ions as functions of ionic radii of R^{3+} ions. (c) Schematics of magnetic structure and two different Mn^{4+}–Mn^{4+} bonds.

1-1-23

Hypothetical Phase Transitions and soft modes in A2BX4-type Dielectrics

H. Shigematsu(A) and K. Nomura(A)
(A)Department of Physics, Faculty of Education, Shimane University

Rubidium selenate, Rb2SeO4, and Cesium selenate, Cs2SeO4, belong to a family of A2BX4-type (X = O, Cl, Br) crystals with the Beta-K2SO4 type structure. As the temperature decrease, the crystals transform from a high-temperature phase I to an orthorhombic phase II (Beta-K2SO4-type structure) at T1. At lower temperature, many of the A2BX4-type crystals, for example K2SeO4, Rb2ZnCl4 and Rb2ZnBr4, transform into an incommensurate phase with the modulation wavevector along the a-axis at T2. However, the phase transition could not be found for many A2BO4-type (X=O) crystals below T1, although the calculated dispersion curves contain an unstable Sigma-2 phonon branch whose qualitative and quantitative features are similar to those obtained for the prototype incommensurate crystal K2SeO4. Indeed, a softening tendency of the Sigma-2 phonon branch around 0.7a* was observed in Rb2SeO4 and Cs2SeO4. The estimated hypothetical temperature is below -150 K.

In A2BX4-type (X = Cl, Br) crystals, further phase transitions take place at T3 and T4. Soft phonon mode which make contribution to the phase transition at T4 has been observes around T-point (0,1/2,1/2). In order to clarify the mechanism of low-temperature phase transition and the hypothetical one in A2BO4-type crystals, we have to obtain additional information about the behavior of the low-energy optical branches around T-point in various A2BO4-type crystals. Therefore, we performed inelastic neutron scattering experiments by use of the triple-axis spectrometers (4G and T1-1) at JRR-3M of JAERI. Figure 1 shows the phonon dispersion curves in an extended-zone scheme along the (0 x x) direction for K2SeO4. The low-frequency mode softens slightly in the vicinity of x = 1/2 as the temperature approaches T2 = 131 K from above, and does not vanish, but hardens with further decreasing temperature. In Rb2SeO4, the hollow was not observed around T-point. The phonon dispersion frequency was essentially unchanged below room temperature. The inelastic neutron scattering study on other A2BO4-type crystals is now in progress.

Present address: Department of Physics, Faculty of Education, Yamaguchi University

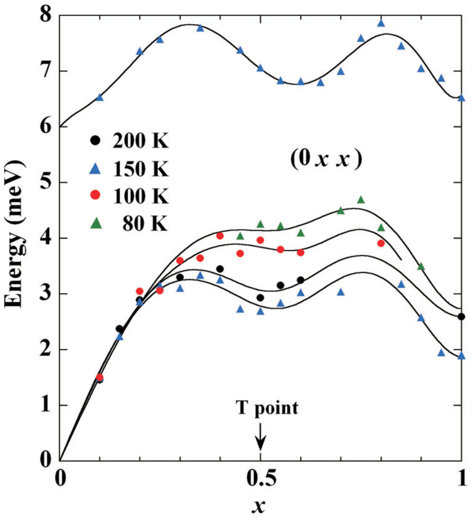

Fig. 1. Phonon dispersion curves in an extended-zone scheme on the (0 x x) for K2SeO4.

1-1-24

Crystal and magnetic structure of multiferroic material $BiFeO_3$-$BaTiO_3$

R. Kiyanagi, T. Yamazaki, Y. Sakamoto, H. Kimura, Y. Noda, and K. Ohyama
Institute of Multidisciplinary Research for Advanced Materials, Tohoku university, Institute for Materials Research, Tohoku university

A perovskite compound $BiFeO_3$ is known as a multiferroic material with ferroelectricity ($T_C \sim 1100$ K) and antiferromagnetism ($T_N \sim 650$ K). In the course of exploration of an enhanced multiferroicity of $BiFeO_3$, solid solutions of $BiFeO_3$ and other perovskite compounds have been investigated. It has been reported that the solid solution of $BiFeO_3$ and $BaTiO_3$, (1-x)$BiFeO_3$-$x$$BaTiO_3$, exhibits weak ferromagnetism as well as the ferroelectricity in the range of $0 \leq x \leq 0.5$ [1]. Meanwhile, structural studies by X-ray powder diffraction suggested that the crystal structure of (1-x)$BiFeO_3$-$x$$BaTiO_3$ is hexagonal in $x \leq 0.33$ and cubic in $0.33 \leq x \leq 0.92$ [2]. These results are contradictory since neither ferromagnetism nor ferroelectricity can be realized in a cubic system. In oder to clarify the structure of (1-x)$BiFeO_3$-$x$$BaTiO_3$, (1-$x$)$BiFeO_3$-$x$$BaTiO_3$ with various x were studied by means of neutron powder diffraction.

The samples were synthesized by solid state reaction from powders of Bi_2O_3, Fe_2O_3 and $BaTiO_3$ with various molar ratios, corresponding to x = 0, 0.1, 0.2, 0.25, 0.33, 0.4, 0.45, 0.5, 0.6, 0.7, 0.8, 1.0. The neutron powder diffraction experiments were carried out on the neutron powder diffractometer, HERMES, installed at T1-3 beam port in JRR-3M. Each sample was measured at several temperatures between 13 K and 650 K. The obtained powder diffraction patterns were analyzed by the Rietveld method with the General Structure Analysis System (GSAS) with EXPGUI [3, 4].

With the results of the structural analyses on various compositions and temperatures, the phase diagram of (1-x)$BiFeO_3$-$x$$BaTiO_3$ with respect to x and temperature was obtained as shown in Fig. 1. Coexistence of the hexagonal phase and the cubic phase in a wide range of x was observed. The hexagonal phase persists up to $x = 0.8$, and the cubic phase was recognized in $0.2 \leq x \leq 0.6$ at room temperature. This coexisting hexagonal phase is considered to be the origin of the observed ferroelectricity in (1-x)$BiFeO_3$-$x$$BaTiO_3$. Note that the hexagonal phase is rich in Bi and Fe, and the cubic phase is rich in Ba and Ti. T_N and T_S, the expected structural phase transition temperature, were estimated from the magnetic reflection, (1 0 1), and the hexagonal-phase-specific reflection, (2 1 $\bar{5}$), respectively. Decreases of T_N and T_S were found as x increased. These changes are apparently attributed to internal structural deformation, namely the decrease of hexagonality in the hexagonal phase surrounded by the cubic phase.

References

[1] T. Ozaki, *et al.*: Ferroelectrics (2009) in press.

[2] M. M. Kumar, A. Shrinivas, S. V. Suryanarayana: J. Appl. Phys. **87** (2000)855.

[3] A. C. Larson, R. B. von Dreel: Los Alamos National Laboratory Report LAUR (2004)86-748.

[4] B. H. Toby: J. Appl. Crystallogr. **34** (2001)210.

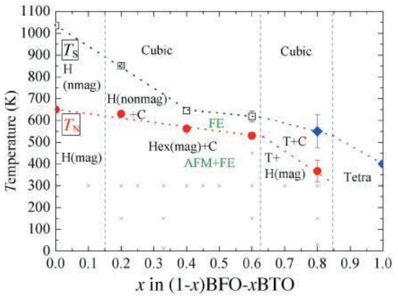

Fig. 1. Obtained phase diagram of (1-x)$BiFeO_3$-$x$$BaTiO_3$ with respect to x and temperature

1-1-25

Phase transition in a lead-based inorganic-organic perovskites C5H10NH2PbI3

Miwako Takahashi(A), Munehiko Nakatsuma(A), Kunimitsu Kataoka(A), Takurou Kawasaki(A), Ken-ichi Ohshima(A), Yukio Noda(B)
(A)IMS., Univ. of Tsukuba, (B)IMRAM, Tohoku Univ.

C5H10NH2PbI3 has a lead-based inorganic-organic perovskites structure consisting of semiconducting parts which are composed of one-dimensional chains of face-sharing lead-iodide octahedra and barrier parts composed of C5H10NH2+ molecules. The lead-iodide chain is isolated by the organic molecules to be a quantum wire, so this material can be regarded as a naturally self-organized one-dimensional system. The crystal structure at room temperature is orthorhombic with space group of C2221. It has been shown by Raman scattering, DSC and optical absorption measurements that the structure undergoes temperature-induced successive phase transitions: phase I at room temperature, phase II for 255.5K to 284.5K, phase III for 250K to 255.5K and phase IV below 250K, which involve rotational/orientational ordering of the organic C5H10NH2+ parts. However, its precise structure has not been determined yet. We have been studying structures and phase transitions in this material by combining the data obtained by neutron and x-ray diffraction techniques, and found interesting structural changes take place in the successive phase transitions. The lattice parameters show step-like changes at the transition temperatures with considerable large contraction along direction vertical to lead-iodide chain while it expands along the chain. Below 285K in phase II, 400 peak is found to separates in two indicating that the crystal lattice changes from orthorhombic to monoclinic. The angle between the splitting peaks increases linearly with decreasing temperature down to 255K and decreasing again up to room temperature without any hysteresis. Below 255K, diffuse peaks appear at the reciprocal points at which reflection is forbidden in the C-centered lattice. These results show that the large structural changes are accompanied with the successive phase transitions. Structural analysis measurement for the phase II has been performed by using a single crystal diffractometer T2-2, FONDER. Since creation of twined crystals in the process of phase transitions is inevitable, Bragg peak intensities were measured at 280K just below the transition temperature where monoclinic angle is close to 90 degree and intensities from twined crystals were integrated together. The intensity data at phase II has been analyzed with the model of monoclinic P21/n which has been suggested by X-ray measurement. The refinement was not successful and structure at phase I gives better R value. Powder diffraction measurement was also performed by using HERMES. The obtained data shows quite high background due to the incoherent scattering from H atoms. Figure 1 shows diffraction pattern at room temperature analyzed by the Rietveld method "RIETAN-2000" [1]. The Rietveld analysis for the data at low temperatures is now going on.

[1] F. Izumi and T. Ikeda, Mater. Sci. Forum, 321-324 (2000) 198-203.

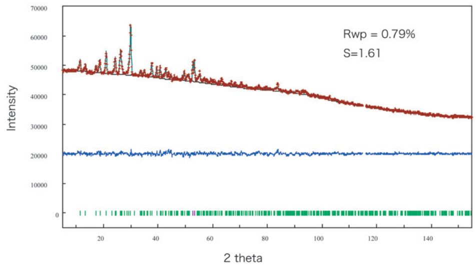

Fig. 1. Diffraction pattern at phase I analyzed by Rietveld method.

1-1-26

Magnetic Fluctuations in a Ternary Alloy CuFePt6

M. Takahashi(A), T. Shishido(A), K. Ohshima(A), M. Matsuura(B)
(A)IMS., Univ. of Tsukuba, (B)ESS., Ohsaka Univ.

CuFePt6 has fcc fundamental structure and forms Cu3Au-type ordered structure below 1313 K[1]. In the ordered structure, Cu and Fe occupy corner sites with equal occupation probabilities while Pt occupies face centered sites. In spite of the simple atomic arrangement in the ordered structure, its magnetic behavior is complicated. In the process of zero-filed cooling (ZFC) it undergoes successive transitions of ferromagnetic at Tc1=200K and ferrimangetic at Tc2=100K. In the process of field cooling, on the other hand, only a ferromagnetic phase appears below Tc. The behaviors indicate existence of competitive interactions of ferromagnetic and antiferromagnetic which are sensitively dependent on the magnetic field. To investigate field dependence of the magnetic structure, elastic and inelastic neutron scattering measurements were performed at the triple-axis-spectrometer PONTA. In the measurements, intensity of magnetic scattering at around Gamma and M points of the ordered structure have been investigated under FC and ZFC processes. Magnetic field was applied up to 70 Oe with using Helmholtz coil. In order to compare the behavior of elastic and inelastic components of magnetic scattering, elastic intensities have been measured under triple axis mode.

Figure 1(a) shows X point magnetic Bragg scattering for FC and ZFC process. Intensities of the ferrimagnetic component does not change under FC and ZFC processes, though ferrimagnetic phase does not appear in the magnetization measurement. It has been confirmed in the measurements at FONDER that ferrimagnetic component remains under the magnetic field of up to 1.5kOe. Ferromagnetic Bragg scattering at Gamma point also shows no dependence of magnetic field. Figure 1(b) shows inelastic intensities of dE=2 meV along 0kk with and without magnetic field below Tc2. Without magnetic field, inelastic peaks have been observed at k=0.45 and 0.65. When applying field of only 70 Oe, peaks disappear and intensities of higher back ground were observed. The results show that there exists dynamical fluctuation in the magnetic structure which is easily suppressed by weak magnetic field. Further experiments should be necessary to clarify the origin of the magnetic fluctuation.

[1]M. Takahashi, E. Ahmed, A. K. Das, Y. Fujii, H. Iwasaki, and K. Ohshima; Journal of Alloys and Compounds 453, 75-78 (2008).

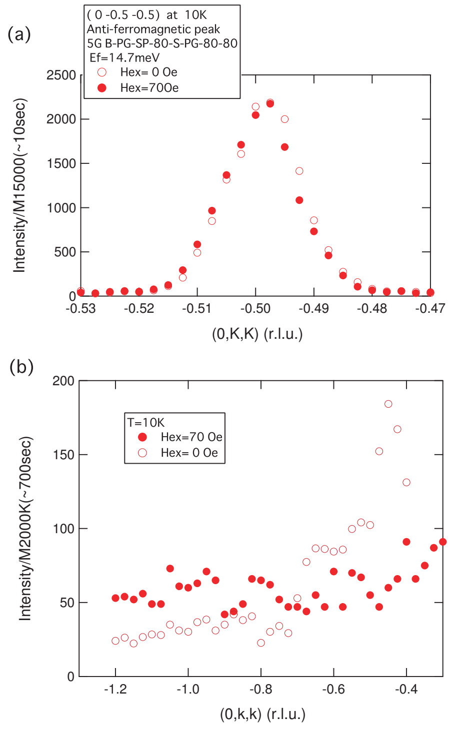

Fig. 1. (a)Magnetic Bragg scattering at X point under FC and ZFC processes. (b)Inelastic intensities around X point with and without magnetic field below Tc2.

1-1-27

Kinetics of crystalline-noncrystalline phase transition of sucrose crystal

M. Takahashi(A), K. Kawasaki(A) and K. Ohshima(A)
(A)Institute of Materials Science, University of Tsukuba

Sugar, in which sucrose (C12H22O11) is the main ingredients, attracts a great deal of attention in the field of food, medicines, preservative and battery material adjusting to surroundings. However, melting points among sucrose crystals with high purity are occasionally different from each other and are given as in the range from 433 to 459K. It has been thought that the impurity, the water content or the manufacturing method would contribute such different melting points. There are few diffraction studies for understanding of the melting phenomena, though the macroscopic observation has been carried out by an optical microscope and a calorimeter. We have, therefore, performed in-situ diffraction study for the kinetics of crystalline-noncrystalline phase transition in sucrose. Since information on the hydrogen atom positions is indispensable, neutron diffraction measurement was performed by using a single crystal diffractometer T2-2, FONDER. In the diffraction measurement, a sucrose single crystal with a volume of 24mm3 was mounted in a aluminium cell with a heater coil. Intensities of Bragg peaks were measured at room temperature for a structural analysis, and then the sample was heated to 366 K which is far below the melting points. Time dependence of the Bragg peak intensities was measured with keeping the sample at the fixed temperature.

Crystal structure at room temperature is determined by combination of X-ray and neutron data. Figure 1(a) shows nuclear density distribution on a-c plane calculated by MEM using PRIMA[1]. It clearly shows negative peaks (blue part) which indicate hydrogen atom positions. Figure 1(b) shows temperature dependence of 401 and 442 Bragg peaks. The Bragg intensities decrease monotonically indicating that the sample gradually changed to noncrystalline state. In the x-ray measurements, the incubation time, which was defined as waiting time until the noncrystalline phase transition starts at a fixed temperature, has been observed in a range between 422K and 443K[2]. Time dependence of the Bragg intensities in the present neutron measurement did not show any incubation time. Structure analysis for the data in the successive time spans is now going on to study microscopic change of crystalline to noncrystalline phase.

[1]F. Izumi and R. A. Dilanian, "Recent Research Developments in Physics," Vol. 3, Part II, Transworld Research Network, Trivandrum (2002), pp. 699-726.
[2]T. Fujita, Doctor Thesis of Univ. of Tsukuba (2006).

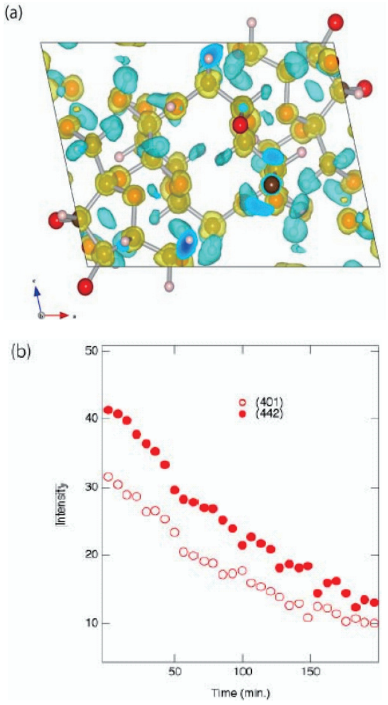

Fig. 1. (a)Nuclear density distribution of sucrose at room temperature calculated by MEM. (b)Time dependence of 401 and 442 Bragg peaks at 366K.

1-1-28

Crystal structure of Pb-free silver niobate perovskite

Masatomo Yashima, †,* Takahiro Wakita, † Takafumi Komatsu, † Yong Phat, †
Hiroki Taniguchi, ‡ Tomoyasu Taniyama, ‡ and Mitsuru Itoh ‡
† *Department of Materials Science and Engineering, Interdisciplinary Graduate School of Science and Engineering, Tokyo Institute of Technology, Nagatsuta-cho 4259, Midori-Ku, Yokohama, Kanagawa 226-8502, Japan,* ‡ *Materials and Structures Laboratory, Tokyo Institute of Technology, 4259 Nagatsuta-cho, Yokohama 226-8503, Japan*

Lead-free piezoelectrics with high performance are important in material sciences. Materials with a large internal polarization that can be strongly coupled to an electric field are required. But, the crystal structure of AgNbO3 has not been studied satisfactorily [1]. In the present work, we have investigated the crystal structure and phase transition of AgNbO3 with neutron powder diffractometry.

AgNbO3 materials were prepared by solid state reactions. Appropriate amounts of high purity Ag2O and Nb2O5 were mixed with ethanol in an agate pot and calcined at 980 °C for 6 h in O2 atmosphere. The calcined powder was then milled again, pressed in a 10 mm steel die with a pressure of 1000 kgf/cm2 to make pellets, followed by sintering at 1050 °C for 6 h in O2 atmosphere. A phase purity of AgNbO3 was confirmed by x-ray diffraction measurements.

We performed neutron powder diffraction experiments on the Kinken powder diffractometer for high-efficiency and high-resolution measurements, HERMES [2], of Institute of Materials Research, Tohoku University, installed at the Japan research reactor, JRR-3M in Japan Atomic Energy Association, Tokai, Japan. Incident neutrons with a fixed wavelength of 1.82646 were obtained by a vertically focusing (331) Ge monochromator and a 12 '-∞-22 ' collimator. Diffraction data were collected at step intervals of 0.1? over a 2? range from 20 to 152?, using 150 3He counters set at 1 intervals. We have utilized a furnace with MoSi2 heaters [3], which was devised for neutron diffraction study by the HERMES, to heat the AgNbO3 rod in air under atmospheric pressure at high temperatures. There were two thermocouples in the furnace. One thermocouple near the heater was used to control the temperature and the other near the rod sample monitored the sample temperature.

Figure 1 shows the Rietveld pattern of AgNbO3 at room temperature. The reliability factors were Rwp=5.41%, RB=1.96% and RF=0.98%. Unit-cell parameters were a=5.5526(3) , b=5.6091(3) and c=15.6462(7) . Increasing temperature phase transitions were observed.

References

1. D. Fu, M. Endo, H. Taniguchi, T. Taniyama and M. Itoh, Appl. Phys. Lett., 90, (2007) 252907.
2. K. Ohoyama, T. Kanouchi, K. Nemoto, M. Ohashi, T. Kajitani and Y. Yamaguchi, Y. Jpn. J. Appl. Phys. Part 1, 37 (1998) 3319.
3. M. Yashima, J. Am. Ceram. Soc., 85 (2002) 2925.

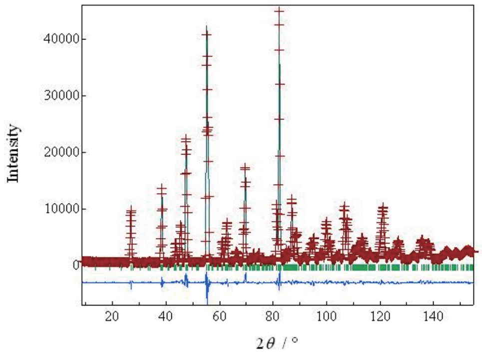

Fig. 1.

Activity Report on Neutron Scattering Research: Experimental Reports **16** (2009)
Report Number: 819

1-1-29

Structure Analysis of Oxide Ions in a Doped Pr2NiO4-based Mixed Conductor

Hiroki Yamada †, Masatomo Yashima †, Tomoya Takizawa †, Shinji Yamamoto †, Tatsumi Ishihara ‡

† Department of Materials Science and Engineering, Interdisciplinary Graduate School of Science and Engineering, Tokyo Institute of Technology, Nagatsuta-cho 4259, Midori-ku, Yokohama, Kanagawa 226-8502, Japan and ‡ Department of Applied Chemistry, Faculty of Engineering, Kyushu University, Motooka 744, Nishi-ku, Fukuoka 819-0395, Japan

Mixed oxide-ionic and electronic conducting ceramics (MIECs) are attracting much interest as materials for oxygen separation membranes. Oxygen can permeate through MIECs membranes when a gradient of oxygen chemical potential exists. A2BO4-based oxides with K2NiF4-type structure have extensively been studied as a new mixed ionic-electronic conductor, where A and B are cations. The development of improved MIECs requires a better understanding of the mechanism of ionic conduction, and crucial to this is a comprehensive knowledge of the oxide ion conduction in the A2BO4-based oxides occurs by diffusion of excess oxide ions along the rock-salt-type AO layers. However, the diffusion of excess oxide ion has not been determined yet. Pr2NiO4-based oxides have high oxygen permeability and high diffusivity of oxide ions. Here, we report the structure analysis of a K2NiF4-type mixed conductor Pr2(Ni0.75Cu0.25)0.95Ga0.05O4+ δ (PNCG), through a high-temperature neutron powder diffraction study. We chose this chemical composition, because it exhibits high oxygen permeability. The present result would give hints for the design of K2NiF4-type conductors.

A PNCG sample was prepared by a solid-state reaction at 1350 oC for 6 h in air. Neutron powder diffraction data of PNCG were in situ measured at 20.4-1011.2 oC using a furnace and 150 detector system HERMES at a neutron wavelength of 1.8204(5) angstrom. Neutron diffraction data were analyzed by Rietveld analysis. A computer program RIETAN-FP was utilized for the Rietveld analysis.

Rietveld refinements of the neutron diffraction data of PNCG at 20.4 oC and 1011.2 oC were performed on the basis of the K2NiF4-type structure with I4/mmm space-group symmetry. Reliability factors and goodness of fit at 20.4 oC were Rwp = 6.66%, RI = 3.06%, RF = 1.78% and GOF = 3.17. Lattice parameters were a = b = 3.8364(2) angstrom, c= 12.5374(7) angstrom. Reliability factors and goodness of fit at 1011.2 oC were Rwp = 6.33%, RI = 2.06%, RF = 0.98% and GOF = 4.93 (Fig.1). Lattice parameters were a = b = 3.8793(4) angstrom, c= 12.7326(13) angstrom.

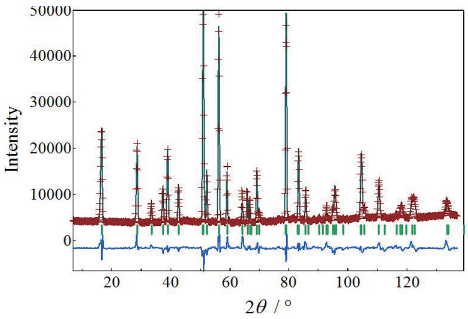

Fig. 1. Neutron diffraction profiles at 1011.2 oC for Pr2(Cu0.75Ni0.25)0.95Ga0.05O4+ δ using a single phase I4/mmm model.

Activity Report on Neutron Scattering Research: Experimental Reports **16** (2009)
Report Number: 824

1-1-30

Structure analysis of automotive exhaust catalysts, Ce2Zr2O7.32 by neutron powder diffraction measurement

Tomoya Takizawa, Masatomo Yashima, Takahiro Wakita
Department of Materials Science and Engineering, Interdisciplinary Graduate School of Science and Engineering, Tokyo Institute of Technology, Nagatsuta-cho 4259, Midori-Ku, Yokohama, Kanagawa 226-8502, Japan

CeO2-ZrO2 solid solutions have been investigated due to their high oxygen storage capacity [1,2]. In particular, it is known that Ce2Zr2O7+x (0<x<1) has higher oxygen storage capacity in CexZr1-xO2-d solid solutions. Sasaki et al reported Ce2Zr2O7 and Ce2Zr2O7.5 belong to the Fd-3m and F-43m space groups, respectively [3]. However, structure analysis of Ce2Zr2O7+x (0<x<1) has not been studied satisfactorily. In this study, we report the structure analysis of Ce2Zr2O7.32.

Ce2Zr2O7 powders were prepared by a coprecipitation route. The amount of oxygen atom was analyzed by thermogravimetric measurement, and the composition of sample was determined as Ce2Zr2O7.32. The powders were put into vanadium holder and neutron powder diffraction measurement was performed in air with a 150-detector system, HERMES [4], installed at the JRR-3M reactor in Japan Atomic Energy Agency, Tokai, Japan. Neutron with wavelength 1.81386 angstrom was obtained by the (331) reflection of a Ge monochromator. Diffraction data were collected in air at 299.7 K. The experimental data were analyzed by Rietveld method. Computer program RIETAN-FP [5] was utilized for the Rietveld analysis.

Rietveld analysis of Ce2Zr2O7.32 at 299.7 K was carried out assuming the F-43m space group. The reliability factors and goodness of fit were Rwp = 8.64%, RI = 1.63%, RF = 0.85% and S = 3.70. Unit-cell parameter was 10.6404(3) angstrom. Atomic displacement parameters of cation and anion were 0.0043(5) and 0.0097(5) angstromˆ2, respectively.

References

[1] M. Yashima et al., J. Am. Ceram. Soc. 76 (1996) 2865.
[2] M. Yashima et al., Appl. Phys. Lett. 72 (1998) 182.
[3] T. Sasaki et al., J. Ceram. Soc. Japan. 112 (2004) 440
[4] K. Ohoyama et al., Jpn. J. Appl. Phys. 37 (1998) 3319.
[5] F. Izumi and K. Momma, Solid State Phenomena. 15-20 (2007) 130.

Activity Report on Neutron Scattering Research: Experimental Reports **16** (2009)
Report Number: 825

1-1-31

Lattice dynamics of cubic $NaNbO_3$

I. Tomeno(A), Y. Tsunoda(B), K. Oka(C), M. Matsuura(D), M.Nishi(E)
(A)Akita Univ., (B)Waseda Univ., (C)AIST, (D)Osaka Univ., (E) Univ. of Tokyo

Sodium niobate $NaNbO_3$ has a simple cubic perovskite structure above T_{c1}=913 K. $NaNbO_3$ undergoes at least six phase transitions. First, the cubic to a tetragonal phase transition takes place at T_{c1}. Next, three distinct orthorhombic phases appear between T_{c5}=643 K and T_{c2}=848 K. An AF monoclinic P phase exists in the range between T_{c6}=193 K and T_{c5}. Finally, $NaNbO_3$ exhibits a FE rhombohedral N phase below T_{c6}. We studied the phonon dispersion relations for cubic $NaNbO_3$. The inelastic-neutron-scattering experiments were mainly performed using the T1-1 triple-axis spectrometer. Most of the measurements were performed at 970 K.

The important features of the phonon dispersion are the simultaneous softening of M_3 and R_{25} phonon modes. Present results indicate the instabilities of in-phase and out-of-phase rotations of the oxygen octahedra about the [001] direction. These zone-boundary modes exhibit an extremely gradual softening as the temperature is lowered toward T_{c1}=913 K. Figure 1 shows the phonon dispersion relations along the [110] direction. The TO_1 phonon modes along the [110] direction polarized with the [001] direction also soften around **q**=[0.15,0.15,0] and merge into the lower-energy TA phonon modes. This is basically similar to the waterfall phenomenon observed for Pb-based perovskite relaxor ferroelectrics. The coexistence of long-wavelength and zone-boundary phonon instabilities above T_{c1}=913 K is closely related to the complex sequence of phase transitions in $NaNbO_3$.

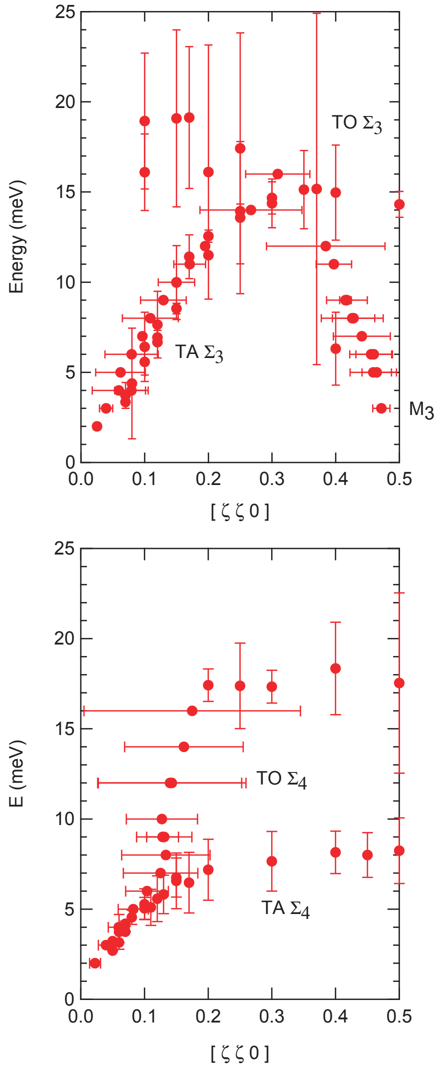

Fig. 1. Phonon dispersion relations for cubic $NaNbO_3$ at 970K.

1-1-32

Phonons in tetragonal $BiVO_4$

I. Tomeno(A), N. Sato(A), K. Oka(B)
(A)Akita Univ., (B) AIST

Bismuth vanadate $BiVO_4$ undergoes a second-order ferroelastic phase transition at T_C=525 K. The high-temperature paraelastic phase has a tetragonal scheelite structure with space group $I4_1/a$ (C^6_{4h}). In the sheelite structure, the isolated VO_4 tetrahedra are separated by the Bi^{3+} ions. The low-temperature ferroelastic phase has a monoclinic distorted scheelite structure with $I2/a$ (C^6_{2h}). Brillouin scattering studies revealed a dramatic softening of transverse acoustic (TA) modes polarized on the (001) plane at T_C.[1-2] We studied the lattice dynamics of $BiVO_4$ in the paraelastic phase. Inelastic neutron scattering measurements were performed using the triple-axis spectrometer T-11 (HQR) at JRR-3M.

We performed transverse constant-**Q** scans at $q = [\sqrt{2}\xi\cos\theta, \sqrt{2}\xi\sin\theta, 0]$ polarized in the (001) plane, where θ is an absolute value of the angle from [100] in the (001) plane. The angular dependence of the TA phonon energy corresponds reasonably to the results of Brillouin-scattering studies. Figure 1 shows that a difference in the TA phonon energy between $q = [\sqrt{2}\xi\cos 35°, \sqrt{2}\xi\sin 35°, 0]$ and $q = [\xi, \xi, 0]$ becomes large with increasing ξ. These results demonstrate that the acoustic symmetry axes in a tetragonal scheelite structure deviate from the crystallographic high-symmetry $[\xi, \xi, 0]$ direction. We measured the phonon dispersion relation along the $[\sqrt{2}\xi\cos 35°, \sqrt{2}\xi\sin 35°, 0]$ direction at T=533 and 773 K. The results plotted in Fig.1(b) indicate that the softening of the TA mode along $[\sqrt{2}\xi\cos 35°, \sqrt{2}\xi\sin 35°, 0]$ occurs in the small ξ region. Brillouin-scattering measurements revealed that the frequency of the TA phonon propagating along the $[\sqrt{2}\xi\cos 35°, \sqrt{2}\xi\sin 35°, 0]$ direction becomes small toward T_c. Thus we expect that the TA phonon branch at T=533 K have a relatively flat slope in the vicinity of zone center. We also found a central peak associated with the softening of TA modes. Further experiments are necessary to investigate the lattice dynamics of tetragonal $BiVO_4$ in a wide temperature range.

References [1]G. Benyuan, M. Copic and H. Z. Commins, Phys. Rev. B24, 4098 (1981). [2]H. Tokumoto and H. Unoki, Phys. Rev. B27, 3748 (1983).

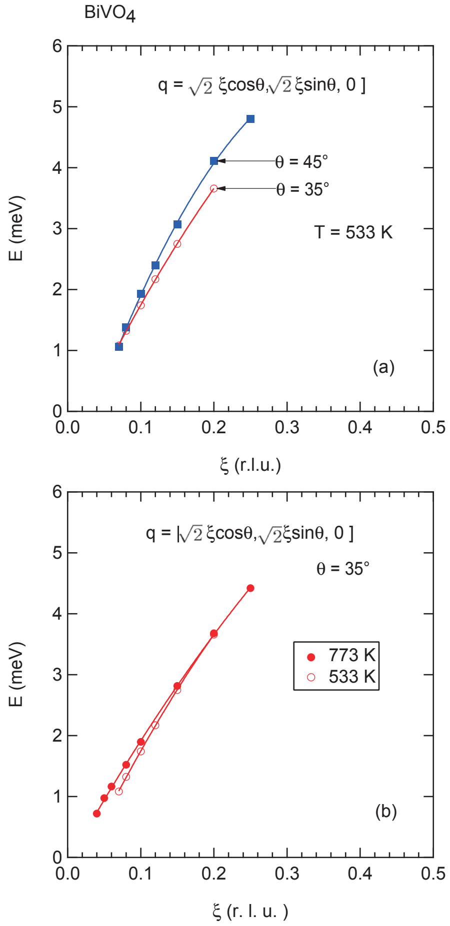

Fig. 1. The TA phonon dispersion curves in tetragonal $BiVO_4$.

1-1-33

Inelastic neutron scattering in the impurity-induced ferroelectric phase of $CuFe_{1-y}Ga_yO_2$

N. Terada[1], T. Nakajima[2], and S. Mitsuda[2]
[1] *National Institute for Materials Science, 1-2-1 Sengen, Tsukuba, 305-0047*
[2] *Fac. of Sciences, Tokyo University of Science, 1-3 Kagurazaka, Shinjuku-ku, Tokyo, 162-0825*

Since the discovery of the magnetic-field-induced ferroelectric phase transition in $CuFeO_2$,[1] the magnetoelectric coupling in this compound has attracted considerable attention. Although the static features, such as magnetic structure and ferroelectric polarization, in this system have been relatively well understood, the magnetic excitation has not been fully understood so far.

This time, in order to determine the spin wave dispersion relation of the nonmagnetic impurity induced ferroelectric incommensurate (FEIC) phase in $CuFe_{1-y}Ga_yO_2$, we have performed the inelastic neutron scattering measurements on $CuFe_{0.965}Ga_{0.035}O_2$. Unlike the FEIC phase of the Al-doped sample with spatially distributed magnetic domains with two different wave numbers, the FEIC phase of the Ga-doped sample is characterized by a single wave number.[2]

The experiment was carried out with the cold neutron triple-axis spectrometer HER installed at C1-1 beam port in the guide hall of JRR-3. The single crystal sample is of the mass 4.8 g. Constant $E_f (= 3 \text{ meV})$ mode was used. To cut off the higher order contamination, the Be filter was put back of the sample.

As shown in Fig. 1, we obtained the contour map of the neutron scattering intensity corresponding to the dynamic structure factor $S(\mathbf{Q}, \omega)$ along the $[H, H, 3/2]$ direction in the FEIC phase of $CuFe_{0.965}Ga_{0.035}O_2$. In the previous neutron diffraction measurements[2], the Bragg reflections at $(q\ q\ \frac{3}{2})$ and $(\frac{1}{2}-q\ \frac{1}{2}-q\ \frac{3}{2})$ with $q = 0.203$ were observed. The lowest energy spin wave branch starts from the two reflection points, where the energy gap of the branch is smaller than 0.2 meV. We confirmed that the spin wave with energy gap in the 4-sublattice (4SL) phase of pure system of $CuFeO_2$[3, 4] is soften and the energy gap goes to zero by a small amount of nonmagnetic impurity.

The relatively complex dispersion relation has not been solved completely at the present stage. There are two types of model for geometric pattern of the exchange interaction. One is a simple triangular lattice model that is considered up to third nearest neighbor exchange interactions, which was applied to the pure $CuFeO_2$ by the other group.[4] However, the lattice distortion occurs in both the 4SL and the FEIC phases. We therefore expect that the scalene triangular lattice model, where the nearest neighbor interactions splits into the three different interactions as the result of the lattice distortion, could explain the dispersion relation.

References

[1] T. Kimura *et al.*: PRB **73**, 220401 (2006).
[2] N. Terada *et al.*: PRB **78** 014101 (2008).
[3] N. Terada *et al.*: JPCM **19** 145241 (2007).
[4] F. Ye *et al.*: PRL **99** 157201 (2007).

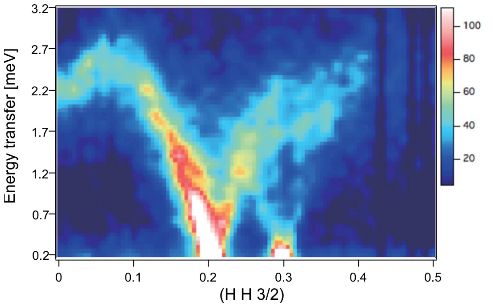

Fig. 1. The spin wave dispersion relation along the $[H, H, 3/2]$ direction in the ferroelectric incommensurate phase of $CuFe_{0.965}Ga_{0.035}O_2$.

1-1-34

Crystal structure analyses of layered thermoelectric manganites

Yuzuru Miyazaki, Fumiya Kawashima, Kei Hayashi and Tsuyoshi Kajitani
Department of Applied Physics, Graduate School of Engineering, Tohoku University

Perovskite based layered manganites have recently attracted much interest owing to their high n-type thermoelectric (TE) performance at higher temperatures. We have studied the effects of detailed structure, in particular the Mn-O distances and Mn-O-Mn angles, on the TE properties. Here, we report the structure of Sr- and (Bi, Sr)-substituted Ca2MnO4 at room temperature; the chemical formulas of the substituted samples are (Ca1.4Sr0.5Bi0.1)MnO4 and (Ca1.5Sr0.5)MnO4. Neutron powder diffraction (ND) data were collected at several temperatures by the use of HERMES diffractometer. The ND data were analyzed using the Rietveld refinement program RIETAN2000. In Fig.1(a), we show the observed, calculated and difference patterns of ND data for Ca2MnO4, based on the I41/acd space group. All the samples were refined with the identical space group and converged with reasonably low R-factors. In Fig.1(b), we plot the relationship between the effective ionic radii (Reff) at the Ca site and the Mn-O2 distance as well as the Mn-O2-Mn angles of the MnO6 octahedra. With increasing Reff, both the dMn-O lengths and Mn-O2-Mn angles increase. The increase in the Mn-O2 lengths reduces the overlapping of the Mn3d-O2p orbitals, while the increase in the Mn-O2-Mn angles enhances such overlapping. In fact, the latter effect plays a dominant role to increase TE performance and a further substitution by Sr would be effective to prepare potential n-type TE materials in the Mn-oxides.

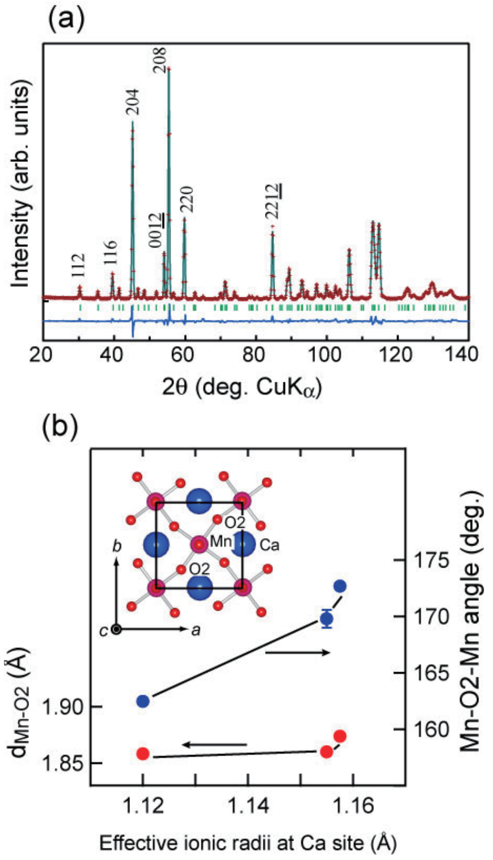

Fig. 1. Rietveld refinement patterns of Ca2MnO4 (a) and the relationship between the effective ionic radii (Reff) at the Ca site and the Mn-O2 distances as well as the Mn-O2-Mn angles of the MnO6 octahedra (b).

1-1-35

Low-Energy Phonon Anomaly of $CeRu_4Sb_{12}$

K. Iwasa[1], R. Igarashi[1], L. Hao[2], Y. Murakami[1]
Tohoku Univ.[1], *China Institute of Atomic Energy*[2]

Anomalously anharmonic lattice properties of the rare-earth filled skutterudites RT_4X_{12} (R = rare earth, T = transition metal, X = pnictogen) have been studied, in addition to the various strongly correlated electron phenomena originating from 4*f* electrons. The filled ions locating within the icosahedral X cage vibrate with large amplitude, as evidenced by the large Debye-Waller factors. One of the attractive lattice properties is the dispersion of elastic constants of $PrOs_4Sb_{12}$, interpreted as low-energy Pr-ion motion within the Sb cage (T. Goto *et al.*: Phys. Rev. B **69** (2004) 180511). We have reported the anomalous softening of phonon due to Pr vibration with decrease of temperature and the possible electron-phonon interaction in $PrOs_4Sb_{12}$ and $PrRu_4Sb_{12}$ (K. Iwasa *et al.*: Physica B **378-380** (2006) 194, J. Phys. Conference Series **92** (2007) 012122). In the present study, we have investigated the low-energy phonon spectra of $CeRu_4Sb_{12}$ using the triple-axis spectrometer TOPAN (6G).

The figure shows temperature dependence of the peak energy position corresponding to the phonon excitation measured at the reciprocal lattice point **Q** = (6 -0.4 -0.4) of $CeRu_4Sb_{12}$. It shows decreasing behavior of excitation energy with decreasing temperature from 300 down to 13 K. This softening mode was confirmed to be less dispersive like an optical mode assigned to the Ce motion in the Sb cage of $CeRu_4Sb_{12}$ (C. H. Lee *et al.*: J. Phys. Soc. Jpn. **75** (2006) 123602). The presence of such anharmonic low-energy phonon is seen also in the previously investigated three compounds of $PrOs_4Sb_{12}$, $PrRu_4Sb_{12}$, $CeOs_4Sb_{12}$ which was reported in the Meeting of Physical Society of Japan (Sep. 2007). Therefore, the anharmonicity appearng in the low-lying optical mode of rare earth ions inside the Sb cages is a characteristic property among the rare-earth filled skutterudite with the Sb cage.

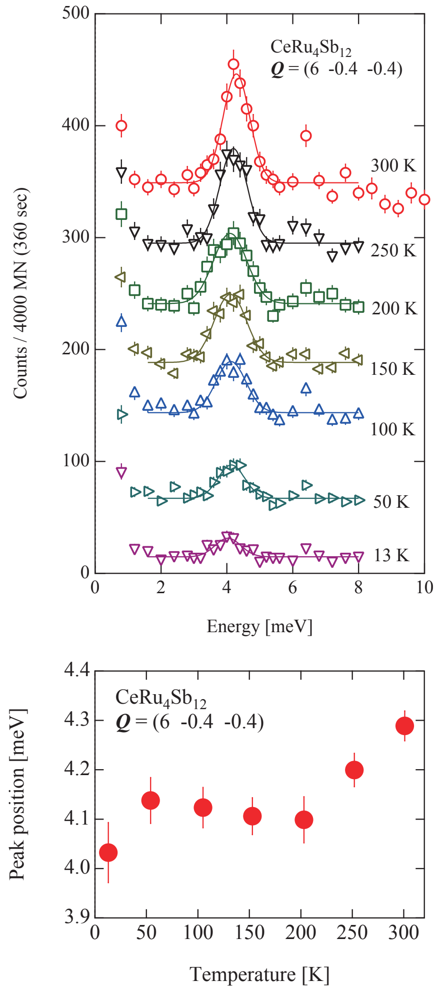

Fig. 1. Temperature dependence of the phonon spectra and the peak energy at **Q** = (6 -0.4 -0.4) of $CeRu_4Sb_{12}$.

1-1-36

Neutron Diffraction Study on SnO2-MOx (M = Ce, Sb) System

K. Nomura (A), H. Kageyama (A), T. Maekawa (B), C. Minagoshi (B), H. Miyazaki (B),
and Y. Kawabata (B)
(A) National Institute of Advanced Industrial Science and Technology (AIST), (B) New Cosmos Electric Co., Ltd.

Recently, SnO2-based materials have been investigated as transparent conductive oxides, oxidation catalysts, and the sensing materials of semiconductor gas sensors [1]. Of these, as the sensing materials of sensors, SnO2-MOx (M = Al, Ce, etc.) systems have been mainly used. However, the detailed crystal structures of these systems are not clear yet. In a previous study, we measured the neutron diffraction data of SnO2-MOx (M = Al, Ce) system [2], and investigated the crystal structure and the nuclear density distributions. In this study, we have investigated the crystal structure and the nuclear density distributions of SnO2-MOx (M = Ce, Sb) system.

Neutron diffraction measurements of high purity (SnO2)(CeO2)a(SbOx)b (0.01<=a<=0.03, 0.01<=b<=0.03) samples were performed with HERMES installed at JRR-3M in JAEA (Tokai) [3]. Neutron wavelength was 1.8204(5)A. Diffraction data were collected in the 2 θ range from 20 to 157 deg. in the step interval of 0.1 deg. The diffraction data obtained were analyzed by the combination technique of Rietveld analysis using a computer program RIETAN-2000 [4] and a maximum-entropy method (MEM)-based pattern fitting. MEM calculation was carried out using a computer program PRIMA [5].

The neutron diffraction patterns of (SnO2)(CeO2)a(SbOx)b (0.01<=a<=0.03, 0.01<=b<=0.03) samples showed larger peak widths and higher background intensities compared to that of pure SnO2. All the reflection peaks of these samples were indexed by a tetragonal symmetry (P42/mnm, No.136). The assumed structure model was as follows: Sn, Ce, and Sb atoms occupy 2a sites (0, 0, 0) and O atoms occupy 4f sites (x, y, 0) (x = y ˜ 0.306) [1] with isotropic atomic displacement parameters. The lattice parameters and unit cell volume increased with increasing Ce and (or) Sb contents, suggesting the introduction of larger Ce4+(0.97A) and (or) Sb3+(0.76A) ions [6] into Sn4+ (0.69A) sites. Figure. 1 shows the equicontour surfaces (0.5fm/A^3) of scattering amplitude of (SnO2)(CeO2)0.03(SbOx)0.03. Not only 2a (Sn, Ce, Sb) sites but also 4f (O) sites showed nonspherical equicontour surfaces with large distributions (compared to SnO2), suggesting the disturbed atomic arrangements on the 2a and 4f sites by introducing Ce and Sb atoms into Sn sites.

References
[1] M. Batzill and U. Diebold, Progress in Surface Science, 79, 47 (2005).
[2] T. Maekawa, C. Minagoshi, S. Nakamura, K. Nomura, H. Kageyama, Chemical Sensors, 24, 19 (2008).
[3] K. Ohoyama, T. Kanouchi, K. Nemoto, M. Ohashi, T. Kajitani, and Y. Yamaguchi, Jpn. J. Appl. Phys., 37, 3319 (1998).
[4] F. Izumi and T. Ikeda, Mater. Sci. Forum, 321-324, 198 (2000).
[5] F. Izumi and R.A. Dilanian, in: Recent Research Developments in Physics, vol.3, Transworld Research Network, Trivandrum, 2002, p.699.
[6] R.D. Shannon, Acta Cryst, B51, 751 (1976).

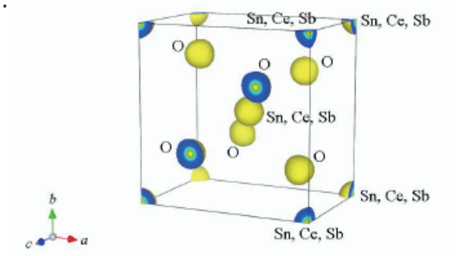

Fig. 1. Equicontour surfaces (0.5fm/A^3) of scattering amplitude of (SnO2)(CeO2)0.03(SbOx)0.03.

1-1-37

Observation of Hydrogen Tunneling in Pd nanoparticles by Low-temperature Neutron Scattering Measurement

Miho Yamauchi(A), Hiroshi Kitagawa(B), Osamu Yamamuro(C)
(A)CRC, Hokkaido Univ., (B)Faculty of Sci. Kyushu Univ., (C)ISSP-NSL Univ. Tokyo

2H NMR spin-lattice relaxation times (T1) for deuteron atoms in the Pd nanoparticles showed a particular minimum below 30 K while T1 for the bulk sample increase monotonously with decreasing temperature. In order to clarify the origins of the unusual T1 minima, neutron scattering experiments were carried out for the bulk and nanoparticle of Pd with AGNES spectrometer installed at JRR-3 (JAEA, Japan). Pd nanoparticles, that are homogeneous in size, were synthesized by a chemical reduction method with water-soluble polymer, poly[N-vinyl-2-pyrrolidone] abbreviated as PVP. By TEM measurements, homogeneity in size of Pd nanoparticles was confirmed and the mean diameter was estimated to be 6.3 ± 1.0 nm. 800 mg of Pd nanoparticles were loaded into the sample tube that was connected to a vacuum line and a hydrogen gasbag. In this system, pressure inside the sample tube can be monitored and hydrogen gas provided. Measurements for bulk Pd and Pd nanoparticles with and without hydrogen gas were performed at 7, 14 and 28 K. The data were accumulated for 32 hours. Scattering intensity from absorbed hydrogen atoms was evaluated from the intensity difference between the samples with and without hydrogen atoms. Difference scattering intensities for the Pd nanoparticle are shown in Fig. 1. Although, in general, scattering intensity is increased due to thermal vibration, that is, the intensity at high temperature is larger than that at low temperature, the scattering intensity at 7 K of hydrogen absorbed in Pd nanoparticles seems to be slightly larger than that at 28 K under magnification in the energy region below 3 meV. This unusual tendency of the scattering intensity is attributed to the same origin of the NMR T1 minima observed below 30 K.

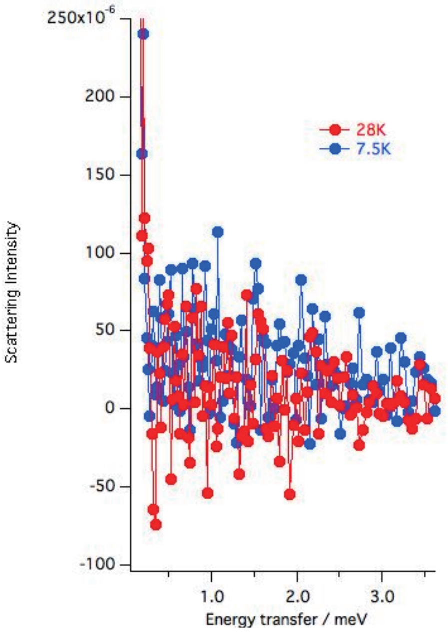

Fig. 1. Fig. 1. Scattering intesity of hydrogen absorbed Pd nanoparticles.

1-1-38

Structural, magnetic and thermoelectric properties of half-Heusler compounds

G. Nakamoto (A), H. Murakami (A), M. Kurisu (A), A. Tanaka (B), T. Tsutaoka (B), Y. Andoh (C)
(A) School of Materials Science, Japan Advanced Institute of Science and Technology, (B) Graduate School of Education, Hiroshima University, (C) Faculty of Regional Sciences, Tottori University

Recently, half-Heusler compounds have attracted much attention because of the high potential as a thermoelectric material originating from the anomalous electronic band structure near the Fermi level called a half-metallic state. It has been reported firstly that the TiNiSn-based half-Heusler compounds show the high thermoelectric performance with the dimensionless figure of merit, ZT=1.5 at 700 K [1]. Our group has investigated the thermoelectric property of the rare-earth based half-Heusler compounds RPdSb (R: rare-earth elements). The Seebeck coefficient, electrical resistivity and thermal conductivity have been measured as a function of temperature. It is found that the temperature dependence and absolute values of theses thermoelectric quantities depend strongly on the sample-preparation condition. It is also expected that defects or instability of the lattice giving strong influence on the electronic state are easily introduced in the half-Heusler structure. However, the effect of the structural property on the thermoelectric one has not been fully understood yet in the half-Heusler system.

In the present study, in order to elucidate the correlation between the structural and thermoelectric properties in the half-Heusler compounds, the powder neutron diffraction study have been performed on the rare-earth based half-Heusler RPdSb system to examine the existence of defects and the degree of disorder. Furthermore, the magnetic properties like the magnetic transition temperature and magnetic moment have been also investigated.

The polycrystalline samples were prepared by arc melting the constituent elements in purified Ar atmosphere. The excess amount of Sb was added to compensate the weight loss due to evaporation during melting. The ingot was melted and flipped over several times to ensure the complete mixing of the elements. The single-phase formation was confirmed by a powder X-ray diffraction measurement. The thermoelectric and magnetic properties were studied below room temperature by a PPMS and a SQUID magnetometer. The powder neutron diffraction experiments were carried out by the T1-3, HERMES installed at JRR-3M in JAEA. The precise structural refinement of the powder neutron diffraction data was performed by the Rietveld analysis using the pattern profile fitting program, RIETAN-2000 to determine the crystal parameters.

The detailed structural analysis is now under way to have a definite conclusion about the correlation between the structural and thermoelectric properties in the half-Heusler compounds.

Reference

[1] N. Shutoh and S. Sakurada, 22nd International Conference on Thermoelectrics (2003), p. 312.

1-1-39

Dependence of crystal structure and thermodynamic stability on different synthetic method and Li content for Lix(Ni,M)O2 (M=Mn,Co) as a cathode active material for Li ion battery

Yasushi Idemoto, Naoto Kitamura and Takuya Hasegawa
Department of Pure and Applied Chemistry, Faculty of Science and Technology, Tokyo University of Science, 2641 Yamazaki, Noda-shi, Chiba 278-8510

As a cathode active material for lithium ion battery, LiCoO2 with a layer structure is the most widely used. Due to high cost and high toxicity of the Co, however, nickelate-based materials have drawn much attention. From such background, we have studied Lix(Ni,M)O2 (M=Mn,Co); especially LixMn0.5Ni0.5O2 and LixNi0.8Co0.2O2, which have lower Co content. As a result, we found that their cathode performance depended on the synthetic process. However, less information on their crystal structures make the synthetic process effects ambiguous at this moment.

In this work, we investigated crystal structures of LixMn0.5Ni0.5O2 and LixNi0.8Co0.2O2 prepared by two different methods. We investigated the crystal structures by Rietveld analysis using neutron diffraction and nuclear densities by MEM. Based on the results, we discussed relationship between thermodynamic stability, crystal structure and cathode performance, and then tried to reveal how the synthetic process affected them.

LixMn0.5Ni0.5O2 and LixNi0.8Co0.2O2 were prepared by two methods; that is, conventional solid-state method and solution method using citric acid as an additive. Their cathode performances were studied by CV and charge-discharge cycle tests. In order to clarify crystal structure at the charged state, chemical delithiation using 0.5N-(NH4)2S2O8 was also performed. Thermodynamic stabilities of the samples were evaluated from their heats of dissolution which were measured by a twin-type multi-calorimeter. The crystal structures were determined by neutron diffraction using HERMES[1] of IMR at JRR-3M in JAERI. The data was refined using the Rietan-FP[2]. The nuclear densities were determined with PRIMA program[3].

From XRD patterns, it was found that main phases of LixMn0.5Ni0.5O2 (x=0.98~1.08) synthesized in this work had the α-NaFeO2-type layer structure (S. G.: R-3m) although Li2MnO3 was slightly observed as a secondary phase depending on preparation process. Cycle performance tests revealed that the samples with the same analytical composition exhibited different cathode performance depending on synthetic method, that is, the samples synthesized by solid state reaction exhibit more stable cycle performance than those prepared by solution method. From formation enthalpies of the samples evaluated by the calorimetry, it could be concluded that higher thermodynamic stability induced better cathode performance.

In order to discuss effects of the synthetic processes on their crystal structure, the Rietveld analysis using the neutron diffraction was carried out. As a result, it was found that cation mixing — that is, Ni content at Li site and Li content at Ni site — was essentially independent of the synthetic process. However, local distortion around the transition metal site, which was evaluated from the results of the Rietveld analysis, was larger in the samples exhibiting worse cycle performance. Such a distortion also became larger by a chemical delithiation although the crystal structure kept the layer structure even after the delithiation. In the case of LixNi0.8Co0.2O2[4], similar results to LixMn0.5Ni0.5O2 were also obtained.

[1] K. Ohoyama, T. Kanouchi, K. Nemoto, M. Ohashi, T. Kajitani, Y. Yamaguchi, Jpn. J. Appl. Phys. 37, 3319 (1998) .
[2] F. Izumi, and T. Ikeda, Mater. Sci. Forum, 321, 198 (2000).
[3] F. Izumi and R. A. Dilanian, ”Recent Research Developments in Physics, ” Vol.3, Part II, Transworld Research Network, Trivandrum (2002), pp.699-726.
[4] Yasushi Idemoto, Yu Takanashi, Naoto Kitamura, J. Power Sources, 189(1), 269 (2009).

1-1-39

1-1-40

Crystal structure and ionic conduction path of $Ln_2Ni_{1-x}Cu_xO_{4+d}$ for solid oxide fuel cells

Yasushi Idemoto and Naoto Kitamura
Departme nt of Pure and Applied Chemistry, Faculty of Science and Technology, Tokyo University of Science, 2641 Yamazaki, Noda-shi, Chiba 278-8510

Recently, solid oxide fuel cell (SOFC) has drawn much attention, and many researches on the device have been carried out. Lanthanum nickelate-based materials with the K_2NiF_4-type structure are considered as promising candidates for cathodes of SOFC. It is well-known that excess oxygens are incorporated at interstitial sites in the rock-salt La_2O_2 layer and the oxygens can be a conduction species in the lanthanum nickelate-based materials. Due to the difficulty in an analysis on crystal structures at elevated temperature, however, it is still ambiguous how the host crystal structure affects excess oxygen sites and their conduction path.

From such background, we investigated $Ln_2Ni_{1-x}Cu_xO_{4+d}$ with the K_2NiF_4-type structure in this work. By using neutron diffraction patterns, crystal structures of the materials at high temperature were refined with the Rietveld method, and their nuclear density distributions were also estimated by the maximum entropy method (MEM).

We synthesized $LaNi_{0.8}Cu_{0.2}O_{4+d}$ with a solution method using citric acid as an additive. Phase identification of the sample was carried out by XRD, and the composition was evaluated by ICP. Conductivity of the sample was also measured at elevated temperature. In order to study the crystal structure in detail, we measured neutron diffraction patterns at the temperature range from 298 to 673 K using HERMES of IMR at the JRR-3M[1], and analyzed the patterns with the Rietan-FP[2]. We also estimated nuclear density of the sample by MEM technique with PRIMA program[3].

It was confirmed with X-ray diffractions that $LaNi_{0.8}Cu_{0.2}O_{4+d}$ had a single phase of the K_2NiF_4-type structure. From ICP measurement, it was indicated that metal composition of the sample was almost equal to the nominal one.

As for the lanthanum nickelate-based sample, Rietveld analysis using neutron diffractions was performed. In the analysis, we assumed the space group as I4/mmm and excess interstitial oxygens in the rock-salt layer. As a result, it was found that lattice constants of the material increased as temperature increased. The content of the excess oxygen, which was calculated from the occupancy, became lower with increasing temperature although their sites were essentially independent of temperature. Because bond valence sum of (Ni,Cu) site became lower at higher temperature, it was considered that the effective negative charge of the excess oxygens was compensated by an oxidation of Ni and/or Cu. From the nuclear density distribution at elevated temperature, it was suggested that oxygens at the interstitial site and an apex site of the perovskite layer moved significantly compared with the other oxygens.

[1] K. Ohoyama, T. Kanouchi, K. Nemoto, M. Ohashi, T. Kajitani, Y. Yamaguchi, Jpn. J. Appl. Phys. 37, 3319 (1998) .
[2] F. Izumi, and T. Ikeda, Mater. Sci. Forum, 321, 198 (2000).
[3] F. Izumi and R. A. Dilanian, ”Recent Research Developments in Physics, ” Vol.3, Part II, Transworld Research Network, Trivandrum (2002), pp.699-726.

1-1-41

Structural Analysis of Interface between DLC films Having Various Wettabilities and Lubricants Using Neutron Reflectometry

*Tomoko Hirayama, *Takashi Torii, *Takashi Kashihara, *Takashi Matsuoka, **Kazuko Inoue, ***Masahiro Hino
**Doshisha University, **Waseda University, ***Kyoto University*

Structures of interfaces between materials and lubricants were analyzed using neutron reflectometry and discussed in the series of studies. In this paper, three kinds of DLC films having various wettabilities (normal DLC, hydrophilic DLC and hydrophobic DLC) were prepared as base materials, and water and 2-propanol were selected as lubricants. The instrument we used was a neutron reflectometer ’MINE’ in Japan Atomic Energy Agency (JAEA). The DLC films were soaked into the lubricants in a specially-designed sample holder, and the neutron reflectivity profiles from the interface between DLC films and lubricants were directly obtained. Through an analytical fitting approach with Parratt’s theory to the obtained profiles, authors presented the strict structure of the interface.

First, each DLC film was soaked into water in a sample holder, and the neutron reflectivity profiles from the interface between DLC films and water were obtained. Then, deuterated water (D2O) was used for clearer analysis because of its high sensitivity for neutron. Fitting operation to the obtained reflectivity profiles showed that density of water at the interface between normal DLC and water was same as density of bulk water and uniform along vertical direction. On the other hand, at the interface between hydrophilic DLC and water, water was infiltrating from the top surface of DLC to the 15 nm depth. In addition, we found that the ’dense water layer’ existed from the top surface of DLC to the 2 nm depth. At the interface between hydrophobic DLC and water, ’low density water layer’ existed on the film surface. The fitting approach confirmed that the thickness of the layer on the hydrophobic surface was 3nm, and its density was almost half of bulk water.

Structures of interfaces between each DLC film and deuterated 2-propanol (CD3CD(OD)CD3) were also analyzed using neutron reflectometry. We found that the 2-propanol was also infiltrating from the top surface of hydrophilic DLC to the 15 nm depth and was infiltrating from the top surface of normal DLC to the 9 nm depth.

The coefficients of friction of each DLC film under boundary lubricated condition were measured using a ball-on-disk friction tester. The ball material and size are SUJ2 and 3/16 inch in diameter. The applied load to the ball was 0.2 N. The obtained coefficient of friction of each DLC film under water lubricated or 2-propanol lubricated condition is shown in Fig. 1. This figure shows that the friction coefficient of hydrophilic DLC is lower and that of hydrophobic DLC is higher than that of normal DLC. It may be because that for the hydrophilic surface, lubricants are enough to reduce the friction, while that for the hydrophobic surface, friction surface runs short of lubricants under boundary lubricated condition. We conclude that the nano structure of interface between DLC and lubricants are very influential to the lubricated friction property.

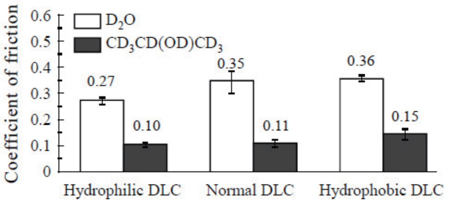

Fig. 1. Coefficients of friction under lubricated condition

1-1-42

High Temperature Neutron Diffraction Study of (La0.6Sr0.4)(Co0.8Fe0.2)O3-d Perovskite

K. Nomura (A), K. Kakinuma (B), T. Kojima (A), N. Takeichi (A), H. Kageyama (A),T. Maekawa (C), C. Minagoshi (C), H. Miyazaki (C), and Y. Kawabata (C)
(A) National Institute of Advanced Industrial Science and Technology (AIST), (B) University of Yamanashi, (C) New Cosmos Electric Co., Ltd.

Recently, (La,Sr)(Co,Fe)O3-d perovskites have been investigated as the cathode materials of solid oxide fuel cells, because of the high electronic and high oxide-ion conductivity [1]. However, the detailed crystal structures under cell operation conditions, i.e., at elevated temperatures under oxygen partial pressures, P(O2) <= 0.21atm, have not been reported yet. In this study, we have measured high temperature neutron diffraction data of 40 mol% Sr- and 20 mol% Fe-doped LaCoO3, (La0.6Sr0.4)(Co0.8Fe0.2)O3-d (LSCF), at elevated temperatures, 299<=T<=1273K, under 0.002<=P(O2)<=0.21atm, to investigate the detailed crystal structures and the oxide-ion conduction path.

Neutron diffraction measurements were performed with a 150-detector system, HERMES [2], installed at the JRR-3M reactor in JAEA (Tokai). The neutron wave length was 1.8204(5)A and the diffraction data were collected in the 2 θ range from 20 to 153 deg. in step interval of 0.1 deg. A furnace with Pt-Rh heaters installed in a vacuum chamber was placed on the sample stage, and used for neutron-diffraction measurements at high temperatures. The diffraction data obtained were analyzed using the Rietveld program RIETAN-2000 [3]. The diffraction data of LSCF could be indexed assuming a trigonal symmetry (R-3c, No.167) at 299, 475, and 671K in P(O2) = 0.21atm, or a cubic one (Pm-3m, No.221) between 873 and 1273K under 0.002<=P(O2) <=0.21atm. The Rietveld refinement result of LSFC measured at 1273K in P(O2) = 0.002atm was as follows: Z = 1, a = 3.9333(2)A, α = 90 deg., V = 60.854(6)A^3. The reliability factors were as follows: Rwp = 6.48%, Re = 3.43%, S = Rwp/Re = 1.89. Figure 1 shows the refined crystal structure of LSFC at 1273K in P(O2) = 0.002atm. Oxide ions showed larger atomic displacement parameters than those of La, Sr, Co, and Fe ions. Oxide ions also indicated larger thermal motion perpendicular to (Co, Fe)-O bonds. These results suggest the oxide-ion conduction in LSCF with an arc shape path [4].

References

[1] N. Minh, J. Am. Ceram. Soc., 76, 563 (1993).
[2] K. Ohoyama, T. Kanouchi, K. Nemoto, M. Ohashi, T. Kajitani, and Y. Yamaguchi, Jpn. J. Appl. Phys., 37, 3319 (1998).
[3] F. Izumi and T. Ikeda, Mater. Sci. Forum, 321-324, 198 (2000).
[4] M. Yashima and T. Kamioka, Solid State Ionics, 178, 1939 (2008).

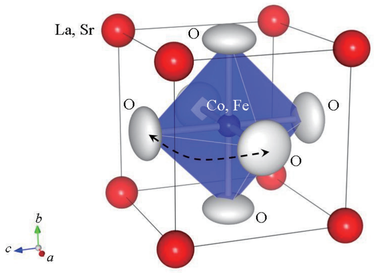

Fig. 1. Refined crystal structure of (La0.6Sr0.4)(Co0.8Fe0.2)O3-d at 1273K under P(O2) = 0.002 atm. The dotted curve with arrows denotes possible conduction path of oxide ions.

1-1-43

Phonons in FCC-Fe precipitates in Cu

Kohtaro Horiguchi and Yorihiko Tsunoda
School of Science and Engineering, Waseda University, 3-4-1 Ohkubo, Shinjuku-ku, Tokyo 169-8555

An fcc-Fe is stable only at temperature between 1185K and 1667K. However, Fe precipitates which are grown in supersaturated Cu-Fe solid solution retain fcc structure even at room temperature. The lattices of Fe precipitates are coherent with Cu matrix. At low temperature (T<70 K), Fe precipitates undergo a structural phase transition. The lattice structure in the low temperature phase is described by the shear wave propagating along the [110] direction and the [1-10] polarization vector. In related to the structural phase transition, drastic softening of the elastic moduli C ’ and C11 is observed below 150 K.

The purpose of the present experiments is two points. There are no experimental data of phonon dispersion relation of fcc Fe at the room temperature because of no bulk specimen. Thus, the first purpose is to observe the phonon peaks and to determine the dispersion relations of fcc Fe at room temperature using the coherent precipitates. If observation of phonons is possible, the second purpose is to observe the phonon softening towards the structural phase transition.

A super-saturated Cu97Fe3 single crystal was grown by Bridgmann method. The sample was quenched into water from 1000 C, then precipitation anneal was performed at 600 C for 53.5 hours. Averaged precipitation particle size is estimated to be 50 nm. Phonon measurements were performed at the T1-1 triple axis spectrometer.

For small q regions, it was impossible to separate the phonons of Cu matrix and Fe precipitates. At high q regions, phonon intensity is too weak to observe because of small effective volume of fcc-Fe precipitates. However, we succeeded to observe phonon peaks of the [1 1 0] T1-branch at room temperature. Since the elastic modulus C ’ shows softening towards the structural phase transition, to study the phonon dispersion relation of the [1 1 0] T1 branch would be interesting. Temperature variation of phonon peaks for fcc-Fe precipitates studied at q=0.3 is given in Fig. 1. At low temperature, phonon peak intensity is too weak and it is hard to discuss the phonon softening. However, phonon peak shift with temperature decreasing (hardening) between RT and 150 K is very large. The reason is considered to be increasing of mis-fitting parameter of the lattices between Cu and Fe precipitates. We would like to discuss this point thoroughly.

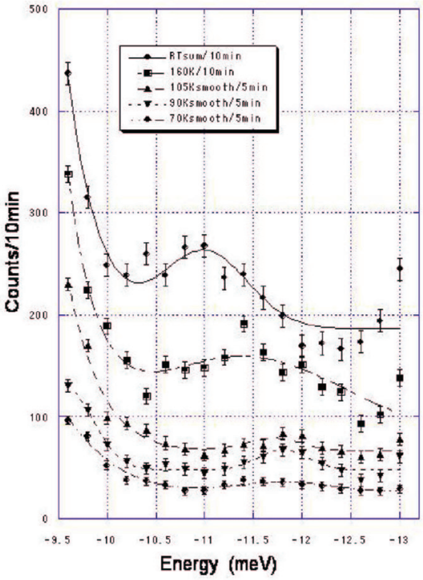

Fig. 1. Fig.1 temperature variation of phonon peaks of fcc Fe precipitates studied at q=0.3.

1-1-44

Crystal Structure Analysis of a Supramolecular Ferroelectric 55DMBP-H2ia at Low-temperature Phase

Reiji Kumai1, Daisuke Okuyama2,3, Sachio Horiuchi1, Takahisa Arima3, Ryoji Kiyanagi3, Yukio Noda3, and Yoshinori Tokura1,2,4
1National Institute of Advanced Industrial Science and Technology (AIST), 2Cross-Correlated Materials Research Group (CMRG), ASI, RIKEN, 3Institute of Multidisciplinary Research for Advanced Materials, Tohoku University, 4Department of Applied Physics, The University of Tokyo

Ferroelectrics have been motivated not only by basic science but also by application because of those various utilizations for electronics. Recently Horiuchi et al. have reported a new ferroelectric realized by proton dynamics in a hydrogen-bonded chain with supramolecular structure, the cocrystal of 5,5’-dimethyl-2,2’-bipyridine (55DMBP, C12H12N2) and iodanilic acid (H2ia, C6H2O4I2) [1], in which the corrective proton motion should be playing an important role for the development of the ferroelectricity. Here, we report crystal structure of 55DMBP-H2ia in a low-temperature phase obtained by the neutron diffraction in order to make clear the more precise hydrogen atom position.

Large single crystals of 55DMBP-H2ia (3 x 1 x 10 mm3) were prepared by slow evaporation from methanol solution. The neutron diffraction experiments were performed at the T2-2 guide-hall of JRR-3M in JAEA, utilizing a four-circle diffractometer “ FONDER ” with 1.23960 neutron beam monochromized by a Ge(311) monochromater. We used the program SHELX-97 for the least-square fitting in order to refine the parameters. [2]

The crystal of 55DMBP-H2ia consists of one-dimensional chain made from O⋯H⋯N type hydrogen bond between acid and base molecules. Figure 1a shows the hydrogen bonded chain structure of ferroelectric phase of 55DMBP-H2ia (T = 50 K) obtained by a neutron crystal structure analysis. Lattice parameters, space group (P1), and atomic coordinates except for hydrogen atoms, consist with those obtained by the X-ray diffraction experiments. It can be clearly observed that there are two types of hydrogen bonded site, a neutral O-H⋯N site and a ionic O-⋯H-N+ site, in the chain. From a comparison between ferroelectric structure and paralectric structure (Fig. 1b), which was determined by the previous neutron diffraction study, one can find the corrective proton motion along the one-dimensional hydrogen bonded chain. The alternating O-H⋯N and O-⋯H-N+ constitute a polar chain and a polar three-dimensional structure. That is to say, the proton migration can be an origin of the polarization in this system.

References and notes

[1] S. Horiuchi, R. Kumai, Y. Tokura, Angew. Chem. Int. Ed., 46, 3497 (2007).
[2] 55DMBP-H2ia 300K: C18H14N2O4I2, Z = 2, Triclinic P1, a = 9.996(5) , b = 8.729(2) , c = 12.650(3) , alpha= 66.54(2), beta= 67.57(2),gamma= 66.45(2), V = 895.1(5) 3, R = 0.0433 for 3115 independent reflections (|Fo| > 4sigma(|Fo|)).

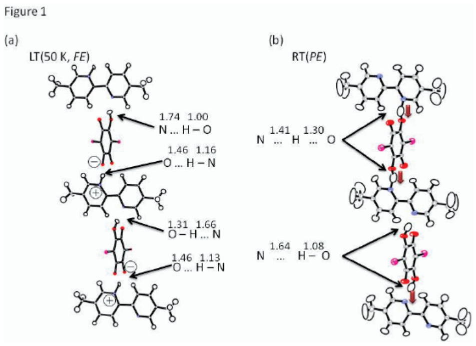

Fig. 1. Crystal Structure of 55DMBP-H2ia at (a) ferroelectric phase (50 K) and (b) paraelectric phase (room temperature).

1-1-45

Crystal Structure of Lithium Battery Electrode Materials with Tunnel Structure

N. Kijima(A), J. Akimoto(A), K. Kataoka(A,B)
(A) National Institute of Advanced Industrial Science and Technology (AIST), (B) University of Tsukuba

A great deal of research into the application of a-MnO2 as an electrode material for lithium-ion batteries has been conducted because a-MnO2 has large (2 × 2) tunnels presenting a privileged pathway for Li ion diffusion [1-3]. The a-MnO2 electrode can be intercalated in lithium cells at about 3 V, and the initial discharge capacity exceeds 200 mAh/g. To clarify the structural properties of a Li inserted a-MnO2 specimen, neutron diffraction investigations have been made in this work.

A well-crystallized a-MnO2 specimen was prepared by oxidation of MnSO4 with ozone gas in H2SO4 solution at 353 K. A Li inserted a-MnO2 specimen was obtained by soaking the parent a-MnO2 powder in a mixed solution of 0.1 mol/dm3 LiOH and 0.1 mol/dm3 LiNO3.

Neutron powder diffraction data were taken at room temperature on the HERMES powder diffractometer installed at the JRR-3M research reactor of the Japan Atomic Energy Agency. Incident neutrons with a fixed wavelength of 1.8204(5) angstroms were obtained by a vertically focusing (331) Ge monochromator. The powder diffraction data were measured over a 2 theta range of 7-157 degrees with a step interval of 0.1.

The diffraction data were analyzed by the Rietveld method with RIETAN-2000, and the nuclear scattering density distribution of specimens were visualized by the maximum-entropy-method based pattern fitting.

Figure 1 depicts the preliminary result of the nuclear scattering density distribution of Li inserted a-MnO2 specimen. This image clearly shows the Li and O atoms in the tunnel space.

The parent a-MnO2 specimen showed a poor discharge property although no cationic residues or residual H2O molecules remained in the tunnel space. In contrast, the Li inserted a-MnO2 specimen showed a good charge-discharge property as the cathode. These facts suggest that the presence of stabilizing O atoms within the (2 × 2) tunnel is necessary to facilitate the diffusion of Li ions during cycling.

References
[1] N. Kijima, T. Ikeda, K. Oikawa, F. Izumi, Y. Yoshimura, J. Solid State Chem. 177 (2004) 1258.
[2] N. Kijima, Y. Takahashi, J. Akimoto, J. Awaka, J. Solid State Chem. 178 (2005) 2741.
[3] N. Kijima, Y. Sakata, Y. Takahashi, J. Akimoto, T. Kumagai, K. Igarashi, T. Shimizu, Solid State Ionics 180 (2009) 616.

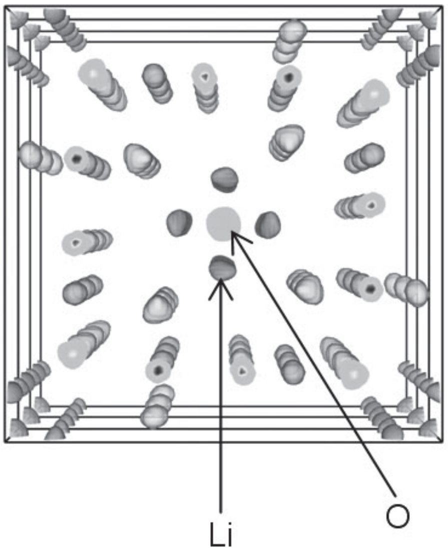

Fig. 1. Nuclear scattering density distribution image of the Li inserted a-MnO2 specimen.

1.　中性子散乱 2）磁　性

1. Neutron Scattering　2）Magnetism

1-2-1

Magnetic Bragg Peaks of Quasi-One-Dimensional Antiferromagnets $Cu_6Ge_6O_{18}$-xD_2O (x = 0, 6)

M. Hase, N. Terada, H. S. Suzuki, H. Kitazawa, K. Ozawa, K. Kaneko[1], N. Metoki[1],
M. Matsuda[1] and K. Kakurai[1]

National Institute for Materials Science (NIMS), 1-2-1 Sengen, Tsukuba, Ibaraki 305-0047, Japan
[1] *Japan Atomic Energy Agency (JAEA), 2-4 Shirakata Shirane, Tokai, Naka, Ibaraki 319-1195, Japan*

The spin systems of insulating cuprates $Cu_6Ge_6O_{18}$-xD_2O ($x = 0 - 6$) are spin-1/2 Heisenberg chains with first- and second-nearest-neighbor antiferromagnetic (AF) exchange interactions.[1)] The space group is $R\bar{3}$ (No. 148).[2)] Helical spin-1/2 chains of Cu are formed parallel to the c axis. Each chain has three Cu ions in the unit cell. Magnetic long-range order appears below T_N. The value of T_N/T_{max} decreases with decrease in x from $x = 6$, while it is nearly constant below $x = 1.54$. Here, T_{max} is temperature where the magnetic susceptibility has a broad maximum. At $x = 1.54$, T_N/T_{max} jumps abruptly from 0.23 to 0.39, and two magnetic transitions are seen. The jump indicates that magnetic long-range orders at $x < 1.54$ and $x > 1.54$ belong to essentially different phases. The difference, however, has not been unveiled. Accordingly, we performed neutron-diffraction measurements of powders with $x = 0$ or 6 using the TAS-2 (the wave length $\lambda = 2.444$ Å) and MUSASI ($\lambda = 2.474$ Å) spectrometers to investigate magnetic structures.

Figure 1 shows diffraction patterns of $Cu_6Ge_6O_{18}$-$6D_2O$.[3)] As indicated by arrows, we can see a resolution-limited magnetic Bragg peak in each figure below T_N. We could find two magnetic Bragg peaks in each sample. The index (h, k, l) of the scattering vector $\mathbf{Q}$ is $(2, 1, -0.5)_{hex}$ and $(1, 2, 0.5)_{hex}$ for the low-angle peak and $(3, 1, 0.5)_{hex}$ and $(1, 3, -0.5)_{hex}$ for the high-angle one. We adopt the hexagonal unit cell. The l value is half integer. Therefore, the spin arrangement is collinear AF in each chain.

We calculated scattering cross sections (SCSs) of magnetic Bragg peaks when the nearest-neighbor interchain interaction (J_a) is AF or ferromagnetic. Here, we assume that the ordered spins are parallel to the c axis, because the spin is almost parallel to the c axis in the AF long-range order in isostructural $Cu_6Si_6O_{18}$-xH_2O (x = 0, 6).[4,5)] The calculated SCSs in the case that J_a is AF are consistent with the experimental results.

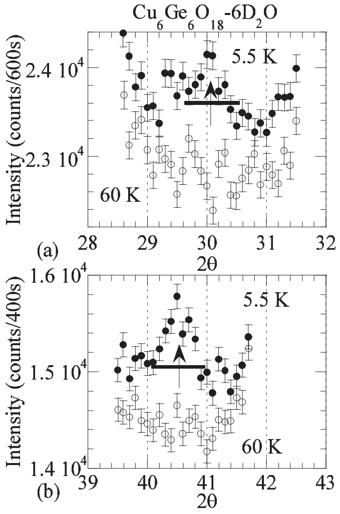

Figure 1: Diffraction patterns of $Cu_6Ge_6O_{18}$-$6D_2O$.

References

1) M. Hase, K. Ozawa and N. Shinya : "Phys. Rev. B", 68, pp. 214421 (2003).
2) H.-J. Brandt and H. H. Otto : "Z. Kristallogr.", 212, pp. 34 (1997).
3) M. Hase, N. Terada, H. S. Suzuki, H. Kitazawa, K. Ozawa, K. Kaneko, N. Metoki, M. Matsuda and K. Kakurai : "J. Phys.: Conference Series", 150, pp. 042051 (2009).
4) M. Wintenberger, G. André and M. F. Gardette : "Solid State Commun.", 87, pp. 309 (1993).
5) E. L. Belokoneva, Y. K. Gubina, J. B. Forsyth and P. J. Brown : "Phys. Chem. Minerals", 29, pp. 430 (2002).

原子炉：JRR-3　装置：TAS-2(T2-4)　分野：中性子散乱（磁性）

1-2-2

Spherical Neutron Polarimetry Analysis in the Ferroelectric Phase of the Magnetoelectric Multiferroic $CuFe_{1-y}Ga_yO_2$

N. Terada[1,3], T. Nakajima[2], S. Mitsuda[2], M. Matsuda[3], K. Kakurai[3] and H. Kitazawa[1]
[1] *National Institute for Materials Science, Tsukuba, Ibaraki 305-0047*
[2] *Department of Physics, Faculty of Science, Tokyo University of Science, Tokyo 162-8601*
[3] *Quantum Beam Science Directorate, JAEA, Tokai, Ibaraki 319-1195*

Recently, as one of magnetoelectric multiferroics, $CuFeO_2$ has been intensively studied for understanding the microscopic mechanism regarding the magneto-ferroelecticity.[1,2] There has been several theories to explain ferroelectricity in multiferroics. One of the mechanisms was proposed for explaining the ferrelectricity in $CuFeO_2$, which originates from Fe $3d$-O $2q$ hybridization with the spin-orbit coupling.[3] For the verification of the mechanism, the detail magnetic structural determination was strongly required. Although the previous unpolarized neutron diffraction experiments have determined the magnetic structure to be proper helical one,[4] its ellipticity has not been clarified. Our recent study demonstrated that nonmagnetic Ga doping leads to the ferroelectric phase with the single magnetic modulation wave number.[5]

This time, we have performed the spherical neutron polarimetry analysis on the ferroelectric phase of $CuFe_{0.963}Ga_{0.037}O_2$ at the triple-axis spectrometer TAS-1 with the CRYOPAD option installed at JRR-3 in JAEA. In this experiment, we can measure the neutron polarization matrix with three dimensional components for incident and scattered neutrons.

Figure 1 shows scattering vector (of the magnetic reflection) dependence of the neutron polarization matrix term P_{yy} $(= -P_{zz})$. The experimental data was refined by least square analysis, where the refined parameter is the ellipticity $(\mu_{1\bar{1}0}/\mu_c)$. μ_c and $\mu_{1\bar{1}0}$ mean the momentum amplitude in the c and $1\bar{1}0$ spin components, respectively. As clearly seen in this figure, the refined ellipticity is not 1.0 but about 0.9.

For the verification of the theory above mentioned,[3] the understanding of the spacial modulation of the electric dipole moments coupled with magnetic moments, which was predicted to be with two times larger wave number than the magnetic one, is strongly desired. The presently determined elliptic magnetic structure will help understanding the microscopic coupling between spin and electric dipole moment.

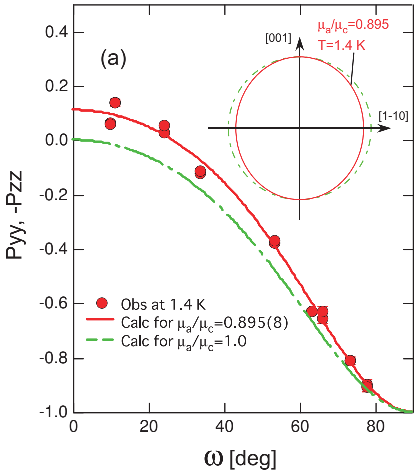

Figure 1: Comparison of the calculated curves and experimental data for the neutron polarization matrix terms, $P_{y,y}$ and $-P_{zz}$. ω is the relative angle between the hexagonal [110] axis and the scattering vector of each magnetic reflection. The dashed and solid lines denote the calculated curves for the ellipticity of 1.0 and 0.895, respectively.

References

1) T. Nakajima et al. :"Phys. Rev. B", 78, pp. 024106 (2008).
2) T. Nakajima et al. :"Phys. Rev. B", 78, pp. 214423 (2009).
3) T. Arima et al. :"J. Phys. Soc. Jpn." 76, pp. 073702 (2007)
4) T. Nakajima et al. :"J. Phys. Soc. Jpn.", 76, pp. 043709 (2007).
5) N. Terada et al. :"Phys. Rev. B", 78, pp. 014101 (2008).

原子炉：JRR-3　　装置：TAS-1(2G)　　分野：中性子散乱（磁性）

1-2-3

Magnetic and Structural Phase Transitions of $RbFeBr_3$

Y. Nishiwaki, K. Kakurai[1] and T. Kato[2]

Department of Physics, Tokyo Women's Medical University, Shinjuku-ku, Tokyo 162-8666
[1]*Quantum Beam Science Directorate, Japan Atomic Energy Agency, Tokai, Ibaraki 319-1195*
[2]*Faculty of Education, Chiba University, Inage-ku, Chiba 273-8522*

Among magnetic compounds with the ABX_3 chemical formula, the $CsNiCl_3$-type antiferromagnets take the perovskite-like structure with hexagonal close packed AX_3 layers, in which face-sharing BX_6 octahedra run as forming a -BX_3- chain along the *c*-axis. Their nearest-neighbor magnetic B^{2+} ions on the *c*-plane form a triangular lattice and give rise to spin frustration. There are several compounds, such as $KNiCl_3$, $RbMnBr_3$, $TlCoCl_3$ and $RbCoBr_3$, crystal structures of which are distorted from the prototype $CsNiCl_3$-structure through structural phase transitions. The lattice distortions are characterized by the shifts of the chains either upwards or downwards along the *c*-axis. The spin frustration is released by the distortion. In a certain case, breaking of inversion symmetry by the lattice distortion is accompanied with and the crystal structure is polar. We call these crystals members of the $KNiCl_3$-family. Most $KNiCl_3$-family compounds exhibit ferroelectricity at certain phases. We have been interested in how these lattice distortions and electric polarization affect the magnetism of those crystals and vice versa. In past, we determined the magnetic and crystal structures of $RbMnBr_3$[1)] (Heisenberg spin with easy plane anisotropy), $TlCoCl_3$[2)] (Ising spin), and $RbCoBr_3$[3)] (Ising spin) through the neutron diffraction measurements. In the present study, we performed the single-crystal neutron diffraction measurements in $RbFeBr_3$ which is one of the $KNiCl_3$ compounds. The magnetic phase transitions of $RbFeBr_3$ are described as the XY spin systems.

$RbFeBr_3$ undergoes successive structural phase transitions at $T_{\rm st1} = 109$ K and $T_{\rm st2} = T_{\rm C} = 39.5$ K. Below $T_{\rm C}$, ferroelectricity exhibits. In the present measurements, $(\frac{1}{3}\ \frac{1}{3}\ 2)$ peak was observed below $T_{\rm st1}$. The temperature dependence of this peak height shows an anomaly at $T_{\rm C}$. The antiferromagnetic phase transitions occur at $T_{\rm N1} = 5.5$ K and $T_{\rm N2} = 2.0$ K.[4)] Therefore, ferroelectricity and spin order are coexisted below $T_{\rm N1}$. The temperature dependence of the $(\frac{1}{3}\ \frac{1}{3}\ 1)$ and $(1\ 1\ 1)$ magnetic peak heights are shown in Fig. 1. The $(\frac{1}{3}\ \frac{1}{3}\ 1)$ peak is observed below $T_{\rm N1}$ but the $(1\ 1\ 1)$ peak is observed only below $T_{\rm N2}$. The spin structures at $T_{\rm N2} < T < T_{\rm N1}$ and $T < T_{\rm N2}$ are determined as the partial disordered and the triangular ones, respectively. We observed the small spontaneous magnetization perpendicular to the *c*-axis below $T_{\rm N1}$.

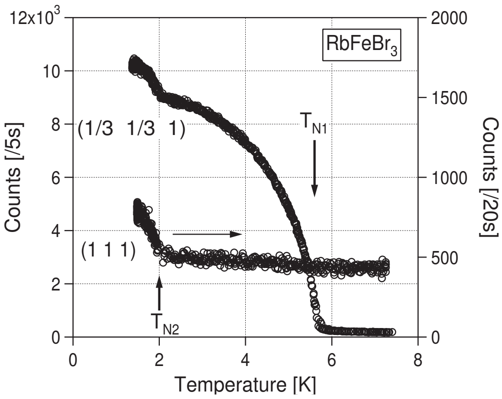

Figure 1: Temperature dependence of $(\frac{1}{3}\ \frac{1}{3}\ 1)$ (left axis) and $(1\ 1\ 1)$ (right axis) neutron diffraction peak heights of $RbFeBr_3$.

References

1) T. Kato: J. Phys. Soc. Jpn. **71** (2002) 300.
2) Y. Nishiwaki, T. Kato, Y. Oohara, A. Oosawa, N. Todoroki, N. Igawa, Y. Ishii, and K. Iio: J. Phys. Soc. Jpn. **75** (2006) 034707.
3) Y. Nishiwaki, T. Nakamura, A. Oosawa, K. Kakurai, N. Todoroki, N. Igawa, Y. Ishii, and T. Kato: J. Phys. Soc. Jpn. **77** (2008) 104703.
4) K. Adachi, K. Takeda, F. Matsubara, M. Mekata and T. Haseda: J. Phys. Soc. Jpn. **52** (1983) 2202.

原子炉：JRR-3　装置：TAS-2(T2-4)　分野：中性子散乱（磁性）

1-2-4

Crystal Structure Analysis and Magnetic Properties of Multiferroic System $\mathbf{Ni_{3(1-x)}Cu_{3x}V_2O_8}$

T. Kai, Y. Yasui, M. Sato, H. Fukazawa[1], N. Igawa[1], and K. Kakurai[1]

Department of Physics, Nagoya University, Furo-cho, Chikusa-ku, Nagoya 464-8602
[1]*Quantum Beam Science Directorate, JAEA, Tokai, Ibaraki 319-1195*

$Ni_3V_2O_8$ is an insulating system with Ni^{2+} spins (spin S=1) arranged in a kagomé staircase or in a buckled kagomé plane. The system exhibits three magnetic transitions at temperatures T_{c1}=9.1 K, T_{c2}=6.3 K and T_{c3}=3.9 K. In the region $T_{c2} < T < T_{c1}$, the spins have a sinusoidally modulated incommensurate structure with the spin direction along a and the modulation vector along a (HTI phase). In the region $T_{c3} < T < T_{c2}$, they have a helically modulated structure within the ab-plane with the modulation vector along a (LTI phase). Below T_{c3}, the weak spin canted ferromagnetic structure is realized with a commensurate modulation vector along a (C phase). The multiferroic behavior or the coexistence of magnetic and ferroelectric orders can be found in the region $T_{c3} < T < T_{c2}$.[1)] The helical magnetic structure originates from the competing nearest neighbor(J_1) and next nearest neighbor(J_2) interactions. For this system, impurity doping effects has been studied, because the Zn, Co, Mn and Cu substitution for Ni may change the magnetic and dielectric behaviors, and present information on the mechanism of the multiferroic phenomenon. Another interesting view point of the system is the existence of the successive magnetic transitions, because the system has the geometrical frustration inherent in the crystal structure. First, we have carried out measurements of the magnetization, specific-heat and dielectric properties of $Ni_{3(1-x)}M_{3x}V_2O_8$ (M=Zn, Co, Mn and Cu). For $Ni_{3(1-x)}M_{3x}V_2O_8$ (M=Zn, Co and Mn), all the three transition temperatures (T_{c1}, T_{c2} and T_{c3}) are found to monotonically decrease with increasing x. In contrast, for $Ni_{3(1-x)}Cu_{3x}V_2O_8$, T_{c3} was found to increase and T_{c1} and T_{c2} were found to decrease (The C phase is stabilized). In the samples with $x > 0.1$, the LTI phase is not found and the ferroelectricity does not exist. The crystal system changes from orthorhombic to monoclinic ones at around x=0.25 with increasing x. Next, to obtain detailed information on the crystal and magnetic structures of $Ni_{1.5}Cu_{1.5}V_2O_8$, the powder neutron diffraction measurements have been carried out at 50K and 3K by using the high resolution powder diffractometer (HRPD) installed at JRR-3 of JAEA in Tokai. The horizontal collimations were 12'-40'-6' and the neutron wavelength was 1.8231 Å. We have carried out the Rietveld analysis on the data at 50 K (paramagnetic phase), and the data can be almost explained by using the space group $P2_1/c$, where a=11.4369 Å, b=8.1350 Å, c=6.0880 Åand $\beta = 89.01°$. A schematic of the (Ni,Cu)O_6 octahedron is shown in the upper part of the figure. The z' axis of the local coordinates expands by the Cu-doping, which is considered to be due to the Jahn-Teller effect of the Cu^{2+} ions. The lower part of the figure shows the view of the cut plane parallel to the ab-plane of the one-dimensional chains of edge-sharing (Ni,Cu)O_6 octahedra. It indicates that the doped Cu^{2+} ions disconnect the some exchange interactions J_1 and J_2. The results seem to be related to the stability of the C phase at low temperature. We have determined the magnetic structure at T=3 K of $Ni_{1.5}Cu_{1.5}V_2O_8$; The characteristics of the ordering pattern are similar to those of C phase of $Ni_3V_2O_8$ except for the easy axis direction of spins.

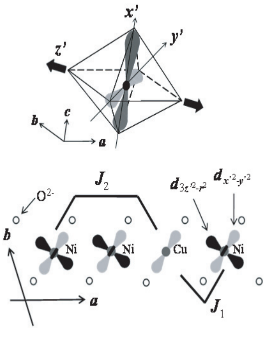

References

1) G. Lawes *et al.*; Phys. Rev. Lett. **95** (2005) 087205.

原子炉：JRR-3　　装置：HRPD(1G)　　分野：中性子散乱（磁性）

1-2-5

Studies of Multiferroic System of $LiCu_2O_2$ -Magnetic Structures of Two Ordered Phases with Incommensurate Modulations-

K. Sato, Y. Yasui, T. Moyoshi,Y. Kobayashi, M. Sato, and K. Kakurai[1]

Department of Physics, Nagoya University, Furo-cho, Chikusa-ku, Nagoya 464-8602
[1] *Quantum Beam Science Directorate, JAEA, Tokai, Ibaraki 319-1195*

By the combined work of neutron diffraction and ^{7}Li-NMR, the three dimensional magnetic structures of the multiferroic system $LiCu_2O_2$, which has four chains (ribbon chains) of edge-sharing CuO_4 square planes in a unit cell have been determined.[1,2] In the course of the studies, we have first realized that for the complete determination of its magnetic structures, it is insufficient to reproduce, by choosing a set of parameters, only one kind of experimental data, because we have to use a number of parameters to describe the modulated magnetic structures of the four ribbon chains. We have therefore applied experimental means of ^{7}Li-NMR and neutron magnetic scattering on single crystal samples, trying to consistently explain the data of these methods. The neutron experiments have been carried out on a single crystal of $^7LiCu_2O_2$ by using the triple axis spectrometer TAS-1 installed at JRR-3 of JAEA in Tokai. To avoid the large neutron absorption of Li nuclei, we used the ^{7}Li isotope in the measurements. The horizontal collimations were 40'-40'-80'-open, and the neutron wave length was 2.359 Å. The 002 reflection of Pyrolytic graphite (PG) was used as the monochromator. A PG filter was placed after the second collimator to suppress the higher-order contamination. The crystal was oriented with the [100] and [010] axes, in one case, and the [102] and [010] ones, in another case, in the scattering plane. The size of the crystals was $\sim 18 \times 16 \times 1$ mm^3, and the integrated intensities of 20 nonequivalent magnetic Bragg reflections were measured. In the analyses of the data, the anisotropic magnetic form factor for Cu^{2+} ions deduced from the $x^2 - y^2$ orbit was used, and the absorption corrections considering the shape of the single crystal were made. First, we have confirmed that the system has two successive magnetic transitions at $T_{N1} \sim 24.5$ K and $T_{N2} \sim 22.8$ K. In the temperature region between T_{N1} and T_{N2}, the magnetic structure has been found to be a sinusoidally modulated incommensurate one. At $T < T_{N2}$, an ellipsoidal helical spin structure with the incommensurate modulation has been found (Fig. 1). As stated above, by combining the NMR and neutron data, we have succeeded in the determination of detailed parameters related to the modulation amplitudes, helical axis vectors and relative phases of the modulations of four ribbon chains, which can reproduce both the NMR and neutron results, in the two magnetically ordered phases. This finding of the rather precise magnetic structures enables us to discuss the relationship between the magnetic structure and the multiferroic nature of the present system in zero magnetic field, and open a way how to understand the reported electric polarization under the finite magnetic field.

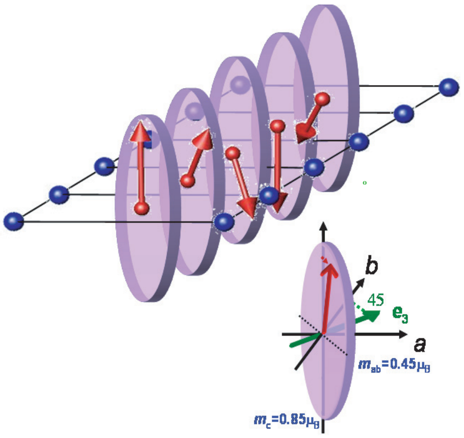

Figure 1: Magnetic structure of a CuO_2 ribbon chain in $LiCu_2O_2$ below T_{N2} is shown schematically. There are four chains in a unit cell and the relative phases of their modulations have also determined.

References

1) Y. Kobayashi, K. Sato, Y. Yasui, T. Moyoshi, M. Sato, and K. Kakurai: J. Phys. Soc. Jpn. **78** (2009) No. 8.
2) Y. Yasui, K. Sato, Y. Kobayashi, and M. Sato: J. Phys. Soc. Jpn. **78** (2009) No. 8.

原子炉：JRR-3　装置：TAS-1(2G)　分野：中性子散乱（磁性）

1-2-6

Crystal-Field Study of Clathrate Rare-Earth Compounds $Ce_3Pd_{20}(Si_{1-x}Ge_x)_6$ with Multi-Polar Ordering

H. Kitazawa, N. Terada, Y. Tsuchiya, Y. Kawamura, A. Kikkawa, A. Dönni, O. Sakai, M. Matsuda[1], K. Kakurai[1], Y. Nemoto[2] and T. Goto[2]

National Institute for Materials Science, 1-2-1 Sengen, Tsukuba, Ibaraki 305-0047
[1]*Japan Atomic Energy Agency (JAEA), 2-4 Shirakata Shirane, Tokai, Naka, Ibaraki 319-1195*
[2]*Graduate School of Science and Technology, Niigata University, Niigata 950-2181*

The rare-earth clathrate compounds $Ce_3Pd_{20}X_6$ (X = Si, Ge) crystallize in the C_6Cr_{23}- type structure belonging to the space group symmetry Fm$\bar{3}$m. In this structure, Ce atoms occupy two different crystallographic sites, 4a and 8c, both with a cubic point symmetry O_h and T_d, respectively. The heavy fermion compounds $Ce_3Pd_{20}Si_6$ [1)] and $Ce_3Pd_{20}Ge_6$ [2)] undergo successive quadrupole ordering (below $T_Q = 0.5$ K and 1.2 K, respectively) and antiferromagnetic ordering (below $T_N = 0.31$ K and 0.7 K, respectively). The inelastic neutron scattering (INS) experiment [3)] revealed that the crystalline field (CEF) scheme of Ce ions for both sites in $Ce_3Pd_{20}Ge_6$ consists of a Γ_8 quartet ground state and a excited Γ_7 doublet state, with a splitting energy of 4.0 meV at the 8c-site and 5.2 meV at the 4a-site. Very recently, however, we observed only one well-defined excitation of 3.7 meV at 5 K in $Ce_3Pd_{20}Si_6$, In order to investigate the origin of the single CEF excitation in $Ce_3Pd_{20}Si_6$, we have performed INS experiments in the pseudo-ternary systems $Ce_3Pd_{20}(Si_{1-x}Ge_x)_6$ using TAS2 spectrometer of JRR-3 in Tokai.

The INS spectrum of polycrystalline samples $Ce_3Pd_{20}(Si_{1-x}Ge_x)_6$ (x = 0, 0.1 0.3, 0.5 1) are shown in Fig. 1. Our data for x = 1 demonstrates a main peak at 4.0 meV (peak A) and a shoulder peak at 5.3 meV (peak B) which is consistent with the previous data [3)]. With decreasing x value, the peak B becomes unclear and the shape of the combined peak (A and B) remains asymmetric. In order to decompose the overlapping peaks into two Gaussian peaks, we assumed that the background forms a linear function and the ratio of their integrated intensity is equal to 2 : 1, which corresponds to the ratio of the number of Ce ions on the 8c- and 4a-site, respectively. We could fit all the experimental data by this simple model as shown by broken lines in Fig. 1. The x dependence of peak A is very weak. In contrast, with decreasing x value, the amplitude of peak B strongly decreases and the peak width increases. The CEF splitting at the 4a-site is affected by replacement of Si atoms for Ge atoms. It suggests that the characteristic of 4f electrons at 4a-site changes from localized state to itinerant or well-hybridized state.

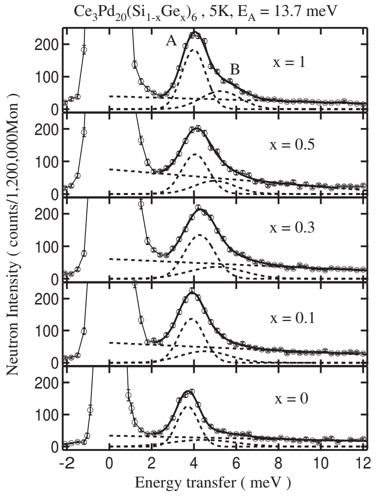

Figure 1: INS spectrum of $Ce_3Pd_{20}(Si_{1-x}Ge_x)_6$ (x = 0, 0.1 0.3, 0.5 1) at 5 K.

References

1) A. M. Strydom, et al. :“J. Phys. Conf. Ser.”, 51, pp. 239-242 (2006).
2) J. Kitagawa, et al. :“Phys. Rev. B”, 53, pp. 5101-5103 (1996).
3) L. Keller, et al. :“Physica B”, 259-261, pp. 336-337 (1999).

原子炉：JRR-3　　装置：TAS-2(T2-4)　　分野：中性子散乱（磁性）

1-2-7

Enhancement of the Two-Dimensional Spin Correlations in Ag doped $CuCrO_2$

R. Kajimoto, M. Matsuda[1], T. Kishimoto[2], K. Uto[2], T. Hokazono[2] and T. Okuda[2]
J-PARC Center, Japan Atomic Energy Agency, Tokai, Ibaraki 319-1195
[1] *Quantum Beam Science Directorate, Japan Atomic Energy Agency, Tokai, Ibaraki 319-1195*
[2] *Department of Nano-structures and Advanced Materials, Kagoshima University, Kagoshima 890-0065*

$CuCrO_2$ has a delafossite structure, where edge-shared CrO_6 octahedral layers and Cu layers stack alternatively. Since Cr^{3+} ions have $S = 3/2$ spins and they form a two-dimensional (2D) triangular lattice, $CuCrO_2$ attracted attention as one of the 2D antiferromagnet. In spite of the layered crystal structure, the spins of Cr ions have finite interplanar coupling, which yields three-dimensional (3D) magnetic ordering below $T_N = 26$ K. The magnetic structure is a 120° structure with the spins lying on the *ac* plane.$^{1)}$ Recently, however, it was revealed by a specific heat study that substitution of Cu^+ ion ($3d^{10}$) with Ag^+ ion ($4d^{10}$) induces crossover from 3D to 2D low-energy magnetic excitations in addition to the decrease of T_N.$^{2)}$ In the present study, we studied $Cu_{1-x}Ag_xCrO_2$ by neutron diffraction to confirm the dimensional crossover of magnetic correlations by Ag doping. The sample was powders of $x = 0$ and 0.15 ($T_N = 14$ K). The neutron diffraction measurements were performed using the triple-axis spectrometer TAS-2 with an incident energy $E_i = 14.7$ meV.

Figure 1(a) shows powder diffraction patterns of $Cu_{0.85}Ag_{0.15}CrO_2$ at 6, 15, and 100 K. At 6 K, 3D magnetic Bragg peaks are observed at $(q, q, 0)$, $(q, q-1, 0)$, $(q-1, q, 2)$, $(q, q, 3)$, etc. with $q \sim 1/3$. By investigating the peak positions in detail, we found that q is slightly different form 1/3 and it was 0.328. Interestingly, this incommensurability is almost same as that reported in the end compound, $AgCrO_2$ (0.327).$^{3)}$ At a temperature just above T_N (15 K), the Bragg peaks disappear, but intense broad scattering remains around $(q, q, 0)$. The profile of this broad scattering has a skewed structure, which is a typical profile of a 2D system. The 2D correlations were also evidenced by the fact that this scattering profile can be well fitted to the Warren function$^{4)}$, as shown by a broad solid line in Fig. 1(a). As a comparison, we also performed similar measurements on the non-doped ($x = 0$) sample [Fig. 1(b)]. The non-doped sample also shows the 2D scattering just above T_N, but the ratio of the 2D scattering intensity to the 3D Bragg peaks is much reduced compared with $x = 0.15$. These results clearly indicate that 2D character in the magnetic correlations is much enhanced by the Ag doping.

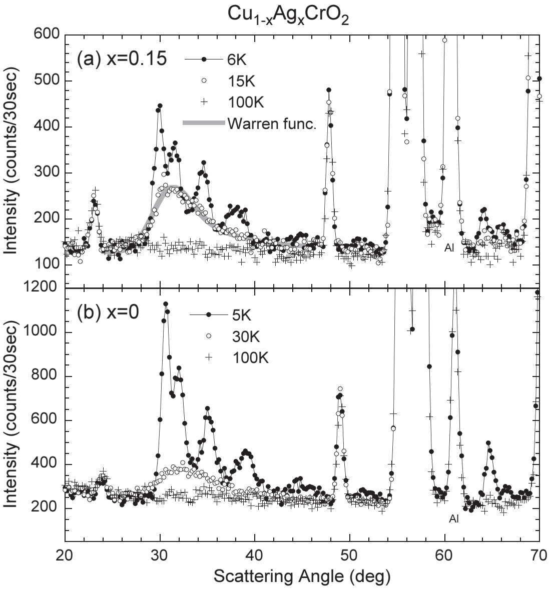

Figure 1: Powder neutron diffraction patterns of (a) $Cu_{0.85}Ag_{0.15}CrO_2$ and (b) $CuCrO_2$.

References

1) H. Kadowaki *et al.*, J. Phys.: Condens. Matter 2, 4485 (1990).
2) T. Okuda *et al.*, J. Phys. Soc. Jpn. 78, 013604 (2009).
3) Y. Oohara *et al.*, J. Phys. Soc. Jpn. 63, 847 (1994).
4) B. E. Warren, Phys. Rev. 59, 693 (1941).

原子炉：JRR-3　装置：TAS-2(T2-4)　分野：中性子散乱（磁性）

1-2-8

Dynamical Character of the Two-Dimensional Spin Correlations in Ag doped $CuCrO_2$

R. Kajimoto, M. Matsuda[1], T. Kishimoto[2], K. Uto[2], T. Hokazono[2] and T. Okuda[2]

J-PARC Center, Japan Atomic Energy Agency, Tokai, Ibaraki 319-1195
[1]*Quantum Beam Science Directorate, Japan Atomic Energy Agency, Tokai, Ibaraki 319-1195*
[2]*Department of Nano-structures and Advanced Materials, Kagoshima University, Kagoshima 890-0065*

Delafossite oxide $CuCrO_2$ is one of the two-dimensional (2D) triangular antiferromagnets. In this compound, $S = 3/2$ spins of Cr^{3+} ions form a 2D triangular lattice. The Cr layers are separated from each other by Cu layers. However, the coupling between the Cr layers is strong enough to yield a three-dimensional (3D) magnetic ordering with a 120° structure below $T_N = 26$ K.$^{1)}$ Recently, however, it was revealed by a specific heat study that substitution of Cu^+ ion ($3d^{10}$) with Ag^+ ion ($4d^{10}$) induces crossover from 3D to 2D low-energy magnetic excitations.$^{2)}$ As mentioned elsewhere, we have performed neutron diffraction measurements on the powder sample of $Cu_{0.85}Ag_{0.15}CrO_2$ using the triple-axis spectrometer TAS-2, and confirmed that the 2D scattering at a temperature just above T_N is much enhanced compared with the non-doped compound.$^{3)}$ In the present study, we performed high-energy-resolution neutron scattering measurements on a powder sample of $Cu_{0.85}Ag_{0.15}CrO_2$ to clarify the character of the 2D magnetic correlations. The measurements were performed using the triple-axis spectrometer LTAS with a scattered neutron energy E_f being fixed at 3.5 meV.

Figure 1 (a) shows temperature dependence of elastic scattering profiles of the magnetic scatterings. In contrast to the result at TAS-2,$^{3)}$ the 2D scattering at 15 K is much reduced. The difference in the 2D scattering intensity can be attributed to the difference in the energy resolution ($\Delta E = 1.2$ meV at TAS-2 and 0.2 meV at LTAS). If the 2D scattering is dominated by an inelastic component, the elastic scattering intensity is apparently reduced in the high-energy-resolution measurement at LTAS. The dynamical character was more directly evidenced by an energy scan, which is shown in Fig. 1(b). We observed that the magnetic scattering spreads to the energy of ~0.8 meV. From the present study, we confirmed that the 2D magnetic correlations in $Cu_{0.85}Ag_{0.15}CrO_2$ consists mostly of dynamical component.

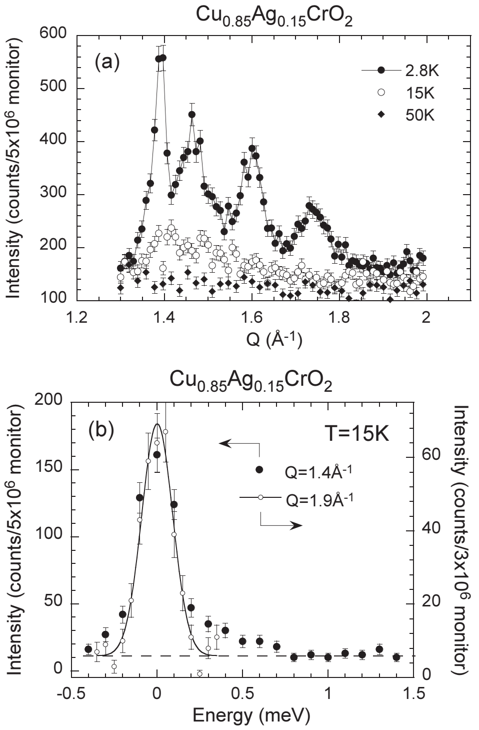

Figure 1: (a) Powder neutron diffraction patterns of $Cu_{0.85}Ag_{0.15}CrO_2$ at 2.8, 15, and 50 K. (b) Energy scan profiles of $Cu_{0.85}Ag_{0.15}CrO_2$ at 15 K measured at $Q = 1.4$ Å^{-1} and 1.9 Å^{-1}. The latter profile represents the energy resolution.

References

1) H. Kadowaki *et al.*, J. Phys.: Condens. Matter 2, 4485 (1990).
2) T. Okuda *et al.*, J. Phys. Soc. Jpn. 78, 013604 (2009).
3) R. Kajimoto *et al.*, this issue.

原子炉：JRR-3　装置：LTAS(C2-1)　分野：中性子散乱（磁性）

1-2-9

Spin Correlations in a Frustrated Spinel Antiferromagnet LiCrMnO$_4$

M. Matsuda, Z. Honda[1], H. Aruga Katori[2], H. Takagi[2], H. Ueda[3], Y. Ueda[3], H. Mitamura[3]
and K. Kindo[3]

Quantum Beam Science Directorate, JAEA, Tokai, Ibaraki 319-1195
[1] *Graduate School of Science and Engineering, Saitama University, Saitama, Saitama 338-8570*
[2] *RIKEN, Wako, Saitama, 351-0198*
[3] *The Institute for Solid State Physics, The University of Tokyo, Kashiwa, Chiba 277-8581*

Geometrically frustrated antiferromagnets show interesting phenomena originating from the macroscopic ground state degeneracy. The pyroclore lattice, in which corner-sharing tetrahedra of the magnetic ions are linked three-dimensionally, is known as highly frustrated magnetic system.

LiCrMnO$_4$ has the spinel structure, in which the Cr^{3+} and Mn^{4+} moments with S=3/2 are randomly located at the corners of the tetrahedron in pyrochlore lattice. 1) It shows a spin-glass behavior below $T_g \sim$13 K suggested from the magnetic susceptibility experiments. In order to clarify the magnetic properties from the microscopic point of view, we performed neutron scattering experiments on TAS-2. It was found that short-range spin correlations with characteristic $Q \sim$0.6 and 1.6 Å^{-1} develop at low temperatures, as shown in Fig.1. The spin correlation with $Q \sim$1.6 Å^{-1} (phase I) is explained by the antiferromagnetic fluctuations originating from the hexagonal spin clusters, which is proposed in ZnCr$_2$O$_4$ above T_N. 2) Although the origin of the spin correlation with $Q \sim$0.6 Å^{-1} (phase II) is still unknown, the spin correlation probably originates from a new magnetic state in highly frustrated pyrochlore lattice.

LiCrMnO$_4$ also shows an interesting behavior in magnetic field. Magnetization in LiCrMnO$_4$ gradually increases and saturates at $\sim$1/2 of the full moment ($3\mu_B$). This phenomenon is similar to the half-magnetization plateau observed in ACr$_2$O$_4$ (A: Cd and Hg), which originates from a strong spin-lattice coupling. 3) We performed neutron scattering experiments in LiCrMnO$_4$ in magnetic field up to 10 T to clarify the origin of the plateau-like state. It was found that the magnetic peak at $Q \sim$0.6 Å^{-1} is suppressed with increasing magnetic field although the magnetic peak at $Q \sim$1.6 Å^{-1} is robust. This result suggests that the saturation of the magnetization is not related with the spin-lattice coupling as in ACr$_2$O$_4$ but spins in phase II first align ferromagnetically in low magnetic field. This indicates that the magnetic interactions in phase II are relatively small, suggesting that the phase II is formed by further-neighbor interactions.

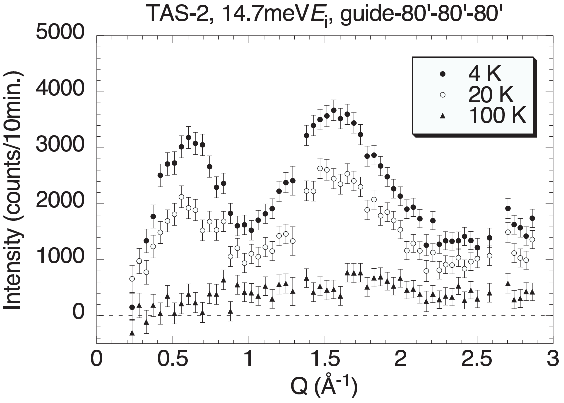

Figure 1: Neutron diffraction patterns at 4, 20 and 100 K in LiCrMnO$_4$. The background intensity measured at 200 K is subtracted.

References

1) M. Tachibana *et al.*: Phys. Rev. B 66, 092406 (2002).
2) S.-H. Lee *et al.*: Nature 418, 856 (2002).
3) H. Ueda *et al.*: Phys. Rev. Lett. 94: 047202 (2005); H. Ueda *et al.*: Phys. Rev. B 73, 094415 (2006); M. Matsuda *et al.*: Nature Phys. 3, 397 (2007).

原子炉：JRR-3　　装置：TAS-2(T2-4)　　分野：中性子散乱（磁性）

1-2-10

Magnetic Field-Induced Transitions in the Spinel $GeCo_2O_4$

M. Matsuda, T. Hoshi[1,2], H. Aruga Katori[2], M. Kosaka[1] and H. Takagi[2]
Quantum Beam Science Directorate, JAEA, Tokai, Ibaraki 319-1195
[1] *Graduate School of Science and Engineering, Saitama University, Saitama, Saitama 338-8570*
[2] *RIKEN, Wako, Saitama, 351-0198*

The spinel $GeCo_2O_4$ shows an antiferromagnetic ordering with a characteristic wave vector of $\mathbf{Q}_M$=(1/2, 1/2, 1/2) below T_N ∼21 K accompanied with a structural phase transition from cubic to tetragonal symmetry. Recently, magnetic properties of $GeCo_2O_4$ in magnetic field were studied by magnetization measurements. 1,2) It was reported that magnetization in polycrystalline $GeCo_2O_4$ exhibits an anomaly at H=4.25 and 9.70 T, which correspond to magnetic transitions. 1) The magnetization measurements using single crystal also show magnetic phase transitions at H ∼4.5 and 10 T, depending on the magnetic field directions. 2) The anomaly at H ∼4.5 T is observed only when the field is applied along the (110) and (111) directions. In order to understand the magnetic interactions in $GeCo_2O_4$, it is important to determine the magnetic structure in the magnetic field-induced phases.

In order to clarify the magnetic structure in magnetic field, we performed neutron diffraction experiments on TAS-2 using polycrystalline sample of $GeCo_2O_4$. We first confirmed that the magnetic structure in zero magnetic field is consistent with that reported previously. 1) The magnetic structure is basically the same as that in $GeNi_2O_4$ below $T_{\mathrm{N}2}$, in which the spin arrangement is ferromagnetic in the kagomé and triangular planes and antiferromagnetic between the kagomé and triangular planes. 3) With applying magnetic field, the magnetic Bragg intensities change drastically, originating from both change in magnetic structure and orientation of magnetic domains, as shown in Fig. 1. We found that the effect of the domain orientation is not so distinct at higher temperatures and performed Rietveld refinement analysis. Fortunately, an overall feature of the magnetic structure in magnetic field could be determined even with powder sample. The spin arrangement between the triangular planes becomes ferromagnetic around 4 T and the spin arrangement between the kagomé planes also becomes ferromagnetic gradually above ∼4 T. Finally, all the spins align ferromagnetically along the field direction at ∼10 T. These results suggest that the kagomé and triangular planes become more decoupled in magnetic field, which is similar to the behavior of $GeNi_2O_4$ in zero magnetic field. 3)

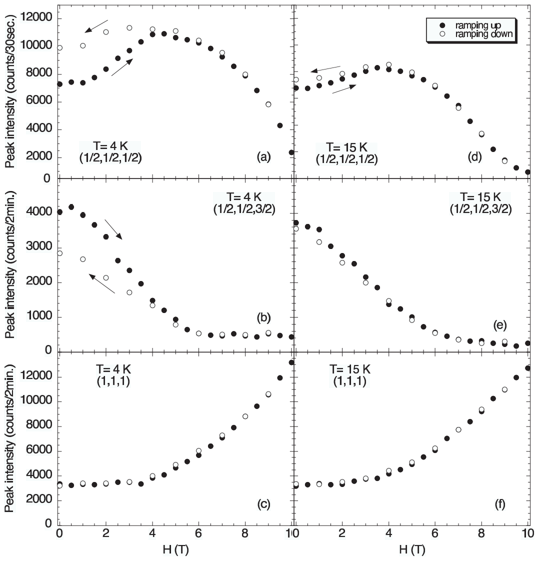

Figure 1: Magnetic field dependence of the magnetic Bragg intensities at (1/2, 1/2, 1/2), (1/2, 1/2, 3/2) and (1, 1, 1).

References

1) S. Diaz *et al.*: Phys. Rev. B 74, 092404 (2006).
2) T. Hoshi *et al.*: J. Mag. Mag. Mater. 310, e448 (2007).
3) M. Matsuda *et al.*, Europhys. Lett. 82,37006 (2008).

原子炉：JRR-3　　装置：TAS-2(T2-4)　　分野：中性子散乱（磁性）

1-2-11

High-Pressure Neutron Diffraction Study of Magnetic Properties in DyB_2C_2

H. Yamauchi and T. Osakabe

Quantum Beam Science Directorate, JAEA, Tokai, Ibaraki 319-1195

The tetragonal DyB_2C_2 shows an antiferroquadrupolar (AFQ) order below $T_Q = 24.7\,K$ in zero magnetic field$^{1)}$. Below $T_N = 15.3\,K$ the antiferromagnetic (AFM) order competitively coexists with the AFQ order. The magnetic structure in the coexistent phase is described by $\boldsymbol{k}_1 = (1, 0, 0)$ and $\boldsymbol{k}_2 = (0, 1, 1/2)$ to give the basic 90° structure along the c-axis, plus $\boldsymbol{k}_3 = (0, 0, 0)$ and $\boldsymbol{k}_4 = (0, 0, 1/2)$ to give the additional slight canting of magnetic moments in the c-plane. The situation with the variation of DyB_2C_2 magnetic properties under pressure is not so clear as that with ambient pressure properties. There is only one published report where the electrical resistivity studies were carried out on application of hydrostatic pressure up to $3.1\,GPa^{2)}$. We performed the neutron diffraction experiments under high pressures up to 8.8 GPa on a single crystal DyB_2C_2 in order to investigate the $P-T$ phase diagram and magnetic structure under pressure.

The single crystal of $Dy^{11}B_2C_2$ was prepared by the Czochralski method with a tetra-arc furnace. The sample was cut and shaped in a rectangle of $0.7 \times 0.7 \times 0.2\ mm^3$. We succeed in experiments using an opposed pair of large anvils, named “hybrid-anvil cell”$^{3)}$. The measurements were carried out in the a^*- a^* reciprocal lattice plane with a neutron wavelength of 2.444 Å. All the collimators and PG filter were taken away to intensify the possible neutron beam flux.

Figure 1-(a) shows the pressure dependence of T_N in DyB_2C_2. The transition temperatures are determined from the temperature dependence of the peak intensity of AFM 1 0 0 reflection under pressure. The results of ref. 2) are concurrently shown for comparison in the figure. The T_N increases linearly with pressure up to ~6 GPa and seems to decrease above ~7 GPa. On the other hand, the T_Q decreases with increasing pressure and seems to merge with T_N at ~7 GPa. Contrary to the pressure dependence of T_N, it is mysterious that the $\boldsymbol{k}_1$ components of magnetic structure is suppressed by pressure as shown in Fig. 1-(b), since the AFM order described by the wave vector of $(1, 0, 0)$, which is observed in most of the RB_2C_2 system, are considered to reflect the basic magnetic interactions in DyB_2C_2. It is, therefore, necessary to measure $\boldsymbol{k}_2$ components which reflect the existence of the competitive AFQ interactions and to consider the effects of the frustration between the AFQ and AFM interactions.

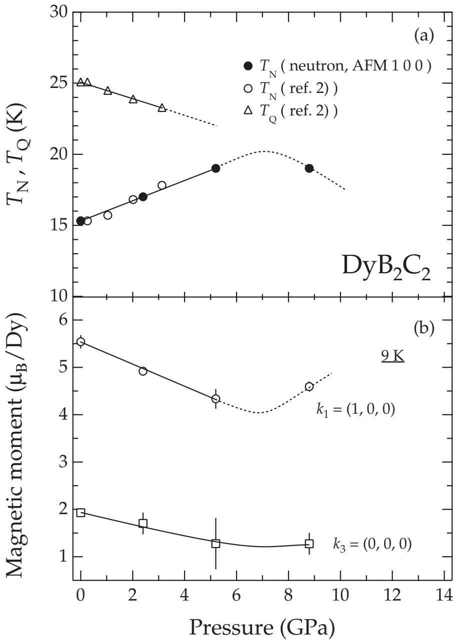

Figure 1: The pressure dependence of (a) T_N, T_Q and (b) $\boldsymbol{k}_1$, $\boldsymbol{k}_3$ components of magnetic structure at ~9 K in DyB_2C_2. Lines are guide for eyes.

References

1) H. Yamauchi *et al.*: J. Phys. Soc. Jpn., 68, 2057 (1999).
2) M. Kosaka *et al.*: “Spring Meeting of Phys. Soc. Jpn.”, 22pZF-5 (March, 2000).
3) T. Osakabe *et al.*: J. Magn. Magn. Mater. 310, 2725 (2007).

原子炉：JRR-3　　装置：TAS-1(2G)　　分野：中性子散乱（磁性）

1-2-12

Nematic-to-Smectic Transition of Magnetic Texture in Conical State

M. Takeda[1,2], Y. Endoh[1,3], K. Kakurai[1], Y. Onose[4], J. Suzuki[2] and Y. Tokura[4,5]

[1] *Quantum Beam Science Directorate, Japan Atomic Energy Agency, Tokai, Ibaraki 319-1195, Japan*
[2] *J-PARC Center, Tokai, Ibaraki 319-1195, Japan*
[3] *International Institute for Advanced Studies, Kizugawa, Kyoto 619-0225, Japan*
[4] *Department of Applied Physics, University of Tokyo, Tokyo 113-8656, Japan*
& ERATO Multiferroics Project, JST, c/o University of Tokyo, Tokyo 113-8656, Japan
[5] *Cross-Correlated Materials Research Group, ASI, RIKEN, Wako 351-0198, Japan*

Unconventional magnetic properties such as the anomalous Hall effect$^{1)}$ and quantum phase transition under high pressure$^{2)}$ in the helimagnetic phase of the MnSi family have currently attracted considerable interest. The non-centrosymmetric crystal structure of a simple cubic lattice (P_{2_13}, or B20 type) is inherent in the MnSi family including $\mathrm{Fe}_{1-x}\mathrm{Co}_x\mathrm{Si}$. This low symmetry of the crystal structure hosts a long-range helimagnetic spiral spin modulation via the Dzyalosinsky-Moriya (DM) interaction.

The microscopic structure of spin moments, particularly the complex structures of an antiferromagnet with a long-range spin modulation cannot be exclusively determined without neutron magnetic scattering study$^{3)}$. In this study, we found unique neutron diffraction patterns manifesting the existence of a complex magnetic texture in the bulk material of $\mathrm{Fe}_{0.7}\mathrm{Co}_{0.3}\mathrm{Si}$.

Measurements of SANS have been performed using SANS-J-II. A single crystal of $\mathrm{Fe}_{0.7}\mathrm{Co}_{0.3}\mathrm{Si}$ ($\sim$0.1 cm^3) grown by the floating zone method$^{4)}$. The helical spin modulation is changed to the commensurate ferromagnetic order through a conical spin state by applying external magnetic field. The external field was applied up to 0.2 T where the spiral phase disappears. Temperature was controlled between 4 and 60 K.

Figure 1 shows magnetic field dependence of the color-coded scattering profiles on a common logarithmic scale at 4.5 K. The representative patterns show clear changes in scattering profiles, i.e., circular → ellipsoidal → crescent → double dots, with field application along the [100] axis. This indicates that a phase transition of magnetic texture occurs. Throughout this phase transition, the change in the diffraction patterns is very similar to that observed in the nematic and smectic phase transitions of liquid crystals. The details of this study will be reported elsewhere$^{5)}$.

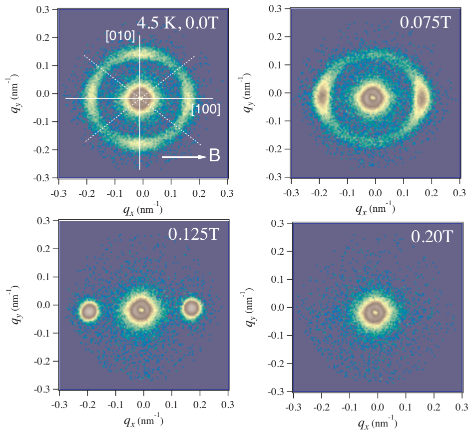

Figure 1: Magnetic field dependence of the color-coded scattering profiles. The external magnetic field was increased from $\mu_0 H = 0$ to 0.2 T at 4.5 K.

References

1) M. Lee, Y. Onose, Y. Tokura, and N. P. Ong: Phys. Rev. B **75** (2007) 172403.
2) C. Pfleiderer, G. J. McMullan, S. R. Jurian, and G. G. Lonzarich: Phys. Rev. B **55** (1997) 8330.
3) G. L. Squires: *Introduction to the Theory of Thermal Neutron Scattering* (Dover, New York, 1996) p. 186.
4) Y. Onose, N. Takeshita, C. Terakura, H. Takagi, and Y. Tokura: Phys. Rev. B **72** (2005) 22443.
5) M. Takeda, Y. Endoh, K. Kakurai, Y. Onose, J. Suzuki, and Y. Tokura: J. Phys. Soc. Jpn. in press.

原子炉：JRR-3　　装置：SANS-J(C3-2)　　分野：中性子散乱（磁性）

1-2-13

Anisotropic Spin Freezing in Lightly-Doped $La_{2-x}Sr_xCuO_4$

M. Matsuda, M. Fujita[1], M. Takeda, K. Kakurai and K. Yamada[1]

Quantum Beam Science Directorate, JAEA, Tokai, Ibaraki 319-1195
[1]*Institute for Materials Research, Tohoku University, Sendai 980-8577*

The interplay between magnetism and conductivity is crucial to understand the mechanism of superconductivity in high-T_c cuprate superconductors. The mother compound La_2CuO_4 shows a Néel ordering below ∼320 K. When hole carriers are doped, the magnetic ordering is quickly destroyed at $x{\sim}0.02$. The short-ranged magnetic correlations remain even above $x{\sim}0.02$. Extensive neutron-scattering studies have shown that the spin correlations of the short-ranged magnetic phase are incommensurate. Furthermore, the static spin modulation in $La_{2-x}Sr_xCuO_4$ changes from being diagonal to parallel at $x{\sim}0.055$, coincident with the insulator-to-superconductor transition [1,2]. This shows an intimate relation between magnetism and conductivity. One possibility to explain the diagonal incommensurate spin correlations is the stripe model. On the other hand, the diagonal incommensurate spin correlations can be explained using the spiral model, originating from magnetic frustration caused by the localized hole spins. In order to understand the nature of the incommensurate spin correlations in this region, it is important to clarify the magnetic anisotropy (Heisenberg, XY, or Ising) and determine the spin Hamiltonian.

Inelastic neutron scattering experiments were performed to observe the zone center gap originating from the magnetic anisotropy in the diagonal incommensurate phase [3]. Since the magnetic excitations become broadened, it is not clear whether the gap disappears or the magnetic excitations are just smeared out so that the gap is difficult to be identified.

Polarized neutron scattering is an important tool to clarify the magnetic anisotropy in the magnetic materials. Using three-dimensional (3D) polarization analysis [4], we clarified the magnetic anisotropy in $La_{1.982}Sr_{0.018}CuO_4$ and determined that the XY model is the most suitable model to describe the low energy spin fluctuations.

Unpolarized neutron scattering measurements were performed on TAS-2. The fixed initial neutron energy was 14.7 meV with an instrumental energy resolution of $\Delta E \sim 1.6$ meV. Polarized neutron scattering measurements were performed using CRYOgenic Polarization Analysis Device (CRYOPAD) installed on TAS-1[5]. Heusler alloy (111) crystals were used as monochromator and analyzer. A flipping ratio of ∼30 was measured at the nuclear (200) reflection, corresponding to 93% polarization of the beam. The incident neutron energy was fixed at E_i=14.7 meV with an instrumental energy resolution of $\Delta E \sim 1.7$ meV.

It was previously reported that $La_{1.982}Sr_{0.018}CuO_4$ exhibits a Néel ordering and spin-glass behavior at low temperatures [6]. The spin-glass phase shows short-ranged antiferromagnetic ordering with diagonal incommensurate correlations. Since the magnetic correlation perpendicular to the CuO_2 plane is finite, a modulation of scattering intensity along L direction is observed, as shown in Fig. 1. The correlation length along the c axis was estimated to be 11 Å[6], which almost corresponds to c. The signal contains quasi-elastic component with finite energy fluctuations ($|E| < \Delta E$). It is noted that the incommensurate magnetic peaks are not in the scattering plane, as shown in Fig. 1. The vertically elongated instrumental resolution integrates the two peaks effectively. There also exist magnetic Bragg peaks at the commensurate positions (1, 0, *even*), which originate from the Néel ordering. However, since the peaks are very sharp, the broad signal shown in Fig. 1 purely comes from the spin-glass phase.

In the porlarization analysis we measured

原子炉：JRR-3　　装置：TAS-1(2G)　　分野：中性子散乱（磁性）

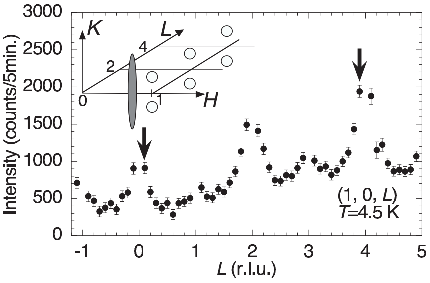

Figure 1: Magnetic elastic scattering in $La_{1.982}Sr_{0.018}CuO_4$ at (1, 0, L) at T=4.5 K, measured with unpolarized neutrons. The background signal measured at 60 K was subtracted. The arrows show the positions where the neutron polarization analysis was performed. The inset shows the configuration of incommensurate magnetic Bragg peaks in the ($H0L$) scattering plane. The vertically elongated instrumental resolution, shown by a shaded ellipsoid, effectively integrates the two magnetic peaks (open circles), which are located above and below the scattering plane.

Table 1: Polarization matrix elements P_{if} observed at (1, 0, 0.1).

$i \setminus f$	x	y	z
x	-0.9(1)	0.09(8)	0.03(7)
y	0.11(9)	-0.7(1)	0.00(7)
z	0.04(8)	-0.05(8)	0.7(1)

two diffuse magnetic peaks at (1, 0, 0.1) and (1, 0, 3.9). The neutrons observe only the spin component perpendicular to Q. Therefore, at (1, 0, 0.1), where Q is almost along the a axis, the magnetic anisotropy in the bc plane can be observed. On the other hand, at (1, 0, 3.9), where Q is ~60° tilted from the ab plane, the magnetic anisotropy mostly in the ab plane can be observed. Combining these two results, it is possible to estimate the magnetic anisotropy in the spin-glass phase.

Table 1 shows the results of 3D polarization analysis at (1, 0, 0.1) in the spin-glass phase of $La_{1.982}Sr_{0.018}CuO_4$. The polarization matrix has nine elements P_{if} with i, f=x, y, and z, where i and f represent "initial" and "final", respectively. Since the signal is purely magnetic in origin, P_{xx} corresponds to initial beam polarization. It was observed that all the non-diagonal terms are negligibly small. P_{yx} and P_{zx} are chiral terms that should become finite in the presence of helicity in the magnetic structure. In the present experiment, the chiral terms should become zero in principle even when the structure has helicity, since two incommensurate peaks, which are related with positive and negative helicities, are integrated so that two contributions are cancelled out. We plan to perform polarized neutron scattering experiments to clarify the helicity in the future. From the polarization components P_{yy}, P_{yz}, P_{zy} and P_{zz}, it was estimated that the ratio between the spin components along the b axis (S_b) and along the a axis (S_a) is S_b/S_a ~1.2.

Table 2: Polarization matrix elements P_{if} observed at (1, 0, 3.9).

$i \setminus f$	x	y	z
x	-0.90(8)	0.00(4)	0.03(4)
y	0.04(4)	-0.25(3)	0.05(4)
z	0.01(4)	-0.01(4)	0.32(6)

Table 2 shows the results of 3D polarization analysis at (1, 0, 3.9). The polarization components are similar to those at (1, 0, 0.1) except P_{yy} and P_{zz}. From these values, it was estimated that the ratio between S_b and the spin component along the c axis (S_c) is S_c/S_b ~0.15.

From the above two results, we conclude that $S_a : S_b : S_c$~0.8 : 1.0 : 0.15. It was found that the low energy spin fluctuations ($|E|$<1.7 meV) have the XY anisotropy in $La_{1.982}Sr_{0.018}CuO_4$ although there also exists a small Ising anisotropy along the b axis in the ab plane. This reminds us that pure La_2CuO_4 shows a Néel ordering with an easy axis along the b axis.

References

1) S. Wakimoto *et al.*, Phys. Rev. B **60**, R769 (1999).
2) M. Fujita *et al.*, Phys. Rev. B **65**, 064505 (2002).
3) M. Matsuda *et al.*, Phys. Rev. B **62**, 9148 (2000).
4) F. Tasset, Physica B **156-157**, 627 (1989).
5) M. Takeda *et al.*, Physica B **356**, 136 (2005).
6) M. Matsuda *et al.*, Phys. Rev. B **65**, 134515 (2002).

1-2-13

1-2-14

Magnetic Structural Analysis of Magnetic Multilayers for Read Sensor Heads by Polarized Neutron Reflectometry

M. Takeda[1,2], D. Yamazaki[1,2] and T. Hirano[3]

[1] *Quantum Beam Science Directorate, Japan Atomic Energy Agency, Tokai, Ibaraki 319-1195, Japan*
[2] *J-PARC Center, Tokai, Ibaraki 319-1195, Japan*
[3] *Hitachi Research Laboratory, Hitachi Ltd., Hitachi, Ibaraki, Japan*

A read sensor head is one of key elements to achieve higher recording density of hard disk drives (HDDs). The read sensor head of HDD consists of several ferromagnetic, antiferromagnetic, and noble metal layers. The characterization of the magnetic interfacial structure in these magnetic multilayers is indispensable for producing the high-performance and high-reliability read sensor heads, because the device properties strongly depend on the structure.

Neutron reflectometry is a powerful and nondestructive technique to investigate the internal layered structures, and gives us the information on the depth profile of magnetization vector of the magnetic multilayers in the reflection plane. When polarized neutron is used, the sensitivity to the magnetization is much enhanced$^{1)}$. Therefore, polarized neutron reflectometry is an unrivaled way to analyze the internal magnetic structure in magnetic multilayers.

Figure 1 shows a typical example of the investigation of the magnetic multilayers for the read sensor heads using a new neutron reflectometer, SUIREN, installed at the C2-2 cold neutron beam port of the beam hall in JRR-3, of JAEA$^{2)}$. Structures of the samples are described as Si(substrate)/Ta(5 nm)/Ru(5 nm)/MnIr(x nm)/CoFe(2 nm)/Cu(1nm)/Ru(2 nm) (x = 3.0 (sample A) and 5.0 (sample B)). Exchange bias between the CoFe and MnIr layers of sample B is larger than that of sample A.

The reflectivity was measured under an external magnetic field of 1.8 kOe perpendicular to the magnetized direction. An intermediate layer at the interface between the CoFe and MnIr layers was found only in sample B. This intermediate layer may be a key to elucidate the mechanism of the exchange bias effect. The details of this experiment will be reported elsewhere.

References

1) G. P. Felcher, R. O. Hilleke, R. K. Crawford, J. Haumann, R. Kleb, and G. Ostrowski, Rev. Sci. Instrum. **58**, 609 (1986).
2) D. Yamazaki, M. Takeda, I. Tamura, R. Maruyama, A. Moriai, M. Hino, K. Soyama, Physica B **404**, 2557 (2009).

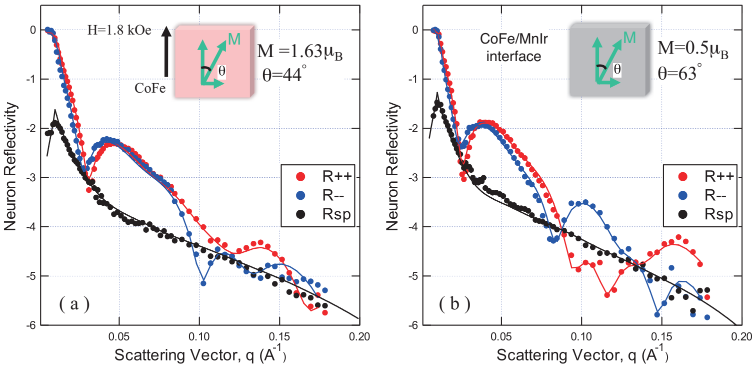

Figure 1: Difference of the polarized neutron reflectivity curves with a change of thickness of the MnIr layer; (a) 3 nm and (b) 5 nm. An external magnetic field of 1.8 kOe was applied perpendicular to the magnetized axis.

原子炉：JRR-3　　装置：SUIREN(C2-2)　　分野：中性子散乱（磁性）

1-2-15

Acquirement of a Guiding Principle Towards the Dy-free or Dy-less High Performance Nd-Fe-B Sintered Magnets by Investigation of the Origin of the Coercivity with Interfacial Structural Analysis

M. Takeda[1,2,4], J. Suzuki[2], D. Yamaguchi[3], T. Akiya[4],H. Kato[4,5], Y. Une[6] and M. Sagawa[4,6]
[1]*QuBS, Japan Atomic Energy Agency, Tokai-mura, Ibaraki, 319-1195, Japan*
[2]*J-PARC Center, Tokai-mura, Ibaraki, 319-1195, Japan*
[3]*ASRC, Japan Atomic Energy Agency, Tokai-mura, Ibaraki, 319-1195, Japan*
[4]*New Industry Creation Hatchery Center, Tohoku Univ., Sendai, Miyagi, 980-8579, Japan*
[5]*Depertment of Applied Mathematics and Physics, Yamagata University,*
Yonezawa, Yamagata, 992-8510, Japan
[6]*Intermetallics Co., Ltd., Kyodaikatsura #303, 1-36 Goryo Ohara, Nishikyo-Ku,*
Kyoto, 615-8245, Japan

Nd-Fe-B magnets are useful permanent magnets utilized in many applications such as motors, HDD and mobile phones. Recently, they are used in motors of hybrid electric vehicles (HEV) which is one of the most promising application of Nd-Fe-B magnets. As high heat resistance and high coercivity are strongly required in HEVs, some amounts of Dy are added to Nd-Fe-B magnets.

However, the natural abundance of Dy is quite low and producing countries are limited. Therefore, the development of Dy-free or Dy-less Nd-Fe-B sintered magnets with high coercivity is strongly demanded. In order to enhance the coercivity, grain refinement of microstructure in sintered magnets and the microstructural control at the interface between $Nd_2Fe_{14}B$ and Nd-rich phases are important.

We performed small-angle neutron scattering (SANS) measurements of the Nd-Fe-B sintered magnets using unpolarized and polarized neutrons to get information on the averaged internal inhomogeneous structure of Nd-Fe-B sintered magnets including the interfacial structures which is the key parameter to achieve the high-coercivity Dy-free Nd-Fe-B sintered magnet. The SANS experiments were performed using PNO and SANS-J-II.

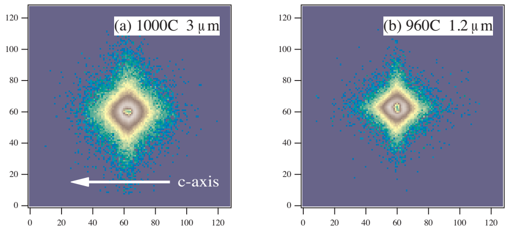

Figure 1: Color-coded intensity maps of Nd-Fe-B sintered magnets with different sintering process; (a) 3 μm powders sintered at 1000 °C, and (b) 1.2 μm powders sintered at 960 °C.

Intensity distributions of SANS from the Nd-Fe-B sintered magnets on a 2-dimensional position-sensitive detector of SANS-J-II (intensity maps) were sensitive to the sintering and annealing condition of the samples, as shown in FIg. 1. The patterns were also drastically changed by changing the temperature and applying magnetic field during measurements. These observations indicate that the SANS measurement is a promising tool to investigate the correlation between the coercivity and the internal structure of Nd-Fe-B sintered magnets. We are going to extend this work to elucidate the high-magnetic-field annealing phenomenon1), which improves the coercivity, in the next fiscal year.

This work was supported by New Energy and Industrial Technology Development Organization (NEDO), Grant-in-Aid for ”Development of technology for reducing dysprosium usage in a rare-earth magnet” in ”Rare Metal Substitute Materials Development Project”.

References

1) H. Kato, T. Miyazaki, M. Sagawa, and K. Koyama, Appl. Phys. Lett., **84** (2004) 4230.

原子炉：JRR-3　装置：SANS-J(C3-2)　PNO(3G)　分野：中性子散乱（磁性）

1-2-16

Polarized Neutron Diffraction Study of Magnetic Chirality in Multiferroic Compound $TmMn_2O_5$

S. Wakimoto, H. Kimura[1], M. Fukunaga[1], M. Takeda, K. Kakurai, and Y. Noda[1]

Quantum Beam Science Directorate, JAEA, Tokai, Ibaraki 319-1195
[1]*Institute of Multidisciplinary Research for Advanced Materials, Tohoku University, Sendai 980-8577*

Multiferroic materials RMn_2O_5 show antiferromagnetic order and ferroelectricity concomitantly at low temperatures with strong coupling. To date, two models are suggested as an origin of the magnetic driven ferroelectric in this system. One suggests $P \propto S_i \times S_j$ [2] while the other suggests $P \propto S_i \cdot S_j$. [3] Previously we have shown that the magnetic chirality is proportional to the FE polarization for materials with R =Ho and Er, consistent with the $S \times S$ model. [4] Recenltly it is found that $TmMn_2O_5$ shows polarization flop transition at 4 K from $P//b$ to $P//a$ as temperature decreases. [5] Since the $S \times S$ model requires one to one correspondence between the chiral plane and the polarization, a study of the magnetic chirality at the flop transition should give another test of the model.

Polarized neutron diffraction study was carried out at TAS-1 spectrometer with PG monochromator and Huesler analyzer. In this case, diffracted neutron cross-sections with different polarizations σ_+ and σ_-, i.e. spin up and down, correspond to the different chirality. During the measurement, external electric field has been applied to the a-axis.

Figure 1 shows the cross-sections σ_+ and σ_- measured near $(1.5, 0, 0.25)$. At this Q, one can observe the magnetic chirality in the bc-plane which gives $P//b$ on the basis of the $S \times S$ model. As shown in Fig. 1, the magnetic chirality which can be characterized by the difference in σ_+ and σ_- disappears in the $P//a$ phase. This proves that the polarization flop transition is indeed accompanied by the change of the chiral plane consistent with the $S \times S$ model.

References

1) T. Kimura *et al.*, Nature **426**, 55 (2003).
2) H. Katsura, N. Nagaosa, and A. V. Balatsky, Phys. Rev. Lett.**95**, 057205 (2004).
3) L. C. Chapon *et al.*, Phys. Rev. Lett.**96**, 097601 (2006).
4) S. Wakimoto *et al.*, doi:10.1016/j.physb.2009.06.012.
5) M. Fukunaga *et al.*, J. Phys. Soc. Jpn. **77**, 094711 (2008).

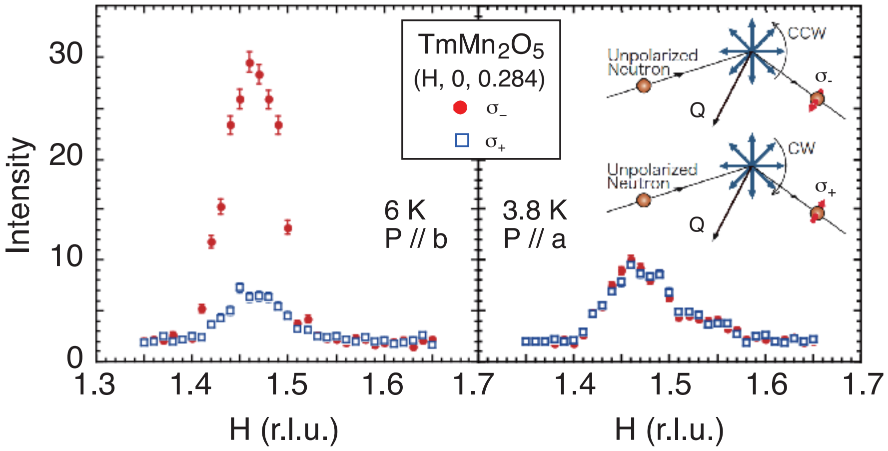

Figure 1: Polarized neutron diffraction data at 6 K and 3.8 K near $(1.5, 0, 0.25)$. Cross-sections σ_+ and σ_- correspond to the different chiralities as shown in the inset.

原子炉：JRR-3　　装置：TAS-1(2G)　　分野：中性子散乱（磁性）

1-2-17

A Small-Angle Polarized Neutron Scattering Experiment of Spherical $Fe_{16}N_2$ Nano-Particles for High Density Magnetic Recording Tape

H. Hagiya[1,3], T. Oku[1], H. Kira[1], T. Shinohara[1], J. Suzuki[1],Y. Tamai[2,3], M. Takeda[2],
K. Kakurai[2], Y. Sasaki[4], M. Kishimoto[4], M. Yokoyama[3], Y. Nishihara[3]

[1]*Japan Proton Accelerator Research Complex center, JAEA, Tokai, Ibaraki 319-1195*
[2]*Quantum Beam Science Directorate, JAEA, Tokai, Ibaraki 319-1195*
[3]*Department of Science, Ibaraki University, Mito, Ibaraki 310-8512*
[4]*Hitachi Maxell, Ltd., Koizumi, Oyamazaki-Cho, Otokuni-Gun, Kyoto 618-8525*

$Fe_{16}N_2$ exhibits a large magnetic moment and large crystalline anisotropy. Hence, the industrial researchers have developed magnetically stable spherical $Fe_{16}N_2$ nano-particles for high density magnetic recording tape. The surface of the particles is coated with a non-magnetic layer to prevent oxidization and sintering. The optimization of the surfactant layer thickness is important to maximize recording performance of the magnetic tape. Then, in this study, we performed polarized small-angle neutron scattering (SANS) experiments to evaluate their non-magnetic surfactant layer thickness quantitatively. According to the previous study $^{1)}$, it was suggested that scattering intensity profiles which reflect the information of surface layer thickness would appear intensively in the range $q \gtrsim 1\ \mathrm{nm}^{-1}$. Thus, we performed SANS experiments in the range of $0.15\ \mathrm{nm}^{-1} < q < 2\ \mathrm{nm}^{-1}$ about 2 samples (M2 and M6) of $Fe_{16}N_2$ nano-particles with different surface layer thicknesses. We applied a magnetic field of 1 T to the samples and measured SANS intensities of I^+ and I^- of the cases that the spin polarity of incident neutrons is positive and negative, respectively. Fig. 1 shows the scattering intensities $I_\perp^+$ and $I_\perp^-$ along the direction perpendicular to the applied magnetic field direction. Here, we analyzed the data with 2 core-shell models in which we made assumptions as follows: 1) In model 1, the thickness of the nonmagnetic surfactant layer is independent of the particle diameter. 2) In model 2, the ratio of the volumes of the magnetic core and nonmagnetic surfactant layer regions is constant. The fitting results with the models are shown in Fig. 1. It was found that the experimental data were reproduced better with model 2 than model 1 for the 2 samples. According to the sample preparation method $^{2)}$, model 2 is considered more appropriate for the samples. Therefore, we evaluated the surface layer thicknesses of the samples based on the analysis with model 2, and the non-magnetic surfactant layer thicknesses were determined to be 3.4 nm and 3.6 nm for sample M2 and M6, respectively.

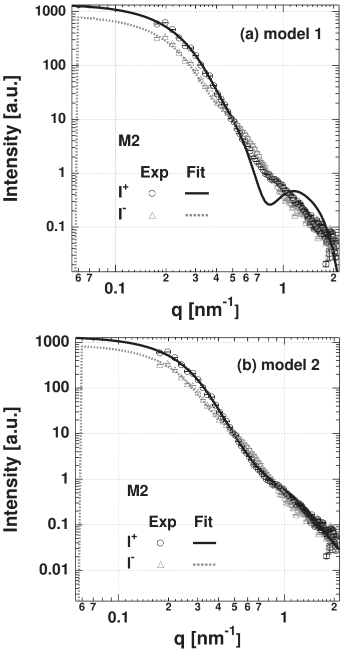

Figure 1: I vs. q.

References

1) T. Oku, et al. :"Physica B" (2009) in press.
2) Y. SASAKI, et al. :"IEEE Trans. Mag." 41 (10) pp. 3241-3243 (2005).

原子炉：JRR-3　　装置：SANS-J(C3-2)　　分野：中性子散乱（磁性）

1-2-18

Magnetic Structure in the Shastry-Sutherland Lattice TmB_4

Iga F.(a), Shigekawa A.(a), Michimura S.(a), Takabatake T.(a), Yoshii S.(b), Yamamoto T.(b), Hagiwara M.(b), Kindo K. (c), Ohoyama K.(d)
(a) ADSM, Hiroshima Univ., (b) KYOKUGEN, Osaka Univ., (c) cInstitute for Solid State Physics, Univ. of Tokyo, (d) IMR, Tohoku Univ.

Rare-earth tetraborides RB4 have a tetragonal crystal structure with a space group P4/mbm which is characterized by the 2-dimensional orthogonal dimers in the c-plane. Such dimer systems are equivalent to the Shastry-Sutherland lattice (SSL) [1] where nearest-neighboring dimers geometrically frustrated.

The previous study of TmB4 indicates an antiferromagnetic order at 11.7 K by the measurements of temperature dependences of electrical resistivity and magnetic susceptibility [2]. From our recent experimental results, we have found that TmB4 exhibits three phase transitions at TN1=11.7K, T*=11K and TN2=10K [3]. The phase transitions at TN1 and TN2 were already reported by Fisk et al [2]. In order to clarify these ordering vectors in these magnetic phases, we have performed neutron diffraction experiment on Tm11B4.

First, high-quality single crystal TmB4 was grown by floating zone method using a four-xenon lamps image furnace. Next, these crystals were crushed to powder. The neutron powder diffraction experiment was performed on the powder diffractometer for high efficiency and high resolution measurements, HERMES. Measured temperatures were set at 3K (antiferro-magnetic phase, IV), 10.7K (unknown phase, III), 11.7K (unknown phase, II) and 20K (paramagnetic phase, I).

Figure 1 shows the powder pattern for the four phases of TmB4. The pattern at 20 K was used for the nuclear scattering standard. Phase IV shows a simple antiferromagnetic pattern with a propagation vector of k4=(1, 0, 0). This is consistent with the previous report [2]. The Phase III has been assigned with propagation vector k4 and an additional long period modulation vector k3=(0.13, 0, 0). Furthermore, the phase II was also indexed with the k4 and k2=(0.012, 0.012, 0) and k2=(0.036, 0.012, 0). However, we have not yet succeeded in obtaining complete fitting parameter.

Magnetization process M(B//c) in TmB4 shows 1/8 and 1/2 plateaus at 1.7-1.4 T and 2-3 T, respectively. These characteristic behavior may be originated from geometric frustration in not only magnetic dipole interactions but also electric multipole interactions.

References
[1] B. S. Shastry and B. Sutherland, Physica B & C 108B (1981), p. 1069.
[2] Z. Fisk et al., Solid State Commun. 39 (1981), p. 1189.
[3] F. Iga et al., J. Magn. Magn. Mater. (2007) in press.

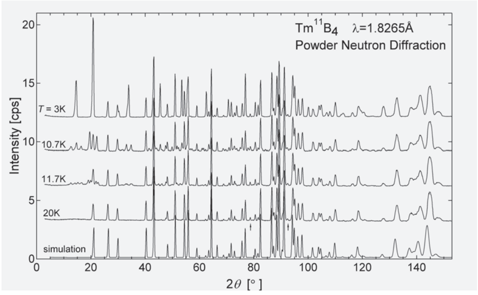

Fig. 1. Fig. 1 Neutron powder diffraction patterns for the four phases of TmB4. The bottom shows a simulation in the paramagnetic state.

1-2-19

Successive metamagnetic behavior in an easy-plane type antiferromagnet ErNi2Ge2

Y. Tabata(A), M. Okue(A), H. Nakamura(A), N. Matsuura(B)
(A) Graduate School of Engineering, Kyoto University, (B) ISSP, University of Tokyo

A rare earth intermetallic compound ErNi2Ge2 with a tetragonal ThCr2Si2-type structure is a long-period antiferromagnet with TN =3.0K and magnetic wave vector km=(0,0,0.75). Our recent magnetization measurements by using single crystalline samples and crystalline-electric-field (CEF) analysis indicate that ErNi2Ge2 is an easy-plane type magnetic anisotropy, where the c-plane is a magnetic easy-plane. Interestingly, a successive metamagnetic behavior has been found in a magnetization process along the magnetic hard-axis, c-axis. Such a metamagnetism along a magnetic hard-axis had also been found in another easy-type anitferromagnet TbB4, which has the Shastry-Surthreland lattice. Recently, the multi-step metamagnetic transition in TbB4 had been explained based on a model with a XY-type ground spin state and an Ising-type exited spin state[1]. Now we are trying to understand the metamagnetism in ErNi2Ge2 based on a similar model.

On the othre hand, a colinear sinusoidal modulated magnetic structure of ErNi2Ge2 was reported by Andre et al. [2], where the Er magnetic moment forms an angle 64 degree with the c-axis. In their model, the c-axis component of the Er magnetic moment is about half the size of the c-plane component, contradicting the results of our magnetization measurements mentioned above. In order to determine the direction of Er magnetic moment in the antiferromagnetic state, we performed polarized neutron scattering experiments by using a single crystalline sample on the triple-axis spectrometer 5G installed at JRR-3M reactor.

Figure 1 shows spin-flip (SF) and non-spin-flip (NSF) magnetic scattering profiles with a scattering vector K = (2,0,0.75) in the condition of the polarization vector of neutron P being perpendicular to the scattering vector. In this experimental condition, the direction of P or K is almost parallel to the c- or the a-axis respectively, and hence, the b- or the c-axis component contributes the SF or the NSF scattering respectively. As shown in Fig. 1, the NSF scattering is almost absent, indicating the c-axis component is almost 0. Hence, we have concluded that ErNi2Ge2 is the easy-plane type antiferromagnet, as expected from the magnetization measurements.

[1] T. Inami et al., cond-mat/0709.0977.
[2] G .Andre et al., J. Alloys and Comp. 224, 253 (1995).

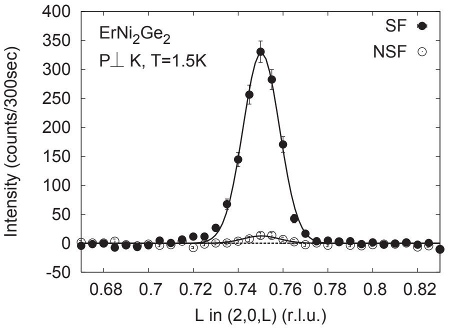

Fig. 1. Magentic scattering profile of polarized neutron at the magnetic wave vector K = (2,0,0.75) in the condition of the polarization vector P being perpendicular to K. Closed and oped circles denote the SF- and the NSF-scattering profiles respectively.

1-2-20

Anisotropic magnetic diffuse scattering in an easy-plane type antiferromagnet ErNi2Ge2

Y. Tabata, H. Taguchi, K. Matsuda, H. Nakamura
Graduate School of Engineering, Kyoto University

A rare earth intermetallic compound ErNi2Ge2 with a tetragonal ThCr2Si2-type structure is a long-period antiferromagnet with TN =3.0K and magnetic wave vector km=(0,0,0.75). Our recent magnetization measurements by using single crystalline samples and crystalline-electric-field (CEF) analysis indicate that ErNi2Ge2 is an easy-plane type magnetic anisotropy, where the c-plane is a magnetic easy-plane. Absence of the third harmonic scattering and weak anisotropy in the c-plane strongly suggest a helical magnetic order in this compound. We have found an anomalous anisotropic magnetic diffuse scattering in the magnetic ordered phase.

Figure 1 shows magnetic scattering profiles along the [1,0,0]-, the [1,1,0]- and the [0,0,1]-direction with the scattering vector Km = (0,0,3.25). The profiles along the [1,0,0]- and the [1,1,0]-directions contains a widespread diffuse-scattering component, while the profile along the [0,0,1]-direction has only a sharp Gaussian component. This result indicates that the long-range and the short-range orders coexist in the antiferromagnetic region and the short-range order is quite anisotropic. The correlation length of the short-range order along the c-axis is enough long that the peak profile is within the resolution limit, suggesting the short-range order consists of 1-dimensional long-range helices along the c-axis. The diffuse-scattering component in the c-plane is better fit by a modified Lorentzian with an anomalous exponent theta = 1.34, the form is written in Fig.1, than by a simple Lorentzain. The physical meaning of the shift of theta away from 1 is unclear.

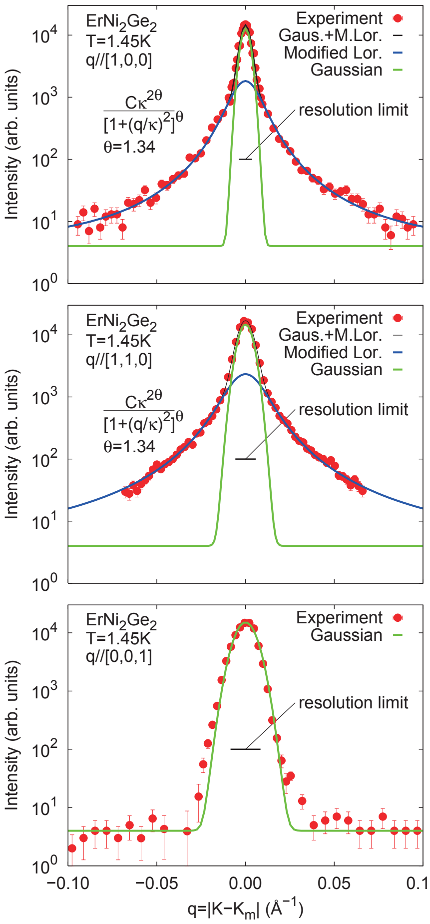

Fig. 1. Magnetic scattering profiles along (upper) the [1,0,0]-, (middle) the [1,1,0]- and (lower) the [0,0,1]-direction with the scattering vector Km = (0,0,3.25).

Activity Report on Neutron Scattering Research: Experimental Reports **16** (2009)
Report Number: 607

1-2-21

Magnetic structure of RCoSn (R=Tb, Ho and Er)

M.Kurisu, G.Nakamoto, T.Tsutaoka(1) and Y.Andoh(2)
Japan Advanced Institute of Science and Technology, Ishikawa 923-1292, Japan
(1)Graduate School of Education, Hiroshima University, Hiroshima 739-8524, Japan
(2)Faculty of Regional Sciences, Tottori University, Tottori 680-8551, Japan

RTX (R: rare earths, T: transition metals, X: metalloids) compounds crystallize in the epsilon-TiNiSi-type orthorhombic structure. We have shown that the crystalline electric field effect plays an dominant role in their anisotropic magnetic behaivior. The temperature dependence of magnetic susceptibility is well explained by the systematic variation of CEF parameters in TbTX compounds, TbNiSn, TbPdSn and TbRhGe[1]. The easy axis of magnetization is the b-axis in these three compounds. Recently, we have found that it is the a-axis in the isostructural compound TbCoSn. The sign of second order CEF parameters of the compound have opposite sign to other TbTX. In the present report, we show preliminary experimental results of single crystal neutron diffraction on TbCoSn to examine its magnetic strucure.

Single-crystalline TbCoSn ingots were grown by a Czochralski method using a tetra-arc furnace in purified Ar atmosphere. The neutron diffraction measurements were performed at T1-1:HQR spectrometer installed at JRR-3M.

The SQUID magnetic susceptibility shows that antiferromagnetic ordering takes place at TN = 20.2 K. Below TN, an anomaly indicative of another magnetic transition is observed at 4 K for the three principal axes. The specific heat measurement also indicates the two magnetic phases.

The magnetic reflection is observed in the a*-b* reciprocal lattice plane below TN as shown in Fig.1. The magnetic structure appears to be represented by the wave vector (0 0.25 0). The analysis is in progress.

References

[1] Specific heat and high field magnetization of a TbPdSn single crystal, Yoshikazu Andoh, Do Thi Kim Anh, Hiroyuki Hoshino, Go Nakamoto, Makio Kurisu, and Shinji Kawano, Physica B, 373 (2006) 150-153.

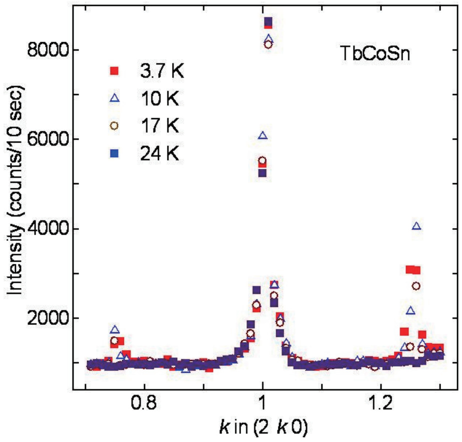

Fig. 1. Magnetic and nuclear reflections in a*-b* plane of TbCoSn.

1-2-22

Relationship between Magnetic Structure and Ferroelectricity of LiCu2O2

Y. Yasui, K. Sato, Y. Kobayashi, T. Moyoshi, M. Sato and K. Kakurai*
*Dept of Phys., Nagoya Univ., *JAEA*

Materials with magnetic and ferroelectric coexisting orders are called multiferroics and attract much attention. The authors ’ group have found that LiVCuO4 is a multiferroic with quasi one-dimensional spin S=1/2 chains of Cu2+ ions formed of edge-sharing CuO4 square planes (called CuO2 ribbon chains).1,2) For physical understandings of multiferroic nature, this kind of spin 1/2 systems seem to be useful, because they do not have any complications arising from the multi-orbital effects, and because quantum effects may also induce interesting phenomena.

LiCu2O2 with the CuO2 ribbon chains was also reported to be multiferroic.3) However, because its correct magnetic structure has not been reported, there are many unsolved problems on the relationship between observed ferroelectiric behaviors3) and the magnetic structure:4,5) Concerning the magnetic structure, several groups have reported their results obtained by just one of experimental methods, such as neutron scattering4) and 7Li-NMR,5) where we can find that any of the reported structure cannot explain the other reported structures. Actually, the existence of the four CuO2 ribbon chains in the unit cell makes it difficult to correctly determine the modulated magnetic structure of the present system. Here, we have determined the magnetic structure2, applying both the neutron scattering and 7Li-NMR measurements for single-crystal samples of LiCu2O2, and the relationship between the magnetic structure and dielectric or ferroelectric properties also studied here, has been discussed.

From the temperature (T) dependences of the specific heat and 7Li-NMR spectra, the magnetic transitions has been found at 24.5 K (≡ TN1) and 22.8 K (≡ TN2), where the ferroelectric transition has also been observed at TN2. To determine the magnetic structures of intermediate (TN2<T<TN1) and low temperature (T <TN2) phases, the neutron scattering intensities were measured in the (h k 0) and (h k 2h) planes in the reciprocal space at 12 K (<TN2), 23.3 K (TN2<T<TN1) and 50 K (>TN). To avoid the large neutron absorption of Li, we used 7Li isotopes. At 12 K and 23.3 K, we observed magnetic superlattice reflections at Q = (h, k ± δ , 0) and (h, k ± δ , 2h) (h = half-integer, k = integer and δ ˜0.172). The system has an incommensurate magnetic structure with the modulation vector Q=?b* (or the pitch angle ˜62 along the CuO2 ribbon chains). We have determined the magnetic structures of intermediate and low temperature phases to reproduce the neutron data and 7Li-NMR spectra simultaneously. At 23.3 K(in the intermediate phase), the system has been found to have a collinear structure with the spins along the c-axis and modulated in a sinusoidal way. It is consistent with the nonappearance of ferroelectricity in this phase. The magnetic structure of the low temperature phase has also been determined. Basically, it is helical, and parameters to describe the detailed structure will be published soon.

We have found that the relation P ? Q ? e3 holds (e3 is the helical axis) in zero magnetic field, which is consistent with the existing theories. The existence of the collinear phase above TN2, and the observed anisotropy of the amplitudes of the modulations, which form the helical structure may be related to a possible effect of the quantum fluctuation.

References

[1] Y. Naito et al.: J. Phys. Soc. Jpn. 76 (2007) 023708.
[2] Y. Yasui et al.: J. Phys. Soc. Jpn. 77 (2008) 023712.
[3] S. Park et al.: Phys. Rev. Lett. 98 (2007)

057601.
[4] T. Masuda et al.: Phys. Rev. Lett. 92 (2004) 177201.
[5] A.A. Gippius et al.: Phys. Rev. B 70 (2004) 020406.

1-2-22

1-2-23

Magnetic Properties of Honeycomb System Na2Co2TeO6

Y. Yasui, Y. Miura, T. Moyoshi, M. Sato and K. Kakurai*
*Dept of Phys., Nagoya Univ., *JAEA*

Na2Co2TeO6, has Co2TeO6 layers, consisting of edge-sharing CoO6- and SbO6-octahedra with Na layers between them. The Co2+ ions are considered to have high spin state S=3/2. For this system, polycrystalline samples of Na2Co2TeO6 were prepared, and their magnetic susceptibility and specific heat were first measured, where clear anomalies due to the antiferromagnetic transition1) were found in the temperature dependences of these quantities at TN=23.7 K. The magnetic susceptibility data have been analyzed using the high temperature expansion method, and the first-, second- and third-neighbor interactions J1, J2 and J3 among the spins are estimated to be 11.4 ± 0.5 K (Ferro), -4.1 ± 0.1 K (AF) and 0.3 ± 0.1 K (Ferro), respectively. Based on the J1/J3-J2/J3 phase diagram of Heisenberg spin system proposed by Fouet et al.,2) the magnetic structure of this system is expected to be screw type one. To see if the structure is actually found in this system, neutron scattering measurements were carried out using the triple axis spectrometer HQR (T1-1), where the double axis condition was adopted. At T=4 K, we observed the magnetic reflections at commensurate Q-points. Figure shows the T-dependence of the integrated intensity of 1 0 1 magnetic reflection. From the figure, the magnetic ordering is found to grow with decreasing T below TN. By the preliminary analyses of the neutron scattering data, the magnetic structure which can reproduce the observed magnetic scattering intensities at 4 K is obtained (shown schematically in the inset of the figure). The details of the obtained structure at 4 K can be described as follows. The collinear ordering of the Co2+ moments can be found with the moment direction parallel to the c-axis. In the honeycomb layer, the one-dimensional zig-zag ferromagnetic chains exist and these ferromagnetic chains order antiferromagnetically. The discrepancy between the predicted and actual magnetic structure of Na2Co2TeO6 seems to be originated from the anisotropy of the Co2+ spins with strong Ising anisotropy.

References

[1] Y. Miura et al.: J. Phys. Soc. Jpn. 75 (2006) 084707.
[2] J.B. Fouet et al.: Eur. Phys. J. B 20 (2001) 241.

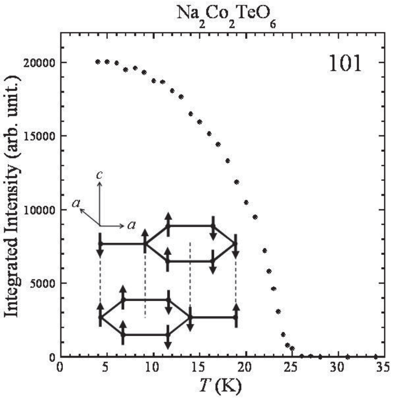

Fig. 1.

1-2-24

Magnetic structure of multiferroic $DyMnO_3$ studied by polarized neutron diffraction

D. Okuyama(A), H. Murakawa(B), K. Iwasa(C), H. Sagayama(D), Y. Kaneko(B), Y. Taguchi(A), T. Arima(D), and Y. Tokura(A,B,E)
(A)RIKEN-CMRG, (B)ERATO-MF, (C)Tohoku Univ., (D)Tohoku Univ.-IMRAM, (E) Univ. of Tokyo

Recently, perovskite manganites have been intensively studied from the view points of multiferroics properties [1]. In typical multiferroics material $TbMnO_3$ and $DyMnO_3$, polarization flop phenomena are observed under the magnetic field [1]. Recent theoretical studies [2, 3] suggest that the cycloidal magnetic structure of Mn ion plays an important role to the ferroelectric state. In Ref. [2], ferroelectric polarization of multiferroics $TbMnO_3$ and $DyMnO_3$ can be expressed by cross product between the magnetic propagation vector and magnetic chirality from cycloidal structure as $P=\alpha\, k \times (S_i \times S_j)$. On the basis of this theory, the origin of polarization flop phenomena from $P//c$ to $P//a$ can be understood as being due to the magnetic structural phase transition from *bc*-cycloidal magnetic structure to *ab*-cycloidal magnetic structure. For ensuring this theoretical prediction, the magnetic structure of $P//c$ phase at zero filed and $P//a$ phase under hight magnetic fields should be clarified. Therefore, we utilized polarized neutron diffraction method and tried to decide the precise magnetic structure in both zero and high magnetic fields.

As the target material, we chose $DyMnO_3$, which shows the polarization flop phenomenon at low magnetic filed (∼2 Tesla). Neutron diffraction experiments were performed on TOPAN triple-axis spectrometer. Neutron beam with an energy 80 meV was used. A single crystal of $DyMnO_3$ was mounted in longitudinal magnetic filed-type superconducting magnet (Endoh-magnet) so that the [1 0 0]-[0 0 1] direction on *Pbnm* setting were parallel to the scattering plane.

First, we tried to measure the eight magnetic reciprocal lattice points marked with red circles in Fig. 1 with unpolarized neutron diffraction mode for charactering the magnetic properties at low temperature of $DyMnO_3$. In Fig. 1, the peak profiles of magnetic reflections at (0 k 5), (0 k 6), (1 k 5), (1 k 6), (5 k 0), (6 k 0), (4 k 1), (5 k 1) positions are shown. Black triangle, red triangle, and blue circle indicate the peak profiles at T=15 K, 8 K, and 6.5 K near the ferroelectric ordering temperature T_C=18 K and the magnetic ordering temperature of Dy moment T_{N-Dy}=6.5 K, respectively. In the data at 8 K (6.5 K$\leq T \leq$18 K), only (0 0.38 5) and (4 0.38 1) reflections were observed, in which the magnetic moment of Mn ion is mainly involved. In contrast, in the data at 3 K ($T \leq$6.5 K), additional (0 1/2 5) and (5 1/2 0) were observed. These experimental results are consistent with the data of Ref. [4].

In order to decide the magnetic structures of Mn moment at both zero and high magnetic fields, we utilized polarized neutron diffraction method. For the limitation of the experimental configuration, we measured only (0 0.38 5) magnetic reflection. In this case, we can mainly observe the magnetic reflection from *a*-axis (*b*-axis) magnetic component at spin flip (non-filp) process, respectively. In Fig. 1, at 0.5 Tesla (near zero field $P//c$ phase), only the magnetic reflection from non-spin flip process was observed. This result strongly suggests the *bc*-cycloidal magnetic structure of Mn moment, which is consistent with the data of Ref. [4]. On the other hand, at 3.5 Tesla ($P//a$ phase), the small magnetic reflections from both non-spin flip and spin flip processes were observed with slightly poor statistics. From this result, we concluded that the *ab*-cycloidal magnetic structure of Mn moment is realized in $P//a$ phase at high magnetic fields.

In summary, we determined roughly the magnetic structure of Mn moment of multiferroic $\mathrm{DyMnO_3}$ in both $P//c$ phase at low magnetic fields and $P//a$ phase at high magnetic fields. These magnetic structures support the theoretical prediction that the polarization flop phenomenon is due to the change of the cycloidal spin plane from *bc*-plane to *ab*-plane.

[1] T. Kimura *et. al.*: Nature **426**, 55 (2003).; Phys. Rev. **B 71**, 224425 (2005). [2] H. Katsura *et. al.*: Phys. Rev. Lett. **95**, 057205 (2005). [3] M. Mochizuki *et. al.*: e-print available at arXiv:0811.4015. [4] O. Prokhnenko *et. al.*: Phys. Rev. Lett. **98**, 057206 (2007).

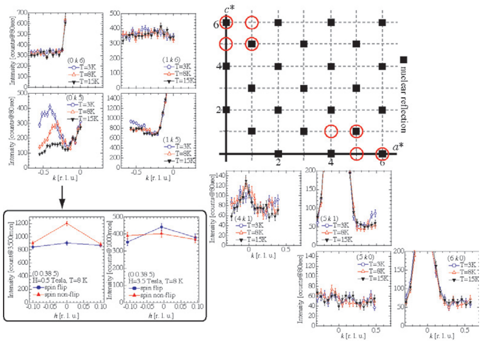

Fig. 1.

1-2-24

1-2-25

Neutron Diffraction Studies on Dy7Rh3Dx

T. Tsutaoka(A), A. Tanaka(A), G. Nakamoto(B), M. Kurisu(B), Y. Andoh(C), R. Sato(D),
S. M. Filipek(D)
(A)Graduate School of Education, Hiroshima University, (B)Japan Advanced Institute of Science and Technology, (C)Faculty of Regional Sciences, Tottori University, (D) Institute of Physical Chemistry, Polish Academy of Sciences

The rare earth intermetallic compounds R7Rh3 based hydrides can have the hexagonal Th7Fe3 type structure with the space group P63mc in the relatively high hydrogen content up to R7Rh3H30; magnetic property of the Tb7Rh3 and Dy7Rh3 changes from antiferromagnetic to ferromagnetic or ferrimagnetic and the electrical property changes from semimetallic to metallic by the hydrogenation[1]. In this study, we have performed powder neutron diffraction measurements on the magnetic deuteride Dy7Rh3D28 to investigate the magnetic structure. Hydrogenation of R7Rh3 samples were carried out in the pressure up to 10 kbar at 25 and 100 degree Celsius in the high pressure apparatus [2]. Neutron diffraction measurements have been carried out by using the HERMES spectrometer of JRR-3M in the temperature range from 10 to 100 K with a wave length of 1.82645(6) A.

Figure 1(a) shows the powder neutron diffraction profiles of Dy7Rh3 at 3.5 K, 40 K and 70 K. A large (000)+ magnetic reflection was observed in the magnetically ordered states below TN = 59 K. Nuclear peaks can be indexed by the Fe7Rh3 type structure. Figure 1(b) shows the powder neutron diffraction profiles of Dy7Rh3D28 at 4.5 K and 70 K. The (000)+ magnetic reflection was also observed in the duteride Dy7Rh3D28. This result indicates that the Dy7Rh3Dx also has the antiferromagnetic interactions. From the past studies, since R7Rh3 compounds tend to have helical or conical magnetic structures, Dy7Rh3 can have the helical magnetic structure. For the R7Rh3 deuterides, the configuration of the hydrogen has not been determined. Thus the study for the magnetic structure as well as the hydrogen structure investigation for Dy7Rh3 and its hydrides is now in progress.

References
[1] R. Sato, T. Tsutaoka, S.M. Filipek, J. Alloys and Comp., 446-447 (2007) 610.
[2] B. Baranowski, S.M. Filipek, J. Alloys and Comp., 404-406 (2005) 2.

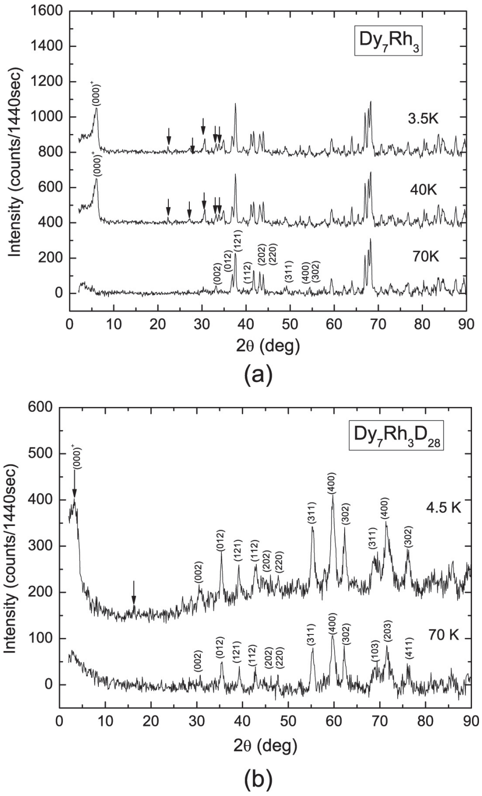

(a)

(b)

Fig. 1. Fig.1 Neutron diffraction profiles for Dy7Rh3 (a) and Dy7Rh3D28 at several temperatures.

1-2-26

Quantum Phase Transition in the Solid Solution

Kitada A., Tsujimoto Y., Kageyama H., Yoshimura K., Nishi M.
Department of Chemistry, Graduate School of Science, Kyoto University; Institute for Solid Staet Physics, University of Tokyo

The structure of (CuCl)LaNb2O7, a metastable phase prepared using an ion-exchange reaction, consists of Cu2+Cl layers sandwiched by non-magnetic double-layered perovskite LaNb5+2O7 blocks. Thus it is regarded as an S = 1/2 quasi-2D system. Previous magnetic studies of this compound revealed the spin-singlet ground state with a zero-field gap of 2.3 meV to the low-lying triplet excited states. The Br-based counterpart (CuBr)LaNb2O7 exhibits collinear anti-ferromagnetic (CAF) order at TN = 32 K characterized by the propagation vector q = (pi, 0, pi). Apparently, the superexchange interactions through Cu-X-Cl (X = Cl, Br) substantially influence their magnetic properties. The solid solution (CuCl1-yBry)LaNb2O7 has been recently prepared to investigate the correlation between the two states.15, 16 However, it should be noted that (CuCl1-yBry)LaNb2O7 is subject to random disorder due to the differing ionic radii of Cl and Br anions and that the CuCl layer inherent to the magnetism is directly disrupted.

Thus we have decided to study the magnetism of (CuCl)LaTa2O7 and the solid solution (CuCl)La(Nb1-xTax)2O7 [1. 2]. A crucial advantage of studying the Nb-Ta system (over the Cl-Br system) is that the CuCl layers are unaffected by the substitution and that Nb and Ta ions have nearly the same ionic radius (0.64 angstrom). We observed persistence of the spin-singlet state in (CuCl)LaNb2O7 up to x ˜ 0.4, accompanied by a slight reduction of the spin gap with increasing x. (CuCl)LaTa2O7 exhibits collinear antiferromagnetic (CAF) order with TN ˜ 7 K, similar to what is observed in (CuBr)LaNb2O7. In the intermediate region (0.4 < x < 1), we observed CAF order with a significantly reduced magnetic moment but with a nearly constant TN, suggesting that the CAF state coexists with the spin-singlet state in agreement with recent MuSR results.

References
[1] A. Kitada et al., submitted to Phys. Rev. B.
[2] Y. J. Uemura et al., submitted to Phys. Rev. B.

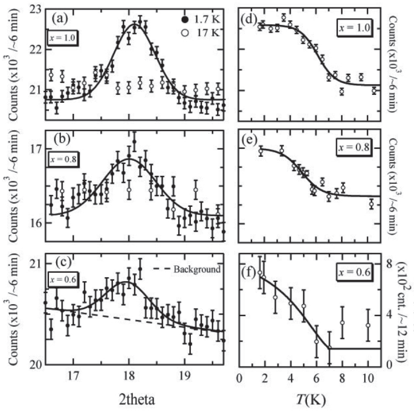

Fig. 1. Neutron diffraction of (CuCl)La(Nb1-xTax)2O7 demonstrating the collinear (pi, 0, pi) magnetic order at low temperatures.

1-2-27

Electric polarization flop induced by magnetic phase transition in multiferroic $YbMn_2O_5$

H. Kimura[1], Y. Sakamoto[1], M. Fukunaga[1], Y. Noda[1], and H. Hiraka[2]
[1]*IMRAM, Tohoku University*
[2]*IMR, Tohoku University*

A rare-earth (*R*) manganite of RMn_2O_5 is one of the typical multiferroic materials, which has been extensively studied[1]. However the origin of ferroelectricity is not yet fully understood. We have recently found in $TmMn_2O_5$ the flop of electric polarization from *b*-axis to *a*-axis around 5 K with decreasing temperature[2], which is the first discovery of *a*-polar phase in RMn_2O_5 system. It was reported previously that the polarization along *b*-axis disappear below ~ 6 K in $YbMn_2O_5$[3]. This is a suggestive result being expected the polarization flop from *b*- to *a*-axis below ~ 6 K. We thus carried out neutron diffraction measurements and magnetic structure analysis to clarify the microscopic magnetism in $YbMn_2O_5$.

Microscopic magnetic properties were measured using AKANE spectrometer. The results show that all the magnetic phases which successively occur with decreasing temperature are incommensurate and there is no commensurate magnetic order at all in $YbMn_2O_5$ unlike the other RMn_2O_5 families. Fig. 1(a) shows the magnetic Bragg peak profiles around $Q = (2.55\ 4\ 0.265)$ taken at 2.5 K and 7 K, showing the change of Bragg peak intensity. This indicates that the magnetic phase transition takes place between 2.5 K and 7 K. We measured the electric polarization of this material and found that, as shown in Fig. 1(b), the polarization flop from *b*- to *a*-axis occurs below ~ 6 K, indicating the strong relevance between the direction of electric polarization and the magnetic structure. To clarify the microscopic origin of this polarization flop, we have performed magnetic structure analysis in both *b*-polar phase and *a*-polar phase using FONDER diffractometer. A sufficient number of the integrated intensities of magnetic Bragg peaks were successfully measured at both the phases. The magnetic structure analysis is now in progress.

References

[1] N. Hur *et al.*: Nature **429** (2004) 392.
[2] M. Fukunaga *et al.*: JPSJ **77** (2008) 094711.
[3] Y. Koyata *et al.*: JPSJ **65** (1996) 1383.

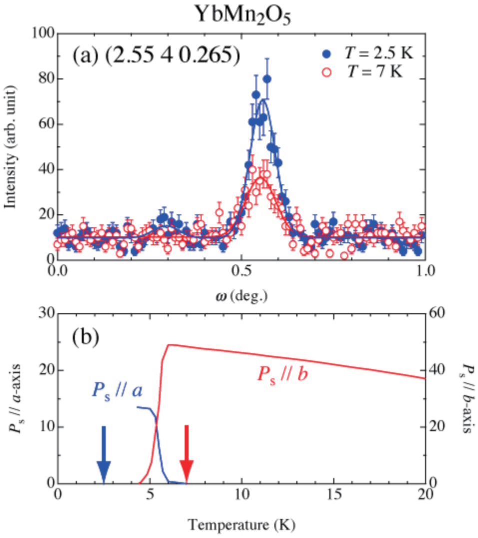

Fig. 1. (a) Peak profiles of magnetic Bragg reflection around (2.55 4 0.265) of $YbMn_2O_5$ taken at 2.5 K and 7 K. (b) Spontaneous electric polarization measured along *a*- and *b*-axes as a function of temperature.

1-2-28

Relationship between Spin Helicity and Electric Polarization in Multiferroic Material CuCrO2

Minoru Soda1, Kenta Kimura2, Tsuyoshi Kimura2, Masato Matsuura1 and Kazuma Hirota1
1Department of Earth and Space Science, Graduate School of Science, Osaka University
2Division of Material Physics, Graduate School of Engineering Science, Osaka University

Ferroelectricity induced by a noncollinear spin arrangement has been investigated experimentally and theoretically with respect to delafossite CuCrO2. CuCrO2 undergoes an antiferromagnetic transition at TN ˜25 K. A powder neutron diffraction study reported by H. Kadowaki et al. has indicated that CuCrO2 has an out-of-plane 120 deg. magnetic structure below TN. [1] Within the framework of the spin-current model, an electric polarization P does not appear macroscopically for this out-of-plane 120 deg. magnetic structure. However, the ferroelectricity has been recently reported in the out-of-plane 120 deg. magnetic structure. [2,3] In the present work, the spin-polarized-neutron studies have been carried out on the multiferroic material CuCrO2 to clarify the relationship between the spin helicity and the electric polarization P.

Below TN, the magnetic reflections were observed at Q-points (h ’/3,h ’’/3,l) (h ’ and h ’’ = 3n+1 or 3n+2 where n is integer). To discuss the magnetic domains, the crystal was oriented with the [001] axis vertical, and the electric field E was applied to the [110] direction. (The intensities of the magnetic reflections with the neutron spin parallel and antiparallel to the scattering vector are defined as Ion and Ioff.) After applying E=-73 kV/m, the difference between Ion and Ioff was observed at all the Q-points (1/3,1/3,0), (-1/3,2/3,0) and (-2/3,1/3,0), although the relations between Ion and Ioff at (-1/3,2/3,0) and (-2/3,1/3,0) are opposite to that at (1/3,1/3,0). (The Q-points (-1/3,2/3,0) and (-2/3,1/3,0) correspond to those rotated by 60 and 120 degrees from (1/3,1/3,0).)

In the present CuCrO2 studies, the spin helicities can be controlled by E without the change of T. For E=-73 kV/m, Ioff was larger than Ion at (1/3,1/3,0). The relation between Ion and Ioff was reversed at (2/3,2/3,0). These results are consistent with the helical magnetic structure or the out-of-plane 120 deg. magnetic structure. At (-1/3,2/3,0) and (-2/3,1/3,0), Ioff was smaller than Ion, which is opposite to that at (1/3,1/3,0). For -73 kV/m < E < +73 kV/m, the sum of the spin helicities were reversible by the reversal of the electric field without changing T at all the Q-points (1/3,1/3,0), (-1/3,2/3,0) and (-2/3,1/3,0). These results can be explained qualitatively by a theoretical prediction proposed by T. Arima.[4] However, for E > +73 kV/m, the relation between Ion and Ioff at the Q-point (1/3,1/3,0) changes. A large difference between Ion and Ioff was observed not at (1/3,1/3,0) but at (-1/3,2/3,0). These results indicate a possibility that the magnetic domains and the magnetic structures are controllable by the electric field.

[1] H. Kadowaki, H. Kikuchi and Y. Ajiro, J.Phys.: Condens.Matter 2 4485 (1990)
[2] S. Seki, Y. Onose and Y. Tokura, Phys. Rev. Lett. 101 067204 (2008)
[3] K. Kimura, H. Nakamura, K. Ohgushi and T. Kimura, Phys. Rev. B 78 140401(R) (2008)
[4] T. Arima, J. Phys. Soc. Jpn. 76 073702 (2007)

Activity Report on Neutron Scattering Research: Experimental Reports **16** (2009)
Report Number: 787

1-2-29

Competition between Relaxor-like behavior and Magnetic Ordering in (1-x)BiFeO3-xBaTiO3

Minoru Soda and Kazuma Hirota
Department of Earth and Space Science, Graduate School of Science, Osaka University

In relaxors, the temperature dependences of the dielectric permittivity show a broad maximum and a frequency-dependence. Because the relaxors have the high dielectric constant around room temperature, they are industrially important. To explain the T-dependences of the refraction indices and the dielectric permittivity of the relaxor systems, Burns and Dacol proposed the idea that randomly oriented, very local polar regions start to appear below a characteristic temperature Td (Burns temperature). This " Polar Nano Region " (PNR) is most important concept to consider the origin of the relaxor properties.

As a new example of such relaxor systems, we have studied (1-x)BiFeO3-xBaTiO3. Because (1-x)BiFeO3-xBaTiO3 with the relaxor-like dielectric property has the magnetic ions Fe3+, a question immediately arises as regards what magnetic behaviors appear in this relaxor system. [1] In the present studies, the neutron scattering studies have been carried out on single crystalline samples of 0.67BiFeO3-0.33BaTiO3(0.67BFO-BTO), which is around Morphotropic Phase Boundary(MPB), to clarify the relationship between relaxor-like dielectric property and magnetization.

Anisotropic nuclear diffuse scatterings, which have disappeared at about 900 K, have been observed around nuclear Bragg reflections at T=550 K˜900 K. (The T-dependence of the dielectric permittivity of 0.67BFO-BTO shows a broad maximum at Tmax=500 K˜700 K.) Although these nuclear diffuse scatterings are expected to indicate the existence of PNR, the change of these nuclear diffuse scatterings has been observed below the antiferromagnetic transition temperature TN. The intensities of the magnetic Bragg reflections, which originate from G-type antiferromagnetic order, begin to grow gradually at around TN˜500 K with decreasing T. Furthermore, the intensities of the nuclear Bragg reflections increase gradually below TN with decreasing T. This increase of the intensities of the nuclear Bragg reflections corresponds to the decrease of the nuclear diffuse scatterings around them, indicating that the volume of PNR decreases below TN. The simple G-type antiferromagnetic order is expected to compete with PNR and their domain walls. We think that the crystal structure begins to be formed regularly below TN with decreasing T. These results indicate the possibilities that the relaxor dielectric property and the antiferromagnetic order can be controlled by the magnetic field and the electric field, respectively.

Neutron scattering studies have been also carried out on single crystalline sample of 0.75BiFeO3-0.25BaTiO3(0.75BFO-BTO) with no relaxor behavior. The magnetic behavior of 0.75BFO-BTO is different from that of 0.67BFO-BTO. The magnetism of 0.67BFO-BTO is suppressed more than that of 0.75BFO-BTO. For 0.75BFO-BTO with no relaxor behavior, PNR which are related to the relaxor behavior are expected to be small or few. The magnetic behavior of 0.75BFO-BTO is consistent with the idea that the antiferromagnetic order competes with PNR and their domain walls.

[1] M. Mahesh Kumar, A. Srinivas and S. V. Suryanarayana, J. Appl. Phys. 87 (2000) 855.

1-2-30

Magnetic structure analysis of Crednerite $CuMnO_2$

Noriki Terada
National Institute for Materials Science

Crednerite $CuMnO_2$ has a distinct two dimensional crystal structure instructed by isosceles triangular lattice layers of the magnetic Mn^{3+}. Despite the large negative value of Weiss temperature $\theta_p = -450$ K, $CuMnO_2$ exhibits the antiferromagnetic phase transition at relatively low temperature $T_N = 64$ K, which is reported by the previous bulk measurements.[1, 2] The further cooling produces the week-ferromagnetic phase transition at 42 K.[1, 2] Considering the two dimensional isosceles triangular lattice crystal structure and the relatively large ratio between θ_p and T_N, $CuMnO_2$ is considered to be characterized by the geometric frustration. Thus, a complex magnetic structure could be expected in the low temperature phase. However, the magnetic structural determination has not been performed so far.

This time, in order to investigate magnetic orderings of $CuMnO_2$, we have performed the neutron powder diffraction measurements. The experiments were carried out with the diffractometer HERMES installed in the guide hall at JRR-3. The incident neutron wave length was 1.8204 Å. The powder sample was mounted on the cold head of the closed cycle He refrigerator.

We have performed the rietveld refinements for the data measured at the several temperature from 10 K to 300 K, using FullProf refinement program.[3] We observed the magnetic Bragg reflection below 70 K at the reciprocal lattice positions indexed as $(h, k, l)\pm(0.5,0.5,0.5)$. The typical result of the refinements for the data measured at 60 K, where the system is in the antiferromagnetic phase, is shown in Fig. 1. The refined magnetic structure is collinear magnetic structure with the magnetic moments aligned to the direction perpendicular to the b axis (monoclinic unique axis).

We also observed the magnetic diffuse scattering above T_N, suggesting the two dimensional character of $CuMnO_2$. For further investigation of the diffuse scattering, the inelastic neutron scattering measurements are desired.

References

[1] M. Trari *et al.*: J. Solid State Chem. **178** (2005) 2751.

[2] Y. Bessekhouad *et al.*:J. Mater. Sci. **42** (2001) 6469.

[3] J. Rodriguez-Carvajal: Physica B **192** (1993) 55.

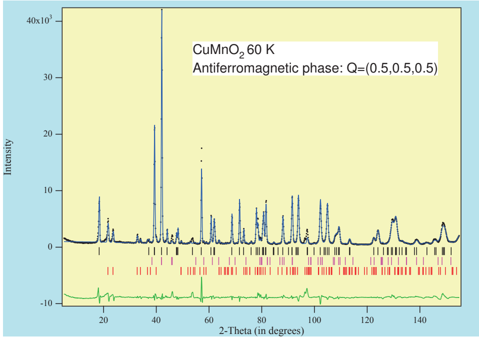

Fig. 1. Rietveld refinement of the neutron diffraction data obtained at 60 K for $CuMnO_2$.

Activity Report on Neutron Scattering Research: Experimental Reports **16** (2009)
Report Number: 798

1-2-31

Long-time variation of magnetic structure in a multistep metamagnet CeIr3Si2

K. Motoya, Y. Muro and T. Takabatake (a)
Tokyo University of Science, (a) Hiroshima University

Time variation of magnetic property has been extensively investigated in the spin-glass study. In a system without randomness or imperfections we have not thought to observe a time variation of magnetic structures in an attainable time scale. We report the first observation of a long-time transformation of magnetic structures in a non-diluted magnet $\mathrm{CeIr_3Si_2}$.

A ternary compound $\mathrm{CeIr_3Si_2}$ shows successive magnetic transitions at T_{N1}=4.1 K and T_{N2}=3.3 K. At $T < T_{\mathrm{N2}}$ it shows three-step metamagnetic transitions below H=1.43 T.[1,2] When a sample is rapidly cooled below T_{N2}, the magnetic Bragg peaks corresponding to the medium temperature (MT) phase ($T_{\mathrm{N2}} < T < T_{\mathrm{N1}}$) are observed. The amplitude of these Bragg peaks gradually decreases as time goes on. On the other hand, another group of Bragg peaks corresponding to the low temperature (LT) phase ($T < T_{\mathrm{N2}}$) gradually grow with time. Figure 1 shows the time variations of the amplitudes of the MT and LT phase signals measured at various temperatures. At T=0.7 K the MT-phase signal was observed without detectable change up to 10 h and no LT phase signal was observed.

The time variations of the signal amplitude are well expressed by simple exponential functions with a characteristic time t^*. The value of t^* for each measurement is posted in the figure. We analyzed the temperature variation of t^* in terms of the Arrhenius model. The activation energy of the time variation was obtained as E_a/k_B =4 K.

Although the magnetic structure in each phase has not been determined, we presume that the transition from the MT phase to the LT phase is basically an incommensurate to commensurate phase transition. We note that in the present measurements, only the amplitude of Bragg peaks varied with time. Neither the position nor the line width of Bragg peaks showed appreciable time variation. These results strongly suggest that we have observed the change of the volume fractions of two magnetic regions with a commensurate and an incommensurate structures.

We believe this is the first real-time observation of magnetic structural change in a uniform magnetic system. In future experiments with high intensity apparatus, we will be able to observe the change of domain size at very early stage of the time evolution.

References

[1] Y. Muro et al.: J. Mag. Mag. Mater. **310** (2007) 389.
[2] K. Shigetoh et al. : Phys. Rev. B **76** (2007) 184429.

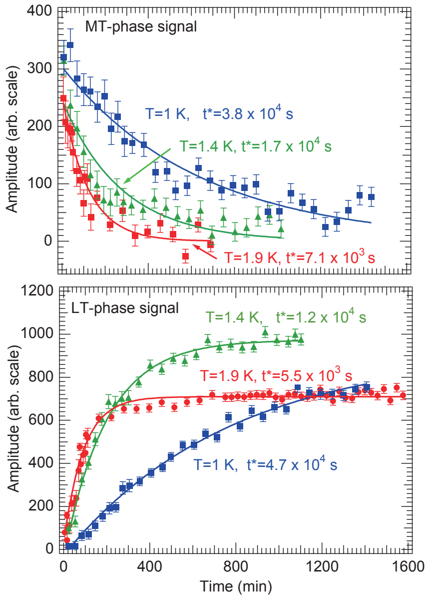

Fig. 1. Time variations of the amplitude of the MT and LT phase signals at various temperatures.

1-2-32

Inelastic neutron scattering study in O2 adsorbed deuterated CPL-1

Takatsugu Masuda, Suguru Hondo an Masato Matsuuda
Yokohama City University, Osaka University

We have studied the spin dynamics of oxygen molecules adsorbed in coordination polymers complex for a few years. In the nano-scale porous O2 molecues are aligned periodically and consequently an articficially designed O2 crystal is realized. In case of {[Cu2(pyrazine-2,3-dicarboxylate)2(pyz)]2H2O}n abbreviated as CPL-1 the O2 forms ladder-like structure. Previously we studied the magnetic excitation of the adsorbed O2 molecule in the protonated CPL-1 by inelastic neutron scattering. Though we succeeded in extracting the main excitation of O2 (singlet-triplet excitation at hw = J) by elaborate data analysis, the huge background from protons smeared detailed information. Particularly we could not conclude the existence of the triplet-quintet excitation (presumed to be observed at hw = 2J) because of the poor signal noise ratio (signal/noise ˜ 1/10). In addition the obtained temperature dependence of the singlet-triplet excitation was of poor quality. Hence we prepared 2 g of deterated CPL-1 sample and performed inelastic neutron scattering. We used PONTA spectrometer with horizontally focuse analyzer. The collimation was open-80′-radial collimation-open and Ef=14.7 meV. ORANGE type cryostat with specially designed sample probe for O2 induction experiment was used.

The energy scans on non O2 adsorbed (filled circles) and O2 adsorbed (open circles) CPL-1 are shown in Fig. (a). A well defined peak due to singlet-triplet excitation is observed at 7.8meV. The energy is consistent with previous study on protonated sample. The signal noise ratio is remarlably improved. In Fig. (b) we show the net contribution of O2 molecule at T = 2 K and 60 K. No signal is observed at hw =2J ˜16meV. This means that the O2 magnet realized in the nanoporous is not a simple spin dimer but probably a dimer magnet strongly coupled to lattice. Detail study on the exotic magnet will be published elsewhere.

The difficulty of this experiment is that we must collect a pair of scans on O2 adsorbed and O2 non-adsorbed samples for background subtraaction. Since the O2 adsorption process takes 12 hours, we perform all the presumably necessary scans on O2 adsorbed sample first. Then we do O2 de-adsorbtion process. After that we do the scans on non O2 adsorbed sample. The set of meaningful data can be obtained after these steps, that is, the end of maschine time. After the experiment we found that temperature dependence data is not enough for publication. We will continue this study in fisical year of 2009.

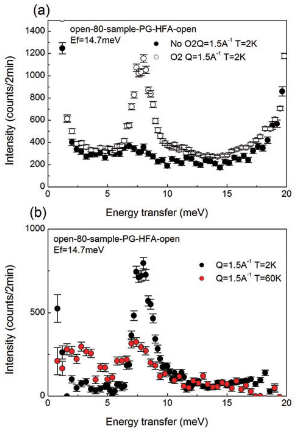

Fig. 1. (a) Energy scans in O2 adsorbed and non-adsorbed CPL1. (b) Energy scans at T = 2 K and 60 K after background subtraction

1-2-33

Chiral Helimagnetic Order in T1/3NbS2 (T=Cr, Mn)

Y. Kousaka1, Y. Nakao1, H. Furukawa2 and J. Akimitsu1
1Department of Physics and Mathematics, Aoyama-Gakuin Univ., 5-10-1 Fuchinobe,
Sagamihara 229-8558; 2Department of Physics, Ochanomizu Univ., 2-1-1 Ohtsuka,
Bunkyo-ku, Tokyo 112-8610

Systematic understanding of the interplay between a crystallographic structure and magnetic order is an important issue in the field of magnetism. In particular, the magnetic chirality triggered by crystallographic chirality has been discussed as a long-standing problem. An intercalate system of 2H-NbS2 type chiral crystal structure T1/3NbS2 (T = transition metal) has been paid attention as a candidate of chiral helimagnetic compounds. It shows a variety of magnetic order; paramagnetic (T = Ti, V), ferromagnetic (T = Mn) and antiferromagnetic (T = Fe and Co). Cr1/3NbS2 shows an magnetic anomaly at around Tc ˜ 130 K and small-angle neutron scattering experiments show helimagnetic ordering.[1] While neutron diffraction in Mn1/3NbS2 shows ferromagnetic, magnetization shows a magnetic anomaly as observed in Cr1/3NbS2.[2] Angle resolution of thermal neutron diffraction experiments is not high enough to separate fundamental Bragg peaks and magnetic satellite peaks. Therefore, Mn1/3NbS2 may be misinterpreted as a ferromagnetic ordering.

To examine the helimagnetic ordering in Cr1/3NbS2 and Mn1/3NbS2, we performed small angle neutron scattering experiments at SANS-U, a small-angle neutron scattering instrument with a 64 cm-wide position sensitive area detector, installed at JRR-3M, Tokai, Japan. The wavelength of incident neutron beam was 11 A. The data was taken by using powder samples. The magnetic satellite peak was detected by subtracting the room temperature data from the low temperature data, though the intensity at lower q position is negative value due to failing to subtracting paramagnetic scattering. Fig. 1 shows the observed magnetic peak position q and magnetic peak intensities. We succeed in observing the magnetic satellite peak, which indicates helimagnetic ordering with the pitch of 420 A for Cr1/3NbS2 and 700 A for Mn1/3NbS2. Therefore, the magnetic ordering in Mn1/3NbS2 is not ferromagnetic, but helimagnetic.

[1] T. Miyadai et al.: J. Phys. Soc. Jpn. 52 (1983) 1394.
[2] Y. Kousaka et al.: Nucl. Instr. and Meth. A 600 (2008) 250.

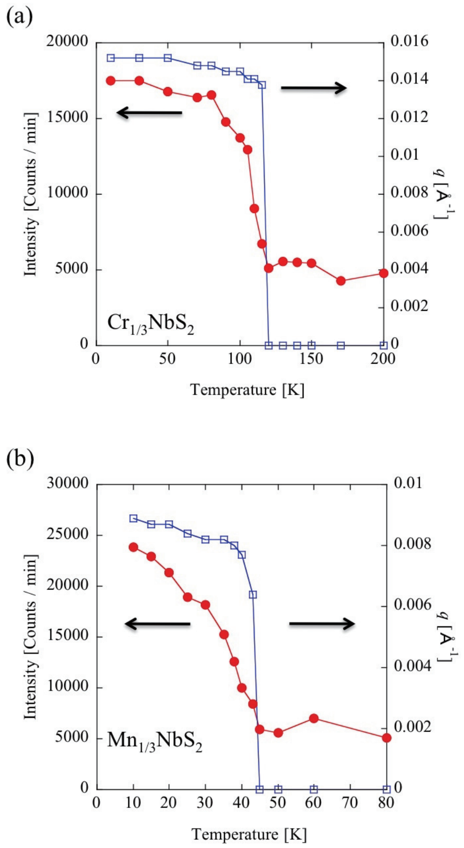

Fig. 1. Magnetic peak position q and the peak intensity in (a) Cr1/3NbS2 and (b) Mn1/3NbS2

1-2-34

Neutron powder diffraction of Tb1-xGdxB2C2(x=0.15,0.2)

E. Matsuoka(A), Y. Sasaki(A), K. Ohoyama(B), H. Onodera(A)
(A)Department of Physics, Tohoku University, (B)Institute for Materials Research, Tohoku University

The compound TbB2C2 shows an antiferromagnetic (AFM) ordering at TN = 21.7 K with a main [1 0 1/2] propagation vector and field-induced antiferroquadrupolar transitions [1]. The AFM phase in TbB2C2 that has been called phase IV shows some anomalous features in its magnetic behavior. The [1 0 1/2] wave vector in phase IV is peculiar to TbB2C2 since the other RB2C2 exhibit [1 0 0]-type AFM structure. Furthermore, the magnetic susceptibility anomalously increases below TN without any spontaneous magnetization. To obtain more precise information with respect to the anomalous magnetic behavior, effects of substitution of Tb3+ ions by Gd3+ have been examined and the T-x phase diagram of Tb1-xGdxB2C2 has been constructed [2]. The Gd substitution with a small content (x<0.075) induces drastic change of magnetic properties, namely, an intermediate magnetic phase named AFM1 appears at TO<T<TN. Here, TO is a transition temperature from AFM1 to phase IV. The neutron diffraction experiments of Tb0.94Gd0.06B2C2 have revealed that the magnetic structure of AFM1 phase is a long periodic one whose wave vector is [1+delta delta 0] with delta˜0.114 [3]. The magnetic structure below TO (phase IV) is described by the main wave vector of [1 0 1/2] in addition to the long-periodic component [3]. The results of neutron diffraction support the assumption proposed in ref. [2] that the antiferro-octupolar (AFO) order occurring at TO forces to align the magnetic moments with their wave vector of [1 0 1/2]. This assumption explains satisfactorily the anomalous properties of TbB2C2 and the Gd-substitution effects [2].

TO decreases very rapidly and disappears at x = 0.075, while TN increases with x. For compounds with x > 0.075, a new transition temperature T1 appears below TN. Although the magnetic phase for T1<T<TN is considered to be the same to AFM1 phase described above, that for T<T1 is not phase IV. The magnetic phase below T1 is called as AFM2 [2]. In this study, neutron powder diffraction experiments of Tb0.85Gd0.15B2C2 (x = 0.15) have been performed using HERMES installed at the JRR-3M reactor in JAEA to determine the magnetic structures for T1<T<TN and T<T1. Neutrons with a wavelength of 1.8204(5) A were obtained by the 331 reflection of the Ge monochromator. Since the natural boron is a strong neutron absorber, the 11B-enriched boron was used for the sample preparation.

Fig. 1 shows the neutron diffraction patterns of Tb0.85Gd0.15B2C2 measured at several temperatures. At paramagnetic region (T>TN), all of the Bragg peaks can be indexed as a LaB2C2-type tetragonal structure as shown in Fig. 1(a). On the other hand, weak satellite peaks around (101) and (211) are observed at 17 K (T1<T<TN) as shown in Fig. 1(b). The positions of these satellite peaks can be explained by considering a long periodic one whose wave vector is [1+delta delta 0] with delta˜0.11, implying that the magnetic structure at T1<T<TN is almost identical to AFM1 for Tb0.94Gd0.06B2C2. These satellite peaks disappears at 3.8 K and the other magnetic Bragg peaks appears as shown in Fig. 1(c). The magnetic Bragg peaks at 3.8 K (T<T1) can be explained by considering the wave vector of (100). Therefore, the magnetic structure of AFM2 is identical to that of GdB2C2.

[1] K. Kaneko et al., J. Phys. Soc. Jpn. 70 (2001) 3112.
[2] E. Matsuoka et al., J. Phys. Soc. Jpn. 75

(2006) 123707.
[3] Y. Sasaki et al., to be published in Physica B.
[4] Y. Yamaguchi et al., Appl. Phys. A 74 [Suppl.] (2002) S877.

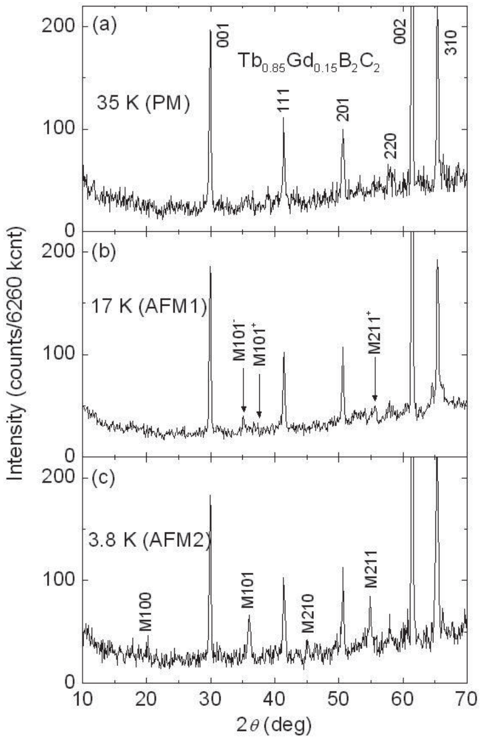

Fig. 1. Neutron powder diffraction patterns of Tb0.85Gd0.15B2C2 measured at several temperatures.

1-2-34

1-2-35

Elastic diffuse scattering of neutrons in Fe3Pt Invar alloys

M. Takasaka, Y. Tsunoda
School of Science and Engineering, Waseda University, 3-4-1 Ohkubo, Shinjuku-ku, Tokyo 169-8555

Very recently, we have found elastic diffuse scattering of neutrons around various Bragg peak positions for the typical Invar alloys Fe1-XNiX (0.35<X<0.60) alloys. The scattering intensities depend on temperature and Ni concentration and increase with decreasing temperature and decrease with increasing Ni concentration. Since the ranges of temperature and Ni concentration, for which diffuse scattering is observed, coincide with those for which the Invar anomalies are observable, the diffuse scattering seems to have strong correlations with the Invar effect. The experimental data were well reproduced as diffuse scattering due to the formation of clusters with the local lattice deformation wave propagating along the <1 1 0> direction and the <1 -1 0> polarization vector. Since an Fe65Ni35 Invar alloy is located close to the phase boundary of fcc-bcc martensitic transformation, the origin of the diffuse scattering would be explained as a pre-martensitic phenomenon of an fcc-bcc phase transition of the alloy.

Another archetypical Invar alloys, ordered and disordered Fe3Pt alloys are also located close to the phase boundary of an fcc-bcc martensitic transformation. Thus, we can expect similar diffuse scattering for these Invar alloys. We report observation of similar elastic diffuse scattering of neutrons for ordered and disordered Fe3Pt Invar alloys as those for the FeNi alloys. The experimental data were analyzed using the Huang diffuse scattering. In Fig 1, diffuse scattering observed around (200) for ordered Fe72Pt28 alloy and calculated one using the expression of Huang diffuse scattering are given. This pattern is very similar to that observed for the Fe65Ni35 alloy. Since the similar diffuse scattering is observed for the disordered Fe72Pt28 alloy, appearance of elastic diffuse scattering is a common feature of typical Invar alloys, ordered and disordered Fe3Pt and Fe1-xNix (0.35<x<0.5). Various anomalous magnetic behaviors have been reported by previous authors as common properties for the Invar alloys. The local lattice deformation observed here would give a strong effect to the magnetism of the Invar alloys. Spin modulations coupled with the local lattice deformation would be the future problem.

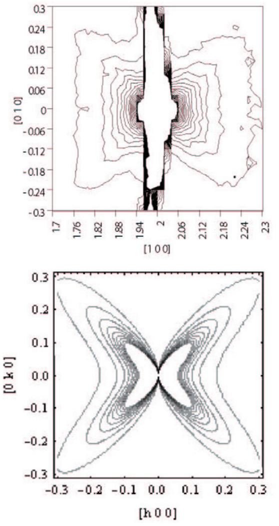

Fig. 1. Fig.-1 Observed and calculated diffuse scattering around (2 0 0)

Activity Report on Neutron Scattering Research: Experimental Reports **16** (2009)
Report Number: 843

1-2-36

Refinement of magnetic structure in the ferroelectric phase of Cu(Fe,Ga)O_2

T. Nakajima[1], S. Mitsuda[1], K. Yoshitomi[1], H. Kimura[2], Y. Noda[2]
[1] *Department of Physics, Faculty of Science, Tokyo University of Science, Tokyo 162-8601*
[2] *Institute of Multidisciplinary Research for Advanced Materials, Tohoku Univ., Sendai 980-8577*

Delafossite compounds $CuFeO_2$ (CFO), $CuFe_{1-x}Al_xO_2$ (CFAO) and $CuFe_{1-x}Ga_xO_2$ have been the subjects of increasing recent interest as a magneto-electric (ME) multiferroics, because of the discovery of the ferroelectricity in the field-induced or impurity-induced phase from the ground state.[1, 2] In the previous study, we have reported that the magnetic structure in the ferroelectric phase of these systems is a 'proper-screw-type' magnetic structure shown in Fig.1(a),[2] suggesting that the origin of the ferroelectricity is not the 'spin-current' model but the *d*-*p* hybridization model.[3] However, the previous measurements was not so sensitive to the direction of the helical axis and the ellipticity of the magnetic structure. In order to confirm the origin of the ferroelectricity in this system, it is critical to refine the magnetic structural parameters in detail. In the present measurements, therefore, we have performed precise refinement of the magnetic structure using 4-circle neutron diffraction and a single-crystal CFGO ($x = 0.035$) sample, which exhibits the ferroelectric phase under zero magnetic field.

The neutron diffraction measurements were performed using the four-circle neutron diffractometer FONDER installed at JRR-3 in JAEA. The incident neutron beam with wavelength 1.239 Å was obtained by a Ge(311) monochromator. The sample was mounted on a closed-cycle He-gas refrigerator.

For the magnetic structure analysis, we have measured integrated intensities of more than 130 magnetic Bragg reflections at $T = 2.8$ K and 6.5 K. The effect of neutron absorption was corrected by the DABEX software. Using a homemade least-square fitting program, we have refined the lengths of the magnetic moments along x and z axes (μ_x and μ_z), the phase shift in the magnetic modulation (δ), and the direction of the helical axis. As a result, the direction of the helical axis was determined to be parallel to the b-axis within the experimental accuracy, and the ellipticity and the phase shift were determined to be $\mu_x/\mu_z = 0.895$ and $\delta = 73.4°$ at $T = 2$K, respectively. These results strongly confirm that the origin of the ferroelectricity in this system is not the 'spin-current' model but the *d*-*p* hybridization model.[3] We also found that the ellipticity and the phase shift slightly decrease with increasing temperature. More comprehensive analysis including results of spherical neutron polarimetry will be published elsewhere.

References

[1] T. Kimura *et al.*: PRB **73** 220401(2006).
[2] T. Nakajima *et al.*: JPSJ **76** 043709 (2007).
[3] T. Arima: JPSJ **76** 073702 (2007).

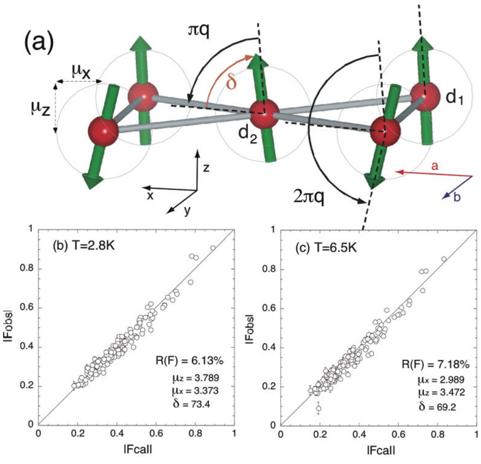

Fig. 1. (a) Magnetic structure in the ferroelectric phase. [(b)-(c)] Comparison between $|F_{cal}|$ and $|F_{obs}|$ obtained from the magnetic structure analysis at (b) $T = 2.8$ K and (c) $T = 6.5$ K.

1-2-37

Magnetic Structure in $Ba_2Mg_2Fe_{12}O_{22}$

H. Sagayama(A), K. Taniguchi(A), T. Arima(A), Y. Nishikawa(B), S. Yano(B), J. Akimitsu(B), H. Kimura (A), Y. Noda(A)
(A)IMRAM, Tohoku Univ., (B)Dept. Phys., Aoyama-Gakuin University

It has been recently found that a Y-type hexaferrite $Ba_2Mg_2Fe_{12}O_{22}$ (BMFO) exhibits a nonlinear magnetoelectric effect [1,2]. It is proposed that the conical magnetic structure at low temperatures is modified by the application of a weak magnetic field perpendicular to the cone axis of the *c* axis, which produces the electric polarization. To reveal the correlation between the magnetic structure and the electric polarization in the presence of magnetic field, we carried out a magnetic structure analysis of a single crystal of BMFO with $H \parallel b^*$.

Single crystals of BFMO were grown from Na_2O-Fe_2O_3 flux. Neutron diffraction measurement was performed with a four-circle neutron diffractometer FONDER at JRR-3. A single crystal was set in a magnetic field of about 0.3 T between two permanent magnets. The direction of the magnetic field was parallel to the b*-axis. The crystal was then cooled down to 4 K. Profiles of 397 fundamental reflections and 105 pure magnetic reflections with the magnetic modulation vector Q=(0 0 3/2) were measured.

From the least-square fit of the intensities of the pure magnetic reflections, we determine the antiferromagnetic component with a period of 2/3 c. Figure 1 shows the projection of the magnetic structure along the magnetic field. It clearly shows the noncollinear nature of the magnetic structure. In fact, the spin current model [3] or the inverse Dzialoshinskii-Moriya interaction [4], defined as

$$\Delta p_{ij} \propto e_{ij} \times (S_i \times S_j),$$

can explain the macroscopic electric polarization along the a-axis. Here, Δp_{ij} is a local electric polarization induced by a nonlinear pair of adjacent spin moments S_i and S_j, connected by a unit vector e_{ij}.

References

[1] K. Taniguchi et al., Appl. Phys. Express **1**, 031301 (2008).

[2] S. Ishiwata et al., Science **319**, 1643 (2008).

[3] H. Katsura et al., Phys. Rev. Lett. **95**, 057205 (2005).

[4] I. A. Sergienko and E. Dagotto, Phys. Rev. B **73**, 094434 (2006).

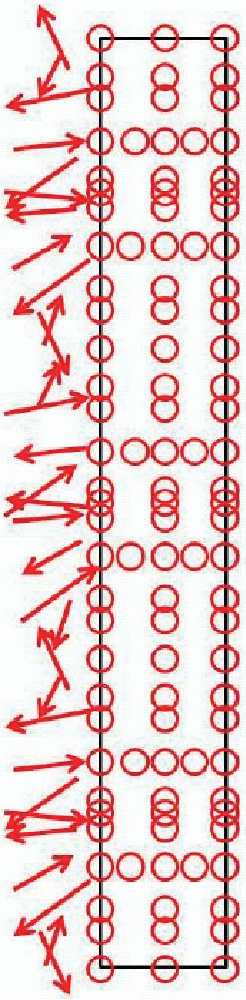

Fig. 1. Projection of the magnetic structure of a Y-type hexaferrite $Ba_2Mg_2Fe_{12}O_{22}$ along the b*-axis at 4 K. A magnetic field of 0.3 T is applied perpendicular to the projection.

1-2-38

Effective random-fied domain-state in Ga-substituted $CuFeO_2$

T. Nakajima, S. Mitsuda, M. Yamano, H. Yamazaki, K. Kuribara
Department of Physics, Faculty of Science, Tokyo University of Science, Tokyo 162-8601

The effects of random field on the stability of a long-range magnetic ordering have been extensively studied from 1980s. In the early stage, the random-field effect was experimentally investigated using diluted antiferromagnets under applied magnetic field.[1] The recent experimental studies on $CsCo_{1-x}Mg_xBr_3$ have revealed that a combination of a partially-disordered magnetic structure, which often shows up in some magnetically frustrated systems, and site-random magnetic vacancies can generate 'effective-random-field' without an application of external magnetic field.[2]

In the previous works, we have found that $CuFe_{1-x}Al_xO_2$ ($x > 0.10$) exhibits the effective random-field domain-state, in which the local magnetic structure is a sinusoidally amplitude modulated incommensurate structure.[3] We also found that the scattering function $S(q)$ broadens as the Al-concentration increases. This indicates that the magnetic correlation length is shortened by the Al-substitution. However, the recent studies on $CuFe_{1-x}Ga_xO_2$ have pointed out that the Al-substitution produces not only the magnetic vacancies but also local lattice distortions due to the difference between the ionic radii of Fe^{3+} and Al^{3+}.[4] Although this local distortion might disturb the long-range magnetic ordering, this should be distinguished from the effective random-field effect. In order to purely investigate the effective random-field effect, in the present study, we used Ga-substituted $CuFeO_2$ samples, in which the local lattice distortion is relatively small.

We performed neutron diffraction measurements on $CuFe_{1-x}Ga_xO_2$ samples with $x = 0.20$ and 0.30, using the triple-axis neutron spectrometer HQR(T1-1) installed at JRR-3. The collimation open- '40- '40- '40 was employed. The wavelength of the incident neutron is 2.44 Å. The single crystal of $CuFe_{1-x}Ga_xO_2$ samples were mounted in a ^{4}He-pumped cryostat with a hexagonal (H, H, L)-scattering plane. In order to evaluate the magnetic correlation length quantitatively, we analyzed the scattering profile, using Multi-Profile-Deconvolution (MPD) method presented in Ref. [3].

Figures 1(a) and 1(b) show the $(H, H, 3/2)$ diffraction profiles at $T = 2.0$K and results of the MPD-analysis. For both samples, the functional form of $S(q)$ are well described by the sum of a Lorentzian term and Lorentzian-Squared term shown in Fig. 1(c). The Lorentzian-squared component dominating at low temperature indicates the domain state as seen in the prototypical random-field Ising model.[1] While the ratio between the amplitudes of Lorentzian and Lorentzian-squared terms are comparable to each other ($B/A = 0.02 \sim 0.09$), the widths of $S(q)$ are rather different. The further detailed analysis is now in progress.

References

[1] D. Belanger *et al.*: PRB **31** 4538 (1985).
[2] J. van Duijn *et al.*: PRL **92** 077202 (2004).
[3] T. Nakajima *et al.*:JPCM **19** 145216 (2007).
[4] N. Terada *et al.*: PRB **78** 014101 (2008) .

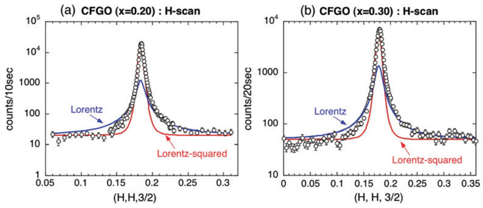

(c) Scattering Function

$$S(\boldsymbol{q}) = \frac{A}{(1+(q_a^2+q_b^2)/K_{ab}^2+q_c^2/K_c^2)^2} + \frac{B}{1+(q_a^2+q_b^2)/K_{ab}^2+q_c^2/K_c^2}$$

Fig. 1. [(a)-(b)] $(H, H, 3/2)$ diffraction profiles of (a) $x = 0.20$ sample and (b) $x = 0.30$ sample at $T = 2.0$K, and results of the MPD-analysis.(c) The definition of the functional form of the scattering function $S(q)$.

1-2-39

Competing Interactions in Two Dimensional Square Lattice CuSb2-xTaxO6

M. Nishi, M. Kato(A) and K. Hirota(A)
ISSP Univ. of Tokyo, (A)Inorganic Chemistry Lab. Doshisya Univ.

CuSb2O6 compound has a tri-rutile type structure in which Cu2+ ions form a square lattice [1]. The magnetic susceptibility of CuSb2O6 indicates a typical behavior for S=1/2 one-dimensional Heisenberg antiferromagnet above 20K and shows a antiferromagnetic (AF) long-range order at 8.7 K in which Cu spins are aligned ferromagnetically along b-axis (namely collinear order) with a propagation vector (1/2, 0, 1/2) [2, 3]. If nearest neighbor coupling J1 is too stronger than next nearest coupling J2 along diagonal, Neel order will be stabilized. Then J2 interaction through Cu-O-O-Cu bond is dominant on the collinear order of CuSb2O6. The substitution of Ta atom instead of Sb atom causes the decreasing of transition temperature of long-range order which disappears above x=1 [4]. TaO6 octahedron occupies inter CuO layers and the inter layer coupling may be decreased with the substitution of Ta atom; x. In this reason we can study the J1 and J2 couplings about CuO layer only at the compound with x=1. When J2 coupling is AF, there are the spin frustrations between J1 and J2 couplings even if J1 coupling is ferromagnetic or AF [5].

The results of first neutron inelastic scattering measurements of CuSbTaO6 powder samples were reported at last year (#461, #464) that the magnetic spin gap was observed at 0.8 meV with the use of PONTA (5G) spectrometer. High energy resolution experiments were done for the confirmation of the spin gap by the cold neutron triple-axis spectrometer HER (C11) installed at the JRR-3M reactor at JAEA. Magnetic excitation peak was observed at Q=0.6A-1 for constant E=0.4 meV, 1.0 meV and 1.4 meV scans at the temperature 5K as shown in figure 1. The spin gap in magnetic scattering could not be observed with the energy resolution 0.14 meV. This result indicates that CuSbTaO6 is typical one-dimensional magnetic substance. The peak position along Q is near 0.6 A-1 in deviation from the expected value 0.4735 A-1 in Cu-O-O-Cu chain.

References
[1] A. M. Nakua et al., J. Solid State Chem. 91 (1991) 105.
[2] M. Kato et al., J. Phys. Soc. Jpn. 71S (2002) 187.
[3] B. J. Gibson et al., J. Mag. Mag. Mater. 272-6 (2004) 927.
[4] M. Kato et al., J. Phys. Chem. Sol. 63 (2002) 1129.
[5] N. Shanon et al., Eur. Phys. J. B38 (2004) 599.

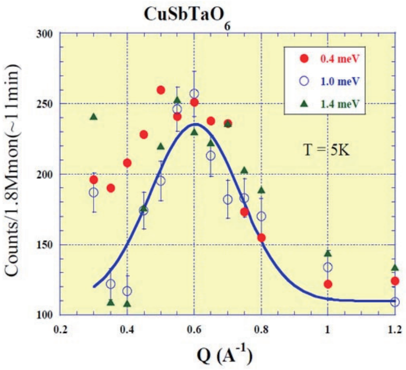

Fig. 1. The experimental results of CuSbTaO6 powder sample by the cold neutron-scattering. Magnetic spin gap was not observed and the peak by antiferromagnetic correlation was observed at several constant E-scan.

1-2-40

Spin-driven dielectric relaxation in a paraelectric phase of magneto-electric multiferroic $CuFeO_2$

S. Mitsuda , M. Yamano , K. Kuribara , T. Nakajima , K. Masuda, and K. Yoshitomi
Department of Physics, Faculty of Science, Tokyo University of Science, Tokyo 162-8601

Magnetic oxide $CuFeO_2$ is a rare magneto-electric multiferroic where magnetic field-induced or nonmagnetic impurity-induced proper helical magnetic ordering generates a spontaneous electric polarization. We have measured the complex permittivity in various magnetic phases under an applied magnetic field up to 15 T, and found Debye-type-like dielectric dispersion with low relaxation frequency in only 4-sublattice(4SL) antiferromagnetic ground state. The relaxation frequency of dielectric dispersion shows interesting anisotropic magnetic field as well as temperature dependences. Although so-called Maxwell-Wagner effect in a dielectric system with heterogeneous nature can often explain this kind of magnetodielectric effect [1], we speculated that 4SL-specific magnetic domain wall motion must be responsible for the dielectric dispersion; As shown in Fig. 1(a), the magnetic domain wall moving back and forth, and corresponding displacement of oxygen near magnetic domain wall can be responsible for the dielectric dissipation. Here, we consider the magnetic domain wall is essentially the same as AD-type domain wall discussed in domain growth kinetics in the isosceles triangular Ising antiferromagnet $CoNb_2O_6$ [2].

In order to check the existence of the magnetic domain state in 4SL phase of $CuFeO_2$, we have performed neutron diffraction experiments to determine the functional form of the scattering function, using the triple-axis neutron spectrometers HQR(T1-1) installed at JRR-3. The collimation open-'40-'40-'40 was employed, and the wavelength of the incident neutron was 2.44 Å. As shown in Fig. 1(b), scattering profile of 4SL $(1/4, 1/4, 3/2)$ magnetic reflection is entirely different from resolution-limited Gaussian and rather close to Lorentzian-squared specific to the magnetic domain state. The further detailed analysis using Multi-Profile-Deconvolution method [3] is now in progress.

References

[1] G. Catalan, APL. **88**, 102902 (2006).
[2] S. Kobayashi et al., PRB **69**, 144430 (2004).
[3] T. Nakajima *et al.*:JPCM **19** 145216 (2007).

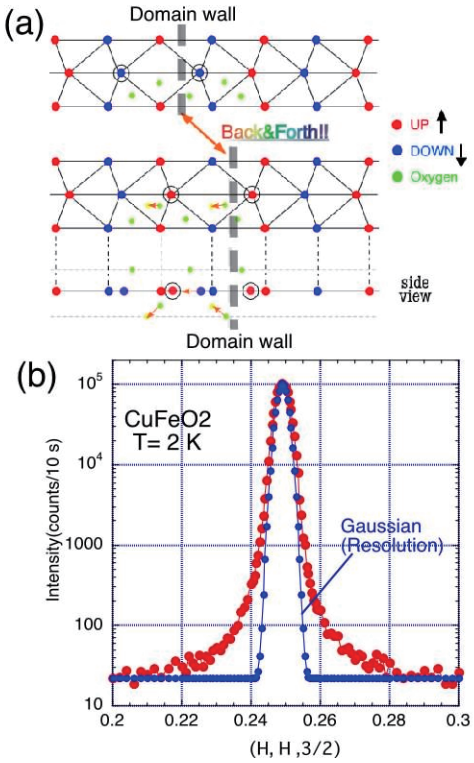

Fig. 1. a) Schematic drawings of magnetic domain wall moving back and forth, (b) scattering profile of 4SL (1/4, 1/4,3/2) magnetic reflection.

1-2-41

Inelastic Neutron Scattering Study on Triangular Lattice Antiferromagnet $CuCrO_2$

T. Nozaki, K. Hayashi, and T. Kajitani
Department of Applied Physics, Graduate School of Engineering, Tohoku University, Sendai, 980-8579

Delafossite-type oxide $\mathrm{Cu}B\mathrm{O}_2$ has received much attention as a model material of the magnetically frustrated triangular lattice antiferromagnets. $CuFeO_2$ reaches Ising-like antiferromagnetic state thorough 2-step phase transitions at T_{N1} = 14 K and T_{N2} = 10.5 K. On the other hand, $CuCrO_2$ shows Heisenberg-type antiferromagnetic state below T_N = 24 K. Recently both systems have been intensively studied due to the local ferroelectric polarization[1,2]. Previously we measured the inelastic neutron scattering (INS) spectra of $CuFeO_2$ powder. Below 12.5 K the INS peaks corresponding to the creation of localized magnon mode were observed. Above 11 K, the quasi-elastic neutron scattering (QNS) peak was observed. In this study, we measure the INS spectra of $CuCrO_2$ powder using a cold neutron spectrometer, AGNES (C3-1-1), to compare the magnetic behavior with $CuFeO_2$.

Figure 1 shows neutron scattering intensity, $S(E)$, being the summation of $S(|\boldsymbol{Q}|, E)$ in the $\boldsymbol{Q}$-space of $CuCrO_2$ powder taken at 10, 20, 30, and 150 K. In the $CuCrO_2$ case, only the QNS peak is observed. The maximum QNS intensity is observed at 30 K, just above T_N. Below 30 K, the QNS intensity exists in the $\boldsymbol{Q}$-space below $|\boldsymbol{Q}| = 1.5\ \mathrm{A}^{-1}$. In comparison, the QNS intensity at 150 K appears in the observed Q-space, conceivably due to the Heisenberg paramagnetic scattering. For further understanding of the corresponding spin dynamics, INS measurements on $CuFeO_2$ and $CuCrO_2$ using the triple-axis spectrometer HER (C1-1) is underway.

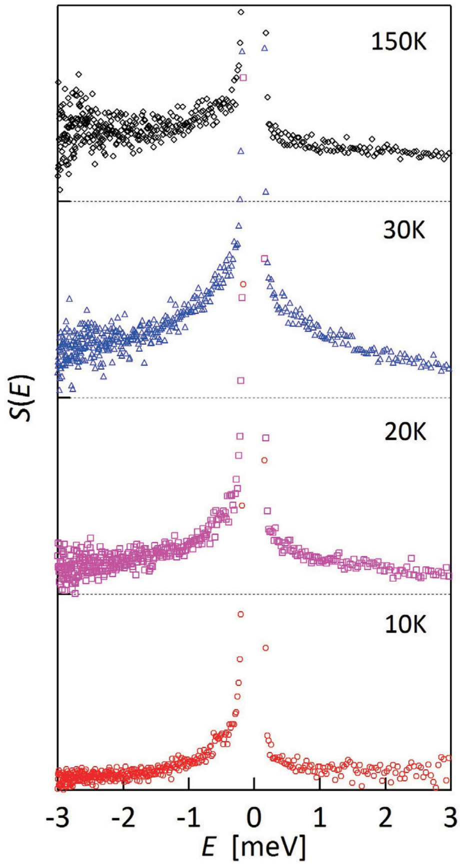

Fig. 1. Inelastic neutron scattering spectra of $CuCrO_2$ powder at 10, 20, 30, and 150 K.

References

[1] T. Kimura, J. C. Lashley, and A. P. Ramirez: Phys. Rev. B **73** (2006) 220401.

[2] S. Seki, Y. Onose, and Y. Tokura: Phys. Rev. Lett. **101** (2008) 067204.

1-2-42

Observation of magnetic fluctuation in Ni2(OD)3Cl by neutron scattering

Y. Oohara1, M. Hagihala2, X.G. Zheng2
1, ISSP, Univ. of Tokyo, 2, Faculty of Sci. and Engineer. Saga Univ.

As the temperature is decreased, conventional magnetic materials exhibit a slowing down of the magnetic fluctuations as the temperature approaches the critical point, Tc (namely the critical slowing down). Crossing Tc, the fluctuations disappear rapidly and the magnetic moments are frozen into static at T << Tc. All conventional magnetic materials of ferromagnets, antiferromagnets or spin glasses are featured by the freezing of magnetic moments into static. Recently there are reported new dynamical magnetic states of spin ice and spin liquid in rare earth pyrochlores where magnetic fluctuation persist down to 0 K. However, these states are basically disordered and do not have an order over a macroscopic range (long range order). It is believed that a long range order in magnet must be fully frozen (static).

However, recently we observed an exotic dynamical antiferromagnetic order below TN=4.5K in Ni2(OH)3Cl by muon spin relaxation (1). The present neutron scattering study was designed to further investigate this magnetic order. Elastic and inelastic measurements were performed at HQR and HER, respectively, at JAEA. The elastic measurement showed a clear long range order extending over a spacing of approximately 56 (Fig. 1). Inelastic measurements suggested spin fluctuation of 0.5 meV at 0.8 K, which is less than 1/5 of its transition temperature. The analysis to reveal its magnetic structure is in progress.

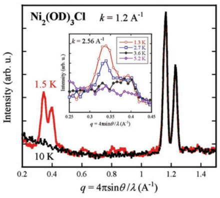

Fig. 1. Elastic scattering data showing magnetic reflections in the ordered state. The inset plot shows the evolution of two magnetic peaks below TN.

References:
[1] X. G. Zheng, M. Hagihala, K. Nishiyama, T. Kawae,Physica B 404 (2009) 677-679.

1-2-43

Study of spin gap in two-dimensional frustrated triangular lattice: YbAl3C3

M. Kosaka(A), T. Kobiyama(A), A. Yamada(A), K. Ohoyama(B), N. Aso(C)
(A)Grad. School of Sci. and Engi., Saitama Univ., (B)IMR Tohoku Univ., (C) ISSP-NSL Univ. Tokyo

YbAl3C3 shows the highly frustrated phenomena with a spin gap. The inelastic neutron spectra of low-lying magnetic excitations at low temperatures are quite similar to those of SrCu2(BO3)2 and (CuCl)LaNb2O7 that exhibit a dimer ground state in a two-dimensional quantum spin system. In order to investigate low-lying magnetic excitations at low temperature, we performed inelastic neutron scattering (INS) measurements on the triple-axis spectrometer C1-1 (HER) installed at the JRR-3M reactor. The collimations after the monochromator were open-(Sample)-radial collimator-open.

Figure 1 shows the spectra measured using Ef=2.4 meV with a high resolution of 0.06 meV at T=0.7 K. As a result, it became clear that the first excited state consists of three excitations and the second excited state is composed of many excitations. The solid line shows the least-squares fit to the experimental data where the peaks are approximated by three Gaussian curves. The excitation energies are estimated to be 1.22, 1.42, and 1.62 meV using the same full widths at the half maximum of 0.18 meV. In single crystalline SrCu2(BO3)2, the three resolved branches of the triplet excitation, which are attributed to the Dzyaloshinski-Moriya interaction, were observed by high-resolution INS experiments. The crystal symmetry of YbAl3C3 lowers below the phase transition at 80 K; this will satisfy the condition of the Dzyaloshinski-Moriya interaction. When we consider the analogy between the results of the INS measurements for these two compounds, the first and the second excitations are expected to be the single-triplet excitations and two-triplet excitations, respectively. Moreover, the energy gaps, $\Delta_1 \simeq 1.5$ and $\Delta_2 \simeq 2.9$ meV, satisfy the relation $\Delta_2 \approx 2\Delta_1$.

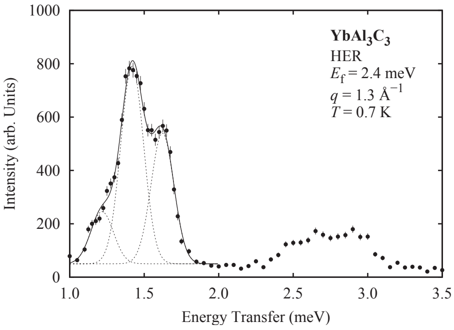

Fig. 1. Detailed inelastic neutron spectra of YbAl3C3 at 0.7 K with Ef=2.4 meV. The full curve represents the least-squares fit where the peaks are approximated by three Gaussian curves.

1-2-44

Spin Waves in MnP

S. Yano(1) , M. Nishi(2), M. Matsuura(3), K. Hirota(3) and J. Akimitsu(1)
(1)Department of Physics and Mathematics, Aoyama-Gakuin Univ., 5-10-1 Fuchinobe, Sagamihara(2) Institute for Solid State Physics, The Univ. of Tokyo 106-1 Shirakata, Tokai 319-1106(3)Department of Earth and Space Sceince, Graduate School of Science

Manganese phosphide MnP is a ferromagnetic intermetallic compound below TC = 291K, and it transforms into a proper screw state at T* = 47K.

The crystal structure is a slightly distorted NiAs structure with the lattice parameters of a = 5.916 , b = 5.260 , c = 3.173 at room temperature. In the ferromagnetic state, the easy-axis of the magnetization is the c-axis. In the proper screw state, the spin rotates in the b-c plane with a propagation vector $\delta = 0.117a^*$ along the a-axis.

One of our interests of MnP is the mechanism of transition from ferromagnetism to helimagnetism which had not been explained by theoretical viewpoint. In order to elucidate the mechanism, the information of spin wave in the whole Brillouin zone is crucially important.

The ferromagnetic spin-waves along the three principal axes had been measured by Todate et al[1]. They reported that the dispersion relation along the a-axis exhibits anomalous wave vector and temperature dependence, and also the quadratic q dependence was observed both along the b- and c-axes. In the proper screw state, spin-waves along the a- and b-axes had been measured by Tajima et al[2]. They reported the anomalous jump around T* along the a-axis which may be related to 3δ.

In order to obtain the spin wave dispersion relations, we performed the neutron inelastic scattering experiments at triple-axis spectrometer PONTA (5G), JRR-3M reactor in JAERI (Tokai).

The single crystal of MnP, whose size is 9mm φ × 40mm, was grown by the Bridgman method.

The spin wave dispersions have been mearsured along the a-axis at 12 K and 50K, as shown in Fig1. We could observe the spin wave dispersions along the a-axis, however, anomalous jump around T* which Tajima et al reported was not found. It is probably broadened dispersion due to itinerant magnetism.

In order to obtain the spin waves in the whole Brillouin zone, further measurements of spin waves at higher energy (~ 100meV) and lower energy (0 ~ 2 meV) are now in progress.

References

[1] Y Todate et al.: Jou Phys Soc Jpn. 56 36 (1987).
[2] K Tajima et al.: Jou Mag Mag Mat. 15-18 373-374 (1980).

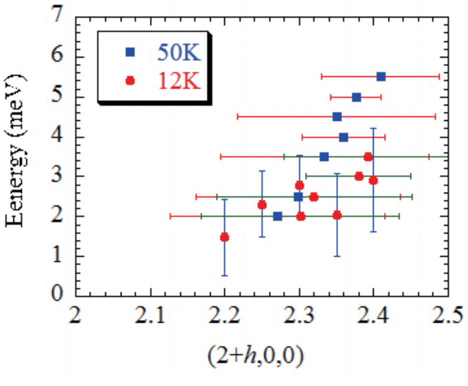

Fig. 1. Spin wave relations along the a-axis

1-2-45

Spin Waves in MnP

S. Yano(1) K. Iwasa(2) and J. Akimitsu(1)
(1)Department of Physics and Mathematics, Aoyama-Gakuin Univ., 5-10-1 Fuchinobe, Sagamihara (2) Department of Physics, Tohoku University, Sendai 980-8587

Manganese phosphide MnP is a ferromagnetic intermetallic compound below TC = 291K, and it transforms into a proper screw state at T* = 47K.

The crystal structure is a slightly distorted NiAs structure with the lattice parameters of a = 5.916 , b = 5.260 , c = 3.173 at room temperature. In the ferromagnetic state, the easy-axis of the magnetization is the c-axis. In the proper screw state, the spin rotates in the b-c plane with a propagation vector δ = 0.117a* along the a-axis.

One of our interests of MnP is the mechanism of transition from ferromagnetism to helimagnetism which had not been explained by theoretical viewpoint. In order to elucidate the mechanism, the information of spin wave in the whole Brillouin zone is crucially important.

The ferromagnetic spin-waves along the three principal axes had been measured by Todate et al[1]. They reported that the dispersion relation along the a-axis exhibits anomalous wave vector and temperature dependence, and also the quadratic q dependence was observed both along the b- and c-axes. In the proper screw state, spin-waves along the a- and b-axes had been measured by Tajima et al[2]. They reported the anomalous jump around T* along the a-axis which may be related to 3 δ.

We performed the neutron inelastic scattering experiments at triple-axis spectrometer TOPAN (6G), JRR-3M reactor in JAERI (Tokai).

The single crystal of MnP, whose size is 9mm φ × 40mm, was grown by the Bridgman method.

The spin wave dispersions have been measured along the a-axis at 14 K, 35K, 54K and 81K, as shown in Fig1. The dispersion curve below T*, there seems to be two lines. However, the indicated lines by an arrow are arised from another Brillouin zone.

In order to obtain the spin waves in the whole Brillouin zone, further measurements of spin waves at higher energy (~ 100meV) and lower energy (0 ~ 2 meV) are now in progress.

References
[1] Y Todate et al.: Jou Phys Soc Jpn. 56 36 (1987).
[2] K Tajima et al.: Jou Mag Mag Mat. 15-18 373-374 (1980).

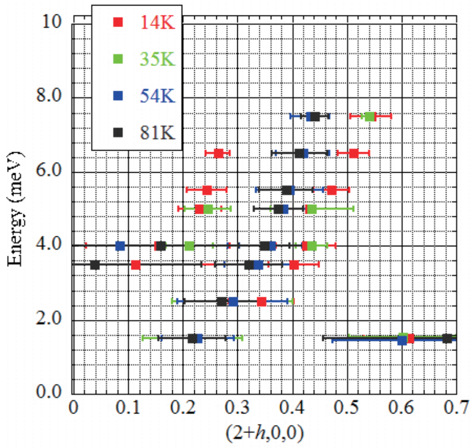

Fig. 1. Spin wave relations along the a-axis

1-2-46

Research for magnetic reflections on HoRh2Si2

T. Shigeoka(A), A. Tanaka(B), G. Nakamoto(C)
(A) Grad. Sch. of Sci. Eng. Yamaguchi Univ, (B) Grad. Sch. of Sci. Eng. Hiroshima Univ.
(C)Japan Advanced Institute of

The ternary compound $HoRh_2Si_2$ crystallizes in the tetragonal $ThCr_2Si_2$-type crystal structure (space group: I4/mmm). It shows an antiferromagnetic order below T_N=29.5 K. Recent magnetic study shows that $HoRh_2Si_2$ has three transitions: T_1=12.4 K, T_2=27.5 K and T_N=29.5 K. The neutron diffraction study were performed on a single crystal compound and following results have been reported [1]; at low temperatures below T_1, an appearance of antiferromagnetic reflections associated with the propagation vector k= (0, 0, 1) has been confirmed. Both (001) and (100) reflections are observed, indicating that magnetic moments tilt from the c- and a-axis. This result is consistent with the previous report [2]. The (001) reflection disappears above T_1. The temperature dependency of intensity of (100) peak changes at T_1. In intermediate temperature region $T_1<T<T_2$, only antiferromagnetic reflections associated with the AFI-type structure are observed. All magnetic reflections disappear above T_2; for $T_2<T<T_N$, magnetic reflections could not detected at all. We believe that new magnetic reflections should appear for $T_2<T<T_N$. Thus neutron study has been carried out on a powdered sample for 4K-35K by using the HERMES spectrometer of JRR-3M with wave length of 1.82645 A.

For low temperatures, the previous results have been confirmed; the antiferromagnetic structure with the propagation vector k= (0, 0, 1) appears below T_2.

Neutron diffraction patterns above T_2 are shown in Fig. 1. New antiferromagnetic reflections (indicated by arrows) appear, indicating a change of the magnetic structure at T_2. The detail analysis is now in progress.

References
[1] T. Shigeoka et al., Activity report on Neutron Scat. Res. Vol.14 (2008)
[2] M. Slaski et al., J. Magn. Magn. Mat. 39(1983)268.

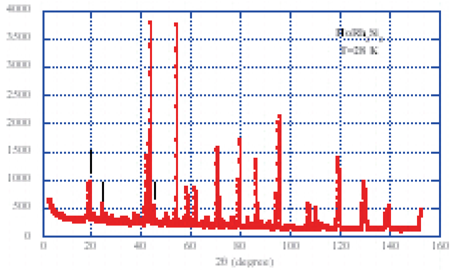

Fig. 1. Neutron diffraction patern at 28 K below TN.

1-2-47

Neutron scattering study on the magnetic moleculars

K. Iida[A], H. Ishikawa[B], T. Yamamse[B], T. J Sato[B]
[A]*ISSP*, [B]*Dept. of Phys. Tokyo Inst. of Tech*

Several triangular spin clusters showed an attractive phenomenon, that is a half-step magnetization change with hysteresis. The avoided level crossing between the $S_{total} = 1/2$ and $S_{total} = 3/2$ states due to the DM interaction is suggested to be the origin of the half-step change [1]. One of such molecular nanomagnets exhibiting the half-step change is the V_3 molecular nanomagnet [2]. Although the DM interaction is of particular importance in these system, there are no report on the DM interaction using the microscopic method. Hence, we have performed an inelastic neutron scattering (INS) to investigate the DM interaction.

Approximately 0.7 grams of deuterated powder sample were used in our INS experiments on HER. We plotted INS spectra in the range of $0.5 \leq \hbar\omega \leq 1.0$ meV in Fig. 1 (a). At lower temperature, the intensity around $\hbar\omega = 0.8$ meV apparently grew up. In contrast, the peak almost disappears at 5.4 K, and there remains only the incoherent component in the INS spectrum. Same results were obtained on $E_f = 3.0$ meV as shown in Fig. 1 (b). As a model Hamiltonian, we here propose the following form consisting of anisotropic exchange and DM interactions and the Zeeman term;

$$\mathcal{H} = -\sum_{i=1}^{3}\left[J^x\left(s_i^x s_{i+1}^x + s_i^y s_{i+1}^y\right) + J^z s_i^z s_{i+1}^z\right] + \sum_{i=1}^{3} D_{i,i+1}^z\left(s_i^x s_{i+1}^y - s_i^y s_{i+1}^x\right).$$

By fitting the calculated intensity to the temperature difference obtained in the experiment using the least-squares method, we estimated the optimum exchange and DM parameters. The obtained parameters are bellow; $J^x = J^y = -6.51 \pm 0.04$K, $J^z = -5.43 \pm 0.05$ K, $D_{1,2}^z = 0.257 \pm 0.10$ K, and $D_{2,1}^z = D_{3,1}^z = 0.284 \pm 0.12$ K. The calculated scattering intensitys are shown in Figs. 1 (a) and 1 (b) using the solid lines: a good coincidence with the observation can be readily seen. This satisfactory correspondence ensures the reliability of the estimated parameters.

By ascribing the 0.8 meV peak to a superposition of four magnetic excitations between two $S_{total} = 1/2$ and two $S_{total} = 3/2$ doublets, we have successfully estimated the anisotropic as well as the antisymmetric interactions. And this result is the evidence that the DM interaction exsist in V_3.

[1] K. Y. Choi et al., Phys. Rev. Lett. 96, 107202 (2006)
[2] T. Yamase et al., Inorg. Chem. 43, 8150 (2004).

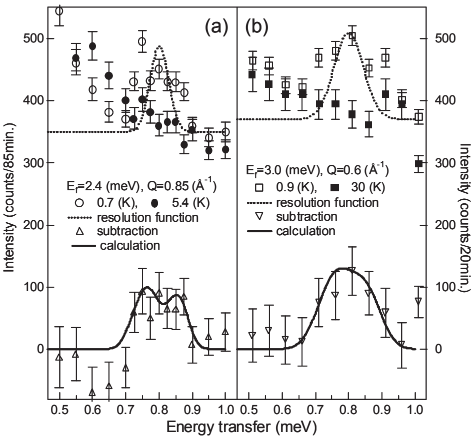

Fig. 1. (a) INS results on $E_f = 2.4$ meV. (b) INS results on $E_f = 3.0$ meV.

1-2-48

Crystal Field Softeing and Magnetic Phase Transition in HoB_4

T. Matsumura and D. Okuyama(B)
AdSM, Hiroshima University, RIKEN CMRG (B)

A tetragonal rare-earth system of RB_4 has attracted interest as a sytem where the quadrupolar and magnetic degrees of freedom are active on the so-called Shastry-Sutherland lattice. HoB_4 exhibits two phase transitions at $T_{N1} = 7.5$ K and at $T_{N2} = 5.9$ K. The details of the magnetic structures and the anomalous nature of the phase transitions have been reported in Ref. 1. Below T_{N1} an incommensurate magnetic order sets in with Q=$(\delta, \delta, \delta')$ ($\delta = 0.022$, $\delta' = 0.07$), followed by a first order transition into a commensurate order with Q=$(1, 0, 0)$ at T_{N2}. One of the anomalous results in the study was the very broad magnetic diffuse scattering around (0, 0, 0.5) and (1, 0, 0). In order to clarify the origin of this diffuse scattering and the anomalous phase transitions, we have carried out an inelastic neutron scattering experiment on a triple-axis spectrometer HER, using cold neutrons to achieve high energy resolution at low energies. Horizontal focusing analyzer, radial collimator, Be and PG filters were used at an final energy of 5.01 meV.

Fig. 1 shows the temperature dependences of the CEF excitation energy at Q=(1, 0, 1) and (2, 0, 0.43). The former and the latter corresponds to the commensurate and incommensurate magnetic structures, respectively. As shown by the plot, the CEF energies at these Q-vectors decrease with decreasing temperature down to T_{N1}. Simultaneously, in the paramagnetic phase above T_{N1}, quasi-elastic peaks gradually develop at these Q-vectors. The temperature dependences of the inverse intensity are plotted in the bottom figure. This clearly demonstrates that the commensurate and incommensurate correlations coexist in the paramagnetic phase, and well follow the Curie-Weiss behavior until they diverge at the respective transition temperatures. This can be understood within the mean-field approximation.

The softening of the CEF can also be understood within the mean-field approximation as reflecting $\chi(Q, \omega) = \chi_0(\omega)/(1 - J(Q)\chi_0(\omega))$. The CEF softening shows that the ground state of a Ho ion is a singlet with no magnetic moment and that the magnetic order of HoB_4 is caused by the mixing with higher CEF states. It was clarified that the diffuse scattering reported in Ref. 1 was these CEF excitations reflecting $J(Q)$.

Therefore, at zero magnetic field, there seems no indication of a magnetic frustration effect caused by the Shastry-Sutherland type lattice.

(1) D. Okuyama *et al.*, J. Phys. Soc. Jpn., **77**, 044709-1-14 (2008).

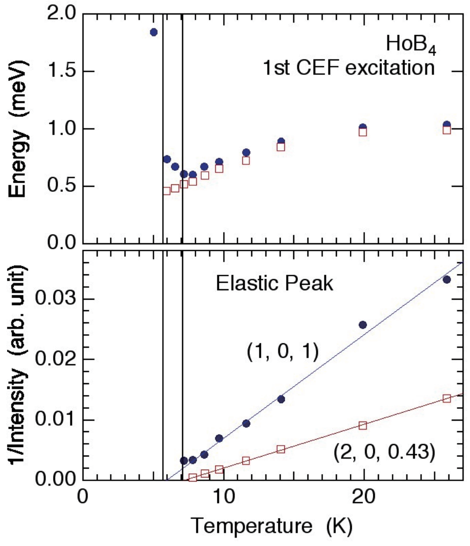

Fig. 1. (top) Temperature dependence of the 1st CEF excitation energy of HoB_4 at Q=(1, 0, 1) and (2, 0, 0.43). (Bottom) Temperature dependence of the inverse intensity of the elastic peak at Q=(1, 0, 1) and (2, 0, 0.43).

1-2-49

Phase Transitions of Non-Kramers Pr Ions in a Trigonal Symmetry in $Pr_4Ni_3Pb_4$

T. Onimaru[1], A. Ishida[1], K. Shigetoh[1], Y. F. Inoue[1], M. Nishi[2], T. J. Sato[2], Y. Oohara[2] and T. Takabatake[1,3]
[1]*AdSM, Hiroshima University, Higashi-Hiroshima 739-8530*
[2]*Neutron Science Laboratory, ISSP, University of Tokyo, Tokai 319-1106*
[3]*IAMR, Hiroshima University, Higashi-Hiroshima 739-8530*

Multipolar degrees of freedom often play an important role in $4f$ electron systems. Non-Kramers ions such as Pr^{3+} and Tm^{3+} possess multipolar degrees of freedom other than magnetic dipoles even in a trigonal symmetry. In the present work, we have focussed on a Pr-based intermetallic compound $Pr_4Ni_3Pb_4$ crystallizing in the trigonal $La_4Ni_3Pb_4$-type structure (space group $R3$) without inversion symmetry.[1, 2] In the unit cell, Pr ions occupy the $3a$ and $9b$ sites with the C_3 and C_1 point symmetries. In the C_3 point symmetry, a nine-fold multiplet $^3H_4$ splits into three Γ_1 singlets and three Γ_{23} doublets with quadrupolar degrees of freedom. The isothermal magnetization shows a shoulder-like anomaly at 4 T only for $B||c$, suggesting that an excited Γ_{23} doublet exists at a low energy of 4 K above the Γ_1 singlet ground state. The specific heat has cusp-type double anomalies at T_{N1}=2.7 K and T_{N2}=2.1 K which are probably attributed to the Γ_1-Γ_{23} quasi-triplet.

Neutron diffraction measurements on a single crystalline sample were performed using the ISSP High Q-resolution Triple-Axis Spectrometer HQR(T1-1), in order to detect magnetic peaks below the transition temperatures. Figure 1 shows the Q-scan along the $(1,0,L)$ line. A magnetic peak appears at $Q=(1,0,\frac{1}{4})$ and its equivalent positions below T_{N2}=2.1 K. At the temperature range between T_{N2} and T_{N1}, the peak at $(1,0,\frac{1}{4})$ splits into two peaks at $(1,0,\frac{1}{4}\pm\delta)$ $(\delta\sim0.1)$ where positions shift on cooling. These behaviors indicate an incommensurate magnetic structure. We observed both peaks at 2.14 K close to T_{N2}, suggesting that the IC-C transition at T_{N2} should be of first order. Comparing the intensities of the equivalent magnetic peaks, they tend to be strongly suppressed as the peak positions approach to the $[001]^*$ direction. It means that the magnetic moments have a trend to align along the c-axis in the ordered structures. Detailed analyses of the magnetic structures are in progress.

References

[1] L. D. Gulay *et al.*: J. Alloys Compd. **392** (2005) 165.
[2] K. Shigetoh *et al.*: J. Phys. Soc. Jpn. **75** (2006) 033701.

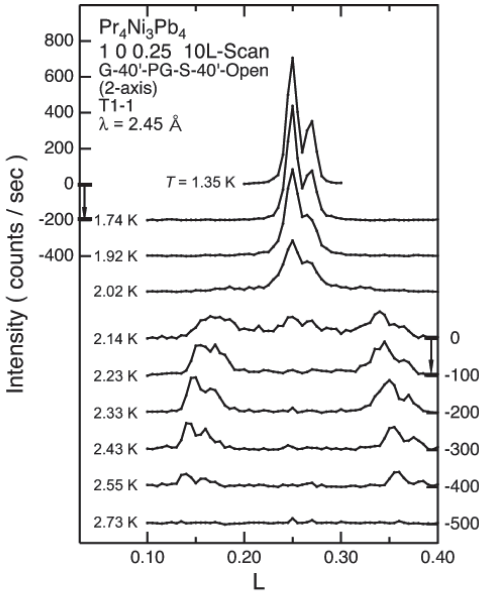

Fig. 1. Q-scan along the $(1,0,L)$ line. The magnetic $10\frac{1}{4}$ peak appears below T_{N2}=2.1 K.

1-2-50

Giant Uniaxial Anisotropy in the Magnetic and Transport Properties of $CePd_5Al_2$

T. Onimaru[1], Y. F. Inoue[1], K. Ohoyama[2] and T. Takabatake[1,3]
[1]*AdSM, Hiroshima University, Higashi-Hiroshima 739-8530*
[2]*Institute for Materials Research, Tohoku University, Sendai 980-8577*
[3]*IAMR, Hiroshima University, Higashi-Hiroshima 739-8530*

$CePd_5Al_2$ crystallizing in the tetragonal $ZrNi_2Al_5$-type structure shows successive antiferromagnetic orderings at T_{N1}=4.1 K and T_{N2}=2.9 K.[1] The temperature dependence of resistivity ρ shows a Kondo metal behavior with large anisotropy, $\rho_c/\rho_a=3.2$ at 20 K, and opening of a superzone gap along the tetragonal **c**-direction below T_{N1}. The magnetic data of $\chi(T)$ and $M(B)$ in the paramagnetic state were analyzed using a crystalline electric field (CEF) model. It led to a Kramers doublet ground state with wave functions consisting primarily of $\left|\pm\frac{5}{2}\right\rangle$,. The excited states are at 230 and 300 K. This CEF effect gives rise to the large anisotropy in the paramagnetic state. In the ordered state, the uniaxial magnetic anisotropy is manifested as $M_c/M_a=20$ in $B=5$ T and at 1.9 K, and $\chi_c/\chi_a=25$ in $B=0.1$ T and at 4 K.[2]

In the present work, we performed powder neutron diffraction experiments using HERMES of IMR. Neutrons with a $\lambda=1.82646(6)$ Å were obtained by the 331 reflection of the Ge monochromator. Figure **??** shows the powder neutron diffraction patterns of $CePd_5Al_2$ at various temperatures 1.4, 3.3 and 5.5 K. The patterns at 1.4 K and 3.3 K are vertically offset by 1000 and 2000 counts, respectively, for clarity. At 5.5 K, all the peaks can be indexed as nuclear Bragg peaks of the tetragonal $ZrNi_2Al_5$-type structure. No secondary phase was found in the patterns being consistent with the X-ray diffraction analysis. Although the intensities of the nuclear peaks do not change between 5.5 K and 1.4 K, weak superlattice peaks appear at 3.3 K and 1.4 K at the scattering angles $2\theta=8.1°$ and $21.7°$, which are shown with the thick arrows. On cooling, the intensity starts to increase at 4 K, which is in good agreement with T_{N1}. Thus the superlattice peaks originate in the magnetic transition at T_{N1}. The propagation vector of magnetic structures does not change at T_{N2}, which hints to a possible magnetic structure. From the analysis of $\chi(T)$, we propose canting of the magnetic moments from the *c*-direction. Another model is square-up of a modulated sine-wave structure with appearance of higher order reflections, because the magnetic entropy changes largely at T_{N2} as is found in the specific heat. However, no higher order reflections was observed in the present experiments. This is probably because the intensity was too weak to detect by means of the powder neutron diffraction technique. These results have already been published in ref. [2]. We plan to perform neutron diffraction experiments on a single crystal to determine the propagation vector.

References

[1] R. A. Ribeiro *et al.*: J. Phys. Soc. Jpn. **76** (2007) 123710.

[2] T. Onimaru *et al.*: J. Phys. Soc. Jpn. **77** (2008) 074708.

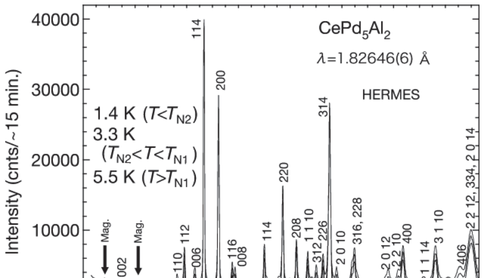

Fig. 1. Powder neutron diffraction patterns at $T=1.4$ K ($T<T_{N2}$), 3.3 K ($T_{N2}<T<T_{N1}$) and 5.5 K ($T>T_{N1}$).

1-2-51

Magnetic structure of Nd0.33Sr1.66MnO4

Y. Oohara, M. Kubota, and H. Kuwahara
ISSP, Univ. of Tokyo, PF, KEK Fac. Sci. & Tech, Sophia Univ.

Order of orbital state plays an important role in magnetic order of manganite compounds. The magnetic order of manganite consists of linear or zigzag ferromagnetic chain, which is influenced by orbital order. In Nd1+xSr1-xMnO4 at x=3/4, the linear ferromagnetic chain is established in the magnetic ordered phase. On the other hand, zigzag one is expected to exhibit at x=2,/3. To see if it is appropriate or not, we have performed neutron diffraction on the crystal sample of x=2/3.

The neutron diffraction measurements were performed with the ISSP triple-axis spectrometer GPTAS and HQR installed at the 4G and T11 experimental port JRR-3 in JAEAI (Tokai).

Figure shows the (h 0 0) line scan at 13 K. The peak position is with h=0.5, which is same position as the x=3/4 position, h=0.5.

The observed data suggests that the magnetic order does not consists of zigzag ferromagnetic chain. However, the order is short-ranged.

It explaines why the crystal structure at x=2/3 is tetragonal.

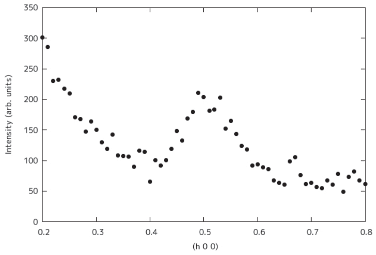

Fig. 1. Line scans along (h 0 0) at 13 K.

1-2-52

Magnetic excitations in YbV4O8

Y. Oohara, M. Kubota, and Y. Kanke
ISSP, Univ. of Tokyo, PF, KEK and NIMS

YbV4O8 exhibits complex magnetic phase transitions with charge order.
In the low temperature, we find that the magnetic moments disappearfrom the magnetic susceptibility measurements. To explore the mechanism of this disappearance, we have performed inelastic neutron scattering measurements.

We prepared the 10cc powder sample.Neutron scattering measurements were performed with ISSP
spectrometer HER and HQR installed at C11 and T11 experimental ports at JRR3 (JAEA). The sample is cooled with closed cycle refrigerator.

Figure shows the energy profile at Q=1 A-1 at 10 K.There is a peak at 2.5 meV. It suggests that a spin-singlet is formed in the low temperature with the 2.5 meV coupling, which disappear the magnetic moment observed in susceptibility measurements.

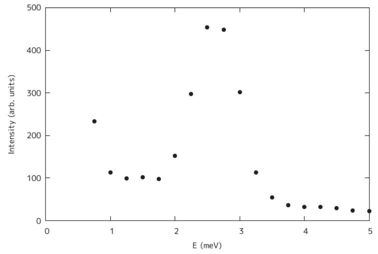

Fig. 1. Energy profiles at 1 A-1 at 10 K.

1-2-53

Multiple temperature and field induced phase transitions in new geometric frustration material Co2(OH)3Br

M. Hagihala^1, X.G. Zheng^1, Taku J Sato ^2
1. Saga Univ. 2. ISSP, Univ. of Tokyo

Co2(OH)3Br is a new geometrically frustrated compound in deformed pyrochlore lattice. Previously we reported the coexistence of ferromagnetic order and spin fluctuation in Co2(OH)3Cl [1]. Later we found its sister compound Co2(OH)3Br is an antiferromagnetor with succssesive transitions at TN1=6.2K and TN2=4.8K [2,3]. Recently we further found field-induced multiple transitions under applied magnetic field. The present study was designed to determine the zero-field as well as the field-induced magnetic structures.

Elastic neutron scattering measurements were performed at 4G:GPTAS using polycrystalline Co2(OD)3Br. Under zero field, we observed the antiferromagnetic reflections of k1=(0 -1/2 1/2) below TN1, and further another independent k2=(0 0 3/2) below TN2. For the lower temperature phase we have succeeded in determining its magnetic structure, which is illustarted in Fig. 1.

For the field-induced phases, we observed a new antiferromagnetic order for H > 6 kOe. At higher fields of H > 30 kOe a ferromagnetic order similar to that in Co2(OH)3Cl appeared. Further work is in progress to determine all of the magnetic structures.

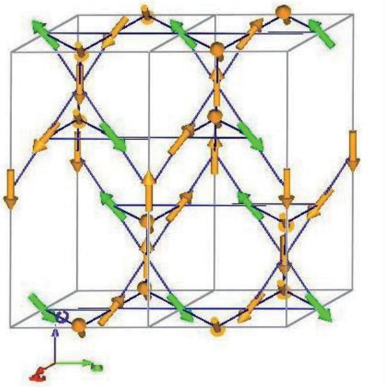

Fig. 1. The magnetic structure for the low temperature antiferromagnetic order in Co2(OD)3Br

References

[1] X. G. Zheng et al. Phys. Rev. Lett. 97 (2006) 247204.
[2] M. Hagihala et al. J. Phys. : Cond. Matt. 19 (2007)145281.
[3] M. Hagihala, X.G. Zheng, T. Kawae,Physica B 404 (2009)607.

1-2-54

Neutron powder diffraction of TbPd3S4 in magnetic fields

E. Matsuoka(A), Y. Sasaki(A), T. Matsumura(B), K. Ohoyama(C), H. Onodera(A)
(A)Department of Physics, Tohoku University, (B)ADSM, Hiroshima University, (C)Institute for Materials Research, Tohoku University

The rare-earth (R) palladium bronzes RPd3S4 crystallizes into a cubic NaPt3O4-type crystal structure. The R atoms form a body-centered cube and are subjected to a cubic crystalline electric field (CEF) represented by the cubic point group of Th [1]. Systematic studies along the R series have revealed that the CEF ground states of 4f electrons in RPd3S4 retain orbital degeneracy [1].

TbPd3S4 shows an antiferromagnetic (AFM) transition at TN=2.5 K. The neutron powder diffraction study of TbPd3S4 has revealed that the magnetic structure below TN is described by a wave vector of k = (100) [2]. TN shows an anomalous magnetic-field dependence. By applying a magnetic field below 0.5 T, TN decreases with increasing magnetic field, while it increases with increasing magnetic field above 0.5 T. The increase of TN above 0.5 T implies that the field-induced antiferroquadrupolar (AFQ) ordering occurs above 0.5 T. To examine the possibility of field-induced AFQ ordering, neutron powder diffraction study of TbPd3S4 in magnetic field has been performed using HERMES installed at the JRR-3M reactor in JAEA. Neutrons with a wavelength of 1.8204(5) A were obtained by the 331 reflection of the Ge monochromator.

Fig. 1 shows the magnetic-field dependence of the integrated intensities of 100 and 110 Bragg peaks measured at 1 K (T < TN). At zero magnetic field, 100 and 110 are magnetic and nuclear Bragg peaks, respectively. The integrated intensity of 100 peak decreases gradually with increasing magnetic field, while that of 110 increase by applying magnetic field. Such field dependence can be understood by considering the process that the AFM structure with wave vector of (100) is destroyed gradually by magnetic field. At 0.5 T, the decrease rate of the integrated intensity of 100 and increase rate of that of 110 become large abruptly, implying that the magnetic structure changes from the (100)-type AFM structure to a canted-AFM structure at 0.5 T. Similar canted-AFM structure has been observed in DyPd3S4[3] and the appearance of such a canted structure is the evidence of a coexistence of AFM and AFQ ordering in DyPd3S4 [3]. We therefore conclude that AFQ ordering is induced for TbPd3S4 above 0.5 T.

[1] K. Abe et al., Phys. Rev. Lett. 83 (1999) 5366.
[2] E. Matsuoka et al., J. Magn. Magn. Mater. 231 (2001) L23.
[3] L. Keller et al., Phys. Rev. B 70 (2004) 060407.

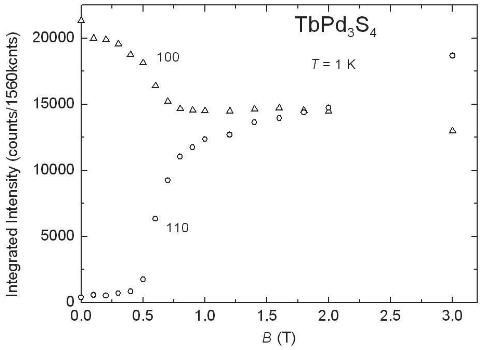

Fig. 1. Magnetic-field dependence of the integrated intensities of 100 and 110 Bragg peaks for TbPd3S4.

1-2-55

Inelastic neutron scattering study on 1/1 approximant Ag-In-Tb

S. Ibuka, K. Matan and T. J. Sato
NSL, ISSP, University of Tokyo

Quasicrystals are characterized by sharp Bragg reflections with a point symmetry which is forbidden in a periodic lattice, such as the five-fold symmetry. Quasicrystal can include magnetic ions, called as ”magnetic quasicrystals”. These magnetic quasicrystals provide us an intriguing playground to experimentally investigate the magnetic ordering and dynamics in the quasiperiodic spin systems.

Macroscopically, the magnetic quasicrystals mostly show the spin-glass-type freezing at low temperatures, as seen in the Zn-Mg-RE (RE: rare-earth) quasicrystals. Nevertheless, the spin dynamics, observed by neutron scattering, is very different from canonical spin-glasses; in several magnetic quasicrystals, highly localized inelastic mode was observed as broad inelastic peak [1]. The origin of the inelastic mode is inferred to be spin-wave-like modes localized in the dodecahedoral spin clusters, which are characteristic clusters in the icosahedral quasicrystals. To confirm this idea, we have performed neutron inelastic scattering study in the Ag-In-Tb 1/1 approximant, which is made of icosahedral clusters arranging periodically.

Polycrystalline samples of the $Ag_{47}In_{39}Tb_{14}$ 1/1 approximant were prepared in usual manner. The powdered sample was loaded in the closed cycle ^{4}He refrigerator, and the inelastic spectrum was observed using the ISSP-GPTAS and ISSP-HER triple-axis spectrometers installed at the JRR-3 research reactor.

Figure 1 shows the inelastic spectra at several temperature in the range of $3.5 < T < 150$ K. In the high temperature range, only the quasielastic response may be seen in the spectrum, whereas as the temperature is decreased, evolution of the low energy peak around 4 meV is evident. We note that this behavior is almost the same as those observed in the Zn-Mg-Tb quasicrystal (except for the characteristic energy scale), and thus conclude that the inelastic mode is due to the local high-symmetry clusters commonly found in the quasicrystalline and crystalline phases.

[1] T. J. Sato *et al.*, Phys. Rev. B 73 (2006) 054417.

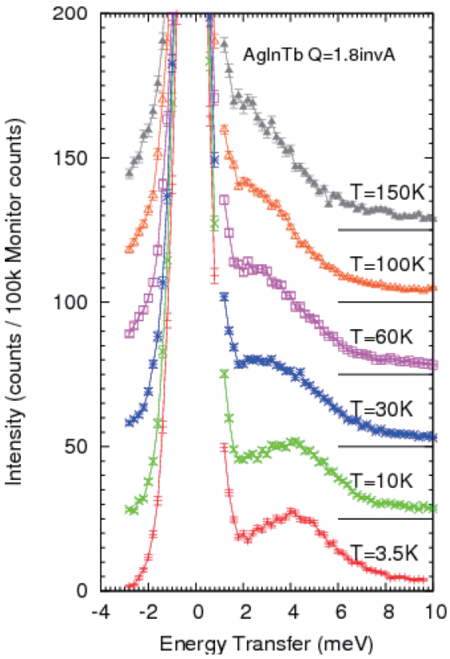

Fig. 1. Inelastic scattering spectrum of Ag-In-Tb. A broad peak at 4 meV appears below 60 K.

1-2-56

Neutron scattering study on magnetic quasicrystal Zn-Mg-(Y,Gd)

S. Ibuka, K. Iida and T. J. Sato
NSL, ISSP, University of Tokyo

Quasicrystals are characterized by sharp Bragg reflections with a point symmetry which is forbidden in a periodic lattice, such as the five-fold symmetry. Quasicrystal can include magnetic ions, called as ”magnetic quasicrystals”. These magnetic quasicrystals provide us an intriguing playground to experimentally investigate the magnetic ordering and dynamics in the quasiperiodic spin systems.

Macroscopically, the magnetic quasicrystals mostly show the spin-glass-type freezing at low temperatures, as seen in the Zn-Mg-RE (RE: rare-earth) quasicrystals. Nevertheless, the spin dynamics, observed by neutron scattering, is very different from canonical spin-glasses, and sometimes exhibits temperature independent $S(Q,\hbar\omega)$ in the neutron scattering spectrum [1].

The temperature independent $S(Q,\hbar\omega)$ is very unusual. One intriguing mechanism of the temperature independence is the proximity to the quantum critical point (QCP) [2]. On the other hand, the temperature independence may be simply due to distribution of the crystalline electric field (CEF) levels. To conclusively judge which is the case for the magnetic quasicrystal, we have performed neutron inelastic scattering experiment in the Zn-Mg-(Y,Gd) quasicrystal, where the half-filld 4f level of the Gd^{3+} ions do not have CEF splitting in principle.

The neutron inelastic scattering study was performed using the ISSP-GPTAS(4G) and ISSP-HER(C11) triple-axis spectrometers installed at the JRR-3 research reactor. A powdered icosahedral sample of the composition $Zn_{60}Mg_{30}Y_{8.5}{}^{160}Gd_{1.5}$ was prepared in the usual manner. It may be noted that to avoid the huge neutron absorption of natural Gd, we used the stable isotope.

Figure 1 shows the resulting inelastic scattering spectra at several temperatures spanning 1.4 K to 50 K, observed using the ISSP-HER spectrometer with the outgoing neutron energy of 2.75 meV. It is clearly seen that the spectrum for the neutron-energy-loss side exhibits almost temperature-independent behavior. This behavior is indeed exactly the same as what has been observed in the Zn-Mg-Ho quasicrystal. Therefore, we can conclude that the origin of the temperature independence is not due to the accidental distribution of the CEF levels. Instead, a closer relation to the QCP mechanism is highly suggested.

[1] T. J. Sato *et al.*, Philos. Mag 87 (2007) 2939.

[2] M. C. Aronson *et al.*, Phys. Rev. Lett. 75 (1995) 725.

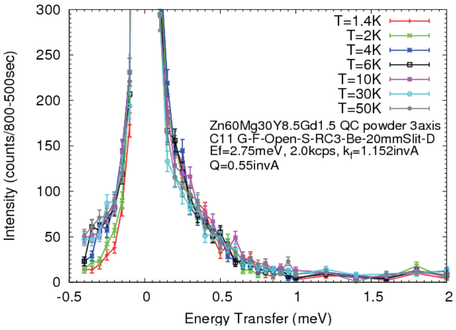

Fig. 1. Inelastic scattering spectrum of Zn-Mg-(Y,Gd)

1-2-57

Magnetic structures in magnetic fields of TmB4 with the Shastry-Sutherland lattice

Iga F. (a) , Michimura S. (a), Matsumura T. (a), Takabatake T. (a), Ohoyama K. (b)
(a) ADSM, Hiroshima Univ., Higashi-Hiroshima, Hiroshimna 739-8530, Japan (b)IMR, Tohoku University, Katahira, Sendai 980-8577, Japan

Rare-earth tetraborides RB4 have a tetragonal crystal structure with a space group P4/mbm which is characterized by the 2-dimensional orthogonal dimers in the c-plane. Such dimer systems are equivalent to the Shastry-Sutherland lattice (SSL) [1] where nearest-neighboring dimers geometrically frustrated.

Our previous study of powder neutron diffraction in TmB4 shows incommensurate antiferromagnetic (IC AFM) orderings at 11.7 K and 10.7K, and incommensurate-commensurate (IC-C) transition at 10 K [2]. From the magnetic phase diagram as shown in Fig.1, phase IV shows a simple antiferromagnetic pattern with a propagation vector of k4=(1, 0, 0). The Phase III has been assigned with propagation vector k4 and an additional long period modulation vector k3=(0.13, 0, 0). Furthermore, the phase II was also indexed with the k4 and k2=(0.012, 0.012, 0) and k2’=(0.036, 0.012, 0). We have found that TmB4 shows a multi-step magnetization process. The magnetization for B//c shows not only a 1/2 Ms plateau in phase VI as in RB4 (R=Dy, Ho, Er, Tb) but also a 1/8 Ms plateau in phase V [3]. Here, Ms means the saturation moment of Tm3+ ion. In order to clarify these ordering vectors in these magnetic phases, we have performed neutron diffraction experiment on a single crystal sample of Tm11B4.

High-quality single crystal sample of TmB4 was grown by floating zone method using a four-xenon lamps image furnace. The neutron diffraction experiment in fields up to 6 T was performed in the triple axis spectrometer, TOPAN (6G). The incident neutron energy Ei was tuned to 30.5 meV (1.64 A). The sample was placed with the (h k 0) plane in order to set parallel to the neutron scattering plane in field applied along [001] axis.

From the neutron diffraction in magnetic fields, the incommensurate and commensurate magnetic structures based on the 8-unit cell period were found in the Plateau phase (V, VI). The magnetic structure ordered in the field accompanied by the magnetic plateau has a similar value as the period determined in phase III with magnetic fluctuation. Frustration on the SSL plays an important role to form the magnetic plateaus. The super-lattice reflections without magnetic origin were found in the 4-unit cell period for a-axis in the phase V. This suggests that the periodic magnetic structure with 8-unit cell period locks into the period crystal lattice.

References

[1] B. S. Shastry and B. Sutherland, Physica B & C 108B (1981), p. 1069.
[2] S. Michimura et al., J. Phys. Soc. Jpn. 78 (2009), 024707.
[3] F. Iga et al., J. Magn. Magn. Mater. 310 (2007) e45-47.

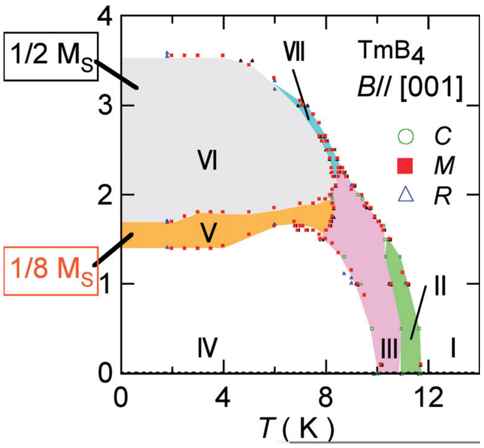

Fig. 1. Fig. 1 Magnetic phase diagram of TmB4.

1-2-58

Magnetic State in the Tm-based Reentrant Superconductor Investigated by the Powder Neutron Scattering

N. Kase[1], Y. Tomiyasu[2], T. Muranaka[1], and J. Akimitsu[1]
[1] *Department of Physics and Mathematics, Aoyama-Gakuin Univ., 5-10-1 Fuchinobe,* [2]
Department of Physics, Tohoku Univ., 6-3 Aoba, Sendai, 980-8578

The Tm-based reentrant superconductor $Tm_5Rh_6Sn_{18}$ exhibits superconductivity at T_c = 2.2 K[1] and reentrant behavior between 1.0 and 1.45 kOe[2]. From the muon-spin rotation/relaxation (μSR) measurements, we reveal the coexistence between magnetism and superconductivity under a zero magnetic field, and a development of magnetic ordering is observed below around 10 K[3]. However, the magnetic ordering cannot be described as a simple long-range magnetic ordering.

To understand magnetic state more precisely, magnetic structure of $Tm_5Rh_6Sn_{18}$ has been investigated by a powder neutron scattering as shown in Figure 1, which represents the neutron powder diffraction pattern at 0.75 K and 10 K. We could not observe any Bragg peak due to a long-range magnetic order in any temperature region and also observe a magnetic diffuse scattering attributed to a short-range order in the low-angle region below 10 K. The diffuse scattering intensity can be described as a conventional Gaussian function. Furthermore, the temperature dependence of the integrated intensity is almost consistent with the results of muon precession frequency obtained from the ZF-μSR measurement.

Therefore, we conclude that the magnetic order can be considered not to be long range ordered but superparamagnetic; ferromagnetically ordered within a certain cluster, but, paramagnetically fluctuating between the cluster, and the superparamagnetic cluster gradually develops below around 8 K. The size of the magnetic cluster is so large that a spontaneous oscillation signal is clearly observed from ZF-μSR measurement. This scenario makes it possible to explain the occurrence of the reentrant superconductivity; the field-induced magnetic order obtained from the electrical resistivity measurements under magnetic fields is originated from an alignment of each spin of magnetic clusters to the same direction. Thus, superconductivity is not destroyed under zero magnetic filed below T_c.

References

[1] J. P. Remeika *et al.*: Solid. State. Commun. **34** (1980) 923.
[2] A. Rojek *et al.*: Phys C **223** (1994) 111.
[3] N. Kase *et al.*: to be submitted in J. Phys. Soc. Jpn..

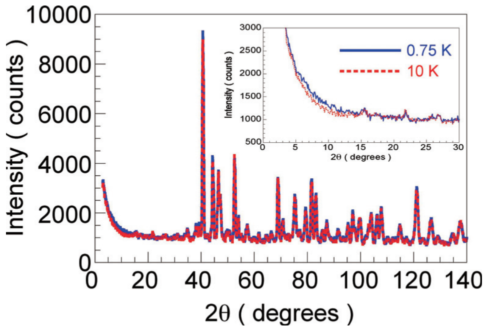

Fig. 1. The neutron powder diffraction pattern at 0.75 K and 10 K of $Tm_5Rh_6Sn_{18}$. The inset shows the expansion of the low-angle region.

1-2-59

Neutron diffraction experiment under high pressure in $YbMn_2Ge_2$

T. Fujiwara^A, N. Aso^B, M. Nishi^C, Y. Uwatoko^D
^{A}*Yamaguchi Univ.*, ^{B} *Univ. Ryukyus*, ^{B}*ISSP Univ. Tokyo*, ^{C}*ISSP-NSL Univ. Tokyo*

$YbMn_2Ge_2$ with $ThCr_2Si_2$ type body-centered tetragonal structure is an intermediate valence system and its magnetic property is dominated by magnetic exchange interactions between Mn moments. This system shows a quite unique magnetism in which two antiferromagnetic states, AFM I at $T_{N2} < T \leq T_{N1} \approx 405$ K and AFM II at $T \leq T_{N2} = 163$ K, compete with each other. With applying hydrostatic pressure, the system indicates valence transition of Yb ions at $P_c \sim 1.25$ GPa. Althogh, magnetic behaviors of the system drastically change above P_c and new magnetic phases, AFM III and IV, induced upon pressurization, the details of magnetic structures in AFM III and IV states are not clarified yet. In this work, we have carried out the neutron diffraction experiment within the reciprocal lattice plane (HHL) of single crystal $YbMn_2Ge_2$ under high pressure using a clamping-type high pressure cell made of hardened Cu-Be alloy.

Figure 1 is rocking curves at $Q = (111)$ in $YbMn_2Ge_2$ under $P = 1.3$ GPa at $T = 8$ K and 300 K. As shown in the figure, magnetic bragg peak is clearly observed in both AFM III (300 K) and AFM IV (8 K) states. This indicates an existence of antiferromagentic component consists of that a ferromagnetic (00ℓ) Mn planes couples antiferromagentically along [001] direction. It is recognizable that an increase of (111) peak intensity occurs simultaneously when the system undergoes a magnetic phase transition from AFM III to IV with decreasing temperature under 1.3 GPa. Unfortunately, we could not observe any magnetic bragg reflection under $P = 1.3$ GPa except (111) and (113). Therefore, it is necessary to perform the similar neutron diffraction experiments on (H0L) and (HK0) reciprocal lattice planes under high pressure to obtain the detail information of the magnetic structures in AFM III and IV states.

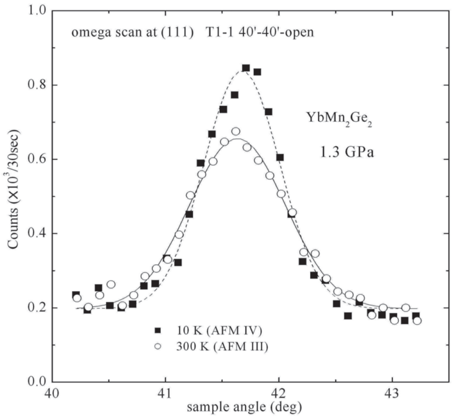

Fig. 1. Rocking curves at $Q = (111)$ in $YbMn_2Ge_2$ under $P = 1.3$ GPa in AFM III ($T = 300$ K) and AFM IV ($T = 8$ K) states.

1-2-60

Magnetic excitation in Co4B6O13

Masuda T., Hondo S. and Matsuura M.
Yokohama City University, Osaka University

Recently spin liquid in triangular lattice, Kagome lattice, Pyrochlore lattice, etc has been attracted much attention. Amongt them regular tetrahedron spin system, Co4B6O13, was discovered recently[1]. Co2+ (S=3/2) ions are on the corner of tetrahedron. Since the Co-Co intratetrahdron distance 3.25 A is shorter than the intertetrahedron 4.26 A this compound is expected to be an isolated tetrahedron spin system. The magnetic susceptibility shows broad maximum at T = 14 K and it decreases drastically at low temperature. No magnetic order is identified at $T > 1.8$ K. These are typical behaviors of spin gap system with nonmagnetic ground state. In the magnetization measurement an drastic increase was identified at H = 10 T and multistep anomalies were observed at 40 T and 60 T. These anomalies are supposed to be transition between eigenstates of Heisenberg antiferromagnetic tetrahedron cluster, S=0 (quartet), S=1 (ninefold multiplet), S=2 (elevenfold multiplet). However, in quantitative level, the data cannot be reproduced and additional terms such as Dzyaloshinskii-Moriya interaction and single ion snisotropy would be required. Even though rather complex, the isolated tetrahedron spin cluster is a rare experimental realization of exact solvable model with spin frustration. Hence to reveal the spin excitation of Co4B6O13 we performed inelastic neutron scattering experiments.

Powder sample was obtained by hydrothermal synthesis. As a starting material we used 11B oxide to reduce the absorption of neutron. Orange type cryostat was used to achieve low temperature. Inelastic neutron scattering experiment was performed at C1-1 beamline. The collimation setup is Guide-PG-40′-radial collimation-Be filter-Horizontally focused analyzer-open with Ef = 3 meV.

In Fig. 1 we show energy scan at q=1A-1. Well dfined peaks are observed at hw = 0.96, 1.18, 1.61, 2.44, 2.92, 4.15, and 4.66 meV. These peaks are identified dispersionless in similar scans at different q. With the increase of temperature the intensity decreases. These results measn that the peaks are of a magnetic cluster. The fine peak structure measn that the degenerated eigenstate of a Heisenberg cluster is splitted by peturbative terms as magnetic susceptibility and heat capacity data indicated. Q scans were also performed at several energies. The detailed data analysis is now under progress. The summary of this study will be published with additional nutron scattering experiment somewhere.

[1] H. Hagiwara et al., fall meeting of Japan Physical Socity, 20aQH (2008).

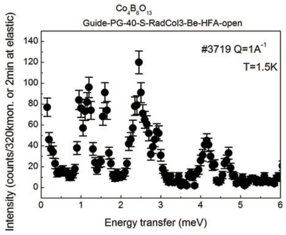

Fig. 1. Energy scan of Co4B6O13 at Q = 1A-1.

1-2-61

Degree of frustration in geometrically frustrated magnets (Co1-xZnx)Cr2O4

Tomiyasu K.(A), Yokobori T.(B), Horigane K.(C), Akimitsu J.(B), Yamada K.(C)
(A)Dep. of Physics Tohoku Univ., (B) Dep. of Physics Aoyama Gakuin, (C)WPI-AIMR Tohoku Univ.

Highly frustrated systems, spinel antiferromagnets ACr2O4 (nonmagnetic A=Mg,Zn,Cd and Hg) consisting of a corner-sharing tetrahedron lattice as B (Cr) sites, are well-known to exhibit the phenomenon of spin hexamer on the kagome plane. On the other hand, it was recently reported that geometric frustration still survives in spinel ferrimagnets ACr2O4 (magnetic A=Co and Mn) as explained below. In these materials a spin forms a conical structure resolved into an Ising-type ferrimagnetic component and an incommensurate spiral one. As the temperature decreases, although the former component forms long-range order at T_C=93 and 51 K, the latter one mainly starts to grow at T_S=25 and 14 K and does not achieve long-range order even in the lowest temperature phase. Therefore, it was proposed that the geometric frustration among the B-site spins can coexist with the A-site spins, and is mainly reflected on the spiral component.

However, the spiral type seems to be too different from the hexamer. Here, in order to validate the expanded concept of geometric frustration, we report the spiral spin correlations of solid solution materials (Co1-xZnx)Cr2O4 by powder neutron diffraction (x=0 to 1).

Figure shows the diffraction patterns measured at elastic condition in the lowest temperature phases. The intensity of 111 fundamental reflection decreases with increasing x from 0 to 0.45, then is almost constant, meaning that the ferrimagnetic component disappears. The magnetic satellite reflections monotonically become broad, most likely validating that the correlation length of spiral order corresponds to the degree of expanded frustration, and the spiral short-range order comes from the frustration. In addition, even at x=0.90 the peak positions of diffuse scattering are different from those of magnetic Bragg reflections in ZnCr2O4, suggesting that the spiral short-range order still survives.

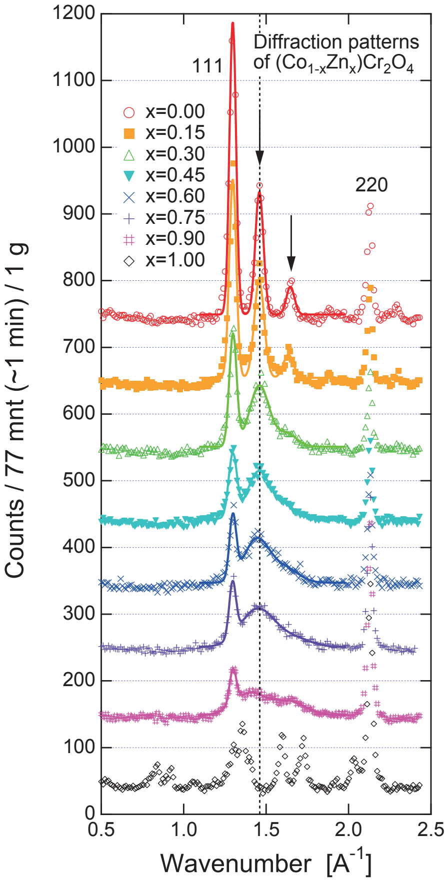

Fig. 1. Figure. Elastic scattering data of (Co1-xZnx)Cr2O4 in lowest temperature phases.

1.　中性子散乱　3）強相関電子系

1. Neutron Scattering　3）Strongly Correlated Electron Systems

This is a blank page.

1-3-1

Competition of different antiferromagnetic correlations in a heavy fermion Ce(Ru1-xRhx)2(Si1-yGey)2

Y. Tabata(A), S. Ohya(B), H. Taguchi(A), C. Kanadani(C), T. Taniguchi(B), H. Nakamura(A)
(A) Graduate School of Engineering, Kyoto University, (B) Graduate School of Science, Osaka University, (C) RCMI, Toho University

CeRu2Si2 is a paramagnetic heavy fermion locating close to an antiferromagnetic (AFM) quantum critical point (QCP). Interestingly, in this compound three AFM correlations with the magnetic wave vector q1=(0.31,0,0), q2=(0.31,0.31,0) and q3=(0,0,0.35) coexist [1], and may compete each other. By substituting Rh for Ru, the q3-AFM correlation develops the long-range magnetic order, q3-phase, in the Rh-concentraion x range of $0.03 < x < 0.35$ [2]. On the other hand, appearance of the q1-AFM order, q1-phase, was reported by substituting Ge for Si or by substituting La for Ce [3]. It takes a great interest in quantum phase transitions among such a competing antiferromagnetic phases and paramagnetic Fermi liquid (FL). As a first step for studying such quantum phase transitions, we have grown many single crystalline samples of Ce(Ru1-xRhx)2(Si1-yGey)2 and have tried to make up the xy phase diagram.

Figure. 1 shows the xy phase diagram of Ce(Ru1-xRhx)2(Si1-yGey)2 obtained from neutron scatteing experiments and magnetization measurements. A 3rd AFM phase where both the q1and the q3 magnetic scattering are observed, q1+q3-phase, has ben discovered between the q1- and the q3-phases. No hysteretic behavior was observed in the q1+q3-phase, and hence, we conclude that the q1+q3-phase is a thermodynamic equilibrium state, may has a double-q structure. And also, we have found that the AFM phase appeared by substituting Ge for Si in CeRu2Si2 is not a simple q1-phase but the q1+q3-phase.

[1] H. Kadowaki et al., Phys. Rev. Lett. 92, 097204 (2004).
[2] S. Kawarazaki et al., J. Phys. Soc. Jpn. 66, 2473 (1997).
[3] S. Dakin et al., J. Magn. Magn. Mater. 108, 117 (1992)., S. Quezel et al., J. Magn. Magn. Mater. 76&77, 403 (1988).

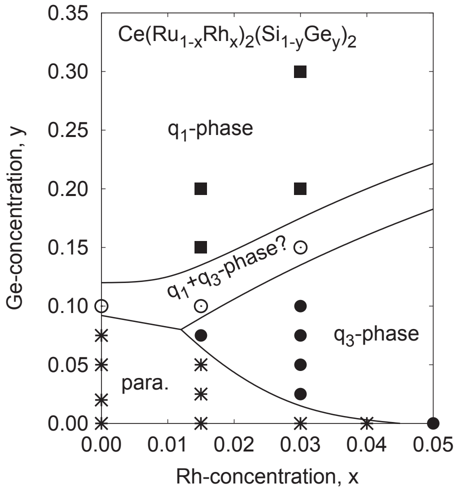

Fig. 1. The xy phase diagram of Ce(Ru1-xRhx)2(Si1-yGey)2 at T = 1.5K obtained from neutron scatteing experiments. Asterisk, closed square, closed circle and open circle denote the paramagnetic FL, the q1-, the q3- and the q1+q3-phases respectively.

Activity Report on Neutron Scattering Research: Experimental Reports **16** (2009)
Report Number: 603

1-3-2

Magnetic phase diagram under low temperature and high pressure in RVO3 II

D. Bizen(A), H. Nakao(A), K. Iwasa(A), Y. Murakami(A), T. Osakabe(B), S. Miyasaka(C), Y. Tokura(D,E,F)
(A) Tohoku Univ., (B) JAEA, (C) Osaka Univ., (D) The Univ. of Tokyo, (E) ERATO-MF, (F) RIKEN-CMRG

Perovskite vanadium oxide RVO3 (R: rear earth or Y) shows various physical properties coupled with the spin and orbital states. [1] The orbital ordering is strongly coupled with the lattice distortion, i.e. Jahn-Teller distortion. Hence the pressure effect for the orbital state interests us, and the pressure-temperature phase diagram of the V 3d-orbital state was investigated by x-ray diffraction under high-pressure and low-temperature. [2] Under high pressure (> 6 GPa), the orbital disorder (OD) - C-type orbital ordering (C-OO) phase transition was newly found in YVO3. At this transition, the space group does not change, although the symmetry is usually broken at an orbital order-disorder transition. Such an orbital order-disorder phase transition without the change of the space group was actually reported in LaMnO3. On the other hand, the magnetic symmetry breaking upon this phase transition can be also expected. To make clear the relation between the spin and orbital states, we have investigated the magnetic phase diagram of YVO3 under high-pressure and low-temperature using a hybrid anvil cell.

In order to determine the magnetic ordering phase, the magnetic scattering was explored by using the triple-axis spectrometer TOPAN. The temperature dependence of the magnetic peak intensities was measured at several pressures as shown in the figure. At ambient pressure (0GPa), the (0 1 0) magnetic peak reflecting the C-type spin ordering (C-SO) was observed below TSO1=118K. Moreover, the second magnetic transition was observed at TSO2=77K: there the magnetic peak at (0 1 0) disappears and that at (0 1 1) reflecting the G-type spin ordering (G-SO) appears. With increasing pressure, TSO2 remarkably increases while TSO1 has few pressure dependence. As a result, the C-SO phase completely disappears above 3GPa. Furthermore, TSO2 continues to increase even after the disappearance of C-SO phase. Finally, we could elucidate that the magnetic transition at TSO2 just corresponds to OD/C-OO phase transition above 6GPa; such a simultanious transition has never been reported in perovskite-type transition metal oxides. The result indicates that the magnetic ordering play an important role for the OD/C-OO phase transition.

[1] S. Miyasaka et al., Phys. Rev. B 68 (2003) 100406.
[2] D. Bizen et al., Phys. Rev. B 78 (2008) 224104; D. Bizen et al., J. Magn. Magn. Mater. 310 (2007) 785.

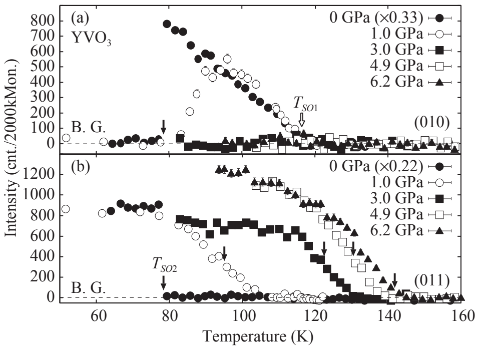

Fig. 1. Temperature dependence of the magnetic peak intensities at (0 1 1) and (0 1 0), which reflect G-SO and C-SO, respectively.

1-3-3

Magnetic-Field Variations of Antiferromagnetic Structure in CeRh1-xCoxIn5

M. Yokoyama(A), Y. Ikeda(B), I. Kawasaki(B), D. Nishikawa(B), K. Tenya(C), H. Amitsuka(B)
(A)Ibaraki University, (B)Hokkaido University, (C)Shinshu University

The Ce-based heavy-fermion compounds CeMIn5 (M=Rh and Co: HoCoGa5-type tetragonal structure) are intensively studied for a rich variety of low-temperature properties ascribed to the interplay of antiferromagnetism (AF) and superconductivity (SC). CeRhIn5 orders in an incommensurate AF phase with a modulation of qh = (1/2, 1/2, 0.297)[1]. It is revealed in the Co-doped alloys CeRh1 − xCoxIn5 [2] that the AF phase is suppressed with increasing x, and then disappears at x_c ˜ 0.7. At the same time, SC appears between x = 0.4 and x = 1. Recent our elastic neutron scattering (ENS) measurements revealed the emergence of a new AF state with modulations of qc1 = (1/2, 1/2, 1/2) in the intermediate x range, followed by the suppression of the qh-AF state[3-5]. To elucidate magnetic instability involved in small and intermediate x ranges, we have further performed the ENS experiment under magnetic field for CeRh1 − xCoxIn5.

Single crystals of CeRh1 − xCoxIn5 were grown by the In-flux method. The samples were shaped into bar (typical size: ˜3 mmˆ2 × 10 mm) in order to minimize the effects of the neutron absorption caused by Rh and In. The ENS experiments were carried out using triple-axis spectrometers GPTAS and PONTA at the JRR-3M research reactor of JAEA. Magnetic field was applied along the [110] direction, which are orthogonal to the (hhl) scattering plane selected in the present study.

Figure 1 shows the neutron scattering pattern obtained from the (1/2, 1/2, L) scan at 1.6 K. It is found that applying field along [110] switches the AF propagation vector from qh to qc2 = (1/2, 1/2, 1/4) at x = 0.23, while it integrates the qc1- and q1-AF components [q1=(1/2,1/2,0.42)] into a single qc1 one at x = 0.7. This result suggests that the properties of the Fermi surfaces significantly vary by Co concentrations.

[1] W. Bao et al., Phys. Rev. B 62 (2000) R14621.
[2] V.S. Zapf et al., Phys. Rev. B 65 (2001) 014508.
[3] M. Yokoyama et al., J. Phys. Soc. Jpn. 75 (2006) 103703.
[4] M. Yokoyama et al., Phys. Rev. B 77 (2008) 224501.
[5] S. Ohira-Kawamura et al., Phys. Rev. B 76 (2007) 132507.

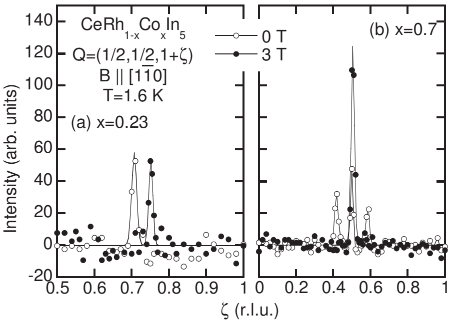

Fig. 1. The AF Bragg-peak profiles at B = 0 and 3 T for CeRh1 − xCoxIn5 with (a) x = 0.23 and (b) 0.7.

1-3-4

Magnetic Excitations of LaFeAsO0.89F0.11

Taketo Moyoshi, San Chul Lee, Ayaka Kawabata, Yoshiaki Kobayashi, Yukio Yasui,
Masatoshi Sato and Kazuhisa Kakurai1
Department of Physics, Nagoya University, Chikusa-ku, Nagoya 464-8602, 1 Quantum Beam Science Directorate, JAEA, Tokai, Ibaraki 319-1195

This project was originally planned to study the dynamical magnetic properties of honeycomb systems of Na3Cu2SbO6and Na2Co2TeO6 to investigate in detail the unusual behavior such as the spin gap phenomena found in the former one. However, the machine time was used to measure the magnetic excitation spectra of newly found superconducting system LaFeAsO1-xFx1) to quickly obtain information on its electronic state useful to investigate the superconducting mechanism.

In LaFeAsO1-xFx, the superconducting phase is derived by the F-doping to the magnetically ordered phase, and the highest transition temperature Tc is ˜ 28 K at x˜0.11. Because the magnetic fluctuation is considered to play a possible role in realizing the superconductivity, to study the magnetic excitation spectra of the system one of the most important things for the study of the superconducting mechanism.

The measurements were carried out for a powder sample of LaFeAsO1-xFx (x˜0.11) with the incident (Ei) or scattered (Ef) neutron energy being fixed at 30.5meV. In the measurements, the horizontal collimations were 40 ’-40 ’-80 ’-80 ’. Scanning the absolute scattering vector Q at various fixed transfer energies E, we found a peak at Q ˜1.1 -1 corresponding to (?, 0) point in the reciprocal space. Because the peak gets sharper with decreasing T, they are considered to be magnetic. The integrated intensities Iint of the peaks have been estimated, and in the figure, Iint/(n+1) (n: Bose factor) are shown against E at T = 3.5 K (< Tc) and 40 K (> Tc).These results should be compared with the so-called resonance peak, the existence of which is discussed by Maier and Scalapino for the s? symmetry of the superconducting order parameter ?.2) Because the expected resonance peak is expected to be very sharp, if it exists, the widths of the peaks of the ? ” (Q,?)-? curve obtained with constant Ei, for which the energy resolution widths are ?3.3 meV, should be sharper than those obtained with constant Ef (the resolution widths ?5.2 meV. As can be found in the figure, we do not see appreciable change of the curves with changing the experimental resolution, which suggests that the resonance peak does not exist. Recently, the neutron scattering measurements on aligned crystals of BaFe1.84Co0.14As23) and BaFe1.9Ni0.1As24) were reported. The present data seems to be very similar to that of BaFe1.9Ni0.1As2. Here, we note that our data are consistent with the fact that the Co doping effect on Tc of LaFeAsO1-xFx (x˜0.11) is much weaker than expected for the s? symmetry first reported by us.5)

1)Y. Kamihara et al., J. Am. Chem. Soc. 130 (2008) 3296.
2)T. A. Maier and D. J. Scalapino, Phys. Rev. B 78 (2008) 020514.
3)M. D. Lumsden et al., arXiv: 0811.4755.
4)S. Chi et al., arXiv:0812.1354
5)A. Kawabata et al., Proc. Int. Symposium on Fe-oxipnikutide Superconductors, June28-29, 2009, Tokyo and also J Phys. Soc. Jpn., 77 (2008) 103704.

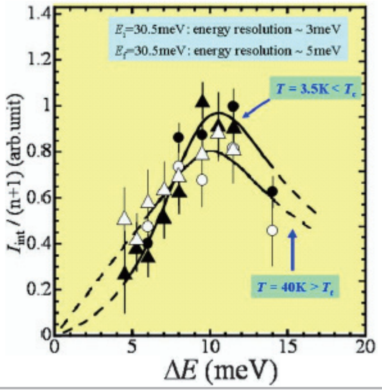

Fig. 1.

1-3-5

Magnetic excitations of NaxCoO2.yD2O

Taketo Moyoshi, Yukio Yasui, Masatoshi Sato and Kazuhisa Kakurai1
Nagoya Univ. 1JAEA

Na0.3CoO2.1.3H2O with the triangular lattice of Co atoms exhibits the superconducting transition at Tc of 4.5 K.1) It attracted much attention as the oxide superconductor with 3d-electrons found after the high-Tc Cu-oxides, and various experimental and theoretical studies have been carried out to identify the superconducting mechanism.

We have carried out the neutron magnetic inelastic scattering to investigate the relationship between the magnetism and the superconductivity. We used aligned crystals of NaxCoO2.yD2O, in which the volume fraction of the superconducting phase or the one with y˜1.3 was about 75%. The remaining non-superconducting phase was found not to contain D2O. On this aligned sample, we have carried out measurements three times. During the periods (nine months) between these experiments, the sample was kept in the He gas with D2O vapor. The c-axis length of the superconducting phase was determined to be 19.7038(7) , 19.706(2) and 19.653(2) just before the first, second and third experiments, respectively. This indicates that the deuterated parts of the crystals are at the boundary between the lower-nuQ3 superconducting and nonsuperconducting regions in the Tc-nuQ3 phase diagram shown in ref. 2 at the first and second experiments and at middle point of the lower-nuQ3 superconducting phase at the third experiment. (nuQ3˜3nu,nuQ being the NMR quadrupolar frequency.)

Scans of the transfer momentum Q along (h, 0, 2.8) in the reciprocal space with fixed transfer energy (E) have been carried out at E= 3 meV at several temperatures between 5 K and 100 K. In all experiments, two magnetic scattering peaks have been observed at h˜0 and h˜1/2. The peak at h˜0 corresponds to an in-plane ferromagnetic fluctuation and the peak at h = 1/2 corresponds to the in-plane antiferromagnetic fluctuation.

We find that the Q-integrated intensity kai ” (omega= 3 meV) estimated for the peak observed at h ˜ 0 decreases with decreasing T and becomes inappreciable at low temperature, while kai ”(omega= 3 meV) at h = 1/2 exists at all temperatures studied here. The disappearance of kai ”(omega= 3 meV) at h˜0 at low T excludes the existence of the hole pockets near the K points in the reciprocal space. We do not show the detailed reasons here, but just mention that the existence of the peak in a relatively high T region is due to the fact that the top of the eg ’band is slightly below the Fermi level.3) Important point is that this result excludes the basis of the predicted triplet superconductivity.4) The incommensurate magnetic fluctuations with a small wave vector q (or h˜0) suggested by Kuroki et al.5) as the excitations among the electron levels of two different Fermi surfaces around the gamma point, are also excluded by the disappearance of the scattering peak at h˜0. The result on the Fermi surface topology is consistent with the simple Fermi surface observed by the angle-resolved photoemission spectroscopy (ARPES) reported by Shimojima et al.6)

The two-dimensional antiferromagnetic fluctuations have been observed in the Q region around (1/2, 0, l). This result indicates that, if spin fluctuations are important for the occurrence of the superconductivity, they should be antiferromagnetic, supporting singlet pairing.

The present results exclude the possibility of the triplet-pairing of the superconductivity, and are consistent with the results of the NMR Knight shift reported by the present authors ’ group.7)

Activity Report on Neutron Scattering Research: Experimental Reports **16** (2009)
Report Number: 740

1) K. Takada et al.: Nature 422 (2003) 53.
2) Y. Kobayashi et al.: J. Phys. Soc. Jpn. 76 (2007) 103705.
3) K. Yada and H. Kontani: J. Phys. Soc. Jpn. 74 (2005) 2161.
4) Y. Yanase et al.: J. Phys. Soc. Jpn. 74 (2005) 430.
5) K. Kuroki et al.: Phys. Rev. B 73 (2006) 184503.
6) T. Shimojima et al.: Phys. Rev. Lett. 97 (2006) 267003.
7) Y. Kobayashi et al.: J. Phys. Soc. Jpn. 77 (2008) 063703.

1-3-5

1-3-6

Fe-doping dependence of magnetic correlations in Bi2201

H. Hiraka and K. Yamada
IMR, Tohoku University, AIMR, Tohoku University

To explain the origin of high-T_c superconductivity, it is important to investigate spin correlations in a wide carrier-concentration range for high-T_c cuprates systematically. Although no magnetic cross section has been experimentally reported yet in one of the most typical cuprate superconductors Bi2201, we succeeded in finding magnetic incommensurate peaks at quasi-elastic channel by using a Fe and Pb co-doped single crystal on AKANE last year [1]. The most striking feature of the magnetic scattering is the anomalously large incommensurability $\delta = 0.20$. Since δ in Sr-doped La214 system saturates in 0.13 $\sim 1/8$, it should be examined first whether the large δ in Fe-doped Bi2201 come from the underlying Cu-spin modulation or merely the Fe-Fe magnetic interaction between localized spins. So, we searched the Fe-doping dependence of the magnetic incommensurate peaks using as-grown single crystals of $Bi_{1.75}Pb_{0.35}Sr_{1.90}Cu_{1-y}Fe_yO_{6+\delta}$ with y =0.03, 0.06, and 0.12. To compare the scattering intensity each other, samples with nearly the same sample volume were prepared for current studies.

Neutron scattering experiments were carried out on triple-axis spectrometers AKANE and TOPAN. Figure 1 shows difference plots of **Q** spectra between 3 K and 70 K about $(1, 0, 0)$ antiferromagnetic zone center. While the magnetic intensity successively increases upon Fe doping, the incommensurate-peak structure is unchanged within the statistics. In fact, the spectra are well reproduced by using the same incommensurability and peak width, already extracted from $y = 0.09$ [1]. This result could be explained by supposing small magnetized clusters around Fe, which grow in number with increasing Fe spins. Hence, the magnetic modulations with large δ detected by Fe doping may come from underlying modulations of Cu spins. The large δ of the current sample in the ocerdoped phase follows a relation $\delta = p$, where p is the effective hole concentration and estimated to $\sim$0.22 from ARPES measurements for $y = 0.09$ [2]. This strongly suggests a different type of spin correlations in Bi2201 from the dominant spin-stripe correlations in Sr-doped La214.

References

[1] H. Hiraka and K. Yamada, Activity Report on Neutron Scattering Research: Experimental Reports **15** (2008), Report Number 398.

[2] T. Sato, private communications.

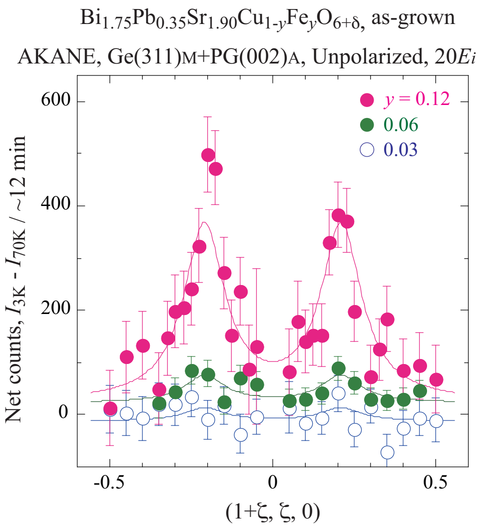

Fig. 1. Difference plots of Q spectra of Fe-doped samples for Fe-doped Bi2201 with $y = 0.03, 0.06,$ and 0.12. The curved lines are fits to a pair of Lorentzians by holding the peak position and the peak width fixed.

1-3-7

Identification of an order parameter in a heavy fermion antiferromagnet $CeTe_3$

K. Deguchi[1], N. Aso[2], 3, H. Iwase[1], T. Okada[1], G. F. Chen[1], N. K. Sato[1], H. Yoshizawa[3]
Nagoya Univ.[1], *Univ. of the Ryukyu*[2], *NSL-ISSP, Univ. of Tokyo, Graduate School of Sci.*[3]

Rare-earth tri-telluride $CeTe_3$, which belongs to the family of quasi-two dimensional compounds RTe_3 (where R = Y, La-Sm, Gd-Tm), has highly two-dimensional crystal structure; bi-layer RTe-sheets and two square Te-sheets are stacked along the b-axis (space group *Cmcm*, weakly orthorhombic structure) [1]. Fermi surfaces consist of inner and outer square sheets, large regions of which are nested by a single incommensurate wave-vector corresponding to the observed lattice-modulation. Because of the characteristic quasi-two-dimensional nature of the Te sheet, the charge-density-wave (CDW) is formed with an extremely large gap [2]. Despite the extensive studies on the CDW in recent years, remarkably little is known about magnetism and low-temperature properties of $CeTe_3$. Recently, it has been reported that $CeTe_3$ exhibits two (magnetic) ordering below $T_{N1} = 3.1$ K and $T_{N2} = 1.3$ K by the specific heat and susceptibility measurements, shown in Fig.1 (a) [3, 4]. From these measurements, the phase below at T_{N2} seems to be a spin-density-wave (SDW).

The goal of this work is to determine the order parameters of the low-temperature two phases by neutron diffraction technique. A single crystal of $m \sim 0.3$ gram was prepared and put in an aluminum can filled with a He gas. It was cooled down to 0.7 K using a ^{3}He cryostat [5]. Neutron diffraction experiments were performed at HQR and PONTA in the research reactor JRR-3.

We have searched magnetic reflections of $CeTe_3$ below T_{N2} with mesh-scans in a scattering plane of $(H, 0, L)$. We have found the Bragg reflection at an incommensurate reciprocal point $Q = (0.18, 0, 1.32)$ at 0.7 K (below T_{N2}). Fig.1 (b) shows temperature dependence of the peak intensities at $Q = (0.18, 0, 1.32)$, which disappeared at 1.5 K (above T_{N2}). The development of the incommensurate magnetic Bragg peak strongly supports that the order below T_{N2} are of itinerant magnetic origin. A series of experiments indicate that the magnetic order of $CeTe_3$ develops from the paramagnetic phase to the SDW phase through the intermediate phase with the formation of heavy quasi-particles.

References

[1] Y. Iyeiri *et al.*, *Phys. Rev.* **B 67**, 144417 (2003); N. Ru *et al.*, *Phys. Rev.* **B 73**, 033101 (2006).
[2] V. Brouet *et al.*, *Phys. Rev. Lett.* **93**, 126405 (2004); H. Komoda *et al.*, *Phys. Rev.* **B 70**, 195101 (2004).
[3] G.F. Chen *et al.*, in preparation.
[4] K. Deguchi *et al.*, *J. Phys. Conf. Series* **150**, 042023 (2009).
[5] TAIYO NIPPON SANSO CORPORATION. Tokyo 142-8558, Japan.

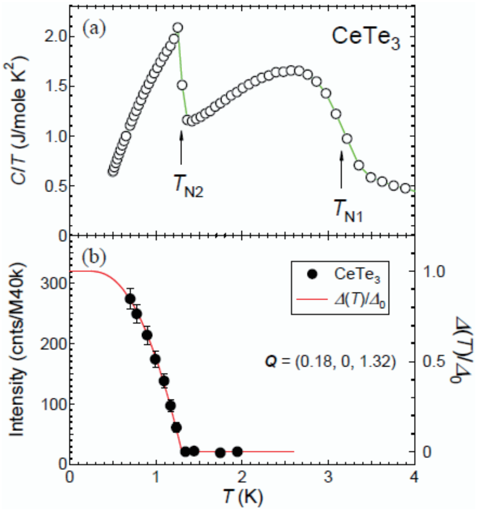

Fig. 1. (a) Temperature dependence of the specific heat divided by temperature of $CeTe_3$. (b) Temperature dependence of Bragg peak intensities of $Q = (0.18, 0, 1.32)$. Solid line represents the square of calculated SDW gap.

1-3-8

Thermal variations of magnetic excitation spectrum in slightly overdoped $Bi_{2.1}Sr_{1.9}CaCu_2O_{8+\delta}$

M. Matsuura[1], Y. Yoshida[2], H. Eisaki[2], N. Kaneko[2], C.-H. Lee[2] and K. Hirota[1]
[1] *Department of Earth and Space Science, Faculty of Science, Osaka University, Toyonaka, 560-0043.*
[2] *AIST, 1-1-1 Umezono, Tsukuba, Ibaraki 305-8568*

Recently, similar magnetic spectra have been reported on several high-T_c families, $La_{2-x}Ba_xCuO_4$ (LBCO) [1], $La_{2-x}Sr_xCuO_4$ (LSCO) [2], and $YBa_2Cu_3O_{6+x}$ (YBCO) [3], namely, a characteristic hourglass-like magnetic excitation. There are, however, important differences concerning their thermal variations of spectra across T_c. In particular, the magnetic resonance peak in YBCO shows an order-parameter like behavior in contrast to no clear enhancement of the (π,π)-peak at T_c in the LBCO and LSCO systems. This discrepancy rises following question. Which part of magnetic excitation is essential and universal for high-T_c superconductors? One way to resolve this issue is to investigate another high-T_c system $Bi_{2.1}Sr_{1.9}CaCu_2O_{8+\delta}$ (Bi2212). We explored the magnetic spectrum in slightly overdoped Bi2212 grown by travelling-solvent-floating zone method. Neutron scattering experiments were performed on the triple-axis spectrometer PONTA installed at the JRR-3 Reactor of the JAEA. We have aligned 9 single crystals on Al plates. The total mass of aligned crystals is 4.6g (0.71cc), which is 12 times as large as the crystal used in the previous report[4].

From our previous studies, we know resonance peak appears at $\omega = 34$ meV and $(\frac{1}{2},\frac{1}{2},-14)$ in our sample. Upon heating above T_c, the intensity at $(\frac{1}{2},\frac{1}{2},-14)$ (open circles) keeps on increasing except a small drop at $T = 200$ K. This dip-structure at $T = 200$ K is more clear for the difference (closed circles) between background (BG: open rectangles) and the intensity at $(\frac{1}{2},\frac{1}{2},-14)$. Here, the background at $(\frac{1}{2},\frac{1}{2},-14)$ was estimated as an average of the intensities at $(0.1, 0.1, -14)$ and $(0.9, 0.9, -14)$. Subtracting temperature-dependent background, the (π,π)-peak keeps on decreasing with increasing temperature up to 200 K, which roughly agrees with the onset of pseudogap $T^* = 150 \sim 200$ K. This suggests that, in slightly overdoped Bi2212, a large magnetic resonance peak remains above T_c and disappears around T^*, which could be associated with pre-formed singlet pairs in the pseudogap phase.

References

[1] J. M. Tranquada *et al.*, Nature **429**, 534 (2004).
[2] N. B. Christensen *et al.*, Phys. Rev. Lett. **93** (2004) 147002.
[3] S. M. Hayden *et al.*, Nature **429** (2004) 531.
[4] H. F. Fong *et al.*, Nature (London) **398**, 588 (1999).

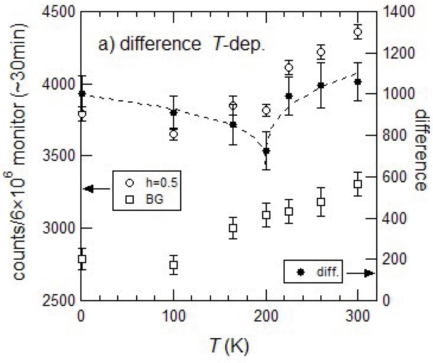

Fig. 1. The temperature dependence of the scattering intensity at $\omega = 34$ meV measured at $(\frac{1}{2},\frac{1}{2},-14)$, background, and the difference between them.

1-3-9

Inelastic neutron scattering experiment on deuterated halogen-bridged nickel complex

S. Itoh and T. Yokoo
High Energy Accelerator Research Organization, Tsukuba, 305-0801

The halogen-bridged nickel complex, [Ni(chxn)2Br]Br2 (chxn=1R,2R-cyclohexandiamine), has a 1D structure, -Br-Ni(III)-Br-Ni(III)-Br-, along the b-axis [1-2]. This spin structure implies the formation of antiferromagnetically coupled S=1/2 Heisenberg chains of Ni(III). Recently, this system has been suggested to be the second d-electron spin-Peiers system following CuGeO3, and the first example of organic d-electron spin-Peiers system (TTF-CuBDT is a p-electron system). In fact, a clear splitting of the spectrum below 40 K has been observed in the Br-81 NQR study [3].

We have initiated inelastic neutron scattering experiments in [Ni(chxn)2Br]Br2, in order to detect magnetic excitations. In the early stage of our investigations, we grew single crystals and tried inelastic neutron scattering experiments. However, since the sample was not deuterated, local modes originating from hydrogen were too strong to detect magnetic excitations.

Very recently, we have successfully synthesized 95%-deuterated polycrystals of [Ni(chxn)2Br]Br2. We measured inelastic neutron scattering spectra from the 95%-deuterated polycrystalline sample on the triple axis spectrometer PONTA (5G) at JRR3M in JAEA (Tokai), with Ef = 14.7 meV, by using the collimation, open-80 ’-80 ’-open, at 10 K and 100 K (below and above the transition temperature). Although we used 95%-deuterated crystals, the background noise was still high as shown in Fig. 1(a) (1Mmon roughly corresponds to 5 minutes). In order to reduce the background noise, fully-deuterated crystals are required. The antiferromagnetic zone center is located at Q = 0.6 A-1. Assuming the signals at Q = 0.8 A-1 to be the background, the spectrum of S(E) = I(Q=0.6,E) - I(Q=0.8,E) was deduced, and the difference of S(E,T=10K) - S(E,T=100K) is plotted in Fig. 1(b). The spectrum in Fig. 1(b) should be magnetic signals at the magnetic zone center if magnetic response is detected.

[1] K. Toriumi et al., J. Am. Chem. Soc. 111 (1989)2341.
[2] H. Okamoto et al., PRB 54 (1996) 8438.
[3] S. Takaishi et al., J. Am. Chem. Soc. 126 (2004) 1614.

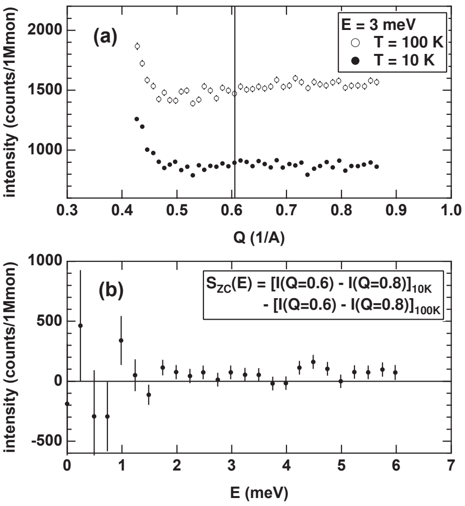

Fig. 1. Fig. 1 Inelastic neutron scattering spectra from deterated [Ni(chxn)2Br]Br2 measured on PONTA with Ef =14.7 meV.

1-3-10

Electric Control of Helimagnetic Chirality in CoCr2O4

Y. Kousaka1, M. Nishi2, K. Tomiyasu3, M. Matsuura4, K. Hirota4 T. Yokobori1 and J. Akimitsu1
1Department of Physics and Mathematics, Aoyama-Gakuin Univ., 5-10-1 Fuchinobe, Sagamihara 229-8558; 2Institute for Solid State Physics, The Univ. of Tokyo, 106-1 Shirakata, Tokai 319-1106; 3Department of Physics, Tohoku Univ., Aoba, Sendai 980-8578; 4 Department of Earth and Space Science, Graduate School of Science, Osaka Univ., 1-1 Machikaneyama, Toyonaka 560-0043, Osaka

Ferroelectricity driven by magnetic order is paid a large attention in the recent study of multiferroics. A cubic spinel CoCr2O4, in which magnetic Co2+ ions occupy the A site and Cr3+ ions occupy the B site, shows ferrimagnetic ordering below TC = 93 K and conical-spiral magnetic ordering below TS = 26 K. [1] As the spiral magnetic ordering induces electric polarization,[2, 3] the right-handed or left-handed spiral magnetic structure can be controlled by the electric polarization.[4] To detect the chiral helimagnetic structure, polarized neutron diffraction is powerful method by comparing magnetic satellite intensity of up-spin and down-spin incident neutron beams.

To detect the helimagnetic chirality, we performed polarized neutron diffraction experiments on a triple-axis spectrometer 5G (PONTA), JRR-3M, Tokai, Japan. The energy of incident neutron beam was 13.7 meV. To make single chiral helimagnetic domains, we cooled the sample with applying a magnetic field of 0.5 T along <0, 0, 1> and electric field of 0 to 0.9 kV/mm along <-1, 1, 0>. After cooling, the magnetic and electric field was turned off and the sample was set on a goniometer. The data was collected at 10 K. By observing nuclear Bragg reflection of (2, 2, 0), the neutron polarization of incident beam was determined to be 95.4 %. As shown in Fig. 1, we observed magnetic satellite peak at (2-q, 2-q, 0), where the magnetic propagation vector kmag was (q, q, 0) (q = 0.616). To investigate the helimagnetic chirality, intensity comparison at (± q, ± q, 2) is necessary. As the peaktop intensity of (± q, ± q, 2) was too weak (0.1 cps), we estimated the intensity by subtracting the background intensity from the peaktop intensity. In any electric field amplitude, the obtained neutron polarization in (q, q, 2) was nearly zero, which indicates the right- and left-handed magnetic screw domains coexist in equal ratio. The magnetic domains might be destroyed in the process of turning off the magnetic field. Therefore, the additional polarized neutron diffraction experiments under an applied magnetic field are now in progress.

[1] K. Tomiyasu et al.: Phys. Rev. B 70 (2004) 214434.
[2] Y. Yamasaki et al.: Phys. Rev. Lett. 96 (2006) 207204.
[3] Y. J. Choi et al.: Phys. Rev. Lett. 102 (2009) 067601.
[4] H. Katsura et al.: Phys. Rev. Lett. 95 (2005) 057205.

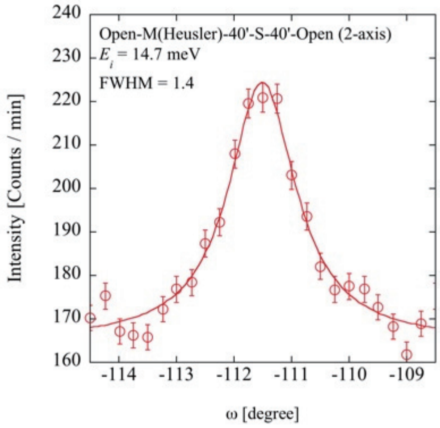

Fig. 1. Omega scan profile in (2-q, 2-q, 0)

1-3-11

Mechanism of Spontaneous Electric Polarization Flop in TbMnO3

H. Sagayama (A), N. Abe (B), T. Arima (A), K. Iwasa (B)
(A)IMRAM, Tohoku univ., (B) Dept. Phys., Tohoku univ

Orthorhombic perovskite TbMnO3 is one of the typical multiferroic systems. Spontaneous electric polarization (P) along the c-axis appears below TC (˜27K) [1]. It originates from the spiral configuration of Mn3+ spins rotating in the bc-plane with propagating vector (0 q 1) (q˜0.27) through an inverse effect of the DM interaction [2,3]. Interestingly, the P//c is turned to the a-axis direction by applying a magnetic field along the a- or b-axis. Magnetic structure analysis and a spin-polarized neutron diffraction study of 160Gd0.7Tb0.3MnO3 strongly suggest that P//a also originates from helical spin structure rotating in the ab-plane [4]. It has been pointed out that anisotropic magnetic moments of Tb3+ play an important role for the complicated electric polarization flop [5].

To clarify mechanism of the electric polarization flop, we have performed a spin-polarized-neutron diffraction measurement using the TOPAN installed at JRR-3. Heusler(111)-Heusler(111) monochromator-analyser configuration was used. The incident neutron energy Ei was 80 meV. Collimators were set as open-80-100-open. A single crystal sample was mounted in a superconducting magnet with the a- and c-axis in the scattering plane. The magnetic field was applied along the b-axis up to 5.5 T.

We observed magnetic field dependences of spin-flip and non-spin-flip scattering at (0, q, 7) and (4, q, 1) at 8 K. These results indicate the basal plane change of spin helix from the bc- to ab- plane. In addition, we observed increasing of (1 0 6) reflection corresponding to the C-type antiferromagnetic structure with increasing magnetic field. It might be caused by the local anisotropy of Tb magnetic moments lying in the ab plane. Based on the experimental results, we considered coupling between Mn3+ spins and anisotropic Tb3+ magnetic moments. We calculated magnetic field dependence of the energy gain of the coupling and succeeded in reproducing the electromagnetic diagram of TbMnO3 [5].

Reference

[1] T. Kimura et al., Nature (London) 426, 55 (2003).
[2] M. Kenzelmann et al., Phys. Rev. Lett. 95, 087206 (2005).
[3] Y. Yamasaki et al., Phys. Rev. Lett. 98, 147204 (2007).
[4] Y. Yamasaki et al., Phys. Rev. Lett. 101, 097204 (2008).
[5] N. Abe et al., Phys. Rev. Lett. 99, 227206 (2007).

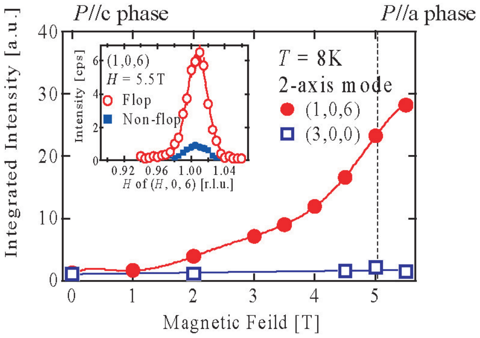

Fig. 1. Magnetic field dependences of integrated intensities of (1 0 6) and (3 0 0) refrection. The inset shows reflection profiles of spin frop and non-spin flop scattering at (1 0 6).

1-3-12

Thermoelectric properties and crystal structures in layered Co oxides

H. Nakatsugawa and K. Nagasawa
Yokohama National University 79-5 Tokiwadai Hodogaya-ku Yokohama 240-8501 Japan

Polycrystalline samples were prepared by a conventional solid-state reaction method. Appropriate amount of starting from a mixture of CaCO3 (99.9%) and Co3O4 (99.9%) powders were mixed with an agate mortar and pressed into pellets. The pellets were calcined in air at 920 ℃ for 12h and sintered at 920 ℃ for 24h under pure flowing oxygen gas. The samples were furnace cooled to room temperature, ground and pelletized again. This process was repeated three times in order to obtain well-crystallized single-phase sample. In addition, one of the obtained well-crystallized single-phase samples were annealed in pure flowing Ar gas at 740 ℃ for 48h and then quenched in distilled water to control oxygen nonstoichiometry δ. In this work, we prepare two samples: "Sample A" and "Sample B". The former is the obtained well-crystallized single-phase sample, and the latter is the annealed sample to control oxygen nonstoichiometry δ in reduction atmosphere.

Neutron powder diffraction (ND) data were collected at room temperature using a Kinken powder diffractometer for the high-efficiency and high-resolution measurements (HERMES) of Institute for Materials Research (IMR), Tohoku University, installed at a JRR-3M reactor in Japan Atomic Energy Research Institute (JAERI). The ND data were collected on thoroughly ground powders in a multiscanning mode in the 2θ range from 3.0 to 153.9 °with a step width of 0.1 °.The incident neutron beam was monochromatized to a wavelength of 1.8205 Å.The XRD and ND data were simultaneously analyzed using a Rietveld refinement program PREMOS 91 designed for modulated structure analyses. We adopt a superspace group of C2/m(1p0)s0 because the CdI2-type [CoO2] subsystem has a C2/m symmetry, whereas the RS-type BL subsystem has a C21/m symmetry. The crystal structures and interatomic distance plots were obtained using the PRJMS and MODPLT routines, respectively; both are included in the PREMOS 91 package.

Figure 1(a) shows the observed, calculated and difference intensities of the HERMES data for Sample A. Short vertical lines below the patterns indicate the peak positions of the main (upper) and satellite (lower) reflections of the two subsystems. The final Rwp factor is 5.37 % and the lattice parameters are refined to a = 4.83353(4) Å, bCoO2 = 2.82380(7) Å, c = 10.8455(3) Å and β = 98.141(5) °for the [CoO2] subsystem and bRS = 4.55757(8) Å for the RS-type BL subsystem. The resulting p = bCoO2/bRS = 0.61958(5) ～0.62 corresponds to the structural formula [Ca2CoO3.08]0.62CoO2.

The crystal structure of Sample B was also analyzed in a similar manner. Figure 1(b) shows the observed, calculated and difference intensities of the HERMES data for Sample B. Short vertical lines below the patterns indicate the peak positions of the main (upper) and satellite (lower) reflections of the two subsystems. The final Rwp factor is 4.69 % and the lattice parameters are refined to a = 4.83804(6) Å, bCoO2 = 2.82533(1) Å, c = 10.86027(2) Å and β = 98.135(8) °for the [CoO2] subsystem and bRS = 4.55128(9) Å for the RS-type BL subsystem. The resulting p = bCoO2/bRS = 0.62077(6) ～0.62 corresponds to the structural formula [Ca2CoO3.08 − δ]0.62CoO2.

Activity Report on Neutron Scattering Research: Experimental Reports **16** (2009)
Report Number: 833

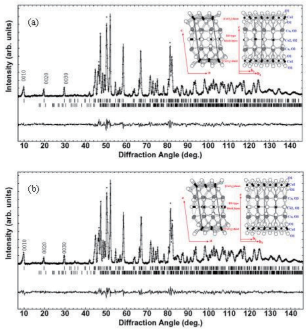

Fig. 1. Fig.1 Observed, calculated and difference intensities of powder ND data for (a) Sample A and (b) Sample, respectively.The inset is the final crystal structure.

1-3-12

1-3-13

Thermoelectric properties and crystal structures in layered Co oxides

H. Nakatsugawa and K. Nagasawa
Yokohama National University 79-5 Tokiwadai Hodogaya-ku Yokohama 240-8501 Japan

Polycrystalline samples were prepared by a conventional solid-state reaction method. Appropriate amount of starting from a mixture of CaCO3 (99.9%) and Co3O4 (99.9%) powders were mixed with an agate mortar and pressed into pellets. The pellets were calcined in air at 920 ℃ for 12h and sintered at 920 ℃ for 24h under pure flowing oxygen gas. The samples were furnace cooled to room temperature, ground and pelletized again. This process was repeated three times in order to obtain well-crystallized single-phase sample. In addition, one of the obtained well-crystallized single-phase samples were annealed in pure flowing Ar gas at 740 ℃ for 48h and then quenched in distilled water to control oxygen nonstoichiometry δ. In this work, we prepare two samples: "Sample A" and "Sample B". The former is the obtained well-crystallized single-phase sample, and the latter is the annealed sample to control oxygen nonstoichiometry δ in reduction atmosphere.

Neutron powder diffraction (ND) data were collected at room temperature using a Kinken powder diffractometer for the high-efficiency and high-resolution measurements (HERMES) of Institute for Materials Research (IMR), Tohoku University, installed at a JRR-3M reactor in Japan Atomic Energy Research Institute (JAERI). The ND data were collected on thoroughly ground powders in a multiscanning mode in the 2θ range from 3.0 to 153.9 °with a step width of 0.1 °.The incident neutron beam was monochromatized to a wavelength of 1.8205 Å.The XRD and ND data were simultaneously analyzed using a Rietveld refinement program PREMOS 91designed for modulated structure analyses. We adopt a superspace group of C2/m(1p0)s0 because the CdI2-type [CoO2] subsystem has a C2/m symmetry, whereas the RS-type BL subsystem has a C21/m symmetry. The crystal structures and interatomic distance plots were obtained using the PRJMS and MODPLT routines, respectively; both are included in the PREMOS 91 package.

Figure 1(a) shows the observed, calculated and difference intensities of the HERMES data for Sample A. Short vertical lines below the patterns indicate the peak positions of the main (upper) and satellite (lower) reflections of the two subsystems. The final Rwp factor is 5.37 %. The crystal structure of Sample B was also analyzed in a similar manner. Figure 1(b) shows the observed, calculated and difference intensities of the HERMES data for Sample B. Short vertical lines below the patterns indicate the peak positions of the main (upper) and satellite (lower) reflections of the two subsystems.

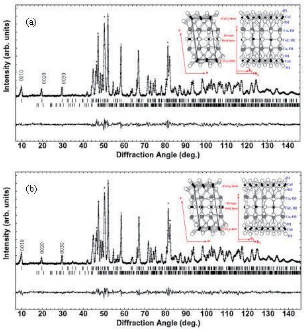

Fig. 1. Observed, calculated and difference intensities of powder ND data for (a) Sample A and (b) Sample B, respectively. The inset is the final crystal structure.

Activity Report on Neutron Scattering Research: Experimental Reports **16** (2009)
Report Number: 835

1-3-14

Nonmagnetic impurity effect in ferroelectric phase of $CuFeO_2$

T. Nakajima[1], S. Mitsuda[1], M. Yamano[1], H. Yamazaki[1], M. Matsuura[2], K. Hirota[2]
[1] *Department of Physics, Faculty of Science, Tokyo University of Science, Tokyo 162-8601*
[2] *Department of Earth and Space Sci., Osaka University, Toyonaka 560-0043*

In the past several years, a magnetic oxide $CuFeO_2$ (CFO) has been intensively investigated as a new class of magnetoelectric (ME) multiferroics, whose ferroelectricity is originated from a proper-screw type magnetic ordering. The recent experimental studies have revealed that the ferroelectric helimagnetic phase, which originally shows up as a magnetic-field-induced phase in pure CFO, also shows up as a ground state in slightly diluted $CuFe_{1-x}Al_xO_2$ (CFAO) and $CuFe_{1-x}Ga_xO_2$ (CFGO). Although the origin of the ferroelectricity must be common to CFO, CFAO and CFGO, the reported values of the observed macroscopic electric polarization, P, are rather different from each other. In particular, the previously reported value of P in CFAO ($\sim 50\mu C/m^2$) is remarkably smaller than the values in CFO and CFGO ($200 \sim 400\mu C/m^2$).

In the present study, we have thus performed polarized neutron diffraction and in-situ pyroelectric measurements on CFAO, in order to answer the question: "What determines the magnitude of P in CFO, CFAO and CFGO systems?". The polarized neutron diffraction measurements on CFAO($x = 0.015$) were carried out at the triple-axis neutron spectrometer PONTA installed by University of Tokyo at JRR-3 in the Japan Atomic Energy Agency(JAEA). Incident polarized neutron beam with energy 34.06 meV was obtained by a Heuslller (111) monochromator. The flipping ratio of the polarized neutron beam was ~ 14. The experimental settings and procedures including pyroelectric measurement were the same as those in the previous polarized neutron diffraction measurement on CFAO ($x = 0.02$).[3]

Since our previous work have revealed a one-to-one correspondence between the spin helicity and the polarity of the induced ferroelectric polarization, in the present work, we have deduced asymmetry in the fractions of the left-handed and right-handed helical magnetic ordering from the results of the polarized neutron measurements. We refer to this asymmetry of the spin helicity as D.

Figures 1(a-1) and 1(a-2) show the measured values of D and P as functions of E_p. We found that P and D in CFAO were rather insensitive to E_p. However, we also found that CFAO can achieve P of $\sim 250\mu C/m^2$, which is comparable to the values of P in CFO and CFGO, as shown in the inset of Fig. 1(b). This implies that the magnitude of the local electric polarization in CFO system does not reduced by the Al-substitution, but the sensitivity of P to E_p is reduced.

References

[1] T. Kimura *et al.*: PRB **73** 220401(2006).
[2] T. Nakajima *et al.*: JPSJ **76** (2007)043709.
[3] T. Nakajima *et al.* PRB **77** 052401 (2007).

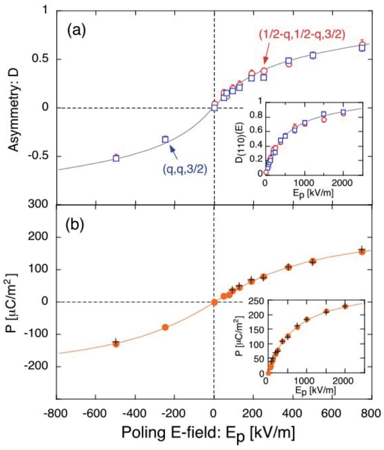

Fig. 1. [(a)-(b)] E_p dependences of (a)P and (b)D in CFAO ($x = 0.015$) at $T = 2.0$K.

1-3-15

Magnetic Phase Diagram in $Ba_2Mg_2Fe_{12}O_{22}$

H. Sagayama(A), K. Taniguchi(A), T. Arima(A), Y. Nishikawa(B), S. Yano(B), J. Akimitsu(B), M. Matsuura(C), K. Hirota(C)
(A)IMRAM, Tohoku Univ., (B)Dept. Phys., Aoyama-Gakuin University, (C)Dept. Earth and Space Science, Osaka Univ.

It has been recently found that a Y-type hexaferrite $Ba_2Mg_2Fe_{12}O_{22}$ (BMFO) exhibits a nonlinear magnetoelectric effect [1,2]. It is proposed that the conical magnetic structure at low temperatures is modified by the application of a weak magnetic field perpendicular to the cone axis of the *c* axis, which produces the electric polarization. However, the magnetic phase diagram of BMFO has not been clarified yet. We performed a neutron diffraction measurement to reveal the magnetic phase diagram with the $H \parallel b^*$ configuration.

Single crystals of BFMO were grown from Na_2O-Fe_2O_3 flux. Neutron diffraction measurement was performed with a triple-axis neutron spectrometer PONTA at JRR-3. A single crystal was set in a ^{4}He refrigerator. A magnetic field was applied parallel to the b-axis using a 1T electromagnet. The diffraction profile along (1 0 L) was measured for various temperatures and magnetic fields.

As cooling down the sample down to 10 K in zero magnetic field, clear magnetic satellite peaks are observed at L=-3.4 and -1.6, indicating a incommensurate conical phase. Considering the M-H curve, the cone axis is possibly parallel to the c-axis. As increasing the magnetic field along the b-axis to 0.2 T, the peak position of the magnetic satellites suddenly moves to L=-4.5. The compound clearly undergoes incommensurate-commensurate magnetic phase transition. A magnetic structure analysis with using FONDER suggests that the magnetic moments form a spiral around the b axis and propagate along the c axis with a period of two unit layers. The magnetic structure does not change at least up to 0.5 T. With decreasing the magnetic field down to 0 T, the magnetic structure does not show the incommenrate alignment but changes to another commensurate phase. The period of the magnetic alignment is six unit layers.

At higher temperatures, we also find the four-fold magnetic phase for an intermediate region between the low-field six-fold phase and high-field two-fold phase. We summarize the magnetic phase diagram in Fig. 1.

References

[1] K. Taniguchi et al., Appl. Phys. Express **1**, 031301 (2008).

[2] S. Ishiwata et al., Science **319**, 1643 (2008).

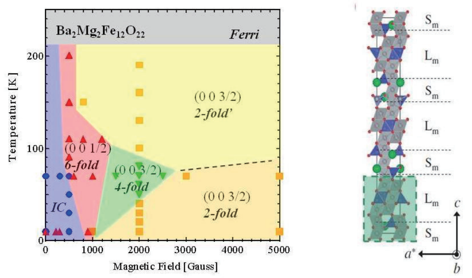

Fig. 1. Magnetic phase diagram of a Y-type hexaferrite $Ba_2Mg_2Fe_{12}O_{22}$ for magnetic fields along the b-axis.

1-3-16

Magnetic Property of $Pr_xFe_4Sb_{12}$

K. Iwasa[1], T. Orihara[1], Y. Murkami[1],K. Kuwahara[2], H. Sugawara[3]
Tohoku Univ.[1], *Ibaraki Univ.*[2], *The Univ. of Tokushima*[3]

Rare-earth filled skutterudite compounds have been studied for various phase transitions of $4f$ electron states. $Pr_xFe_4Sb_{12}$ has been considered to exhibit magnetic ordering at around 4 K, that is composed by not only Pr $4f$ but also Fe $3d$ electrons (N. P. Butch *et al.*: Phys. Rev. B 71 (2005) 214417), since the magnitude of effective magnetic moment estimated from the high temperature magnetic susceptibility is larger than that of Pr^{3+} free ion. The ordered structure of the two kinds of magnetic moments depending on the Pr filling has been unsolved yet. It is notable that the magnetic phse transition is reported to disappear in case of full occupation of the Pr-ion sites ($x = 1$). The effect of Pr filling to the magnetic ordering has also not been explained.

We performed neutron scattering experiment using the triple-axis spectrometer TOPAN (6G) in order to reveal Pr-ion crystal field levels by using powdered simple and the four-circle diffractometer FONDER (T2-2) to investigate the magnetic ordered structure by using a single crystalline sample. These samples were synthesized by the so-called Sb-self flux method, and the Pr concentration x is expected to be less than unity ($x = 0.7 - 0.9$), as was reported in the previous reports. Figure shows inelastic spectra observed at TOPAN. We succeeded in observing two magnetic excitation peaks at 2.4 and 11 meV. The peak positions are almost equivalent with those of the $x < 1$ sample reported by E. Bauer *et al.* (J. Magn. Magn. Mater. 310 (2007) 286) but also for the x 1 one synthesized by K. Tanaka *et al.* using the high-pressure method (J. Phys. Soc. Jpn. 76 (2007) 103704). Therefore, one can expect that the nature of $4f$ electrons localized at Pr ions does not strongly depend on the Pr ion concentration. In the Experiment at FONDER, we succeeded in observing the increase of fundamental reflection intensities with decreasing temperature thorough the transition temperature. This results is consistent with the previous study, and the magnetic ordering pattern is composed of ferromagnetic component. However, because of the small single crystalline sample, we have not yet achieved to the conclusion of magnetic structure. We will carry out a subsequent measurement with a larger volume sample.

The less dependence of the $4f$ crystal field levels and the apparent dependence of the magnetic ordering on the Pr ion concentration may indicate that the magnetic ordering is predominated by Fe magnetic moments as discussed previously.

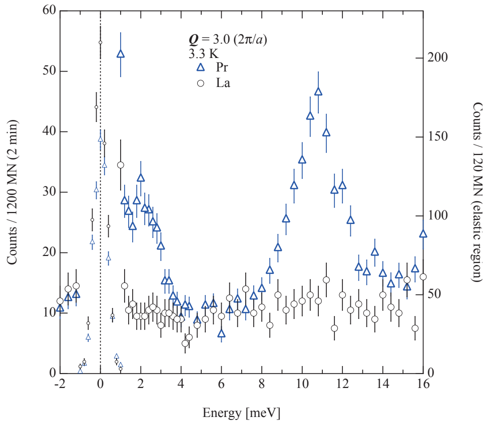

Fig. 1. Magnetic excitation spectra of $Pr_xFe_4Sb_{12}$ and $La_xFe_4Sb_{12}$ at 3.3 K.

1-3-17

Crystal-field excitation and multipolar ordering in $Pr(Ru_{1-x}Rh_x)_4P_{12}$

K. Iwasa[1], K. Saito[1], L. Hao[2], Y. Murakami[1]
Tohoku Univ.[1], *China Institute of Atomic Energy*[2]

Spontaneous ordering of higher-rank multipoles of $4f$ electrons has been detected in various rare-earth based materials. $PrRu_4P_{12}$ is one of typical systems, exhibiting the antiferro-type hexadecapolar (rank-4 multipolar) ordering below the metal-nonmetal transition at 63 K (T. Takimoto: J. Phys. Soc. Jpn. 75 (2006) 034714). The phase transition is a new type of charge density wave formation originating from the coupling of the Fermi surface nesting property to the modulated $4f$ multipolar arrangement. This coupling is due to p-f hybridization between $4f$ and conduction electrons. It should be notable that the ordering is characterized by the crystal field excitations exhibiting the strong temperature dependence in accordance with the evolution of the multipolar order parameter (K. Iwasa *et al.*: Phys. Rev. B 72 (2005) 024414). The substitution of Rh to Ru gives rise to rapid suppress of metal-nonmetal transition; the electrical resistivity at low temperature in the Rh 10% system becomes the same magnitude at around 60 K (C. Sekine *et al.*: Physica B 378-380 (2006) 211). Thus, a study of the doping effect leads to understand the ordered phase of $PrRu_4P_{12}$. Then we have carried out inelastic scattering experiments to measure crystal-field excitation of $Pr(Ru_{1-x}Rh_x)_4P_{12}$.

We have performed experiments using the triple-axis spectrometers HER (C1-1) and TOPAN (6G) for polycrystalline sample of $Pr(Ru_{1-x}Rh_x)_4P_{12}$. These previous studies revealed that the Rh doping systems (x = 0, 0.03, 0.05, 0.10 and 0.15) shows the crystal field excitations at 2.4 and 13 meV, whose peak positions do not show any temperature dependence, in addition to the strongly temperature dependent ones. The most recent measurement for x = 0.01 performed at HER also shows the same excitation spectrum. The peaks appearing in the Rh doped systems indicate appearance of Pr ions without contribution to the ordering. In order to identify the level schemes produced by the Rh doping, we carried out the inelastic measurements under magnetic field for the x = 0.05 system. Figure depicts the magnetic field dependence of the excitation at 2.4 meV measured at 1.6 K. The broadening and asymmetric shape of the peak under finite magnetic field indicate that the peak corresponds to excitation from singlet ground state to triplet state. On the phase transition to the antiferro-type hexadecapolar ordering in the pure system, the crystal field level scheme at one of the Pr ion sites switches from a singlet to a triplet state. Thus, the Rh doping is thought to force the Pr $4f$ electron state to remain at the singlet state, resulting into the suppression of the transition.

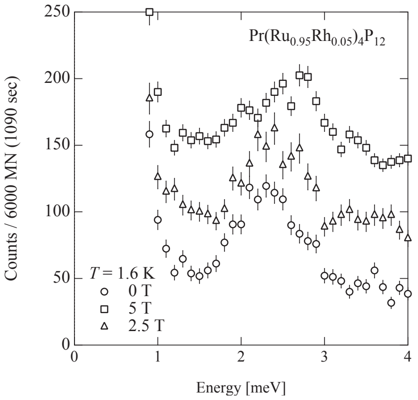

Fig. 1. Magnetic field dependence of crystal-field excitations of $Pr(Ru_{0.95}Rh_{0.05})_4P_{12}$ at 1.6 K.

1-3-18

Electric Field Control of Magnetic Correlation in Multiferric Cu(Fe,Al)O_2

K. Takahashi, Y. Kaneko, T. Ito, T. Nakajima, and S. Mitsuda
Department of Physics, Faculty of Science, Tokyo University of Science, Tokyo 162-8601

Recently, a magneto-electric multiferroic $CuFeO_2$, in which the ferroelectric phase shows up as a magnetic-field- or impurity-induced phase, has been extensively investigated. The recent experimental works have revealed that the magnetic structure in the ferroelectric phase is a 'proper-screw-type' structure[1], whose spin-helicity corresponds to the polarity of the local ferroelectric polarization emerging along the helical axis.[2] In the previous neutron diffraction measurement on $CuFe_{1-x}Al_xO_2$ at FONDER(T2-2),[3] we have discovered that magnetic diffraction profiles in the ferroelectric phase were sharpened by applying electric field parallel to the helical axis. This implies that the magnetic correlation length in the ferroelectric phase can be controlled by an applied electric field.

In order to investigate the electric field dependence of the magnetic correlation length in detail, in the present experiment, we have performed neutron diffraction measurements on $CuFe_{1-x}Al_xO_2$ ($x = 0.02$) under applied electric fields parallel and perpendicular to the helical axis, using the triple-axis neutron spectrometers HQR(T1-1) and HER(C1-1) installed at JRR-3. As shown in Figs. 1(a) and 1(b), we found that a poling electric field applied parallel to the helical axis sharpens the diffraction profile of $(q,q,3/2)$ magnetic reflection in the ferroelectric phase, but that applied perpendicular to the helical axis does not. Figure 1(c) shows that the variance of the diffraction profile, which is relevant to the inverse magnetic correlation length, decreases, with increasing poling electric field. This suggests that the average size of the magnetic domains is enlarged by the poling electric field, owing to the one-to-one correspondence between the magnetic and ferroelectric domains, because the poling electric field should enlarges the ferroelectric domains in which the local electric polarization is parallel to it. Note that this electric field dependence of the magnetic correlation length might not be observed not in the typical multiferroics such as $TbMnO_3$, but is clearly observed in $CuFe_{1-x}Al_xO_2$. This is because the magnetic correlation in the ferroelectric phase of $CuFe_{1-x}Al_xO_2$ ($x = 0.02$) is originally disturbed by site-random Al^{3+}-substitutions, and therefore the change in the magnetic correlation length was easily detected by neutron diffraction measurements. For further research, we will investigate the helicity-dependent magnetic correlation by polarized neutron diffraction measurements.

References

[1] T. Nakajima *et al.*: JPSJ **76** 043709 (2007).
[2] T. Nakajima *et al.*: PRB **77** 052401 (2008).
[3] T. Nakajima *et al.*: ISSP-NSL report #328 (2007).

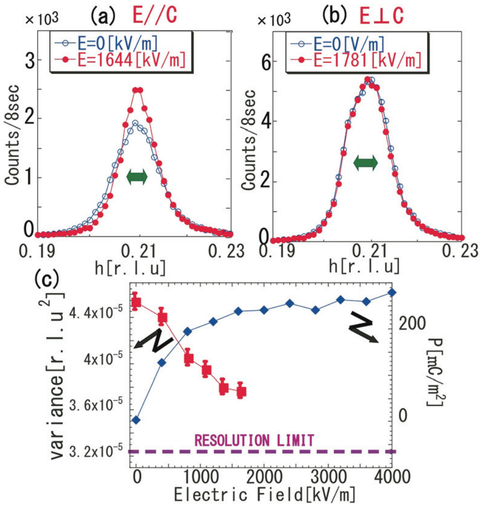

Fig. 1. (a)(b)Diffraction profiles in the ferroelectric phase. Green bar stand for resolution limit. (c)E-field dependence of the variance of diffraction profiles in the ferroelectric phase and the polarization.

1-3-19

Rattling vibration of cage compounds

C. H. Lee(A), H. Yoshizawa(B), K. Kihou(A), T. Onimaru(C), K. Suekuni(C), T. Takabatake(C)
(A) AIST, (B) ISSP, (C) Hiroshima Univ.

A large vibration of an atom in an oversized atomic cage, so called rattling, has attracted great interest since it can be the origin of exotic physical properties. For example, rattling can be responsible for the extremely low thermal conductivity in cage compounds. Electronic properties could be also affected by rattling via electron-phonon coupling. To clarify the effect of rattling motion on these exotic physical properties, it is very important to understand the nature of rattling.

Type-I clathrate X8Ga16Ge30 (X=Ba, Sr or Eu) is one of compounds that has large Ga and Ge atomic cages filled with X guest atoms. According to crystal structure analysis, the positions of Sr and Eu atoms split into four sites. Phonon dynamics of cage compounds with off-centered guest atoms are a controversial issue. Therefoire, we studied the phonon dynamics of Sr8Ga16Ge30 by inelastic neutron scattering [1,2].

Neutron scattering measurements were carried out using a triple-axis spectrometer, TOPAN, at the JRR-3 reactor of JAEA at Tokai. The final neutron energy was fixed at Ef=14.8 meV using a pyrolytic graphite (PG) monochromator and analyzer. The sequences of horizontal collimators were 40′-30′-S-30′-30′ where S denotes the sample position. A single crystal of Sr8Ga16Ge30 was grown by a self-flux method using excess Ga. The volume of the single crystal used for the measurements was about 2 cc. All measurements were conducted at room temperature.

Figure 1 shows the phonon dispersion of Sr8Ga16Ge30 with propagation vector of [100]. The optical phonon mode observed at E = 4 meV corresponds to a guest mode, in which Sr atoms vibrate largely. The guest mode shows anti-crossing behavior with the acoustic phonon mode, though the gap energy is relatively small comparing with that of Ba8Ga16Ge30. Analysis based on a Born-von Karman force model has clarified that the Sr atoms are bound very weakly to surrounding atoms, with a force constant of 0.007 ˜ 0.009 mdyn/A. The results suggest that hybridization between the guest atoms and host lattice vibration is weak in Sr8Ga16Ge30 compounds.

[1] C. H. Lee et al., J. Phys. Soc. Jpn. 77 (2008) 260, Suppl. A.
[2] C. H. Lee et al., J. Phys.: Conf. Ser. 92 (2007) 12169.

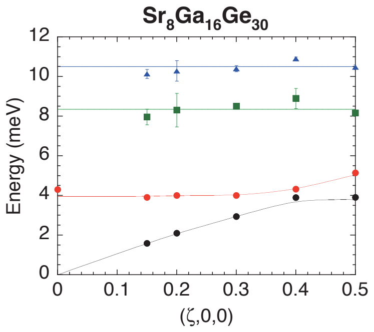

Fig. 1. Phonon dispersion curves of transverse acoustic and optical phonon modes with propagation vector [100] in Sr8Ga16Ge30.

1-3-20

Spin fluctuations of single-layer in Bi2+xSr2-xCuO6+d superconductor

M. Fujita[1], M. Enoki[2], and K. Yamada[3]

[1] *Institute for Materials Research, Tohoku University, Katahira, Sendai 980-8577, Japan*
[2] *Department of Physics, Tohoku University, Aramaki, Sendai 980-8578, Japan*
[3] *World-Premier-International Research Center Initiative, Tohoku University, Katahira, Sendai 980-8577, Japan*

Inelastic neutron-scattering measurement is a powerful technique for the study of spin dynamics and lattice vibrations (phonon) in condensed matters such as high-Tc superconductors. Systematic neutron-scattering experiments on the high-T_c superconducting systems of $La_{2-x}Sr_xCuO_4$ (LSCO) and $YBa_2Cu_3O_{6+\delta}$ (YBCO) revealed an existence of similar dispersion in the spin excitation spectrum [1, 2]. Therefore, the spin correlation is considered to closely connect with the superconductivity. On the other hand, an interaction of the phonon and the electron seems to be also important in the high-T_c superconductor because anomalous softening in the bond-stretching phonons were observed in the superconducting phase of both LSCO and YBCO systems. Thus, the origin of pairing force for the emergence of high-T_c superconductivity, namely spin fluctuations, phonon and others, is still discussed. However, since the high-T_c superconducting systems studied by neutron-scattering experiments are quite limited, other reference systems are highly required for the clarification of universal nature in spin excitations and phonons. Motivated by the above reason, we have started the study on $Bi_{2+x}Sr_{2-x}CuO_{6+\delta}$ (Bi2201) system.

The crystal growth of Bi2201 superconductor is known to be much difficult than that of LSCO and there is no report on the spin dynamic and phonon investigated by neutron-scattering measurement. We have, however, found adequate growth condition of sizable single crystal, and succeeded in observing inelastic magnetic signals in Bi2201 system for the first time.

Figure 1. shows the low-energy spin fluctuations below 11 meV in the x=0.2 sample (hole concentration is ~0.17). Interestingly, the magnetic signals were observed at (0.5±δ, 0.5)/(0.5, 0.5±δ) with δ~0.12 (r.l.u.) in the tetragonal notation, which is consistent with those reported for LSCO system with comparable carrier concentration [3]. This observation of incommensurate structure in the single-layer Bi2201 provides provides important opportunity to explore the generic feature of spin excitation spectra in high-T_c cuprates.

References

[1] J. M. Tranquada *et al.*: Nature **375** (2004) 531.
[2] S. M. Hayden *et al.*: Nature **375** (2004) 534.
[3] K. Yamada *et al.*: Phys. Rev. B **57** 1998) 6165.

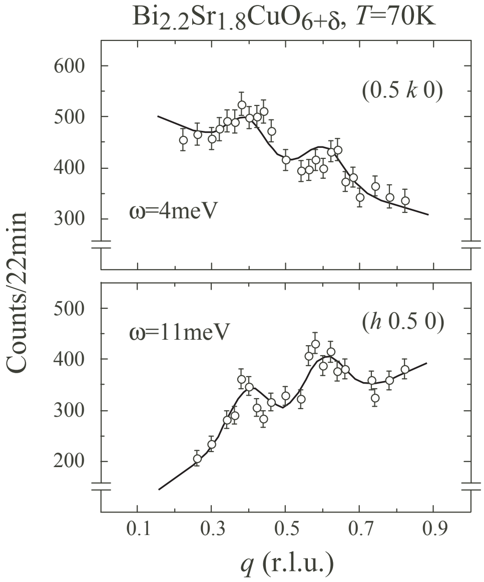

Fig. 1. Inelastic neutron scattering spectra of $Bi_{2.2}Sr_{1.8}CuO_{6+\delta}$ with constant energy of 4 meV and 11meV measured at 70K.

1-3-21

Dual structure in spin excitations of La2-xSrxCuO4 studied through impurity effect

M. Fujita[1], M. Enoki[2], S. Iikubo[3], and K. Yamada[3]
[1] *Institute for Materials Research, Tohoku University, Katahira, Sendai 980-8577, Japan*

Antiferromagnetism in the doped cuprate Mott-insulator has been extensively investigated due to its rich physics and close relation with the high transition temperature (high-Tc) supercoductivity. Recently, Vignolle and co-workers revealed the existence of two energy scales in the spin excitations of optimally doped $La_{1.64}Sr_{0.16}CuO_4$ exhibiting the sharp and broad intensity-maximum at 18meV and 45meV, respectively [5]. Furthermore, even in the optimally-doped region of Y-123 existence of high-energy dispersive magnon-like modes, which is not reproduced by the Fermi liquid theory was reported [6], while the low-energy spin dynamics including resonance feature is well explained by fermiological way. Such structure of spin excitation showing dual nature suggests the different origins for the hourglass-shape spectrum separated by energy. Indeed, phenomenological theory, which treats both itinerant fermions and local spins have well reproduced the overall spin susceptibility in Y-123 [7]. Therefore, two spin degrees of freedom of the itinerant spins and local spins would intrinsically exist in the high-Tc compounds. To make progress on above issue, we investigated the spin excitations in Fe-doped $La_{2-x}Sr_xCuO_4$ system, in which both spin and charge stripe order is significantly stabilized by Fe-doping.

In Fig. 1, the local spin susceptibility (χ'') is plotted for $La_{1.64}Sr_{0.16}Cu_{0.98}Fe_{0.01}O_4$. With decreasing the energy transfer (ω), χ'' below 6 meV decreases toward the minimum intensity at $\sim$2 meV and turn to increase, showing a gap-like structure. Compared to the Fe-free LSCO with the comparable hole concentration shown by dashed line, the low-energy component below 2 meV is strongly enhanced while the high energy component above 8 meV is suppressed. This result suggests that the spectral weight is shifted toward the low energy side by Fe-doping, and therefore, the low energy component is significantly affected by Fe-doping. To conclude the existence of dual nature of spin excitations, study of Fe-doping effects on the high-energy is required, and the neutron-scattering experiment is now under progress.

References

[1] B. Vignolle *et al.*: Nature Physics **3**, (2007)163.
[2] D. Reznik *et al.*: Phys. Rev. B **78** (2008)132503.
[3] Y. Bang: arXiv:cond-mat/0706.1387.
[4] M. Kofu *et al.*: Phys. Rev. Lett. **102** (2009)047001.

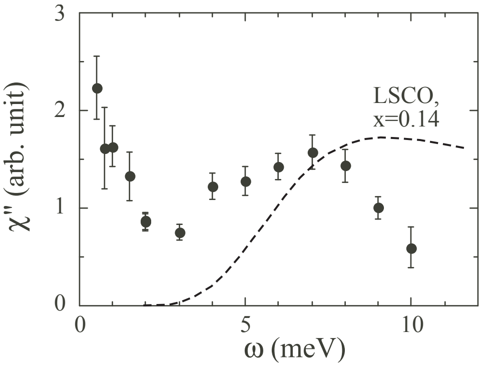

Fig. 1. Local spin susceptibility for $La_{1.94}Sr_{0.16}Cu_{0.98}Fe_{0.02}O_4$ measured at 14K. Dashed line represents the result for Fe-free LSCO with the comparable hole concentration.

1-3-22

Doping evolution of spin correlations in electron-doped Pr1-xLaCexCuO4

M. Fujita[1], J. Kaminaga[2], and K. Yamada[3]

[1] *Institute for Materials Research, Tohoku University, Katahira, Sendai 980-8577, Japan*
[2] *Department of Physics, Tohoku University, Aramaki, Sendai 980-8578, Japan*
[3] *World-Premier-International Research Center Initiative, Tohoku University, Katahira, Sendai 980-8577, Japan*

Antiferromagnetic (AF) spin fluctuations are widely believed to play a crucial role for the appearance of high temperature superconductivity in cuprates. Neutron scattering experiments have revealed the existence of low-energy spin fluctuations in the superconducting phase of electron-doped $Nd_{2-x}CexCuO_4$ and $Pr_{1-x}LaCexCuO_4$ [1]. On the other hand, an evidence for the transition or crossover of superconducting paring symmetry from being *d*-wave to *s*-wave in nature upon doping was reported for the electron-doped (*n*-type) cuprate [2, 3]. This suggests that in the *n*-type superconductors the *d*-wave superconductivity mediated by spin fluctuations can change to the conventional *s*-wave superconductivity mediated by lattice vibrations with increasing doping concentration. Since the observed spin correlation in the electron-doped cuprate is limited to the optimally-doped region, the doping evolution of spin correlation in the superconducting phase is necessary to determine whether the crossover of paring symmetry occurs or not. We, therefore, investigated the low-energy spin fluctuations in $Pr_{1-x}LaCe_xCuO_{4+\delta}$ over a wide concentration range of $0.07 \leq x \leq 0.18$, spanning from the antiferromagnetic phase to the heavily overdoped superconducting (SC) phase.

As seen in Fig. 1(a), the low energy excitations exhibit commensurate peaks centered at the (π, π) position, unlike to the incommensurate one in the hole-doped system. Figure 1(b) shows the imaginary part of the dynamic susceptibility, $\chi''(\omega)$, as a function of ω. In the SC phase with $x \geq 0.11$, the relaxation rate of the spin fluctuations corresponding to the peak-energy is linearly proportional to T_c. These results suggest that the commensurate spin correlations are closely related with the superconductivity in the *n*-type cuprates.

References

[1] K. Yamada *et al.*, Phys. Rev. Lett. **90** (2003)137004.
[2] J.A. Skinta *et al.*: Phys. Rev. Lett **88** (2002)207005.
[3] V.A. Khodel *et al.*: Phys. Rev. B **69** (2004)144501.

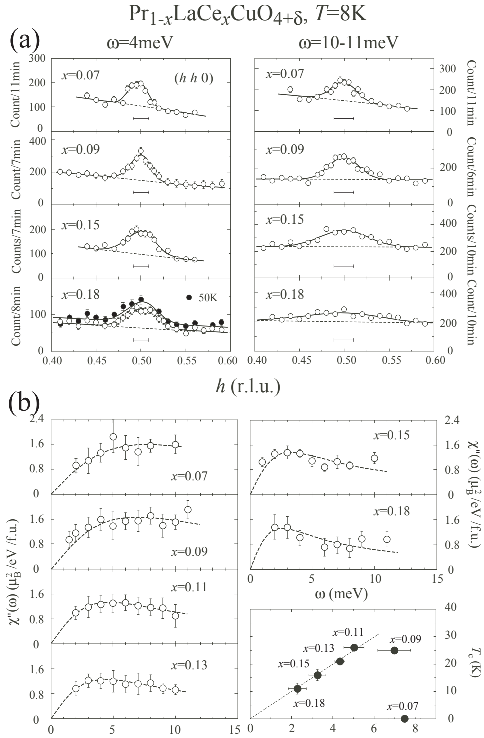

Fig. 1. (Upper panels) Constant-ω scans with $\omega = 4$ meV and 10-11 meV. (Lower panels) ω-dependence of the local spin susceptibility and T_c as a function of Γ.

1-3-23

Crystal structure of the calcium-ferrite type 1-D chain compounds CaCo2O4

Masaaki ISOBE (A), Yoshitaka MATSUSHITA (B)
(A) Superconducting Materials Center, National Institute for Materials Science; (B) Quantum Beam Center, National Institute for Materials Science

The CaFe2O4 (calcium ferrite)-type structure can be described using a general formula AB2O4 (A= alkali or alkali-earth ion; B= transition-metal ion), which crystallizes in an orthorhombic structure with lattice constants a˜9 A, b˜3 A, and c˜10 A (space group: Pnma), built of eight-fold-coordinated A atoms and distorted BO6 octahedra. The BO6 octahedra form an edge-sharing one-dimensional (1-D) double chain network along the b-axis, in which unique quantum behavior characteristic of low-dimensional system may occur due to strong correlation between electrons. Recently, we found a new member of the calcium-ferrite-type structure family, CaCo2O4 ± d, by utilizing high-pressure synthesis technique, and found that the compound can exhibit comparatively large thermoelectric power (>150 microV/K), even though it has finite density of states at Fermi level [1]. This large thermoelectric power may be attributed to residual spin entropy due to orbital degeneration, or distinctive dispersion of the Co t2g bands around Fermi level [2]. In this short paper, we report structural parameters precisely refined using Rietveld analysis with neutron diffraction data, and evaluate bond valences of the Co ions in order to find which crystallographic site, Co1 or Co2, is prior to another site for hole doping.

Polycrystalline sample of CaCo2O4 prepared from a solid-state reaction under 7.7 GPa and 1,600 ℃ was used for the neutron diffraction experiments. Diffraction data were collected using the HERMES diffractometer (IMR, Tohoku Univ.) at room temperature in a step size of 0.1 deg. over a 2theta range of 3-152.9 deg. using 150 3He counters set at 1 deg. intervals. Incident thermal neutron beams were monochromatized to a wavelength of 1.8204 A with the 331 reflection of a bent-crystalline Ge monochromator. Structural refinement was performed using the Rietveld analysis program RIETAN-2000 [3]. Initial structure models and parameters were constructed using the results of the X-ray Rietveld analysis in ref. 1.

Figure 1 shows a powder neutron diffraction pattern of CaCo2O4 for the Rietveld analysis. Some of small extra reflections were purposely excluded from the observed data to improve the reliability factors. The data elimination between 77.0 and 77.9 deg. is due to machine trouble of a 3He counter amplifier. The resultant reliability factors obtained from the refinement were Rwp=3.32%, Rp=2.55%, RI=1.66%, RF=0.94%, and S=1.2787. The obtained positional parameters and isotropic thermal displacement parameters are summarized as follows; x=0.7609(2), z=0.6630(2), B=0.46(3) A2 for Ca; x=0.4161(4), z=0.0975(3), B=0.16(4) A2 for Co1; x=0.4434(4), z=0.6102(3) for Co2; x=0.1974(1), z=0.1554(1), B=0.22(1) A2 for O1; x=0.6141(1), z=0.0225(1) for O2; x=0.5309(1), z=0.7886(1) for O3; x=0.4187(1), z=0.4279(1) for O4. The constraints are B(Co2)=B(Co1) and B(O4)=B(O3)=B(O2)=B(O1). All the y-values are fixed at 1/4, because all the sites are 4c sites of the space group Pnma. Lattice parameters refined were a=8.7911(1) A, b=2.90398(5) A, c=10.2767(1) A, and V=262.357(7) A3. Bondlengths were calculated using the structural parameters and resulted as follows; 1.903(4) A for Co1-O2; 1.921(2) A for Co1-O3 (× 2); 1.924(2) A for Co1-O2 (× 2); 2.013(4) A for Co1-O1; 1.886(3) A for Co2-O4; 1.931(2) A for Co2-O4 (× 2); 1.963(2) A for Co2-O1 (× 2); 1.988(4) A for Co2-O3. The bond valences were calculated from the Co-O distances.

The values are +3.1 for the Co1 sites and +3.0 for the Co2 sites. It suggests that holes should be doped into the Co1 site rather than the Co2 site at least in lightly doped phases, for example, obtained by Na substitution for the Ca site. The structural parameters refined in this work would be utilized for ab-initio band calculation to determine electronic structure of CaCo2O4 in near future.

References
[1] M. Shizuya, M. Isobe, E. Takayama-Muromachi, J. Solid State Chem. 180 (2007) 2550.
[2] M. Isobe, M. Arai, E. Takayama-Muromachi, J. Electronic Mater., in press.
[3] F. Izumi, T. Ikeda, Sci. Forum 321-324 (2000) 198.

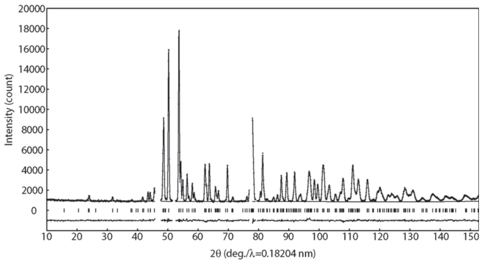

Fig. 1. Powder neutron diffraction pattern of CaCo2O4 for the Rietveld analysis.

1-3-23

1-3-24

Magnetic structure study of the multi-step metamagnet CeIr3Si2

Y. Muro(A), K. Motoya(A), K. Shigetoh(B), T. Takabatake(B)
(A)Department of Physics, Faculty of Science and Technology, Tokyo University of Science,(B)ADSM, Hiroshima University

CeIr3Si2 crystallizes in the orthorhombic ErRh3Si2-type structure (Imma, No. 74), which is a derivative of the hexagonal CeCo3B2-type. The lattice parameters are a=7.1765 A, b=9.7274 A and c=5.5971 A. The results of electrical resistivity, specific heat and magnetic susceptibility measurements reveal that CeIr3Si2 is a Kondo-lattice compound showing two successive magnetic transitions at T_N1=4.1 K and T_N2=3.3 K[1]. Below 3.3 K, the isothermal magnetization of polycrystalline sample displays mult-step metamagnetic transitions at 0.6 T, 0.9 T and 1.2 T. Recent study of a single-crystal CeIr3Si2 has revealed that the metamagnetic transitions at 0.6 T and 1.2 T occurs when the magnetic field applyed along the b-axis while that at 0.9 T occurs when the field applyed along c-axis[2]. We need to obtain the magnetic structures between each transition field in order to study the origin of multi-step metamagnetism of CeIr3Si2. Thus we have been carrying out the elastic neutron scattering of powder and single-crystal samples.

Below T_N2, we observed four magnetic Bragg peaks at Q=(0 4/3 +-2/3) and Q=(0 5/3 +-1/3). The observed magnetic reflections agree with those observed in the previous measurement using a powder sample. These non-integer Q's indicate that the lattice parameters of b- and c-axis below T_N2 becomes three time as large as those above T_N1. The temperature dependence of integrated intensity at Q=(0 4/3 -2/3) and Q=(0 5/3 -1/3) display a maximum at 2.7 K in spite of no further phase transition down to 0.5 K. At last year, we obtained that this peak behavior results from the long time relaxation of the magnetic structure below T_N2.

Figure 1 shows the time dependence of the intensity for Q=(0 4/3 2/3) at 1.5 K. We determined t=0 s when the temperature reached 1.5 K from 10 K. The intensity increases linearly with increasing time and seems to saturate at 12 hour. This behavior indicates that the transition at T_N2 is of first order and that the frustration exists in the magnetic interaction between Ce 4f moments.

[1]Y. Muro, Y. Ohno, T. Okada, K. Motoya, J. Magn. Magn. Mater. 310 (2006), p. 389.
[2]K. Shigetoh, A. Ishida, Y. Ayabe, T. Onimaru, K. Umeo, Y. Muro, K. Motoya, M. Sera, T. Takabatake, Phys. Rev. B 76 (2007), p. 184429.

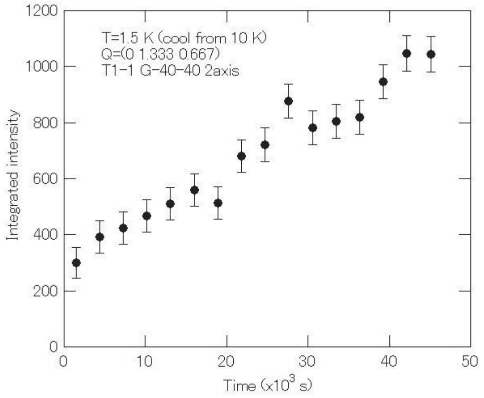

Fig. 1. Time dependence of the integrated intensity at (0 4/3 2/3) when the sample is cooled from 10 K to 1.5 K.

1-3-25

Magnetic structure of a pressure-induced magnetically ordered phase in YbAgGe with a quasi-kagome lattice

K. Umeo[1], H. Kubo[2], T. Onimaru[2], K. Katoh[3], T. Matsumura[2], N. Aso[4] and T. Takabatake[2]
[1] *Cryogenics and Instrumental Analysis Division, N-BARD, Hiroshima Univ.,*
1-3-1 Kagamiyama, Higashi-Hiroshima, 739-8526
[2] *Department of Quantum Matter, ADSM, Hiroshima Univ.,*
1-3-1 Kagamiyama, Higashi-Hiroshima, 739-8530
[3] *Department of Applied Physics, National Defense Acadeny, Yokosuka, 239-8686*
[4] *Institute for Solid State Physics, The University of Tokyo, 106-1 Shirakata, Tokai, 319-1106*

The heavy-fermion antiferromagnet YbAgGe with the ZrNiAl-type structure undergoes two magnetic transitions at T_{M1}=0.8 K with an incommensurate propagation vector $\vec{k}_1$=[0, 0, 0.324] and T_{M2}=0.65 K with $\vec{k}_2$=[1/3, 0, 1/3] .[1, 2] A tail in the specific-heat $C(T)$ extended above T_{M1} was attributed to effects of magnetic frustration inherent to the quasi-Kagome lattice of the Yb sublattice.[1] Recently, an anomalous phase diagram of YbAgGe under pressures has been constructed from the $C(T)$ and resistivity measurements.[3, 4] With applying pressure above 0.5 GPa, the resistivity anomalies at T_{M1} and T_{M2} merge into a sharp drop at T_M=0.85 K.[3] In the pressure range $0.5 < P < 1.5$ GPa, $T_M(P)$ remains constant, while above $P^* = 1.6$ GPa, $T_M(P)$ increases linearly. Concomitantly, the anomaly of $C(T)$ at T_M converts from a first-order type sharp peak to a second-order type jump of a conventional magnetic compound without geometrical frustration. The magnetic entropy at T_M rises for $P > P^*$, while the Kondo temperature does not change.[4] These findings suggest that the sudden rise of $T_M(P)$ for $P > P^*$ is a consequence of the release of the magnetic frustration.

In the present work, in order to determine magnetic structures at ambient pressure, we performed neutron diffraction experiments. Measurements were preformed on a sample prepared by the Bridgman method. The powdered sample was wrapped in an aluminum foil, and was loaded in an aluminum can under 10 atm pressure of purified helium gas. It was cooled down to 35 mK with a ^{3}He-^{4}He dilution refrigerator.

Fig. 1 shows the 2θ scans at T=80 mK $< T_{M2}$ (red) and 1.5 K $> T_{M1}$ (green). At T=80 mK, we found magnetic Bragg reflections which are indexed with $\vec{k}_2$, whereas we obseved no magnetic reflection with $\vec{k}_1$. Measurements at $T_{M2} < T < T_{M1}$ could not be performed, because of temperature instability due to troubles of the dilution refrigerator. We are now in progress to analyse the data to determine the magnetic structure below T_{M2} by using FullProf.[5]

References

[1] K. Umeo *et al.*: J. P. S. J., **73** (2004)537.
[2] B. Fåk *et al.*: Physica B **378-380** (2006)669.
[3] K. Umeo *et al.*: Physica B **359-361** (2005)130.
[4] H. Kubo *et al.*: J. P. S. J., **77** (2008)023704.
[5] J. Rodriguez-Carvajal *et al.*: Physica B **192** (1993) 55.

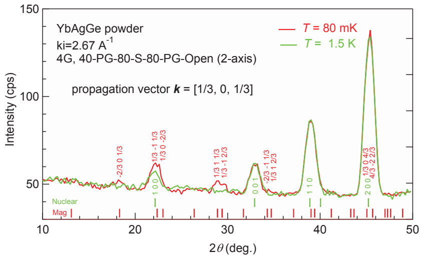

Fig. 1. 2θ scans at T=80 mK and 1.5 K indicated with the red and green curves, respectively. The red and green lines, respectively, are calculated angles of nuclear and magnetic reflections with $\vec{k}_2$=[1/3, 0, 1/3].

1-3-26

Competition between Hidden Order and Pressure-Induced Antiferromagnetism in URu_2Si_2

H. Amitsuka[A], Y. Ikeda[A], I. Kawasaki[A], S. Takayama[A], D. Nishikawa[A], and M. Yokoyama[B],

[A]*Graduate School of Science, Hokkaido University,* [B]*Faculty of Science, Ibaraki University*

Heavy fermion compound URu_2Si_2 shows an elusive phase transition at 17.5 K, whose order parameter and ordering vector have not been found yet. Kiss *et al*. proposed that the magnetic octupoles could be the 'hidden' order parameter on the basis of group theory and a crystal field model. They also predicted that the magnetic dipoles are coupled with the octupoles via quadrupoles, and thus can be induced by lowering the crystal symmetry on U-site from tetragonal to orthorhombic [1]. This lattice distortion can be generated by applying uniaxial stress (σ). In this project, we performed the elastic-neutron-scattering experiments of URu_2Si_2 under uniaxial stress to test this prediction by seaching for the induced dipole moments. Scattering planes (h0l) and (hhl)were chosen for the uniaxial stress $\sigma \parallel$ [100] and [110], respectively. Spectrometers GPTAS(4G) and PONTA(5G) in JAEA were used. The uniaxial pressure devise used were designed by Kawarazaki *et al* [2]. As a consequence, in the present setup with σ applied up to $\sim$2 kbar, the magnetic dipole moments were not detected, except the antiferromagnetic moments observed at $\sigma = 0$ (Fig. 1).

[1] A. Kiss *et al*, Phys. Rev. B 71 (2005) 054415.

[2] S. Kawarazaki *et al*, Jpn. J. Appl. Phys. 41 (2002) 6252.

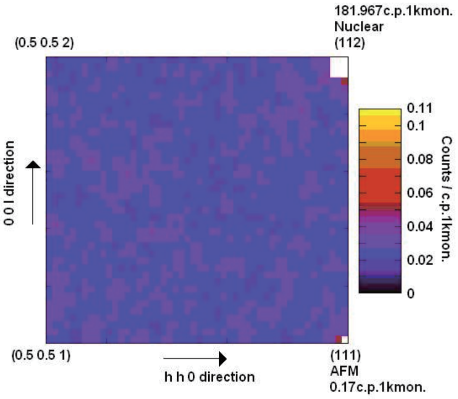

Fig. 1. Neutron scattering intensity observed by a mesh scan in the (*hhl*) scattering plane for uniaxial stress applied perpendicular to the plane.

1-3-27

Quasi-elastic neutron scattering measurements on the kagome lattice antiferromagnet $KFe_3(OH)_6(SO_4)_2$

K. Matan[1], T. J. Sato[1], D. Grohol[2], D. G. Nocera[2], and Y. S. Lee[2]
[1]*ISSP, U. of Tokyo and* [2]*MIT*

Physics of geometrically frustrated spin systems is unconventional due to the collective behavior of interacting electron spins that are influenced by the topology of the underlying lattice. One of the most frustrated lattices in 2 dimensions (2D) is a kagome lattice, which is formed by corner-sharing triangles. One ideal realization of this type of lattice is jarosite. This class of compounds is particular ideal for a study of magnetic properties of the kagome lattice because (1) it consists of single layers of undistorted kagome planes, (2) it can be synthesized with compositions that are stoichiometrically pure, and (3) large crystals can be mode for inelastic neutron scattering. Jarosite is composed of kagome planes formed by magnetic Fe^{3+} ions with spin 5/2. These magnetic ions, which are located inside tilted octahedral cages formed by six oxygen atoms, sit at each corner of the corner-sharing triangles that form the perfect kagome planes. The kagome planes are well separated by non-magnetic ions, making an interlayer coupling negligibly small. The system orders magnetically at T_N = 65 K due to Dzyaloshinskii-Moriya interactions and interlayer coupling. Our previous inelastic neutron scattering measurements show well-defined spin-wave excitations in the ordered state with the first observation of a lifted zero-energy mode [1]. Above T_N, we observe spin fluctuations with uniform spin chirality [2]. In this study, we utilized neutron scattering to investigate temperature dependence of correlation length of spin fluctuations above T_N. The measurements were performed on a single crystal sample at GPTAS (4G) with an incident energy of 14.7 meV and collimations 40-40-S-40-open in a 2-axis mode, where final energy is integrated according to quasi-elastic approximation. Pyrolytic graphite filters were placed in the incident beam to reduce higher-order contamination. The sample was cooled using a closed cycle 4He cryostat. The energy-integrated intensities of the quasi-elastic neutron scattering above T_N were measured at Q=(1,0,0). Figure 1(a) shows a typical Q-scan around (1,0,0) measured at 66 K, slightly above T_N. The intrinsic widths (correlations lengths) were extracted by fitting the data to Lorentzian convolved with the experimental resolution functions. Temperature dependence of correlation length is shown in Fig. 1(b), which shows the results from our measurements at HFIR, Oak Ridge National Laboratory. A solid line shows a fit to the Berezinskii-Kosterlitz-Thouless (BKT) theory for 2D XY model. In summary, our preliminary neutron scattering measurements show a signature of the BKT transition above T_N, consistent with the 2D XY universality class.

[1] K. Matan, D. Grohol, D. G. Nocera, T. Yildirim, A. B. Harris, S.-H. Lee, S. E. Nagler, and Y. S. Lee, Phys. Rev. Lett,. 96, 247201 (2006).

[2] D. Grohol, K. Matan, J.H. Cho, S.H. Lee, J.W. Lynn, D.G. Nocera, and Y.S. Lee, Nature Materials, 4: 323-328 (2005)

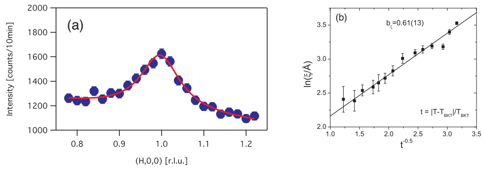

Fig. 1. (a) A representative scan of the quasi-elastic scattering around (1,0,0) at 66 K. A line shows a fit to a Lorentzian. (b) The log of correlation length is plotted as a function of a reduced temperature. A line shows a fit to the BKT theory.

1.　中性子散乱　4）非晶質･液体

1. Neutron Scattering　4）Amorphous・Liquid

This is a blank page.

1-4-1

Analogy on the Self-assembled Fractal-like Structure between the Niobate Nanosheet Colloidal Solution and Block Copolymer Lamellar Morphology

D. Yamaguchi, N. Miyamoto[1], S. Koizumi, T. Nakato[2], S. Akasaka[3], M. I. Kim[3],
H. Hasegawa[3] and T. Hashimoto

Advanced Science Research Center, Japan Atomic Energy Agency (JAEA), Tokai, Ibaraki 319-1195
[1]*Department of Life, Environment and Materials Science, Fukuoka Institute of Technology, 3-30-1 Wajiro-higashi Higashi-ku, Fukuoka 811-0295*
[2]*Division of Bio-Applications and Systems Engineering (BASE), Institute of Symbiotic Science and Technology, Tokyo University of Agriculture and Technology, 2-24-16 Naka-cho, Koganei-shi, Tokyo 184-8588*
[3]*Department of Polymer Chemistry, Graduate School of Engineering, Kyoto University, Katsura, Nishikyo-ku, Kyoto 615-8510*

Introduction

In the previous study, according to the concept of fractal we investigated the structure of an aqueous dispersion of niobate nanosheets by the scattering method within the wide length scales from Åto tens of μm and characterized a fractal-like structure having a specific mass-fractal dimension of $D_m = 2.9$ 1). We attributed this fractal-like structure to some concentration fluctuations of the nanosheets, giving rise to water-rich regions, which originate from undulation of stacks of the nanosheets.

In this study, we further investigate this specific fractal-like structure of $D_m = 2.9$ along the concept of the structural analogy between the aqueous dispersion of niobate nanosheets and lamellar microdomains consisting of block copolymers which are dispersed in the matrix of constituent homopolymer (what is called "dry brush" system 2)).

Experiment

The mixtures of block copolymer (BCP) and constituent homopolymer (HP) were prepared on three different compositions, that is, BCP/HP= 70/30, 50/50 and 20/80 (w/w), respectively. The scattering measurements were performed on the Bonse-Hart type double crystal ultra-small-angle neutron scattering diffractometer(PNO) and the focusing small-angle neutron scattering spectrometer (SANS-J-II) at the research reactor JRR-3. From the scattering profiles shown in Fig.1, we can discern that the different mass fractal dimensions were observed at the different blend composition and the specimen of 50/50 mixture shows a similar mass-fractal dimension of $D_m = 2.9$ to that of the niobate nanosheet specimen.

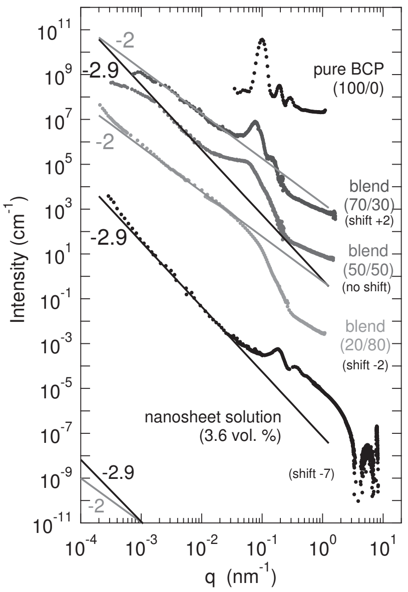

Figure 1: Power-law Behaviors of Niobate Nanosheet Solution and Block Copolymer Lamellar Morphology.

References

1) D. Yamaguchi, et al. :"Hierarchical Structure of Niobate nanosheets in Aqueous Solution", J. Appl. Cryst., 40, s101 (2007).

2) S. Koizumi, et al. :"Ordered Structure of Block Polymer/Homopolymer Mixtures, 4. Vesicle Formation and Macrophase Separation", Makromol. Chem. Macromol Symp., 62, 75 (1992).

原子炉：JRR-3　　装置：PNO(3G)　　分野：中性子散乱（液体・不規則物質）

1-4-2

Hydrophobic hydration and partial molar volume of alcohol aqueous solutions

K. Maruyama(1), M. Nakada(2) and M. Misawa(3)
(1)Fac. of science, Niigata University, (2) Graduate School of Sci. and Tec., Niigata Univ., (3) J-Parc center, KEK

In a previous paper [1], we reported that the characteristic behavior of the excess partial molar volume of 1-propanol-water mixture was interpreted satisfactorily in terms of the hydrophobic hydration of the fractal surface of alcohol clusters. This results were also confirmed on t-butyl alcohol-water mixtures. In this study we investigated two other alcohol, i.e. ethanol and 2-propanol, aqueous solutions. By analysing the dynamic structure factors with a relaxing cage model[2], the common behavior of these samples were revealed.

The quasielastic neutron scattering measurements on alcohol aqueous solutions were performed by using AGNES spectrometer and its standard accessery. The samples, their alcohol composition x, and messured temperature were ethanol x=0.0-0.25, 298, 320 and 343K; 2-propanol x=0.0-0.17, 298, 320, and 343K. The metyl groups of alcohols were deuterized in order to investigate the diffusive properties of water molecules. The sample cell was an aluminum double cylindrical cell with the sample thickness of 0.3 and 0.5mm. The accumurate time was 4 hours for each condition.

The dynamic structure factor S(Q,E) was obtained by a usual process with a program AGDAS. The statistical accuracy of S(Q,E) was good enough for the detailed analysis. The number fraction of hydrating water molecules α was derrived by using two states approximation and some dynamic properties, e.g. diffusion coefficient D and relaxation time τ, were also obtained with a relaxing cage model. Fiugure 1 shows the derrived D as a fuction of α. In this figure D has a good linear dependence on α, which means the α is a good parameter descriving the state of water molecules. Figure 1 also shows that D of all slcohol solutions have nearly the same depenednce on α, which means the dynamics of water in both bulk and hydrating states is independent on the species of alcohol.

References
[1] M. Misawa, Y. Inamura, D. Hosaka and O. Yamamuro, J. Chem. Phys., 125 (2006) 074502.
[2] A. Cunsolo, A. Orecchini, C. Petrillo, and F. Sacchetti, J. Chem. Phys. 124 (2006) 084503.

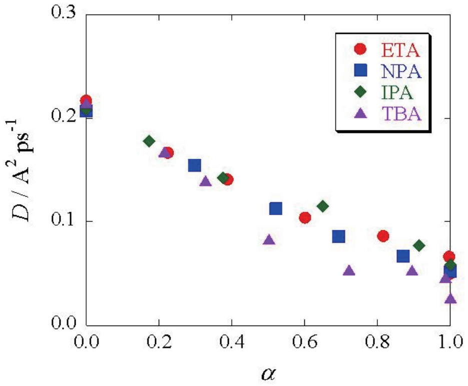

Fig. 1. Diffusion coeficient D of some alcohol aqueous solutions as a function of the number fraction of hysrating water molecules α.

1-4-3

Hydration structure around the nitrogen atom of the pyridine molecule

Yasuo Kameda, Asami Maki, Yuko Amo, Takeshi Usuki
Dept. Material & Biological Chemistry, Faculty of Science, Yamagata Univ.

The coordination property of the pyridinyl nitrogen atom plays an important role in the wide fields of chemical and biological sciences, however, the experimental determination of the hydration structure of the pyridine molecule has not been reported. In the present report, we describe results of neutron diffraction measurements on the aqueous 10 mol% pyridine solutions in which 14N/15 and H/D isotopic ratios were changed.

Neutron diffraction measurements were carried out at 298 K using the ISSP diffractometer, 4G (GPTAS) installed at the JRR-5M research reactor with an incident neutron wavelength of 1.093(3) A. Scattered neutrons were collected over the angular range of $3 < 2$ theta <118 deg. corresponding to $0.3 < Q < 9.8$ 1/A. Preset time was 180 s for each data point. After correction for the background, absorption and multiple scattering, the observed scattering intensities were converted to the absolute scattering cross section by the use of corrected scattering cross section from the vanadium rod.

The first-order difference function between [1] (14N-pyridine-D2O) and (15N-pyridine-D2O) was determined from the difference in the observed scattering cross sections between sample solutions with different 14N/15N compositions. The distribution function around the pyridinyl nitrogen atom was derived by the Fourier transform of the observed first-order difference function (Fig. 1a). In the present experimental condition, contributions from the N-O(water) and N-D(water) partial structure factors are dominant in the observed difference function. The calculated intramolecular contribution within the pyridine molecule was subtracted from the observed total difference function to obtain the intermolecular difference function. The intermolecular distribution function was evaluated by the Fourier transform of the intermolecular difference function (Fig. 1b).

The first peak observed in the intermolecular distribution function is assigned to the nearest neighbor N···D (water) interaction. The least squares fitting analysis of the observed intermolecular difference function revealed that, on the average, 2.4 water molecules are hydrogen-bonded in the N···D-O-D type. The nearest neighbor N···D distance is determined to be 1.93 A.

Reference
[1] J. E. Enderby, G. W. Neilson, “ Water, A Comprehensive Treatise ”, Plenum Press, New York (1979), Vol. 6, p. 1.

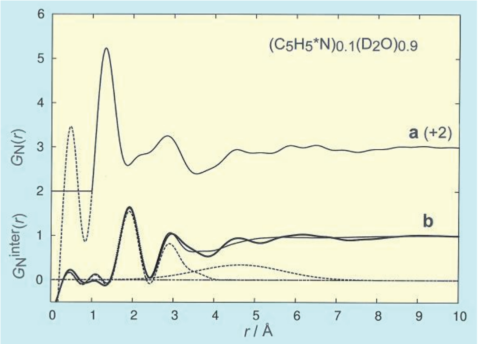

Fig. 1. Fig. 1 a) Total and b) intermolecular distribution functions around nitrogen atom of the pyridine molecule.

1-4-4

DMF-induced Phase Separation of HFIP-Water Mixtures

T. Takamuku, T. Shimomura, M. Tachikawa
Saga University

At an ambient condition, 1,1,1,3,3,3-hexafluoro-2-propanol (HFIP) is miscible with water at any ratio. However, the mixing state of HFIP-water solutions at a nano-scale is not homogeneous [1]. We have been found in the previous study that phase separation of HFIP-water solutions occurs by adding amide molecules, such as N-methylformamide (NMF) [2]. The amide-induced phase separation of HFIP-water mixtures occurs in a circular area of triangle phase diagram, and the area becomes wider with increasing hydrophobicity of amide in the sequence of N-methylpropionamide (NMP) > N-methylacetamide (NMA) > NMF. This may be due to the enhancement of nano-heterogeneity of HFIP-water solutions arising from solvation for hydrophobic parts of amide molecules by hydrophobic HFIP clusters formed in the solutions. In the present study, phase separation of HFIP-water solutions by addition of N,N-dimethylformamide (DMF) has been clarified by using small-angle neutron scattering (SANS) technique. A DMF molecule cannot form N-H···O-H hydrogen bond due to the methylation of both amino hydrogen atoms, although the carbonyl oxygen can form C=O···H-O hydrogen bond as well as the other amide molecules.

The phase diagram of amide-induced phase separation of HFIP-water solutions at 298 K indicated that the circular area of DMF-induced phase separation of HFIP-water solutions is wider than that of the NMA system, but slightly narrower than that of the NMP one. According to the phase diagram, SANS experiments using the SANS-U spectrometer have been made on DMF-HFIP-D2O ternary solutions at HFIP mole fraction of 0.14, which corresponds to the volume ratio of HFIP to water of 1:1, with varying DMF content. The Ornstein-Zernike correlation lengths Xi were estimated from SANS spectra for the ternary solutions. Figure 1 (a) and (b) show the Xi values for all the ternary solutions below and above the circular area of phase separation, respectively. As seen in Figure 1 (a), the Xi values for all the amide systems increase with increasing amide content, suggesting that the nano-heterogeneity of the solutions is enhanced when the amide content increases. The increase in the Xi with increasing amide content agrees with the fact that the amide-induced phase separation toward the lower critical line takes place at lower amide content in the sequence of NMP = DMF < NMA < NMF. On the other hand, Figure 1(b) reveals that the nano-heterogeneity of the solutions diminishes with lower amide content in the sequence of NMF < NMA = DMF < NMP. This is consistent with that one-phase solution is recovered above the upper critical line with lower amide content in the sequence. The present results suggest that the hydrophobicity of DMF is between those of NMA and NMP.

References

[1] K. Yoshida, T. Yamaguchi, T. Adachi, T. Otomo, D. Matsuo, T. Takamuku, and N. Nishi, J. Chem. Phys., 119, 6132-6142 (2003).
[2] T. Takamuku, H. Wada, and K. Fujii, Activity Reports on Neutron Scattering Research, #361, (2007).

Activity Report on Neutron Scattering Research: Experimental Reports **16** (2009)
Report Number: 706

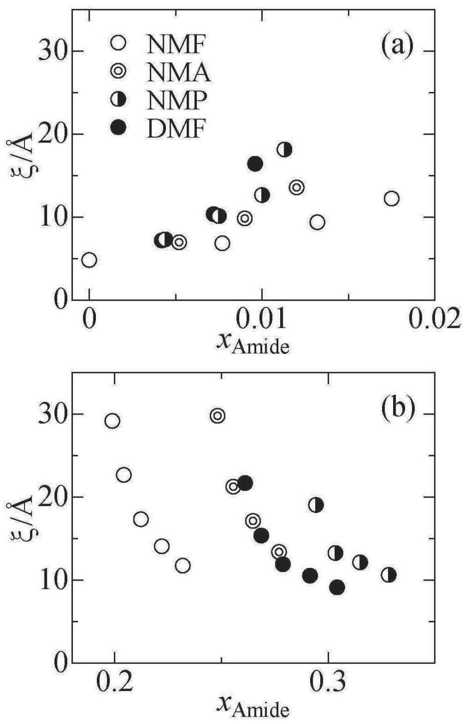

Fig. 1. Amide mole fraction dependence of Xi for amide-HFIP-D2O ternary solutions (a) below and (b) above two-phase area of phase diagram.

1-4-4

1-4-5

Alkyl-chain Dependence of Mixing State for Methanol Solutions of Imidazolium-based Ionic Liquids

T. Takamuku, T. Shimomura, K. Fujii
Saga University

Room temperature ionic liquids attract much attention in various chemical fields, such as organic synthesis, extraction, and electric device, because of their properties of novolatility, noflammability, and high electroconductivity. However, their high viscosity is a serious problem for application of ionic liquids in such fields. Thus, ionic liquids are often utilized by mixing them with cosolvent like water, methanol, and acetonitrile. The microscopic state for mixtures of ionic liquid and molecular liquid is essential to evolve the application of ionic liquids. In the present work, the mixing state of methanol solutions of imidazolium-based ionic liquid has been evaluated by using small-angel neutron scattering (SANS) technique.

1-alkyl-3-methylimidazolium bis(trifluoro methanesulfonyl) amides Cnmim+TFSA- with the different length of alkyl chain of n = 4, 6, 8, 10, and 12 were synthesized by a conventional method. Sample solutions were prepared by mixing Cnmim+TFSA- with deuterated methanol at various methanol mole fractions XCD3OD. SANS spectra for the sample solutions at 298 K were measured by using the SANS-U spectrometer with the camera lengths of 1 and 4 m.

Figure 1 shows the Ornstein-Zernike correlation lengths Xi for Cnmim+TFSA–CD3OD mixtures estimated from SANS spectra as a function of XCD3OD. The dependence of the length of alkyl chain is clearly observed in the figure. The Xi value for the methanol mixture of C4mim+TFSA- reaches a maximum at XCD3OD = 0.95 when the mole fraction increases from 0.8 to 1, suggesting that the mixing of the ionic liquid and methanol is the most inhomogeneous at XCD3OD = 0.95 among the mole fractions examined. However, those for the methanol mixtures of Cnmim+TFSA- with n = 6-12 indicate a maximum at the higher mole fraction of XCD3OD = 0.97. Furthermore, the maximum of Xi increases with increasing length of the alkyl group. The present results thus suggest that the longer the alkyl group of imidazolium, the more the heterogeneity of the mixtures is evolved. This is because the hydrophobic field is easily formed by the longer alkyl chain and methanol molecules aggregate by hydrogen bonds in the field.

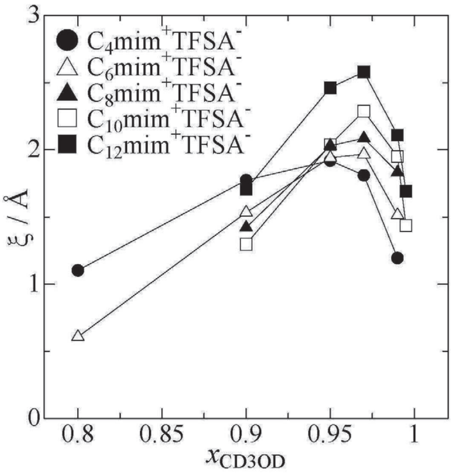

Fig. 1. Figure 1. Xi for Cnmim+TFSA–CD3OD mixtures as a function of methanol mole fraction.

1-4-6

Nano-scale aggregation structure formed in room temperature ionic liquid and its application to the new reaction field

K. Fujii (A), T. Shimomura (A), T. Takamuku (A), Y. Umebayashi (B), S. Ishiguro (B)
(A) Saga University, (B) Kyushu University

Small-angle neutron scattering (SANS) experiments were made on the 1-alkyl-3-methylimidazolium bis(trifluoromethanesulfonyl)amide, [C(n)H(2n+1)mim+][TFSA-] (n: alkyl-chain length of the imidazolium cation) ionic liquids containing a hydrophobic solute such as surfactant and alcohol, and we discussed the aggregation structure of hydrophobic solute in the ionic liquids. SANS measurements were carried out by using SANS-U spectrometer at 298 K and the scattering intensities for the samples were accumulated on the detector at the camera lengths of 1 and 4 m for 10 min and 1 h, respectively. In this work, the deuterated ionic liquids, [C(n)D(2n+1)mim+][TFSA-] where alkyl-chain H atoms is substituted by D atoms were synthesized and were used as the solvents on SANS measurements.

(1) Dodecyl-trimethylammonium bromide (DTAB) in [C(n)D(2n+1)mim+][TFSA-] with n =2 and 4.

SANS profile observed for DTAB/[C2D5mim+][TFSA-] solution did not show a significant peak to obtain a flat SANS pattern at all DTAB concentrations (C = 0 - 0.04 mol kg-1). The same was obtained for DTAB/[C4D9mim+][TFSA-] system. These results indicate that nano scale structure such as DTAB micelle is not formed in the ionic liquids. Here, it has revealed by our density measurement that the apparent molar volume estimated in DTAB/[C2D5mim+][TFSA-] system markedly increases with DTAB concentration up to ca. 0.01 mol kg-1 and is kept a constant at C > 0.01 mol kg-1. We concluded on the basis of SANS and molar volume studies that DTAB molecules are not form a nano scale micelle due to a specific interaction between DTAB and ionic liquid. It is need to elucidate the intermolecular interaction at micro scale level, and we are trying now large-angle X-ray scattering and MD simulation.

(2) Alcohols, C(n)D(2n+1)OH (n = 2, 4 and 6) in [C12H25mim+][TFSA-].

According to our previous SANS study, it is established that neat [C12mim+][TFSA-] shows an intense SANS peak at around Q = 0.2-0.3 A-1 and the peak is ascribed to the long-range TFSA-TFSA correlation in the ionic liquid. In this study, the peak position was unchanged with adding C2D5OH and C4D9OH, implying that liquid structure in neat [C12H25mim+][TFSA-] remains in both alcohol/IL binary systems and the solvation of alcohol molecule by IL is weak. On the other hand, in C6D13OH/[C12H25mim+][TFSA-] system, the peak position slightly shifts to a higher Q-range and the intensity decreases with C6D13OH, implying that liquid structure of neat [C12H25mim+][TFSA-] is destroyed due to hydrophobic interaction between alkyl groups of [C12H25mim+] cation and C6D13OH to give the shifted Q and the decrease in the SANS intensity.

References

[1] J. N. A. C. Lopes, A. A. H. Padua, J. Phys. Chem. B 110, 3330-3335 (2006)
[2] L. M. N. B. F. Santos, J. N. C. Lopes, J. A. P. Coutinho, J. M. S. S. Esperanca, L. R. Gomes, I. M. Marrucho, L. P. N. Rebelo, J. Am. Chem. Soc. 129, 284-285 (2007)

1-4-7

Temperature variation of the diffusional motion of water molecules in n-propyl alcohol aqueous solution

K. Maruyama(A), M. Nakada(B), T. Kikuchi(C), C. Matsumoto(A), and O. Yamamuro(C)
(A)Fac. Sci., Niigata Univ., (B) Grad. Sch., Niigata Univ., (C)ISSP-NSL Univ. Tokyo,

We carried out the quasielastic neutron scattering (QENS) measurements for n-propyl alcohol aqueous solutions, the composition of n-propyl alcohol xp = 0.0 to 0.167, by using High Resolution Clod Neutron Scattering Spectrometer AGNES. The temperature range was 268 to 298 K. We could obtain quasielastic spectra with good resolution. Hence the experimental data for samples are well distinguishable from the S(Q,E) of vanadium, which was used as the resolution function.

In order to get an information of diffusive dynamics of water molecules in n-propyl alcohol aqueous solutions, we analysed S(Q,E)'s with relaxing cage model (RCM)[1]. The fitting by RCM analysis to experimental data was good in whole E range. Then, we obtained diffusion coefficients D of water molecules in every measured solution. The D obtained from high-resolution mode measurement and RCM analysis at 298 K shows good agreement with the values in ref. 2. This agreement is quantitatively better than the values for standard mode measurement and RCM analysis which we had carried out in previous study.

Furthermore, since we were interested in temperature dependence of diffusive dynamics of water molecules in solutions, an Arrhenius plot of D of water molecules is shown in Fig. 1. As seen in Fig. 1, D for the solution of xp = 0.167 turns down around 298 K, which suggests that the diffusive dynamics of water molecules in the solution of xp = 0.167 seems to change at this condition, and is consistent with previous result, in which we found that at the condition of xp = 0.167 and at 298 K, the almost all water molecules hydrophobically hydrate to alcohol molecules or clusters. Thus we believe that this result relates to the behaviour of hydrophobic hydration in alcohol aqueous solution.

[1] M. Nakada, K. Maruyama, O. Yamamuro, and M. Misawa, J. Chem. Phys. 130 (2009) 074503.
[2] E. Hawlicka, and L. A. Woolf, J. Phys. Chem. 96 (1992) 1554.

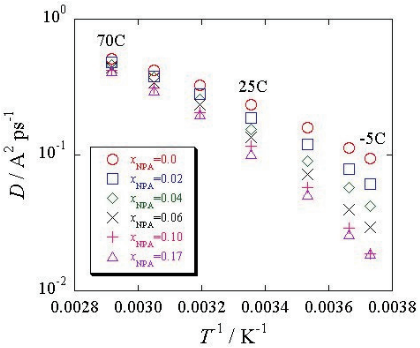

Fig. 1. The Arrhenius plot of diffusion coefficients of water molecules in the n-propyl alcohol aqueous solutions.

1-4-8

Study on micro-solvent extraction mechanism using ionic liquid-water mixed solvents by SANS

K. Fujii, S. Homi, T. Takamuku and M. Tabata
Saga Univevrsity

Aqueous mixed solvents of ionic liquids (ILs) were measured by small-angle neutron scattering (SANS) to elucidate the liquid structure on nanometer scale. The aqueous IL samples examined were prepared by weighting imidazolium based ionic liquid [Cnmim+X-, X = Cl, Br, CF3SO3, bis(trifluoromethansulfonyl)amide (TFSA)] with the alkyl-chain length n = 4, 8 and 12. SANS measurements were carried out by using SANS-U spectrometer at 298 K and the scattering intensities for the samples were accumulated on the detector at the camera lengths of 1 and 4 m for 10 min and 1 h, respectively. Typical results are given below.

With regard to 1-butyl-3-methylimidazolium (C4mim+) ionic liquid system (IL concentration, m = 0 - 1 mol kg-1), aqueous mixed solvents of C4mim+Cl- and C4mim+Br- show no scattering above the background over the whole Q range examined (0.01 < Q/A-1 < 0.35). On the other hand, that of C4mim+CF3SO3- shows a weak SANS profile based on a general Ornstein-Zernike function. This implies that a hydrophobic IL anion such as CF3SO3- is not easily solvated with water relative to Cl- and Br- anions, and then the CF3SO3- aggregates with hydrophobic C4mim+ cation to form IL cluster.

With aqueous C8mim+Br- system, No significant SANS profile is observed for the concentration m = 0.09 mol kg-1, which is shown in Figure 1. The SANS intensity increases with increasing IL concentration up to 1 mol kg-1. Note that those for m = 0.46 and 0.97 mol kg-1 fall on the straight line with a I(Q) = Qˆ-4 relationship on a range of Q = 0.15 - 0.25 A-1, suggesting that the ionic liquids aggregate with each other to form the charged micelle in the solutions. By assuming a spherical charged micelle, we analyzed the obtained data by using core-shell spherical model (form factor) with a Hyter-Penforld structure factor for charged macroions. As seen in Figure 1, the observed I(Q) is good agreement with the theoretical one (solid line), as the result, the core radius and shell thickness in the IL micelle were estimated to be 14.8 and 3.3 A, respectively, for m = 0.97 mol kg-1 and the same values were obtained for m = 0.46 mol kg-1.

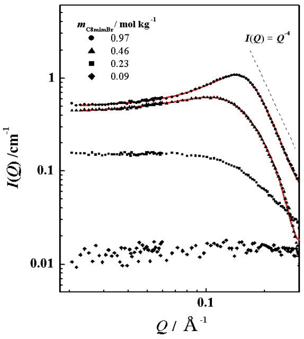

Fig. 1. SANS profiles observed for aqueous C8mimBr system. The solid lines correspond to the model fit results.

1-4-9

Structural investigation on super crtical CO_2 and co-solvent system

Masaaki Sugiyama, Takashi Sato, Keiji Ito, Kazuhiro Mori and Toshiaru Fukunaga
Research Reactor Institute, Kyoto University

Supercritical carbon dioxide (sc-CO_2) is widely recognized as an environmentally accepted solvent for reaction chemistry. Unfortunately, this green solvent has lesser solubility than the other major organic solvents. To overcome this point, small amount of the second chemical, entrainer (co-solvent), is added to enhance the solubility. Therefore, it is very important to understand this entrainer effect from the both of fundamental and application chemistry.

The solvent property of sc-CO_2 is deeply related with its structure of density fluctuation in nano-scale. It means that the clarification of the nanostructure is very important to understand the solvent property of sc-CO_2 and that with co-solvent. Small-angle neutron scattering (SANS) is one of the most suitable technique to clarify the nanostructure. Because neutron has very high trasmission for many substances comaped with X-ray: artificial sapphire with the thickness of 10 mm can be used for the window of a pressure cell. In this study, we observe the SANS of sc-CO_2 with protonaed ethanol and deuterated-ethanol, and pure sc-CO_2 as a reference.

SANS experiments were performed with SANS-U spectrometer. Samples were sc-CO_2, sc-CO_2 with 1 mol% protonated ethanol, sc-CO_2 with 1 mol% deuterated ethanol. Along the isothermal line at 39˚C, we observed the nanostructure at 10 different density points from 0.275 g/cm^3 to 0.609 g/cm^3 (presuure: 7.89 MPa to 10.00 MPa, critical point of pur CO_2: 31.1˚C, 0.468 g/cm^3, 7.38 MPa).

The observed SANS data were analyzed with Ornstein-Zernike formula. The results were shown in Fig. 1. As you can see, the peak positions of correlation length and density fluctuation are shifted to lower density. In the peak position, several characteristic values, for example dissolving power, show drastical change: in the higher density, the dissolving power becomes enhanced. Therefore, from the view point of nanostructure, the entrainer effect has been confirmed in this study.

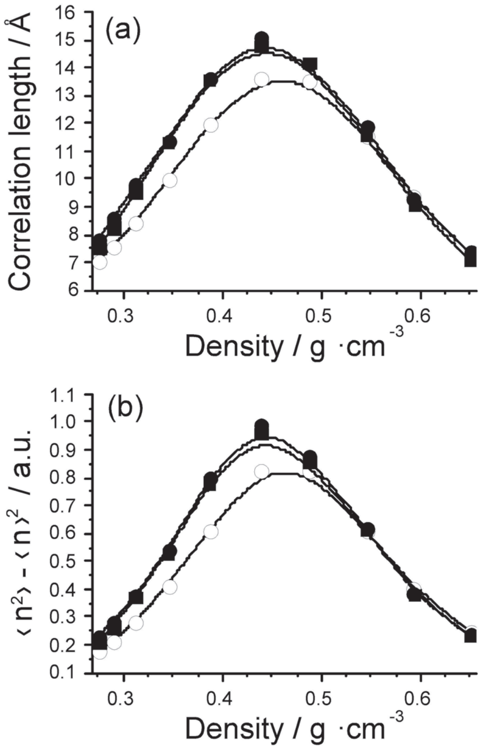

Fig. 1. Density dependece of observed correlation-length (a) and density fluctuation (b). Open circles, closed squares and closed circle shows those of sc-CO_2 and sc-CO_2 with 1 mol% protonated ethanol, respectively,

Activity Report on Neutron Scattering Research: Experimental Reports **16** (2009)
Report Number: 875

1-4-10

QENS Studies of Fast Molecular Reorientation in Isotropic, Glass, Smectic, and Crystalline Phases of 6O2OCB

H. Suzuki(A), A. Inaba(A), J. Krawczyk(B), M. Massalska-Arodz(B), T. Kikuchi(C), O. Yamamuro(C)

(A)Osaka Univ., (B)Inst. Nuclear Physics, Krakow, Poland, (C)ISSP-NSL, Univ. Tokyo

Some of cyanobiphenyl compounds are well known as liquid crystalline materials. These molecules are rod-shaped consisting of two parts (rigid cyanobiphenyl part and flexible alkyl-chain part), which is one of the keys of forming a liquid crystalline phase. The phase behavior of liquid crystalline material is quite sensitive to a small change in molecular shape. Branching modification of the alkyl-chain for cyanobiphenyl compounds is one of such changes, which varies not only the behavior of liquid crystalline phases but also the crystalline polymorphisms. We have been interested in the relation between the phase behavior and alkyl-chain motion of such compounds. In the past two years, we reported the results of the quasi-elastic neutron scattering (QENS) measurement of (S)-4-(2-methylbutyl)-4-cyanobiphenyl (5*CB) and (S)-4-(1-methylheptyloxy)-4-cyanobiphenyl (8*OCB) both of which are the structural isomer of famous liquid crystalline materials 5CB and 8OCB having branching structure in their alkyl-chains. From those investigations, it has been revealed that the chain branching significantly slows down the motion of alkyl-chain as well as the rotational motion of whole molecule around its long axis. This year, we report the results of QENS measurement for another cyanobiphenyl compound 4-(2-hexyloxy-ethoxy)-4′-cyanobiphenyl (6O2OCB) which is analogous to 8OCB having ?OCCO? structure in its alkyl-chain.

Various kinds of measurements have already been made for 6O2OCB. From the calorimetric measurements, the phase behavior of 6O2OCB has been established [1]. The isotropic liquid is easily undercooled and forms glassy state on further cooling below 218 K. There exist two liquid crystalline phases (both of which are metastable smectic) and two crystalline phases (metastable and stable). The phase behavior of 6O2OCB is significantly different from that of 8OCB which has two liquid crystalline phases (nematic and smectic). The dielectric relaxation measurements have also been made, and they showed that the molecular reorientation around its short axis becomes quite slow near the glass transition temperature at 218 K [1]. The purpose of this experiment was to investigate the molecular reorientation around its long axis and the internal molecular motions.

We performed QENS experiments on 6O2OCB using AGNES spectrometer at JRR-3M. The measurements were made at 370 K, 350 K, 330 K, 310K, 290 K for isotropic liquid phase with a low-resolution mode (delta E = 120?micro-eV). As a spectrum of rotational motion is approximately described by sum of a delta function (an elastic component) and a Lorentz function (a quasielastic component), we first fitted the spectra with these two functions. However, the result was not quite. We next tried to fit the data with two Lorentz functions, which was actually better. The HWHM of the Lorentz function for narrow component increases with increasing momentum transfer (Q), indicating the narrow component as a diffusive motion. The diffusion constants were obtained by using the continuous diffusion model. An Arrhenius plot for the diffusion constant gives the activation energy 22.1 kJ /mol (Fig. 1). This motion may be the mixture of the alkyl-chain tumbling motion and the rotation of whole molecule around its long axis.

One of the interesting points is that the diffusion constant of 6O2OCB is smaller than that of 8OCB while it is larger than that of 8*OCB, which indicates that the ?OCCO? structure in its alkyl-chain slows down the chain motion less significantly than the chain-branching effect. Since 6O2OCB shows two liquid crystalline phases while no liquid crystalline phase is found for 8*OCB, there seems some correlation between the speed of alkyl-chain motion and the formation of liquid crystalline phase.

[1] Massalska-Arodz M., Sciesinska E., Sciesinski J., Krawczyk J., Inaba A., Zielinski P.M., Dielectric Properties of Liquid Crystals, eds Z. Galewski, L. Sobczyk (Research Signpost Publ.); ISBN: 978-81-7895-288-8 (2007) 160.

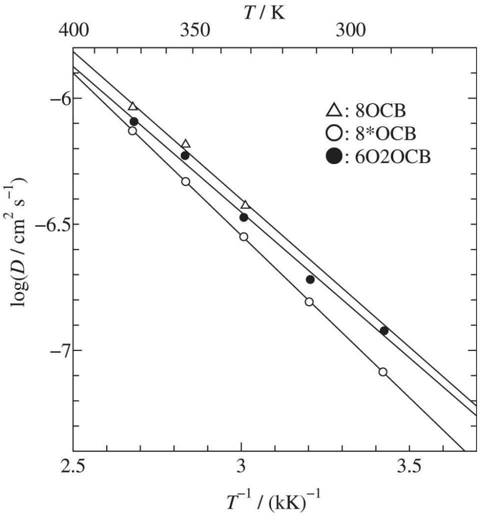

Fig. 1. Fig. 1 An Arrhenius plot of the diffusion constant for 6O2OCB, 8OCB and 8*OCB.

1-4-10

1.　中性子散乱　5）高分子

1. Neutron Scattering　5）Polymer

1-5-1

SANS Study of PEEK-Based Polymer Electrolyte Membrane Prepered by Radiation-Induced Graft Polymerization

S. Hasegawa, S. Takahashi, H. Iwase[1], S. Koizumi[1] and Y. Maekawa

Quantum Beam Science Directorate, JAEA, Takasaki, Gunma, 370-1292
[1] *The Advanced Science Research Center, JAEA, Tokai, Ibaraki 319-1195*

Development of alternative polymer electrolyte membrane (PEM) well working under low humidity condition has been needed to realize practical application of polymer electrolyte fuel cells (PEFCs). Recently, by using radiation-induced graft polymerization technique, poly(ether ether ketone) (PEEK)-based PEMs were sucessfully prepered and showed high ion-conductivity under low humidity conditions in comparison with that for Nafion. Small-angle angle neutron scattering (SANS) measurements also have been performed in order to reveal higher-order structure and morphology of these PEEK-based PEMs, because ion-conductivity closely is related to the higher-order structure. In this study, we observed morphological change of the PEEK-based PEM during the preparation by SANS.

SANS measurements were performed on Focusing and polarized neutron small-angle scattering spectrometer (SANS-J-II) at the research reactor (JRR-3) in Japan Atomic Energy Agency (JAEA), Tokai, Japan. The SANS profiles were obtained with a sample-to-detector distances of 10 and 2.5 m, covering from $Q = 0.04$ to $1\ nm^{-1}$, where $Q = (4\pi/\lambda)\sin(\theta/2)$ (θ and λ are the scattering angle and the wavelength, respectively). All SANS measurements were performed at room temperature.

Figure 1 shows SANS results of original PEEK substrate, grafted PEEK with a grafting degree (GD) of 46%, and PEEK-PEM with a sulfonation degree (SD) of 90%, respectively. The SANS profiles of the grafted PEEK was much larger scattering in the whole Q-range and showed new shoulder-like peak at around $Q = 0.35\ nm^{-1}$ ($d = 2\pi/Q = 13.7\ nm$). The d-spacing of 13.7 nm corresponds to the size of ethyl 4-styrenesulfonate (E4S) grafts phase. The Q^{-2} behavior in the Q-range of $Q > 0.35\ nm^{-1}$ indicated the no sharp interface between the grafts and PEEK substrate; namely, the E4S grafts are miscible to the substrate PEEK chains owing to a similar hydrocarbon structures. The SANS profile of the PEEK-PEM shows a similar one with a shoulder-like peak profile, appeared at $Q = 0.38\ nm^{-1}$, which is slightly higher than that of the grafted PEEK, i.e., smaller $d = 13.2\ nm$. It is surprising to observe Q^{-2} behavior in the Q-range of $Q > 0.38\ nm^{-1}$, which also showed the no sharp interface between the grafts and PEEK substrate, even though the hydrolyzed PSSA grafts must be hydrophilic compared with the E4S grafts and substrate PEEK chains. The SANS results also showed the 2.5 times larger size (13 nm) of ion channels consisting of poly(styrenesulfnoic acid) (PSSA) grafts than that in Nafion.

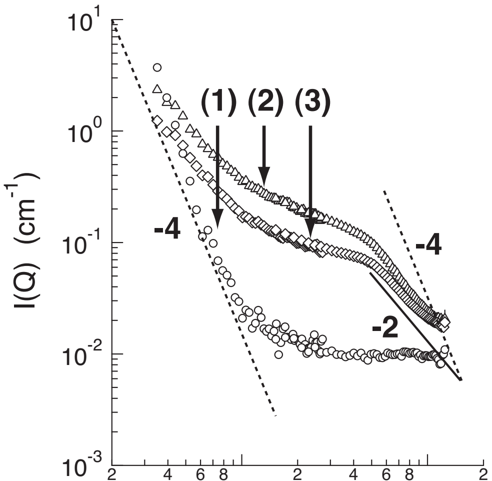

Figure 1: The SANS profiles of (1) original PEEK substrate, (2) E4S-grafted PEEK with 46% GD, and (3) PEEK-PEM with 90% SD.

原子炉：JRR-3　　装置：SANS-J(C3-2)　　分野：中性子散乱（高分子）

1-5-2

Combined SANS, WANS, and Weighing Studies of Microbial Cellulose: Elucidation of Hierarchical Structures in Drying Process

Y. Zhao, S. Koizumi and T. Hashimoto
Advanced Science Research Center, JAEA, Tokai, Ibaraki 319-1195

We studied the structural change of the microbial cellulose in the drying process by means of combined time-resolved measurements of small-angle neutron scattering (SANS), wide-angle neutron scattering (WANS), and weighing, as schematically illustrated in Fig.1. Combining the three Tr-techniques, we are able to observe the structural change of the cellulose network in two different length scales on a rigorously common time scale, e.g., the changes in microscopic structure (the concentration fluctuations of cellulose fibrils and the air voids generated upon drying), the geometry and structure change in mesoscopic scale (the size and total weight of the specimen, the water concentration or hydrogen density in the scattering volume), and interrelationships between the structural changes. We found the drying process is divided into three time regions, defined by Region I, II and III. In Region I, 3-dimensional shrinkage occurs and the weight loss is fast. While in Region II, only 1-demensional shrinkage is observed, hence the weight loss slows down. In Region III, all changes stop, indicating the drying process is over, however, still partial of water remains, which is believed to be bound water. Time evolution of SANS profiles at representative time during the drying process for two sample specimens in either water or heavy water is shown in Fig.2. We observe that the microscopic structure of cellulose fibrils itself, at q-range (q denotes magnitude of scattering vector) covered in this study, does not change upon drying, but the amount of air voids does. In addition, the drying ways are found to influence the size of the air voids dramaticly. The faster the drying process is, the larger the air voids are.

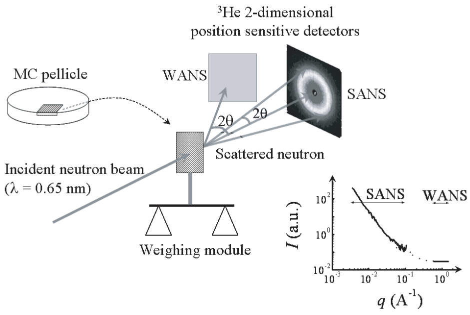

Figure 1: Schematic illustration of experimental setup of time-resolved SANS, WANS and weighing measurements for the same cellulose specimen in a single batch.

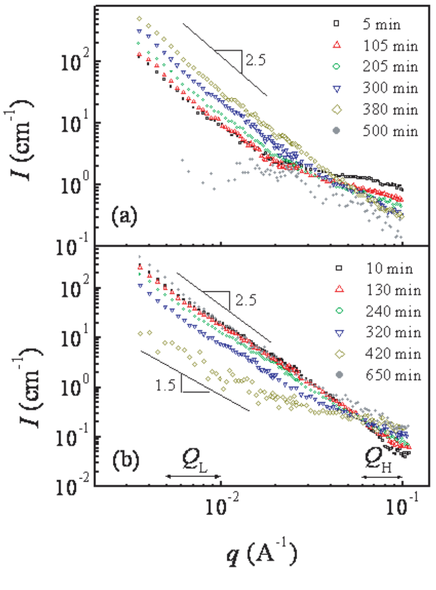

Figure 2: Time evolution of SANS profiles at representative times for (a) specimen 1 in water; (b) specimen 2 in heavy water during the drying process.

原子炉：JRR-3　　装置：SANS-J(C3-2)　　分野：中性子散乱（高分子）

1-5-3

Effect of Dynamic Nuclear Polarization on Small Angle Neutron Scatterings of Diblock Copolymer with a Lamellar Structure

Y. Noda, T. Kumada, T. Hashimoto and S. Koizumi

Advanced Science Research Center, JAEA, Tokai, Ibaraki 319-1195

We have carried out small angle neutron scattering (SANS) measurements for 2,2,6,6-tetramethylpiperidine 1-oxyl (TEMPO) doped polymers with its proton spins polarized by a dynamic nuclear polarization (DNP) technique, in which the sample was irradiated by a microwave with frequency of 94 GHz, at 3.3 T and 1.1 K 1). Recently, we applied this method to polystyrene (PS) polyisoprene (PI) diblock copolymer, in which TEMPO molecules selectively doped into the PI phase by a vapor permeation process, since the PS phase is glassy and the PI phase is fluid at the temperature of the doping process (40 °C). And the sample with a lamellar morphology was obtained by getting the molecular weight of the two blocks to be close to each other. So far, there have been no SANS study for a dynamically polarized sample having a lamellar structure, although a lamellar structure can be treated as a one-dimensional system, which allows us a simple analysis.

As shown in Figure 1, the sample showed a 1st, 2nd, and 3rd peaks due to the lamellar structure. And the q value of the 1st peak (0.1 nm^{-1}) gave the thickness of a lamellar period to be 63 nm. The positive polarization of $P = +37$ % decreased the scattering intensity by a factor of 0.04, and the negative polarization of $P = -37$ % increased the scattering intensity by a factor of 3.4. The P dependence of the scattering intensity agreed well with that of the contrast factor calculated with assuming P to be homogeneous through the sample. In the calculation, we used the two phases' mass density, atomic composition, and polarization determined by ^{1}H-NMR measurements. From this result, it was shown that the sample was polarized almost homogeneously.

On the other hand, at $P = -37$ %, the relative peak height of 2nd/1st increased to twice as that at $P = 0$ %. This result can be explained by the small deviation from the homogeneous P distribution; at the PI phase $|P|$ is homogeneous (38 %), and at the PS phase $|P|$ decreases down to 36 % as being far from the interface with neighboring PS phases 2). The successful observation of the quite small P inhomogeneity through SANS profile was owing to the sharp peaks from the lamellar structure with a high periodicity and thickness uniformity.

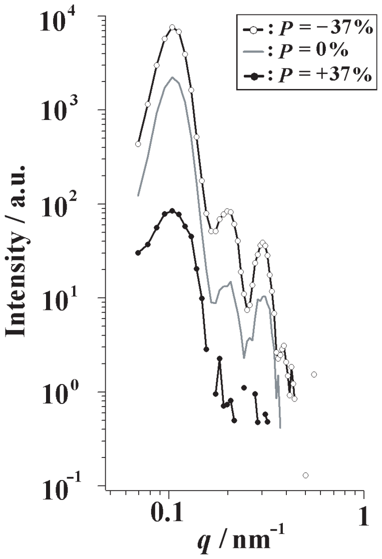

Figure 1: SANS profile of the PSPI block copolymer at the unpolarized and dynamically polarized states.

References

1) Y. Noda, T. Kumada, T. Hashimoto and S. Koizumi :"Physica B", in press.
2) Y. Noda, T. Kumada, T. Hashimoto and S. Koizumi :"J. Appl. Crystallogr.", in preparation.

原子炉：JRR-3　装置：SANS-J(C3-2)　分野：中性子散乱（高分子）

1-5-4

Gel structure with excess water in a surfactant solution

Youhei Kawabata,Akimi Matsuno,Tomoaki Shinoda,Tadashi Kato
Tokyo Metropolitan University

In a binary system consisting of surfactant and water, a hydrated solid phase is formed below the Kraft temperature, where the hydrophobic tails extend to the length with all trans. Figure 1 shows the T-ϕ phase diagram of a non-ionic surfactant $C_{16}E_7$ ($C_{16}H_{33}$ $(OC_2H_4)_7OH$) and water system. As shown in Fig. 1, the hydrated solid phase is a two-phase coexistence of excess water and lamellar structure L_β of bilayers whose hydrophilic tails are " solid-like " gel and interdigitated. The hydrated solid phase is strongly turbid and has a viscoelastic property, which is applied in cosmetic industry and so on. So far, we have investigated the structural formation of the hydrated solid phase in the $C_{16}E_6$/water and $C_{16}E_7$/water system by means of small angle X-ray scattering (SAXS) and optical microscope. Even though those surfactants are slightly different from each other in the head length, we found clearly different structures in nm $\sim$ μm scale. In μm scale observation using optical microscope, vesicle structures and worm-like lamellar domains are observed in the $C_{16}E_7$ system and $C_{16}E_6$ system, respectively. The SAXS experiments showed that the formation processes of membranes are different between the both system. The hydrophobic parts of surfactants hinder extends of the hydrophilic tails of the $C_{16}E_7$ system, while those of the the $C_{16}E_6$ system tend to extend to the full length. In this report, we compare the dynamic and static structures of the $C_{16}E_7$ system with those of the $C_{16}E_6$ system by using the results obtained from the SANS and NSE experiments.

The SANS experiments were carried out using the SANS-U spectrometer. The momentum transfer q ranged over $0.003 \leq q \leq 0.2$ Å^{-1}. The NSE experiments were performed using the iNSE spectrometer. The observed range of momentum transfer q and Fourier time t, were $0.09 \leq q \leq 0.15$ Å^{-1} and $0.15 \leq t \leq 15$ ns, respectively. Temperature was set to 8 °C for the $C_{16}E_7$ system, and to 20 °C for the $C_{16}E_6$ system. The concentration of $C_{16}E_7$ and $C_{16}E_6$ is 10 wt.%, respectively. For the NSE experiments, we started the experiments after waiting 1 hour from setting each sample to the sample cell holder because the sample structures should be stable.

In order to investigate the head and tail length of surfactants, we analyzed those profiles using the form factor of bilayers taking the hydration of hydrophilic parts into account. Figure 2 indicates the time evolutions of the length of hydrophilic tails in each system after the temperature jump, which are obtained from the SAXS experiments. The results obtained from SANS experiments are consistent with those obtained from SAXS experiments. We confirmed that the hydrophilic tails of the $C_{16}E_7$ system are hindered from extending to the full length around $\sim 2000 sec$. Figure 3 shows the universal plot of the intermediate correlation functions obtained from the NSE experiments. If the NSE results obey the theory proposed by Zilman and Granek [1], these plots should be straight lines. The solid lines in Fig. 3 are the fitting results by using Zilman and Granek model. From this analysis, we found that the bending modulus κ of bilayers in the $C_{16}E_7$ system is $\sim k_BT$, while that in the $C_{16}E_6$ system is $\sim 10k_BT$. This indicates that the bilayers of the $C_{16}E_7$ system are flexible because the tail length becomes short, while those of the $C_{16}E_6$ system are rigid because the tails tend to extend to the full length.

References

[1] A. G. Zilman and R. Granek, Phys. Rev. Lett., **77**, 4788 (1996).

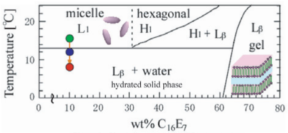

Figure 1 : Phase diagram of C16E7-water system.

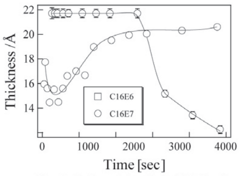

Figure 2 : The time evolution of hydrophilic tail length.

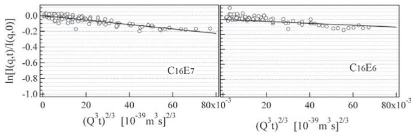

Figure 3 : Universal plot of the intermediate correlation function.

Fig. 1. Figure 1 : Phase diagram of C16E7-water system. Figure 2 : The time evolution of hydrophilic tail length. Figure 3 : Universal plot of the intermediate correlation function.

1-5-4

1-5-5

Structure characterization of Tetra-PEG gel having homogeneous network structure

Takamasa Sakai(A), Takuro Matsunaga(B), Mitsuhiro Shibayama(B), Ung-il Chung(A)
(A)Dep. of Bioeng, Univ. of Tokyo, (B)ISSP, Univ. of Tokyo

The structure of Tetra-PEG gel, a new class of biocompatible, easy-made, and high-strength hydrogels consisting of a four-arm polyethylene glycol (PEG) network, has been investigated by means of small-angle neutron scattering (SANS). Since the Tetra-PEG gel is prepared by cross-end-coupling two kinds of four-arm PEG macromers having different functional groups at the ends, i.e., amine group and succinimidyl ester group respectively, coupling reaction occurs exclusively between PEG chains carrying different functional groups. Structure analyses of Tetra-PEG gels were carried out by means of swelling experiments and SANS, and the results were discussed by taking into account the mechanical properties of the same systems. The following facts were disclosed.
(1) Tetra-PEG gels are stoichiometrically prepared irrespective of the initial polymer concentration, and their swelling behaviors are well predicted by the Flory-Rehner theory. (2) The mechanical moduli of Tetra-PEG gels, E and G, are proportional to the initial polymer concentration and is one order of magnitude larger than the corresponding gels made with similar tetra-arm PEG gels prepared with a low-molecular-weight coupling reagent. This indicates that cross-end-coupling of A- and B-type tetra-PEG is essential for gel preparation with extremely low defects. (3) The scattering functions of the macromers can be well reproduced by the scattering function for star polymers. (4) SANS functions of Tetra-PEG gels can be described by simple Ornstein-Zernike function without excess scattering component originating from cross-linking inhomogeneities. This means that Tetra-PEG gels are extremely homogeneous, and an “ ideal ” network free from defects is formed. (5) Preparation in non-stoichiometric composition leads to formation of defects in the polymer chain network and results in a significant depression of the mechanical properties. Structural models of macromer solutions and of Tetra-PEG gels, which account for the advanced mechanical properties of Tetra-PEG gels, are proposed.

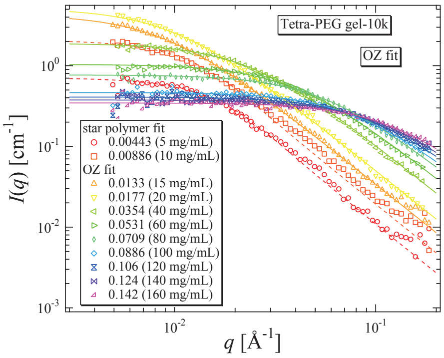

Fig. 1. SANS intensity functions of Tetra-PEG gel. The solid and dashed lines are fitting results of Ornstein-Zernike function for gels at high macromer concentration and 4-arm star polymer for imperfect gels prepared at low macromer concentrations, respectively.

1-5-6

Dispersion Stability of Carbon Black Suspensions by the Addition of Polymers

Masami Kawaguchi, Hiroki Mizukawa, and Yoshiaki Takahashi
Mie University, Kyushu University

In order to confirm changes in the aggregates in the carbon black suspensions dispersed in Nafion solutions under shear flow, an experiment using a rheometer-base shear flow apparatus for a small angle neutron scattering SANS-U instrument of Institute for Solid State Physics, the University of Tokyo at JAERI Tokai has been performed as functions of the scattering vector and the shear rate at the carbon black concentrations of 5.0 wt and 8.0 wt % and the ambient temperature. Nafion was adsorbed on the carbon black surfaces and it played a role in the stabilization of carbon black suspensions. After sedimentation of the carbon black suspensions, whose surfaces were covered by adsorbed Nafion using a centrifuge, the sedimented carbon black suspensions were washed several times to remove free Nafion chains by the dispersion media and the re-dispersed carbon black suspensions were obtained. The neutron scattering intensities of the re-dispersed carbon black suspensions clearly depended on the shear rate. However, it is noticed that the scattering patterns show two power-law regimes, irrespective of the shear rate: At at low q, a weak slope of ?2.3 corresponds to a mass fractal regime, whereas at high q, a power law ?3.6 is observed for the surface fractal of the primary particle. This means that the basic fractal structures of the carbon black suspensions are maintained even under shear flow. Moreover, changes in the neutron scattering intensities with an increase in the shear rate are well correlated with the shear flow behavior of the corresponding carbon black suspension. Therefore, for the first shear thinning regions and the plateau shear viscosity regions at the shear rates less than 50 s-1 the neutron scattering intensity rapidly decreases and attains the minimum due to the partial breaking down the aggregated structures of the carbon black suspensions under shear flow, whereas for the second shear thinning regions with an increase in the shear rate beyond at the shear rate of 50 s-1 the corresponding neutron scattering intensity grows up and approaches to a constant value above at the shear rate of 200 s-1 due to the formation of some newly ordered structures of the partial ruptured carbon black suspensions under higher shear flow. Thus, changes in the neutron scattering intensities seem to be well correlated with changes in the structures in the carbon black suspensions under shear flow.

1-5-7

Study on Structural Nonuniformity of Cross-linked Natural Rubber

Y. Ikeda(A), N. Higashitani(A), H. Asai(A), Y. Kokubo(A), T. Suzuki(B), N. Osaka(B), H. Endo(B), M. Shibayama(B), and S. Kohjiya(C)
(A)Dept. Chem. Mater. Technol., Kyoto Inst. Tech., (B)ISSP-NSL, Univ. Tokyo, (C)Fac. Sci., Mahidol Univ.

Natural rubber (NR) is one of the most important industrial materials among many polymeric ones. Generally, NR products are prepared by cross-linking reaction, and the network has been thought to give characteristic properties as rubber materials. However, it is difficult to elucidate the microscopic structure of cross-linked NR due to non-rubber components in NR such as proteins and lipids [1]. In this study, we applied small-angle neutron scattering (SANS) experiments by varying a deuterated toluene (D-toluene) fraction in solvents in order to investigate the network inhomogeneity of cross-linked NR. Two peroxide cross-linked NR samples with different network-chain densities (SP-NR-P1 and SP-NR-P2) and uncross-linked NR (NR milled) were subjected to the SANS experiments. Dicumyl peroxide (DCP) was used as a cross-linking reagent. The measurements were performed at SANS-U diffractometer of Institute for Solid State Physics, the University of Tokyo. For a contrast matching technique, matching point of NR was determined to be ca. 15 vol% D-toluene fraction in a mixture of D- and H-toluene as shown in Fig.1. However, this result can not be utilized to delete an excess scattering from the non-rubber components due to similar scattering length densities between the components and poly(isoprene). Increase of DCP decreased scattering intensities in the solvents whose fractions of D-toluene were over 0.3 as shown in Fig.1(b). Contrast variation SANS technique, on the other hand, qualitatively suggested that a network inhomogeneity decreased with an increase of DCP, i.e., network-chain density, when a scattering length density of proteins was assumed to be 1.8e10 cm-2.

Reference : [1] T. Karino et al., Biomacromolecules, 8, 693(2007).

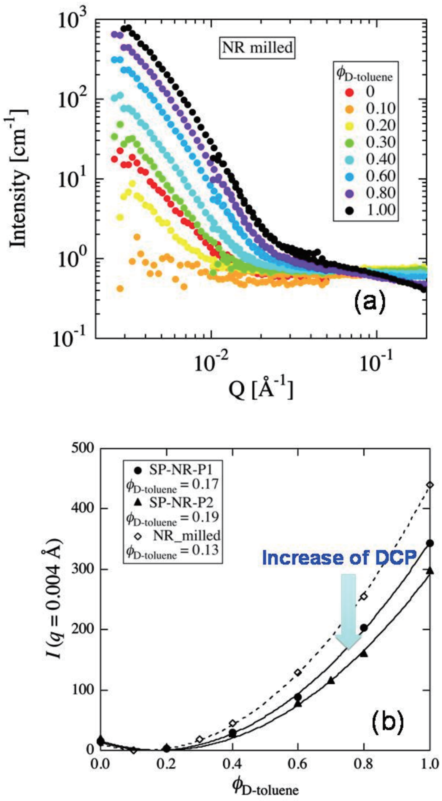

Fig. 1. Fig.1 (a) SANS profiles of uncross-linked NR in toluene with various D-toluene contents, (b) Effect of D-toluene fraction on scattering intensity at q = 0.004 angstrom for three samples.

1-5-8

Structure and compressibility of worm-like lamellar domain in a hydrated solid phase

Youhei Kawabata[1],Tomoaki Shinoda[1],Yuko Nagai[2], Akira Murakami[1] and Tadashi Kato[1]
Tokyo Metropolitan University[1], *Kao Corp.*[2]

In a binary system consisting of surfactant and water, a hydrated solid phase is formed below the Kraft temperature, where the hydrophobic tails extend to the length with all trans. The hydrated solid phase is a two-phase coexistence of excess water and lamellar structure L_β of bilayers whose hydrophilic tails are " solid-like " gel and interdigitated. So far, we have investigated the structural formation of the hydrated solid phase in the $C_{16}E_6$/water and $C_{16}E_7$/water system [$C_{16}H_{33}(OC_2H_4)_{6,7}OH$] by means of small angle X-ray and neutron scattering (SAXS, SANS) and optical microscope. We found clearly different structures in nm $\sim$ μm scale, even though those surfactants are slightly different from each other in the hydrophilic segment length. Figure 1a shows vesicle structures and worm-like lamellar domains observed in the $C_{16}E_7$ system and $C_{16}E_6$ system, respectively. In this study, to clarify the formation process of the lamellar domains, we performed SANS experiments. Especially here, we report the hyper-swollen lamellar structure in the $C_{16}E_7$ system.

The SANS experiments were carried out using the SANS-U spectrometer. The momentum transfer q ranged over $0.003 \leq q \leq 0.2$ Å^{-1}. The Krafft temperatures are 287 K for the $C_{16}E_7$ system. Temperature was jumped from 289 K to 277 $\sim$ 287 K. The concentration of $C_{16}E_7$ is 10 wt %, respectively.

Figure 1b shows a typical SANS profile obtained at 279 K in the $C_{16}E_7$ system at about 1 hour after temperature quench. Bragg peaks can be clearly seen, and they correspond to a swollen lamellar structure whose repeat distance is 84 nm. These Bragg peaks in such a low-Q region only appear below 279 K and at least above 281 K, they never appear. Coincidentally, from the microscope experiments, we found that below 279 K, small pieces of lamellar domains as shown in the inset of Figure 1b coexist for a few hours. It has been considered that lamellar domains hardly fuse each other because of the low temperature and they become quasi-equilibrium state. From all evidences, at present, we conclude that this hyper-swollen lamellar structure might be related to those small pieces of lamellar domains.

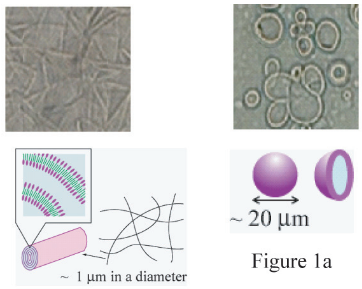

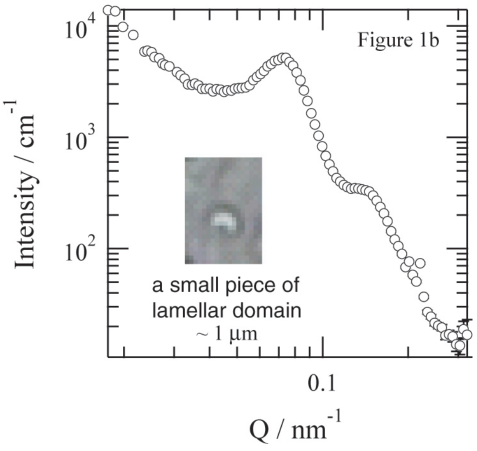

Fig. 1. The SANS profile obtained at 279 K in the $C_{16}E_7$/water system. A swollen lamellar structures whose repeat distance is 80 nm is formed.

1-5-9

Shear-induced onion formation of complex bilayer membrane systems

Shuji Fujii(A), Yohei Kawabata(B), and Yoshiaki Takahashi(C)
(A)Nagaoka University of Technology, (B)Tokyo Metropolitan University, (C) Kyushu University

The influence of a triblock copolymer, poly(ethylene oxide)m-b-poly(propylene oxide)n-b-poly(ethylene oxide)m (Pluronic series with different PEO and PPO chain length) on the phase behavior and on the shear induced onion formation in the lyotropic lamellar phase of the nonionic surfactant C10E3 was investigated by means of rheology, small angle neutron scattering (SANS) and small angle light scattering (SALS). At quiescent state, added triblock copolymer significantly shifted the La-L3 phase transition to lower temperatures. Under shear, the onion structure was not stable and easily transformed back into the lamellar phase with increasing polymer concentration and with increasing the polymer chain length, both of m and n. As a typical example of the results we obtained, polymer chain length dependence of the time development of 2D-SANS pattern in the shear-induced lamellar-to-onion formation process is shown in figure 1. Here, only the results on the PPO chain length dependence are shown. At short time region, anisotropic SANS pattern with the Bragg peak in the neutral direction, which was a representative for the parallel oriented lamellae along the flow direction, was observed for every samples. As PPO chain length, m, of triblock copolymer was increased, however, the time development of the onion formation process was remarkably affected. Samples with short PPO chain length showed an isotropic SANS pattern, which is a signal of the onion formation. As the PPO chain length was increased, the isotropic SANS pattern, i.e., the onion formation, was remarkably prohibited, and the sample with the longest PPO chain, m=69, showed no onion formation but the parallel oriented lamellar phase. In the rheology measurements, we found an increase of the critical shear rate for the onset of the shear-thickening, which also indicates the instability of onion in the presence of the triblock copolymer. Suppression of the shear-induced onion formation might be attributed to the enhancement of the effective surface tension, which might be also influenced by added triblock copolymer. These results clearly indicate that not only the hydrophilic polymer chain, PEO, but also the hydrophobic polymer chain, PPO, influences the dynamic properties of the lamellar membranes, which would be controlled by a combination of hydrophilic and hydrophobic chain length. To make clear the effect of guest components on the shear-induced nonequilibrium phenomena, it is necessary to perform experiments with different series of complex lamellar phase and elaborate analysis of structure on the basis of SANS.

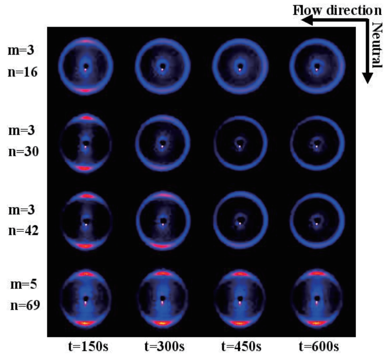

Fig. 1. Hydrophobic polymer chain length dependence of the time development of 2D-SANS patterns for complex lamellar phase in the onion formation process. Polymer mole fraction was fixed at 1mol%. Shear rate was fixed at 10s-1.

1-5-10

Small Angle Neutron Scattering Study on Metal-containing Gels Composed of Co(II) Ion and Oligopyridines

Jun Yoshida, Shin-ichi Nishikiori, Takuro Matsunaga, Mitsuhiro Shibayama
Graduate School of Arts and Sciences, The University of Tokyo; Institute for Solid State Physics, The University of Tokyo

In recent years, supramolecular gels composed of metal ions and organic ligands are attracting great attentions. Metal-containing gels (metallogels) have a potential to be responsive to external stimuli such as magnetic and electric ones so that they can exhibit unique properties among the gels. However, metallogels are still minor due to their synthetic and analytic difficulties.

We recently found that the combination of oligopyridines (L1 and L2) with CoCl2, Co(NO3)2, or AgBF4 forms gels easily(Fig. 1). The formation of these gels depended on the M(metal ion)/L(oligopyridine ligand) ratio. In every case, no gel was formed in low M/L conditions, while gelation occurred with increasing the M/L ratio. Dynamic light scattering (DLS) study for the solutions containing the metal ions and the ligands confirmed that the metal ions were effective in forming the supramolecular type metallogel and the solutions showed more gel-like behavior with an increase in the M/L ratio. However, at a certain M/L ratio, it abruptly turned into a sol state. The details of this change could not be traced by DLS and other spectroscopic methods. To obtain more information about this phenomenon, we used SANS technique, which is applicable to samples even in the sol state.

SANS intensity profiles for CoCl2-L1 are shown in Fig.1. In a low q region, the slopes of the profiles for the samples in the gel state (M/L = 1/10, 1/4, 1/2 and 1/1) were almost -4, while those for the samples in the sol state (M/L = 1.5/1, 2/1) were close to -1. These two profile types correspond to the gel and the sol state, and they indicate that the sol-gel transition is accompanied by some structural change. Although a model for the gel state is under investigation at the present stage, the profiles for the sol samples could be analyzed based on a model where rods with a large aspect ratio(length >> diameter) are randomly oriented. The diameters for the samples in the M/L ratio of 1.5/1 and 2/1 were evaluated to be 6.8 and 10.2 nm, respectively.

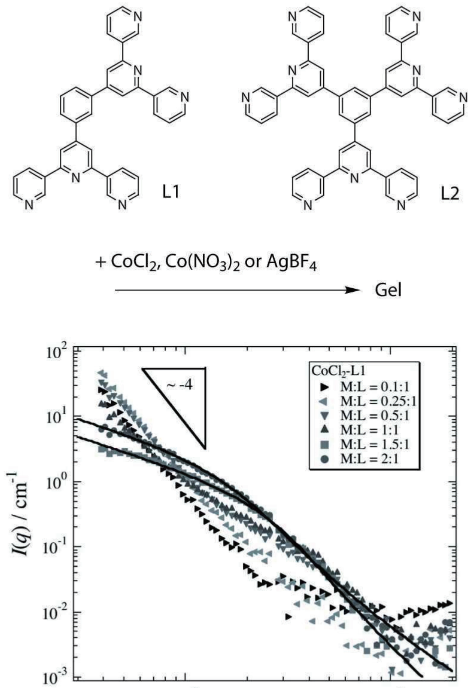

Fig. 1. Gel formation from oligopyridines (L1, L2) and metal salts, and SANS intensity profiles for the combination of L1 and CoCl2

1-5-11

Breathing Mode in Polymer Micelles and Second Virial Coefficient

K. Kawashima (a), T. Kanaya (a), G. Matsuba (a), H. Endo(b)
(a) ICR, Kyoto University, (b) ISSP, University of Tokyo

When diblock or triblock copolymers are added to a selective solvent, they aggregate into spherical micelles consisting of an inner core of insoluble blocks and an outer corona of soluble blocks, similar to micellization of surfactants. In previous papers [J. Chem. Phys. Solids, 60, 1367-1369 (1999) , J. Chem. Phys., 122, 144905 (2005)] we have investigated dynamics of micelles of deuterated styrene-protonated butadiene diblock copolymers (PSD-PB) and deuterated styrene-protonated isoprene diblock copolymers (PSD-PI) in deuterated n-decane, focusing on the chain dynamics in the corona using neutron spin echo (NSE). We observed the collective breathing mode for PSD-PI. On the other hand, it disappeared but the Zimm mode (single chain motion) was observed for PSD-PI although the molecular weight of PSD-PB and PSD-PI were almost identical. This has been assigned to the difference of the second virial coefficient (A_2) between PB and PI in deuterated n-decane. In this work we have studied the second virial coefficient and the dynamic crossover from a cooperative motion (gel mode) to a single chain motion (the Zimm mode) to elucidate why the collective breathing mode disappears in the DPS-PB micelles.

We used PB with Mw=22600 and Mw/Mn=1.05 and PI with Mw=24500, Mw/Mn=1.06. The solvent was deuterated n-decane. Small-angle neutron scattering and neutron spin echo measurements were done using SANS-U spectrometer and iNSE spectrometers in JRR-3 reactor, Tokai. First we have evaluated the second virial coefficient A_2 of PB and PI to find that A_2 of PB is smaller than that PI, showing the interactions among PBs are smaller than those among PI. We have also performed NSE measurements on the 20 wt % PB and PI solutions. The decays of intermediate scattering functions I(Q,t) were analyzed to evaluate the first cumulant G. Dividing the first cumulant G by Qˆ2, we plotted G /Qˆ2 as a function of Q in Figure 1. In the high Q region the first cumulant is proportional to Qˆ3, suggesting that the mode we observed is the Zimm mode. On the other hand, in the low Q range G is proportional to Qˆ2. It shows that the collective gel mode is dominant in this Q range. What we have to emphasize is that the crossover Q from the Zimm mode to the gel mode depends on sorts of polymers. The crossover Q of PI is located to the higher value than that of PB, showing that PI has longer-range (stronger) interaction and the collective dynamics arises in PI in the more local region than PB. This must be a reason why the collective breathing mode disappeared in PSD-PB micelles.

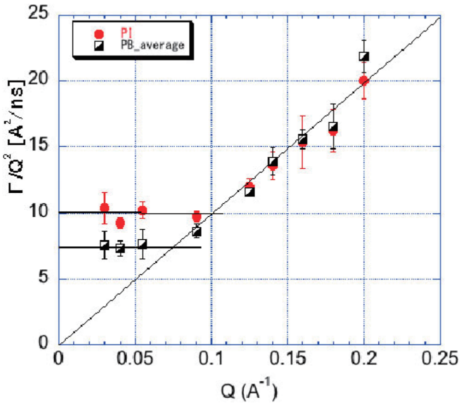

Fig. 1. Figure 1. Q dependence of G /Qˆ2 fpr PB and PI.

1-5-12

Distribution of Glass Transition Temperature Tg in a Polymer Thin Film by Neutron Reflectivity

K. Kawashima (a), T. Kanaya (a), G. Matsuba (a), K. Nishida (a), M. Hino (b)
(a) ICR, Kyoto University, (b) RRI, Kyoto University

Recent extensive studies on polymer thin films have revealed very interesting but unusual properties of polymer thin films. It was reported that the glass transition temperature Tg of polystyrene thin films supported on silicon substrate decreases with decreasing thickness below 40 nm. Similar results were reported by many researchers on Tg of polystyrene thin films supported on silicon substrate. These results were explained in terms of multi-layer structure consisting of surface mobile layer, middle bulk-like layer and interfacial immobile layer near the substrate. It is now believed that revealing the multi-layer structure is essential to understand the unusual properties. This has been already pointed out by de Gennes [2000, Eur. Phys. J. E 2 201], and he mentioned that further experiments should not aim at the determination of a single Tg, but at a distribution of Tg ’s. In this report we have studied the distribution of glass transition temperature Tg in a three-layer polystyrene thin film by neutron reflectivity, aiming to elucidate the multi-layer structure of polymer thin films.
For neutron reflectivity (NR) measurements we used deuterated polystyrene (d-PS) and hydrogenated polystyrene (h-PS) with molecular weight Mw = 7.31 x 10ˆ5 and Mw = 7.69 x 10ˆ5, and molecular weight distributions were Mw/Mn = 1.18 and 1.08, respectively. The bulk glass transition temperatures Tg of h-PS and d-PS are 100 C and 103 C, respectively. NR measurements were performed using MINE spectrometer at JRR-3 reactor in Tokai.
Figure 1 shows neutron reflectivity profiles from the three-layer thin film at 30, 60, 85 and 110 C. It is very clear that the reflectivity profiles gradually shifts to lower q with increasing the temperature, showing thermal expansion of the film. The temperature dependence of the total film thickness is shown for the total film thickness, the top (surface), the middle and the bottom layers are shown in Figures 2(a), (b), (c) and (d), respectively. The surface layer increases in thickness with the thermal expansivity of ˜1.3 x 10ˆ-4 Kˆ-1, which is close to the expected value (= 1.1 x 10ˆ-4 Kˆ-1), while it begins to increase above ˜85 K more steeply, showing that the glass transition temperature of the surface layer is ˜18 K lower than the bulk Tg. The middle layer shows a very similar thermal expnsivity in the glassy state with the top layer, but the glass transition temperature is ˜105 K which is very close to or little bit higher than the bulk Tg. The middle layer behaves as the bulk layer. On the other hand, the bottom layer shows very different temperature dependence of the thickness from other layers. The film thickness is almost independent of temperature below ˜130 C, suggesting that the glass transition temperature of the bottom layer must be higher than 130 C. The present results clearly show that the thin film has a distribution of Tg.

Activity Report on Neutron Scattering Research: Experimental Reports **16** (2009)
Report Number: 729

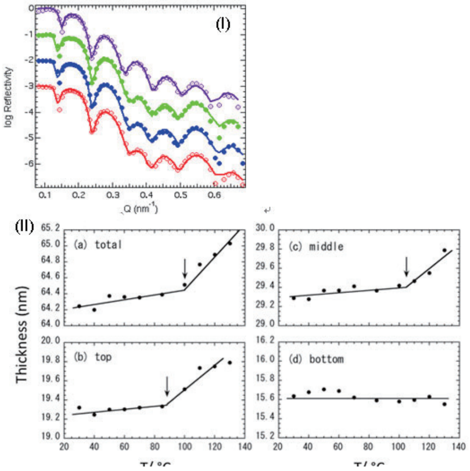

Fig. 1. (I) Neutron reflectivity profiles of three-layer polystyrene thin film. (II) Temperature dependence of film thickness. (a) total, (b) top layer, (c) middle layer, (d) bottom layer.

1-5-12

1-5-13

Role of Low Mw Components in Polymer Crystallization under Shear Flow

C. Ito, G. Matsuba, K. Nishida, T. Kanaya
ICR, Kyoto University

It is well known that when polymers in melts and solutions are crystallized under elongational and/or shear flows the so-called shish-kebab structure is formed, which consists of long central fiber core (shish) surrounded by lamellar crystalline structure (kebab) periodically attached along the shish. In the previous research, it was found that high molecular weight component composed mainly shish structure. Now, we carried out the structural formation processes of shish-kebab during drawing was confirmed by in-situ small-angle neutron scattering (SANS) measurements on a polyethylene (PE) blend of low molecular weight deuterated PE and high molecular weight hydrogenated PE(3 wt%). Time-resolved SANS measurements were performed with SANS-U spectrometer at the JRR-3M reactor in JAPAN Atomic Energy Research Institute (JAERI), Tokai.

On drawing process of the blends, it was observed that the isotropic crystal structure gradually formed the anisotropic shish-kebab structure with in-situ SANS measurements in Figure 1. At first 10 min, the isotropic pattern changed horizontally long ellipsoid-like profiles. This suggested that the isotropic lamella was stretched and distorted. Between 20 min and 80 min, the shish-kebab formation processes were observed. In high temperature condition, the long spacing period increased with drawing process, while the long spacing period decreases in low temperature condition. In high temperature, the “ tie chain ” between lamella could extend and be pulled off from lamella crystal because of high mobility. On the other hand, low mobility in low temperature prevented the “ pulled off ” process and then the lamella crystal could be broken. After 80 min, we observed the processes of “ kebab evaporating ”. Such disappear of kebab structure could be caused by “ shish-formation process ” from kebab structure.

Furthermore, we evaluated the detailed shish-kebab structure from these 2D SANS profiles. The shish kebab structure can be described as core-shell cylinder model. The radius of core cylinder was about 45 nm and the shell cylinder had two core cylinders.

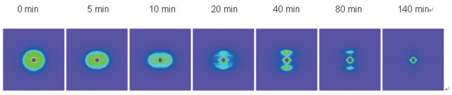

Fig. 1. Time evolution of 2D SANS patterns during crystallization process of PE at 110 C, drawing rate = 6 micron/ s

1-5-14

Neutron Scattering Study on Miscibility of Statistical Copolymer / Homopolymer Blends

Siti Sarah A. R., D. Kawaguchi, Y. Matsushita
Dept.Appl. Chem., Nagoya Univ.

We have recently found that 4-substituted polystyrene derivatives and polyisoprene (I) are weakly interacted and likely to be miscible with each other. Among the various combinations, poly(4-tert-butylstyrene) (B) and I exhibit a lower critical solution temperature (LCST) type phase diagram, while poly(4-tert-butoxystyrene) (O)/I blend shows an upper critical solution temperature (UCST) type one. Hence, competition between two interactions having opposite temperature dependence is expected when a copolymer consists of B and O is blended with I. The objective of this study is to investigate the phase behavior of statistical copolymers composed of B and O, abbreviated as s-BO, with I by optical microscopic (OM) observation and small-angle neutron scattering (SANS) measurements. Several blends of s-BOs having mol fraction of B, mB, comparable to 0.50, with I showed both UCST and LCST type phase diagram. Furthermore, UCST type phase behavior was observed for blends having small mB, while LCST type one was for that of large mB at all employed temperatures. These results imply that the attractive interaction of B/I leads to miscibility and that the repulsive interaction of O/I induces immiscibility of the blends within the temperature range studied. Hence, the phase behavior of s-BO/I blend can be understood as a result of the competition of two interactions having opposite temperature dependence.

To elucidate the interaction between blend components indirectly from SANS data, the structure factors at q=0, S(0)s, which correspond to the thermodynamic susceptibility were determined by using the Ornstein-Zernike equation. S(0)s were obtained from the fittings of inverse S(q) vs. q^2 data to Ornstein-Zernike equation. Figure 1 gives the relation between inverse S(0) and inverse temperature, for s-BO/d-I blends together with those for O/d-I and B/d-I blends for comparison. The inverse S(0) for O/d-I blend in Figure 1(a) decreased with a decrease in inverse T, whereas that for B/d-I blends increased with inverse T as shown in Figure 1(e). This shows that the interaction of O/d-I becomes less repulsive as temperature becomes higher and vice versa for the interaction of B/d-I. Hence, these results indicate that O/d-I blend shows an UCST and B/d-I blend has a LCST type phase behavior.

Figure 1(b) for s-BO35/d-I blend showed qualitatively the same trend as that O/d-I, however, the temperature dependence of the inverse S(0) for s-BO/d-I blends changed dramatically when mB reaches to 0.49 as shown in Figure 1(c). Namely, the inverse S(0) first increased, but went through a maximum at 170 °C and then turned to decrease. This implies that s-BO49/d-I blend shows both UCST and LCST type phase behavior. Furthermore, as mB goes up more, opposite temperature dependence was observed as shown in Figure 1(d) for s-BO66/d-I blends. The inverse S(0) increased with decreasing inverse T, indicating LCST behavior which is similar to B/d-I blend. These results revealed by SANS experiments for s-BO/d-I blends are in good accordance with OM observation. Thus, we were able to display that the phase behavior of s-BO/d-I blends change from UCST to LCST type one with an increase in mB due to the competition of B/I and O/I opposite interactions and show both UCST and LCST type phase behavior at balanced condition.

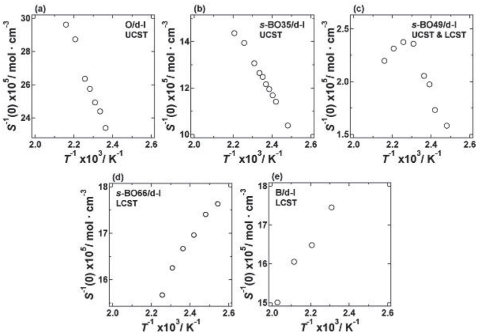

Fig. 1. Temperature dependence of the inverse S(0) of (a) O/d-I, (b) s-BO35/d-I, (c) s-BO49/d-I, (d) s-BO66/d-I and (e) B/d-I blends.

1-5-14

1-5-15

Dynamical Properties of Nanoporous Structure in Syndiotactic Polystyrene

Fumitoshi Kaneko, Tatsuya Kawaguchi, Kenji Okuyama
Graduate School of Science, Osaka University

Syndiotactic polystyrene (sPS) is a relatively new commodity polymer, which exhibits a variety of crystalline states. The δ_e phase of sPS occupies a unique position from the viewpoints of structure chemistry of polymers. In the δ_e phase, there exist two relatively large cavities between sPS helices taking TTGG conformation. Each cavities has a volume of nearly 120A^3. This nanoporus structure is regarded as the first example of molecular sieve in polymeric materials. Unlike the ordinary crystalline states of polymers, the density of the δ_e phase (0.977 g cm^{-3}) is less than that of the amorphous state (1.05 g cm^{-3}). It seems that this unique structure exerts a considerable influence on the dynamical properties of the δ_e phase.

In this study, we compared the QNS spectrum of the δ_e phase with that of the γ phase and the glass state of sPS. In the γ phase, sPS helices takes TTGG conformation like those of the δ_e phase but they are much more densely packed. All QNS spectra were measured with AGNES spectrometer of JRR3M (Tokai). The mean-square displacement $< u^2 >$ of hydrogen atoms was evaluated from the Q dependence of the elastic scattering intensity $I(Q)$ by using the following the Debye-Waller formula: $I(Q) = I(0)$ exp[-(1/3)$< u^2 > Q^2$], where $I(0)$ is the elastic intensity at $Q = 0$. In order to reduce the effect of coherent scattering, $I(Q)$ was devided by that at 20K.

Figure 1 shows the temperature dependence of $< u^2 >$ for the δ_e, γ and glass samples. The mean square displacement of the glass sample is larger than that of the γ and δ_e phases in the whole temperature range of 100-350K. Although there is no conspicuous difference in $< u^2 >$ between the two crystalline phases, δ_e and γ, up to 250K, the δ_e phase shows a clearly larger displacement in the higher temperature region, which is attributable to the weaker interchain interaction in δ_e phase. As for the QNS component, these samples exhibit their own characteristics; the δ_e phase shows a larger contribution to the high $Q$and low ΔE region, suggesting the activation of local motions.

According to the previous ^{13}C-NMR study by Gomez and Tonelli, the spin-lattice relaxation times T_1 are shorter in the δ_e phase than the glass. We conjecture that the difference in the NMR and QNS experiments is due to the time scale of detectable molecular motion. Considering all the various factors together, we infer that the influence of the nonoporous structure appears most conspicuously in slow and large motions. However, we can see from the results of QNS that smaller molecular motions of shorter time scale, which are probably the phenyl group's motions, are more activated in the nanoporous δ_e phase. To clarify the more detailed dynamical properties of the δ_e phase, it is necessary to study the larger molecular motion of longer time scale.

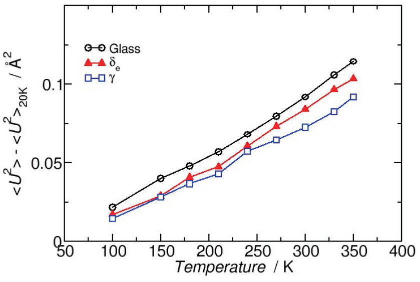

Fig. 1. Temperature dependence of mean square displacement in sPS solid states

1-5-16

Static/Dynamic Structural Investigation of Lipid Nanodiscs

M. Nakano(A), M. Fukuda(A), M. Miyazaki(A), Y. Wada(A), H. Endo(B)
(A)Graduate School of Pharmaceutical Sciences, Kyoto Univ., (B)ISSP-NSL, Univ. of Tokyo

Phospholipid Nanodiscs are lipid-protein complexes in which amphipathic helices, such as apolipoprotein A-I (apoA-I) and its truncated proteins surround the edge of the bilayer. Nanodiscs can be formed by simply mixing apoA-I and lipids (such as dimyristoylphosphatidylcholine (DMPC)) at the gel-liquid crystalline phase transition temperature of the lipid, or by solubilizing these compounds into a micellar solution of cholate with subsequent removal of the surfactant. The reported size of Nanodiscs constituted by apoA-I ranges from 7 to 12 nm, depending on the lipid used or lipid/protein composition. However, their detailed structure and characteristics, especially the dynamic properties of lipids in Nanodiscs, are not well understood.

We previously succeeded in determining the rates of interbilayer exchange and flip-flop of dimyristoylphosphatidylcholine (DMPC) in large unilamellar vesicles (LUVs) by small-angle neutron scattering (SANS) technique [1]. In the present study, we elucidated the static and dynamic properties of apoA-I/DMPC Nanodiscs with SANS.

ApoA-I was isolated from pig plasma. DMPC was mixed with buffer containing apoA-I (DMPC:apoA-I = 80:1 (mol/mol)) and incubated at 25 °C for 8h. Nanodiscs formed were separated from coexisting vesicles and lipid-free proteins by density gradient ultracentrifugation. Nanodiscs consisting of either d54-DMPC (D-disc) or DMPC (H-disc) were prepared.

SANS profiles of D- and H-disc with different scattering contrasts were fitted simultaneously, and whole diameter was estimated at 9.4 nm. From the core volume, the molecular area of DMPC was calculated as 0.50 nm2, which is much smaller than the molecular area in vesicles (0.66 nm2), suggesting closer lipid packing.

Time-resolved SANS measurement was started immediately after mixing an equivalent volume of D-disc and H-disc. Time-course of the normalized contrast was calculated from the scattering intensity. The decay curves at four different temperatures were reproduced well by single-exponential function to provide the rate constant (kex). Noteworthy, the decays were more than 20-fold faster than the theoretical decay with the exchange rate for LUVs. Arrhenius plot for kex suggested that DMPC desorbs from Nanodiscs via enthalpically unfavorable but entropically favorable process. These distinct dynamic properties of lipids in Nanodiscs, including a decreased activation energy compared with LUVs, could be ascribed to the entropically more unstable state in Nanodiscs as suggested by the static SANS measurements. That is, the lower entropy state derived from the closer lipid packing countervails the decremental entropy on the lipid desorption.

In conclusion, the static and time-resolved SANS study clarified the fast lipid dynamics in Nanodiscs, which is connected with the static properties of bilayers altered by the envelopment with the proteins.

References

[1] M. Nakano, M. Fukuda, T. Kudo, H. Endo, T. Handa, Phys. Rev. Lett. 98 (2007) 238101.

1-5-17

nano-meter-sized domain formation in model bio-membrane

Y. Sakuma and M. Imai
Department of Physics, Ochanomizu University

Using a contrast matching technique of small angle neutron scattering (SANS) we have investigated a phase separation to liquid-disordered and liquid-ordered phases on ternary small unilamellar vesicles (SUVs) composed of deuterated-saturated, hydrogenated-unsaturated phosphatidylcholine lipids and cholesterol, where the equilibrium size of these domains is constrained to less than 10 nm by the system size. Below a miscibility temperature, we observed characteristic scattering profiles with a maximum, indicating formation of nano-meter-sized domains on the SUVs. The observed profiles can be described by a multi-domain model rather than a mono-domain model. The nano-meter-sized domain is agitated by thermal fluctuations and eventually ruptured, which may result in the multi-domain state. The kinetically trapped nano-meter-sized domains grow to a mono-domain state by decreasing temperature. Furthermore, between the miscibility and disorder-order transition temperature of saturated lipid, the integrated SANS intensity increased slightly, indicating the formation of nano-meter-sized heterogeneity prior to the domain nucleation.

1-5-18

Neutron Reflectivity Studies of the Swelling States of Polysulfobetaine Brush at Water Interface

Y. Terayama1, M. Kobayashi 1 ,2, A. Takahara1,2
1Institute for Materials Chemistry and Engineering, 2Graduate School of Engineering, Kyushu University

Water-swollen states of hydrophilic polymer brushes have been paid great attention because they relate to biointerface performance and water lubrication. We studied the swollen structure of polymer brushes containing zwitter inonic and nonionic macromolecules in aqueous solution by neutron reflectivity (NR). This article describes a part of them, focusing on swelling behavior of polysulfobetaine brush prepared by surface-initiated radical polymerization polymerization of (3-dimeth yl(methacryloxyethyl) ammonium propane sulfonate) (DMAPS). Poly(DMAPS) is insoluble in pure water due to the strong attractive electrostatic interaction between ammonium cations and sulfonyl anions. In contrast, poly(DMAPS) is soluble in salt solution because of the screening of the inter- or intramolecular interaction by ions in aqueous solution[1,2]. The dependence of ionic strength on swelling behavior of poly(DMAPS) brush was investigated by NR.

The poly(DMAPS) brush on quartz was prepared by surface-initiated atom transfer polymerization of DMAPS. NR was measured by a multilayer interferometer for neutrons (MINE) in JRR-3 at TOKAI, using wavelength $\lambda = 0.88$ nm with an accuracy of 2.7 %. A neutron beam was irradiated from a quartz substrate to the interface between heavy water (D2O) and the poly(DMAPS) brush on quartz glass. The incident slit width were adjusted to maintain a 55 mm footprint size on the sample surface. The scattering vector, q, in specular reflectivity is defined by $q = (4\pi / \lambda) \sin\theta$. The NR profiles were analyzed by fitting calculated reflectivity from model scattering length density profiles to the data using Parratt32 software.

Figure 1 shows the neutron reflectivity curves and scattering length density profiles of poly(DMAPS) brush in D2O and 0.5 M NaCl/D2O. The neutron scattering length density (SLD) of poly(DMAPS) brush in D2O was dramatically increased from 4.80 × 10-4 to 6.32 × 10-4 nm-2 along with the distance from the substrate, and was slightly increased up to 6.39 × 10-4 nm-2 at the pure D2O region. Volume fraction distribution of DMAPS segments in D2O solution was evaluated from SLD curve, and was fitted by the parabolic function to estimate the brush thickness in solution, which was 130 nm in pure D2O. On the other hand, the SLD profile in 0.5 M NaCl/D2O drastically increased to 5.50 × 10-4 in 50 nm region from the substrate, and gradually increase to 6.29 × 10-4 nm-2 at the external solution interface. Polymer brush chains at the outermost region were stretched up to 260 nm from quartz surface. Hydrated salt ions screened the attractive electrostatic interaction of sulfobetaine groups to give an extended chain structure like as an osmotically swollen brush of an electrically neutral polymer.

References
(1) Huglin M B and Radwan M A 1991 Makromol. Chem 192 2433.
(2) Kato T and Takahashi A 1996 Ber. Bunsenges. Phys. Chem. 100 784.

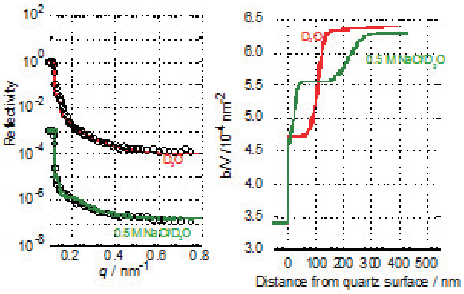

Fig. 1. Figure 1. NR of PDMAPS brush in D2O and 0.5 M NaCl/D2O solution and the corresponding fits (Left). The SLD profiles in D2O and 0.5 M NaCl/D2O solution to calculate the fitting curves for reflectivity (Right).

1-5-18

1-5-19

Structure-Property Relationship of Particle-Polymer Mixture Solution under shear field

M. Shibayama, T. Matsunaga, T. Suzuki, N. Osaka, T. Nishida, H. Endo
ISSP, The University of Tokyo

The microscopic structure clay nanoparticles (Laponite XLG) and poly(ethylene oxide)(PEO) suspension under steady shear has been investigated by contrast-variation small-angle neutron scattering(CV-SANS). It is noted that the radius and thickness of the clay are 150 and 10 , respectively. The molecular weight of the PEO used is Mw = 1,000 kg/mol. The stock solution of clay and PEO was prepared by adding PEO solution to clay and stirring with a magnetic stirrer until well-blended. Laponite (clay) platelet dispersions in poly(ethylene oxide) (PEO) aqueous solutions with various deuterious/hydrogeneous water compositions were prepared and contrast-variation SANS experiments were carried out.

Reversible shear-thinning behaviors were observed in both clay dispersions and PEO solutions. No anisotropy was observed in SANS patterns even clay platelets are highly anisotropic, indicating turbulent rotation of platelets by shearing. In the presence of PEO, on the other hand, the viscosity showed a hysteresis loop with strong anisotropy (see figure). This suggests that clay platelets are well aligned along the flow direction due to bridging together by oriented polymer chains.

Furthermore, by contrast-variation SANS experiments, the following facts were disclosed. In a stationary state, a significant number of PEO chains are adsorbed on the clay surface. Because of the presence of tie-chains bridging neighboring clay platelets, the viscosity is higher than that of clay dispersion without PEO chains. When the system is sheared, the adsorbed layer is destroyed and desorption occurs. However, by reducing the shear rate, polymer chains start to adsorb on the clay platelets again. Here, the desorption/adsorption process is very much dependent on the history of shearing, leading to a strong hysteresis behavior.

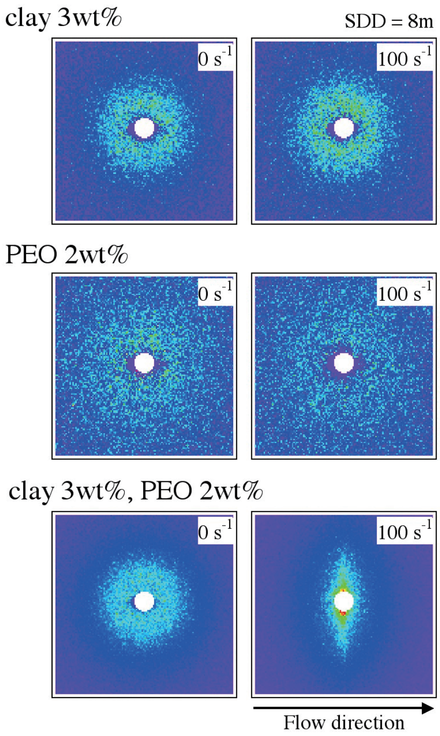

Fig. 1. SANS 2D-patterns for clay(3 wt%) dispersion, PEO(2 wt%) solution and clay(3 wt%)-PEO(2 wt%) mixed solution

Activity Report on Neutron Scattering Research: Experimental Reports **16** (2009)
Report Number: 887

1-5-20

Kinetic process on transition from small to large uni-lamellar vesicles

N. L. Yamada
High Energy Accelerator Research Organization

It has been reported that the mixture of dimyristoylphosphatidylcholine (DMPC; 14 carbons/chain) and dihexanoylphosphatidylcholine (DHPC; 6 carbons/chain) spontaneously form small uni-lamellar vesicles (SUVs; several hundreds of angstroms in radius) [1]. Due to high stability and monodispersity, SUVs consisting of long- and short-chain phospholipid mixtures have a potential for drug delivery, micro reactor, as well as biomimetic system. According to experimental reports, the SUVs are formed from small bilayered-micelles (bicelles; approximately one hundred angstroms in radius) above the chain melting temperature of long-chain lipids T_c [2, 3, 4].

In this study, the transition not from bicelles but from small SUVs to large SUVs has been found in this system. As far as I know, this is the first observation of the SUV-SUV transition in aqueous solution of amphiphilic molecules. The purpose in this study is to clarify the mechanism of this transition from the viewpoint of kinetics by using time-resolved small angle neutron scattering (SANS) by using SANS-U.

Figure 1(a) shows the time evolution of SANS profiles after temperature jump from 50°C to 27°C. The fringes due to large SUVs gradually appeared for over five hours after cooling as shown in Fig. 1(a), while those due to small SUVs gradually disappeared. This indicates that the size of SUVs discontinuously changed at the SUV-SUV transition. If small SUVs fused each other to be large SUVs, continuous increase in the vesicle size should be observed. Hence, this result implies that transient bicelles were formed during the transition.

To confirm the assumption, model fitting of SANS profiles have been performed. Solid lines in Fig. 1(a) are the results of the fitting. Since scattering intensities are proportional to the number density of particles, the volume fractions of SUVs and bicelles can be estimated by the fitting as shown in Fig. 1(b). A minimal model describing time evolution from small to large SUVs via transient bicelles well agrees with the experimental results as solid lines in Fig. 1(b). This indicates that the deformation from small SUVs to bicelles is the trigger for the transition to large SUVs, which is induced by the stabilization of rim structure by decreasing temperature to near T_c.

References

[1] N. E. Gabriel and M. F. Roberts, Biochemistry **23**, 4011 (1984).

[2] K. M. Eum, G. Riedy, K. H. Langley, and M. F. Roberts, Biochemistry **28**, 8206 (1989).

[3] M. P. Nieh, C. J. Glinka, and S. Krueger, Langmuir **17**, 2629 (2001).

[4] N. L. Yamada, M. Hishida, and N. Torikai, Phys. Rev. E, **79**, 032902 (2009).

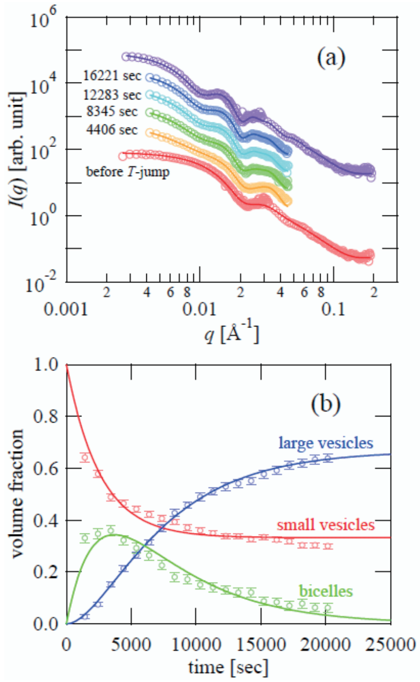

Fig. 1. Results of time-resolved SANS experiments (a) and time evolution of volume fraction of SUVs and bicelles (b) after the temperature jump from 50°C to 27°C.

1-5-21

Structural Analysis of N-isopropylacrylamide / Rod-like silica Hybrid Gels by Contrast-variation Small-angle Neutron Scattering

Takuya Suzuki, Noboru Osaka, Hitoshi Endo, Mithuhiro Shibayama
ISSP-NSL, Univ. Tokyo,

Polymer gels, which are soft materials that retain large amounts of solvent, can be functionalized or strengthened by incorporation of inorganic compounds. The organic/inorganic hybrid gels thus obtained can be of various morphologies, such as semi-interpenetrating polymer networks with inorganic domains as well as polymer networks that are organically cross-linked and then strengthened by the incorporation of inorganic compounds. In addition, there exist organic hybrid gels free of organic cross-links, but which are cross-linked by the inorganic compounds via chemical or physical cross-linking. Detailed studies on hybrid polymer morphology, gelation dynamics, and interfacial structures between polymers and inorganic compounds have so far been limited by the inherent complexity of the systems. This complexity originates from the molecular interactions of the multi-component systems (i.e., the polymers, the inorganic compounds, and the solvent).

In this study, we investigated the microscopic structure of N-isopropylacrylamide (NIPAm)/rod-like silica hybrid gels. NIPAm gel is one of the widely studied thermo-responsive gels and a model system for studying hydrophobic interactions. It is prepared by using redox-polymerization and shows an attractive interaction with the silica surface via hydrogen bonding. It can be possible to discuss the influence of the distribution of inorganic compounds in the gel by flexibly changing not only the concentration but also the size or the shape (sphere or rod) of silica particles. The systematic study on the mechanical property and microstructure of hybrid gel, which can be tuned by these quantitative or geometrical arrangements of inorganic compounds, should be of great importance in order to design the high-performance gel. One of NIPAm/rod-like silica gel and three types of NIPAm/spherical silica gels, each having different silica sizes, were prepared while maintaining an equal total volume fraction. Contrast-variation small-angle neutron scattering measurements were performed to clarify the silica shape dependence of the hybrid gel microstructure. The presence of an adsorbed layer of NIPAm chains on the silica surface and its dependence on silica particle size are addressed.

Fig.1 shows the intensity profiles for (left) rod-like silica and (right) NIPAm/Rod-like silica hybrid gels. In the case of rod-like silica, the distinct peak appeared in the low Q region indicating the repulsive interaction of each particle. On the other hand, for the hybrid gels, the power law behavior was observed due to the fractal-like aggregation of each particle. Moreover, it should be noted that the shoulder was observed for each sample indicating the form factor of each particle. By using these experimental data, the surface structure around silica particles was discussed.

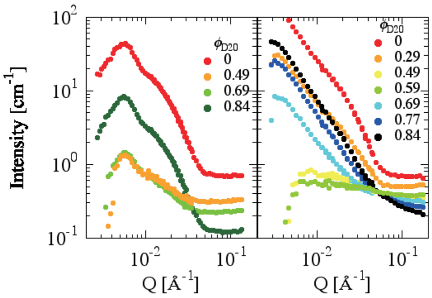

Fig. 1. Intensity profiles for Rod-like silica (left) and NIPAm/Rod-like silica hybrid gels (right).

1-5-22

Structural Analysis of Polyurethane Resin by Small-angle Neutron Scattering

(A) Takuya Suzuki, Mitsuhiro Shibayama, (B) Kazuhiro Hatano, Masahiko Ishii
(A) Institute for Solid State Physics, The University of Tokyo, (B) Paint & Finishing Design Dept., Vehicle Material Engineering Div., TOYOTA MOTOR CORPORATION

Polyurethane resin is one of the most familiar materials consisting of polyisocyanate and polyol groups. Due to the good mechanical properties like adherence and durability, polyurethane resin is widely used as industrial materials in the wide ranges such as adhesives, fabrics, paints, and inks. Polyurethane resin including isocyanurate groups, which is formed by a trimerization reaction of isocyanate groups, provides better thermal stability and rigidity than that composed of linear urethane bonding because of more functional groups and of stiffer hard segments in the former one.

As for the effect of the stoichiometric ratio, [NCO] / [OH], into the network structure of polyurethane resin, various studies have been carried out so far. Redman reported the effect of the [NCO] / [OH] ratio on molecular weight and on the rheological, thermal, and mechanical properties of two series of ester-based polyurethanes.[1] Nierzwicki and Wysocka also studied the effect of the [NCO] / [OH] ratio on the micro-phase separation of ester-based polyurethanes, which can be induced by the soft segments and hard segments, by thermo-mechanical analysis (TMA).[2]

In this paper, we discuss the gelation kinetics and the microstructure of polyurethane gels by focusing on the network concentration and the stoichiometric ratio of isocyanate to hydroxyl groups, [NCO] / [OH]. The purpose of this study is to clarify the following matters, i.e., the effect of the total concentration and [NCO] / [OH] on the microscopic inhomogeneities of the network. We used acryl-polyol as a soft segment component and polyisocyanate as a hard segment component.

Fig.1 shows the intensity profiles of polyurethane resin having different total concentration(wt%) and [NCO] / [OH]. In the case of 12.8 wt%, the [NCO] / [OH] dependence is so little and the intensity is low. This is due to the fact that at 12.8 wt%, the system was at liquid state while the sample became gel-like state by further increasing the total concentration. It should be noted that at 17.1 wt%, the intensity became the maximum. At more than 17.1 wt%, the intensity decreased with the total concentration due to the decrease of the concentration fluctuation of the polymer network. These experimental results were also in good agreement with our previous work by dynamic light scattering.[3] At 54 wt%, the intensity profiles were flat due to the strong incoherent scattering of the concentrated polymers.

References

[1]Redman RP. Developments in Polyurethanes. London: Applied Science Publishers, 1978.
[2]Nierzwicki W and Wysocka E. J. App. Polym. Sci. 1980;25:739-746.
[3]T. Suzuki, M. Shibayama, K. Hatano, and M. Ishii. Polymer, in press.

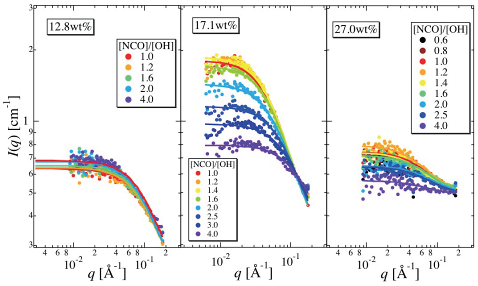

Fig. 1. Intensity profiles of polyurethane resin.

1-5-23

Small-angle neutron scattering study of block copolymers in supercritical carbon dioxide

M. Itoh, H. Yokoyama, K. Mayumi, K. Ito, N. Osaka, H. Endo, M. Shibayama
University of Tokyo

Depending on volume fraction of each block, degree of polymerization and interaction between blocks, several microphase-separated morphologies are observed in diblock copolymers. These morphologies are kinds of micro-phase separation of each blocks: Examples are spheres, cylinders and lamellae ordering in long-ranged periodic structures, such as cubic lattice of spheres and hexagonal lattice of cylinders. In addition to those classic morphologies, 3D contineous networking structures, which are called bicontinuous structures, have been reported. We have succeeded in inducing multiple order-to-order phase transitions by swelling selectively CO2-philic blocks with supercritical CO2 and changing pseudo-volume fraction. This morphology change was anticipated by ex-situ analysis of the samples frozen and removed from supercritical CO2. However, in-situ measurement of selectively swollen block copolymers in supercritical CO2 has never been conducted. Thus this time we performed in-situ measurement of swollen block copolymers in CO2 by neutron scattering analysis.

We analyzed the morphologies of Poly(styrene-b-perfluorooctylethyl methacrylate)s (PS-PFMAs), using small angle neutron scattering measurement system ,SANS-U, at JRR-3. PFMA is CO2-philic and highly swollen in CO2. We prepared three samples differing with the ratio of PS to PFMA and total degree of polymerization, of which molecular weights and weight fraction of PFMA are 18,600 and 20 % (S1), 17,400 and 48% (S2), and 23,000 and 28 wt% (L), respectively. Samples for SANS were made by casting from trifluorotoluene solutions. Then the samples were placed into high-pressure cell with CO2 pressure and temperature controls. This time, temperature was fixed at 60 degree C and pressure was varied from atmospheric pressure to 30MPa.

Fig.1 shows the pressure dependence of SANS profiles. Profiles in each graph are seriated in increasing order of pressure. Fig1a is scattering patterns of S1. At 0.1MPa the peak positions of q (1:1.73), corresponding to Hex lattice of PFMA Cylinders is found. Similarly, the profile at 15MPa agrees with lamellar peak pattern. At 10 MPa, at which the effective volume fraction is between cylinderical and lamellar morphologies, unknown peak pattern appeared. Because the first and second order peaks were not well separated due to limited resolution, we cannot assign the morphologies at this point, but the peak ratio is inconsistent with either cylinder or lamellar. Pressurizing from 15MPa to 20MPa we observed sudden change of the first peak position followed by BCC/SC lattice of spheres at 25MPa and 30MPa(1: 1.44). The sudden change of the first order peak position can be interpreted as evidence of exchange of the matrix. Scattering profiles of S2 with higher PFMA fraction (48%) is shown in Fig.1b. In as cast state, peaks appear at 1, 1.99, 2.97 relative to the first order, which is lamella. In pressurizing process at 15 MPa, peak ratio 1:1.74:1.86 was observed. This pressure and hence the effective volume fraction is in bicontinuous regime, but identifying this structure requires additional experiments. As pressurizing continuously, the polymer structure changed to Hex of cylinder at 25MPa and finally the structure factor vanished at 30MPa.

Fig.1c shows the scattering function of L with the higher mass. From peak ratios of as cast specimen and at the pressure upto 20MPa, the morphology is always Lamella.

At a pressure over 25MPa peak becomes weak, and at 30MPa structure factor completely disappears.

As can be seen from these three samples, we observed multiple order-to-order transitions. We are continuing in-situ measurement with SANS on new additional samples with different ratio of PFMA and the degree of polymerization.

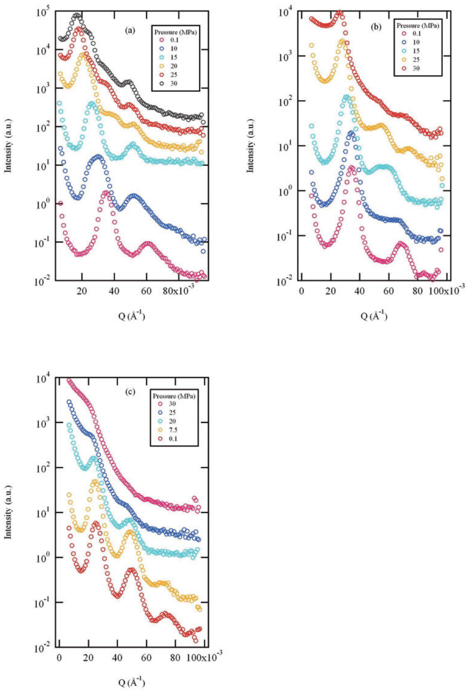

Fig. 1. Fig. 1. Small angle neutron scattering patterns of PS-PFMAs with different molecular weight and fractions at several different CO2 pressures: (a) Mn = 18,600 and PFMA wt% = 20; (b) 17,400 and 48%; (c) Mn = 23,000 and PFMA = 28 wt%.

1-5-23

1-5-24

Reconstruction of uni-lamellar vesicles induced by addition of polymers

N. L. Yamada
High Energy Accelerator Research Organization

It has been reported that the mixture of long-chain phospholipids (14 carbons/chain or more) and short-chain phospholipids ($6-8$ carbons/chain) spontaneously forms small uni-lamellar vesicles (SUVs; several hundreds of angstroms in radius) [1]. Since a membrane consisting of phospholipid molecules is the main component of biomembranes, such SUVs have a potential to create biomimetic system for studying bioactivities in cells. Recently, it has been reported that nanopores are sponetaneously formed on the surface of SUVs consisting of dimyristoylphosphatidylcholine (DMPC; 14 carbons/chain) and dihexanoylphosphatidylcholine (DHPC; 6 carbons/chain) mixture [2]. If translocation of polymers thorough the nanpores can be observed, this system would be an ideal system to investigate the material transportation in real cells.

In this study, the effect of polyethyleneglycol (PEG) on the stability of SUVs consisting of DMPC and DHPC mixture has been investigated by small angle neutron scattering (SANS) for the first step. The SANS experiments were performed using SANS-U at the C1-2 port of JRR-3 at Japan Atomic Energy Agency (JAEA), Tokai [3]. The lipid mixture of [DHPC]:[DMPC] = 1:3.2 was dissolved in a D_2O solution of 3 mM $CaCl_2$. The lipid concentration of the solution was controlled to be 0.9 vol%. The obtained solution was kept at 30°C for thirty minutes to make homogeneous SUV solution, and mixed with the twice amount of PEG solution (100 mg/mL PEG and 3 mM $CaCl_2$).

Figure 1 shows the SANS profiles after the addition of PEG solution. The period of fringes becomes shorter than that before the addition. This result indicates that the reconstruction of SUVs occured, because the period of fringes is inversely proportional to the size of SUVs. The size of SUVs after the addition of PEG solution depends on the molecular weight of the PEG. However, the origin of the reconstruction of SUVs has not been understood yet.

References

[1] N. E. Gabriel and M. F. Roberts, Biochemistry **23**, 4011 (1984).

[2] N. L. Yamada, M. Hishida, and N. Torikai, Phys. Rev. E, **79**, 032902 (2009).

[3] S. Okabe, M. Nagao, T. Karino, S. Watanabe, T. Adachi, H. Shimizu, and M. Shibayama, J. Appl. Cryst. **38**, 1035 (2005).

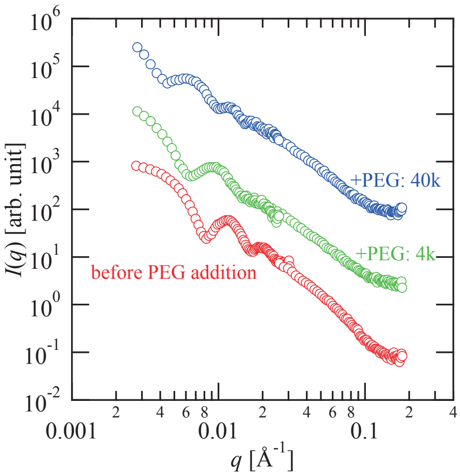

Fig. 1. SANS profiles before and after the addition of PEG solution.

1-5-25

Relation between bending modulus and spontaneous curveture in DGI/SDS/D2O system

H. Mayama(A), X. J. Chen(A), M. Nagao(B), H. Seto(C) and K. Tsujii(A)
(A)Nanotechnology Research Center, RIES, Hokkaido Univ., (B)ISSP-NSL Univ. Tokyo, (C)Dept. Phys, Kyoto Univ.

A non-ionic surfactant, n-dodecyl glyceryl itaconate (DGI), self-assembles into bilayer membranes in water having a spacing distance of sub-micrometer in the presence of small amounts of ionic surfactants, and forms multi-lamellar structure which indicates beautiful iridescent color because of Bragg diffraction. We have found that the repeat distance between the bilayers distributes in the scale range between 130 nm (red) and 180 nm (blue) in the suitable concentration range of ionic surfactant and it decreases with increasing the concentration (J. Colloid Inf. Sci. 305 (2007) 308). In order to understand fundamental question why this system maintains long repeat distance on the order of 100 nm, we have studied on membrane dynamics in the DGI/SDS/D2O system. We found that the membrane dynamics can be described very well by the theory of Zilman and Granek (PRL 77 (1996) 4788) and bending modulus kappa was increased from 20 kT to 40 kT with increasing the concentration of SDS (decreasing of repeat distance) as shown in Fig. 1. Through other experiments on direct observation of multilamellar structure in our previous study, we found that self-assembled DGI forms giant onions consisted of the stacked DGI bilayers and the radius of curvature is changed between 10 (higher SDS concentration, onion structure) and several hundred micrometer (lower SDS concentration, flat onion structure). The relation between the spontaneous curvature and the bending modulus would give us a clue to understand the question.

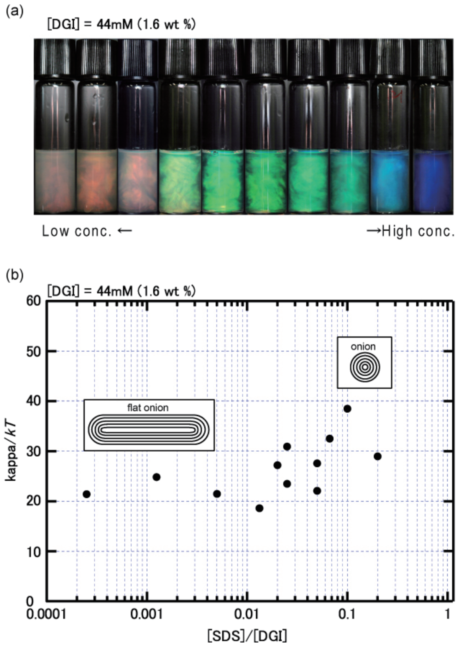

Fig. 1. Iridescent color of DGI/SDS/D2O system (a) and dependence of bending modulus kappa on SDS concentration. The insets: schematic representation of onion structures consisted of stacked layers at lower (left) and higher SDS concentrations (right).

1-5-26

Conformation and Dynamics of Polyrotaxane in Solution

Koichi Mayumi, Hitoshi Endo, Noboru Osaka, Hideaki Yokoyama, Mitsuhiro Shibayama, Kohzo Ito
Graduate School of Frontier Sciences, The University of Tokyo, Institute for Solid State Physics, The University of Tokyo

Polyrotaxane (PR) is a typical supramolecule, in which cyclic molecules are threaded onto a linear polymer chain [1]. The cyclic molecules in PR can slide and rotate on the polymer chain, and the degree of freedom of movement within a chain is the most unique feature of PR. This additional kinetic freedom has been utilized to produce functional nanomaterials having novel dynamical properties [2]. For example, PR, composed of polyethylene glycol (PEG) and α-cyclodextrins (CDs), was applied to a novel kind of polymer network, called “slide-ring gel” [3], which was prepared by cross-linking CDs belonging to different PR. The cross-linking point of slide-ring gels can slide along the polymer chain, and this unique structure causes the high extensibility and huge degree of swelling ratio in slide-ring gels. These remarkable physical properties were derived from nanoscale sliding motion of cyclic molecules.

We investigated the conformation and dynamics of polyrotaxane (PR) composed of polyethylene glycol (PEG) and α-cyclodextrins (CDs) by means of small angle neutron scattering (SANS) and neutron spin echo (NSE) technique, respectively. We analyzed the scattering functions for polyrotaxane in DMSO using a form factor based on the wormlike chain model, and it was found that the persistence length for PR dissolved in DMSO was approximately 30 , which is three times as large as that of PEG dissolved in DMSO [4]. Furthermore, the monomer dynamics of PR observed by NSE measurements was slower than that of PEG [5]. These findings indicate that threading CDs into PEG stretched the PEG chain and suppressed the local dynamics.

[1] A. Harada, J. Li, M. Kamachi, Nature (London) 356, 325 (1992)..
[2] J. Araki, K. Ito, Soft matter 3, 1456 (2007).
[3] Y. Okumura, and K. Ito, Adv. Mater. 13, 485 (2001).
[4] K. Mayumi, N. Osaka, H. Endo, H. Yokoyama, Y. Sakai, M. Shibayama, K. Ito, Macromolecules, 41, 6480 (2008).
[5] K. Mayumi, N. Nagao, H. Endo, N. Osaka, M. Shibayama, K. Ito, Physica B, in press.

Activity Report on Neutron Scattering Research: Experimental Reports **16** (2009)
Report Number: 946

1-5-27

Mechanically Interlocked Structure of Polyrotaxane Investigated by Contrast Variation Small Angle Neutron Scattering

Koichi Mayumi, Hitoshi Endo, Noboru Osaka, Hideaki Yokoyama, Mitsuhiro Shibayama, Kohzo Ito
Graduate School of Frontier Sciences, The University of Tokyo, Institute for Solid State Physics, The University of Tokyo

Advances of supramolecular chemistry has realized novel polymer architectures composed of several components noncovalently bonded [1]. One of the most promising supramolecules is polyrotaxane (PR) in which cyclic molecules are threaded into a liner polymer chain [2]. Covering the axial polymer chain with the cyclic molecules resulted in various applications to nanomaterials such as molecular tubes formed by cross-linking adjacent cyclic molecules in a single polyrotaxane and insulated molecular wires incorporating conductive polymers. The cyclic molecules in polyrotaxane are mechanically interlocked with the axial polymer, and slide and rotate on the chain. This additional kinetic freedom has been utilized to produce functional nanomaterials having novel dynamical properties, examples of which are drug delivery systems, multivalent ligand systems, energy transfer systems, and three-dimensionally cross-linked polyrotaxane networks with movable crosslinks. In particular the mechanically interlocked structure of polyrotaxane leads to various application to nanomaterials.

We performed contrast variation small angle neutron scattering measurements on polyrotaxane composed of polyethylene glycol (PEG) and α-cyclodextrins (CDs) in order to determine the detailed structure of PEG and CD in polyrotaxane. The scattering intensities I(Q) ’s for PR in mixtures of DMSO-d6 and DMSO were successfully decomposed into partial scattering functions for the components of polyrotaxane. The CD-PEG cross-term is positive, which corresponds to the mechainically interlocked connection between PEG and CD. In addition, the self-term of CD showed almost the same Q-dependence as the self-term of PEG. This indicated that the CDs in polyrotaxane are distributed randomly along the PEG chain. Contrast variation SANS is efficient to investigate static structures of components in supramolecular systems such as the conformations of and the correlations between the components in the system.

[1] Lehn, J. M. Supramolecular Chemistry: Concepts and Perspectives, VCH, Weinheim, 1995.
[2] Harada, A.; Hashidzume, A.; Takashima, Y. Adv. Polym. Sci. 2006, 201, 1.

1-5-28

QENS Study on Thermal Gelation in Agarose Aqueous Solution

N. Onoda-Yamamuro(A) and O. Yamamuro(B)
(A) Tokyo Denki Univ., (B) ISSP-NSL, Univ. Tokyo

Thermoreversible gelation of aqueous solution of macromolecules is due to the formation of a physically crosslinked network structure. Macroscopic properties, such as viscosity, change drastically with gelation. It is of interest whether microscopic motions such as diffusion of water molecules and segmental vibration of macromolecular chains change or not with gelation. Methylcellulose (MC) gels on heating due to hydrophobic interactions between methoxyl groups. We have shown that dynamic slowing down occurs not only for macroscopic properties but also for microscopic motion of both MC and water molecules by quasi-elastic neutron scattering (QENS) measurements [1]. In this study thermal gelation of agarose was examined. Agarose (AG) gels on cooling due to formation of hydrogen bonds.

QENS experiments were performed on AG solution using AGNES spectrometer, installed at C3-1 port of JRR-3M in Tokai. D2O, not H2O, was used as a solvent to observe both dynamics of water and AG molecules. The relative scattering intensity from H atoms of agarose to that from D atoms of D2O is expected to be comparable in this sample solution. The sample (3.0 wt-% solution) in this study geled around 315K on cooling and soled around 370K on heating.

The data were fitted well to the sum of a Lorentzian function and a Delta function, both of which are convoluted by resolution function as shown in Fig. 1 (a). The former is attributed to diffusive motion of water molecules and the latter to local vibrational motion of AG molecules. The self-diffusion coefficient D of water molecules was obtained from the Q-dependence of the HWHM of the Lorentzian function, while the mean square displacement u2 of AG molecules was obtained from the Q-dependence of the intensity of the Delta term. Temperature dependence of D and u2 are shown in Fig.1 (b). The mean square displacement abruptly decreased and the slope of the self-diffusion coefficient changed with gelation on cooling. The present results revealed that the microscopic motions of both water and AG molecules give rise to dynamic slowing down on thermal gelation.

[1] N. Onoda-Yamamuro et al. Physica B Condens. Matter, 393, 158 (2007).

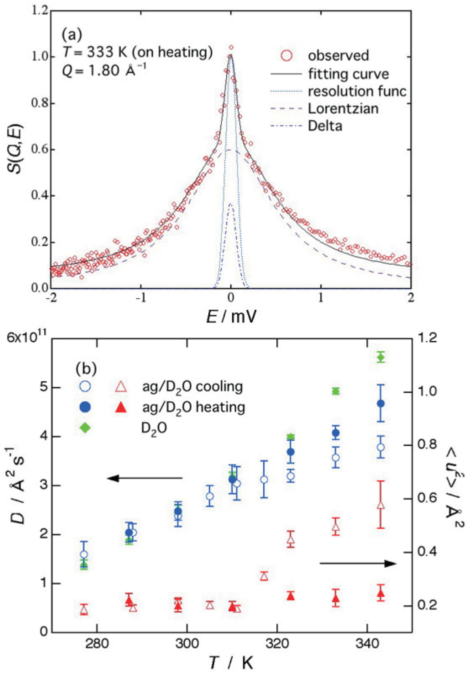

Fig. 1. Figure 1(a) An example of fits to S(Q,E) of the AG solution. (b) T dependence of the self-diffusion coefficient D of water and the mean square displacement <u2> of the local motion in AG molecules.

1-5-29

Aggregation Structure and Dynamics of Polymers at the Interface with Water I: Analysis of Aggregation Structure by Neutron Reflectivity

Hironori Atarashi(1), Toshihiko Nagamura(1), Masahiro Hino(2), Keiji Tanaka(1)
1.Department of Applied Chemistry, Kyushu University, Fukuoka 819-0395, Japan, 2. Research Reactor Institute, Kyoto University, Kumatori, Osaka 590-0494, Japan

Recently, a microwave treatment has been widely adopted for polymer synthesis because the treatment accelerates the movement of reactants in the system. The advantage of the treatment is not only shortening of the reaction time but also easy controlling of the yield and tacticity. However, it seems to us that the effectiveness of the microwave treatment on time evolution of aggregation states in polymer solids has not been discussed yet. In this study, we examined the microwave effect on interfacial evolution of polystyrene (dPS) bilayers with the aid of neutron reflectivity (NR) so that acceleration of chain diffusion by microwave can be discussed.

Monodisperse PS and deuterated PS (dPS) were used as samples. Molecular weights of PS and dPS were 87k and 80k, respectively. A dPS film was prepared on a silicon (Si) substrate with a native oxide layer by a spin-coating method. And, a PS film, which was independently spin-coated on a glass substrate, was mounted onto the dPS film by a floating method. Each film thickness was approximately 50 nm. The PS/dPS films so-prepared were dried under vacuum for 24 h at room temperature, and microwave with the power of 150 W was irradiated on them under the ambient atmosphere for 1.5 min and 3 min. Then, the specimens were applied to NR measurements using MINE2 spectrometer.

Figure 1 (a) shows the NR profiles for the PS/dPS bilayer films before and after the microwave treatment. The open symbols denote experimental data and solid lines show bets-fitting curves calculated on the basis of the model scattering length density (b/V) profiles shown in the panel (b) of Figure 1. The interface between PS and dPS layers before the treatment was sharp. The width is basically arisen from the surface roughness of the original PS and/or dPS film/s. On the other hand, once the bilayer was treated by microwave, the interface disappeared and the (b/V) value in the internal region became 3.72 x 10-4 nm-2, which was almost the middle of the (b/V) values for PS and dPS. This means that PS and dPS chains interdiffused each other, resulting in the formation of homogenous phase in the film. The (b/V) profiles treated for 1.5 min and 3 min were almost the same. Thus, chain interdiffusion in the bilayer reached a quasi-equilibrium state even by the 1.5 min.-treatment. Interestingly, the (b/V) value was higher near the substrate interface than in the interior region. This makes it clear that the dPS component was enriched at the substrate interface in the film being in a quasi-equilibrium state. The detail mechanism of how the treatment affects on chain diffusion, especially, a thermal effect induced by surrounding substance, will be reported in the near future.

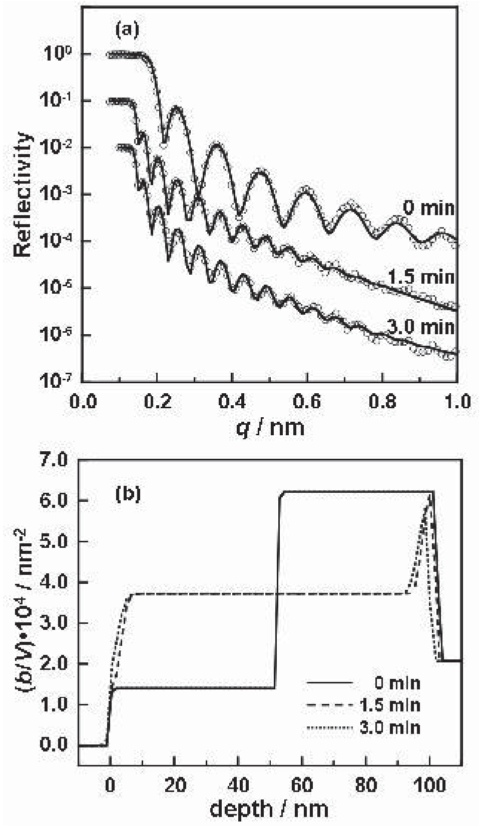

Fig. 1. Figure 1 (a) Neutron reflectivity for a PS/dPS film treated by microwave for 0, 1.5, and 3 min. The scattering length density profiles is shown in (b). For clarify, each data is off-set by a decade.

1-5-29

1-5-30

Aggregation Structure and Relaxation Dynamics of Polymers at the Interface with Water: II. Analysis of Relaxation Dynamics by Neutron Spin Echo

Hironori Atarashi(1), Toshihiko Nagamura(1), Keiji Tanaka(1), Hitoshi Endo(2), and Mitsuhiro Shibayama(2)

1. Department of Applied Chemistry, Kyushu University, Fukuoka 819-0395, Japan, 2. Institute for Solid State Physics, The University of Tokyo, Chiba 277-8581, Japan

Recently, polymer and liquid interface is widely studied, because aggregation states of polymers at liquid interface are important for science and technological application such as lubricate, adhesive, and biocompatibility. We have studied about the structure of poly(methyl methacrylate) (PMMA) contacted with non-solvent by using neutron reflectivity and scanning force microscope.[1] As a result, water and methanol, in spite of non-solvent for PMMA, made PMMA film swollen. In this study, the swollen structure, especially the interface structure between PMMA and non-solvent, of PMMA particles were studied by using small angle neutron scattering instrument, University of Tokyo (SANS-U) and new issp neutron spin echo (iNSE).

PMMA particles with diameter of about 300-500 nm (MP-2200 produced by Soken Chemical & Engineering Co., Ltd.) were used as a sample. Deuterated water (D2O) and deuterated methanol (CD3OD) was used as a non-solvent. The PMMA particles mixed with non-solvent were filled into quartz cell with 2 mm optical length. The sample-to-detector distance was chosen to be 2 and 12 m.

Figure 1 (a) shows the SANS profiles for PMMA particles on 25 and 40 °C mixed with water. Incoherent component was bated as background, and the profiles were fitted with power function. The value of fitted power was almost about 4 both in whole q region. It means that the shape of PMMA particles was not changed with temperature change. Additionally, to see more detail in small range, Porod plot was carried on. As a result, the power for q increased with increasing temperature. It means that the interfacial thickness between PMMA and water became broader with temperature increasing. Figure 1(b) shows the SANS profiles for PMMA particle mixed with methanol. In high q region, it is clear that the value of power was lower than it in low q region. That means the interfacial thickness between PMMA and methanol is broad and that broadening is bigger in compared with the case of water. We performed iNSE measurement using same sample. A certain relaxation was observed in the case of PMMA particles in D2O at 85 °C. We will clarify the dynamics of PMMA chain at the interface between PMMA and non-solvent.

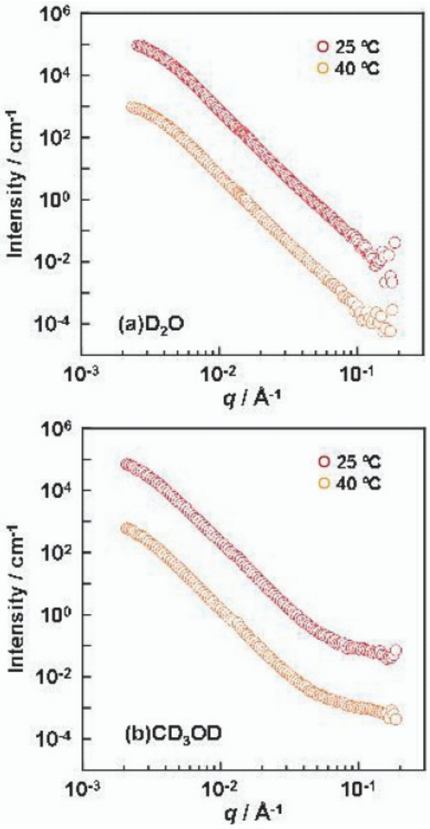

Fig. 1. Figure 1 Temperature dependence of SANS profiles (a) in D2O and (b) in CD3OD.

1-5-31

An Effect of Electromagnetic Wave Treatment on Polymer Diffusion

Hironori Atarashi(1), Toshihiko Nagamura(1), Masahiro Hino(2), Keiji Tanaka(1)
1. Department of Applied Chemistry, Kyushu University, Fukuoka 819-0395, Japan, 2. Resarch Reactor Institute, Kyoto University, Kumatori, Osaka 590-0494, Japan

Recently, a microwave treatment has been widely adopted for polymer synthesis because the treatment accelerates the movement of reactants in the system. The advantage of the treatment is not only shortening of the reaction time but also easy controlling of the yield and tacticity. However, it seems to us that the effectiveness of the microwave treatment on time evolution of aggregation states in polymer solids has not been discussed yet. In this study, we examined the microwave effect on interfacial evolution of polystyrene (dPS) bilayers with the aid of neutron reflectivity (NR) so that acceleration of chain diffusion by microwave can be discussed.

Monodisperse PS and deuterated PS (dPS) were used as samples. Molecular weights of PS and dPS were 87k and 80k, respectively. A dPS film was prepared on a silicon (Si) substrate with a native oxide layer by a spin-coating method. And, a PS film, which was independently spin-coated on a glass substrate, was mounted onto the dPS film by a floating method. Each film thickness was approximately 50 nm. The PS/dPS films so-prepared were dried under vacuum for 24 h at room temperature, and microwave with the power of 150 W was irradiated on them under the ambient atmosphere for 1.5 min and 3 min. Then, the specimens were applied to NR measurements using MINE2 spectrometer.

Figure 1 (a) shows the NR profiles for the PS/dPS bilayer films before and after the microwave treatment. The open symbols denote experimental data and solid lines show bets-fitting curves calculated on the basis of the model scattering length density (b/V) profiles shown in the panel (b) of Figure 1. The interface between PS and dPS layers before the treatment was sharp. The width is basically arisen from the surface roughness of the original PS and/or dPS film/s. On the other hand, once the bilayer was treated by microwave, the interface disappeared and the (b/V) value in the internal region became 3.72 x 10-4 nm-2, which was almost the middle of the (b/V) values for PS and dPS. This means that PS and dPS chains interdiffused each other, resulting in the formation of homogenous phase in the film. The (b/V) profiles treated for 1.5 min and 3 min were almost the same. Thus, chain interdiffusion in the bilayer reached a quasi-equilibrium state even by the 1.5 min.-treatment. Interestingly, the (b/V) value was higher near the substrate interface than in the interior region. This makes it clear that the dPS component was enriched at the substrate interface in the film being in a quasi-equilibrium state. The detail mechanism of how the treatment affects on chain diffusion, especially, a thermal effect induced by surrounding substance, will be reported in the near future.

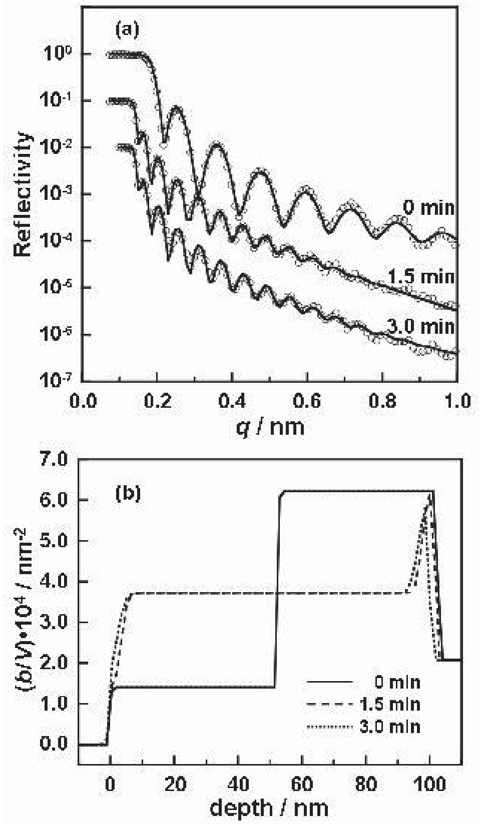

Fig. 1. Figure 1 (a) Neutron reflectivity for a PS/dPS film treated by microwave for 0, 1.5, and 3 min. The scattering length density profiles shown in (b). For clarify, each data is off-set by a decade.

1-5-31

1-5-32

Aggregation Structure and Relaxation Dynamics of Polymers at the Interface with Water: I. Analysis of Aggregation Structure by Neutron Reflectivity

Hironori Atarashi(1), Toshihiko Nagamura(1), Masahiro Hino(2), Keiji Tanaka(1)
1. Department of Applied Chemistry, Kyushu University, Fukuoka 819-0395, Japan, 2. Research Reactor Institute, Kyoto University, Kumatori, Osaka 590-0494, Japan

When a polymer material is used as a biomaterial in human body, the polymer surface is contact with liquid such as blood. Thus, to know the detail of interface between polymer and liquid is important to make high functional materials. In this study, we evaluated the swollen structure of poly(methyl methacrylate) (PMMA) contacted with alcohols.

A deuterated PMMA (dPMMA) with molecular weight of 296k was used as a sample. A dPMMA film was spin-coated onto quartz from dPMMA toluene solution. The film thickness was adjusted to about 65 nm. The film was annealed for 24 h at 423 K under vacuum. Ethanol, 1-propanol, and 2-propanol were used as non-solvent.

Figure 1 (a) shows the NR profiles for the dPMMA films under air, ethanol, 1-propanol, and 2-propanol. The open symbols denote experimental data and solid lines show bets-fitting curves calculated on the basis of the model scattering length density (b/V) profiles shown in the panel (b) of Figure 1 (Figure 1 (b) was normalized with initial thickness in air). The dPMMA films were swollen under all alcohols. However, the swollen behavior was different by alcohol. In the case of ethanol, ethanol diffused into dPMMA film and the ethanol contents in whole film was 13 vol.%. Then film thickness of dPMMA contacted with ethanol increased and the ration of increasing film thickness was 1.19, and the interface between dPMMA and ethanol became rough. Also, in the case of both 1-propanol and 2-propanol, dPMMA films were swollen and alcohol contents was 5.7 vol.%. Then the film thickness of dPMMA in contact with both 1-propanol and 2-propanol increased and the ratio was 1.12. Interestingly, all alcohols through the dPMMA film and segregated to quartz interface. The detail of swollen structure and swollen mechanism of dPMMA under alcohols will be reported in the near future.

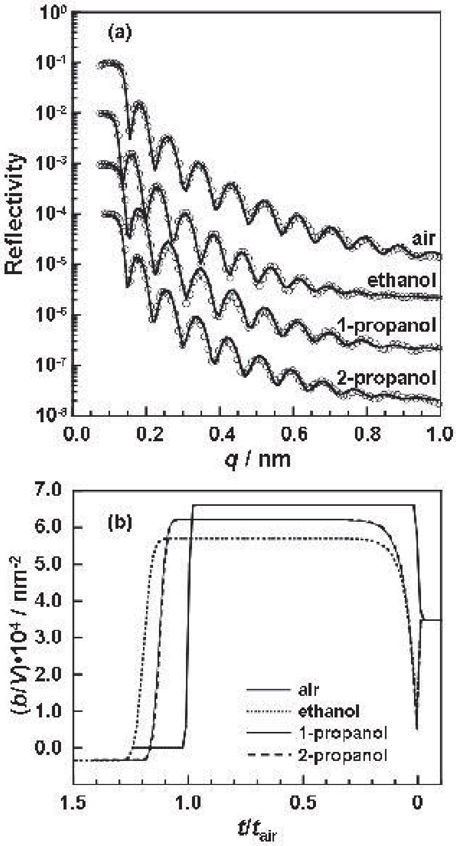

Fig. 1. Figure 1 (a) Neutron reflectivity for a dPMMA films under air, ethanol, 1-propanol, and 2-propanol. The scattering length density profiles is shown in (b). For clarify, each data is off-set by a decade.

1-5-33

Aggregation Structure and Relaxation Dynamics of Polymers at the Interface with Water: I. Analysis of Aggregation Structure by Neutron Reflectivity

Hironori Atarashi(1), Toshihiko Nagamura(1), Masahiro Hino(2), Keiji Tanaka(1)
1. Department of Applied Chemistry, Kyushu University, Fukuoka 819-0395, Japan, 2. Research Reactor Institute, Kyoto University, Kumatori, Osaka 590-0494, Japan

New tools for tailor-made diagnostics are generally made from polymers. In these applications, the polymer surface is in contact with a water phase. However, despite the importance of detailed knowledge of the fundamental interactions of polymer interfaces with liquids, such studies are very limited. We have hitherto studied aggregation structure of poly(methyl methacrylate) (PMMA) at the interfaces with non-solvents such as water, hexane and methanol by neutron reflectivity.[1] As a result, the liquid/polymer interfaces were diffuse in comparison with the air/polymer interface, probably due to interfacial roughening and the partial dissolution of segments at the outermost region of the film. In this study, we focus on alcohol with different alkyl lengths as non-solvents so that an impact of solubility parameter on the interfacial aggregation states can be discussed. A deuterated PMMA (dPMMA) with number-average molecular weight of 296k was used as a sample. A film of dPMMA was spin-coated onto a quartz block from a toluene solution. The film thickness was adjusted to be about 65 nm. The film was annealed for 24 h at 423 K under vacuum. Ethanol, 1-propanol, and 2-propanol were used as non-solvents.

Figure 1 (a) shows the NR profiles for the dPMMA films under air, ethanol, 1-propanol, and 2-propanol. The open symbols denote experimental data and solid lines show best-fitting curves calculated on the basis of the model scattering length density (b/V) profiles shown in the panel (b), where the abscissa was normalized with the initial thickness in air. While the dPMMA film was discernibly swollen under all alcohols, the extent was not the same among them. Interestingly, the segregation of alcohol molecules was observed at the substrate interface for all the cases. The overall contents of ethanol, 1-propanol and 2-propanol in the film were 13, 5.7 and 5.7 vol.%, respectively. The solubility parameters for ethanol, 1-propanol, 2-propanol and PMMA are, respectively, 26.0, 24.3, 23.5 and 22.7. Thus, to what extent alcohol molecules penetrate into the film can be hardly explained only in terms of the solubility parameter. The size of penetrants should be also taken into account.

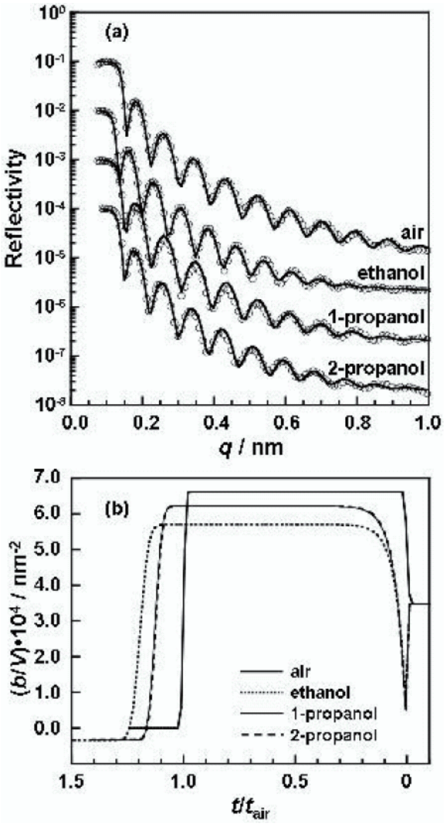

Fig. 1. Figure 1 (a) Neutron reflectivity for a dPMMA films under air, ethanol, 1-propanol, and 2-propanol. The scattering length density profiles are shown in (b). For clarify, each data is off-set by a decade.

1-5-34

Aggregation Structure and Relaxation Dynamics of Polymers at the Interface with Water: II. Analysis of Relaxation Dynamics by Neutron Spin Echo

Hironori Atarashi(1), Toshihiko Nagamura(1), Keiji Tanaka(1), Hitoshi Endo(2), and Mitsuhiro Shibayama(2)
1. Department of Applied Chemistry, Kyushu University, Fukuoka 819-0395, Japan, 2. Institute for Solid State Physics, The University of Tokyo, Chiba 277-8581, Japan

New tools for tailor-made diagnostics are generally made from polymers. In these applications, the polymer surface is in contact with a water phase. However, despite the importance of detailed knowledge of the fundamental interactions of polymer interfaces with liquids, such studies are very limited. We have hitherto studied aggregation structure of poly(methyl methacrylate) (PMMA) at the interfaces with non-solvents by neutron reflectivity.[1] As a result, the liquid/polymer interfaces were diffuse in comparison with the air/polymer interface, probably due to interfacial roughening and the partial dissolution of segments at the outermost region of the film. In this study, relaxation dynamics of PMMA chains at the interfaces with typical non-solvents such as water and methanol was discussed on the basis of small angle neutron scattering (SANS-U) and neutron spin echo (iNSE) measurements. PMMA particles with diameter of about 300-500 nm (MP-2200 produced by Soken Chemical & Engineering Co., Ltd.) were used as a sample to increase the scattering volume rather than a film. Deuterated water (D2O) and ethanol (CD3OD) were used as non-solvents. The PMMA particles mixed with a non-solvent were filled into a quartz cell with 2 mm optical length. The sample-to-detector distance was chosen to be 2 and 12 m.

Figure 1 (a) shows the SANS profiles for PMMA particles with water, which the incoherent contribution was subtracted, at 25 and 40 °C. The power for the linear relation was approximately 4 for both cases. Taking into account that the specimen was PMMA particles, the result is quite reasonable. Interestingly, the power seems to deviate from 4 at q>10-1 A-1 at 40 ℃. This may indicate that the interface between PMMA and water became broader with increasing temperature. Figure 1(b) shows the SANS profiles for PMMA particles with methanol. In this case, the slope transformed 4 to smaller once q went beyond 5*10-2 A-1. This means that the interface between PMMA and methanol was quite diffused in comparison with the case of water. Then, iNSE measurement was made using the same sample. A certain relaxation was somehow observed both in the case of PMMA particles with D2O and CD3OD. The detail analysis for the results has undergone several revisions.

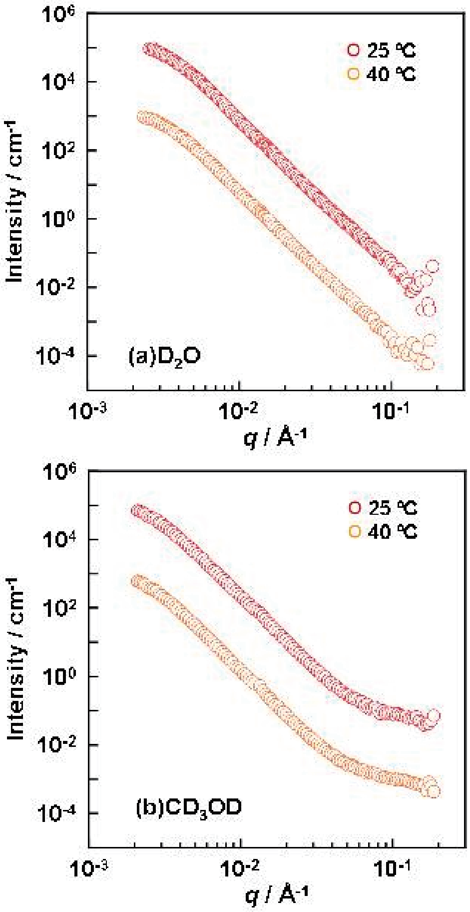

Fig. 1. Figure 1 Temperature dependence of SANS profiles (a) in D2O and (b) in CD3OD.

1-5-34

1-5-35

Large scale structure and crossover of critical phenomena induced by solvation effect

Seto H., Sadakane K. [1], Iguchi N.[1], and Endo H.[2]

Institute of Materials Research Science, KEK, [1] Department of Physics, Kyoto Univ., [2] ISSP, Univ. of Tokyo

The binary mixture of water and 3-methylpyridine, which shows LCST type phase separation, is known to have a large salt effect. In this study, we selected sodium tetraphenylborate ($NaBPh_4$), whose affinities of anion and cation with water are largely different, as a salt because the solvation effect should be intensive and the formation of large clusters is expected theoretically. In cases of the lower amount of $NaBPh_4$ and water-rich concentration, the mixture becomes colored in blue, and changes to orange with approaching critical temperature. This result suggests that a periodic structure is formed, and its repeat distance increases with increasing temperature. For the mixtures with 100 mM $NaBPh_4$, the SANS profiles have a peak around Q =0.1 A^{-1}, and the peak position shifts to lower-Q with increasing temperature. (K. Sadakane et al., J. Phys. Soc. Jpn. 76, 113602 (2007).)

In order to investigate the solvation effect by adding $NaBPh_4$, further experiments are performed at SANS-U. The scattering profiles are successfuly interpreted with the function proposed by Onuki and Kitamura. The temperature dependence of the critical concentration fluctuation shows 3D-Ising behavior when the salt concentration is low enough. On the other hand, the critical behavior is changed to 2D-Ising with increasing the salt concentration. This result can be interpreted that the concentration fluctuation is limited in 2 dimensional region due to the emergence of the layered structure. This crossover is reproduced in the cases of adding ionic surfactant such as AOT and SDS. Thus we conclude that a membrane-like structure is formed near the critical point by the coupling of the salvation effect and the critical concentration fluctuation as suggested by Onuki and Kitamura theoretically.

Neutron Spin Echo experiments are performed at iNSE in the mixture of water, 3MP and $NaBPh_4$. The intermediated correlation function can be interpreted with the model proposed by Zilman and Granek. This evidence verifies the formation of the membrane-like structure by adding $NaBPh_4$.

1-5-36

Aggregation Structure and Relaxation Dynamics of Polymers at the Interface with Water: I. Analysis of Aggregation Structure by Neutron Reflectivity

Hironori Atarashi(1), Toshihiko Nagamura(1), Masahiro Hino(2), Keiji Tanaka(1)
1. Department of Applied Chemistry, Kyushu University, Fukuoka 819-0395, Japan, 2. Research Reactor Institute, Kyoto University, Kumatori, Osaka 590-0494, Japan

New tools for tailor-made diagnostics are generally made from polymers. In these applications, the polymer surface is in contact with a water phase. However, despite the importance of detailed knowledge of the fundamental interactions of polymer interfaces with liquids, such studies are very limited. We have hitherto studied aggregation structure of poly(methyl methacrylate) (PMMA) at the interfaces with non-solvents such as water, hexane and methanol by neutron reflectivity.[1] As a result, the liquid/polymer interfaces were diffuse in comparison with the air/polymer interface, probably due to interfacial roughening and the partial dissolution of segments at the outermost region of the film. In this study, we focus on alcohol with different alkyl lengths as non-solvents so that an impact of solubility parameter on the interfacial aggregation states can be discussed. A deuterated PMMA (dPMMA) with number-average molecular weight of 296k was used as a sample. A film of dPMMA was spin-coated onto a quartz block from a toluene solution. The film thickness was adjusted to be about 65 nm. The film was annealed for 24 h at 423 K under vacuum. Ethanol, 1-propanol, and 2-propanol were used as non-solvents.

Figure 1 (a) shows the NR profiles for the dPMMA films under air, ethanol, 1-propanol, and 2-propanol. The open symbols denote experimental data and solid lines show best-fitting curves calculated on the basis of the model scattering length density (b/V) profiles shown in the panel (b), where the abscissa was normalized with the initial thickness in air. While the dPMMA film was discernibly swollen under all alcohols, the extent was not the same among them. Interestingly, the segregation of alcohol molecules was observed at the substrate interface for all the cases. The overall contents of ethanol, 1-propanol and 2-propanol in the film were 13, 5.7 and 5.7 vol.%, respectively. The solubility parameters for ethanol, 1-propanol, 2-propanol and PMMA are, respectively, 26.0, 24.3, 23.5 and 22.7. Thus, to what extent alcohol molecules penetrate into the film can be hardly explained only in terms of the solubility parameter. The size of penetrants should be also taken into account.

References

[1]K. Tanaka, Y. Fujii, H. Atarashi, M. Hino, and Nagamura, Langmuir, 24, 296 (2008).

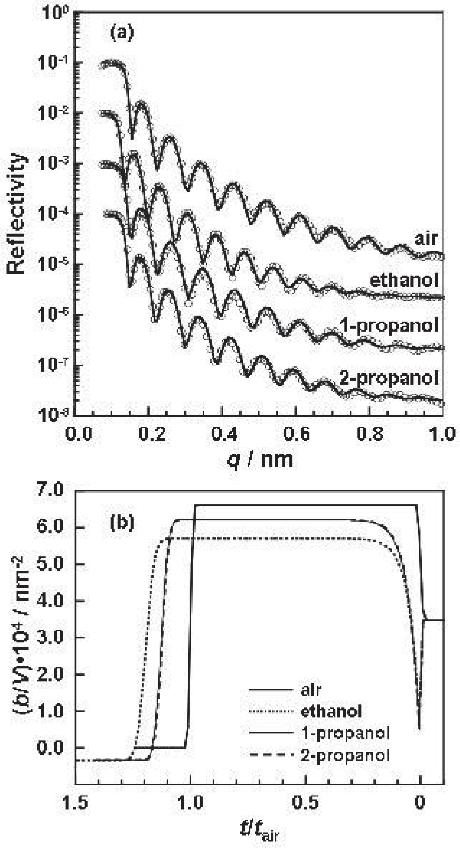

Fig. 1. (a) Neutron reflectivity for a dPMMA films under air, ethanol, 1-propanol, and 2-propanol. The scattering length density profiles are shown in (b). For clarify, each data is off-set by a decade.

1-5-36

1-5-37

An Effect of Electromagnetic Wave Treatment on Polymer Diffusion

Hironori Atarashi(1), Toshihiko Nagamura(1), Masahiro Hino(2), Keiji Tanaka(1)
1. Department of Applied Chemistry, Kyushu University, Fukuoka 819-0395, Japan, 2. Resarch Reactor Institute, Kyoto University, Kumatori, Osaka 590-0494, Japan

Recently, a microwave treatment has been widely adopted for polymer synthesis because the treatment accelerates the movement of reactants in the system. The advantage of the treatment is not only shortening of the reaction time but also easy controlling of the yield and tacticity. However, it seems to us that the effectiveness of the microwave treatment on time evolution of aggregation states in polymer solids has not been discussed yet. In this study, we examined the microwave effect on interfacial evolution of polystyrene (dPS) bilayers with the aid of neutron reflectivity (NR) so that acceleration of chain diffusion by microwave can be discussed.

Monodisperse PS and deuterated PS (dPS) were used as samples. Molecular weights of PS and dPS were 87k and 80k, respectively. A dPS film was prepared on a silicon (Si) substrate with a native oxide layer by a spin-coating method. And, a PS film, which was independently spin-coated on a glass substrate, was mounted onto the dPS film by a floating method. Each film thickness was approximately 50 nm. The PS/dPS films so-prepared were dried under vacuum for 24 h at room temperature, and microwave with the power of 150 W was irradiated on them under the ambient atmosphere for 1.5 min and 3 min. Then, the specimens were applied to NR measurements using MINE2 spectrometer.

Figure 1 (a) shows the NR profiles for the PS/dPS bilayer films before and after the microwave treatment. The open symbols denote experimental data and solid lines show bets-fitting curves calculated on the basis of the model scattering length density (b/V) profiles shown in the panel (b) of Figure 1. The interface between PS and dPS layers before the treatment was sharp. The width is basically arisen from the surface roughness of the original PS and/or dPS film/s. On the other hand, once the bilayer was treated by microwave, the interface disappeared and the (b/V) value in the internal region became 3.72 x 10-4 nm-2, which was almost the middle of the (b/V) values for PS and dPS. This means that PS and dPS chains interdiffused each other, resulting in the formation of homogenous phase in the film. The (b/V) profiles treated for 1.5 min and 3 min were almost the same. Thus, chain interdiffusion in the bilayer reached a quasi-equilibrium state even by the 1.5 min.-treatment. Interestingly, the (b/V) value was higher near the substrate interface than in the interior region. This makes it clear that the dPS component was enriched at the substrate interface in the film being in a quasi-equilibrium state. The detail mechanism of how the treatment affects on chain diffusion, especially, a thermal effect induced by surrounding substance, will be reported in the near future.

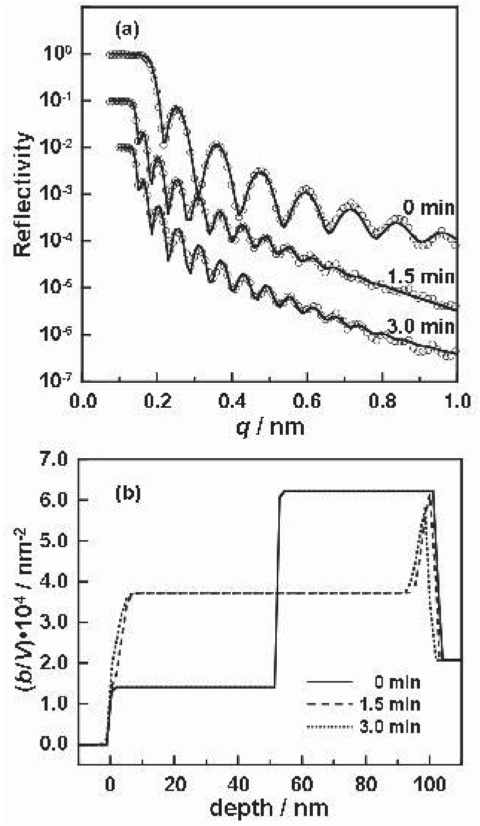

Fig. 1. (a) Neutron reflectivity for a PS/dPS film treated by microwave for 0, 1.5, and 3 min. The scattering length density profiles are shown in (b). For clarify, each data is off-set by a decade.

1-5-37

1-5-38

Aggregation Structure and Relaxation Dynamics of Polymers at the Interface with Water: II. Analysis of Relaxation Dynamics by Neutron Spin Echo

Hironori Atarashi(1), Toshihiko Nagamura(1), Keiji Tanaka(1), Hitoshi Endo(2), and Mitsuhiro Shibayama(2)
1. Department of Applied Chemistry, Kyushu University, Fukuoka 819-0395, Japan, 2. Institute for Solid State Physics, The University of Tokyo, Chiba 277-8581, Japan

New tools for tailor-made diagnostics are generally made from polymers. In these applications, the polymer surface is in contact with a water phase. However, despite the importance of detailed knowledge of the fundamental interactions of polymer interfaces with liquids, such studies are very limited. We have hitherto studied aggregation structure of poly(methyl methacrylate) (PMMA) at the interfaces with non-solvents by neutron reflectivity.[1] As a result, the liquid/polymer interfaces were diffuse in comparison with the air/polymer interface, probably due to interfacial roughening and the partial dissolution of segments at the outermost region of the film. In this study, relaxation dynamics of PMMA chains at the interfaces with typical non-solvents such as water and methanol was discussed on the basis of small angle neutron scattering (SANS-U) and neutron spin echo (iNSE) measurements. PMMA particles with diameter of about 300-500 nm (MP-2200 produced by Soken Chemical & Engineering Co., Ltd.) were used as a sample to increase the scattering volume rather than a film. Deuterated water (D2O) and ethanol (CD3OD) were used as non-solvents. The PMMA particles mixed with a non-solvent were filled into a quartz cell with 2 mm optical length. The sample-to-detector distance was chosen to be 2 and 12 m.

Figure 1 (a) shows the SANS profiles for PMMA particles with water, which the incoherent contribution was subtracted, at 25 and 40 °C. The power for the linear relation was approximately 4 for both cases. Taking into account that the specimen was PMMA particles, the result is quite reasonable. Interestingly, the power seems to deviate from 4 at q>10-1 A-1 at 40 ℃. This may indicate that the interface between PMMA and water became broader with increasing temperature. Figure 1(b) shows the SANS profiles for PMMA particles with methanol. In this case, the slope transformed 4 to smaller once q went beyond 5*10-2 A-1. This means that the interface between PMMA and methanol was quite diffused in comparison with the case of water. Then, iNSE measurement was made using the same sample. A certain relaxation was somehow observed both in the case of PMMA particles with D2O and CD3OD. The detail analysis for the results has undergone several revisions.

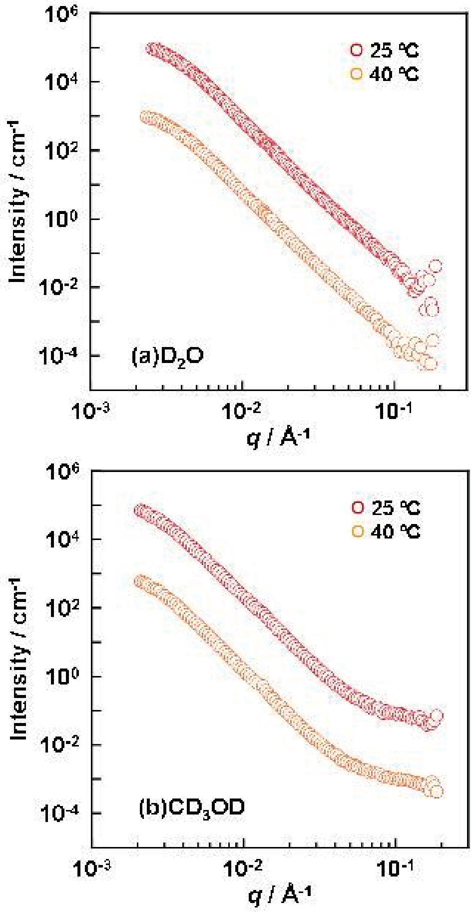

Fig. 1. Temperature dependence of SANS profiles (a) in D2O and (b) in CD3OD.

1-5-38

1.　中性子散乱　6）生　物

1. Neutron Scattering　6) Biology

1-6-1

Hydration Level Dependent Protein Dynamics Studied by Neutron Inelastic Scattering

H. Nakagawa and M. Kataoka

Quantum Beam Science Directorate, JAEA, Tokai, Ibaraki 319-1195

Water is indispensable for life. In physiological condition most proteins work in the solvated environment and water molecules on the protein surface strongly affects the protein dynamics. The dynamical transition of a protein, evidenced as an inflection in atomic mean-square displacements (MSDs) as a function of temperature, has been observed at 200 - 240 K with the hydrated protein [1]. In this study, we measured the hydration level dependent dynamical transition of protein Staphylococcal nuclease by incoherent neutron scattering. The neutron scattering experiments were performed with the triple axis spectrometer, LTAS, in the JRR-3M reactor in Tokai with an energy resolution of about 80 μ eV. The hydration levels of protein samples are 0.10 to 0.62 (g water/g protein). Inset of figure shows the temperature dependent atomic mean-square displacement (MSD) of protein with hydration level of 0.62 (g water/g protein). As the temperature increase, the MSD monotonously increases. At around 240 K, the protein shows the sharp rise in the MSD. This is so called dynamical transition, which is generally observed with the hydrated biomacromolecules [1]. The slope of the regression line of the temperature-dependent MSD is related to the resilience of molecular structure as a force constant [2]. The equation is below, d(MSD)/dT=0.00276/k ,where k is force constant (N/m). Figure shows the hydration level dependent slope. At higher hydration level, slope is larger, which indicates that the dynamical transition is enhanced by hydration. It was found that dynamical transition was more significant above the threshold hydration level around 0.4 (g water /g protein). This suggest that hydration water network on the protein surface with fully hydrated is closely related to the protein dynamics. The dynamical behavior of hydration water is coupled with the protein dynamics. Such a dynamical coupling drives the hydration dependent protein dynamical transition.

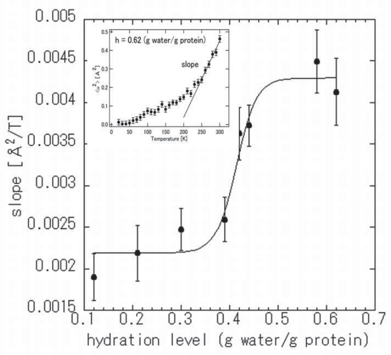

Figure 1: The slope of the regression line as a function of hydration level estimated by temperature dependent mean-square displacement between 250 K and 300 K as shown in inset.

References

1) W. Doster et al. :“Nature”,337, 754(1989).
2) G. Zaccai et al. :“Science”,288, 1605(2000).

原子炉：JRR-3　　装置：LTAS(C2-1)　　分野：中性子散乱（生物）

1-6-2

Neutron Diffraction Study of Porcine Pancreatic Elastase under Active Conditions

T. Tamada, T. Kinoshita[1], T. Ohhara, K. Kurihara, T. Tada[1] and R. Kuroki

Quantum Beam Science Directorate, JAEA, Tokai, Ibaraki 319-1195
[1]*Graduate School of Science, Osaka Prefecture University, Sakai, Osaka 599-8531*

Porcine pancreatic elastase (PPE) is a serine protease classified in the chymotrypsin family that is possibly the most destructive enzymes having the ability to degrade virtually all of the connective components in the body. Uncontrolled proteolytic degradation by pancreatic elastase (EC 3.4.21.36) causes the fatal disease pancreatitis. We have already determined the complex structure between PPE and its peptidic inhibitor at JRR-3 in JAEA by neutron crystallography.1),2) This neutron structure elucidated the tetrahedral intermediate state of catalysis by serine protease. For further clarification of catalytic mechanism of serine protease, we carried out the neutron diffraction analysis of PPE only at active conditions (pD8.0).

The single crystals of PPE were prepared under 0.2 *M* sodium sulfate in acidic condition (pD 5.0) using sitting-drop vapor diffusion method. The crystal was grown to the size of 1.3 mm^3 for neutron diffraction experiment by repeating macro-seeding trchniques under basic condition (pD8.0), and then sealed in quartz capillary for the diffraction study (Figure 1). Diffraction data were collected at room temperature using monochromatic neutron beam ($\lambda = 2.9$ Å) and recorded on a neutron imaging plate on a single-crystal diffractometer (BIX-3) at JRR-3 in JAEA. The crystal of PPE belongs to the space group $P2_12_12_1$ with cell dimensions of a = 52, b = 58, c = 75 Å. The total rotation ranges of 97.8° were covered by 326 still images with exposure time of 4 h./flame by step scanning method at BIX-3, respectively. Data were processed with the programs DENZO and SCALEPACK. Data set was integrated and scaled to 2.3 Å resolution. Data collection and processing statistics are shown in Table 1. Structural analysis is now in progress. Production of larger crystals is also proceeding to collect higher resolution data.

Table 1: Data collection and processing statistics

Resolution (Å)	2.3 (2.38-2.30)
No. of reflections	
obserbed	14,230
independent	8,140
Redundancy	1.7 (1.4)
Completeness (%)	77.0 (69.6)
Mean $I/\sigma(I)$	8.5 (3.5)
R_{merge}	0.116 (0.292)

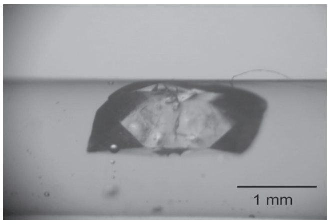

Figure 1: Crystal of porcine pancreatic elastase.

References

1) T. Kinoshita, T. Tamada, K. Imai, K. Kurihara, T. Ohhata, T. Tada, R. Kuroki : "Acta Crystalgr.", F64, 217 (2008).
2) T. Tamada, T. Kinoshita, K. Kurihara, M. Adachi, T. Ohhata, K. Imai, R. Kuroki, T. Tada : "J. Am. Chem. Soc.", in press.

原子炉：JRR-3　　装置：BIX-3(1G-A)　　分野：中性子散乱（生物）

1-6-3

Contrast Variation Measurements of Various Intermediates of Hen Egg White Lysozyme Amyloid Fibrils

S. Fujiwara, F. Matsumoto and H. Nakagawa
Quantum Beam Science Directorate, JAEA, Tokai, Ibaraki 319-1195

In neurodegenerative diseases such as Altzheimer's disease and Parkinson's disease, filamentous protein aggregates called amyloid fibrils are thought to be related to pathogenesis of these diseases. Elucidation of the mechanism of the amyloid fibril formation is thus important for the development of therapeutic strategies against the amyloid diseases. Moreover, since the amyloid fibrils are found to be formed by proteins that have nothing to do with diseases, it should be of considerable help to gain an insight into the generic properties of proteins related to the mechanisms of folding and stability. It was found that hen egg white lysozyme (HEWL) forms the amyloid fibrils in highly concentrated ethanol solution$^{1)}$. The HEWL-water-ethanol system is suitable to study the general mechanism of the amyloid fibril formation. From small-angle X-ray and neutron scattering (SAXS and SANS) measurements, we showed that a pathway of the amyloid fibril formation of HEWL consists of three stages; the formation of the dimers, the formation of the protofilaments, and the formation of the amyloid fibrils via a lateral association of the protofilaments$^{2)3)}$.

In order to understand the mechanism by which the amyloid fibril formation occurs in more detail, it is necessary to obtain detailed structural information of each intermediate structure. Here, we performed SANS experiments of three samples: 2 mg/ml HEWL solution in 90% ethanol, 10 mg/ml HEWL solution in 90% ethanol, and 10 mg/ml HEWL solution containing 1mM NaCl in 90% ethanol, which correspond to the protofilament state, the state where the lateral association of the protofilament occurs, and the final amyloid fibril state, respectively. The SANS curves of these HEWL solutions, prepared in various fractions of deuterated solvents, were measured with SANS-J at the guide hall of the reactor JRR-3M in JAEA, and cross-sectional Guinier analysis was done to estimate the cross-sectional radius of gyration at each contrast. Figure 1 shows the Stuhrmann plots$^{4)}$, the plots of square of the cross-sectional radius of gyration against a reciprocal of the contrast, of these solutions. The data of the 10 mg/ml HEWL solutions were fit with a linear function of $1/(\Delta\rho)$ while the data of the 2 mg/ml HEWL solution was fit with a quadratic function. These results imply that the protofilament has a low density region in a part of the peripheral region, while the amyloid fibrils have the low density region in a central region of the fibrils. Detailed analysis with aid of model calculation is currently underway.

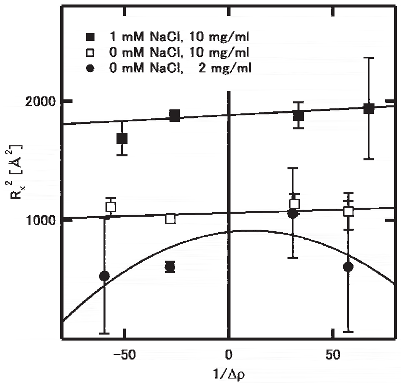

Figure 1: The Stuhrmann plots of the cross-section of the amyloid protofilament of HEWL. Filled and open squares denote the data at 10 mg/ml and 2 mg/ml, respectively.

References

1) S. Goda et al: "Protein. Sci." 9, 369 (2000).
2) Y. Yonezawa et al.: "J. Mol. Biol." 323, 237 (2002).
3) S. Fujiwara et al: "J. Mol. Biol." 331, 21 (2003).
4) H. B. Stuhrmann: "J. Appl. Cryst." 7, 173 (1974).

原子炉：JRR-3　　装置：SANS-J(C3-2)　　分野：中性子散乱（生物）

1-6-4

Small-Angle Neutron Scattering Measurements of Rhodanase-GroEL-GroES Complex

K. Ichimura, Y. Matsuura[1], S. Fujiwara[2], Y. Kawata[3] and H. Kihara[1]

Department of Biochemistry, Dokkyo University Medical Schoo, Mibu, Tochigi 321-0293
[1] *Department of Physics, Kansai Medical University, Hirakata 573-1136*
[2] *Quantum Beam Science Directorate, JAEA, Tokai, Ibaraki 319-1195*
[3] *Department of Biotechnology, Tottori University, Tottori 680-8552*

Elucidating how a protein is folded into the unique tertiary structure is one of the most important problems in biophysics. *In vivo*, they are apt to fold with the aid of chaperon proteins. GroEL, a chaperon protein from *E. coli*, forms hydrophobic bonds with the newly synthesized target protein, assisting the folding of the target protein. In order to elucidate the molecular mechanism of folding the target protein with the aid of the chaperon protein, it is important to elucidate various intermediate structures including the structure of the target protein when they are bound to chaperon protein, and the structure of GroEL in the ternary complex formed with GroES. As a first step towards this purpose, we employed neutron scattering to investigate the structure of the target protein bound to GroEL.

We used rhodanase as a target protein. Rhodanase is a monomeric protein of the molecular weight of 33-kDa, and its folding intermediate is known to bind to GroEL. Employing the mutated GroEL[1)], which takes stable complex with the target proteins and binds GroES at its complex with the target protein, made it possible to measure small-angle neutron scattering (SANS) curves of the rhodanase-GroEL complex. We prepared deuterated (d-) and undeuterated (h-) rhodanase, and mixed with GroEL and GroES at 1:1:1 stoichiometry in solvent containing 42% D_2O, at which the scattering length density of the solvent was matched to that of the undeuterated proteins.

We measured SANS curves of d-rhodanase-GroEL-GroES complex and h-rhodanase-GroEL-GroES complex with the Small-Angle Neutron Scattering Instrument (SANS-J) at the guide hall of the reactor JRR-3M in Japan Atomic Energy Agency. The measurements were done with the incident neutrons of the wavelength of 6.5 Å($\lambda/\Delta\lambda$=13.4%). To cover the Q-range as wide as possible, the measurements were done at two sample-to-detector distances, 6 m and 2.5 m. Figure 1 shows the difference curve of the SANS curve of d-rhodanase-GroEL-GroES and that of h-rhodanase-GroEL-GroEs, corresponding to the curve arising from rhodanase within the GroEL-GroES complex. The curve shows that under the condition where the measurements were done, rhodanase formed large complexes. It, however, clearly demonstrates the feasibility of the experiments.

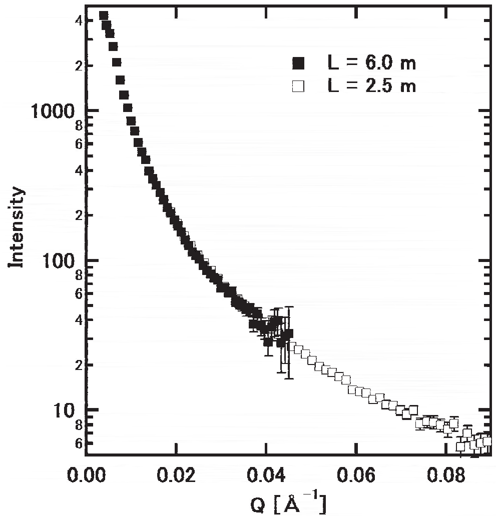

Figure 1: SANS curves of d-rhodanase-GroEL-GroES, h-rhodanase-GroEL-GroES, and the difference curves.

References

1) Y. Kawata et al: "Biochemistry" 38, 15731 (1999).

原子炉：JRR-3　　装置：SANS-J(C3-2)　　分野：中性子散乱（生物）

1-6-5

Neutron Diffraction of Protein Single Crystals in H_2O

S. Fujiwara, T. Ohhara and T. Chatake[1]

Quantum Beam Science Directorate, JAEA, Tokai, Ibaraki 319-1195
[1]*Research Reactor Institute, Kyoto University, Kumatori, Osaka 590-0494*

Neutron scattering and diffraction provide unique information that cannot be obtained from other methods for structural studies of biological macromolecules. Because of a large difference in the scattering length density of water and heavy water (-0.00562 × 10^{-12} cm $Å^{-3}$ for H_2O and 0.064 × 10^{-12} cm $Å^{-3}$ for $^2H(=D)_2O$) due to the difference in the scattering length of hydrogen (-0.3742 × 10^{-12} cm) and deuterium (0.6671 × 10^{-12} cm), it is possible to vary widely the scattering length density of solvent by changing the fraction of D_2O in the solvent. This "contrast variation" technique has found wide applications not only in small-angle neutron scattering but also in low-resolution neutron crystallography. Application of the contrast variation technique in neutron crystallography provides information on individual components in a very large macromolecular complex such as nucleic acid regions within viruses and nucleosomes, and on disordered components in the complex such as lipid moiety in lipoproteins and detergent moiety in membrane proteins. Essence in these applications is obtaining structural information of the region having distinct scattering length density. Thus, there is a possibility that the scattering density of amino acids is estimated because each amino acid has distinct scattering length density. Furthermore, neutron fiber diffraction measurements using the contrast variation technique obtained the results suggesting the possibility of distinguishing the static disorder and dynamic fluctuations1).

To explore such possibility of low-resolution neutron crystallography using the contrast variation technique, we started a project of the contrast variation measurements in the neutron diffraction. As a first step, we prepared a single crystal of proteins in H_2O, and measured diffraction patterns.

A crystal of RNase A was used in the measurements. The crystal, grown in H_2O solution to the size of about 2 mm^3, belongs to the space group $P2_1$ with cell dimensions of $a = 30.10$ Å, $b = 38.20$ Å, $c = 53.21$ Å, $\alpha = \gamma = 90°$, and $\beta = 108.17°$. Diffraction images were collected at room temperature using monochromatic neutron beam ($\lambda = 2.9$ Å) and recorded on a neutron imaging plate on a single-crystal diffractometer (BIX-3) at JRR-3 in JAEA. A total rotation range of 187° was covered by 375 oscillation images with an exposure time of 1800 sec/image by a rotation angle of 0.5°. Figure 1 shows an example of the diffraction images. The diffraction spots out to the resolution of about 2.0 Åwere observed. The data were processed with DENZO and SCALEPACK. Full data set out to 2.5 Åresolution was integrated and scaled. The observed reflections were merged into 3364 unique reflections with an R_{merge} of 0.096 and completeness of 84.3%. Structure analysis is now in progress.

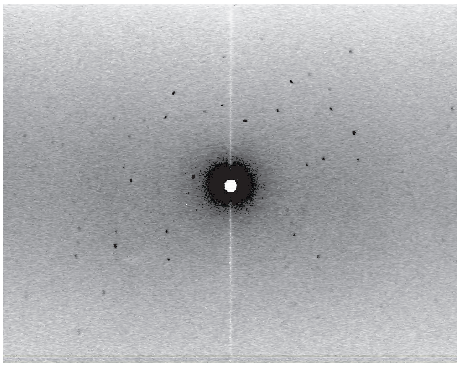

Figure 1: Example of the diffraction patterns collected at BIX-3.

References

1) S. Fujiwara et al.: "J. Struct. Biol." 167, 25 (2009).

原子炉：JRR-3　　装置：BIX-3(1G-A)　　分野：中性子散乱（生物）

1-6-6

Enhancement of Lipid Flip-Flop by Membrane Proteins and Transmembrane Peptides

M. Nakano(A), M. Fukuda(A), M. Miyazaki(A), Y. Wada(A), H. Endo(B)
(A)Graduate School of Pharmaceutical Sciences, Kyoto Univ., (B)ISSP-NSL, Univ. of Tokyo

Interbilayer transport and transbilayer movement of phospholipids are crucial for cell growth, development and survival, and are controlled by lipid transfer proteins and translocase enzymes. The endoplasmic reticulum (ER), in which phospholipids are newly synthesized on the cytosolic leaflet, maintains membrane symmetry, presumably by flippase activity, which is bidirectional and energy-independent. On the other hand, the plasma membrane retains asymmetric lipid distribution via aminophospholipid translocase that mediates the unidirectional transport of phosphatidylserine and phosphatidylethan-olamine from the ectoplasmic to cytoplasmic leaflet of the bilayer. Disruption of the asymmetry in cells by the action of phospholipid scramblase is involved in apoptosis and is associated with increased binding and phagocytosis of these cells by macrophages. Understanding and control of these lipid dynamics quantitatively is therefore a key challenge in biophysics and cell biology.

Although this transbilayer movement of lipids is considered protein-mediated, it is unclear whether it involves a dedicated flippase or the mere presence of proteins in the ER bilayer. Kol et al. have observed that peptides that mimic the alpha-helices of transmembrane proteins can stimulate flip-flop of fluorescence-labeled phospholipids in liposomes [1], which indicates that the ability to catalyze flip-flop in the ER is not necessarily restricted to one specific protein.

We previously demonstrated by SANS that shorter acyl chain lipid, dimyristoylphosphatidylcholine (DMPC) can flip-flop in large unilamellar vesicles (LUVs) [2], while longer acyl chain lipid, 1-palmitoyl-2-oleoylphosphatidylcholine (POPC) can not. In this study, similar experiments were carried out with small unilamellar vesicles (SUVs) of DMPC, and POPC LUVs in the presence of a transmembrane peptide.

LUVs consisting of deuterated (D-LUV) or hydrogenated POPC (H-LUV) were prepared by extrusion method in the presence and absence of 0.5 mol% a transmembrane peptide KALP23. DMPC SUVs (D- and H-SUV) were prepared by sonication. TR-SANS measurement was started immediately after mixing equivalent volume of D- and H-vesicles. Time-course of the normalized contrast was calculated from the scattering intensity.

In the presence of methyl-β-cyclodextrin, the normalized contrast for POPC LUVs reached around 0.5 and became constant, which suggests that POPC does not flip-flop at all. In the presence of KALP23, however, no flip-flop was observed. This result suggests that a mere insertion of transmembrane helices into bilayer does not mediate the lipid flip-flop.

DMPC in SUVs showed faster flip-flop compared with the same lipid in LUVs. Curvature of the membranes is considered to alter the environment of lipids, such as acyl chain packing and/or headgroup hydration, and affect the lipid dynamics.

References

[1] M. A. Kol, A. N. C. van Laak, D. T. S. Rijkers, J. A. Killian, A. I. P. M. de Kroon, B. de Kruijff, Biochemistry 42 (2003) 231.
[2] M. Nakano, M. Fukuda, T. Kudo, H. Endo, T. Handa, Phys. Rev. Lett. 98 (2007) 238101.

1-6-7

Structure and dynamics of β-lactogloblin in alcohol-water mixture

Koji Yoshida and Toshio Yamaguchi
Department of Chemistry, Faculty of Science, Fukuoka University

The secondary and the higher-order structures of protein are affected by the hydrophilic and lipophilic balance (HLB) of solvent. In alcohol-water mixture, we can control the HLB of solvent by changing the composition of alcohol. In fact, alcohol-induced α-helix formation of peptides and proteins is well known and has been widely used in biophysics and biochemistry. So far, in order to investigate the alcohol effect on the native structure of monomer protein, we have measured the circular dichroism (CD) spectra of chymotrypsin inhibitor 2 (CI2) as a function of alcohol mole fraction in aqueous mixtures of methanol, ethanol, trifluoroethanol (TFE), and hexafluoro-isopropanol (HFIP)[1]. The CD spectra have shown that the secondary structure of CI2 changes from β-strand to α-helical structure at alcohol mole fractions characteristic of the individual alcohols in an order of HFIP > TFE > ethanol > methanol. In the present study, small-angle neutron scattering (SANS) and neutron spin echo (NSE) measurements were performed on alcohol aqueous solutions of β-lactogloblin (β-Lg) in order to investigate the alcohol effect on the higher-order structure and dynamics of the protein.

The β-Lg powder (>90 %) was lyophilized in D_2O to exchange labile hydrogens with deuterons. The β-Lg powder was resolved in D_2O with deuterated hydrochloric acid and stirred with a vortex mixer for 30 s. The concentration of DCl was adjusted to 0.1 M in the final solution. And then alcohols were added to the solution up to a desired alcohol concentration and stirred with a vortex mixer for 30 s. Deuterated alcohols used were methanol-d_4, ehtanol-d_6, 2-propanol-d_8, and 2,2,2-trifuluoroethanol-d_3. In this study, the unit of alcohol concentration is volume percent.

The wavelength used for small-angle neutron scattering was 6 Å. The neutron beam size at the sample position was 7 mmϕ. A sample solution was kept in a quartz cell of 2 mm path length. The cell was inserted into a temperature-controlled chamber. The temperature in the chamber was 298K and controlled within ±0.1K. The distances between the sample and detector were 1 and 4 m, corresponding to the momentum transfer (Q) of 0.007 - 0.14 Å^{-1}. The measuring time was 10 min to 1 h depending on scattering intensity. Measurements were also made for background, an empty cell, and lupolen used for intensity normalization. The SANS data of the sample solutions and the empty cell were corrected for absorption by using transmission data measured, and then the empty cell data were subtracted as background from the data of the sample solutions. Correction for the detector efficiency and normalization to absolute units were made by using the intensity of lupolen. The SANS profiles of β-Lg in alcohol-water mixtures showed that β-Lg exists as a monomer at low alcohol concentrations (<30% methanol, <20% ethanol, <20% 2-propanol, and <10% TFE). The radius of gyration (R_G) of β-Lg was calculated with the Gunier equation. The values of R_G of β-Lg were almost independent of alcohol in these alcohol concentrations. The CD spectra indicated that the degree of α-helical structure enhanced with the alcohol addition was less than 20% in these alcohol concentrations [2]. Hence, β-Lg is likely to still keep the native structure in these alcohol concentrations. With increasing alcohol concentration, the large scattering intensity in a low Q region was observed. The SANS profile could be fitted with a power function whose exponent was 1.7 independent of alcohol. This implies that a homogenous network of β-Lg was grown. The CD spectra exhibited that the α-helical structure of β-Lg was dominant in these alcohol concentrations [2].

For the NSE measurements, the wavelength used was 7.3 Å. The scattering vector Q covered was 0.01 - 0.1 $Å^{-1}$. The Fourier time was varied from 0.15 to 15 ns. The measuring time was 4 to 12 h for each Q range depending on scattering intensity. A plate of Grafoil was measured for resolution correction. The sample temperature was 292K and was controlled within ±0.3K. The intermediate scattering functions (ISF) of β-Lg at various Q values were measured in pure D_2O, 20% ethanol-, and 10% TFE- D_2O mixtures. The ISFs were fitted with a single exponential function. The Q^2 dependence of the relaxation rate in pure D_2O, 20% ethanol-, and 10% TFE-D_2O mixtures are shown in Figure 1. The diffusion coefficients (D) were obtained by using a least-square fitting procedure over $0 < Q^2 < 0.01$ $Å^{-2}$. Hydrodynamic radius (Stokes radius) R_H was determined by the Stokes-Einstein equation. The R_H value in pure water (40.2Å) is smaller than that in alcohol-water mixtures (43.4 and 43.1Å in 20% ethanol- and 10% TFE-D_2O mixtures, respectively). Because the radii of gyration of β-Lg in these solvents are almost the same as mentioned above, the increase in R_H in alcohol-water mixture would not arise from an increase of the Stokes friction. On the other hand, the R_H values obtained from dynamical light scattering (DLS) measurements were almost the same irrespectively of solvents [3]. This difference would be explained in terms that NSE would detect internal motion of β-Lg due to a smaller wave length of neutrons. That is, even small addition of alcohol which seldom affects the ternary structure of β-Lg would retard internal motion of the protein. This is consistent with the results of molecular dynamics simulation of a small peptide in TFE-water mixture [4].

[1] K. Yoshida, J. Kawaguchi, S. Lee, T. Yamaguchi, Pure Appl. Chem. 80, 1337 (2008).

[2] D. Hong, M. Hoshino, R. Kuboi, Y. Goto, J. Am. Chem. Soc. 121, 8427 (1999).

[3] K. Yoshida, T. Yamaguchi, unpublished.

[4] M. Fioroni, M. D. Diaz, K. Burger, S. Berger, J. Am. Chem. Soc. 124, 7737 (2002).

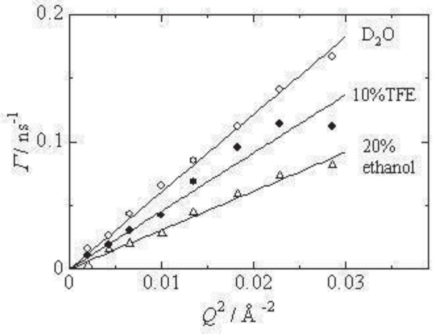

Fig. 1. Q^2-dependence of the relaxation rates of β-lactoglobulin obtained from ISF of NSE in aqueous solutions of 10% TFE and 20% ethanol.

1-6-7

1-6-8

Effect of temperature and pressure on protein dynamics studied by inelastic neutron scattering

Hiroshi Nakagawa[1], Yasumasa Joti[2], Osamu Yamamuro[2] and Mikio Kataoka[1,3]
JAEA[1], Univ. of Tokyo[2], NAIST[3]

Protein structure fluctuates thermally, and the protein dynamics contributes to the stability and biological function. Protein dynamics has been described from the view point of the energy landscape. The structural fluctuation accompanies the volume fluctuation, indicating that protein dynamics should be characterized by the compressibility. Therefore, the effect of pressure as well as temperature on the protein energy landscape is essential for understanding the protein dynamics [1]. Inelastic neutron scattering (INS) is an effective method for studying the protein dynamics between picosecond and nanosecond time scales. So far the temperature dependence of protein dynamics in the powder state is well characterized, but the pressure effect on protein dynamics has not been studied well. Recently, the gas pressure system has introduced by O.Y. into the neutron spectrometer, AGNES. We performed INS experiment with AGNES, whose energy resolution is 120 μ eV, using Staphylococcal nuclease (SNase) of dehydrated samples at several sets of temperatures and pressures. Ar gas was used as pressure medium because of the relatively low background. Figures are the INS spectra at 160 K and 300 K under 1 atm and 900 atm. At 160 K pressure affects the low energy dynamics, whereas the vibrational spectrum with high frequency is not affected by high pressure. In the low energy region, the boson peak was observed, and the peak shifts to higher frequency at high pressure, suggesting potential hardening of protein collective modes. At 300 K and 1 atm, the quasi-elastic scattering appears aside the elastic peak, suggesting onset of the structural relaxation and/or diffusive dynamics. The quasi-elastic scattering significantly suppressed at high pressure and the boson peak was observed clearly, indicating that the protein conformation falls into a local minimum on the energy landscape at high pressure. Anharmonic motions were strongly suppressed by pressure. The anharmonic motions lost at high pressure should contribute to the biological function. Therefore, INS experiment along the axis of pressure as well as that of temperature is essential for analysis of the relationship between protein dynamics and function. Furthermore, the systematical studies of protein dynamics by the high-pressure INS experiment will open a new way to analyze the stability and function of the protein originated from the living organism in the deep sea (ex. Why is a deep-sea fish alive?) and give an important insight into the piezo-biology.

1) L. Meinhold et al. : ”Proc.Natl.Acad.Sci. ”, 104, 17261 (2007).

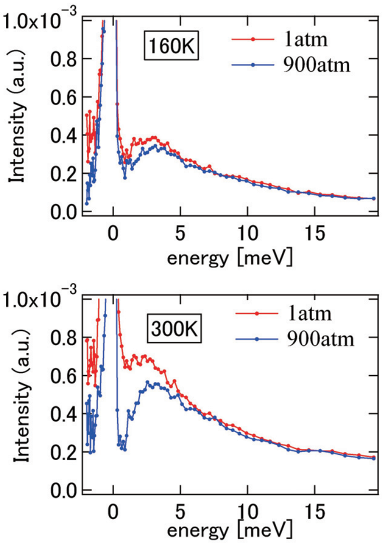

Fig. 1. INS spectra at 160 K and 300 K under 1 atm and 900 atm.

Activity Report on Neutron Scattering Research: Experimental Reports **16** (2009)
Report Number: 786

1-6-9

Denaturation of alpha-Crystallin by replacement of amino-acid residue

Masaaki Sugiyama, Norihiko Fujii, Toshiharu Fukunaga and Noriko Fujii
Research Reactort Institute, Kyoto University

We have investigated on the mechanism of the abnormal aggregation of protein with the eye lens protein, α-Crystallin. Alpha-Crystallin with its molecular weight of ca 800 kDa is a major protein in eye lens. Native α-Crystallin is a hetero-aggregate with 20-30 subunits. There are two kinds of subunits, αA-Crystallin and αB-Crystallin. On the molecular level study, Fujii found that there exist racemized aspartyl residues (D-Asp) in the abnormal aggregates of α-Crystallin of Cataractous and elder eye lens. Therefore, we have supposed the racemization of aspartyl residue should be a trigger of abnormal aggregation. In addition, we have also proposed a pathway to Cataract as follows: Under external stresses such as UV irradiation, X-ray irradiation, low temperature and so on, aspartyl residues are racemized. The D-Asp on the polypeptide chain induces the strain in the regular folding of the polypeptides and the strain makes the structural deformation of the subunits, αA-Crystallin and/or αB-Crystallin. The aggregates with these deformed subunits gather and make the abnormal aggregates.

As the first step to prove above the hypothesis, we prepared for two mutant samples of which an aspartyl residue was replaced with an asparagine residue.
Mutant αA-crystallin (Asp → Asn@151)
Mutant αB-crystallin (Asp → Asn@36)
In addition, as a reference, we also prepared for normal αA-crystallin and αB-crystallin. It is espected that asparagine acid can make racemization more easily than aspartyl acid.

With these samples, SANS experiments were perfomed with SANS-U spectrometer. Figure 1 shows the SANS profiles of nromal and mutant αA-crystallins and those of nromal and mutant αB-crystallins. The structual change of mutant αB-crystallin is larger than that of mutant αA-crystallin. It means that an aspartyl residue in αB-crystallin plays more important role than that in αA-crystallin.

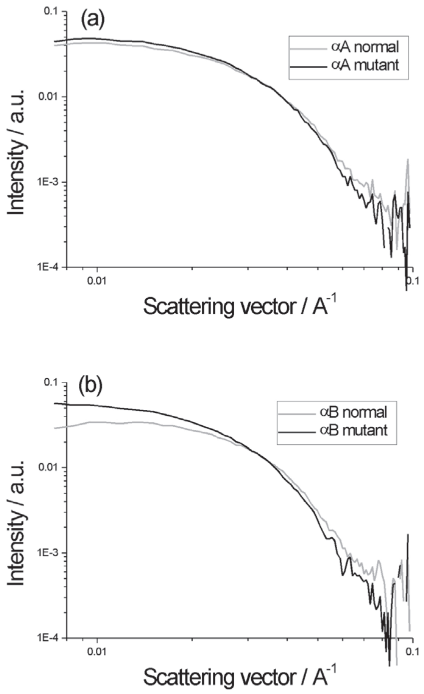

Fig. 1. SANS profiles of nromal and mutant αA-crystallins (a) and those of nromal and mutant αB-crystallins (b).

1-6-10

Analysis of the relationship between the dynamics and the structural polymorphism of F-actin

S. Fujiwara (A), F. Matsumoto (A), H. Nakagawa (A), T. Oda (B)
(A) Japan Atomic Energy Agency, (B) RIKEN SPring8 Center

Actin is one of the most abundant proteins in eukaryotic cells and plays crucial roles in various aspects of cell motility. The actin monomers (G-actin) polymerize to form a helical polymer (F-actin). Flexibility of F-actin has been suggested to be important for such a variety of functions. Understanding the flexibility of F-actin requires characterization of a hierarchy of dynamical properties, from internal dynamics of the actin monomers through domain motions within the monomers and relative motions between the monomers within F-actin to large-scale motions of F-actin as a whole. As one of the ongoing projects towards this ultimate goal, we have been studying the dynamics of actin at pico- to nano-second time range by neutron spin-echo (NSE) spectroscopy.

We carried out the NSE experiments on solutions of F-actin and G-actin in the Q-range between 0.03 A^-1 and 0.2 A^-1 at the Fourier time up to 30 nsec during the machine time in 2007, and found that there are differences in the intermediate functions obtained, from which it was suggested that behavior of the effective diffusion coefficients of G-actin as a function of Q^2 corresponds to free diffusion in solution whereas that of F-actin reflects the collective motions within F-actin.

Here, as a continuation to the experiments on G-actin and F-actin, we investigated effects of solution conditions on the dynamics of F-actin. It was shown that the flexibility of F-actin changes corresponding to a variety of the solution conditions (Isambert et al., 1995). In particular, F-actin polymerized in the presence of Mg2+ (Mg2+-F-actin) was shown to have a distinct structural conformation and be more flexible than F-actin polymerized in the presence of Ca2+ (Ca2+-F-actin), and it was suggested that such modulation of the flexibility by Ca2+ and Mg2+ may have important physiological consequences within the cell (Orlova and Egelman, 1993). We thus carried out the NSE measurements of Mg2+-F-actin and Ca2+-F-actin.

Actin was purified from rabbit skeletal muscles. Actin in the presence of Ca2+ or Mg2+ was polymerized by adding KCl. Solutions of Mg2+-F-actin and Ca2+-F-actin were prepared in D2O. The NSE measurements on these solutions were carried out on the NSE spectrometer, iNSE, run by the University of Tokyo, installed at the guide hall of the research reactor, JRR-3M, Ibaraki, Japan. The measurements were done over the Q-range between 0.03 A^-1 and 0.2 A^-1 at the Fourier time up to 30 nsec. During the measurements, the samples were kept at 10 °C. The normalized intermediate scattering functions obtained showed that each intermediate function can be fit with a single exponential, from which effective diffusion coefficients can be estimated, and that there are differences in the decay times of Mg2+-F-actin and Ca2+-F-actin. It appears that the decay times of Mg2+-F-actin are somewhat faster than those of Ca2+-F-actin, suggesting that Mg2+-F-actin is more flexible than Ca2+-F-actin. This result is consistent with the previous reports. Detailed analysis of the intermediate functions is currently underway.

1. 中性子散乱 7）基礎物理学・中性子光学

1. Neutron Scattering 7）Fundamental Physics・Neutron Optics

1-7-1

Development of Neutron Interferometer using polychromatic mirrors

M. Kitaguchi(A), M. Hino(A), Y. Seki(B), H. Funahashi(C), K. Taketani(D), H. M. Shimizu(D)
(A)KURRI, (B)Kyoto Univ., (C)Osaka Electro-Communication Univ. (D)KEK

Neutron interferometry is a powerful technique for studying fundamental physics. A large dimensional interferometer for long wavelength neutrons has the advantage to increase the sensitivity to small interactions. Such a kind of interferometer was realized by using multilayer mirrors. We demonstrated Jamin-type interferometer for cold neutrons using beam splitting etalons (BSEs), which enables us to align the four independent mirrors within required precision [1]. The BSE contains two parallel mirrors. A couple of the BSEs in the Jamin-type interferometer separates and recombines the two paths spatially. A neutron supermirror is one of the multilayer with continuous latice constants, which reflects the wide range of the wavelength of neutrons. The BSEs with neutron supermirrors enable us to arrange Jamin-type geometory of the interferometer for white neutrons. The interferometer can be applied to pulsed neutrons by using the BSEs with supermirrors. Such interferometer increase the neutron counts for high precision measurements, for example, Aharonov-Casher effect. Wevelength dependence of the interaction in the interferometer also can be measured by the time of flight detection for pulsed neutrons.

As the first test we made polychromatic mirrors. The polychromatic mirror contained two multilayers with the different latice constants. The lattice constants were 15.8nm and 21.0nm respectively. We fabricated two polychromatic mirrors with intermediate gap layer on the top of Si substrate continuously. This device enabled us to provide two separated paths of the Jamin-type interferometer for two wavelength of neutrons.

The experiment has been performed using the cold neutron beam line MINE2 at the JRR-3 reactor in JAEA. The beam has a wavelength of 0.88nm and a bandwidth of 2.7% in FWHM. In the case of monochromatic beam of MINE2, the polychromatic mirrors functions at two Bragg angles. The interferometer can be constructed at the two incident angles. We observed clear interference fringes at the incident angle of 1.14 degree and 1.62 degree, which were corresponding to the two multilayers in the polychromatic mirror (figure 1).

Now we are planning to apply the supermirror for BSEs and to construct the interferometer for pulsed neutrons. We are also planning the experiments using the interferometer as one of fundamental physics investigations at J-PARC.

[1] M. Kitaguchi, et. al., Phys. Rev A 67 (2003) 033609

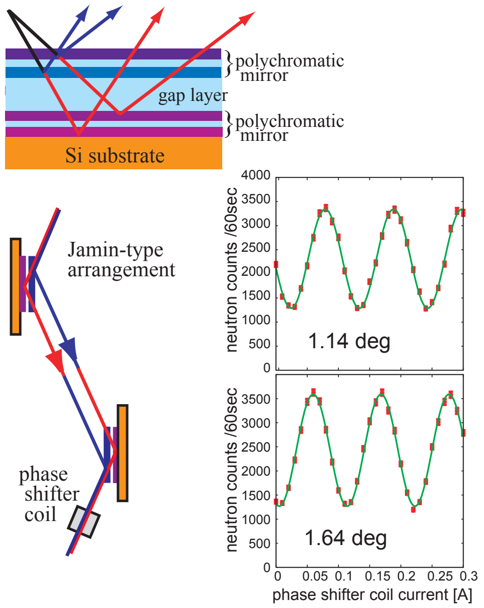

Fig. 1. Interferometer using polychromatic mirrors. Interference fringes are observed at two incident angles.

1-7-2

Measurement of magnetic diffuse scattering from Ni2MnAl

Kouichi Hayashi, Kenji Ohoyama, Tokujiro Yamamoto, and Toetsu Shishido
Insitute for Materials Research, Tohoku University

Neutron holography is relatively local structural analysis method, which visualize 3D local atomic arrangements around selected elements in solids. This technique is attracted as local structural analysis of dopants like X-ray and neutron holography, which have been developed in last two decades. However, the photoelectron or X-ray holography has a disadvantage that they cannot apply to hydrogen system because hydrogen dose not emit any fluorescent X-rays and photoelectrons. In order to overcome this difficulty, neutron holography was proposed in 2001. First demonstration of the neutron holography was realized using a single crystal of simpsonite (Al4Ta3O13(OH)) by Sur et al. They measured angular anisotropy of incoherently scattered neutrons from hydrogen nuclei, and reconstructed surrounded oxygen nucleus images. In 2004, Cser et al. applied this technique to a palladium hydride single crystal, and determined the location of hydrogen in the PdH. We also measured efficiently the neutron hologram of a palladium hydride single crystal using the powder diffrcatometer of HERMES in JRR-3M reactor, and found the thermal diffuse scattering effect in the measured hologram.

Neutron scattering has mainly two ways of scatterings such as nucleus scattering and magnetic scattering. Here, in order to investigate the effect of magnetic scattering on neutron hologram, we measured angular anisotropy of incoherently scatterings by Ni in Ni 2 MnAl single crystal at room temoerature. The present sample shows ferro-antimagnetic property below the Nell temperature of 295 K. The incoherent scattering cross section of Ni was much larger than those of Ni and Al. The single sample of Ni 2 MnAl was grown by floating zone method, its size was 6 mm in a diameter and 5 mm in a thickness. Its microstructure and crystal structure were checked by SEM and TEM, respectively.

Wavelength of the neutron was 0.182 nm. Sample was rotated in the range of 0 - 359 with the step of 1 , where rotation axis was parallel to the incoming beam direction. Neutrons incoherently scattered by Ni nuclei in the sample were detected by HERMES 150 He3 counters at each sample rotation angle. Polar angle of the measured hologram defined by the counter ranged from 7 to 157 . Dwelling time at each angle was 600 sec. The average neutron intensity at each pixel was about 500 counts. Figures 1 show the 2D angular distributions of the neutron intensities around the sample at room temperature and 100 K, respectively. The displayed patterns exhibit strong spots reflecting the sample crystal symmetry, due to thermal diffuse scattering and magnetic diffuse scattering. In order to extract hologram pattern due to pure magnetic scattering, we must measure holograms of Ni 2 MnAl at different temperatures above and below the Nell temperature of 295. Further analysis is now in progress.

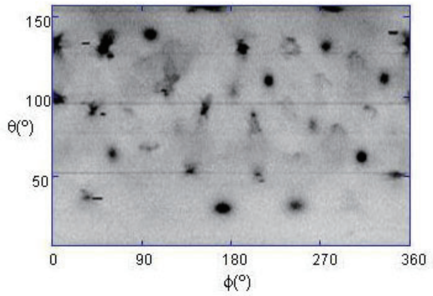

Fig. 1. Fig. 1 2D distributions of neutron intensities around Ni2MnAl.

1-7-3

A study on reflectivity limit of neutron supermirror

M.Hino[1], M.Kitaguchi[1], H.Hayashida[2], T.Ebisawa[2],R.Maruyama[2], N.Achiwa[3],
Y.Kawabata[1]
KURRI[1], *JAEA*[2], *Osaka Univ*[3]

Multilayer mirror is one of the most important devices for slow neutron experiments. A multilayer with small d-spacing and supermirror with large-m are desirable to enlarge utilization efficiency for neutron scattering experiments. Here m is a maximum critical angle of the mirror in unit of critical angle of nickel and Q of nickel ($m = 1$) is 0.215 nm^{-1}. It is also very important to fabricate high reflectivity supermirror even in low-m. Ion beam sputtering (IBS) technique enables us to fabricate smooth layer structure with sharp edge. Indeed, we have succeeded in fabricating $m > 5$ supermirrors and very small d-spacing multilayer using ion beam sputtering (IBS) technique, and neutron optics group in JAEA has installed a large IBS machine and is producing supermirror for J-PARC project. In these reports, the effect of interface roughness and intermixing at each layer boundary in multilayer seems to be less than surface of substrate even in $m > 5$ supermirrors. In our previous result, the measured reflectivities were well reproduced by the simple interface roughness model given in Debye-Waller factor. The surface roughness of ordinary substrate, for example commercial silicon wafer and float glass, is almost larger than 0.4 nm in rms (root-mean-square). The supermirrors were deposited on silicon wafer using IBS instrument installed in the Kyoto University Research Reactor Institute (KURRI).The deposition rates of NiC and Ti were determined by X-ray and neutron reflectometry. The real and imaginary nuclear potential values of NiC were estimated to be 230 and 0.063 neV, respectively. Those of Ti were -51 and 0.038 neV, respectively. The deposition rates of NiC and Ti were estimated to be 0.0315 and 0.037 nm/s, respectively. We have fabricated $m = 2.9$ NiC/Ti supermirror on ordinary silicon wafers in which surface roughness are about 0.4 nm by ion beam sputtering technique. As shown in the inset of Fig.1, the measured reflectivity at $m < 2.8$ was much better than the expected theoretical lines with σ=0.3 and 0.4nm. It was well reproduced by the theoretical line with ideal smooth layer structure in which surface and interface roughness is nothing or very little ($\sigma < 0.1$). In case of IBS technique, supermirror reflectivity is not restricted with in the simple surface roughness model. We realized almost theoretical reflectivity limit of $m = 2.9$ NiC/Ti supermirror by ion beam sputtering technique. It is effective for high reflectivity low-m supermirror deposited on an ordinary substrate to increase the number of layer. It is also useful for realization of small d-spacing monochromator with high reflectivity although we have to estimate the effect of interface roughness with more realistic model.

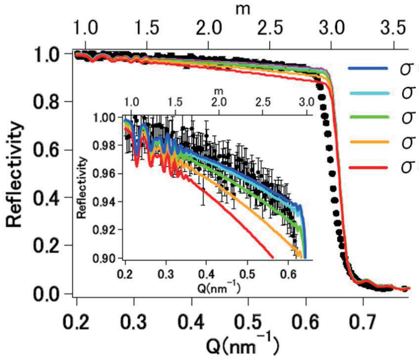

Fig. 1. Measured reflectivity of m=3 supermirror in which number of layers is 650. The solid lines indicate theoretical ones with σ=0, 0.1, 0.2, 0.3 and 0.4 nm. The inset is enlarged at high reflectivity ($R \geq 0.9$).

1.　中性子散乱　8）装　置

1. Neutron Scattering　8）Instrument

1-8-1

Develpoment of U-shaped ^{3}He PSDs for DNA, A New Backscattering Spectrometer at J-PARC

N. Takahashi[1], K. Shibata[1], T. Yokoo[1,2], S. Satoh[1,2] and K. Nakajima[1]

[1] *Neutron Science Section, MLF Division, J-PARC Center*

[2] *Institute of Materials Structure Science, High Energy Accelerator Reseach Organization (KEK)*

Since detectors are one of the most important key components, it is indispensable to evaluate feasibility and performance of new detectors and related electronics prior to actual construction of instruments. From this point of view, in JFY2008, we have continued to perform R&D of U-shaped ^{3}He position sensitive detectors (PSDs), which are planned to be used at new backscattering spectrometer DNA which will be constructed at BL02 in Materials and Life Science Experimental Facility (MLF) at Japan Proton Accelerator Research Complex (J-PARC) by using neutron beam at MUSASI_L port.

The U-shaped PSDs are sequentially coupled detectors. Since one of the both sides of two independent simple PSDs is connected each other by a resistance line, no-detectable area, so-called dead area, can be reduced for one-side, which is corresponding to right side of Figure 1. Such a contrivance is necessary for backscattering instrument at pulsed neutron source facility and BASIS spectrometer at the Spallation Neutron Source (SNS) is also using this type PSDs already.

We have tested a U-shaped PSD made by General Electric/Reuter Stokes (GERS) which is shown in Figure 1. Diameter of tubes and partial pressure of ^{3}He are 1/2 inch and 7.7 atmospheres, respectively. Neutron beam with wavelength of ∼ 2 A was collimated into 1mm^{2} and irradiated the U-shaped PSD which was on a X-Y stage with stepping motor as shown in Figure 2. Applied voltage was 1.37 kV. Pulse-height spectrum has shown good neutron/gamma selectivity. Satisfactory position resolution of 4.0 mm was obtained. The dead area was evaluated from neutron sensitivity of the detector (see Figure 3) and obtained to be 41 mm.

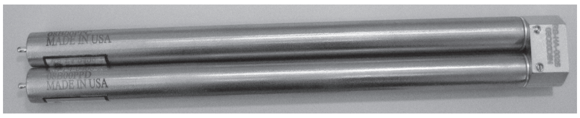

Figure 1: A prototype U-shaped PSD made by GERS.

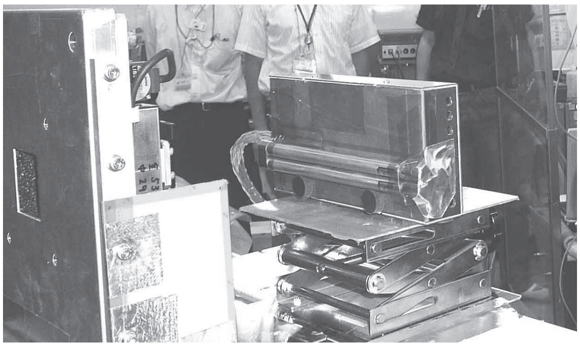

Figure 2: Experimental setup at MUSASI_L port.

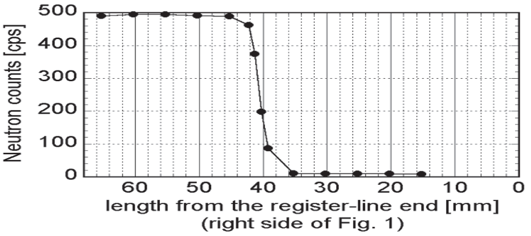

Figure 3: Neutron counts as a function of position of the U-shaped detector.

原子炉：JRR-3　装置：MUSASI-L(T2-3-1)　分野：中性子散乱（装置）

1-8-2

Effect of Interfacial Roughness Correlation on Diffuse Scattering Intensity in a Neutron Supermirror

R. Maruyama, D. Yamazaki, T. Ebisawa, and K. Soyama
J-PARC Center, Japan Atomic Energy Agency, Tokai, Ibaraki 319-1195

Multilayer structure consisting of Ni and Ti are widely used for neutron optical elements such as supermirrors. The thickness of the layers of a supermirror is gradually decreased with the number of the layers to increase the effective critical angle, which is expressed by the ratio m of the effective critical angle of the supermirror to that of natural nickel. High-performance supermirrors allow the realization of focusing systems. Reflected neutrons are divided into specular and off-specular (diffuse) components. Although the specular component contributes to the focused intensity, the diffuse component generates background noise around the focal point. This causes the serious problem of low signal-to-noise ratio in focusing systems such purposes as small angle neutron scattering measurement, in which the diffuse component cannot be removed by slits. The suppression of the diffuse component is, therefore, an important problem along with the realization of higher reflectivity and larger value of m.

There is a technique of adding carbon atoms to the nickel layer that leads to higher reflectivity that has been demonstrated by several groups to be effective in improving the reflectivity of the supermirror. The diffuse intensity from a NiC/Ti supermirror was found to be lower than that from a Ni/Ti suppermirror by more than one order of magnitude. Figure 1 shows the measured diffuse intensity profiles from Ni/Ti and NiC/Ti supermirror with $m = 3$. This result implies that a high-performance focusing system with a diffuse intensity down to the order of 10^{-5} for the specular intensity can be realized by using a NiC/Ti supermirror. In this study, in order to discover the mechanism that controls the diffuse intensity from a supermirror, we investigated the crystal structures of Ni and NiC monolayers and interface structures of Ni/Ti and NiC/Ti multilayers[1)].

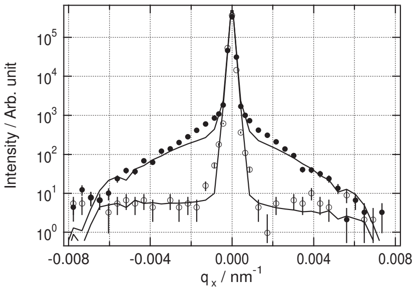

Figure 1: Diffuse intensity profiles from Ni/Ti (●) and NiC/Ti (○) supermirrors. Solid lines indicate the calculated profiles.

Ni/Ti and NiC/Ti multilayers consisting of 300 layers with a bilayer thickness of 10 nm were fabricated in order to investigate the correlation between the multilayer interfaces. Since the measured reflectivity difference between these multilayers was very small over the momentum transfer range up to 2.7 nm^{-1}, where the average interfacial roughness was estimated to be 0.60 nm rms, it can be said that the interface roughness of the NiC/Ti multilayer is the same as that of the Ni/Ti multilayer. The diffuse intensity from the NiC/Ti multilayer was found to be lower than that from the Ni/Ti multilayer by more than one order of magnitude except for the Bragg condition ($q_z = 0.645$ nm^{-1}) as shown in Fig. 2. This result suggests the following explanation of the diffuse intensity difference between the Ni/Ti and NiC/Ti supermirrors. When a multilayer has a variable bilayer thickness distribution structure, the diffuse intensity at every point on the q_x-q_z plane includes a diffuse intensity component from those layers that do not satisfy the Bragg condition. That component from the NiC/Ti multilayer is much smaller than that from the Ni/Ti multilayer, which leads to the diffuse intensity difference between the supermirrors shown in Fig. 1.

In order to verify this explanation, Ni/Ti

原子炉：JRR-3　装置：SUIREN(C2-2)　分野：中性子散乱（装置）

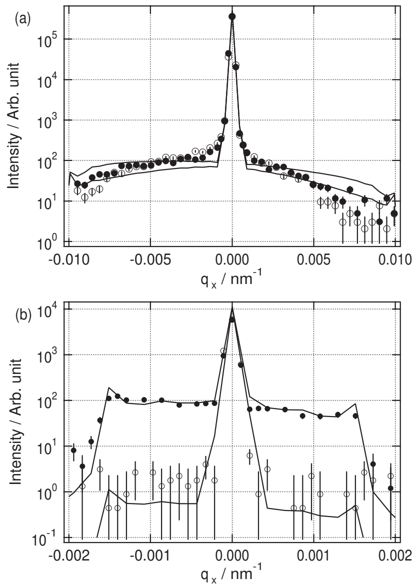

Figure 2: Diffuse intensity profiles from Ni/Ti (●) and NiC/Ti (○) multilayers consisting of 300 layers with a bilayer thickness of 10 nm. Solid lines indicate the calculated profiles. (a) Rocking scan with $q_z = 0.645$ nm^{-1}. (b) Rocking scan with $q_z = 0.31$ nm^{-1}.

and NiC/Ti multilayers were fabricated consisting of 350 layers with a bilayer structure in which thicknesses were distributed in the range of $10 \leq d \leq 17$ nm. Figure 3 shows the result of the rocking scan with $q_z = 0.62$ nm^{-1}, which is within the broad Bragg condition distributed in the range of $0.43 \leq q_z \leq 0.645$ nm^{-1}. In the previous result for the multilayers without a bilayer thickness distribution, the difference between the diffuse intensity of the two multilayers was very small under the Bragg condition as shown in Fig. 2(a). However, the diffuse intensity from the NiC/Ti multilayer is much smaller than that from the Ni/Ti multilayer even within the Bragg condition when the multilayers have bilayer thickness distribution.

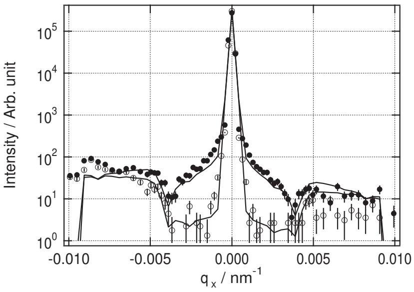

Figure 3: Diffuse intensity profiles from Ni/Ti (●) and NiC/Ti (○) multilayers consisting of 350 layers with a distribution of bilayer thickness of $10 \leq d \leq 17$ nm. (Rocking scan with $q_z = 0.645$ nm^{-1}.) Solid lines indicate the calculated profiles.

In order to investigate the interface structure that controls the diffuse intensity from the multilayers, the measured diffuse intensity profiles were compared with the calculations where the perturbation theory based on the distorted wave Born approximation was used. Upon diffuse intensity measurement of the multilayers without a bilayer thickness variation, the difference between the diffuse intensity of the Ni/Ti and NiC/Ti multilayers was found to be dependent on the Bragg condition. This is closely related to the vertical correlation between different interfaces. From the result of the diffuse intensity calculation for the multilayers consisting of 300 layers with a bilayer thickness of 10 nm (Fig. 2), the parameters of the interface structure were obtained as $\sigma = 0.60$ nm, $h = 1.0$, $\xi_{\|} = 250$ and 70 nm, $\xi_{\perp} = 2.0$ and 50 nm for the Ni/Ti and NiC/Ti multilayers, respectively. Here σ is the average interface roughness, h is the Hurst parameter, $\xi_{\|}$ is the lateral correlation length, and $\xi_{\perp}$ is the vertical correlation length. Using the same parameter sets, diffuse intensity calculations for multilayers consisting of 350 layers with a distribution of bilayer thickness of $10 \leq d \leq 17$ nm and for the supermirrors with $m = 3$ were preformed. The difference between the diffuse intensity of the multilayers and supermirrors were well reproduced by introducing the difference in the lateral and vertical correlation length (Fig. 1 and 3). These results indicate that a multilayer with a large vertical correlation length and a small lateral correlation length effectively suppresses the diffuse intensity from a supermirror.

References

1) R. Maruyama, D. Yamazaki, T. Ebisawa, and K. Soyama :"J. Appl. Phys.", 105, 103527(2009).

1-8-2

1-8-3

Performance Test of Scintillator-based Small Neutron Detector

K. Sakasai, T. Nakamura, K. Toh, A. Moriai, E. Shooneveld[1] and N. Rhodes[1]

J-PARC Center, JAEA, Tokai, Ibaraki 319-1195
[1]*ISIS Science Diffraction and Muon Division, RAL, Didcot, OX11 0QX, UK*

A small linear scintillation neutron detector was fabricated and tested at RESA-II. The detector was originally developed in RAL for the engineering diffractometer, ENGIN-X, at ISIS. In this paper, some results of the performance test of the detector is described.

The fabricated detector was designed to have a small detection pixel with a spatial resolution of 3 mm. The detector had only 14 pixels to confirm the characteristics such as neutron detection efficiency and gamma-ray sensitivity. Scattered neutrons were detected based on a nuclear reaction of ^{6}Li(n,α) in ZnS/LiF scintillators in the pixel. Incident neutron position was determined by a $_2C_n$ coding method. The applied voltages of PMTs are individually set to have a gain of 3×10^7. The Si monochrometer was used for generation of 2.2 Å-neutrons. Figure 1 shows neutron sensitivity of the detector as a function of the threshold voltage of the amplifier. One can see that the detector had a neutron sensitivity of 84 % at a threshold voltage of 250 mV. One the other hand, we have confirmed that the detector had a gamma-ray sensitivity of 4×10^{-7} for 1.3 MeV gamma-ray at the same threshold voltage in the other experiments. After confirmation of fundamental performances such as output linearity, demonstration experiments for neutron diffraction were carried out at a neutron wavelength of 1.5 Å. In the experiment, Ni powder sample was used to check the performance.

Figure 2 shows neutron diffraction pattern of the Ni powder sample after calibration of scattering angle. After determination of each scattering angle in the figure by Gaussian fitting method, lattice spacings of the sample were estimated. In summary, the detector has an excellent performance for neutron scattering experiments. New detectors that meet the actual requirements, e.g., a sensitive area of 196 mm×1,000 mm and the secondary flight path of 2.0 m, for the engineering diffractometer, "TAKUMI", at J-PARC, were constructed and installed for the first commissioning in 2008.

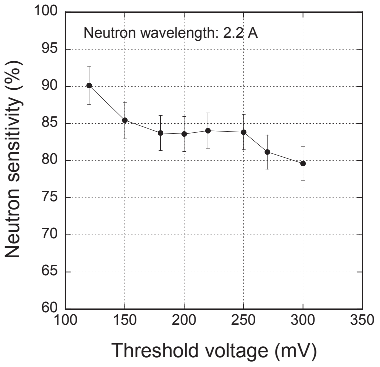

Figure 1: Neutron sensitivity as a function of the thershold volatge.

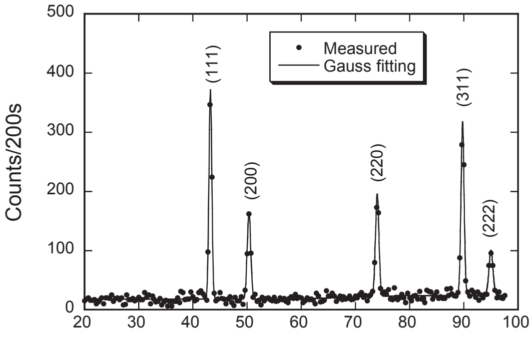

Figure 2: Neutron diffraction pattern of the Ni powder sample.

原子炉：JRR-3　装置：RESA-2(T2-3-2)　分野：中性子散乱（装置）

1-8-4

Measurement of Energy Spectrum of Neutron Beam at MUSASI-H Port

K. Toh, H. Yamagishi and K. Sakasai

J-PARC Center, JAEA, Tokai, Ibaraki 319-1195

The high angle MUSASI beam port provides neutron beam with a scattering angle of about 80 degrees. When pyrolitic graphite (PG) is used as a monochromater, however, neutrons with higher harmonic ones will be generated because of intrinsic characteristics of PG. To provide neutron energy information to users who adopt PG as a monochromater, neutron energy spectrum was measured by a TOF method.

The experimental setup is schematically shown in Fig.1. The neutron signals were measured by a multi-channel scalar (Turbo MCS, EG&G Ortec) through an amplifier (570, Ortec) and a single channel analyzer (551, Ortec). Neutron beam was chopped by a chopper and the chopped neutrons were detected by a ^{3}He detector with a flight path of 0.5 m. The dwell time of MCS was 10 μs.

Measured neutron spectrum is shown in Fig.2. The TOF time was converted to neutron wavelength according to relationship between TOF time and the flight path. Three strong peaks at 1.2, 2.0, and 4.0 Å were observed as seen in Fig. 2. No noticeable peaks was observed above 5 Å. The most intense component was 2.0 Å-neutrons. Note that the data were not corrected by the neutron detection efficiency of the ^{3}He counter.

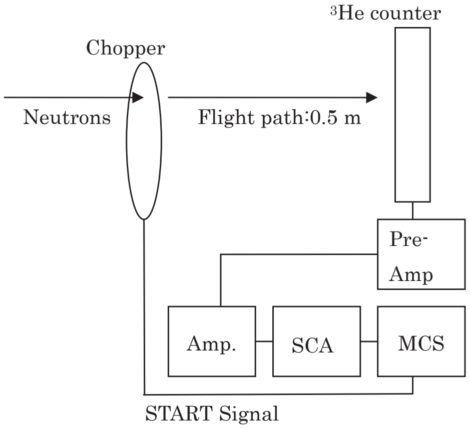

Figure 1: Experimental setup.

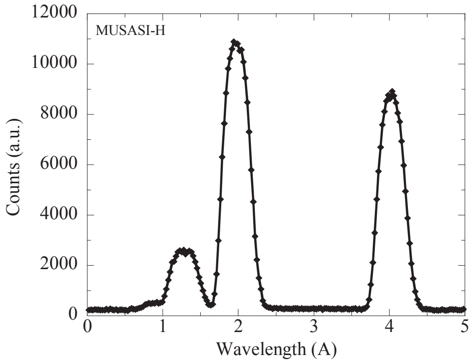

Figure 2: Measured neutron spectrum at MUSASI-H.

原子炉：JRR-3　装置：MUSASI-H(T1-4-6)　分野：中性子散乱（装置）

1-8-5

Development of a Multiplet Magnetic Lens System to Focus a Pulsed Neutron Beam

T. Oku, H. Kira, T. Shinohara, S. Takata, M. Arai, J. Suzuki, H.M. Shimizu[1]
J-PARC center, JAEA, Tokai, Ibaraki 319-1195
[1]*KEK, Tsukuba, Ibaraki 305-0801*

As a magnetic lens based on a sextupole magnet has neutron wavelength-dependent focusing property, namely chromatic aberration, it has been proposed that the chromatic aberration can be compensated in the pulsed neutron beam focusing by changing the focusing and defocusing functions of the magnetic lenses of the multiplet magnetic lens system synchronously with time-of-flight of neutrons [1,2]. In this study, we designed and constructed a triplet magnetic lens system composed of three sextupole permanent magnets and two spin flippers, and performed a pulsed neutron beam focusing experiment with the system. The design of the system and the experimental results are shown and discussed.

The experimental setup is shown in Fig.1. We performed a pulsed neutron focusing experiment at the beamline C3-1-2-1 (NOP) of JRR-3 at Japan atomic energy agency (JAEA). The sextupole magnet functions as neutron focusing and defocusing lens for neutrons with positive and negative spin polarity, respectively [3]. The three sextupole permanent magnets (M1, M2, M3) and two spin flippers (SF1, SF2) were located in series as shown in Fig. 1. The neutron beam was pulsed by using a chopper, and then polarized by using a quadrupole magnet (Fig. 1). The neutrons which transmit through the quadrupole magnet is highly polarized with polarization degree $P > 0.99$ [4,5]. The pulsed polarized neutrons are delivered through the guide field and enter the triplet magnetic lens system. The spatial intensity distribution of the neutrons, which transmitted through the triplet magnetic lens system, were measured by using a 2d-position sensitive detector [6].

At first, we performed the pulsed neutron focusing experiments of the triplet magnetic lens system without changing the spin flipper state synchronously with the time-of-flight of the neutrons. The spin flipper states were fixed during the single measurement. The measuring conditions are shown in Table 1. The measured full widths at the half maximum (FWHMs) of the neutron beam focused onto the detector position are plotted as a function of the neutron wavelength λ in Fig. 2. It was found that neutron focal wavelength changes depending on the spin flipper states. The focal condition of the magnetic lens based on the sextupole magnet is determined by the magnet length L_{mag} and λ as follows:

$$f = \frac{L_{mag}}{2} + \frac{h}{\sqrt{G\alpha} m_n \lambda} \cot\left(\frac{h}{\sqrt{G\alpha} m_n \lambda} \cdot \frac{L_{mag}}{2}\right) \tag{1}$$

Here, f is the focal length, h Plank's constant, G the coefficient of the magnetic field gradi-

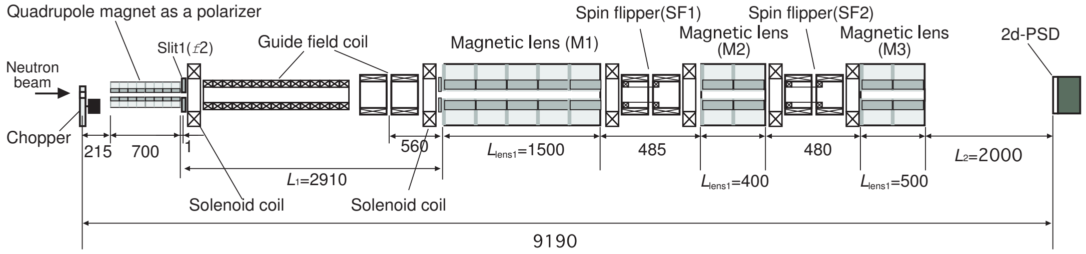

Figure 1: Experimental setup.

原子炉：JRR-3　　装置：NOP(C3-1-2-1)　　分野：中性子散乱（装置）

ent, $\alpha = |\mu_n/m_n| = 5.77\mathrm{m}^2\mathrm{s}^{-2}\mathrm{T}^{-1}$, m_n the neutron mass and μ_n the neutron magnetic moment (Fig. 3). By changing the states of the spin flippers at the wavelength λ_{CO} at which the FWHM curves of Fig. 2 cross over, we can satisfy the focal condition for the pulsed neutrons in a wide wavelength range. Then, we performed the pulsed neutron focusing experiment by turning on and off the spin flippers SF1 and SF2 synchronously with the time of flight of the neutrons at the cross over wavelengths $\lambda_{\mathrm{CO1-3}}$ (Fig. 2). The obtained results are shown in Fig. 2. As the result, the neutron beam size at the detector position were realized to be the narrowest among the cases 1 to 4. The FWHMs were kept less than 4 mm between $\lambda = 7.4$ Å and 10.8 Å (Fig. 2) and the tail of the intensity peak decreased sharply down to the background level with increasing distance from the peak center. The magnetic lens system is applicable to a focusing geometry small-angle neutron scattering (FSANS) instrument with pulsed neutrons. In the application, pulsed neutrons in a wide wavelength range should be focused with a fixed focal length for efficient utilization of the neutrons. Moreover, the neutrons should be focused on the detector so sharp that the peak tail intensity goes down to the background level rapidly.

In conclusion, we have constructed a triplet magnetic lens system composed of three sextupole magnets and two spin flippers to focus a pulsed neutron beam in a wide wavelength range with same focal lengths. We performed the pulsed neutron beam focusing experiment with the system. By choosing the focusing or defocusing functions of each sextupole magnet adequately and synchronously with the time-of-flight of the neutrons, we could focus the neutrons in a wavelength range of between λ = 7.4 Å and 10.8 Å with nearly same focal length. As the application of the magnetic lens system, it is considered to be applicable to a neutron focusing device for the FSANS instruments with pulsed neutrons, since we can focus the pulsed neutrons in a wide wavelength range so sharply onto the detector by using it.

Table 1: The states of the spin flippers and functions of the magnetic lens.

Case	States of the spin flippers		Functions of the magnetic lenses		
	SF1	SF2	M1	M2	M3
1	Off	Off	Focus	Focus	Focus
2	Off	On	Focus	Focus	Defocus
3	On	On	Focus	Defocus	Focus
4	On	Off	Focus	Defocus	Defocus

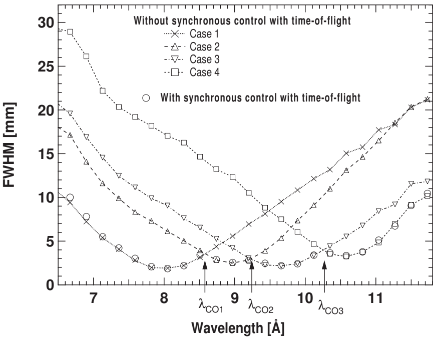

Figure 2: The FWHM of neutron beam focused onto the detector position as a function of the time of flight of the neutrons.

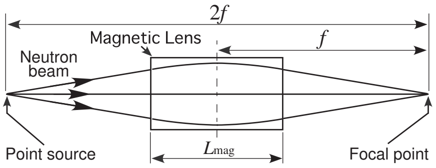

Figure 3: A schematic layout of a magnetic lens which focuses the neutron beam with focal length f.

References

1) J. Suzuki et al., the presentation at the International symposium on Pulsed Neutron and Muon Science, IPS08.
2) T. Oku, et al. :"NIM-A" 600 pp. 100-103 (2009).
3) H.M. Shimizu, et al. :"NIM-A" 430 pp. 423-434 (1999).
4) T. Oku, et al. :"Physica B" 397 pp. 188-191 (2007).
5) T. Oku, et al. :"Meas. Sci. Technol." 19 034011 (4pp) (2008).
6) K. Hirota, et al. :"Phys. Chem. Chem. Phys." 7 pp. 1836-1838 (2008).

1-8-5

1-8-6

Neutron Beam Focusing with a m= 4 Supermirror on a Precisely Figured Elliptic Surface

D. Yamazaki, R. Maruyama, K. Soyama, H. Takai[1], M. Nagano[1] and K. Yamamura[1]
J-PARC Center, JAEA, Tokai, Ibaraki 319-1195
[1]*Research Center for Ultra-Precision Science and Technology, Osaka University, Osaka 565-0871*

We have developed a ultra-precise focusing mirror combining a high-performance supermirror deposition technique and a very precise surface figuring method. This mirror is a first step of developing a focusing mirror which satisfies the following requirements simultaneously: (1)large critical angle of total reflection, (2) high reflectivity, (3) low diffuse scattering, (4)large size and (5) precise surface figure.

The mirror is a one dimensional elliptic mirror of 90 mm (elliptic) × 40 mm (straight). A fused silica surface was figured into an elliptic shape with the numerically controlled local wet etching technique 1). NiC/Ti supermirror (m= 4) was deposited on the figured surface with an ion-beam sputtering technique 2). A photo of the mirror is shown in Fig 1.

Figure 1: A elliptic focusing mirror.

The focal length is 1050 mm. The mirror accepts a neutron beam at a nominal glancing angle of 1.40 deg with acceptance angle 0.12 deg. It, therefore, reflects and focuses wide-band neutrons of $\lambda \geq 3.5$Å. Detailed descriptions is found elsewhere 3).

Focusing of a monochromatic beam was performed at the SUIREN reflectometer 4). The neutron wavelength is 3.93 Å. Incident beam slit was installed at 1050 mm before the focusing mirror, which was placed on the sample stage. The slit width was 0.10 mm.

Figure 2 compares the focused, unfocused and transmit beam intensities measured with translating scans of a slit placed at the focal position. Focused peak width of ∼0.35 mm and intensity gain ∼6 has been obtained. Diffuse scattering from the mirror was found less than 10^{-3} of the peak intensity.

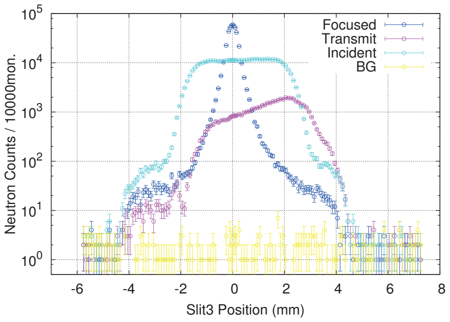

Figure 2: Vertical profiles measured with 2θ scan.

In conclusion, we have developed a one dimensional focusing mirror which shows a high performance with a monochromatic beam. We are now preparing a performance test with wide-band neutron beam. The fabrication method is readily applied to larger mirror substrates or two dimensional mirrors. Stacked focusing mirrors could also be fabricated with these methods.

References

1) K. Yamamura, Annals of the CIRP, 56, 541 (2007).
2) R. Maruyama, D. Yamazaki, T. Ebisawa, K. Soyama, Nucl. Instrum. Meth., A600, 68 (2009).
3) K. Yamamura, H. Takai, N. Zettsu, D. Yamazaki, R. Maruyama, K. Soyama, Opt. Express, 17 6414 (2009).
4) D. Yamazaki, M. Takeda, I. Tamura, R. Maruyama, A. Moriai, M. Hino, K. Soyama, Physica B (2009), doi:10.1016/j.physb.2009.06.022

原子炉：JRR-3　装置：SUIREN(C2-2)　分野：中性子散乱（装置）

1-8-7

Development of a Wavelength-Shifting-Fibre-Based Neutron Imager With a Fibre-Optic-Taper With a High Spatial Resolution

T. Nakamura, M. Katagiri, K. Toh, K. Sakasai and S. Soyama

Neutron Instrumentation Section, Materials and Life Science Division, J-PARC Center, Tokai 319-1195

A great deal of interest has been paid on the energy-selective neutron radiogphy at a pulsed neutron source. The detector specifications required in such applications are generally a spatial resolution of less than 100 μm and a moderate detector efficiency with a capability of time of flight measurement. We have recently developed a compact neutron image detector for the iBIX instrument in the J-PARC [1,2]. The detector comprising a neutron-sensitive scintillator and wavelength-shifting fibers exhibited a spatial resolution of less than 1 mm with a coverage area of 133 × 133 mm^2 with a pulse pair resolution of a few μs. This paper describes the detector implementing the fibre optic taper (FOT) in between the scintillator screen and the WLS fiber ribbons to improve a spatial resolution.

The FOT is a bundle of numbers of fine glass fibers. The each fiber has a taper along the length, thus the bundle works as an image magnifier. The small-sized FOT that has a smaller-face diameter of 8 mm with a taper ratio of 3.1 is implemented in the demonstrator. The effective pixel size becomes 0.16 mm since the side length of the fiber is 0.5 mm. The scintillation light created in the ZnS/^6LiF is partly collimated and propagated on to the WLS fibers while the light image is enlarged.

Figure 1 shows the measured neutron beam profile (y direction) when the up half of the detector was covered with the cadmium mask. The edge profile was fitted with an edge spread function. The spatial resolution was evaluated as 0.33 ± 0.03 mm in full width at half maximum. The measured edge profile in the x direction was similar to that in the y direction. The spatial resolution of the detector was improved by more than a factor two compared with the original detector that equipped without a FOT.

The measured spatial resolution of the demonstrator detector can be understood by the product of the thickness of the scintillator (0.3 mm) and the inherent spatial resolution of the original detector (0.8 mm). Further optimization on the scintillator thickness and the taper ratio of the FOT would improve a spatial resolution. The detector also exhibited a temporal resolution of a few μs and a moderate gamma sensitivity of 10^{-6} as in the iBIX detector.This kind of detector would be quite unique and useful for the neutron transmission measurements at the pulsed neutron source.

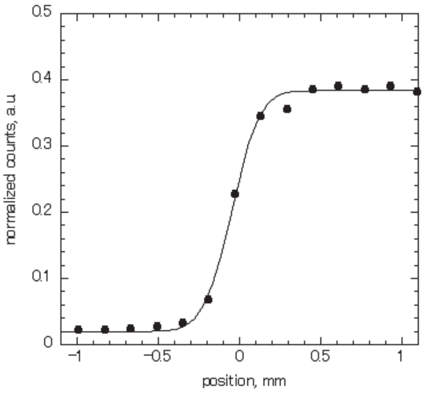

Figure 1: Neutron beam profile measured with the Cadmium mask covering up half of the detector.

References

1) M. Katagiri, et. al: Nucl. Instrum. Meth. A, 573, 149(2007).
2) T. Hosoya, et. al: Nucl. Instrum. Meth. A, 600, 217(2009).
3) T. Nakamura, et al: Nucl. Instrum. Meth. A, 604, 158(2009).

原子炉：JRR-3　装置：CHOP(C2-3-3)　分野：中性子散乱（装置）

1-8-8

Development of the Rradiation-resistant Neutron Mirrors for Neutron Guides

I. Tamura, R. Maruyama[1], D. Yamazaki[1], K. Yamamoto, and K. Soyama[1]
Nuclear Science Research Institute, JAEA, Tokai, Ibaraki 319-1195
[1] *J-PARC Center, JAEA, Tokai, Ibaraki 319-1195*

The neutron guides have been installed in the fixed plug in JRR-3 to increase the intensity of cold neutron beam. In view of the neutron beam transportation, it is important to install the neutron guides there. Since they are near for the cold neutron source, the radiation resistance of the neutron mirror and its substrate become problems. For the reduction in the maintenance cost, we developed the radiation resistance neutron mirror. Therefore, neutron mirror with the radiation resistance was fabricated by choosing the substrates with radiation resistance.

Ni mirrors were employed the ion beam sputtering technique. Substrates whose size 105mm in diameter and 1.5 mm in thickness were selected. The measurements of neutron reflectivity of neutron Ni mirrors on the Soda-lime glass and Glass-like carbon substrate have been carried out at SUIREN[1)] at JRR-3 in the Japan Atomic Energy Agency. The incident neutron wavelength was 3.93Å.

Figure 1 shows the neutron reflectivity of Ni mirror on the Soda-lime glass substrate and figure 2 shows the neutron reflectivity of Ni mirror on the Glass-like carbon substrate. Because reflectivities at the effective critical momentum transfer were almost 1.0, We succeeded in the manufacturing of Ni mirrors with m=1 on both substrates.

However, the performances of the reflectivities of mirrors on the Soda-lime glass substrate were not same as that on the glass-like carbon substrate. The fringe of reflectivity was observed only in the Ni mirror on the Soda-lime glass substrate and the thickness of a Ni layer was 2500∼3000Å clarified from the period of it. From the existence of the fringe of reflectivity, the performance of the reflectivity of the Ni mirror on the Soda-lime glass substrate is better than that of the Ni mirror on the glass-like carbon substrate.

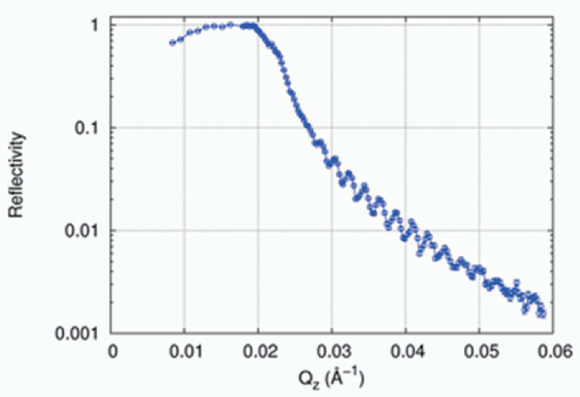

Figure 1: Neutron reflectivity of Ni mirror on the Soda-lime glass substrate carried out at SUIREN.

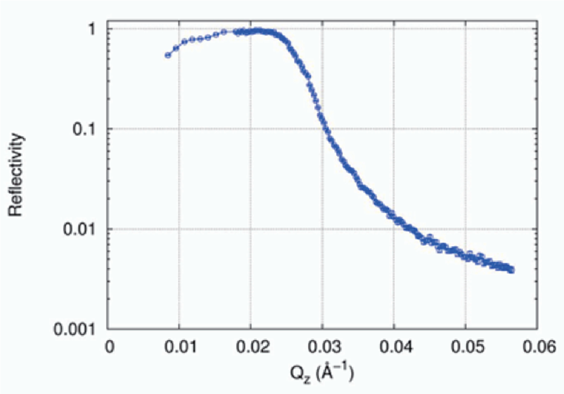

Figure 2: Neutron reflectivity of Ni mirror on the Glass-like carbon substrate carried out at SUIREN.

References

1) D. Yamazaki, et al. :"Development of a Neutron Reflectometer SUIREN at JRR-3", JAEA-Technology 2007-030 (2007).

原子炉：JRR-3　　装置：SUIREN(C2-2)　　分野：中性子散乱（装置）

1-8-9

Development of a Hybrid-Anvil Type High-Pressure Device for Single-Crystal Magnetic Neutron Diffraction under 10 GPa

T. Osakabe, H. Yamauchi

Quantum Beam Science Directorate, JAEA, Tokai, Ibaraki 319-1195

We developed a hybrid-anvil high-pressure (HA) device for single-crystal magnetic neutron diffraction beyond 3 GPa. The device consists of an opposed pair of a lower sapphire anvil and an upper WC anvil with a hollow in the center of the culet. The essential point of the device is the hollow of the WC anvil. A gasket between the anvils is strongly caught by the edge of the hollow when the gasket is pressed. As a result, the deformation of the gasket is highly suppressed and the pressure generation efficiency is improved. Obviously, the hollow can enlarge the volume of the sample chamber. Maximum pressure generated by the device is 7 GPa $^{1)}$.

To increase the maximum pressure up to 10 GPa, we tried three types of the lower anvil instead of the simple sapphire anvil in the HA device. One is a sapphire anvil with a thin diamond cap, another is a sapphire anvil supported by a MP35 alloy, and the other is a SiC anvil supported by a MP35 alloy. We found that the modified hybrid-anvil (mHA) device of the combination of the WC anvil and the supported SiC anvil could generate the pressure of 10 GPa at the load of 3.8 tons. Fig. 1 shows a schematic drawing of the mHA device. Fig. 2 also shows the result of the pressurization test of the mHA device. The size of the sample chamber under 10 GPa was about 1 mm diameter and 0.3 mm height, which was the same volume as that of the HA device under pressure and was sufficient for single-crystal magnetic neutron diffraction experiments. We succeeded in the single-crystal magnetic neutron diffraction experiments on the RB_2C_2 (R=Dy, Ho) up to 9.6 GPa using the mHA device.

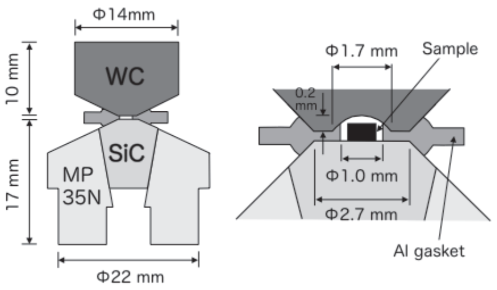

Figure 1: Schematic drawings of a modified hybrid-anvil device.

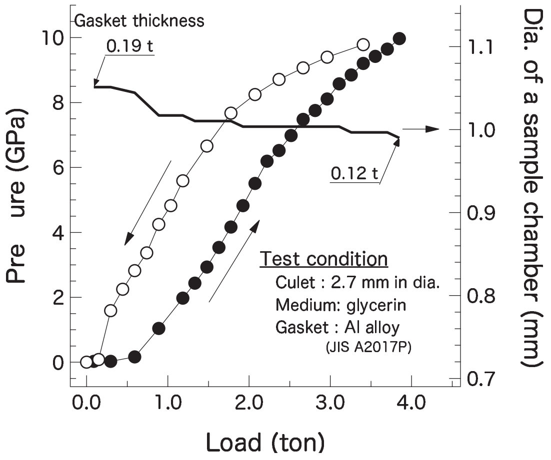

Figure 2: Generated pressure and diameter of the sample chamber vs. applied load for the mHA device.

References

1) T. Osakabe, K Kakurai, D Kawana, K Kuwahara: “J. Magn. Magn. Matt.”, 310, pp. 2725-2727 (2007).

原子炉：JRR-3　　装置：TAS-1(2G)　　分野：中性子散乱（装置）

1-8-10

Renewal of a Software and a Data Acquisition System for the Neutron Reflectometer SUIREN

M. Takeda[1,2], D. Yamazaki[1,2], H. Izunome[1] and A. Birumachi[1]

[1] *Quantum Beam Science Directorate, Japan Atomic Energy Agency, Tokai, Ibaraki 319-1195, Japan*
[2] *J-PARC Center, Tokai, Ibaraki 319-1195, Japan*

Neutron reflectometry has been widespread as a powerful and nondestructive technique to investigate the internal layered structures now. The new neutron reflectometer SUIREN has been installed at C2-2 beam hole in the JRR-3 beam hall in 2007 and is now open to many users. Polarized neutron reflectivity measurements with the full polarization analysis can be performed using this reflectometer by inserting the polarized neutron devices1).

An original software package for controlling the reflectometer and a data acquisition system (DAQ) were constructed based on LabVIEW®, and DAQ hardwares of National Instruments®. This system was satisfactory and worked well. However, we had to wait for a long time to fix minor bugs and to add new components to the reflectometer such as additional stepping motors and a one-dimensional position sensitive detector because a company who constructed the system was too busy to manage the system.

Therefore, we decided to use the same software package and DAQ as those used for three triple-axis spectrometers TAS-1, TAS-2, and LTAS installed at JRR-3. The software package was coded by in-house programmers in JAEA, and ran on HP Tru64 UNIX®on Alpha system. This package was ported to Red Hat Enterprise Linux on x86 based system. A new DAQ is mainly composed of Multi NT-2400 Series which is a commercial product of Laboratory Equipment Corporation.

A variety of modules and interfaces such as a stepping motor controller, a MCA, a timer/scaler, a GPIB controller, a mechanical relay, and an isolated digital input devices are available with a NT-2400 chassis, and these modules and devices are controlled by a library software. Figure 1 shows a schematic diagram of the new system using a workstation operated by the Linux and NT-2400.

We also introduced devices for the neutron polarization analysis (the 2nd spin-flipper, an analyzing mirror, and so on) concurrent with this replacement of the software and DAQ. We completed the construction of SUIREN using this new system, and the full polarization analysis of the polarized neutron reflectivity can be performed as a routine work on SUIREN.

References

1) D. Yamazaki, M. Takeda, I. Tamura, R. Maruyama, A. Moriai, M. Hino, K. Soyama, Physica B **404**, 2557 (2009).

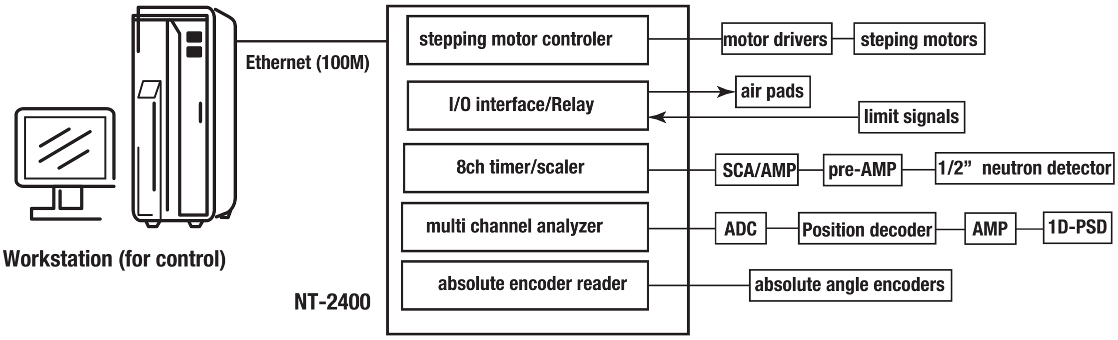

Figure 1: Schematic diagram of new control and data acquisition system for SUIREN.

原子炉：JRR-3　　装置：SUIREN(C2-2)　　分野：中性子散乱（装置）

1-8-11

A beam divergence correction mirror for neutron resonance spin echo

R. Maruyama^A, M. Hino^B, H. Hayashida^C, M. Kitaguchi^B, N. Achiwa^D, D. Yamazaki^A, T. Ebisawa^A, K. Soyama^A

^{A}*J-PARC Center, Japan Atomic Energy Agency*
^{B}*Research Reactor Institute, Kyoto University*
^{C}*Quantum Beam Science Directorate, Japan Atomic Energy Agency*
^{D}*Graduate School of Science, Osaka University*

Neutron resonance spin echo (NRSE) enables us to measure neutron quasielastic scattering with high energy resolution. Its energy resolution is limited by a path length variation due to the beam divergence. Neutron focusing technique using a neutron supermirror can be used to overcome this problem.

A neutron supermirror with cylindrical surface was fabricated as follows. Supermirror with $m = 3$ was deposited on Si wafer with a length of 250 mm, a width of 30 mm, and a thickness of 0.2 mm. When we assume an incident angle of the central flight path to the cylindrical mirror of $\theta = 42$ mrad, the object and image distance from the center of the mirror of $a = b = 500$ mm, and the length of the mirror of $l = 250$ mm, the radius of the cylindrical surface of $R = 12$ m are obtained from the imaging equations. The cylindrical profile was produced by numerically controlled machining of an aluminium plate. The back side of the Si wafer was glued on the cylindrical surface of the aluminium plate using Araldite epoxy glue.

The experiment was performed using the JRR-3/MINE1 beam line at JAEA. To investigate the effect of the cylindrical mirror on the path length variation due to the beam divergence, MIEZE (Modulation of Intensity by Zero Effort) spin echo measurement was performed as shown in Fig. 1(a). The width of the slit (S2) was narrowed to 1 mm to choose a particular flight path from the entire beam. Figure 1(b) shows the measured spin echo signals for the different flight paths chosen by S2. The phase of the measured echo signals is plotted in Fig. 1(c). The solid line indicates the calculated phase where the path length variation is assumed to be corrected in the flight path between the first and the second bootstrap RSF. The calculated phase is in good agreement with the measured value. This result demonstrated that a cylindrical mirror effectively corrects a path length variation due to the beam divergence.

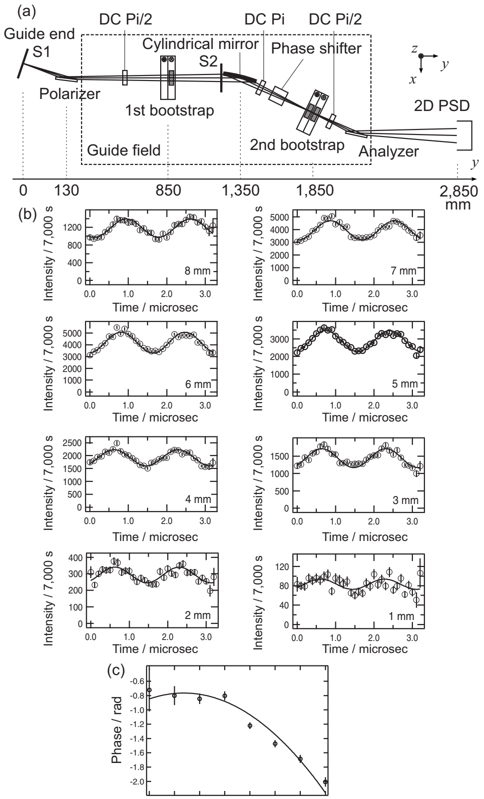

Fig. 1. (a) Experimental geometry of MIEZE spin echo measurement. (b) Measured echo signals for the different flight paths. (c) Phase of the measured and calculated echo signals.

1-8-12

Development of Cubic Anvil type pressure cell for neutron scattering experiments under pressure

Koji Munakata(A), Kazuyuki Matsubayashi(A), Masakazu Nishi(A), Hiroyuki Kagi(B)
and Yoshiya Uwatoko(A)
(A)ISSP, Univ. of Tokyo, (B)Grad. Sch. of Sci., Univ. of Tokyo

During last few decades, intensive studies have been performed on strongly correlated electron systems and/or magnetic materials under high pressure. As a result, with discovery of many interesting physical phenomena at high pressure and low temperature, new technique and know-how of high pressure experiments have been accumulated. However, in the field of neutron experiments, high pressure technique is less common compared to other experiments due to the inevitable difficulty, such is a significant decrease in intensity by absorption and scattering when the neutrons pass through a pressure device that surrounds the sample: it is difficult to conduct experiments with reliability and accuracy.

Recently, we have developed small high pressure apparatus for transport and magnetic measurements, a clamp type of palm cubic anvil cell (PCAC) [1]. This cubic anvil type pressure apparatus can generate superior hydrostatic pressure to other high pressure apparatus. Then, we optimized anvil material for neutron scattering experiments [2], from tungsten carbide (WC) to ZrO2, relatively transparent to neutron beams. In this work, pressurization test was carried out at room temperature. For gasket, two types of material are used, a duralumin (A7057) and a mesoalite (Meso10) which is Al-based hard material. Glycerol is chosen as a pressure transmitting medium because of its good hydrostatic property. A single crystal of NaCl, 1.5 x 1.5 x 1.5 mm3 in size, was set in the gasket and pressurized with a hydraulic press. Generated pressures in the gasket were estimated from a compressibility of NaCl by determining a lattice constant from (200) reflection at each external load. Fig. 1 shows load dependence of the profiles of (200) reflection in θ-2θ scan. As shown in the figure, palpable profiles were obtained. No significant difference was found between the two materials of gasket. We confirmed in generating pressure about 7 GPa at the load of 80 ton. We expect that PCAC will be useful apparatus in the field of high pressure neutron experiments.

[1] Y. Uwatoko et al., Recent Absorbing Topics in the Research of the Earth's Interior, 18 (2008) 230. (in Japanese)
[2] T. Fujiwara et al., Activity Report on Neutron Scattering Research: Experimental Reports 15 (2008) 658.

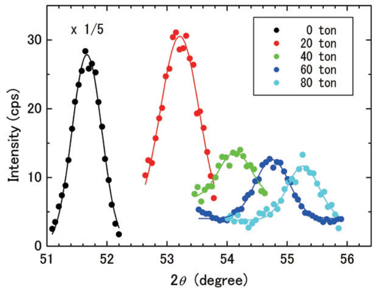

Fig. 1. Profiles of (200) reflection of NaCl in θ-2θ scan at various external loads. At the result of 0 ton, intensity is multiplied by factor of one fifth. The load of 80 ton is equivalent to 7 GPa.

Activity Report on Neutron Scattering Research: Experimental Reports **16** (2009)
Report Number: 996

1-8-13

Development of resonance spin flipper with iron yoke

M. Kitaguchi(A), M. Hino(A), Y. Kawabata(A), S. Tasaki(B), H. Hayashida(C), R. Maruyama(C), T. Ebisawa(C)
(A) KURRI, (B) Kyoto Univ., (C) JAEA

Neutron spin echo (NSE) is one of the techniques with the highest energy resolution for quasi-elastic scattering by measuring rotation of the neutron spin[1]. In neutron resonance spin echo (NRSE), two resonance spin flippers (RSFs) replace a homogeneous static magnetic field for spin precession in the conventional NSE[2]. An RSF, which flips the spin of a neutron by exchanging energy between the neutron and an oscillating magnetic field, gives the difference of wavenumber between up- and down-spin components of the neutron. The relative phase between the two spin components, which is equivalent to spin rotation, is provided by the difference of wavenumber in the area between the RSFs.

A RSF consists of a static magnetic field and an oscillating magnetic field. The static field is proportional to the frequency of the the oscillating field. It was quite difficult to provide the strong static field corresponding to the high frequency up to 500kHz by using air-core coils. New type of RSF has been developed by using dipole magnet with iron poles for the static magnetic field (figure 1). It could provide strong magnetic field with less current, however, magnetic flux leak and its surface was not well-defined.

The gap between the two iron poles had the height of 150mm. The dipole magnet had the uniform magnetic field with the center area of 15mm width, 15mm height and 50mm long. The uniformity was less than 10% . About 20mT was measured at the center of the uniform field area with the current of 8A. The magnetic field was quite stable by using the regulated power supply. Temperature of the coil was also stable for the magnetic field which was less than 20mT without any additional cooling system. The return field was enclosed by iron yoke around the magnet well.

Test experiments to observe MIEZE signals with high frequency by using the new RSFs have been performed using the cold neutron beam line MINE1 at JRR-3 reactor at JAEA. The beam had the wavelength of 0.81nm and the bandwidth of about 10 % . Figure 2 shows the MIEZE signal with normalization of the detector efficiency. Neutron counts modulated according to the phase of the oscillating field of the RSFs. The effective frequency of the modulation was 600kHz. The contrast of the signal was 0.58.

This demonstrated the stability and the smoothness of the magnetic fields provided by the dipole magnets. MIEZE spectrometer is under final process to practical use. We are also continuing to develop RSF with much higher frequency for NRSE spectrometer with high resolution. We will utilize the new system including the new RSFs for the development of a neutron spin echo spectrometer at J-PARC[3].

[1] F. Mezei, Z. Phys. 255(1972)146.
[2] R. Gaehler, R. Golub, Z. Phys. B65(1987)43.
[3] Y. Kawabata, et. al., Nucl. Instr. and Meth. A574(2006)1122.

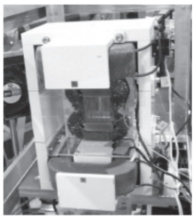

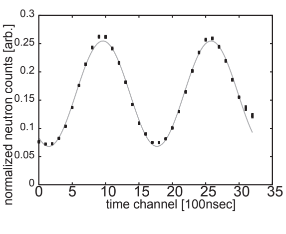

Fig. 1. (Left) RSF with dipole magnet with iron pole.
Fig. 2 (Right) MIEZE signal with 600kHz.

1-8-14

Magnetic Imaging with Neutron Spin Interferometry

Yamazaki D., Hayashida H., Ebisawa T., Maruyama R., Soyama K., Takenaka N.[a],
Kageyama M.[b], Tasaki S.[b], Hino M.[c], Kawabata Y.[c], IIkura H., Yasuda R., Sakai T.,
Matsubayashi M.

Japan Atomic Energy Agency, [a]Kobe University, [b]Kyoto University, [c]KURRI

Stress-induced magnetization change in Permalloy foils was observed using neutron spin interferometry.

Without samples in a spin interferometer, phases and visibilities of interference patterns are stable and almost fixed to their initial values. If a sample which has magnetic field *B* is placed or a field *B* is applied in the interferometer, the field rotates neutron spin around itself and consequently gives rise to phase shifts and visibility damping. By analyzing phase shifts and visibility damping, we can obtain both amplitude and direction of field. In addition, 2-dimensional field distributions can be observed by measuring interference patterns with a position sensitive detector (PSD) and analyzing phase shifts and visibility damping at each pixel of the PSD. In our experiment, we utilized a 2-dimensional PSD with ^{6}Li scintillator glass.

We prepared three Permalloy foils (A,B,C) of 100 μm in thickness. The foil A and B were stressed by bending and stretching them just once. The angles of bent were different for the two foils, 45 degree for foil A and 180 degree for foil B. The foil C was as is.

A foil was placed vertically in the interferometer and illuminated by monochromatic (8.8 Å) neutron beam of 25 mm (H) × 1 mm (W). As for foils A and B, they were placed so that the bend lines are horizontal.

The figure shows the phase shifts and relative visibilities of foil A and B as functions of vertical position. The red lines show data from foil A and the blue lines foil B. Phase shifts are obtaind by subtracting phases of foil C and relative visibilities by dividing by visibilities of foil C.

It is seen that all lines have a dip at 16.5 mm, where the bend line exists. The dips mean magnetization changes, in amplitude and direction, at the bend lines of Permalloy foils. The fact that Foil B, bent with the higher angle, shows the deeper dips in phase and visibility might show the stress-dependence of the magnetization change.

We have also obsereved phase shifts and visibility damping due to a magnetic field induced by two parallel electric currents.

Detailed analysis of these data is now underway and the results will appear elsewhere.

In summary, we showed the capability of neutron spin interferometry to identify magnetic field and magnetization distribution. It could be used to explore the current distribution in fuel cells, magnetization properties of ferromegnetic foils and other applications.

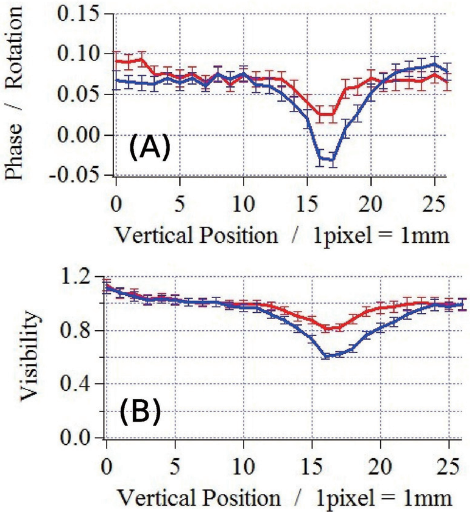

Fig. 1. (A) Phases and (B) Visibilities as functions of vertical position : (Red) 45deg-bent permalloy (Blue) 180deg-bent permalloy

1-8-15

A new MIEZE technique for investigation of relaxation on magnetic nanoparticles

M. Hino[1], H.HAYASHIDA[2], M.Kitaguchi[1], N.Achiwa[3], Y.Kawabata[1]
KURRI[1], JAEA[2], Osaka Univ.[3]

In the MIEZE, sample is placed after the analyzer and there are no optical components between sample and detector. Therefore, the MIEZE spectrometer can be applied to small angle neutron scattering and neutron reflectometry. The contrast of MIEZE signal can be observed without reduction even in magnetic scattering although the contrasts of NSE and NRSE are less than half. However, in general, it is not easy for simple MIEZE setup to separate magnetic and nonmagnetic fluctuations of magnetic nanoscale particles since it measures the both intensities of qausielastic scattering, simultaneously. We propose a new MIEZE technique which is to set a second analyzer and an additional π flipper, in order to separate the magnetic and nonmagnetic quasielastic scattering intensities. We succeeded in observing the superparamagnetic fluctuations of magnetite particles in ferrofluid by using the new technique(Fig.1)[1]. Magnetic ferrofluid consists of magnetite particles and solvent (heavy water). The magnetite particles with a diameter on the order of 10 nm are coated by oleic acid. There are two kinds of dynamical mode in magnetite ferrofluid. One is Brownian diffusion mode of magnetite particles and the other is superparamagnetic fluctuation which is a relaxation of magnetic moment in magnetite particles. Both relaxation time depends on particle size and temperature. The Brownian relaxation time of the particle with the diameter 10 nm is reported to be longer than 2 ns which is out of measurable Fourier time range in this MIEZE experimental setup. On the other hand, the relaxation time of superparamagnetism (Neel) is much faster than the Brownian relaxation time. We tried to observe the effect of relaxation on superparamagnetism. Here MIEZE signal is sensitive to the path length dispersion in neutron trajectories from sample to detector. We estimated instrumental resolution function of the MIEZE spectrometer by using Monte Carlo(MC) simulation. The contrasts from nuclear scattering were well reproduced by MC simulation. On the other hand, these contrasts from magnetic scatterings were almost less than half of nuclear scattering ones.It is clear that the superparamagnetism relaxation contributes to reducing the contrast of MIEZE signal from magnetic scattering.

[1]H.Hayashida, M.Hino, *et. al.*, Nucl.Inst.Meth.A**600**(2009)56.

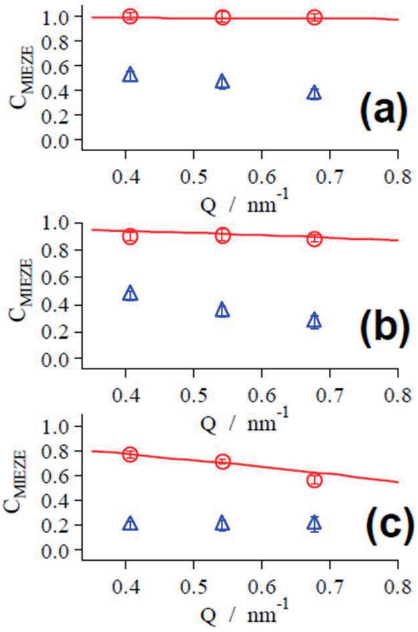

Fig. 1. Contrasts of MIEZE signals of nuclear (open circles), magnetic (open triangles) scattering with the ferrofluid and resolution functions at (a) τ= 0.3, (b)τ =0.8, (c)τ= 1.6 nsec as a function of *Q*, respectively.

1-8-16

Development of Cubic Anvil type pressure cell for neutron scattering experiments under pressure

Koji Munakata, Kazuyuki Matsubayashi, Masakazu Nishi and Yoshiya Uwatoko
ISSP, Univ. of Tokyo

During last few decades, intensive studies have been performed on strongly correlated electron systems and/or magnetic materials under high pressure. As a result, with discovery of many interesting physical phenomena at high pressure and low temperature, new technique and know-how of high pressure experiments have been accumulated. However, in the field of neutron experiments, high pressure technique is less common compared to other experiments due to the inevitable difficulty, such is a significant decrease in intensity by absorption and scattering when the neutrons pass through a pressure device that surrounds the sample: it is difficult to conduct experiments with reliability and accuracy.

Recently, we have developed small high pressure apparatus for transport and magnetic measurements, a clamp type of palm cubic anvil cell (PCAC) [1]. This cubic anvil type pressure apparatus can generate superior hydrostatic pressure to other high pressure apparatus. Then, we optimized anvil material for neutron scattering experiments [2], from tungsten carbide (WC) to ZrO2, relatively transparent to neutron beams. In this work, pressurization test was carried out at room temperature. For gasket, two types of material are used, a duralumin (A7057) and a mesoalite which is Al-based hard material. Glycerol is chosen as a pressure transmitting medium because of its good hydrostatic property. A single crystal of NaCl, 1.5 x 1.5 x 1.5 mm3 in size, was set in the gasket and pressurized with a hydraulic press. Generated pressures in the gasket were estimated from a compressibility of NaCl by determining a lattice constant from (200) reflection at each external load. Fig. 1 shows load dependence of the profiles of (200) reflection in θ-2θ scan. As shown in the figure, palpable profiles were obtained. No significant difference was found between the two materials of gasket. We confirmed in generating pressure about 7 GPa at the load of 80 ton. We expect that PCAC will be useful apparatus in the field of high pressure neutron experiments.

[1] Y. Uwatoko et al., Recent Absorbing Topics in the Research of the Earth's Interior, 18 (2008) 230. (in Japanese)
[2] T. Fujiwara et al., Activity Report on Neutron Scattering Research: Experimental Reports 15 (2008) 658.

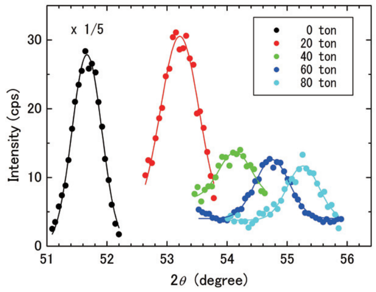

Fig. 1. Profiles of (200) reflection of NaCl in θ-2θ scan at various external loads. At the result of 0 ton, intensity is multiplied by factor of one fifth. The load of 80 ton is equivalent to 7 GPa.

1-8-17

Development of pixel detector for ultra-cold neutrons

Y. Kamiya(A), S. Kawasaki(B), G. Ichikawa(B), S. Sonoda(B), S. Komamiya(A)(B), M. Hino(C), M. Kitaguchi(C), T. Sanuki(D)
(A) ICEPP, The Univ. of Tokyo, (B) Graduate School of Science, The Univ. of Tokyo, (C)KURRI Kyoto Univ., (D)Graduate School of Science, Tohoku Univ.

A CCD-based pixel detector for ultra-cold neutrons has been developed. The detector consists of a back-thinned CCD (S7170-0909, Hamamatsu Photonics K. K.) with a thin neutron converter directly deposited onto the sensor surface. The active area is 12.3 x 12.3 mmˆ2 (512 x 512 pixels of 24 x 24 microns). Two nuclear reactions, 10B(n,alpha)7Li and 6Li(n,alpha)3H, are considered for converter design, where strongly ionizing particles are emitted via those reaction. The thicknesses for the boron based and lithium based converters are both decided to be 200 nm in consideration of conversion efficiency and production easiness. They are sandwiched between titanium layers of 20 nm thickness to prevent oxidizing and crumbling. We used the Neutron Mirror Fabrication System at the KURRI to make the detectors with the converter. Here we report about detection efficiency, uniformity and spatial resolution which were measured using cold neutron beams supplied at the MINE2 line.

The ionizing particle converted from the neutron makes a cluster of charged up pixels distributing around an incident point. Charge sum corresponds to the particle’s kinematic energy and an weighted center of the pixels is a good estimation of the point. Distribution of the charge sum has two edges that correspond to the initial energies of the emitted particles (monochromatic), and has tails to the low energy region that represent an energy loss when the particle transmits through the converter and a thin insensitive volume on the CCD. To separate signal events from a background or thermal noise, we apply a cut to the charge sum distribution. The threshold corresponds to 0.15 MeV energy deposit. The detector was set on the sample stage which continuously move right and left in horizontal to be irradiated uniformly. Detector efficiency was measured to 1.7%(0.3%) with Boron(Lithium) based converter by comparing with the 3He reference detector. Uniformity was evaluated to less than 3% over the sensitive area. Spatial resolution was estimated by analyzing edges of shadow of the Gadolinium neutron mask, which is located in front of the detector surface. Fig.1 shows a neutron distribution taken with the Boron converter. By fitting with error functions for each edges, the spatial resolution was estimated to 3 microns.

In conclusion, we measured basic performances of the CCD-based pixel detector using the cold neutron beams. The results show that the detector has a fine spatial resolution and enough uniformity. Detector with Boron based converter shows better performance than that with Lithium based converter.

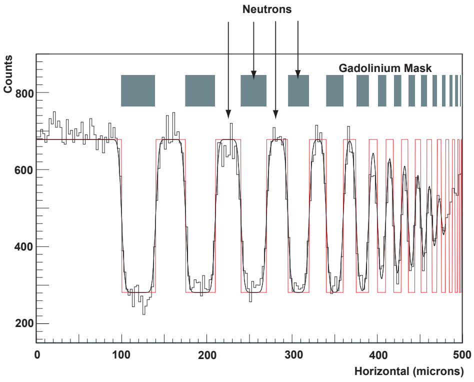

Fig. 1. Neutron distribution. Red line shows an ideal shadow of the Gadolinium mask. Black line shows the fitted distribution. Spatial resolution of 3 microns is measured.

1.　中性子散乱　9）超伝導現象

1. Neutron Scattering　　9）Superconductivity

1-9-1

Structural Analysis on Fe-Based Superconductors, PrFeAsO$_{1-x}$F$_x$ and PrFeAsO$_{1-y}$

K. Kodama[1,2], M. Ishikado[1,2], F. Esaka[3], A. Iyo[4,2], H. Kito[4,2], H. Eisaki[4,2] and S. Shamoto[1,2]

[1] *Quantum Beam Science Directorate, JAEA, Tokai, Ibaraki 319-1195*
[2] *JST, Transformative Research-Project on Iron Pnictides (TRIP), Tokyo 102-0075*
[3] *Nuclear Science and Engineering Directorate, JAEA, Tokai, Ibaraki 319-1195*
[4] *Nanoelectronics Research Institute, AIST, Tsukuba, Ibaraki 305-8562*

Among Fe-based superconductors, a superconductivity in so-called 1111-system is induced by substituting fluorine for oxygen or by oxigen deficiency for parent compound RFeAsO (R:rare earth elements). [1,2] Generally, it is considered that above two effects reduce the valence of Fe-ion from +2 and dope electrons, resulting in the superconductivity. However, comparing the phase diagram of the F-substituted system with that of the O-deficient system, the superconducting transition temperature (T_c) is not scaled by the Fe-valence, indicating that the Fe-valence is not unique parameter for the superconductivity. The atomic substitution and deficiency also change structural parameters, which modify the electric state and may induce the superconductivity. Then we have performed the structural analysis on neutron powder diffraction data of PrFeAsO$_{1-x}$F$_x$ and PrFeAsO$_{1-y}$, including parent compounds.

Powder diffraction data were collected using the high-resolution powder diffractometer (HRPD) at room temperature. Rietveld analysis was performed by using the program RIETAN-2000.[3] Typical diffraction pattern and fitted result are shown in Fig. 1. The occupancy at O (O$_{1-x}$F$_x$) site is refined in the analysis and F-concentration is determined by the secondary ion mass spectrometry in order to determine the valence of Fe-ion. The lattice canstants, a and c of PrFeAsO$_{1-x}$F$_x$ and PrFeAsO$_{1-y}$, are plotted against the Fe-valence in Fig. 2. The lattice constant a (c) of PrFeAsO$_{1-y}$ is larger (smaller) than that of PrFeAsO$_{1-x}$F$_x$ even for the parent compounds with Fe-valence of ∼ +2. It is due to the difference of the sample preparation condition; under high pressure for PrFeAsO$_{1-y}$ and in a quartz tube sealed in vacuum for PrFeAsO$_{1-x}$F$_x$. This result suggest that the difference of structural parameters modifing the electric state causes the difference of the T_c-Fe-valence phase diagram between PrFeAsO$_{1-x}$F$_x$ and PrFeAsO$_{1-y}$.

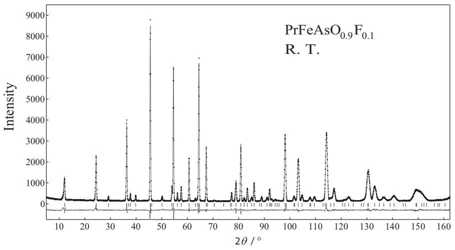

Figure 1: Powder diffraction pattern and the result of Rietveld analysis on PrFeAsO$_{0.9}$F$_{0.1}$.

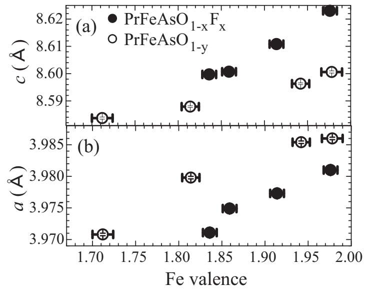

Figure 2: The lattice constants, (a) a and (b) c of PrFeAsO$_{1-x}$F$_x$ and PrFeAsO$_{1-y}$ with tetragonal structure are plotted against the valence of Fe-ion, by closed and open circles, respectively.

References

1) Y. Kamihara, et al. :“J. Am. Chem. Soc.”, 130, 3296 (2008).
2) H. Kito, H. Eisaki, and A. Iyo :“J. Phys. Soc. Jpn.”, 77, 063707 (2008).
3) F. Isumi and T. Ikeda :“Mater. Sci. Forum”, 321-324, 198(2000).

原子炉：JRR-3　　装置：HRPD(1G)　　分野：中性子散乱（超伝導）

1-9-2

Magnetic Excitations in $LaFeAsO_{1-x}F_x$ Superconductors

S. Wakimoto[1,2], K. Kodama[1,2], M. Ishikado[1,2], M. Matsuda[1,2], R. Kajimoto[2,3], M. Arai[2,3],
K. Kakurai[1,2], A. Iyo[2,4], H. Kito[2,4], H. Eisaki[2,4], and S. Shamoto[1,2]

[1] *Quantum Beam Science Directorate, Japan Atomic Energy Agency, Tokai, Ibaraki 319-1195*
[2] *JST, Transformative Research-Project on Iron Pnictides (TRIP), Tokyo 102-0075*
[3] *J-PARC Center, Japan Atomic Energy Agency, Tokai, Ibaraki 319-1195*
[4] *Nanoelectronics Research Institute, National Institute of Advanced Industrial Science and Technology, Tsukuba, Ibaraki 305-8562*

The recently discovered Fe-pnictide superconductor $LaFeAsO_{1-x}F_x$ has provided a unique opportunity to study the high temperature superconductivity other than the cuprates. 1) Band calculations indicate cylindrical Fermi surfaces at Γ- and M-points. From the early stage of the Fe-pnictide superconductor research, many authors have pointed out the importance of spin fluctuations arising from the Fermi surface nesting between the two points in realizing the superconductivity. In fact spin fluctuations have been observed as significant inelastic neutron scattering for the 122-type superconducting compounds, $Ba_{1-x}K_xFe_2As_2$ 2) showing a resonance behavior. On the other hand, the NMR study of the $LaFeAsO_{1-x}F_x$ system shows dramatic decrease of spin fluctuations near $\omega = 0$ in superconducting compositions. 3)

To reconcile these facts, systematic study of low energy spin fluctuation ($\omega \leq 15$ meV) has been performed using polycrystalline $LaFeAsO_{1-x}F_x$ with nominal compositions $x = 0, 0.05, 0.075$, and 0.10 ($T_c = 0, 25, 25$, and 29 K, respectively). High-quality polycrystalline samples were synthesized by solid state reaction. 25 g for each composition was used for inelastic neutron scattering experiments at TAS-1 and TAS-2.

Figure 1 shows doping dependence of the imaginary part of dynamic spin susceptibility $\chi''(\omega)$ at 11 meV. In contrast to the dramatically diminished magnetic fluctuation observed by NMR, the cross section exclusively at 11 meV observed by neutron inelastic magnetic scattering decreases little with doping in the superconducting compounds and, to our surprise, it is comparable to that of the non-doped LaFeAsO. These facts suggest that the antiferromagnetic spin fluctuation remains in deep inside the superconducting regime, implying the importance of spin fluctuation in this system. In addition, we have observed that the magnetic intensity at ~ 11 meV increases below ~ 30 K, consistent with the resonance behavior. More detailed study of doping dependence is now in progress.

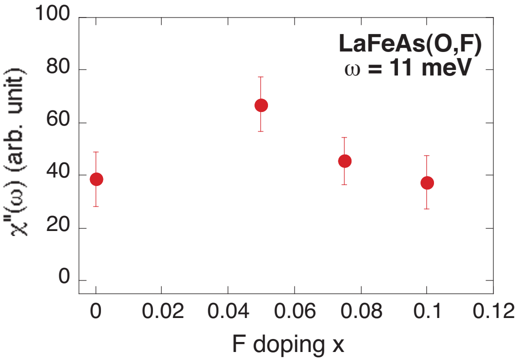

Figure 1: Doping dependence of q-integrated dynamical spin susceptibility $\chi''(\omega)$ measured at 11 meV. The data at $x = 0$ is measured at just above the Néel temperature where the spin fluctuation becomes maximum. The other data are measured at 4K.

References

1) Y. Kamihara, T. Watanabe, M. Hirano, and H. Hosono, J. Am. Chem. Soc. **130**, 3296 (2008).
2) A. D. Chirstianson, E. A. Goremychkin, R. Osborn, S. Rosenkranz, M. D. Lumsden, C. D. Malliakas, I. S. Todorov, H. Claus, D. Y. Chung, M. G. Kanatzidis, R. I. Bewley, and T. Guidi Nature **456**, 930 (2008).
3) Y. Nakai, K. Ishida, Y. Kamihara1, M. Hirano, and H. Hosono, J. Phys. Soc. Jpn. **77** 073701 (2008).

原子炉：JRR-3　　装置：TAS-1(2G), TAS-2(T2-4)　　分野：中性子散乱（超伝導）

1.　中性子散乱　10）残留応力

1. Neutron Scattering　　10）Residual Stress

1-10-1

Behavior of Crack Growth of Austenitic Stainless Steels under Decrease in Stress

H. Ogawa, I. Ioka and M. Yamamoto

Nuclear Science and Engineering Directorate, JAEA, Tokai, Ibaraki 319-1195

It has been shown that the crack growth caused by stress corrosion cracking (SCC), which is located near welded parts at primary loop recirculation system's pipes of BWRs, is inhibited. It seems that this inhibition arises from the reduction of residual stress as the crack growth. The residual stress becomes a key factor to control the crack growth. Therefore, it is important to measure residual stress around the crack. The residual stress using RESA was measured to clarify the relationship between the crack growth and the residual stress.

The specimens with a crack induced by fatigue test were prepared. The specimens were type 316L stainless steel (SS) with high stress at crack tip. The specimens were subjected to heat treatment (850Cx1h, 30%CW). The stress at the crack tip was generated by a taper pin as shown in Fig.1. The estimated initial stress intensity factor (K) is about 50 (MPa$\sqrt{m}$). The SCC test for crack growth is conducted in high temperature water (288C, 7.5MPa, saturated dissolved oxygen) for 1000hs. The fracture surface of specimen was observed by SEM after SCC test. Lattice constants corresponded to residual stress were measured along the line of the ligament using RESA.

The stress around the crack tip was compared between " before SCC test " and " after SCC test ". The result of type 316L SS was shown in Fig.2. It is found that SCC enhanced the growth of crack in type 316L SS. The stress at crack tip was not clearly change, though the propagation of crack was estimated about 1mm. Fig.3 shows fracture surface of type 316L SS after SCC test. The mode of crack was transgranular (TGSCC) and the top of crack was not flat. After SCC test, K corresponded to residual stress was calculated from the load yielded taper pin. The calculated K was a decrease in 65% against the initial K. The residual stress calculated by K was different from that by RESA. The difference may be attributed to the non-uniformity of crack propagation or voxel size (2x2x1mm).

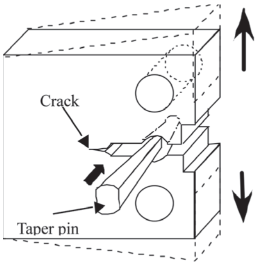

Figure 1: Taper-pin type CT specimen.

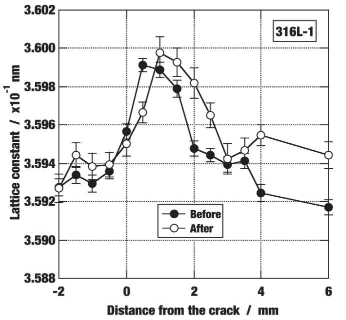

Figure 2: Comparison of lattice constant in type 316L SS between " before " and " after ".

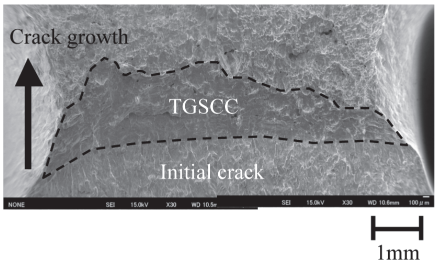

Figure 3: Fracture surface of type 316L after SCC test.

原子炉：JRR-3　　装置：RESA-2(T2-3-2)　　分野：中性子散乱（残留応力）

1-10-2

Stress Measurement of Large Scaled Welded Tube Using Neutron Diffraction Technique

H. Suzuki, J. Katsuyama[1], T. Tobita[1] and Y. Morii

Quantum Beam Science Directorate, JAEA, Tokai, Ibaraki 319-1195
[1]*Safety Research Center, JAEA, Tokai, Ibaraki 319-1195*

Residual stress distributions near weld line of an austenitic large scaled butt-welded tube (500 mm diameter, 760 mm length and 28 mm wall thickness) were measured using the neutron diffraction technique to evaluate effects of crack propagation and repair welding on the residual stress distribution. The through thickness distribution of residual stresses were measured at a position 12.5 mm transverse away from the weld center using the engineering diffractometer, RESA, in the JRR-3 at the Japan Atomic Energy Agency. Two slots (50 mm x 150 mm) were machined on the weld line at 180 deg around the circumference from the centre for minimizing the neutron path length. The lattice constant in stress-free condition was measured using a standard sample cut from the remaining material obtained after machining the slots. Lattice strains of the 311 reflection were measured to avoid the intergranlar effect caused by the accumulated thermal plastic strain due to welding.

Figure 1 shows changes in residual stress distributions before and after slitting and repair welding. In as-welded tube, typical residual stress distributions were observed and it agreed well with the stress distributions calculated by the numerical simulations reported in previous studies. After machining the slit with the size of 30 mm length, 10 mm depth and 0.5 mm width at a position 12.5 mm transverse away from the weld center on the inside wall of the tube, the residual stresses in the axial and the hoop directions were released in the part of the slit. On the other hand, the residual stress distributions after the repair welding on the outside wall were significantly changed compared with the original stress distributions before repair welding. Tensile residual stresses were observed after the repair welding and compressive stresses were disappeared at all positions in all three directions. Tensile residual stresses generated on the inside wall might encourage generation of the stress corrosion cracking, and the tensile residual stresses generated in the middle might drive the crack propagation. Therefore, the repair welding would have an influence on enhancement of crack propagation.

In this study, we indicated that the neutron diffraction technique is useful and powerful tool for measuring residual stress distribution in the large scaled mechanical components.

This research project has been conducted under the research contract with the Japan Nuclear Energy Safety Organization (JNES).

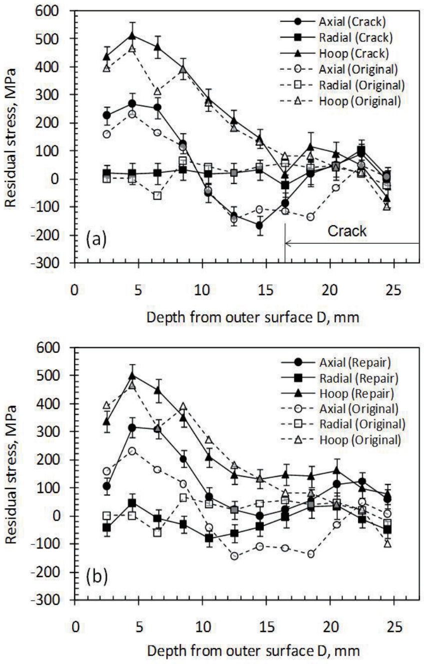

Figure 1: Change in residual stress distributions before and after slitting (a) and repair welding (b).

原子炉：JRR-3　　装置：RESA(T2-1)　　分野：中性子散乱（残留応力）

1-10-3

Strain Measurement in Rebar in Reinforced Concrete by Neutron Diffraction

H. Suzuki and K. Kusunoki[1]

Quantum Beam Science Directorate, JAEA, Tokai, Ibaraki 319-1195
[1]*Department of Architecture, Yokohama National University, Yokohama, Kanagawa 240-8501*

It is typical method to measure the strains on a rebar in a reinforced concrete using strain gauges in the structural engineering field in order to evaluate the bond condition between rebar and concrete. However, waterproof treatment and wiring of the strain gauges around the rebar would affect the bond condition. Therefore, the neutron diffraction technique might be useful for measuring the strains on the rebar in the reinforced concrete without any effects of the bond condition. In this study, a size of anchorage zone was evaluated by measuring strain distributions in the rebar under pull-out loading.

Figure 1 (a) shows the schematic of the specimen used in this study. Rebar with diameter of 10 mm was embedded in the cylindrical concrete with the size of 400 mm length and 50 mm diameter. Pull-out loading was applied to the rebar, and the strain distribution was measured along the rebar by 1 mm pitch. Figure 1 (b) shows the strain distributions in the rebar in the reinforced concrete measured using neutron diffraction technique. Applied stress was gradually decreased from 200 MPa to 150 MPa during strain measurement due to creep of the concrete. The strain distribution under the applied stress of 200 MPa was decreased in the length from X=0 mm to 75 mm. Therefore, it can be said that the length of the anchorage zone measured by neutron diffraction was about 75 mm. Strain distribution measured by strain gauges was also plotted in this figure. Decrease in the strain was observed in the length from X=0 mm to approximately 225 mm, which means that the length of the anchorage zone measured by strain gauges was approximately three times longer than that measured using the neutron diffraction technique. Strain measurement using strain gauge was probably affected by the degradation of the boundary between concrete and rebar due to various treatments around strain gauges. Therefore, it was confirmed that the neutron diffraction technique, which is nondestructive and noncontact method, is useful technique for evaluating bond condition between concrete and rebar accurately. Application of the neutron diffraction technique to the structural engineering field will bring new knowledge regarding design of the concrete structure.

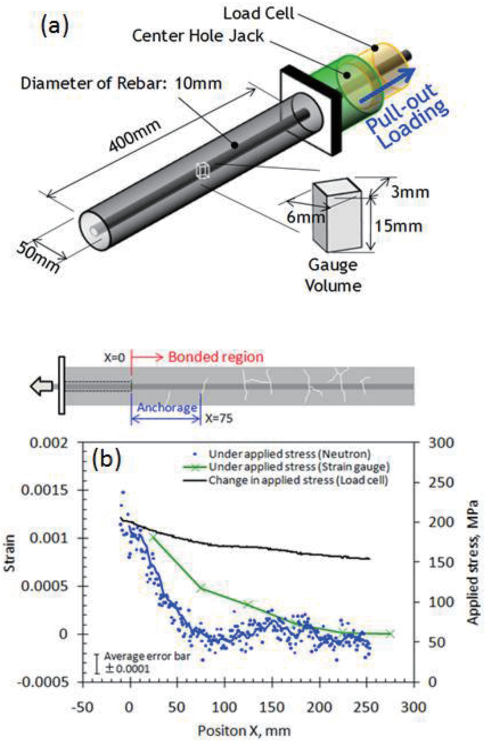

Figure 1: (a) Schematic of the sample used in this study and (b) comparison of strain distributions in the rebar measured using neutron diffraction and strain gauge.

原子炉：JRR-3　　装置：RESA(T2-1)　　分野：中性子散乱（残留応力）

1-10-4

Relaxation of Residual Stress in Engineering Component

K. Akita

Quantum Beam Science Directorate, JAEA, Tokai, Ibaraki 319-1195

Compressive residual stress can enhance the strength for fatigue and stress corrosion cracking of engineering components and it can be introduced on the surface layer by peening technologies such as shot peening and laser peening. The compressive residual stress might be relaxed due to the external mechanical load in service use. To clarify the initial residual stress distribution is important to estimate the relaxation behavior because it superimposes on the external load.

In this study, the initial residual stress distribution was measured on a laser peened sample using neutron diffraction. The material used in this study was an aluminum alloy, A2024-T3. The thickness of the sample was 5 mm. Laser peening was applied on the surface and back surface of the sample. Al-311 diffraction was measured using RESA-II in JRR-3. Lattice strains were obtained from the peak shift of the diffraction profile. The direction of the measured strain was parallel to the surface.

Fig. 1 shows the depth distribution of residual strain in the laser peened sample. Compressive strain induced by laser peening was observed in the surface layer. It decreased and changed into tension at the depth of about 1.2 mm and reached to the maximum tension at the center of the sample. Although the accurate value of the residual stress should be calculated from strains of three directions, the maximum tensile residual stress was estimated from the strain to be about 112MPa under the assumption of equibiaxial plane stress state. It was close to the value analyzed by a finite element method. The tensile residual stress region will be deformed plastically at first while the external tensile load increases. In this study, the existence of the tensile residual stress in the peened sample was confirmed. Relaxation behavior of the residual stress in the external loading will be measured in the next experiment.

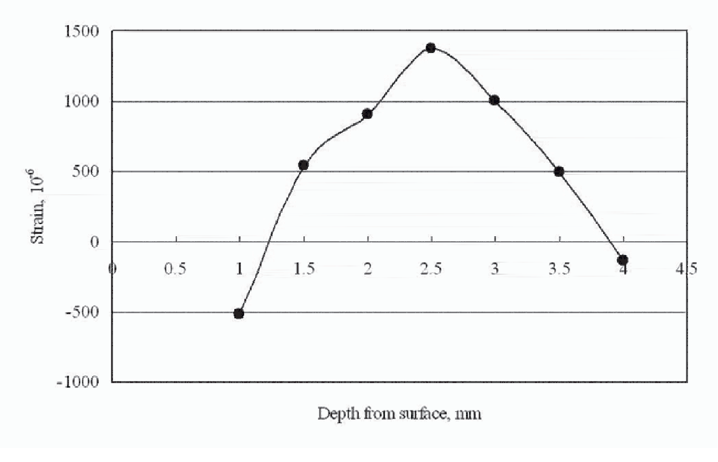

Figure 1: Depth distribution of residual in-plane strain on laser peened sample.

原子炉：JRR-3　　装置：RESA-2(T2-3-2)　　分野：中性子散乱（残留応力）

1-10-5

Residual Stress Measurement of Thick Butt Weld Using Neutron Diffraction

H. Suzuki, J. Katsuyama[1] and Y. Morii

Quantum Beam Science Directorate, JAEA, Tokai, Ibaraki 319-1195
[1]*Safety Research Center, JAEA, Tokai, Ibaraki 319-1195*

Accuracy of a neutron stress measurement near the weldment is affected by changes in microstructure in a weld zone caused by phase transformations, plastic strain generation and crystal grain growth due to heating and cooling process during welding. Therefore, suitable diffraction planes, which are not affected by the plastic strains, and accurate stress-free lattice constant with consideration of changes in microstructure should be figured out in order to measure accurate residual stress distribution near the weldment. In this study, it was confirmed that measuring lattice constant in stress-free condition using a standard sample makes it possible to select suitable reflections which are not affected by the intergranular strains. Specifically, it can be determined that reflections of which lattice constants in three orthogonal directions agree well with average lattice constant of all measured reflections are suitable.

This method was applied to residual stress measurements of 35 mm thick butt weld. It was confirmed that influence of intergranular strain was negligible on the 311 and 220 reflections in austenitic steel and on the 110, 200 and 211 reflections in ferritic steel. Figure 1 shows results of residual stress distributions in transverse path in the center of wall thickness of the 304SS butt weld and the 304SS-low alloy steel (A533B) dissimilar butt weld which were measured using 311 reflection in austenite and 211 reflection in ferrite. It was confirmed that the residual stress distribution of the 304SS butt weld was typical trend agreed well with the stress distributions calculated by the numerical simulations reported in previous studies, and that the residual stress distribution of the dissimilar weld was different from that of the 304SS butt weld since the dissimilar weld was affected by the misfit of thermal expansion coefficient between austenitic steel and ferritic steel.

This research project has been conducted under the research contract with the Japan Nuclear Energy Safety Organization (JNES).

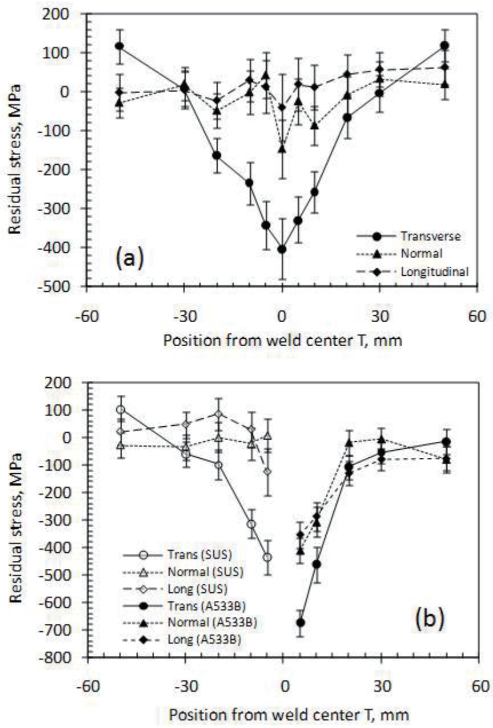

Figure 1: Residual stress distributions in transverse path in the center of wall thickness of the 304SS butt weld (a) and the 304SS-low alloy steel dissimilar butt weld (b).

原子炉：JRR-3　　装置：RESA(T2-1)　　分野：中性子散乱（残留応力）

1-10-6

Development of Cryogenic Load Frame for Neutron Diffraction

H. Suzuki, Y. Tsuchiya[1], T. Umeno[2], S. Machiya[3] and K. Osamura[4]

Quantum Beam Science Directorate, JAEA, Tokai, Ibaraki 319-1195
[1] *Quantum Beam Center, NIMS, Tsukuba, Ibaraki 305-0047*
[2] *Taiyo Nippon Sanso Corporation, Tsukuba, Ibaraki 306-2611*
[3] *Department of Mechanical Engineering, Daido University, Nagoya, Aichi 457-8530*
[4] *Research Institute for Applied Sciences, Kyoto 606-8202*

In the cryogenic engineering field, it is important to know material characterization of engineering materials at low temperature. Especially, evaluations of residual strains as well as deformation behavior at low temperature are required for improving the strength and the functionality of the cryogenic materials. For example, strain evaluations of engineered composite superconductors in service are important to obtain higher performance of superconductivity since that is affected by strains generated during fabrication process and under operation. In order to achieve in-situ strain measurement under loading at low temperature, we have developed a cryogenic load frame for neutron diffraction as shown in Fig. 1 (a). The load capacity of the load frame was 10 kN and the lowest temperature achieved at grips was below 4.8 K by using a GM refrigerator. Figures 1 (b) and (c) show the deformation behaviors of 111, 200 and 220 reflections of type 316 austenitic stainless steel under uniaxial tensile loading at room temperature and 5 K. Linear response was observed in each diffraction at each temperature and this result shows typical relation of which rate of strain change at 5 K were smaller than that at room temperature.

This novel cryogenic load frame shows highest performance compared with similar instruments [1)] prepared in the overseas engineering neutron facilities.

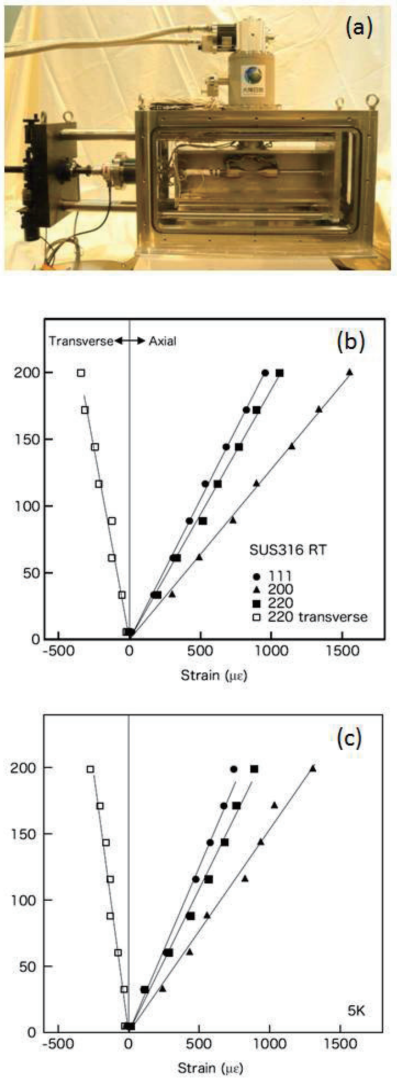

Figure 1: Overview of the developed cryogenic tensile frame (a) and strain changes of three diffractions of an austenitic type 316 stainless steel at room temperature (b) and approximately 5 K (c).

References

1) E. Oliver, B. Evans, M. Chowdhury, R. Major, O. Kirichek and Z. Bowden : "Novel testing chamber for neutron scattering in engineering materials at cryogenic temperatures", Meas. Sci. Technol., 19, 034019(2008).

原子炉：JRR-3　　装置：RESA(T2-1)　　分野：中性子散乱（残留応力）

1-10-7

Development of Multi-channel Vertical Conversing Slit

H. Suzuki, Y. Shinohara[1], T. Oku[1], J. Suzuki[1] and M. Hayashi[2]

Quantum Beam Science Directorate, JAEA, Tokai, Ibaraki 319-1195
[1]*J-PARC Center, JAEA, Tokai, Ibaraki 319-1195*
[2]*Ibaraki Prefectural Government, Tokai, Ibaraki 319-1106*

Neutron stress measurement is very useful to measure residual stresses in large scaled mechanical components such as automobile engines, large scaled welded tubes and so on. In conventional optical system of the RESA engineering diffractometer, the incident neutron beam size has been determined by a cadmium slit. In this case, the cadmium slit should be installed at a position away from the sample to prevent the large scaled sample from bumping the slit during the measurement. Therefore, it was difficult to make the beam size fine at the sample position, because the divergent beam produced by the vertically focusing monochromator transmitts the cadmium slit and reaches the sample. In this study, the multi-channel vertical conversing slit (called "vertical radial collimator") shown in Fig. 1(a) was developed to obtain the expected beam size with high flux at sample position.

Figure 1(b) shows a simple schematic of the optical layout of the RESA diffractometer with the vertical radial collimator. We designed it to obtain 5mm of full width half maximum (H_{FWHM}) of the incident beam height at the sample position. Optimum specification of the vertical radial collimator shown below was decided by the MacStas simulation.

*L1 (Conversing distance) = 500 mm

*L2 (Length of collimator) = 384 mm

*Number of channel = 10 ch

Figure 1(c) shows incident beam profiles along the vertical direction measured by a neutron imaging plate (NIP) at five positions of L1=410 mm, 455 mm, 500 mm, 545 mm and 590 mm. It was confirmed that the beam intensity increased with approaching L1 to the designed value of 500 mm. H_{FWHM} at L1=500 mm was approximately 5.0 mm, showing good agreement with the expected width. The incident beam profile and integrated intensity (I_{int} in Fig. 1(c)) at L1=500mm were almost the same as those at L1=100mm when using a cadmium incident slit. This result indicates that the neutron beam diffracted from all silicon crystals of monochromator system could effectively converge on the sample position by using the vertical radial collimator.

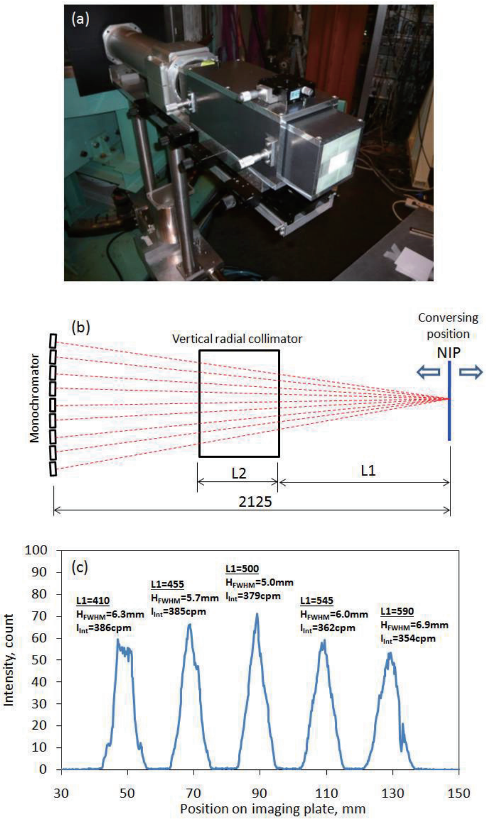

Figure 1: (a) Overview of the vertical radial collimator installed at the RESA diffractometer, (b) schematic of optical system of the RESA diffractometer with the vertical radial collimator and (c) incident beam profiles along the vertical direction by a neutron imaging plate (NIP).

原子炉：JRR-3　　装置：RESA(T2-1)　　分野：中性子散乱（残留応力）

1.　中性子散乱　11）その他

1. Neutron Scattering　11）Others

1-11-1

Anomalous Lattice Dynamics in Relaxor $K_{1-x}Li_xTaO_3$

S. Wakimoto, H. Taniguchi[1], G. A. Samara[2], R. K. Grubbs[2], E. L. Venturini[2], L. A. Boatner[3]

Quantum Beam Science Directorate, JAEA, Tokai, Ibaraki 319-1195
[1]*Materials and Structure Laboratory, Tokyo Institute of Technology, Yokohama 226-8503*
[2]*Sandia National Laboratories, Albuquerque, New Mexico 87185, USA*
[3]*Oak Ridge National Laboratory, Oak Ridge, Tennessee 37831, USA*

Relaxor $K_{1-x}Li_xTaO_3$ shows rich dielectric properties with doping. Undoped compound $KTaO_3$ is a quantum paraelectric material which never undergoes a ferroelectric (FE) transition, $^{1)}$ in spite of the softened FE phonon mode. $^{2)}$ Li-doped system shows relaxor behavior at high temperatures and FE transition at low temperature. This happens because the doped Li^+ ion occupies off-centered position due to the small ionic radius, resulting in a large dipole moment and a precursor to the polar nano-region. Therefore, the dynamics of the doped Li ions are important to understand the relaxor behavior.

So far, there is no conclusive observation of the Li dynamics. Only Raman scattering reported an anomalous mode appears only in the doped samples and only in the relaxor state. $^{3)}$ These data are summarized in Fig. 1 by open symbols. This mode, here we refer as "impurity mode", softens with decreasing temperature following a universal line. However Raman data is restricted to the zone center (ZC) information. We have performed inelastic neutron scattering to investigate q-dependence of this impurity mode.

Crystals with $x = 0.05$ and 0.10 for this study were grown by the slow-cooling method. The neutron inelastic scattering measurements were done at the TAS-2 with fixed final neutron energy at $E_f = 14.7$ meV and collimation sets of Guide($15'$)-80-80-open. The impurity mode has very weak intensity and, furthermore, it locates at the energy close to the strong acoustic phonon. Thus the measurements near the zone center were unsuccessful. However, we succeeded to observe the impurity mode near the zone boundary of M-point, such as $(1.5, 0.5, 0)$ and $(1.5, 1.5, 0)$, where the acoustic phonon goes to well higher energy ($\omega \geq 12$ meV). The observed impurity mode energies for both samples are shown in Fig. 1 by closed symbols. The impurity mode energies at ZC (Raman data) and M points (neutron) agree at higher temperatures (≥ 200 K). It is remarkable that only ZC energy softens with decreasing temperature implying that the impurity mode becomes dispersive at low temperatures. This behavior can be understood that the Li ion dynamics is uncorrelated with each other at high temperature where the relaxor behavior is dominant. As temperature decreases they correlate each other resulting in a ferroelectric transition.

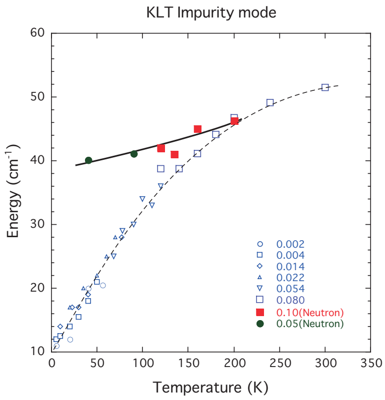

Figure 1: Temperature dependence of the impurity energy mode for various dopings. Open symbols indicate data from Raman scattering, that is the impurity mode energy at the zone center. Closed circles show neutron data measured at the zone boundary (M-point).

References

1) S. H. Wemple, Phys, Rev. 137, A1575 (1964).
2) J. D. Axe, J. Harada, and G. Shirane, Phys. Rev. B 1, 1277 (1970).
3) R. L. Prater, L. L. Chase, and L. A. Boatner, Phys. Rev. B 23, 5904 (1981).

原子炉：JRR-3　　装置：TAS-2(T2-4)　　分野：中性子散乱（その他）

1-11-2

Neutron diffraction experiments of valence fluctuating YbPd

A. Mitsuda^A, M. Sugishima^A, K. Ohoyama^B, H. Wada^A
^{A}*Dept. of Phys., Kyushu Univ.*, ^{B}*IMR, Tohoku Univ.*

The cubic CsCl-type compound YbPd is known to be a valence fluctuating compound and to undergo 4 phase transitions at 0.5, 1.9, 105, and 125 K [1]. ^{170}Yb Mössbauer studies reveal that the one at T_M = 1.9 K is due to magnetic order [2]. However, the mechanisms of the other three phase transitions remain unknown. The Mössbauer studies also suggest magnetic and nonmagnetic Yb ions coexist in equal proportions at low temperatures [2]. Assuming that the difference in magnetism is ascribed to two Yb valence states, of which are nonmagnetic Yb^{2+} and magnetic Yb^{3+}, the two valence states should arrange regularly at low temperatures to make entropy zero. Such behavior, which is called 'charge order', is observed in Yb_4As_3, Fe_3O_4 and so on. These compounds have low carrier density, while YbPd exhibits metallic behavior. We are interested in the charge order of the metallic compound. We take notice of the fact that magnetic order and charge order coexist below 1.9 K according to the Mössbauer studies. If we can determine the spin structure, the structure should include information on structure of the charge order since only Yb^{3+} ions have a magnetic moment. Therefore, in the present study, we perform powder neutron diffraction experiments of YbPd at low temperatures to determine spin and charge structure.

The experiments were carried out at IMR-HERMES powder diffractometer. A powdered sample (about 3 grams) was loaded in the vanadium cell with the diameter of 8.6 mm, and then attached to the 1 K refrigerator. The powder diffraction patterns were taken at 0.72 K and 3.62 K, which is below and above magnetic ordering temperature of 1.9 K. The measurements were carried out twice at the same temperature.

Figure 1 shows the results of the experiments measured at 0.72 K and 3.62 K. The overall diffraction patterns at both temperatures can be indexed as the cubic CsCl-type structure, suggesting absence of the structural transition. At 0.72 K, however, a shallow shoulder is found at around $2\theta = 5^\circ$. Since there exists no shoulder in the patterns at 3.62 K, the shoulder is a magnetic Bragg peak. The low angle of 2θ indicates a long-periodic, possibly incommensurate, magnetic structure. The magnetic Bragg peak, which is obtained by subtracting the diffraction pattern at 3.62 K from that at 0.72 K, is small and not broadened, which suggests shrinkage of the magnetic moment and long-range magnetic order. Analysis of structure of magnetic order and charge order is now in progress.

References:
[1] R. Pott et al., Phys. Rev. Lett. **54** (1985) 481.
[2] P. Bonville et al., Phys. Rev. Lett. **57** (1986) 2733.

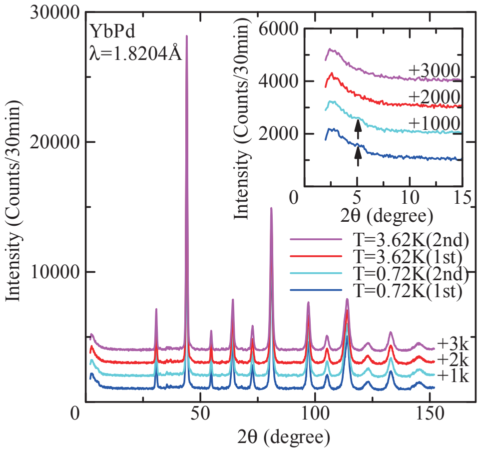

Fig. 1. Neutron diffraction patterns of YbPd at 3.62 and 0.72 K. The inset exhibits an enlarged graph around $2\theta = 5^\circ$. The arrows show a magnetic Bragg peak.

1-11-3

Structural Evaluation of Titanate Nanotube and Nanosheet

A. Nakahira[1], T. Kubo[1] and M. Yashima[2]
Osaka Prefecture University[1] and Tokyo Institute of Technilogy[2]

Nanomaterials with one-dimensional nanostructures have attracted much attention due to their potential applications in a variety of novel devices. Especially, TiO2-derived nanotubes which are prepared by a hydrothermal treatment of TiO2 particles in a concentrated NaOH aqueous solution are expected to be useful for several application studies on such as proton conduction, photoinduced hydrophilicity, photocatalysts,and dye-sensitizing solar batteries. However, the crystalline structure and formation mechanism of TiO2-derived nanotubes are still topics under discussion. The elucidation of the crystalline structure and formation mechanism for TiO2-derived nanotubes will be expected to lead to the further development of novel functional materials with one-dimensional nanostructures. The structural change on the molecular scale of anatase-type TiO2 during a hydrothermal treatment was investigated in detail by various analytic techniques such as neutron diffraction in order to clarify the formation mechanisms of titanate based nanotubes.

Two grams of anatase-type TiO2 powder as a starting material were used. They were added in 10 M NaOH aqueous solution. Then the specimens were treated under the hydrothermal reaction at 383 K for 1 to 96 h. Obtained products after hydrothermal treatments were sufficiently washed with deuterated water and dilute HCl aqueous solution and were subsequently separated from the washing solution by filtration. After the washing treatment, they were filtered and subsequently dried at temperatures above 323 K for more than 12 h in an electric oven. Structural evaluation of titanate nanotube samples were evaluated by neutron diffraction at HEMES station. The neutron powder diffraction experiments were conducted for room temperature using the HERMES powder neutron diffractometer installed on Tl-3 port of JRR-3M reactor in the Japan Atomic Energy Research Institute (JAERI), Tokai, Japan. An incident neutron wavelength λ = 1.8196 Å was obtained from a Ge (311) monochromator. The ND data were collected on thoroughly ground powders by a multiscanning mode in the 2 θ range from 5 ° to 155 ° with a step width of 0.10 °. The 3 g powder sample was wrapped by tungsten foil to form a cylindric shape (10 ϕ × 30 mm).

Fig.1(A) shows the typical structure image of nanotube products prepared by the hydrothermal process. The neutron diffraction pattern shows that the spectrum was unsufficient for the analysis because of the unsifficient substitution of deuterated water in the nanotube structure, as shown in Fig.1(B). It was hard to analysis because there were high backgrounds in the observed data. This is thought to be why the presence of a slight amount of H (H2O) in the measuring sample. For this result, it was found that it was very difficult to prepare a specimen of TiO2-derived nanotubes for ND measurements by using soft chemical process. However, it revealed that the nanosheet-like products composed of highly distorted TiO6 octahedra were generated by a hydrothermal treatment of anatase-type TiO2 and then the anatase-like structures are partially built up with the formative nanotubes by scrolling up these nanosheet-like products.

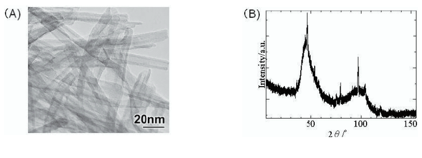

Fig. 1. Fig.1 (A)Typical strucutral image of nanotube and (B) Neutron diffraction of nanotube

This is a blank page.

2.　中性子ラジオグラフィ

2. Neutron Radiography

2-1

Development of the Very High-Frame-Rate and High Resolution Neutron Radiography System for High Speed Multi-Phase Flow Visualizations

M. Kureta

Nuclear Science and Engineering Directorate, JAEA, Tokai, Ibaraki 319-1195

A high-frame-rate neutron radiography system [1] was remodeling in order to keep up to the very high speed multi-phase flow phenomena. The main point of the remodeling was the image intensifier (I.I.). Luminas gain and resolution were increased. The new order-made I.I. system was consisted from two types of the large size and high gain photoelectric multiplayer, one MCP and one imaging buster, with the special relay lens. Resolution could be 1024x1024 pixels when we used the high speed camera (Photron Fastcam-P01BW). Brightness of the image could be controlled by the gain of the MCP. In order to confirm the applicability of the new system to the very high speed phenomena, fundamental test was carried out at the TNRF in the research reactor JRR-3 of JAEA. Sample was very simple bubbling water which was filled in the aluminum can. In the sample, air bubbles were generated by the small pump with a sand stone. Figure 1 shows the instantiates image of the test result. Recording speed of Figure 1 (a) and (b) were 2,000 fps and 6,000 fps, respectively. It was confirmed from the fundamental test that the new system was useful for the very high speed phenomena with 6,000 fps (512x512 pixels) or for high resolution with 1,024 x1,1024 pixels (2,000fps). The new system was applied to the visualization test of the car engine as shown in Figure 2. The test was carried out with NISSAN experimental group who prepared the experimental car engine. The purpose of the test was to make clear the oil phenomena under the working condition. The new imaging system could be used for the high speed driving mode of the car engine.

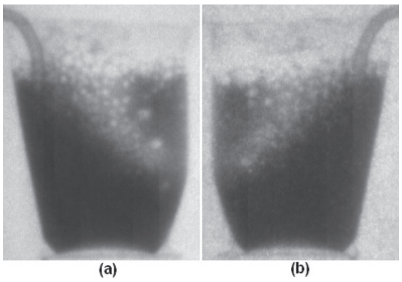

Figure 1: Sample image((a)2,000fps, (b)6,000fps)

References

1) M. Kureta et al. :“Jpn. J. Multi-Phase Flow.”, Vol.23[2], pp. 165-173 (2009).

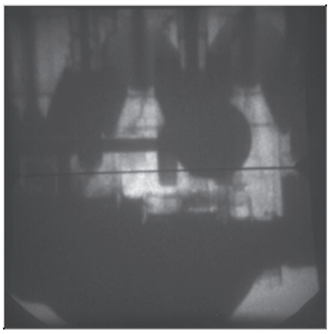

Figure 2: Application of the new system

原子炉：JRR-3　装置：TNRF(7R)　分野：中性子ラジオグラフィー（熱水力）

2-2

Development of Multi-pinhole Collimator for Large Imaging Area with High spatial Resolution

H. Hayashida, M. Segawa, R. Yasuda, H. Iikura, T. Sakai, M. Matsubayashi
Quantum Beam Science Directorate, JAEA, Tokai, Ibaraki 319-1195

There are two kinds of factors affecting to spatial resolution in radiography; one is the resolution of detector system and the other is the beam optimization. In this study, topic is focused to beam optimization.

A multi-pinhole collimator system which is effective for retaining imaging area with high spatial resolution has been demonstrated on Cold Neutron Radiography Facility (CNRF) at JRR-3M in JAEA. The multi-pinhole collimator system consists of a multi-pinhole aperture and an overlap-cutter (Fig. 1). On neutron beam from multi-pinhole aperture, neutrons from each pinholes make overlap at sample position due to beam divergence. In the overlap area, sample images become split images. The overlap-cutter works to cut neutrons contribute to overlap at sample position and enable us to get image without split.

In this study, a demonstration was performed with three conditions as written below, (a), (b) and (c), in order to verify the effect of multi-pinhole collimator system. A plastic model mainly fabricated by polystyrene was used as a sample (Fig. 2) and an imaging plate (IP) was used as a detector with resolution of 50 μm

(a) *Using large single pinhole*

A large size aperture with a size of 35 mm in vertical and 17mm in horizontal was used. The distance between the aperture and sample L was 900 mm and the distance between the sample and detector l was 100 mm. In this condition, unsharpness of image d, a parameter of spatial resolution, is not defined by L/D but by beam divergence of 14 mrad. Thus d is estimated to 1.4 mm. The result is shown in Fig. 3(a). The size of the imaging area is about 50 mm × 50 mm which corresponds to the square area shown in Fig. 2.

(b) *Using multi-pinhole aperture(without overlap-cutter)*

The multi-pinhole aperture was set and the overlap-cutter was not used. The multi-pinhole aperture had 6 pinholes with each diameter of 2 mm and the distances of each pinhole were 10 mm as shown in Fig. 1(a). A geometrical setup was same with the condition (a), the distance between the multi-pinhole aperture and sample $L = 900$ mm and $l = 100$ mm. In this condition, d is estimated to 0.22 mm by $L/D = 450$. The result is shown in Fig. 3(b). An imaging area is about 50 mm × 50 mm which is same with the condition (a) and clear image is obtained. This result shows that using multi-pinhole aperture is effective to ratain imaging area with high spatial resolution. However, neutron beam which contributes to overlap at sample position exists and split image is observed significantly in cheek parts of sample indicated by arrows in Fig. 3(b).

(c) *Using multi-pinhole collimator system*

The multi-pinhole collimator system using both of multi-pinhole aperture and overlap-cutter was set. The distance between the multi-pinhole aperture and sample $L = 900$ mm and $l = 100$ mm. The overlap-cutter was set at 255 mm downstream of multi-pinhole aperture. A picture of overlap-cutter is shown in Fig. 1(b). Neutron beam which contributes to overlap from pinhole (1) and (2) in Fig. 1(a) is cut by (4) part on overlap-cutter shown in Fig. 1(b) and from pinhole (1) and (3) is cut by (5) part, similarly. All the neutron beam contributes to overlap from each pinhole are cut by overlap-cutter in the same way. Since the overlap-cutter works only to cut neutrons contribute to overlap, unsharpness d is same with condition (b) and d is estimated to 0.22 mm. The result is shown in Fig. 3(c). Clear image is obtained without split and an imaging area is about 50 mm × 50 mm.

原子炉：JRR-3　装置：CNRF(C2-3-3-1)　分野：中性子ラジオグラフィー（その他）

Three stripes indicated by arrows shown in Fig. 3(c) are observed. A shape of the stripe is same shape with the overlap-cutter and the stripe can be treated as image of the overlap-cutter. When we have to get image in this region, we have to change a sample position.

The test experiment using the multi-pinhole collimator system was performed at CNRF. Although we have to scan the sample position in order to get images on stripe parts shown in Fig. 3(c), the system is effective to get a wide and clear image without sprit even in compact radiography instrument. In this demonstration, unsharpness d is improved from 1.4 mm to 0.22 mm with a same imaging area of 50 mm × 50 mm. In the system, since the multi-pinhole aperture and the overlap-cutter can be changed easily, it is possible to install another radiography instrument. Furthermore we can control unsharpness d by changing each pinhole diameters.

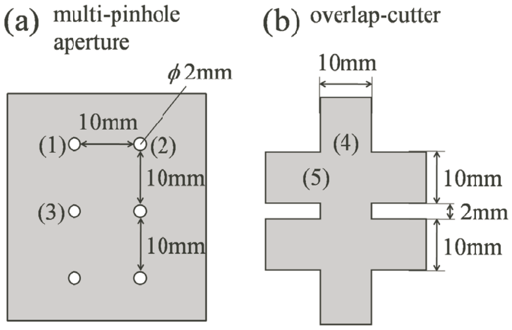

Figure 1: (a) and (b) are the picture of multi-pinhole aperture and overlap-cutter, respectively.

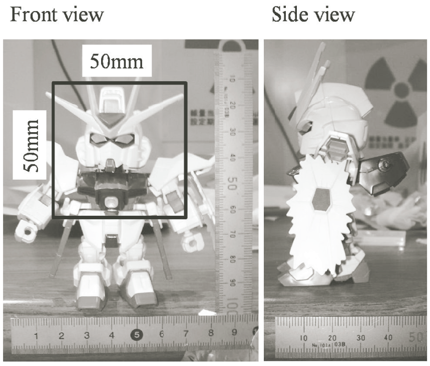

Figure 2: The photograph of a sample.

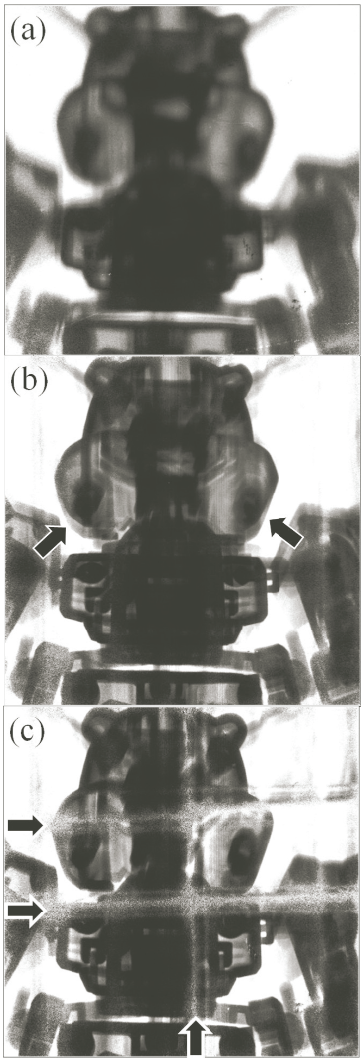

Figure 3: (a), (b) and (c) are the results from experimental conditions of (a), (b), and (c), respectively.

2-3

Evaluation of Spatial Resolution in Computed Tomography Images used Single Aperture Devices in Thermal Neutron Radiography Facility in JRR-3

H. Iikura, R. Yasuda, H. Hayashida, T. Sakai and M. Matsubayashi
Quantum Beam Science Directorate, JAEA, Tokai, Ibaraki 319-1195

Recently, single aperture devices were installed in Thermal Neutron Radiography Facility (TNRF) in JRR-3. Then we evaluated the spatial resolution of computed tomography (CT) images with the devices. In this study, size of aperture we used was 5.1 mm, and L/D with the aperture device was 460 as against 176 without that. In addition, we used not only a standard NE426 scintillator, but also the thinner ZnS:Ag/^{6}LiF scintillator developed by JAEA.

Neutron image was taken through a cooled CCD(Charge-Coupled Device) camera. At first, we used gold wires of five kinds of diameters on an aluminum stick (Fig. 1a). Without the single aperture device, the gold wire was recognized to 200 μm, but the wire of 100 μm was not detected (Fig. 1b). But the gold wire of 100 μm was detected clearly with 5.1 mm aperture and the thinner scintillator (Fig. 1c, arrow). Next, we used gold wires of three kinds of diameters in an aluminum stick in various intervals. CT images were shown by Fig. 2(a) and (b) using pseudo color with and without 5.1 mm aperture and the thinner scintillator. Figure 2(c) shows comparison of spatial profiles in each CT image. With the aperture device and the thinner scintillator, the spatial resolution is improved 2 times higher.

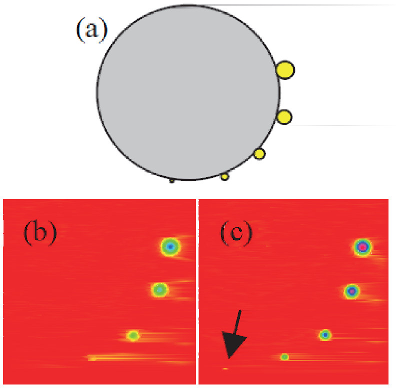

Figure 1: CT images of gold wires of various diameters on an aluminum stick. (a): Configuration of the gold wires setting. (b): CT image of gold wires without single aperture device. (c): CT image of gold wires with 5.1 mm aperture and the thinner scintillator. Arrow shows a gold wire of 100 μm diameter.

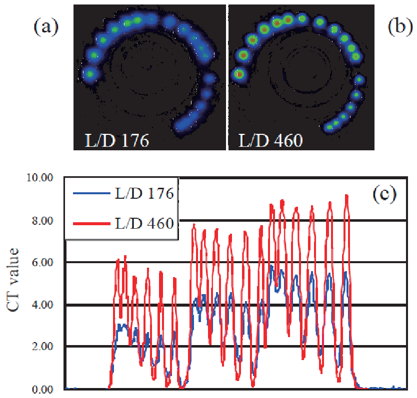

Figure 2: CT images of gold wires which set in various intervals in an aluminum stick. (a): CT image of gold wires without single aperture device. (b): CT image of gold wires with 5.1 mm aperture and the thinner scintillator. (c): Comparison of spatial profiles in each CT image.

原子炉：JRR-3　　装置：TNRF(7R)　　分野：中性子ラジオグラフィー（その他）

2-4

Visualization of Water Behavior in an Operating Fuel Cell

H. Iikura, R. Yasuda, T. Sakai, M. Matsubayashi and Y. Katada[1]

Quantum Beam Science Directorate, JAEA, Tokai, Ibaraki 319-1195

[1]*Fuel Cell Materials Center, National Institute for Materials Science, Tsukuba, Ibaraki 305-0047*

As a collaborative research with National Institute for Materials Science (NIMS), we conducted visualization of water behavior in an operating polymer electrolyte fuel cell (PEFC) using the JRR-3 thermal neutron radiography facility (TNRF). The PEFC is compliant with a Japan Automobile Research Institute (JARI) standard PEFC. On a JARI standard PEFC, an active area is 50 x 50 mm^2 and a flow channel for H_2 and air gases is single parallel serpentine; the width, depth and pitch of which are 1 mm, each. For optimizing the PEFC for neutron imaging, clamping plates (original: stainless steel) were replaced with those of aluminum. Also, for the purpose of experiment, separator plates (original: carbon) were replaced with those of aluminum or high nitrogen steel (HNS).

NIMS is developing high corrosion resistant separator materials, such as HNS. To confirm availability of HNS as separator materials of a PEFC, we started to compare the performance of HNS with those of carbon, aluminum and so on. Thermal neutron transmittance of a 6 mm thick HNS separator plate was worse than that of an original 10 mm thick carbon separator plate. However, we confirmed that the subtraction image showed existence of water in a flow channel of HNS separator clearly.

Real-time neutron imaging system using an EB(Electron Bombard)-CCD(Charge-Coupled Device) camera with frame rate of 30 frames/s coupled with an NE426 equivalent fluorescent converter (NR converter, Kasei Optonix) was used. Captured neutron images were recorded on a hard disk video recorder as NTSC (National Television System Committee) format. A fuel cell operating system which was prepared by NIMS, was installed at the TNRF as shown in Fig. 1.

As a result of power generation of the PEFC, product water was not clearly observed by the real-time neutron imaging system, but condensed water behavior in flow channels of separator plates was clearly observed as shown in Fig. 2. The neutron imaging using an EB-CCD camera system is considered to be available for visualizing of water behavior in flow channels of 1 mm depth and width such as JARI standard PEFCs.

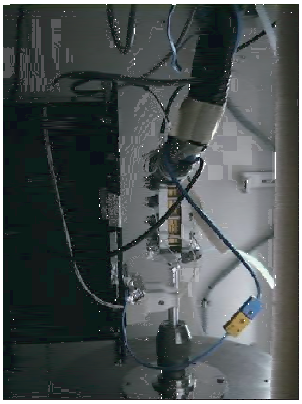

Figure 1: Photograph of an operating PEFC.

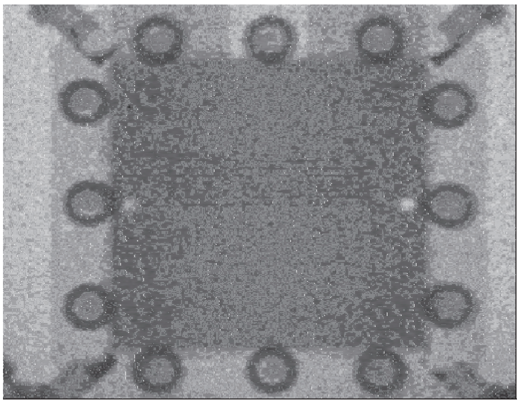

Figure 2: Neutron image of condensed water behavior in PEFC using an EB-CCD camera (1 frame[1/30s]).

原子炉：JRR-3　装置：TNRF(7R)　分野：中性子ラジオグラフィー（その他）

2-5

全固体二次電池における電極・電解質中の水素ならびにリチウムの分布・拡散状態の解明

Investigation of Distribution and Diffusion of Hydrogen and Lithium in the Electrode and Electrolyte Materials for All-Solid State Rechargeable Batteries

研究代表者 鳥取大学大学院　坂口裕樹
研究協力者 鳥取大学大学院 江坂享男，南条真佐人，高井茂臣，飯田貴久
JAEA　松林政仁，飯倉寛

（1）　はじめに

現在リチウム2次電池は携帯端末や自動車用電源に代表されるように，我々の生活に欠くべからざるデバイスとなっており，さまざまな観点から精力的に研究が行われている．現在の2次電池の標準的な構成は，負極(C)/有機電解液/正極 ($LiCoO_2$ や $LiMn_2O_4$，$LiFePO_4$ など)であるが，安全面や取り扱いの範囲の拡張といった点から，電解液を固体電解質とした全固体二次電池がさかんに研究されている．この場合，固体電解質のイオン伝導率や電極/電解質界面での反応が決定的なパラメータになるのはもちろんのこと，正極内部まで入り込んでいたであろう電解液が固体になれば正極自体の拡散係数の絶対値も重要なパラメータとなる．$LiCoO_2$ や $LiMn_2O_4$ などの正極材料は電子・イオン混合伝導体であり，これまでに報告されているリチウムイオンの拡散係数は，GITT (Galvanostatic Intermittent Titration Technique)などの電気化学的手法によって得られたものである．この手法では電極における電荷の出入り(と電圧)のみを観測しているため，別の反応や理想的なモデルからのずれ，あるいは他のパラメータの見積もりに大きく依存し，報告されている値にもかなり幅がある．

我々の研究グループはリチウムの安定同位体 ^{6}Li と ^{7}Li で中性子の吸収係数が数桁違うことを利用して，^{7}Li からなる試料に ^{6}Li が拡散する挙動を，中性子ラジオグラフィー(NR)を用いて観測してきた．これまでは，京大原子炉実験所で固体電解質($Li_{4/3}Ti_{5/3}O_4$，LISICON，$La_{2/3-x}Li_{3x}TiO_3$)を中心にトレーサー拡散係数を測定してきたが，平成 18 年度から中性子ビームの提供を休止しているため，実験施設を原研 JRR-3M 冷中性子ポートに移し，同様の手法でリチウム正極材料に対してトレーサー拡散実験を開始した．NR で同位体濃度分布を測定してトレーサー拡散係数を求める本手法は，他の方法に比べて極めて確度の高い拡散係数測定が可能であり，また化学拡散係数ではなくトレーサー拡散係数が得られるという特徴をもつ．

スピネル型構造を示す $LiMn_2O_4$ は，現在広く用いられている $LiCoO_2$ のように希少金属を含まず，また $LiFePO_4$ と比べてリチウム拡散係数が高いとされていることから，単体としても，あるいは $Li(Co, Mn, Ni)O_2$ のような混晶系としても有望な正極材料である．また，ヤーンテラー歪みが容量低下を引き起こすこと，充電途中の(Li の少ない)試料では Li 空孔が多いにもかかわらず化学拡散係数が低いなどの現象も知られており，電池設計上の基礎データとしてばかりでなく，材料科学の観点からも確度の高いトレーサー拡散係数の測定は切望されている．本報告では，中性子ラジオグラフィーにより $LiMn_2O_4$ の高温領域におけるトレーサー拡散係数を求めた結果について述べる．

JRR-3M　CNRF 中性子ラジオグラフィー装置　材料化学

（２）　実験

拡散試料の ^{7}LiMn$_2$O$_4$ は通常の固相反応法で調製した．^{7}Li$_2$CO$_3$ および Mn$_2$O$_3$ を化学量論比に混合し，600℃および 800℃でそれぞれ 10 時間焼成した．得られた試料は 5 mm×5 mm×7 mm の角柱状に成形し，精密に長さを揃えた．また，同位体濃度校正用に ^{6}Li/^{7}Li の比を 10 %ごとに変化させた LiMn$_2$O$_4$ についても同様に合成し，同一の厚さに成形した．

拡散試料の片面に ^{7}LiNO$_3$ 飽和溶液を微量の酢酸セルロースとともに塗布し，700～800℃で拡散アニールを行った．アニールは 30 分ごとに休止して中性子ラジオグラフィー測定を行い，同一試料でさらに長時間の拡散実験を行った．ラジオグラフィー実験は原研 JRR-3M 炉 CNRF ポートで行った．拡散試料と同位体濃度校正用の標準試料を一列に並べ，中性子用イメージングプレート(NIP) をその背面にセットした．これらを試料ホルダーにセットし，中性子入射方向に垂直に 4 mms^{-1} の一定速度でスキャンすることにより，IP に照射する中性子が走査方向で均一になるようにした．ラジオグラフィーデータはイメージリーダで読み出した．

（３）　結果と考察

Fig. 1 に LiMn$_2$O$_4$ の標準試料と拡散試料の中性子ラジオグラフィー(NR)像とその強度データの例を示す．左から 11 個の標準試料，拡散試料，および拡散試料同じサイズで ^{6}Li を塗布していない試料を並べて測定している．標準試料は Li が自然同位体比の ^{N}Li から ^{7}Li まで 10%ごとに変化させており，^{6}Li 濃度の高い試料(^{N}Li 側)で透過強度が低くなっていることが観測される．拡散試料は ^{6}LiNO$_3$ を塗布後 800°C で 3 時間アニールした LiMn$_2$O$_4$ で，^{6}Li を塗布した試料左端から濃いグラデーションが観測され，^{6}Li が拡散してゆく様子が観測される．

この標準試料部分の NR データを用いて，透過強度と ^{N}Li 濃度の関係を求め，これをもとに拡散試料の同位体濃度プロファイルを求めると，Fig. 2 (a)が得られる．さらに同位体濃度の対数と表面からの距離の2乗の関係をプロットすると(b)のようになり，傾きは$-1/4D^{*}t$ を与える．700，750 および 800℃で様々な時間アニールして得られた NR 像から求めた $D^{*}t$ を t に対してプロットした図が Fig. 3 である．いずれもよく直線に載り，アニール時間と

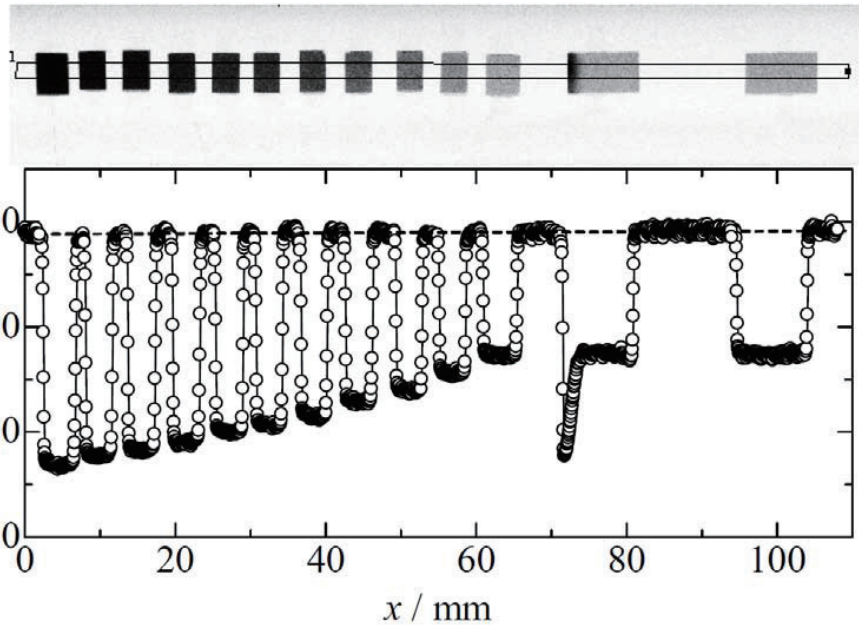

Fig. 1　NR image and transmitted intensities of standard and diffusion samples of LiMn$_2$O$_4$.

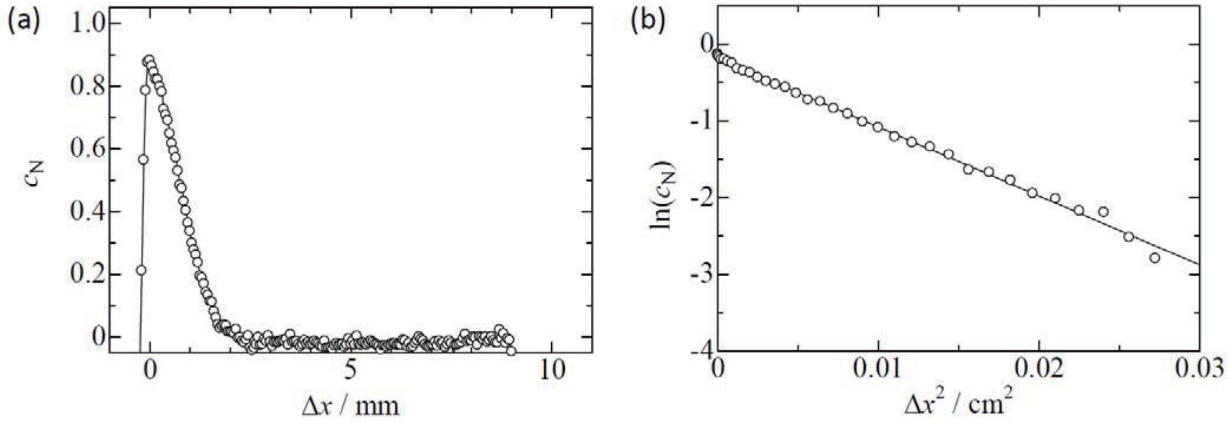

Fig. 2 (a) Isotope concentration profile of $LiMn_2O_4$ diffusion sample annealed at 800°C for 3 hours. (b) ln(c_N) – Δx^2 relationship of the isotope concentration profile.

ともに拡散が進行することがわかる．この傾きから求めた拡散係数をアレニウス型のグラフにプロットすると Fig. 4 が得られた．

本研究は $LiMn_2O_4$ のトレーサー拡散係数を求めた最初の研究である．今回は測定しやすい 10^{-8}～10^{-6} cm^2s^{-1} 程度の拡散係数にするために，700℃以上の領域で拡散アニールを行った．しかし今回のデータでは測定点も少なく高温で範囲も狭いため，リチウム電池の通常の使用領域である室温付近まで拡散係数の値を外挿するのは困難である．今後，より低温(～500℃程度)の拡散試料での測定が望まれる．

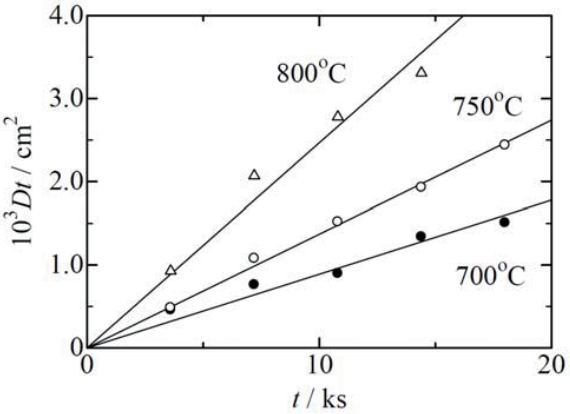

Fig. 3 Annealing time dependence of D^*t obtained from NR data.

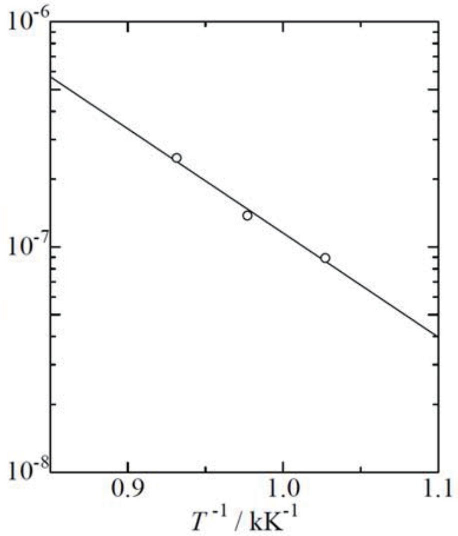

Fig. 4 Arrhenius plots of tracer diffusion coefficients for $LiMn_2O_4$.

2-5

JRR-3M CNRF 中性子ラジオグラフィー装置 材料化学

3. 放射化分析

3. Neutron Activation Analyses

This is a blank page.

3-1

研究テーマ：^{40}Ar/^{39}Ar年代測定による火山活動史及び地殻構造発達史の解明—日本周辺海域及び活動的火山に関する研究—
表　　　題：^{40}Ar/^{39}Ar年代測定による火山活動史及び地殻構造発達史の解明—日本周辺海域及び活動的火山に関する研究—

^{40}Ar/^{39}Ar年代測定による火山活動史及び地殻構造発達史の解明
—日本周辺海域及び活動的火山に関する研究—

石塚治、松本哲一
産業技術総合研究所

１．目的

フィリピン海海域およびその周辺の小笠原海台や南鳥島周辺海域において，採取された地質試料に関する地球科学的分析データ(特に岩石の形成年代)をもとに，各海域におけるマグマ活動およびマントルダイナミクス等を含めた火成活動史を把握することを目的とする．また本研究は現在国により準備されている国連への我が国の大陸棚限界画定申請のための調査の一環である。日本周辺海域の基盤岩の精密な形成年代を決定することを通じて、国連への提出情報作成をサポートする。

２．方法

測定用試料として、火山岩のうちもっとも新鮮な石基部分を主に使用した。試料から厚さ約 1mmの板状試料を切り出し、それを軽く粉砕して約 1mm角の小片にした。その後変質により生じている可能性のある粘土鉱物や炭酸塩鉱物の除去を目的として、3MHCl中で約 30 分、さらに 4MHNO_3中で約 30 分超音波洗浄後、脱イオン水で洗浄した。洗浄時間は、試料の変質程度によって調整した。洗浄後温水中で約 2 日間脱塩処理を行った。乾燥後、顕微鏡下で変質部や斑晶の混入のない試料をハンドピックし、測定用試料とした。

試料はアルミ箔に包み、年代標準試料（フラックスモニタ）とともに、中性子照射用アルミ容器中に各試料の位置を記録しながら、積みかさねて収納した。フラックスモニタとして、米国コロラド州産のFish Canyon Tuff (FC3)中のsanidineを使用した。年代計算には、この標準試料の年代として27.5Maを用いた1)。測定の妨害となるアルゴン同位体の補正は、KとCaをそれぞれ含む合成ガラスを試料とともに中性子照射し、分析することにより行った。試料の中性子照射は、原子力機構東海研究所のJRR3 にて、HR2を使用し 24 時間照射を行った。またカドミウム箔による熱中性子カットを行った。

アルゴンの同位体比分析は、産業技術総合研究所のレーザ加熱^{40}Ar/^{39}Ar年代測定システムにより行った。分析法等については、2) に準じた。測定システムは 2007 年度に改造を実施、２００８年度から本格稼働した。最大の違いは、試料加熱にCO2 レーザを導入したこと、測定を完全自動化したことである。測定に先立ち、試料を真空中にて約 72 時間100°Cで焼きだしを行った。試料の加熱には、CO2 レーザを用い、レーザビームの径は試料全体が均質に加熱されるように約 3.2mmとした。試料の測定は段階加熱法により行った。ステップごとにレーザの出力を上昇させ、試料が融解を開始するまで出力を上昇させた。各ステップで、レーザの出力を一定として、90 秒間加熱し、測定を行った。試料から抽出精製されたガスは、4 個のZr-Alゲッター(SAES AP-10)と 1 個のZr-Fe-Vゲッター（SAES ST707)により 10 分間精製された。精製後、VG Isotech社（現GVI社）製希ガス質量分析計VG3600 によりアルゴン同位体比測定を行った。

３．研究成果

フィリピン海地域から大陸棚限界画定調査により採取された試料について測定を実施した。平成 20 年度は JRR4 の停止の影響で照射は 1 回にとどまり、測定数も限られた。

伊豆小笠原弧西方、四国海盆中に位置する紀南海底崖地域の玄武岩からは 11.8 および 15.69Ma の年代が得られ、海底崖を構成する玄武岩類が四国海盆拡大停止直後から 300 万年程度の間に活動したことを示している。

一方紀南海山列の東側、紀南海底崖の西側に位置する崖から採取された玄武岩から 19.93 Ma の年代が得られた。その玄武岩は、四国海盆底を構成する玄武岩と類似し、中央海嶺玄武岩に近い組成を示す。このことから、この玄武岩は四国海盆拡大末期に、海盆拡大に伴って活動したマグマであると考えられる。海盆拡大軸付近から採取された、同じく中央海嶺玄武岩類似の玄武岩試料について、17.28Ma の年代が得られた。この結果も、この玄武岩が最末期の海盆拡大に伴って形成されたことを強く示唆する。

西マリアナ海嶺から南西方向にのびる小海山列中の海山から得られた玄武岩について、15.64Ma の年代が得られた。これは,マリアナ弧背弧地域においても、背弧海盆拡大停止とほぼ同時に、島弧火山活動が起きていたことを裏付ける結果である。

４．結論・考察

1）背弧海盆拡大終了後の異なるタイプの火山活動の共存

フィリピン海地域の背弧海盆（四国海盆、パレスベラ海盆等）のかつての拡大軸付近において、背弧海盆の他の地域では見られないアルカリ玄武岩の火山体を発見した。この玄武岩溶岩の年代測定を行った結果、背弧海盆拡大終了後５－８００万年後までこの特殊な火山活動が起きていたことを明らかにした。さらに今年度の測定により、四国海盆内で上記の火山活動と化学的特徴が全く異なる、島弧的な火山活動がほぼ同時期に起きていたことが明らかになった。この成果について 2008 年 11 月末に論文投稿を行った。

2）日本南方フィリピン海地域の火山活動史、構造発達史の解明を通じた大陸棚限界画定申請への貢献

^{40}Ar/^{39}Ar年代測定によりフィリピン海地域全体から採取された海底基盤岩の形成年代を明らかにした。これにより、日本南方海域の地質構造の成因について多くの重要な制約を与えた。これらのデータおよび解釈は 2008 年 11 月に国が国連に提出した日本の大陸棚延伸のための申請書に盛り込まれた。今後は、フィリピン海地域の海盆及び古島弧の形成発達史及びマントルプリュームと海盆形成の間の成因的関連等について論文化する予定である。また今後取得するデータは、国連での日本の申請書の審査をサポートするデータとなる。

参考文献

1）Lanphere, M. A., Baadsgaard, H., 2001. Precise K-Ar, ^{40}Ar/^{39}Ar, Rb-Sr and U/Pb mineral ages from the 27.5 Ma Fish Canyon Tuff reference standard. Chem. Geol. 175, 653-671.

2) Ishizuka, O., Uto., K., Yuasa, M., 2003. Volcanic history of the back-arc region of the Izu-Bonin (Ogasawara) arc. Geol. Soc. Spec. Publ., 219, 187-205.

3-2

メスバウアー分光法による無機化合物の研究 VI

Mössbauer spectroscopic studies of inorganic compounds Part VI

東邦大学　高橋　正，綾部剛也，時田紗季，沼野哲朗，平井勇也，三須俊行，今井和貴

(1) はじめに

メスバウアー分光法は 45 元素，91 核種について観測されるが，鉄，スズおよびユウロピウム以外の元素については，市販の線源がないことや低温（通常液体窒素温度以下）での測定が必要なため，化学的には有用な情報を与えると期待されても，研究に用いられない元素が少なくない．この研究は，そういった余りなじみのない元素のメスバウアー分光法を用いて，結合や構造に関する情報を得ることを目的としている．この 3 年間にわたる研究では，(1) ^{197}Au メスバウアー分光法を用いた金→ホウ素逆供与結合を持つ有機金化合物や環状有機金錯体の研究，(2)^{161}Dy メスバウアー分光法によるジカルボン酸で架橋された Dy 錯体の研究，(3) ^{155}Gd メスバウアー分光法によるガドリニウム(III)–トリフェニルホスフィンオキシド錯体の研究，(4) ^{170}Yb メスバウアースペクトル測定のための予備実験をおこなった．

(2) ^{197}Au メスバウアー分光

^{197}Au スペクトルの測定は比較的容易で，これまでも多くの研究が行われてきた．われわれは，環状二核金錯体や有機金化合物の研究に，^{197}Au メスバウアースペクトルを用いてきた．

金原子は通常+I または+III の酸化数をとり，同族の銅とは違って+II を取ることは非常に珍しい. 我々は，長いこと環状二核金(I)化合物を穏やかに酸化すると骨格構造を保持したまま環状二核金(II)錯体となること，およびこれは不均化により Au(I, III)になることを示してきた．一連の研究において，^{197}Au メスバウアー分光法は酸化数の決定だけでなく，配位環境や電子状態の議論において有用であることを示してきた．これまでに，ホスフィンのベンゼン環にメチル基を導入した効果や，配位原子にヒ素を用いた影響を検討してきた．今期は配位炭素を含むベンゼン環をフッ素化したホスフィン錯体についての研究を進めた．

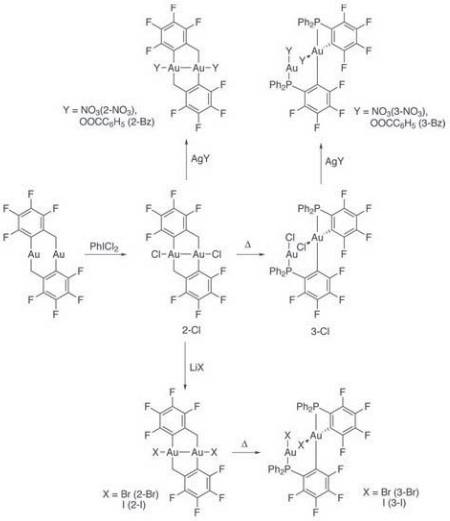

金属錯体あるいは有機金属化合物においては，金属－配位子間の結合は配位子が Lewis 塩基，金属原子が Lewis 酸として相互作用することによっている．ところが最近メルカプトイミダゾールやホスフィンを置換基にもつボラン配位子(**1**，**2**)が設計され，この配位子では配位子が Lewis 酸として作用して，M→B 結合を生成することが示唆されてきた．このような相互作用については，M→BR$_3$でなく M^{2+}←BR$_3$$^{2-}$とする考えも提案されており，電子状態の検討は重要な課題となっている．そこで Bourissou らによって開発されたホスファニルボラン PhB(C$_6$H$_4$PR$_2$)の金錯体(**2a**，**2b**)について ^{197}Au メスバウアー測定を行ない，Au–B 結合について検討した．

［実験］^{197}Au メスバウアー線源は，^{197}Pt を JRR-3 PN 照射孔で照射して作成した．東邦大の低温メスバウアー分光器（Wissel 社の MDU-1200，MDV-1200,

研究施設・装置：JRR-3M (PN-2, HR-1),
研究分野：メスバウアー分光法，錯体化学，有機金属化学

DFG-1200 からなる）を用いて，100~200 mgAu cm^{-2} の吸収体厚みの試料について測定した． 1 回の線源の作成で，4~5 スペクトルを測定することができた。異性体シフトの値は，線源基準で表した。化合物は，既報の方法により合成した．

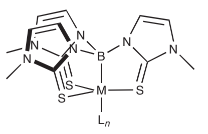

1

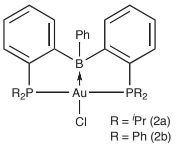

2

［結果と考察］得られたスペクトルを図 1 に示した．Au^{I}_2（**F$_4$-1**）は一組の大きな四極分裂（QS）を持った二重線，Au^{II}_2 化合物（**F$_4$-2**）は Au^{I}_2 よりも小さな QS の二重線であり，二つの Au 原子が等価であることが確認できた．熱分解生成物 **F$_4$-3** は二組の二重線からなり，Au^{I}–Au^{III} の混合原子価化合物であることが確認できた．

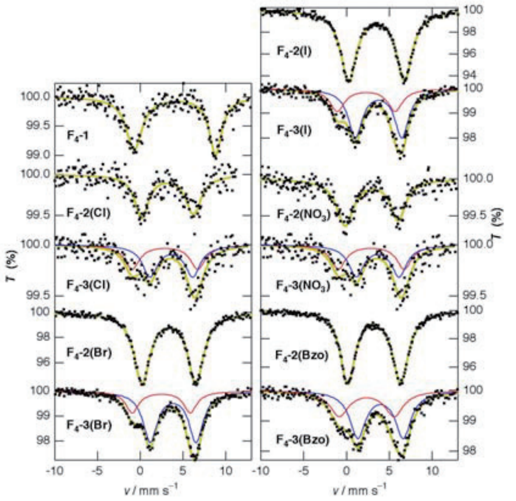

Fig. 1 ^{197}Au Mössbauer spectra of cyclometalated gold compounds and their decomposition products

図 2 に環状二核金錯体の異性シフト（IS）と QS の関係を示す．金化合物では，酸化状態により，IS と QS が固有の領域にプロットされることが知られている．出発物質の二核 Au(I)錯体は P,C-配位のために大きな IS と QS を示すが，低温で穏やかに酸化して生成する二核(II)錯体では，IS も QS も減少している．これは Au(I)から Au(II)になったことに伴う配位構造の変化によるものである．Au(II)化合物では，ハロゲンだけでなく安息香酸イオンや硝酸イオンも配位していることがメスバウアースペクトルから示唆される．Au(I)錯体も Au(II)錯体もホスフィン錯体の場合よりも IS，QS とも小さくなっているが，これはベンゼン環をフッ素化した影響であり，電子供与能の減少が分かる．この減少は，ホスフィンをアルシンに代えたときに近いが，特に IS の減少のほうが大きく，Au 6s 軌道への供与能が今回の錯体では減少したことが示唆される．Au(II)錯体を溶液中で加熱して得られる生成物には，Au(I)と Au(III)に帰属できる 2 サイトが存在し，不均化が起こったことが確認できる．そのメスバウアーパラメータはやはり，フッ素置換体は IS も QS もホスフィン錯体よりも小さくなっている．

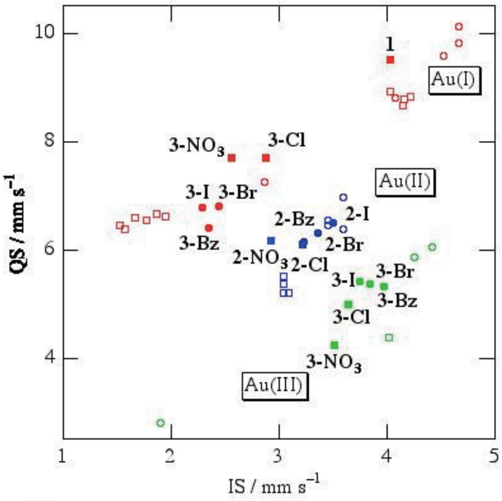

Fig. 2 ^{197}Au Mössbauer spectra of cyclo- metalated and related complexes

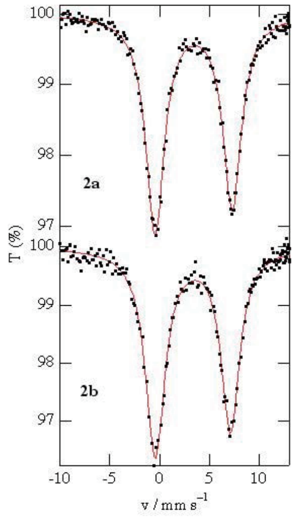

Fig. 3 ^{197}Au Mössbauer spectra of gold-phosphanylborane complexes.

3-2

ホスファニルボラン錯体 2a, 2b の 12 K でのスペクトルを図 3 に示した．メスバウアーパラメータは IS = 3.40, QS = 7.73 mm s^{-1} (**2a**), IS = 3.31, QS = 7.53 mm s^{-1} (**2b**)であった．これらのパラメータの IS と QS の関係を示すと図 4 のようになる．

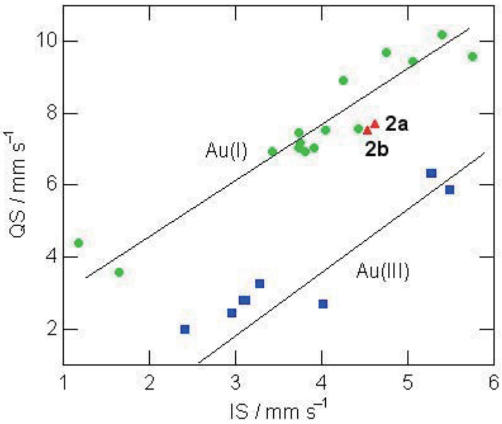

Fig. 4 IS-QS plot of gold-phophanylborane complex. IS values are relative to metallic Au.

図 4 には，種々の Au(I)および Au(III)錯体についての ISと QSの関係もプロットされている．**2a**，**2b** ともに，Au(I)の領域に位置している．このことから，Au–B 結合は $Au^{III}←BR_3^{2-}$でなく $Au^{I}→BR_3$ であり，ボラン配位子が電子受容体として働いていることが明確になった．ところでこれらの錯体は $Au^{I}P_2BCl$ の平面四配位型配置を取っている．Au(I)は通常直線 2 配位をとるのでこの構造は珍しく，比較対象となる Au^{I} 化合物のデータが存在しない．そこで点電荷模型では，平面 4 配位化合物の部分四極分裂は直線構造の 1/2 になることを勘案してパラメータを見てみると，ほぼ合理的な値に見える．

(3) ^{161}Dy メスバウアー分光

^{161}Dy のメスバウアーγ線のエネルギーは 25.7 keV と低いために，室温でもメスバウアー効果が観測できる．このことと，狭い線幅と大きな核磁気モーメントを持つために，磁性体などの物性研究に有用であることが知られている．しかし無機化学的な視点での研究は以外と少ない．

ランタノイドの配位高分子は近年，磁性体，発光材料，分子包接体や触媒などの多孔性物質として注目を集めている．架橋配位子としてのジカルボン酸，特に脂肪族ジカルボン酸は，柔軟に多様な結晶構造を作り出すために広く研究されてきた．我々は色々な鎖長の脂肪族ジカルボン酸$^{-}O_2C(CH_2)_nCO_2^{-}$（n = 0 ~ 5）のランタノイド錯体の次元性に興味をもち，Dy(III)錯体のメスバウアースペクトルを測定した．

［実験］シュウ酸（n = 0; H_2ox），マロン酸（n = 1; H_2mal），コハク酸（n = 2; H_2suc），グルタル酸（n = 3; H_2glu），アジピン酸（n = 4; H_2adi），ピメリン酸（n = 5; H_2pim），リンゴ酸（H_2mali）の錯体 $Ln_2L_3{\cdot}xH_2O$ は，$DyCl_3$ 水溶液にジカルボン酸を加えて pH を 4.5 ~ 5.5 に調製して合成した．重量分析により錯体の組成を次のように決定した．$Dy_2(ox)_3{\cdot}10H_2O$，$Dy_2(mal)_3{\cdot}6H_2O$，$Dy_2(suc)_3{\cdot}2H_2O$，$Dy_2(glu)_3{\cdot}2H_2O$，$Dy_2(adi)_3{\cdot}2H_2O$，$Dy_2(pim)_3{\cdot}5H_2O$，$Dy_2(mali)_3{\cdot}2H_2O$.

^{161}Dy メスバウアー線源 ^{161}Tb/GdF_3（273 MBq）は $^{160}Gd_2O_3$ と NH_4F の固相反応で合成した $^{160}GdF_3$ を，JRR-3 HR-2 照射孔で 20 h 中性子照射をして作成した．スペクトルは，25.7 keV のメスバウアーγ線を比例計数管（$Xe\text{-}CO_2$）で計測して測定した．50 mgDy cm^{-2} となる試料を用いて測定した．Wissel 社のメスバウアー駆動装置を用いスペクトルを測定し，駆動速度（±100 mm s^{-1}）はレーザ干渉計を用いて測定した．スペクトルの解析は，I_g = 5/2 と I_e = 5/2 間の四極遷移について，非対称定数$\eta = 0$ として行った．

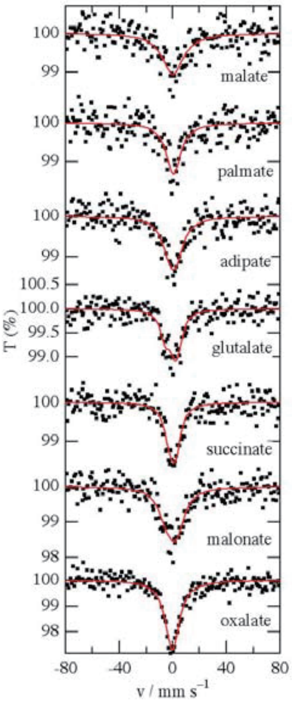

Fig. 5 ^{161}Dy Mössbauer spectra of Dy^{III}–dicarboxylates at 77 K

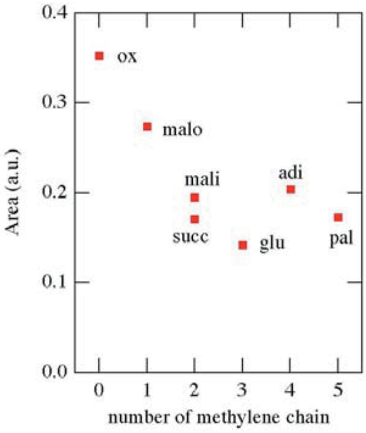

Fig. 6 Relation between absorption area and the number of methylene group n in dicarboxylate anion

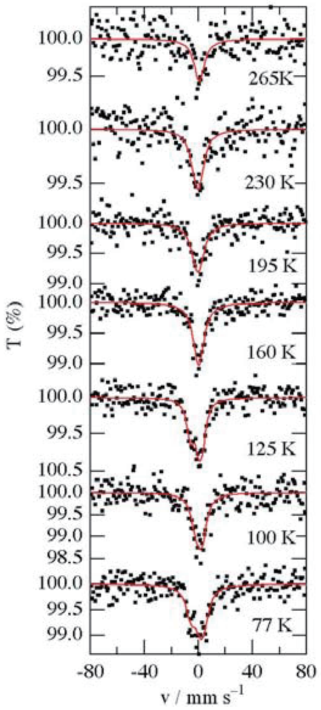

Fig. 7 Temperature dependence of $Dy_2(glu)_3 \cdot 2H_2O$

［結果と考察］50 mgDy cm^{-2}の試料について測定した 77 K でのスペクトルを図 5 に示す．同じ吸収体厚みで測定しているが，ジカルボン酸の鎖長 n が長くなるにつれて吸収強度が弱くなることがわかる．面積強度と鎖長 n の関係を図 6 に示す．$n = 0$（シュウ酸）からコハク酸（$n = 2$）の間で急激に減少しているが，$n = 2$ 以上ではそれほど大きく変化しない．これは短い鎖長のジカルボン酸錯体はリジッドな結晶構造を取っているが，鎖長が長くなるとリジッドさが減少した結晶構造となっていることを示唆している．この研究で用いた錯体の結晶構造は明らかになっていないが，一般にシュウ酸イオンは金属中心間を架橋した 3 次元的ネットワークを作りやすいことや，鎖長が長いジカルボン酸錯体は，通常 2 次元的な pillared layer 構造を取ることを考えると，合理的といえる．

グルタル酸錯体については，温度変化を測定し（図 7），面積強度から格子力学的パラメータ $M\Theta^2$ を求めた．$M\Theta^2 = 4.64\times10^6$ g mol^{-1} K^{-1}であり，デバイ温度Θは 110 K と見積もられた．この値はシアノ架橋 3 次元配位高分子 $DyFe(CN)_4 \cdot 4H_2O$ や $KDyFe(CN)_6 \cdot 4H_2O$ の $M\Theta^2$ の値 7.4×10^6 および 6.3×10^6 g mol^{-1} K^{-1} よりは小さく，最近我々が測定した 2 次元配位 Eu(III)錯体 $4.6_7\times10^6$ (M = Ni), $4.7_8\times10^6$ (M = Co), $6.3_0\times10^6$ g mol^{-1} K^{-1} (M = Mn)と同程度であり，我々が推定している pillared layer 構造と矛盾しない．

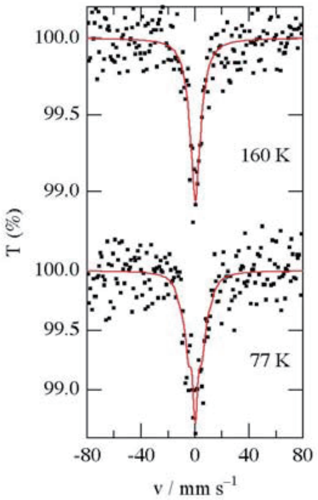

Fig. 8 ^{161}Dy Mössbauer spectra of $Dy_2(glu)_3 \cdot 2H_2O$ simulated by Nowick-Wickman's model.

グルタル酸錯体のスペクトルの線形は緩和スペクトルに見えるので，Nowick-Wickman のスピン緩和模型を用いて解析した（図 8）．77 K における緩和時間τは 30 ps であり，160 K では 0.2 ps まで短くなった．緩和時間はスピン間の距離に関係することが知られている．この錯体の Dy^{3+}–Dy^{3+}距離は不明であるが，多くの Dy(III)–ジカルボン酸錯体では 400－450 pm であり，この錯体も同定の距離を持つと推定される．以前に研究した Er(III)–β-ジケトン錯体（12 K）では，Er^{3+}–Er^{3+} = 558 pm のときτ = 400 ps, Er^{3+}–Er^{3+} = 587 pm で 500 ps, Er^{3+}–Er^{3+} = 382 pm で 100

ps であった．直接の比較はできないが，Er(III)-β-ジケトン錯体の場合とよい対応をしている．

(3) ^{155}Gd メスバウアー分光

^{155}Gd メスバウアースペクトルの特色は，異性体シフトと四極結合定数から，電荷分布や結合についての議論ができることにある．これまでにβ-ジケトン，EDTA，ポリエチレングリコールなどの Gd(III)錯体および CN 架橋 Gd(III)配位高分子などのメスバウアースペクトルの系統的な研究から，窒素原子が配位すると異性体シフトが小さくなる傾向を見いだしている．

トリオクチルホスフィンオキシド（TOPO）に代表されるホスフィンオキシド類は溶媒抽出において，重要であり，溶媒抽出や溶液化学から多数の研究が行なわれてきた．われわれは固体化学的な視点からホスフィンオキシド類の研究を始めた．TOPO 錯体は結晶性がよくなかったので，トリフェニルホスフィンオキシド（TPPO）を用いて錯体を合成し，$\mathrm{Ln(tppo)_4(ClO_4)_3ROH}$（**3A**; Ln = La, Nd, Eu, Gd, Dy, Yb）および $\mathrm{Ln(tppo)_2(NO_3)_3EtOH}$（**3B**; Ln = Eu, Gd）を得た．X 線構造解析から前者は興味深いことに 2 分子の $\mathrm{ClO_4^-}$がキレートした 8 配位十二面体型錯体 $\mathrm{[Ln(tppo)_4(\eta^2\text{-}O_2ClO_2)_2]ClO_4\_ROH}$（Nd~ Yb 錯体は同形）であることがわかった．$\mathrm{Ln–O_2ClO_2}$ 距離（250 ~ 264 pm）は Ln–tppo よりも 27~ 30 pm ほど長く，$\mathrm{ClO_4^-}$ の配位は弱いことが示された．$\mathrm{Ln(tppo)_2(NO_3)_3EtOH}$ は三つの $\mathrm{NO_3^-}$がキレートした 9 配位錯体であった．この課題では，同形の結晶を作る Eu と Gd 錯体の TPPO 錯体について，^{151}Eu および ^{155}Gd メスバウアー測定を行ない，比較検討を試みた．

［実験］$\mathrm{LnX_3{\cdot}\mathit{n}H_2O}$ (Ln = La, Nd, Eu, Gd, Dy, Yb; X = $\mathrm{ClO_4^-}$, $\mathrm{NO_3^-}$）の ROH（R = Me, Et）溶液に 4 倍モルの TPPO の ROH 溶液を加え，ROH を蒸発させると錯体が得られた．

線源は既に報告した線源，すなわち JRR-3 HR-1 で 67 h 照射して作成した $^{155}\mathrm{Eu/SmPd_3}$（半減期 4.96 y）を用いて測定した．測定は，線源と試料（80 mgGd $\mathrm{cm^{-2}}$）を 12 K に冷却しながら，Wissel 社の 1200 駆動システムを使って測定した．線源の駆動速度はレーザ干渉計で測定した．解析は，5/2–3/2 の遷移について，ローレンツ型関数を用いて行なった．δ_{Gd} は線源基準で表わした．

［結果と考察］Eu 錯体の過塩素酸塩（**3-Eu-A** と標記）および硝酸塩（**3-Eu-B** と標記）の 77 K での ^{151}Eu メスバウアーパラメータは，δ_{Eu}, 四極結合定数 e^2qQ_{Eu} の順に，0.20, 5.36 mm $\mathrm{s^{-1}}$ (**3-Eu-A**)，0.30, 3.68 mm $\mathrm{s^{-1}}$ (**3-Eu-B**)であった．δ_{Eu} の値は，**3-Eu-A** は 8 配位としては小さめであるが，妥当な値であった．**3-Gd-A** と **3-Gd-B** の ^{155}Gd メスバウアーパラメータはδ_{Gd}, e^2qQ_{Gd} の順に，0.67, 6.63 (**3-Gd-A**), 0.61, 1.99 (**3-Gd-B**)であった．Gd 錯体で 9 配位の **3B** の方が e^2qQ が小さくなっているのは，おそらく配位数の増加に伴い電荷分布の対称性が増加したためと思われる．これに対し **3A** の EFG が大きいのは，配位子の TPPO と $\mathrm{ClO_4^-}$のもつ電荷が違うことと，二つの $\mathrm{ClO_4^-}$が $\mathrm{Ln^{3+}}$を挟んで直線的に位置していることなどによると思われる．Eu(III)錯体では $^7\mathrm{F}_n \leftarrow {}^5\mathrm{D}_0$ の発光が観測されるが，発光スペクトルから **3-Eu-B** は **3-Eu-A** よりも局所的な対称性が高いことが示唆されており，メスバウアースペクトルの結果と一致している．

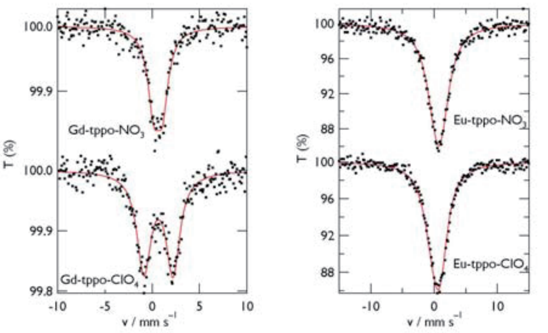

Fig. 9 ^{155}Gd (left) and ^{151}Eu (right) Mössbauer spectra of Ln-TPPO complexes

e^2qQ の値から Eu，Gd 両錯体の EFG V_{zz} を求めると，**3-Eu-A** と **3-Gd-A** は 3.37×10^{21}, 3.66×10^{21} V $\mathrm{m^{-2}}$ とほぼ一致するのに，**3-Eu-B** と **3-Gd-B** は 2.32×10^{21}, 1.10×10^{21} V $\mathrm{m^{-2}}$ と差が見られた．EFG が小さな **3B** で差が見られるのは，Gd(III)は 4f^7 で結晶場の影響が無視できるのに対して，4f^6 の Eu(III)では一つ存在する 4f ホールのために結晶場の効果が存在し，これが格子の EFG に対する寄与が小さくなったために顕在化したためと現在のところ考えている．

(4) ^{170}Yb メスバウアー分光

イッテルビウムは重希土に属し，Eu ほどではないが+2 価を取りやすい元素であり，メスバウアースペクトルから得られる情報は，化学結合や構造について有用であると期待できる．Yb のメスバウアー効果は 5 核種 6 遷移について知られているが，メスバウアー核特性と線源の調製のしやすさから，^{170}Yb が適している．

^{170}Yb のメスバウアー遷移は $E_\gamma = 84.26$ keV の $I_g = 0$ と $I_e = 2$ の間の E2 遷移であり，励起状態の寿命は 1.5 ns（W_o = 2.08 mm s^{-1}）である．これらの特性は ^{166}Er に似ており，既に行った ^{166}Er メスバウアー分光の経験を生かすことができる．

［実験］メスバウアー線源には ^{170}Tm/Al$_2$Tm を使用した．Al$_2$Tm は化学量論比の Al と Tm をアーク溶融してからディスク状に切り出した．Al$_2$Tm 92 mg を JRR-3 HR-2 照射孔（$\phi_{th} = 5.5\times10^{13}$ cm^{-2} s^{-1}）で 55 分間照射して作成した．メスバウアー測定は，^{170}Tm（$t_{1/2}$ = 128.6 d）の 84.26 keV の γ 線を LEPS で計数しておこなった．測定は Wissel 社製 1200 メスバウアーシステムを用い，線源と吸収体を 20 K に冷却しておこなった．線源の駆動速度はレーザー干渉計で測定した．Yb$_2$O$_3$ では 1 スペクトルの測定に 7~ 8 日を要した．

［結果と考察］始めに Yb$_2$O$_3$ を用いて吸収体厚みによるスペクトルの違いを確認するために 56 ~ 336 mgYb cm^{-2} でスペクトルを測定し，以降は 112 mgYb cm^{-2} の厚みで測定することにした．この吸収体厚みで測定したスペクトルを，図 10 に示した．

C 型 Yb$_2$O$_3$ には結晶学的に 2 サイト存在し，S$_3$ 対称の 8a 位置に Yb の 1/4 が，C$_2$ 対称の 24d 位置に 3/4 が存在する．メスバウアースペクトルでは，これら二つのサイトが識別できている．帰属は四極結合定数 e^2qQ = 10.8 mm s^{-1} の吸収が C$_3$ サイトで，25.3 mm s^{-1} が C$_2$ サイトとなる．Gd$_2$O$_3$ も Yb$_2$O$_3$ と同形で，^{155}Gd スペクトルでも，二つのサイトが明瞭に識別できる．C$_3$ サイトは e^2qQ = 10.85 mm s^{-1}. C$_2$ サイトが e^2qQ = 5.53 mm s^{-1} と帰属できる．e^2qQ の値をもとに電場勾配を計算すると，Yb$_2$O$_3$ では C$_3$ サイト 1.5×10^{22} V m^{-2}，C$_2$ サイト 3.4×10^{22} V m^{-2}，Gd$_2$O$_3$ では C$_3$，C$_2$ サイトはそれぞれ 2.5×10^{22} および 1.3×10^{22} V m^{-2} となる．全般的に Yb$_2$O$_3$ のほうが電場勾配が大きくなっているのは，ランタニド収縮によって結晶格子が小さくなったためと考えられるが，Yb$_2$O$_3$ と Gd$_2$O$_3$ では C$_3$ と C$_2$ サイトの電場勾配の大きさが逆になっている．その原因は不明である．

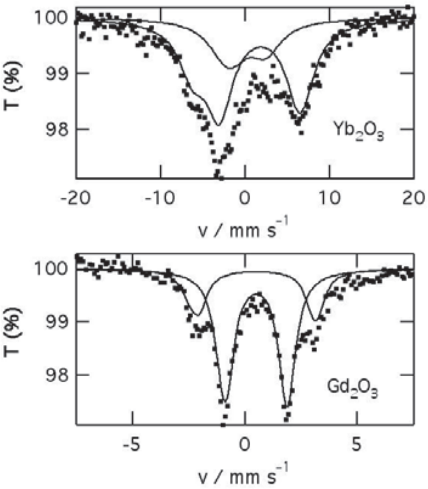

Fig. 10 ^{170}Yb and ^{155}Gd Mössbauer spectra of Yb$_2$O$_3$ and Gd$_2$O$_3$

(5) 今後の計画

原子炉を用いてメスバウアー線源を作成して化学的に有用な知見を与えるメスバウアー分光学的研究を進めるという当初の目的は到達されていると考えている．今後も希土類研究のために ^{155}Gd や ^{161}Dy, ^{170}Yb 測定を続けて行く予定である．^{170}Yb についてはまだ測定ができることが確認できた段階であるが，化学的な応用を進めて行きたい．^{197}Au については，有機金属化合物の研究に有用であることが分かっているので，今後も研究を発展させて行く予定である．有機金属化合物の研究という点からは，^{193}Ir メスバウアースペクトルも有用である．今後 ^{193}Ir メスバウアー測定ができるようにして，^{197}Au と併用しながら，研究を発展させて行くことを計画している．

成果の公表

1. R. Cao, T. M. Anderson, P. M. B. Piccoli, A,. J. Schultz, T. F. Koetzie, Y. V. Geletii, E. Slonkina, B. Hedman, K. O. Hodgson, K. I. Hardcastle, X. Fang, M. L. Kirk, S. K. Knottenbelt, P. Kögerler, D,. G. Musaev, K. Morokuma, M. Takahashi, C. L. Hill, *J. Am. Chem. Soc.*, **129**, 11118 – 11133 (2007): Terminal gold-oxo complexes

2. M. Sircoglou, S. Bontemps, M. Mercy, N. Saffon, M. Takahashi, G. Bouhadir, L. Maron, D. Bourissou, *Angew. Chem. Int. Ed.*, **46**, 8583 – 8586 (2007): Transition-metal complexes featuring Z-type ligands: Agreement or discripancy between geometry and d^n configuration?
3. J. Wang, M. Takahashi, T. Kitazawa, M. Takeda, *J. Rare Earth,* **25**, 647 (2007): Structure and bonding in some Gd(III) metal complexes studied by three-dimensional X-ray analysis and ^{155}Gd Mössbauer spectroscopy
4. M. A. Bennett, S. K. Bhargava, M. Takahashi, N. Mirzadeh, S. H. Privér, *Bull. Chem. Soc. Jpn.,* **82**, (2009), in press: ^{197}Au Mössbauer spectroscopic studies of cyclometalated gold dimers containing 2-$C_6F_4PPh_2$ ligands

国際会議

1. A Nakamura, A.F. Fuentes, Y. Okamoto, M. Takahashi and M. Takeda, International Symposium on the Industrial Applications of the Mössbauer Effect, Budapest, Hungary, Aug. 2008: ^{151}Eu- and ^{155}Gd-Mössbauer Study of Defect-fluorite-type MO_2-$LnO_{1.5}$ Solid Solutions (M^{4+} =Ti, Hf, Zr, Ce, U, Th; Ln^{3+}=Lanthanide)

学会講演

1. 高橋，東舘，竹田，2006 日本放射化学会年会・第 50 回放射化学討論会（2006.10）水戸・東海：（ジハロヨード）ベンゼン類の ^{127}I メスバウアースペクトル.
2. 綾部，高橋，竹田，Costes，2006 日本放射化学会年会・第 50 回放射化学討論会（2006.10）水戸・東海：Gd(III)を含む 3d－4f，4f－4f' 系二核錯体の ^{155}Gd メスバウアースペクトル.
3. 時田，福嶋，北代，竹田，Bhargava，日本化学会第 87 春季年会（2007.3）吹田：*trans*－1,2-ビス（ジフェニルホスフィノ）エチレンが配位した三核金(I)錯体の合成と構造および ^{31}P NMR.
4. 淺香，高橋，宍戸，日本化学会第 88 春季年会（2008.3）東京：イッテルビウム化合物の ^{170}Yb メスバウアー測定.
5. 高橋，淺香，宍戸，第 45 回アイソトープ・放射線研究会（2008.7）東京：無機化合物の ^{170}Yb メスバウアー測定.
6. 高橋，今井，淺香，2008 日本放射化学会年会・第 52 回放射化学討論会（2008.9）広島：Yb 酸化物および塩化物の ^{170}Yb メスバウアースペクトル.
7. 高橋，Mirzadeh, Bhargava, Bennett，2008 日本放射化学会年会・第 52 回放射化学討論会（2008.9）広島：三級ホスフィンを配位子とする二核金錯体の ^{197}Au メスバウアースペクトル
8. 高橋，平井，日本化学会第 89 春季年会（2009.3）船橋：ホスフィンオキシドを配位したランタノイド錯体の構造とメスバウアースペクトル.
9. 藤田，笹森，菊地，高橋，日本化学会第 89 春季年会（2009.3）船橋：二次元正方格子磁性体 BBDTA·$AuBr_4$ における磁気相転移
10. 高橋，根本，Mirzadeh, Bhargava, Bennett，第 46 回アイソトープ・放射線研究会（2009.7）東京：ペルフルオロ基をもつ三級ホスフィンを配位した有機金化合物の Au-197 メスバウアースペクトル
11. 高橋，平井，2009 日本放射化学会年会・第 53 回放射化学討論会（2009.9）東京：ホスフィンオキシドを配位したランタニド(III)錯体の結晶構造と ^{151}Eu および ^{155}Gd メスバウアースペクトル
12. 藤田，笹森，菊地，高橋，日本物理学会 2009 年秋季大会（2009.9）熊本：有機磁性分子が作る二次元正方格子磁性体の基底状態

3-2

3-3

「ガンマ線摂動角相関法を用いた金属タンパク質活性位の超微細場測定」

Measurement of Hyperfine Field of a Metal Site of Protein by the Method of Perturbed Angular Correlation of Gamma-Rays

金沢大学 理工研究域 横山明彦
Akihiko Yokoyama, Institute of Science and Engineering, Kanazawa University

【はじめに】

近年、タンパク質の構造と機能の関係が注目され、盛んに研究が行われている。特に生体分子中の金属イオンは活性中心として重要な役割を担い、その役割を考察する上で pH や酸化還元電位などの化学的環境と関連した状態の情報は、非常に重要である。現在タンパク質の構造を解析するための一般的な手法である X 線構造解析によって、結晶化したタンパク質の詳細な構造を測定できる。しかし、機能を発現しているのは水溶液中であり、タンパク質の溶液中での状態に関する情報が少ない。γ 線摂動相関（PAC）法では試料を溶液のまま（*in situ* 測定）できるので、構造を損なうことなく、または機能が発現できる環境において金属活性部位周辺の超微細場を測定できる可能性がある。

これまでに報告された PAC 法の生体分子への応用としては、以下のような例がある。銅イオンを含むタンパク質の研究として、アズリン、プラストシアニンなどのブルー銅タンパク質中金属位置にプローブ親核を導入することで摂動角相関測定がなされた。これらのタンパク質では二つの His 残基と Cys 残基、Met 残基の四つのアミノ酸残基によって金属が囲まれており、前の三つが金属結合に強く関与し、Met は水の侵入を防いで金属位の安定性に寄与していることが測定結果から論じられた。その他プラストシアニンの His 残基の一つが二つの His 残基と Cys 残基の作る面内で運動していることが PAC スペクトルに反映され、動的な情報についても得られている。他にも銅タンパク質では複数の銅イオンを含むラッカーゼなどのマルチ銅タンパク質の測定例があり、銅以外でも亜鉛イオンを含むタンパク質の研究や、マウスを使った *in-vivo* での測定例もある。これらの研究の多くは生体中の化合物について金属元素の役割を明らかにすることを目指している。

私の研究グループでは、これまでに活性中心に銅サイトを持つ金属タンパク質マビシアニンの野生型や変異体(15 位の Thr を Ala に置き換えたもの)の溶液中の状態についての情報を得ることを目的として、マビシアニンの活性中心での超微細場測定を PAC 法で試みた。この研究において大腸菌により生合成したマビシアニンの銅を PAC プローブ親核 ^{117}Cd（→^{117}In, $T_{1/2}$=2.49 h）に置換し、野生型と変異型それぞれの銅活性部位における超微細場に違いがあることを見出した。[1,2]　また、この測定から得られた情報をより詳しく議論するために、配位元素や配位数が類似した錯体での超微細場測定を ^{117}Cd のほかに ^{111}In（→^{111}Cd, $T_{1/2}$=2.80 d）や ^{111m}Cd（→^{111}Cd, $T_{1/2}$=48.5 min）などの PAC 親核種を用いて行った。[3]しかし、これらの核種は半減期が短く、統計の良いデータを取ることが難しい、また短時間で試料を作成しなければならないといった問題があった。

そこで本研究では金属タンパク質に取り込む PAC 核種に、比較的半減期の長い ^{111}Ag(→^{111}Cd, $T_{1/2}$=7.45 d)を用いて統計の良いデータを得ることを目的とした。^{111}Ag の壊変生成物である ^{111}Cd の酸化数は銅と同じ+2 であるため、この核種を用いることで置換前の銅活性部位により近い化学状態で測定を行えるという利点も期待できる。原子炉での中性子照射で PAC 親核種である ^{111}Ag を製造し、測定に適したトレーサー溶液を調整する手法を確立し、これを用いて種々の銀錯体とタンパク質試料の電場勾配値を測定することを試みた。

【プローブ核の製造】

^{111}Ag の製造は、市販の天然同位体組成の Pd 箔（約 2.55 g）を用いて原子力研究開発機構原子力科学研究所 JRR-3（または JRR-4）原子炉中に送入し、熱中性子照射を 20 分間行った。その後 Pd 箔を 5 日間放置し、^{110}Pd(n,γ)^{111}Pd 反応(反応断面積 0.70 b)によって生じた ^{111}Pd（$T_{1/2}$=23.4 min)を充分に β$^-$壊変させて ^{111}Ag(約 60MBq)を製造するとともに照射時に生成する副生成物を減衰させた。図 1 に放置後の照射試料について、Ge 半導体検出器を用いたガンマ線スペクトルの一例を示した。［4］

JRR-3M および JRR-4　気送管、核物性

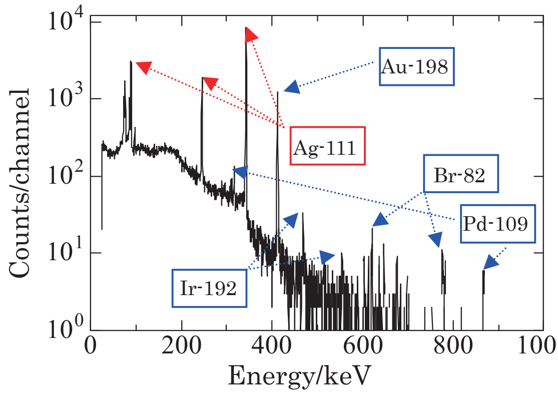

図１．照射試料のγ線スペクトルの一例。

主なγ線は目的の ^{111}Ag であることがわかる。その他はターゲット不純物起源のものと、副生成物（^{109}Pd, $T_{1/2}$=13.43 h）がわずかに確認できる。

【試料調製】

上記の照射試料を京都大学原子炉実験所に運搬し、下記の２つのスキームに従って ^{111}Ag を照射試料から分離してトレーサー溶液とした。銀錯体試料はスキーム１を採用し、タンパク質試料は初期にはスキーム１を、後にスキーム２を採用した。

スキーム１

照射した Pd 箔１枚につき王水を 2 mL 加え、ホットプレート上で加熱して溶解した。担体として硝酸銀を 40 mg 加え、水を加えて約 50ml にした。生成した白色の AgCl 沈殿を遠心分離(3000 rpm、5 min)で取り分け、上澄みは別けておいた。この沈殿にアンモニア水 6 mL を加えて加熱して溶解し、濃塩酸数滴、濃硝酸 4 mL を加えて再び AgCl 沈殿を生成させた。この沈殿を遠心分離で取り分け、6M NaOH を 5mL 加えて湯浴で約 30 分加熱すると沈殿が黒緑色の Ag_2O になった。その後遠心分離でこの沈殿を取り分けて濃硝酸 5 mL で溶かしてトレーサー溶液とした。試料の放射能が少ない場合は、１回目の遠心分離で別けておいた上澄みに同様の操作を行って放射能成分の分離を適宜行った。

スキーム２

試料をビーカーに移し換えて Pd 箔１枚につき王水 2 mL を加え、ホットプレート上で加熱して完全に溶解させた。陰イオン交換樹脂（Dowex 1 × 8 100-200 mesh）をカラム（BIO-RAD 社、容量 20 mL）に充填して濃塩酸でコンディショニングし、試料溶液を流した。その後、まず濃塩酸 10 mL を流して破棄し、次いで濃塩酸 20 mL を流してこれを分取した。全てのカラムから分取した溶出液を１つにまとめ、ホットプレートで約 3 mL まで加熱濃縮し、6M NaOH で pH 7 に調製した後に再び約 2 mL になるまで加熱濃縮し、これを ^{111}Ag のトレーサー溶液とした。

タンパク質試料の調整においては、作成したトレーサー溶液を 6M NaOH で中和し、生合成したマビシアニン溶液（200μM）を加え 6 時間から一晩攪拌して ^{111}Ag を取り込ませた。その後 HEPES 緩衝液を用いて pH 7.5 に調整した Sephadex G25 カラムで、タンパク質に取り込まれなかった余分な ^{111}Ag を除いた後、粘性を高めてタンパク質の拡散運動を抑えるためにスクロースを終濃度 50%になるよう加えて、測定の際にはタンパク質の変性を防ぐためペルチエ素子の上で冷やしながら行った。

銀錯体試料については、作成したトレーサー溶液に各種キレート剤（o-phenanthroline、bismuthiol、オキシン、DDC、BPHA、キナルジン酸）を加えて錯体試料を調製した。

【PAC 測定】

２本のカスケードγ線の角度相関を調べるため、４つの検出器を 0°、90°、180°、270° 方向に設置し、時間微分型 PAC 測定法で計測した。検出器には時間分解能に優れた BaF_2 シンチレータを使用した。

^{111}Ag を親核として用いたときに、電場勾配のみを摂動として考えた場合の摂動係数 $A_{22}G_{22}(t)$は以下のようになる。

$$A_{22}G_{22}(t)=A_{22}\{S_0+S_1\cos(6\omega_Q C_1 t)+S_2\cos(6\omega_Q C_2 t)+S_3\cos(6\omega_Q C_3 t)\}$$

（１）

ここで、S_n, C_n は非対称パラメータ η によって与えられ、η =0 の場合、

$$A_{22}G_{22}(t)=\frac{A_{22}}{5}\left\{1+\frac{13}{7}\cos(6\omega_Q t)+\frac{10}{7}\cos(12\omega_Q t)+\frac{5}{7}\cos(18\omega_Q t)\right\}$$

（２）

となる。

実験で得られた TDPAC スペクトルに（1）式をフィッティングすれば、電気四重極周波数 ω_Q および ^{111}Cd プローブ核位置での電場勾配を求めることができる。ただし、ω_Q はスペクトルによって Gauss 分布の分散を仮定した。測定されたマビシアニンに対する室温付近で測定した TDPAC スペクトルの例を銀錯体のデータと共に図 2 に示す。

統計的にある程度満足できるスペクトルを得ることに成功した o-phenanthroline錯体（図2a）と bismuthiol錯体（図2b）と比較すると、マビシアニ

ン（図2c）についてはAgイオンのタンパク質への取り込み率が悪いため試料の放射能が弱く、あまり統計の良いデータを得ることができなかったが、何とかフィッティング可能な予備的なＰＡＣスペクトルを測定できた。［5］

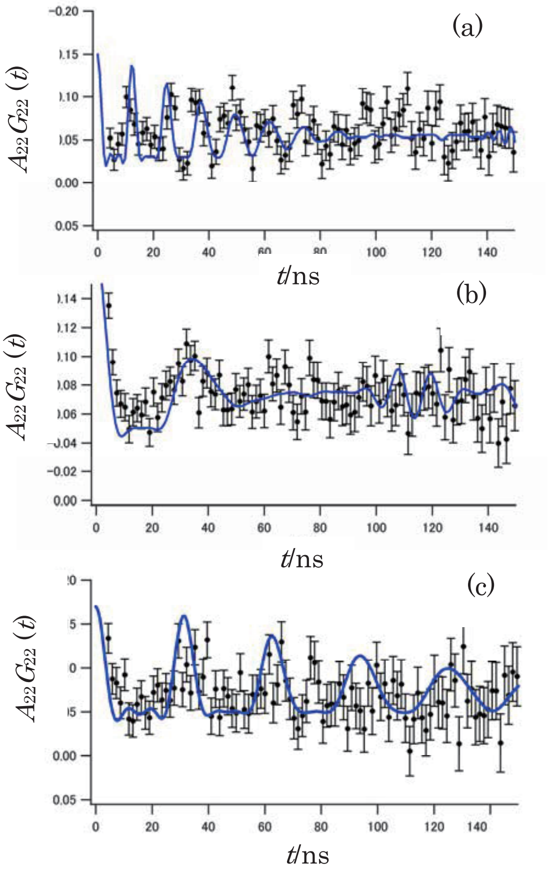

図２．時間微分ＰＡＣスペクトルの例。

【結論】

照射したPd箔より^{111}Agを取り出してトレーサー溶液を作成し、生体試料等に対してPAC測定を行うことに成功した。ただし、今回の実験で測定したタンパク質試料は放射能が弱く、統計の良いデータを取ることが出来なかった。ただし、これまでにスキーム２によって無担体の ^{111}Ag トレーサーの作成手法を確立できたので、これから放射能を増量すれば感度の良い実験を行うことが期待できる。

フィッテングによって求められた四重極周波数 ω_Q 電場勾配は下記のように電気四重極モーメント Q、スピン量子数 I、と非対称パラメータ η で示される。

$$\omega_Q = -\frac{eQV_{zz}}{4I(2I-1)\hbar}$$

この式を使って、現時点までで得られているスペクトルについて、電場勾配を算出した。[6] 今回 ^{111}Ag で測定された電場勾配を、以前に別のプローブ（^{111}In、^{111m}Cd）を用いて測定されたデータと比較すると、オキシン錯体ではプローブ核が同じ ^{111}Cd の中間準位に壊変する ^{111}In、^{111m}Cd と比較して二倍以上大きくなっている。DDC では比較的近い値となっているものの、BPHA でもオキシンと同様、^{111}Ag の方の値が大きくなっている。全体的に ^{111}Ag を用いることにより試料では電場勾配値が大きくなる傾向がみえる。オキシン、DDC、BPHA は誤差が大きいので誤差範囲内で一致している可能性があるが、比較的統計の良いキナルジン酸では、明らかに ^{111}Ag のデータは大きな値を示している。一方、生体試料であるマビシアニンでは、こちらもエラーが大きいが、逆に ^{111}Ag のデータの方が小さい。こういった、プローブ親核による電場勾配値の違いは、プローブ親核の壊変の後遺効果の可能性がある。プローブ核が同じ ^{111}Cd である三つのプローブ親核の壊変は、^{111m}Cd は核異性体転移、^{111}In は EC 壊変、^{111}Ag は β^-壊変と、三つとも異なった壊変である。この効果についても非常に興味深いので、これから検討していきたい。

【参考文献】

[1] 橋本知典、横山明彦、片岡邦重、高田真由子、菊永英寿、木下哲一、村上幸弘、高宮幸一、大久保嘉高、KURRI-KR-118, pp.62-65 (2005).
[2] A. Yokoyama, T. Hashimoto, K. Ihara, H. Kikunaga, N. Kinoshita, I. Yamazaki, K. Kataoka, M. Yanase, M. Takata, Y. Murakami, K. Takamiya, M. Tanigaki and Y. Ohkubo, Hyperfine Int., 181, 69-73 (2008).
[3]横山明彦、橋本知典、片岡邦重、菊永英寿、木下哲一、村上幸弘、高宮幸一、大久保嘉高、佐藤　渉、斎藤　直、KURRI-KR(CD)-6, pp.41-45 (2006).
[4] 横山明彦、山﨑逸郎、村上幸弘、大久保嘉高、佐藤　渉、KURRI-KR(CD)-10, pp.33-36 (2007).
[5] 横山明彦、山﨑逸郎、鈴木大介、片岡邦重、高宮幸一、大久保嘉高、佐藤渉、KURRI-KR(CD)-136, pp.39-42 (2008).
[6] 山﨑逸郎、西尾正樹、片岡邦重、横山明彦、佐藤　渉、高宮幸一、大久保嘉高、KURRI-KR(CD) *in press* (2009).

【成果の公表】
1. 横山明彦、山﨑逸郎、村上幸弘、
　大久保嘉高、佐藤渉、
「PAC法を利用した生体分子活性位における超微細場測定―Ag-111を用いたPAC測定」、京都大学原子炉実験所専門研究会報告書KURRI-KR(CD)-10, pp.33-36 (2007).
2. 横山明彦、山﨑逸郎、鈴木大介、
　片岡邦重、高宮幸一、大久保嘉高、佐藤渉、
「^{111}Agを用いたPAC法によるマビシアニンの超微細場測定」、京都大学原子炉実験所専門研究会報告書KURRI-KR(CD)-136, pp.39-42 (2008).
3. 山﨑逸郎、西尾正樹、片岡邦重、
　横山明彦、佐藤渉、高宮幸一、大久保嘉高、
「親核プローブ^{111}Agを用いたPAC測定」、京都大学原子炉実験所専門研究会報告書KURRI-KR(CD) *in press* (2009).

3-3

3-4

低温核偏極による強磁性体の内部磁場の精密測定
Study of Hyperfine Field using Low-temperature Nuclear Orientation

大矢　進，大坪　隆，泉川卓司[1]，武藤　豪[2]，西村克彦[3]
S. Ohya,T. Ohtsubo, T. Izumikawa, S. Muto, K. Nisimura

新潟大学自然科学研究科
Graduate School of Science and Technology, Niigata University
[1]新潟大学アイソトープ総合センター
[1]Radioisotope Center, Niigata University
[2]高エネルギー加速器研究機構中性子研究所
[2]Neutron Science Laboratory, KEK
[3]富山大学工学部
[3]Faculty of Engineering, Toyama University

１．はじめに

これまで我々は，超低温核整列装置を用いて多くの原子核の超微細相互作用の研究を行ってきた。この場合超微細相互作用の大きさは原子核のｇ因子と内部場の積になる。したがって原子核の磁気モーメントが知られているときは，この超微細相互作用から内部磁場を精度よく求めることが出来るし，逆に内部磁場が知られているときは原子核のｇ因子を決定できる。また実際の実験では低温での温度計として内部磁場と原子核の磁気モーメントがすでに良く知られたものを用いる。普通は Co の単結晶中の ^{60}Co, あるいは鉄中の ^{57}Co および ^{60}Co などが代表的に用いられる。

今回，温度の高いところで用いる鉄中の ^{192}IrF と Co の単結晶は高価であるので Fcc の Co の薄い箔を用いて温度計と超低温核整列の核磁気共鳴のテスト実験用を兼ねたものを製作して，研究に用いることにした。これのきっかけになったのは，旧友の N.J.Stone から CERN/ISOLDE での Hf の High Spin Isomer の磁気モーメントを測定する計画が提案されことに始まる。Hf の鉄中の内部磁場は我々が ^{175}Hf の鉄中の共鳴観測成功していた「１」。

実験は 2008 年８月に CERN/ISOLDE で行われた。日本からは私以外に大坪（新潟大）、西村（富山大）、武藤（KEK）等が参加した。普通は温度計として ^{60}CoFe あるいは ^{57}CoFe が良く使われるが、この研究ではガンマー線の異方性が大変大きいので，温度が高いときに、感度のあるものが必要である。

そこで半減期 74 日の ^{192}IrFe を東海の原子炉を用いて作り、温度計として日本から送ることにした。図１に ^{60}CoFe と比較した ^{192}IrFe の 468-keV のガンマー線の異方性の温度変化（上段）と温度で微分した感度（下段）を示す。^{60}CoFe は温度が５mK あたりが一番感度がよいが、^{192}IrFe は 15mK あたりであり、

JRR-3 水力照射設備　HR-1,2　　　原子核物理学，核物性物理学分野

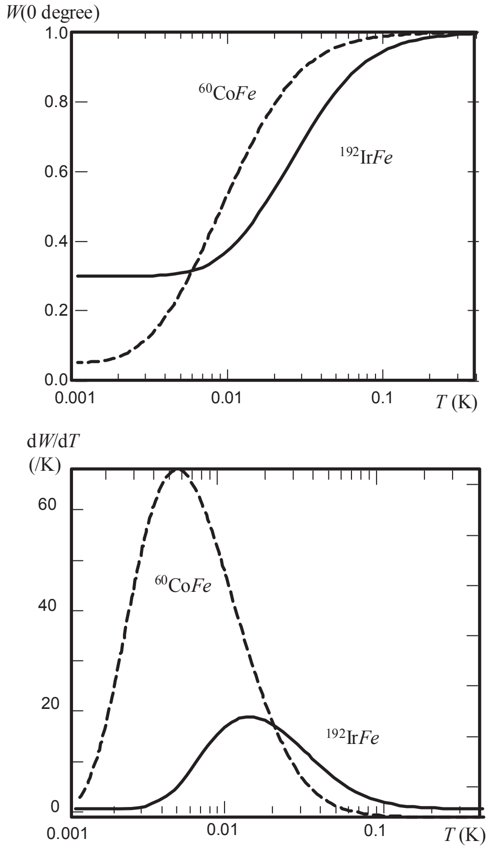

図１.上段は　^{60}CoFe1332-keV ガンマー線と比較した ^{192}IrFe の 468-keV のガンマー線の異方性の温度変化。　下段はそれぞれ温度で微分した感度を示す。

100mK の高温でも異方性があり，高温でも温度計として使用できる。

２．試料の製作

^{192}IrFe 試料は定同位元素を原子炉で照射することにより製作した。　高純度の Ir を高純度の鉄に約 0.17%溶かしたものを（数回，電子ビームによる溶融）ローラで約２０ミクロン薄くしたものを用いた。この試料を原研の３号炉を用いて熱中性子を照射して，鉄の中に非常に希薄な ^{192}IrFe を製作した。　照射後は 800 度でこの試料を真空中で１時間熱処理をした。　^{60}CoCo は Co の４ミクロンの箔を原研の３号炉を用いて熱中性子を照射し，同様に製作した。

^{192}Ir の強度は 100kBq 程度で非密封の条件で CERN に空輸することにした。日本では L 型に相当して、ゆうパックで送れる量である。空輸の国際条約でも強度の弱い Radioactive Material, Excepted Package UN2910 の張り紙をするだけで空輸できた。もちろん CERN の Radiation Safety Office と，やり取りの後，受け取り許可を得てからである。

３．CERN/ISOLDE での Hf の実験

CERN/ISOLDE ではオンラインの超低温核整列装置があり質量分析器から加速された Hf のラジオアイソトープが Fe あるいは Ni に 10mK の温度のまま打ち込むことが出来る。

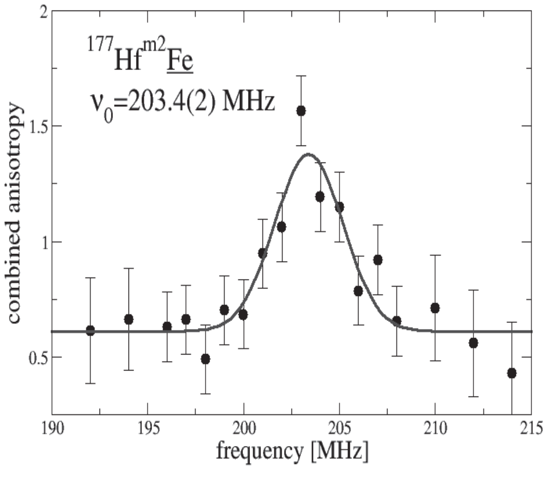

図２　NMR-ON spectrum of ^{177m}HfFe

実験は最初、半減期 51.4 分のスピン 37/2$^-$の ^{177m}Hf のアイソマーから始めた。^{177m}HfFe の NMR-ON 共鳴スペクトルを図２に示す。

このあと ^{180m}Hf と ^{179}Hf の測定を行った。しかし ^{180m}Hf は幅広いパワーレゾナンスのため、また ^{179}Hf は常温で埋め込んだため共鳴は測定できなかったが、ガンマー線の異方性から遷移の混合比など測定できた詳しい解析は現在進められている。また今年度も引き続き実験が行われて解析が行われている。この実験は次の多くの人たちで行われ、やがて正式な結果は発表される予定です。^{60}CoCo の温度計及び NMR-ON 用の共鳴実験の報告は今回の報告には間に合わなかったが，これから行う予定である。最後にこれまで共同研究をやってきた多くの人たち，また原子炉の照射に当たっては開放研の皆様に深く感謝します。

CERN/ISOLDE での共同研究者名

CSNSM – Orsay France: L.Risegari, C.Gaulard, G.Audi

The University of Oxford – UK: N.J.Stone, J.R.Stone

Institut Laue Langevin Grenoble & ISOLDE CERN: U.Köster

University of Tennessee – Knoxville USA: C.Bingham

University of Maryland – College Park USA: W.B.Walters

Niigata University – Japan: S.Ohya, T.Ohtsubo

Toyama University – Japan: K.Nishimura

Neutron Science Laboratory – KEK – Tsukuba Japan: S.Muto

University of Surrey – Guildford UK: P.M.Walker, A.Deo, Z.Podolyak

参考文献

「１」S. Muto, T. Ohtsubo, S. Ohya and K. Nishimura, Hyp. Interact. 158 (2004) 195-198

成果の公表

1. 大矢進，大坪隆，平野晴誉，久保徹，山田亮太，渡部亮太，西村克彦，W.D.Hutchison,武藤豪：^{59}FeNi の NMR-ON，日本物理学会，第 63 回年次大会，2008 年 3 月
2. 大矢進：低温核整列を用いた核物理・核物性の研究，「短寿命核および放射線を用いた物性研究（I）」専門研究会，京都大学原子炉実験所，2008 年 11 月

3-4

3-5

日本海深海底コアの高密度な放射化分析によるアルカリ岩質テフラ降下履歴の高感度検出
Sensitive detection of alkaline cryptotephra layers in deep-sea cores from the Sea of Japan using high-resolution INAA analysis

豊田和弘・任忠完・梅津 茜・川島奈那子・篠塚良嗣・似内真幸（北海道大学・大学院環境科学院）
Kazuhiro Toyoda, Chungwan Lim, Akane Umetsu, Nanako Kawashima, Yoshitsugu Shinozuka, Masayuki Nitanai
（Graduate school of Environmental Science, Hokkaido Univ.）

１．　研究の背景とその意義

地表の堆積層中に挟まれた火山噴出物（テフラ）は、広い地域での厳密な同一時間面を示す鍵層となる。そのため、露頭やコア試料に記録されている高密度なテフラ層序のデータは、地球温暖化の将来予測に有用であるとされる最終氷期末などの気候激変を復元する上で欠かせない、高分解能で高確度な年代軸となりうる。そのため、肉眼では検出できないほど希薄なテフラ層（クリプトテフラ）を、地層中から効率よく数多く検出し、そのテフラの給源火山を特定すること、また同一火山からのテフラ層群を噴火毎に区別する手法について、西欧州を中心に盛んに研究されはじめたという状況が背景にある。

申請者は以前の原子力機構施設の共同利用の成果として得られた、琵琶湖ピストンコアの微量元素の連続垂直分布を詳しく検討したところ、約１万年前に鬱陵島（韓国）から噴出した鬱陵隠岐（U-Oki）テフラ層の、そのすぐ下位の 2 層準で、U-Oki と同様なアルカリ岩質テフラの混入とみられるタンタル／スカンジウム含有量比（Ta/Sc 比）異常を検出することができた。大陸性のアルカリ岩は、日本列島のような島弧火山岩に比べてタンタル含有量が一桁大きく、またスカンジウム含有量は一桁ほど小さいことが多いので、精度良く微量元素分析を連続的におこなうと、わずかな量のアルカリ岩質テフラの混入が検出できる計算になる。しかしこれらの年代での鬱陵島での噴出軽石層準はほとんど報告されてない。

他方、鬱陵島中の噴出軽石層の炭素年代測定では、現在より約五千年前や約八千年前にも大規模なプレニー式噴火があったことが判明している。ところが琵琶湖の他のピストンコアでもその年代で Ta/Sc 比の異常は検出できなかった。よって、この２つの噴火によるテフラ降下分布は鬱陵隠岐（U-Oki）の南西方向ではなく、数万年前に降下した鬱陵大和（U-Ym）テフラのように、北西方向に拡散軸をもつのだろうと推測している。これらの考察から日本海全域の深海底ピストンコアの放射化分析に興味をもった。また、中性子放射化法はテフラの同定法のひとつとして古くから利用されていたが、本研究のように肉眼でも確認できない程の薄いテフラ層の検出法として利用した例はこれまで世界でも日本でも全くないので、その有用性について検証しようというのが、本研究の申請の第一の動機である。

ちなみに、日本列島に降下するアルカリ岩質テフラの供給火山は、日本海西端の韓国・鬱陵島周辺と中朝国境の白頭山の２カ所に限られる。この偏西風によって日本にもたらされる大陸性テフラは、日本の沈み込み帯の島弧火山から供給されるテフラとは大きく異なる組成を持つため、その特異性から日本のテフラ群の中からの判別は容易である。それでも、第四紀後期に鬱陵島も白頭山もそれぞれ数回以上噴火しているのに、広域テフラとして確定していたのは、鬱陵島から約１万年に飛来した U-Oki(鬱陵隠岐)テフラと、約千年前の白頭山の大噴火に由来する

γ線スペクトロメトリー、JRR-4 Tパイプ　　アルカリ岩質テフラと海底堆積物の放射化分析

B-Tm(白頭山苫小牧)テフラの２つのみで、U-Ym や B-J などのテフラに関してはその噴出年代には未だ不確定さが残っていた。

さらに、日本海における第四紀堆積物中は明暗色互層があり、その変遷は氷期と間氷期での世界的な海水準変動やより短期の数千年周期の世界的な気候変動などとも対比されているので、地球環境変化の研究対象として優良である。しかしその色調の変化に乏しいコアもあり、肉眼で見えるアルカリ岩質テフラ層も限られているため、その層序には不明な点が残されている。そこで、今回「日本海深海底コアの高密度な放射化分析によるアルカリ岩質テフラ降下履歴の高感度検出」という本題目で、原子力機構施設利用共同研究の本申請をおこなった。

２．研究の目的

（１）検出の方法論の検証：まず、中性子放射化分析を用いた日本海堆積物中の微量元素の連続垂直分布の測定が、アルカリ岩質クリプトテフラの検出に特に高感度であり、かつ効率的で、有用な手法である事を示す。

（２）クリプトテフラ層の検出：次に、日本海南部から日本海東北部にかけての複数のコアを用いて、鬱陵島周辺から過去９万年間に、また白頭山から過去十数年間に、日本周辺にもたらされたアルカリ岩質テフラ層をすべて走査して、検出する。

（３）検出層の同定とテフラ層序の構築：さらに、検出したテフラ層内から抽出した火山ガラスの分析から、供給火山と噴火毎での化学組成の相違を見つけ出した上で、対比をおこない、明暗色互層の年代とも比較して、これまでほとんど不明であった第四紀後期における日本海海域でのアルカリ岩質テフラ層序を確立する事を目的とした。

３．研究の方法

（１）分析手法

①バルク試料の微量元素分析：中性子放射化分析の長寿命核種の測定のために、乾燥粉末にした堆積物 100ｍｇをポリエチレンで３重に封入した照射試料を、JR-3 と JB1a などの標準岩石試料と一緒に日本原子力機構東海研内の大学開放研に郵送して、東海研内の研究炉ＪＲＲ4のT-A孔で20分間照射を依頼した。照射後１ヵ月ほど冷却してから、大学開放研より北大へ搬送していただき、北海道大学大学院環境科学院内の地下管理区域内のγ線半導体検出器で１試料につき九千秒間測定した。１日に約７試料のペースで測定をして、期間内で約四千個のバルク試料の微量元素分析を行った。定量した元素はクロム、コバルト、セリウム、タンタル、スカンジウム、ハフニウム、ユウロピウムなどの約十元素である。

②抽出したテフラ粒子の放射化分析：肉眼で判るテフラ層と、希薄なテフラの混入を示唆する微量元素組成の異常を示す堆積物試料からは、ふるいと重液分離を用いて、火山ガラス粒または長石粒の抽出をおこない、北海道大学大学院理学研究院内の X 線分析研究室に設置されたエネルギー分散型 EPMA を用いて、これらの粒子の主成分分析をおこなった。微量元素分析については、抽出成分からハンドピックで集めたテフラ粒子約１mg を高純度石英管中に減圧封入した照射試料を標準試料と共に、バルク試料と同様にＪＲＲ4 の T-A 孔で６時間照射した。１週間冷却後に本原子力機構施設内の大学開放研のγ線半導体検出器にて中寿命核種の測定をおこない、１ヶ月冷却後に北大に郵送していただいて、バルク試料と同様に長寿命核種の測定を行った。テフラ粒子中の微量元素含有量の定量は解析が修了して、解析に取りかかっている。

（２）分析試料

①分析に用いた試料は主として日本列島沿いの日本海における産業技術総合研究所所有のピストン

コアである。目的(１)については、以下の５つのコア中のいずれも過去数千年ー約２万年前の堆積年代に相当する部位から連続して１cm 間隔で採取した約千二百個の試料について微量元素分析を行った。

- GH86-2-D:島根沖(対馬海盆南部)コア 18-232 cm
- GH86-4-P510：
  隠岐北東方(大和海盆南西端)コア 76-402 cm
- GH87-2-308：鳥取沖コア 80-295 cm
- GH87-2-KT: 丹後半島沖コア 22-223 cm
- GH88-2-303:金沢沖(北陸沖縁辺台地)コア 10-246 cm

②次に、目的（２）と（３）については、日本海南東部の北陸沖、大和海盆、 山陰沖の５つのコア中から、過去２ー９万年前又は約７万年までの年代の部位から連続して１cm 間隔で分取した約千五百試料について微量元素分析をおこない、鬱陵島周辺および白頭山を供給火山としたアルカリ岩質テフラの検出を行った。

- GH86-2-N: 山陰沖コア 218-558 cm
- GH89-2-28; 北陸沖（大和海盆） 182-524 cm
- GH89-2-26; 北陸沖（大和海盆） 71-465 cm
- GH89-2-25：男鹿半島沖（大和海盆）164-487 cm
- GH99-1259　男鹿半島沖(佐渡海嶺近傍)123-303 cm

③さらに、過去十数万年間の朝鮮半島北部白頭山を供給源とするアルカリ岩質の広域テフラの検出を行うため、連続して１cm 間隔で分取した千数百試料についての微量元素分析がほぼ終わった段階である。

- KR05-09 PC01　松前海台 160-860 cm
- KR05-09 PC02 留萌沖(日本海盆)解析中
- GH96-1212 羽幌沖(日本海盆)150-520 cm

４．研究成果

（１）クリプトテフラ検出の有効性の検証

日本海南部の５本の海底コア中の数千万年から１万数千年前の堆積層のバルク分析のタンタル/スカンジウム含有量比の垂直分布を図１に示す。なお、図１中のハッチをかけた層が肉眼で確認された U-Oki テフラ層序である。

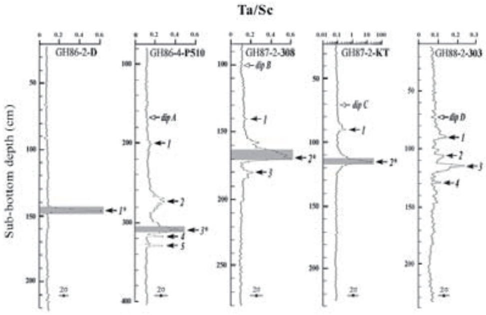

図 1. 日本海南海域の５コア中のTa/Sc 垂直分布

一番西の海域で採取された（図１の左端の）コアを除く４つのコアについて、U-Oki 層以外にもタンタル/スカンジウム含有量比からそれぞれ１ー３層の化学的な異常層が検出された。これらはプレ U-Oki やポスト U-Oki とこれまで呼ばれていた、その存在が不確かなアルカリ岩質テフラに相当する可能性が高い。その異常層から抽出した粗粒な粒子について顕微鏡観察と EPMA-EDS 分析をおこなった結果、その粗粒粒子中の 97%が鬱陵島系火山を給源とするアルカリ岩質テフラ粒と判定された。つまり肉眼では特定できないほど希薄なアルカリ岩質マイクロテフラ層が微量分析から検出できる実例を挙げる事ができた。

さらに、約七千三百年前に西日本に広く降下した鬼界アカホヤ(K-Ah)のテフラ層が確認できたのは、５つのコアのうちの一つ(図２の中央)だけである。K-Ah テフラは日本海堆積物に比べてクロム含有量が小さいのがその化学組成の特徴である。そのコア以外の３つのコア中のクロム/スカンジウム含有量比の垂直分布（図２）には、K-Ah テフラの混入を示唆する化学的異常層（図２中の矢印 A,B,C そして D）が検出された。これらのクロム/スカンジウム含有量比の異常層から抽出された粗粒の流紋岩質火山ガラス粒と長石について、屈折率測定（企業に測定依頼）

と EPMA-EDS 分析（図３）を行った結果、その 94-97％の粒子が K-Ah というテフラ成分と特定された。

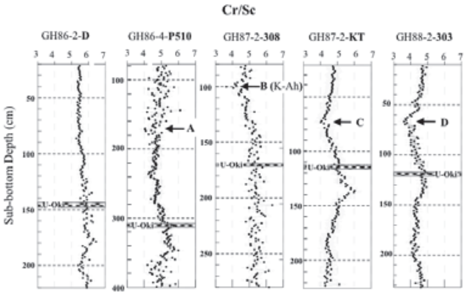

図２．日本海南海域の５コア中の Cr/Sc 垂直分布

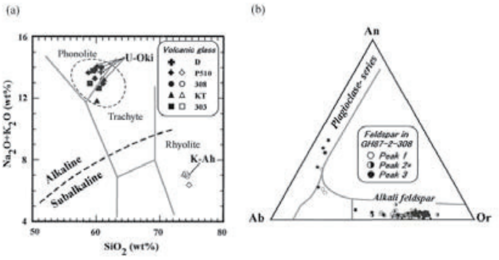

図３．抽出鉱物の主成分組成(a)火山ガラス (b) 長石

本手法によって検出されたクリプトテフラ層と肉眼で確認できるテフラ層との相違は、テフラ成分の他の堆積物成分による希釈率だけでなく、テフラ粒子の粒度の違いにより生じると考えられる。本試料中の肉眼で確認できるテフラ層中のテフラ粒子は 0.2 mm よりも粗粒であるのに対して、本手法で検出されたクリプトテフラ層中のテフラ粒の大部分は 0.04 mm 以下の大きさで、その抽出と分離には１試料でも相当な時間と手間が必要となる。本法はテフラ成分とそれ以外の堆積物成分との間の大きな化学組成の相違を利用して、日本海堆積物中の重量比で約２％に希釈された鬱陵島系テフラ層でも検出できる事を実証できた。

さらに、日本海西南部における過去２万年間のアルカリ岩質テフラ層序を確定するためには、抽出したテフラ粒の噴火毎での微量元素パターンの相違を見いだすことも必要で、現在解析中である。

（２）日本海南東部での過去９万年間のアルカリ岩質テフラ層序の構築

次に本手法を用いて、山陰沖コア１本と東北地方西岸コア４本における３－９万年前の年代での層を走査したところ、タンタル/スカンジウム含有量比の垂直分布（図 4）にあるように、アルカリ岩質テフラの混入を示す多数の化学的異常層が検出された。その異常層のほとんどは肉眼では確認できないものであり、またもうひとつの年代決定法としてよく使用される明暗色互層もやや不明瞭なため、明暗色互層層序のみで確実な年代確定をするのは難しいコアである。

図４　日本海東南域の５コア中の Ta/Sc 垂直分布

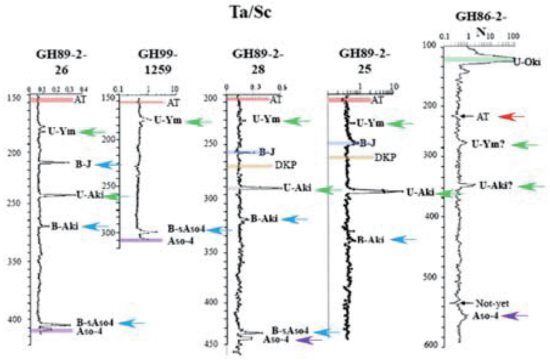

これらの異常層の粗粒相から分離した火山ガラス中の主成分元素の定量（図 5）を行うことで、そのクリプトテフラが、鬱陵島系テフラか白頭山系テフラか、またはタンタル/スカンジウム含有量比がやや高いのが特徴である Aso-4(阿蘇４)テフラなのかを区別する事ができる。

3-5

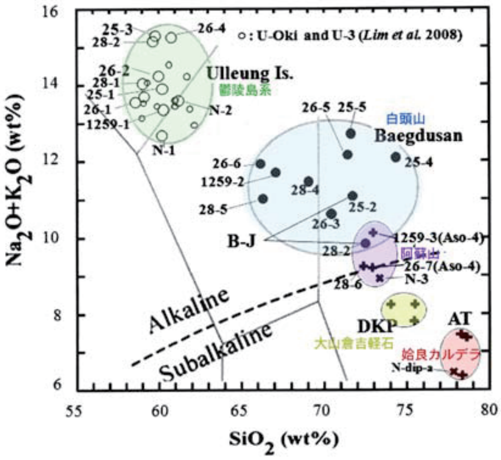

図５抽出した火山ガラスの主成分組成と供給火山

層序学的な考察から、U-Ym（鬱陵-大和）テフラを含むであろう２層の鬱陵島系テフラ、およびB-J(白頭山-日本海盆)テフラを含むであろう３層の白頭山系テフラ層が、それぞれ３つのコアから検出されたと考えられる。新しく検出できたテフラはU-Aki(鬱陵-秋田沖)、B-Aki(鬱陵-秋田沖)、B-sAso4(Aso-4直後の鬱陵系)とそれぞれ命名した。

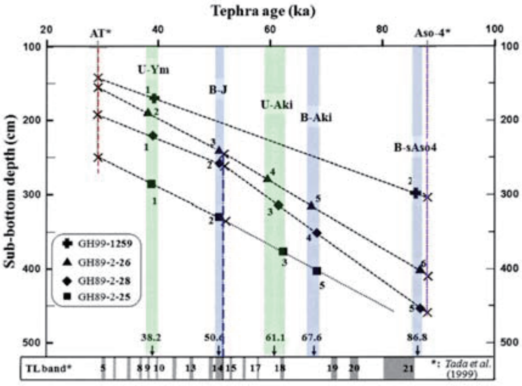

図６日本海東南海域の５コア中のテフラ対比

これらの検出層から抽出したコア間での各テフラ層の対比をおこなう事で、試料コア中の不明瞭な明暗色互層の年代も一部確定する事ができた。AT（姶良）テフラを 29.24 千年前、Aso-4 テフラを 88 千年前の噴出、TL(暗色層)-14 の底面の年代を 51.5 千年前として年代を補間すると、それぞれのテフラの年代は、U-Ym が 38.2 千年前、B-J が 50.6 千年前、61.1 千年前、67.6 千年前、86.8 千年前と計算された（図6)。抽出したテフラ粒中の微量元素の定量もほぼ終わっており、現在、給源火山の違いだけでなく、それぞれの給源火山の噴火毎での微量元素パターンの相違について解析中であり、これらの結論についても国際学術雑誌に投稿準備中である。

（３）日本海北東部での過去１５万年間の白頭山系テフラ層序の構築

さらに本法を用いて、北海道西岸の２つの日本海コア内の 2—15 万年前の層について同様に走査したところ､23 千年前の B-V(白頭山-ウラジオストック)、B-Jおよび前述のB-Aki とB-sAso4のテフラを含む6層のアルカリ岩質テフラ層が検出されており、これらは主成分元素分析の結果、すべて白頭山系テフラ層と判明した。ここで新たに検出された２つの白頭山系テフラの年代は､このコアの明暗色互層層序(池原、未発表データ）から補間して 104 千年前と 148 千年前と計算される。これらの層から抽出したテフラ粒中の微量元素の定量することで、さらに白頭山の詳しい噴火履歴やマグマ溜まりの化学組成の変化を再現できる可能性を示唆できればと考えている。

５．これらの成果に対する評価と今後の方針

以上の研究成果では、近年注目されているクリプトテフラの高感度な新検出法を示し、それが効率的な手法である事を日本海の堆積物で実証して、日本の第四紀後期のアルカリ岩質テフラ層序を確立しつつあることを示した。研究成果（１）は既に Geochimica et Cosmochimica Acta という一流の国際学術雑誌に掲載されており､研究成果（２）と（３）についても、抽出したテフラ粒中の微量元素含有量の解析が完了次第、それぞれ主要な国際学術雑誌に投稿するように準備中である。現在急務とされている最終氷期末の気候激変の日本近郊と世界各地との

時間的なずれ、及び気候激変の機構の解明や、最終氷期末の日本周辺の海流と海面の変化についての編年をおこなう上でも、本研究は重要な役割を果たす。この新手法を活用することで、世界の他の活動的縁辺部地帯におけるテフラ層序も飛躍的に精密になり、過去の地球環境変動の復元に寄与する事が期待される。

今後、さらに、本成果を押し進めて、過去３０万年間の西日本における高密度なテフラカタログ・微量元素データベースの作成を目的に、平成２１年度から「琵琶湖掘削コアの火山灰降灰層準中の火山ガラスの放射化分析」という題目で、本原子力機構施設の共同利用を申請して受理されたので、11 月から原子炉の運転が再開次第、測定を開始したい。2008 年に琵琶湖中央部にて掘削された 100m 級の湖底堆積物コアは、本報告書の日本海コアとは異なり、花粉分析や珪藻分析、有機化学分析等の多数の項目について同一の試料に関して高分解能に解析が行われており、情報量の多い試料である。平成２１年度より３年かけて、琵琶湖 100m 級コア試料についての連続的な放射化分析を行いたいと考えている。

謝辞

本書に記載された試料の放射化と中寿命核種のγ線測定はすべて原子力機構施設利用共同研究を活用させていただいたもので、施設関係者及び大学開放研の皆様に心より感謝申し上げる。また、本研究は独立行政法人産業技術総合研究所・地質情報研究部門・研究グループ長の池原研博士との共同研究という事で行われ、都立大学名誉教授の町田洋先生にもご教示いただいた。心よりお礼を申し上げる。さらに本研究では、文部科学省の科学研究費補助金（課題番号 17340148）基盤研究（B）により購入したオートサンプラー付きのγ線スペクトロメトリーが大活躍した。引き続き、残りの研究成果も一流の国際学術雑誌に掲載されるようにしたい。

５．成果の公表（2006-2008）

〔雑誌論文〕

① Lim C.，Ikehara K.，Toyoda K.，Cryptotephra detection using high-resolution trace-element analysis of Holocene marine sediments, southwest Japan. Geochimica et Cosmochimica Acta 72, 2008, 5022-5036.

〔学会発表〕

①任忠完、池原研、豊田和弘、日本海堆積物コアの中性子放射化分析による第四紀後期のアルカリ岩質テフラ層序の構築、日本地球化学会 2008 年会、2008 年 9 月 19 日、駒場（東京）

②Chungwan LIM、Kazuhiro TOYODA、 Ken IKEHARA、Cryptotephra detection by high-resolution trace-element profiles of hemipelagic sediments.. 京都大学原子炉実験所専門研究会、2008 年１月２３日、熊取（大阪）

③ UMETSU Akane, MACHIDA Hiroshi, Lim Chungwan, TOYODA Kazuhiro、Neutron activation analysis of volcanic glasses in alkaline tephra layers at Baitoushan volcano and Ulreung island, Korea、京都大学原子炉実験所専門研究会、2008 年１月２３日、熊取（大阪）

④Chungwan LIM、Kazuhiro TOYODA、Ken IKEHARA、Identification of multiple cryptotephra layers from Ulleung Island and Baitoushan volcanoes detected by INAA at deep-sea cores in the Japan Sea、日本第四紀学会 50 周年記念国際シンポジウム　2007 年 11 月 20 日、産総研（筑波）

⑤ UMETSU Akane, MACHIDA Hiroshi, Lim Chungwan, TOYODA Kazuhiro、Neutron activation analysis of volcanic glasses in alkaline tephra layers at Baitoushan volcano and

Ulreung island, Korea、日本第四紀学会 50 周年記念国際シンポジウム　2007 年 11 月 20 日、産総研（筑波）

⑥Toyoda K., Shinozuka Y, Lim C.,, Takemura K., Kitagawa H., Yasuda Y. 、GEOCHEMICAL DETECTION OF ALKALINE CRYPTOTEPHRA LAYERS: AN EXAMPLE OF LAST TERMINATION SEQUENCES IN JAPANESE LAKE SEDIMENTS 、The 12th International Conference on Modern Trends in Activation Analysis (MTAA12)、2007 年 9 月 17 日、首都大（東京）

⑦任忠完、池原研、豊田和弘、Geochemical detection of multiple cryptotephra layers from Ulleung Island and Baegdusan volcanoes detected by INAA at deep-sea cores in the Sea of Japan、地球惑星連合学会、2007 年 5 月 22 日、幕張メッセ（千葉）

⑧豊田和弘、篠塚良嗣、竹村恵二、北川浩之、安田喜憲、琵琶湖と水月湖の堆積物コア中から放射化分析で検出した複数の鬱陵島テフラ、日本地球化学会 2006 年会、2006 年 9 月 13 日、日大（東京）

⑨任忠完・豊田和弘・千鍾華・篠塚良嗣・池原研、放射化分析法を用いた日本海・海底コア中のクリプトテフラ検出法の検討、日本地球化学会 2006 年会、2006 年 9 月 13 日、日本大学（東京）

⑩豊田和弘、篠塚良嗣、竹村恵二、北川浩之、安田喜憲、琵琶湖と水月湖の堆積物コア中から放射化分析で検出した複数の鬱陵島テフラとその噴出年代、日本地球惑星科学連合大会、2006 年 5 月 15 日、幕張メッセ（千葉）

⑪任忠完、豊田和弘、Jong-Hwa Chun、篠塚良嗣、池原研，日本海南部コアから放射化分析により検出された複数の鬱陵島系起源のアルカリ岩質テフラ層、日本地球惑星科学連合大会、2006 年 5 月 15 日、幕張メッセ（千葉）

3-5

3-6

海水準変動堆積物の蛍光年代測定と放射化分析による年間線量

Luminescence dating of eustatic sediments and annual dose measurements by NAA

Yoshihiro Ganzawa

雁沢　好博*

Yoshihiro　Ganzawa*

＊北海道教育大学函館校

***Hakodate School, Hokkaido University of Education**

---

1. はじめに

火山石英の RTL（赤熱蛍光）研究は Hashimoto et al. (1989) や Miallier et al. (1991, 1994)によって開始された．RTL は地質年代測定に優れた基本的な性質を有しており，それらは捕獲電子の長い寿命，RTL ホールの安定性，2kGyを越える高い飽和線量，トラップ電子の異常消失の不存などであり，2ka から 1.2Ma に及ぶ広い時代の年代測定が可能とされている(Fattahi and Stokes, 2000, 2005)．一方，加熱によって火山石英から放出される RTL は，350-380°C の高温領域で 600-650nm の放出バンドを示すため，これを加熱装置から放出されるバックグラウンドシグナルと分離する作業は，試料 RTL 測定の要となっている．これを達成するため，フィルター組み合わせ，適切な PMT の利用，そして RTL 検出装置の改善などの技術改良も進められている(Hashimoto 2008; Yawata and Hashimoto,2007)．

また，年間線量を求めるために，一般には ICP マス等の方法が取られるが，我々は U および Th の正確な測定を行うために，原子力機構施設の JRR4 を利用した中性子放射化分析を進めている．しかし，残念ながら，施設故障のため申請 3 年間のうち，2 年半以上にわたって実験できない状況が続いている．したがって，放射化分析に関する内容を十分に反映できない報告になることを予め記しておきたい．

本論では Murray and Wintle (2000)が提唱した単アリコット再現法(SAR 法)を採用した．また，改良された RTL 装置を用いて一粒子による年代測定を試みた結果について報告する．用いた試料は，海水準変動堆積物に含まれる北海道に位置する洞爺カルデラから噴出した洞爺火砕流堆積物である．

2. 実験

2.1. 地質と試料採取地点

洞爺カルデラの噴火は更新統における東北日本の主要な激しい火山活動の一つで，噴出テフラ量は Tpfl 火砕流 20km^3と Tpfa 降下テフラ 150km^3で，合計 170km^3におよぶ（Machida and Arai,2003）(Fig. 1a,b)．洞爺カルデラの周辺（50x70 km^2の範囲）は，3ないし4層の厚い火砕流ユニットに覆われ，各ユニットは挟在する降下テフラやラグブレシアで区分することができる．我々の野外調査では，洞爺カルデラの南側，火砕流堆積物層序のタイプ地点，長流川流域において， Tpfl は連続的な 3 ユニットからなり，下位より Tpfl-A, Tpfl-B と Tpfl-C に区分される（Fig. 1c)．Tpflの層序学的研究によれば，次のようなマグマ活動が復元されている（Machda,1999）．最初の噴火(Tpfl-A)はマグマ貫入による激し

利用施設　JRR4　Tパイプ　　　　コバルト60ガンマ線照射施設（高崎）

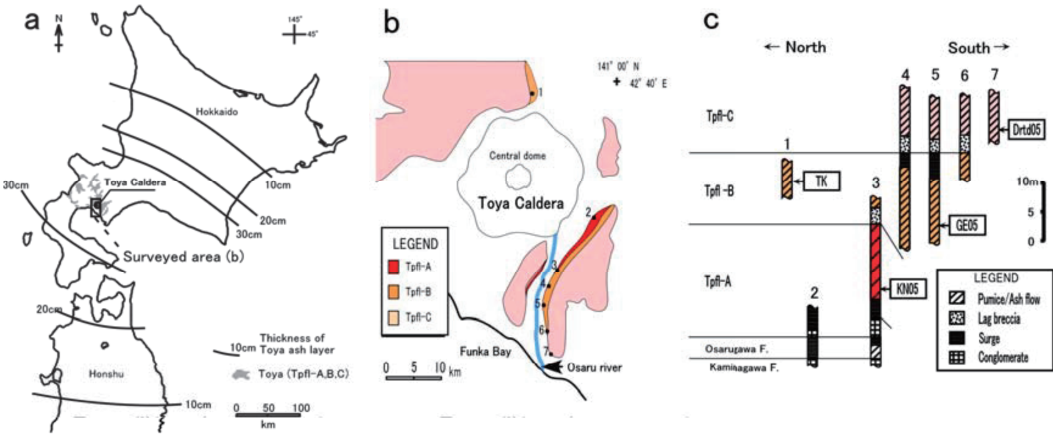

Fig.1 洞爺火砕流の分布と試料採取位置

い破砕と水蒸気爆発に始まり，第 2 ステージの火砕流である中規模な噴火(Tpfl-B)へ引き継がれた．最後ステージは広域な降下テフラ(Tpfa)を伴う軽石流からなるプリニアン噴火型の噴火(Tpfl-C)で終了した．

RTL 年代測定に用いた試料は 3 つの火砕流ユニットから採取され，それらは KN05, TK, GE05 および Drtd05 である．Fig.1b,c にサンプリング地点と採取層準を示した．

2.2. 試料準備

サンプリング試料から以下の手順で石英を分離した．露頭の深さ 40cm から採取された試料は，含水率測定後，水洗し，乾燥後，355-500μm サイズの粒子を分離するため篩い分けを行なった．次に分離粒子の化学処理を，6M NaOH, 6M HCl, 24%HF を用いて，各 2 時間，マグネティックスティーラーによる攪拌をおこなった．試料を乾燥後，ガラス除去のため試料を指で細砕し，篩いわけにより 355-500μm 粒子選別を行った．さらに，2 度目の 24%HF 処理を 2 時間行ない，石英粒子の純度を高めるとともに，粒子表面のエッチングを行なった．最後に，篩い分けを行ない，実験に用いる粒径（355-425μm）を分離した．以上の分離方法により，サンプリング試料，KN05, TK, GE05, Drtd05 から測定に必要な十分な量の石英粒子を得ることができた．

2.3. RTL 測定装置

実験に用いた装置は Ganzawa and Maeda (2009)で用いた装置で，光電子増倍管(PMT)に GaAsP/GaAs 光カソードと電子冷却システムを備えた H7421-40 を用いた．PMT のカソード放電感度(cathode radiant sensitivity)の中心は 580nm にあり，この波長は Kenko R60 と Kenko IRCL65L の 2 つのフィルター組み合わせから得られる透過波長 560-570nm とよく一致する．そのため，従来使用された PMT R649S と比較し，約 2 倍の RTL シグナルの検出に成功した．加熱速度は試料を確実に加熱させるため， 1°C/秒の遅い速度に設定した．また，サンプルホルダーと PMT の間にライトガイドが挿入され，RTL シグナルの透過能力を向上させている．また，ライトガイドはヒーターの熱から PMT を保護する役目を果たしている．

実験では，単粒子測定用の試料ホルダーを用意した．新ホルダーは直径 8mm の銀製で，センターに直径 1mm の試料保持孔があり，測定粒子を挿入できる．さらに，銀サンプルホルダーを覆う黒雲母シールドの使用により，バックグラウンドをさらに低減させた．

RTL 装置には小型 X 線照射装置が導入され，SAR 法測定が可能である．小型 X 線装置の前面には厚さ 120μm のアルミシートが挿入され，低エネルギーの X 線を除去した (Hashimoto et al, 2002)．その結果，50W, 0.1A で 6.1Gy/min の放射線強度を確保することができた.

2.4. SAR 法

Murray and Wintle (2000)により提唱され Fattahi and Stokes(2000)によって石英 RTL 法に初めて試みられた SAR 法を，石英単粒子 RTL 年代測定に採用した.

石英の天然 RTL 強度を測定後，再現 X 線照射を 49Gy あるいは 98Gy から 293Gy まで行いそれぞれの 100−450°C 間の RTL 測定後，テスト測定（テスト照射=49Gy）を行なった．プレヒート温度は 220°C，180 秒で行なった．測定の最後に Dose recovery test (195Gy) を行い，SAR 曲線の信頼性を Recycling ratio (SAR-De/195Gy)により検証した．石英単粒子の SAR 測定は試料 KN05，TK，GE05 and Drtd05 から抽出された 30 から 50 粒子について行なった.

2.5. NAA 分析

試料の年間線量を評価するために，NAA 法とICPマス法によりGanzawa et al.(2005) および Ganzawa and Maeda (2009)の手順に従って，U，Th and K20 濃度を決定した．この 2 つの手法の内，NAAは　UとThの分析感度に優れるので，原子力機構において正確な含有量決定のための試験を進め，最終的に次の測定方法を採用した．中性子照射は原子力機構施設 JRR-4原子炉，Tパイプ(最大出力: 3.5MW，最大中性子フルエンス: $7.0\mathrm{x}10^{13}\mathrm{n/cm^2s}$，Cd 比: 3.9)の A ポジションで 7 分間行った．照射試料は 140 時間冷却し，その後，共同利用大学開放研究室に設置されたAMS42のGeディテクターにより，^{239}Np では 228kev および 278kev，^{233}Paでは 312kevのγ線計測を試料に応じて 5000 から 10000 秒間おこなった．測定試料の重量は 1 試料あたり 80 から 100 mg で NAA 測定は 3 回行ない，その平均値を濃度計算に採用した.

標準岩石試料として産業技術機構から提供された 7 試料を用いたが，それら 2 つの核種の推奨濃度は，Th が 1.27 から 31.6ppm の範囲，U が 0.48 から 11.3ppm の範囲にある．γ線強度と推奨濃度から導かれるカリブレーション線を用いて，年代測定試料の U および Th 濃度が決定された．また，K_2O 濃度は ICP マスにより決定した.

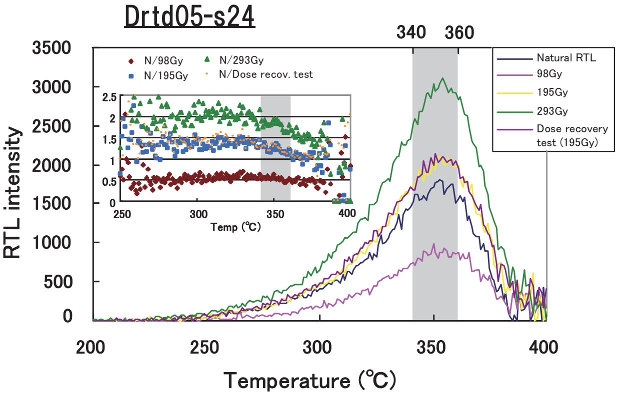

Fig2 石英単粒子の発光曲線

3. 実験結果と考察

3.1. 発光曲線とプラトーテスト

改善した測定装置を用いて行なった石英単粒子の SAR 測定の発光曲線の一例（試料コード：Drtd05-s24）を(Fig.2)に示す．天然 RTL 強度は350°C ピーク付近で約 1800 カウントを示し，再現線量 (Regenerative dose = 98Gy-293Gy)も十分に明瞭な発光カーブ示している．そこで，プラトー領域にある 340-360°C の 20°C 間の RTL 積算値を RTL 強度とした(Fig.2 挿入図)．また，テストドーズ測定においても同じ温度領域の RTL 積算値をテストドーズ RTL 強度とした.

3.2. 蓄積線量と年間線量

SAR 法による De 評価の一例（試料：Drtd05-s24）を Fig.3 に示した．SAR 補正前の線量応答線再現線量 98Gy−293Gy 間でよい直線性を示すが，感度変化率に基づいて，各 RTL 測定値の感度補正（照射 RTL 強度/線量復元 RTL 強度）を行なった．その結果，感度補正線量応答線の傾きはやや減少し，試料の De は感度補正前の 176Gy から 187Gy に増加した.

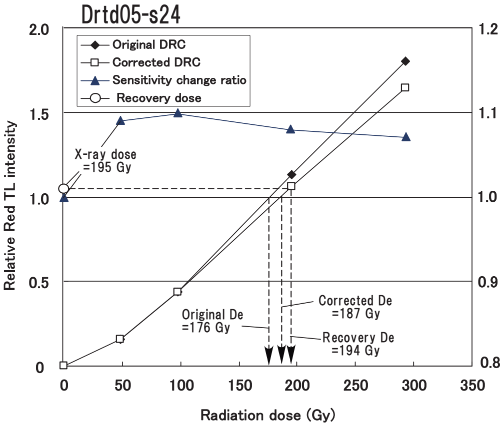

Fig.3 線量応答曲線と石英のSARによる感度変化

また，線量復元テストでは，既知照射量195Gyに対し，感度補正復元Deは194Gyを示し，線量復元率は0.99（＝194Gy/195Gy）のよい値を示した．この結果は，実験で用いた火山石英のDe決定にSAR法が適していることを示している．したがって，本実験ではすべての石英単粒子でSAR-De決定と線量復元テストにより線量応答線の信頼性を評価した．

標準岩石試料のU含有量とNAA分析から得られた^{239}Npのγ線強度の関係，またTh含有量と^{233}Paの関係をFig. 4a, bに示した．両者から導かれるカリブレーション線はともによい直線性（相関係数＝0.99）を示した．その結果，この実験例ではGE05のUとTh含有量として1.65ppm，5.78ppmが決定された．3回のNAA分析から示された各試料(KN05, GE05, TK, Drtd05) のU含有量は，平均値で2.2±0.1，1.5±0.2，1.6±0.1，1.7±0.1ppm，Thは4.6±0.1，4.9±0.2，4.9±0.1，5.8±0.2ppmであった．また，ICPマス分析によって決定した平均K20含有量は，2.17，2.06，1.98，1.50％であった．

これらの放射性核種に起因する石英粒子のβ線透過率は，Adamiec and Aitken (1998)の新コンバージョンファクターから，粒径が355-425μmであることを考慮して計算し，その結果，X=0.209，Y=0.303，Z=0.155 が得られた．試料の含水率は異なる3季節に採取した試料から見積もり，その平均含水率はKN05，GE05，TK，Drtd05 でそれぞれ 0.15，0.14，0.15，0.17であった．宇宙線量評価のために，Prescott and Stephan (1982) および Prescott and Hutton (1994)が示した，北緯40° で海水準0mの値である0.185mGya^{-1}を参考にした．この値をサンプリング地点の高度と深度から査定した結果，宇宙線量はわずか0から0.07 mGya^{-1}であることが示された．

以上の放射性元素濃度，β線透過率および含水率から導かれる年間線量と宇宙線量（0から0.07 mGya^{-1}）の合計から得られるDa（KN05=1.99，GE05=1.91，TK=1.95，Drtd05＝1.63 mGya^{-1}）をTable 1に示した．

3.3. 石英単粒子RTL年代

最初期火砕流Tpfl-A(KN05)の44粒子のSAR年代の測定結果は，測定誤差が2σ内に分布する34粒子と大きくはずれる10粒子が存在した．10粒子を除外した34粒子のSAR年代は90-122kaの範囲を示す．RTL測定計数誤差

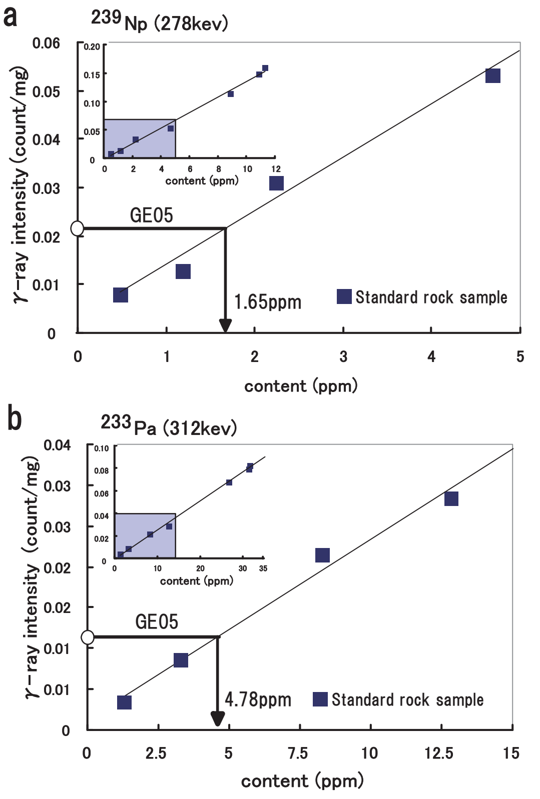

Fig.4 標準岩石試料を用いたNAAによるUおよびTh測定

Table 1　洞爺火砕流石英単粒子によるSAR年代

Flow unit	Sample code	Grain number	U(ppm)	Th(ppm)	K2O(%)	Water content	Cosmic dose (mGy/a)	Da (mGy/a)	Original ave.De (Gy)	Corrected ave.De (Gy)	Corrected ave. age (ka)	Single grain Age range (ka)	Recycling. ratio Ave. (Range)	χ^2 test (%)	Others
Tpfl A	KN05	33	2.2 ± 0.1	4.6 ± 0.1	2.17	0.15	0	2.01	196	210	105 ± 8	90-122	1.01 (0.92-1.10)	46.8	
		10										238-761			Detritus
Tpfl B	GE05	30	1.5 ± 0.2	4.9 ± 0.2	2.06	0.14	0.01	1.85	189	199	114 ± 21	86-133	1.00 (0.88-1.20)	45.8	
Tpfl B	TK	50	1.6 ± 0.1	4.9 ± 0.1	2.30	0.15	0.02	2.01	229	238	118 ± 15	93-149	0.96 (0.74-1.08)	47.3	
Tpfl C	Drtd05	44	1.7 ± 0.1	5.8 ± 0.2	1.50	0.17	0.07	1.61	156	168	104 ± 15	70-156	1.15 (0.63-1.21)	47.1	

および年間線量誤差を考慮した平均年代は106±8ka となった(Table 1). Tpfl-B 火砕流 GE05 および TK の単粒子年代はそれぞれ, 83-129ka, 83-134ka の分布を示し, 誤差を考慮した平均年代は 104±21ka, 114±15ka である. Tpfl-C 火砕流 Drtd05 の単粒子年代は, 73-140ka のやや広い範囲にあり, 平均年代は 103±15ka である.

以上の火砕流 3 ユニットの石英単粒子 RTL 年代は, 103±15ka から 114±15ka の範囲にあり, 火砕流が連続的で短期間に噴火したことを示している. これらの年代は地質学推定年代とよく一致した. この結果は, 本論で進めた単粒子石英による RTL-SAR 法は火砕流堆積物の年代測定に有効に機能し, 中期更新世の年代測定にも優れていることが示している.

文献

Adamiec, G., Aitken, M.J., 1998. Dose -rate conversion factors: update. Ancient TL 16, 37-50.

Fattahi, M., Stokes, S., 2000. Extending the time range of luminescence dating using TL (RTL) from volcanic quartz. Radiat. Meas. 32, 479-485..

Fattahi, M., Stokes, S., 2005. Dating unheated quartz using a single aliquot regeneration-dose red thermoluminescence protocol (SAR RTL). Journal of Luminescence 115, 19-31.

Ganzawa, Y., Furukawa, H., Hashimoto, T., Sanzelle, S., Miallier, D., Pilleyre T., 2005. Single grains dating of volcanic quartz from pyroclastic flows using Red TL. Radiat. Meas. 39, 479-487.

Ganzawa, Y., Maeda, M., 2009. 390-410°C isothermal red thermoluminescence (IRTL) dating of volcanic using the SAR method. Radiat. Meas. 43, 1-6.

Hashimoto, T., Habuki, H., Tanabe, I., Sakai, T., Takahashi, S., 1989. Dating using red thermoluminescence from quartz grains in strata related to fossil bones of Elephas Naumanni. Chikyukagaku (Geochemistry) 23, 35-43 (in Japanese).

Hashimoto, T., Nakagawa, T., Hong, D.G., Takano, M., 2002. An automated system for both red/blue thermoluminescence and optically stimulated luminescence measurements. J. Nucl. Sci. Technol. 39, 108-109.

Hashimoto, T., 2008. An overview of red-thermoluminescence (RTL) studies on heated quartz RTL application to dosimeter and dating. Geochronometria, 30, 9-16.

Machida, H., 1999. The stratigraphy, chronology and distribution of distal maker-tephras in and around Japan. Global and Planetary Change. 21, 71-94.

Machida, H., Arai, F., 2003. Atlas of Tephra in and Around Japan. University of Tokyo Press, Tokyo. (in Japanese)

Miallier, D., Fain, J., Montret, M., Pilleyre, T., Sanzelle, S., Soumana S., 1991. Properties of the red TL peak of quartz relevant to thermoluminescence dating. Nucl. Tracks Radiat. Meas. 18(1/2), 89-94.

Miallier, D., Fain, J., Montret, M., Pilleyre, T., Sanzelle, S., Soumana, S., 1994. Sun bleaching of the red TL of quartz: preliminary observations. Ancient TL. 12, 1-4.

Murray, A.S., Wintle, A.G., 2000. Luminescence dating of quartz using an improved single-aliquot regenerative-dose protocol. Radiat. Meas. 32, 57-73.

Stokes, S., Fattahi, M., 2003. Red emission luminescence from quartz and feldspar for dating applications: an overview. Radiat. Meas. 37, 383-395.

Prescott, J.R., Stephan, L.G., 1982. The contribution of cosmic radiation to the environmental dose for thermoluminescence dating. PACT 6, 17-25.

Prescott, J.R., Hutton, J.T., 1994. Cosmic ray contributions to dose rates for luminescence and ESR dating: large depths and long-term time variations. Radiat. Meas. 23, 497-500.

Yawata, T., Hashimoto, T., 2007. Development of a red TL detection system for single grain quartz. Radiat. Meas. 42, 1460-1468.

成果の公表

〈学会発表〉

1)十和田八戸火砕流堆積物（To-H）の石英単粒子による SAR-RTL 年代測定. 鴈澤好博, 栗田寛子, 細畑有未, 2007 年度日本地質学会 111 年次総会, 2007.9.札幌

2)火山石英単粒子の Red TL－SAR 年代測定. 鴈澤好博, 池麻由美, 2007 年度ルミネセンス年代測定研究会, 2008. 3. 奈良女子大学.

3)SAR 法による Red TL－390℃ITL 年代測定. 前田真, 鴈澤好博, 2007 年度ルミネセンス年代測定研究会, 2008. 3. 奈良女子大学.

4)バイカル湖細粒堆積物のルミネッセンス年代測定. 伊藤一充, 長谷部徳子, 鴈澤好博, 柏谷健二, 2007 年度ルミネセンス年代測定研究会, 2008. 3. 奈良女子大学.

5)Red-ITL dating of volcanic quartz grains using over 390℃ signals. 12th international conference on luminescence and electron spin resonance dating. 2008. 9. 18. Peking University. Chania.

6)Dating the activity of Toya caldera, Japan, using single grains by means of red thermoluminescence (SAR) dating. 5th Japan-Korea-China international workshop on present earth surface process and historical environmental changes in East Asia. 2008. 10. 8. Hakodate.

7)SAR Red-TL daring of late Pleistocene Toya volcano, Japan, Using single quartz grains. 2nd Asia Pacific Conference on luminescence and ESR dating. 2009. 11. 12-15. Ahmedabad. India.

〈公表論文〉

1)SAR 法による洞爺火砕流堆積物の赤色熱ルミネセンス年代測定. 鴈澤好博, 臼井理沙, 田中瞳, 東剛, 地質学雑誌, 113, 470-478 (2007)

2) LA-ICP-MS analysis of pressed powder pellets to luminescence geochronology. K. Ito, N. Hasebe, R. Sumita, S. Arai, M. Yamamoto, K. Kashiwaya, Y. Ganzawa, Chemical Geology, Volume 262, Issue 3, Pages 131-137 (2009)

3) Single-grain two-fragment method for dating terrace deposits using red thermoluminescence from quartz. Y. Ganzawa, T. Azuma, Ancient TL. Volume 27, No.1 1-8 (2009)

4) 390-410 ℃ isothermal red thermoluminescence (IRTL) dating of volcanic quartz using SAR method. Y. Ganzawa, M. Maeda, Radiation Measurements. Volume 44, 517-522 (2009)

3-7

「瀬戸内火山岩類中のヒ素，アンチモン含有量」

Arsenic and antimony contents in the Setouchi Volcanic Rocks

東京経済大学・経営学部・新正裕尚

Hironao Shinjoe (Faculty of Business Administration, Tokyo Keizai University)

（１） 研究の目的と意義

島弧火山岩のマグマ成因を考える上で，沈み込むスラブに由来する成分の評価は極めて重要である．また，そのスラブ由来成分をマントルウェッジにもたらす媒体は，水を中心とする流体相であるのか，ケイ酸塩メルトであるのかも重要な問題の一つである．沈み込むスラブの温度構造により，両者のいずれが主体となるかが決まり，島弧により，さらに島弧の中でも異なるものと見られる．

一般に，海嶺沈み込みの見られるような，高温の海洋プレート沈み込みがおこった場所においては，スラブ由来成分が，主にケイ酸塩メルトとして、マントルウェッジに添加されるものとされる．すなわち，沈み込むスラブが融解して発生したメルトが上位のマントルウェッジを汚染する．

このようなスラブ由来成分の評価は，いわゆる液相濃集元素（incompatible element）の含有量や種々の同位体組成（Sr，Nd，Pb 等）の分析に基づいて行われることが多い．これらの元素濃度は，結晶分化作用等，浅所でのマグマ進化プロセスでも変化する．また，島弧マグマの場合，厚い地殻を通過する際の，地殻物質の同化や混染も評価の妨げになる．そこで，記載岩石学的になるべく未分化な岩石と判断されるものを試料として用いることが望ましい．また，元素種により流体相や，ケイ酸塩メルトの中での挙動が異なるので，様々な元素種，あるいは同位体種の分析により得られる情報を総合的に検討することが望ましい．

上記のような，島弧マグマへのスラブ由来成分の貢献の評価を行う対象の一例として，今回は西南日本弧で中新世中期に活動した瀬戸内火山岩の高 Mg 安山岩および玄武岩中のヒ素，アンチモン含有量の中性子放射化分析の結果を報告する．その意義としては，以下に掲げるようなものがある．

a) 瀬戸内火山岩は日本海形成に伴う，西南日本弧の時計回り回転直後の，高温の四国海盆スラブの沈み込みのもとで活動したものである．

b) 瀬戸内火山岩のなかで，玄武岩および，高 Mg 安山岩マグマは記載岩石学的特徴から，マントルウェッジかんらん岩と平衡に存在し得た，初生的マグマである．

c) 瀬戸内火山岩類の玄武岩および，高 Mg 安山岩については，スラブ融解メルトとマントルウェッジの反応によるマグマ成因が提案され，多種の液相濃集元素や同位体種を取り入れた，そのマグマ成因論に沿ったモデルが検討されている．しかしこれまで，親銅元素であるヒ素やアンチモンについての分析の報告は無い．これらの元素は，沈み込むスラブ上の堆積物や熱水変質を受けた玄武岩には豊富に含まれ，スラブ由来成分の評価には，重要な元素種の一つであると考えられる．比較可能な種々の地球化学的データの蓄積されている，瀬戸内火山岩類の玄武岩および，高 Mg 安山岩についての分析を行なうことで，親銅元素を含めて，スラブ由来成分を総合的に検討することができるかもしれない．

d) ヒ素やアンチモンは非破壊の中性子放射化分析により，他の手法より，比較的精度よく定量することができる．

なお，本研究に用いた試料については後述するように，ヒ素，アンチモンのみならず種々の微量元素濃度の分析も併せて行っている．野外調査や試料の入手および，中性子放射化分析以外の分析については，産業技術総合研究所の角井朝昭氏および，東京大学地震研究所の折橋裕二氏との共同研究として行われたものである．また後述の蛍光Ｘ線分析および，ICP-MS 分析は東京大学地震研究所の共同利用プログラムの援助を受けて行ったものである．

（２） 研究方法

試料は，九州～紀伊半島西部の瀬戸内火山岩分布域の各地から，高 Mg 安山岩および，玄武岩を収集した．列挙すると，大分県の大野火山岩類，愛媛県の高縄半島周辺，香川県の讃岐平野および小豆島，大

阪地域である．粗割した岩石片を洗浄後，メノウ自動乳鉢で細粉化したものを分析に供した．瀬戸内火山岩類は古典的には，東は愛知県の設楽地域から，西は九州東部の大野火山岩類までの分布域を持つとされる．しかし，瀬戸内火山岩類を特徴づける，高 Mg 安山岩が出現するのは，今回分析した試料を調達した九州～紀伊半島西部の範囲に限られる

図１：瀬戸内火山岩類を含む，中期中新世の西南日本弧の海溝寄り火成岩の分布

中性子放射化分析を行なった試料については，合わせて，蛍光 X 線分析により，主成分と一部の微量元素組成を定量し，さらに ICP-MS を用いて，希土類元素を含む多くの微量元素組成を定量した．また，本報告では取り扱わないが，JRR-3 原子炉に敷設の熱中性子ビームラインでの即発ガンマ線分析により，ホウ素含有量の定量も併せて行っている．

ヒ素，アンチモンの定量は日本原子力研究開発機構東海研究開発センターの JRR-4 原子炉を用いた中性子放射化分析で行った．なお，これらの元素をより精度よく定量するために，試料をカドミウム板で包むことにより，主に熱外中性子の照射による放射化を行った．

粉末試料はポリエチレン袋に２重に融封した後，10 試料あまりをとりまとめて，カドミウム板で全体を覆った．さらにそれを厚手のポリエチレン袋内に融封したものを，照射用の試料とした．照射は，JRR-4 原子炉の低出力（350 kW）運転時に，T または S パイプにおいて，20 分間行った．その後 3 日間冷却し，大学開放研究室のガンマ線スペクトロメーター(ASC-20)でガンマ線計測を行った．定量は，産業技術総合研究所，地質調査総合センターの地球化学（岩石）標準試料である JA-3 を標準として対比法で行った

（３） 結果と議論

高 Mg 安山岩については，ヒ素の含有量は，1.2～9.2 ppm，アンチモンの含有量は，0.2～1.2 ppm であった．玄武岩については，ヒ素の含有量は 1.2～2.7 ppm，アンチモンの含有量は 0.2～0.4 ppm であった．分析結果の例を表１に掲げる．先に述べたように，試料は島弧伸長（東西）方向に数地域から収集したものであるが，ヒ素，アンチモン含有量について，東西方向の変化傾向は見られなかった．

マグマ噴出前の結晶分別や，マントルでのマグマ分離時の部分融解度の効果をキャンセルするために，相互にマントル鉱物に対する液相濃集度の類似した元素の比を取ることがある．ヒ素やアンチモンの液相濃集度については，資料が乏しいが Ce と比較的液相濃集度が近いとする Noll et al. (1996)に従い，As/Ce，Sb/Ce 比について検討する．

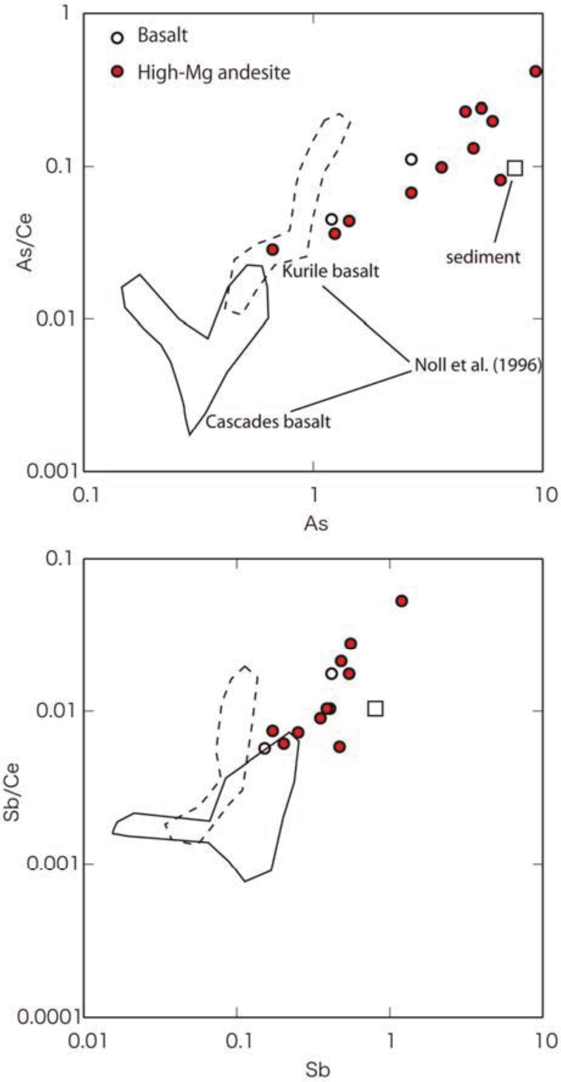

図２:瀬戸内火山岩類の As/Ce 比対 As 含有量および，Sb/Ce 比対 Sb 含有量．比較のために千島弧，カスケード弧の玄武岩の組成範囲（Noll et al.， 1996）を示した．

図２に示したように，As/Ce 比，Sb/Ce 比は広範囲にばらつき，堆積物のマグマソースへの寄与を示唆するトレンドを形成する．

As/Ce 比,Sb/Ce 比についても試料の地域による分散が大きく，東西変化傾向は見られなかった．ただし，同地域で見ると，As/Ce 比，Sb/Ce 比とも，玄武岩よりは高 Mg 安山岩の方が高かった（表１）．一般にこれまで多くの微量元素，同位体組成に基づく議論からは，高 Mg 安山岩について，より，スラブ由来成分の添加の度合いが大きいと判断されることと整合的である．

(Shodo-shima)	As	Sb
SNK92 (basalt)	2.67	0.41
SNK94 (HMA)	4.54	0.55
(Osaka)	As	Sb
SB (basalt)	1.19	0.15
NB (HMA) 9.17	1.17	

表１：小豆島および大阪地域の，玄武岩および高 Mg 安山岩のヒ素，アンチモン含有量（ppm）

また，全般に千島弧，カスケード弧の玄武岩と比較して，As/Ce 比，Sb/Ce 比も，ヒ素，アンチモンの含有量自体も高い試料が多い．

また、図２には，沈み込む堆積物の組成を日本の付加体堆積物（Togashi et al., 2000）や南海トラフの陸源堆積物および四国海盆の遠洋性堆積物（Shimoda et al., 2003）のデータに基づいて推定したものも示した．一部の試料は，堆積物自体より As/Ce 比,Sb/Ce 比が高く、マグマソースへの添加は，メルトまたは流体を媒体にしていることを明確に示している．

（４） 今後の研究方針

2009 年度より「中性子放射化分析による火成岩，堆積岩中の親銅元素の定量」という課題で，ヒ素，アンチモン等の分析をさらに継続して試みようとしている．その中では，以下の２点について留意して研究を進めたい．

a) 標準試料の選定：これまで，未知試料と同時に，様々な標準試料を照射し分析を行なった．先に記したように，今回は産業技術総合研究所，地質調査総合センターの地球化学標準試料 JA-3（安山岩）を標準として対比法で行った分析結果を報告した．それ以外に，同じく産業技術総合研究所の地球化学標準試料の JR-2（流紋岩）や CRM7302a（海底質：産業技術総合研究所，計量標準総合センターの環境分析用組成標準物質），SRM1633b（Coal fly ash: NIST 標準試料）も併せて照射，分析を行った．いくつかの測定回において，JA-3 を標準として求めた分析値と，SRM1633b を標準として求めた分析値を比較した場合,特にヒ素について最大 17%程度の差異が見られた．今のところその原因は不明であり，今後も複数の標準試料を照射しクロスで分析値を検討し，適切な標準試料の選別を行う必要がある．

b) より広い種類の分析試料への適用：これまで記した通り，現在までは瀬戸内火山岩類，特に高 Mg 安山岩および玄武岩を中心に分析を行なってきた．将来的には，より広い試料種について分析を進めたい．火山岩試料としては，西南日本の中新世火山岩と同様に，高温のスラブ沈み込みが見られる地域の島弧火山岩に加えて，比較的低温のスラブが沈み込む地域の島弧火山岩について適応することを計画している．また，これら島弧の火山岩におけるスラブ由来成分として重要であると考えられる，堆積岩類についても適切な試料を収集し分析を行いたいと考えている．特に，今回報告した瀬戸内火山岩類のマグマソースに関連するものとしては，西南日本の付加体堆積物などが重要な対象物であると考えている．さらに，ヒ素や，アンチモンは流体による移動、特に火山弧より浅所の、高圧型変成作用の領域での移動も知られ，変成岩岩石学の立場から議論されている（たとえば Bebout, 1999）．そこで，三波川変成岩などの高圧変成帯の堆積岩由来の結晶片岩も分析対象として，検討してゆきたい．

（５） 成果の公表

【学会発表】

新正 裕尚・折橋 裕二・角井 朝昭・福岡 孝昭・長谷中 利昭・佐野 貴司（2008）瀬戸内火山岩類のホウ素含有量．日本地球惑星科学連合 2008 年大会（幕張メッセ）

3-8

河川・汽水域および海洋底堆積物の放射化分析

Activation analysis of river, estuarine and marine sediments

松尾基之・久野章仁・小豆川勝見・長谷川篤[1]・諸町大地
高橋麻子・山ノ井俊[2]・星野真有美[3]・山野孝嶺[3]・原直樹・藤井政光[3]

東京大学大学院総合文化研究科広域科学専攻
[1] 東京海洋大学大学院海洋科学技術研究科海洋保全学専攻
[2] 東京大学大学院理学系研究科化学専攻
[3] 東京大学教養学部広域科学科

１．はじめに

近年、河口域や干潟の環境保全は人々の重大な関心事となっているが、これらの場所は、淡水と海水が混ざり合う複雑な系であり、そこにおける化学的環境や元素の挙動については、まだ詳しくは理解されていない。放射化分析法は、多元素同時定量分析が可能なため、多くの元素の分布を総合的に判断するのに最適な分析法と言える。我々はこれまで ^{57}Fe メスバウアー分光法を用い、鉄の化学状態を指標として河川底質の化学的環境、特に酸化還元状態を推定してきた。これに対し、従来多くの研究により、試料中の微量元素の分布が化学的環境を反映することも知られている。本研究では、メスバウアー分光法により得られた鉄の化学状態と、出来るだけ多くの微量元素の分布との関連を調べ、比較検討するために多元素同時分析が可能な放射化分析を行った。このような観点から、次に掲げる試料について種々の環境化学的、地球化学的な検討を行ったので、それぞれの試料ごとに研究内容およびその結果を報告する。

２．干潟底質の元素分布に及ぼす周辺部埋立ての影響に関する研究

【序】環境意識が高まり、干潟の埋立て中止や保全・再生の動きが活発化している。一方で、諫早湾干拓事業が断行され、有明海の漁民らが漁業被害を訴えているが、福岡高裁は科学的な証明がないとして訴えを退け、佐賀地裁は水門常時開放と調査を国に命じている。このように、干拓や埋立てが周辺に及ぼす影響は未解明であり、これらを明らかにすることが社会的にも科学的にも求められている。本研究では、埋立ての影響が極端に大きかったと考えられる千葉県谷津干潟と、そのすぐそばにありながら比較的影響が小さいと考えられる三番瀬猫実川河口付近を対象として、当研究室で河口域底質や干潟底質に用いられてきた分析手法および統計的手法を用いて、埋立てが周辺に与えた影響を調査した。また、干潟底質中では硫酸還元菌の活動により硫化水素が発生し、底質中の鉄イオンと反応し硫化鉄や pyrite(FeS_2) を生成することから、メスバウアー分光法により鉄の化学状態を測定した。

【実験】谷津干潟は、元は東京湾奥に広がる広大な前浜干潟の一部であったが、埋立てにより四方が陸地となった長方形の干潟で、東京湾とは２本の細い水路によってつながっている。埋立て後、さらに高架橋によって大小２つのエリアに分断されたことから、それぞれのエリアで底質試料を柱状に約 50 ㎝採取した。得られた試料を３㎝ごとに切り分け、空気による酸化に注意しながら、窒素加圧濾過により間隙水と湿試料に分離し、湿試料の一部を凍結乾燥により乾燥試料とした。こ

研究施設と装置名	研究分野
JRR-4、JRR-3M、気送管、γ線ｽﾍﾟｸﾄﾛﾒｰﾀｰ	環境化学、地球化学、放射化分析

れらの操作の前後の重量変化から含水率を求め、湿試料を用いてメスバウアー分光法により Fe の状態分析を行い、乾燥試料を用いて機器中性子放射化分析(INAA)および中性子誘起即発γ線分析(PGA)により元素の垂直分布を求めた。

【結果及び考察】谷津干潟両地点において周辺埋立ての影響と考えられる大きな変化が各測定の結果に現れていた。一方、三番瀬試料については谷津干潟のような目立った変化は見られなかった。得られた測定結果のうち、INAA と PGA による元素垂直分布のデータに対して主成分分析を行った。主成分分析では、分散共分散行列を用いる方法と相関行列を用いる方法の二手法が存在する。前者はデータの値をそのまま反映させるのに対し、後者はデータを分散 1，平均 0 に標準化した値を用いる。本研究ではまず、両手法の比較を行った。その結果、前者を用いるとばらつきの大きさが影響し、微量元素のデータがほとんど考慮されない結果となった。一方、後者を用いると第２主成分以降がノイズとしてしか解釈できない結果となった。そこで、元素垂直分布のデータを各元素の平均濃度で割り、平均を１に規格化した上で分散共分散行列を用いて主成分分析を行った。図１に、谷津干潟の小さいエリアにおける試料に対する上記３手法による主成分分析の結果を示す。この地点では、周辺埋立ての影響が約 40 ㎝, 分断の影響が 25 ㎝の深さに現れていた。本手法を用いた場合のみ、第一主成分得点も第二主成分得点も埋立てや分断の影響を反映していると思われる値を示し、固有ベクトルの値が平均濃度と相関せずに微量元素が主要元素と同様に扱われていることがわかった。

次に、メスバウアー分光法により得られた pyrite(FeS_2)の垂直分布を図２に示す。これらの結果と含水率や有機物量など他の測定結果との比較から、第一主成分は堆積時の水の流れの弱さを示す指標、第二主成分は堆積後の海水とのインタラクションの強さをあらわす指標となると考えられる。すなわち、埋立てにより海水の流れが弱まり還元的環境となった後、高架橋による分断により狭い水路のような状態になったため、単位面積あたりの流量が増え、海水とのインタラクションが強まり、溶存酸素量が増加して還元度合が弱まったものと考えられる。

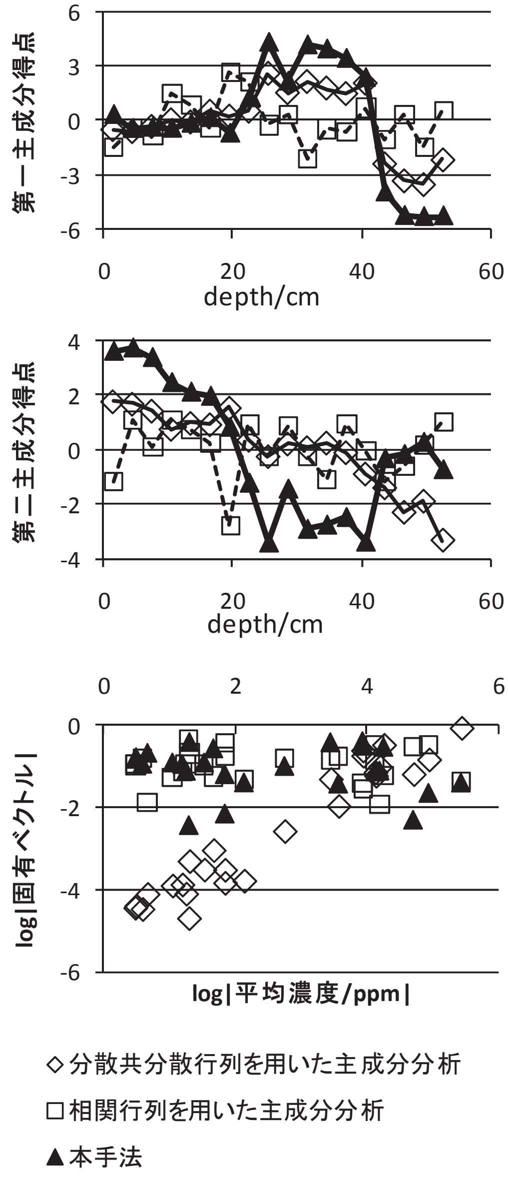

図１．３手法による主成分分析の結果比較
上段：第一主成分得点　中段：第二主成分得点
下段：各元素の第一主成分の固有ベクトルと平均濃度の関係

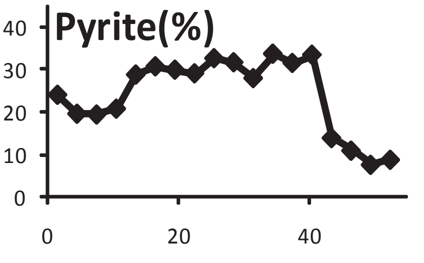

図２．　谷津干潟底質の pyrite の垂直分布

３．東京湾感潮域底質における酸化還元電位と元素の挙動

【序】東京湾では近年水質が改善したと言われているが、青潮の発生により漁業への影響が報告される等、今日でも未解決の問題を抱えている。2008 年 7 月には環境省や各沿岸自治体(46 機関・団体)による水質環境調査が東京湾内 568 カ所で行われ、夏期における東京湾の鉛直方向の溶存酸素量の分布や貧酸素水塊の実態を明らかにしている。しかし、この調査では溶存酸素量・水温・塩分濃度などの水質環境に関する調査結果のみが報告されている現状であり、底質に関するデータは不十分である。特に河口域(感潮域)は、生物の生産性は高いが汚染されやすいという特徴を持っており、近年環境評価の重要性が高まっているが、物質収支等のメカニズムは非常に複雑であり、要素毎の影響を評価することは容易ではない。よって本研究では、東京湾の流入河川である多摩川の河口域について、底質中の元素の定量値に統計的処理を用いることで、元素の挙動の特徴を見出すことを研究の目的とした。

【実験】河口域底質はコアサンプラーで鉛直方向に採取したものを深さ方向に３㎝ごとにカットし、加圧ろ過を行った後、フリーズドライした。得られた乾燥試料について、機器中性子放射化分析と即発γ線分析を用いて多元素の定量分析を行った。定量値はデータの類似度をユークリッド距離の大小で表すクラスター分析と多次元尺度構成法による統計的手法を用いて解析し、深度別、元素別に分類を行い、酸化還元電位等との相関について考察を行った。

【結果と考察】図３に、多摩川河口干潟底質の酸化還元電位(ORP)の鉛直変化を示す。20 ㎝以深の試料では ORP は負の値を取っていた。この酸化還元電位の正負を、元素分析値より得られたクラスター分析等の結果と組み合わせて考えると、ORP が正の試料と負の試料で、ユークリッド距離が大きくなるという傾向が見られた(図４)。また、元素別の比較では、ORP 変化による影響を受けやすいと言われる Fe と S のユークリッド距離が近いという傾向が見られた。河川感潮域においては底質中で還元的環境が生じ、硫酸還元が起こることで、pyrite(FeS_2)が生成することが知られている。よって本研究において Fe と S のユークリッド距離が近い、つまり底質中での挙動が似通っていたということは、硫酸還元の影響を評価する上で意義がある結果だと考えられる。また、還元的環境下では溶出することが知られている Mn は、深層の試料では表層の試料に比べ減少が見られ、他の元素とのユークリッド距離が大きくなっていた。これらから、底質中の元素濃度の鉛直分布が、ORP 変化によって大きな影響を受けていることが示唆された。また、Cr や Zn 等の人為起源が疑われる元素については、特定の深さの試料で顕著に増加が見られ、その他の元素との有意差が見られた。これらの結果から、多元素の定量値に対し、クラスター分析や多次元尺度構成法等の統計的手法を適用することで、河口域底質について特徴的な元素の挙動を分類できることが示唆された。

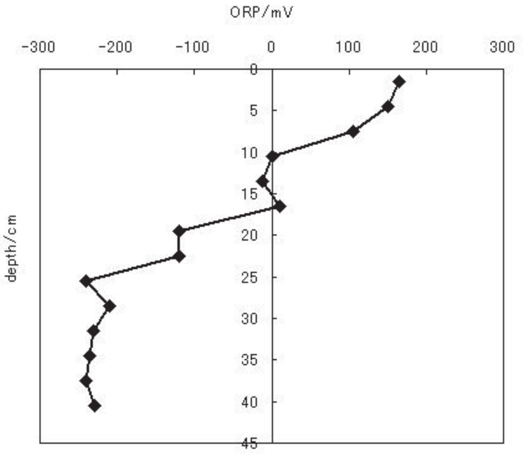

図３．多摩川河口干潟底質の酸化還元電位

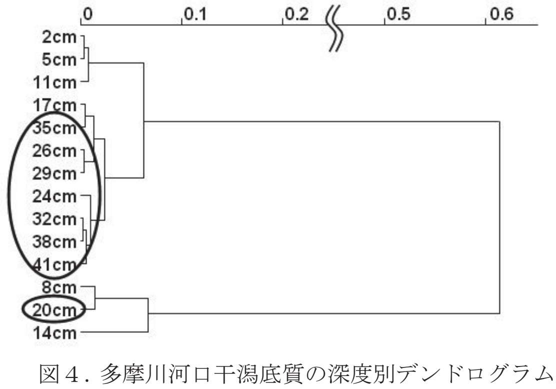

図４．多摩川河口干潟底質の深度別デンドログラム
(ORP が負の試料を丸で囲んで示した)

3-8

４．成果の公表

学術誌、紀要等

1. Estimation of the sources of pelagic sediments from the South Pacific Ocean to the Antarctic Ocean, K. Shozugawa, A. Kuno, Y. Sano and M. Matsuo, J. Radioanal. Nucl. Chem., Articles, 278, 331-335 (2008)
2. Influence of reclamation on the concentrations and chemical states of elements in tideland sediment, D. Moromachi, A. Kuno and M. Matsuo, J. Radioanal. Nucl. Chem., Articles, 278, 495-498 (2008)
3. Elemental analysis of airborne fine particles collected at roadside of an arterial road, M. Hirabayashi, M. Matsuo, S. Hasegawa, S. Kobayashi and K. Tanabe, J. Radioanal. Nucl. Chem., Articles, 278, 479-483 (2008)
4. 南太平洋における遠洋性堆積物をプローブとした堆積当時の気候変動の検討、小豆川勝見・金井豊・佐野有司・松尾基之、「放射化分析法利用に関する国際化」専門研究会報告書、京都大学原子炉実験所、58-69 (2008)
5. Elemental analysis and acid neutralization capacity of soil at the area where the acid rain damage is observed, A. Takahashi, A. Kuno and M. Matsuo, 「放射化分析法利用に関する国際化」専門研究会報告書、京都大学原子炉実験所、70-78 (2008)
6. 谷津干潟及び芝浦運河の底質中における水質浄化作用の解析、長谷川篤・田中美穂・久野章仁・松尾基之, 分析化学, 58, 87-94 (2009)
7. 谷津干潟堆積物中の浄化機能における間隙水の役割に関する研究、長谷川篤・田中美穂・隈倉真・久野章仁・松尾基之, 分析化学, 58, 327-332 (2009)
8. ^{57}Fe Mössbauer study of specific iron species in the Antarctic Ocean sediments, K. Shozugawa, A. Kuno, H. Miura and M. Matsuo, J. Nucl. Radiochem. Sci., 10, 13-17 (2009)
9. 東京湾感潮域底質における酸化還元電位と元素の挙動に関する研究、原直樹・小豆川勝見・松尾基之、「京大原子炉の再開と放射化分析」専門研究会報告書、京都大学原子炉実験所、53-59 (2009)

学位論文

10. 底質の化学分析から見た東京湾周辺の親水環境の評価、星野真有美、東京大学教養学部広域科学科 卒業論文Ⅰ (2006年11月)
11. 酸性雨による土壌の酸中和能の鉛直変化、山野孝嶺、東京大学教養学部広域科学科 卒業論文Ⅰ (2006年11月)
12. 多摩川とその支流における河川環境の評価～人為起源物質の影響を探る～、原直樹、東京大学教養学部広域科学科 卒業論文Ⅰ (2007年11月)
13. 雪氷中の粒子状物質の元素分析による大気汚染物質の挙動に関する研究、藤井政光、東京大学教養学部広域科学科 卒業論文Ⅰ (2008年11月)
14. 干潟底質の元素分布に及ぼす周辺部埋立ての影響に関する研究、諸町大地、東京大学大学院総合文化研究科広域科学専攻 修士論文 (2009年1月)
15. 酸性雨被害が見られる地域における土壌の元素分析と酸中和能との関連性、高橋麻子、東京大学大学院総合文化研究科広域科学専攻 修士論文 (2009年1月)
16. 交換性陽イオンによる土壌の酸中和能の解析、山ノ井俊、東京大学大学院理学系研究科化学専攻 修士論文 (2009年2月)
17. 谷津干潟および芝浦運河の底質・間隙水中における浄化機能に関する研究、長谷川篤、東京海洋大学大学院海洋科学技術研究科海洋保全学専攻 修士論文 (2009年3月)

学会発表

18. 放射化分析法を用いた遠洋性海洋堆積物表層における供給源の検討、小豆川勝見・久野章仁・佐野有司・松尾基之、第51回放射化学討論会 (2007日本放射化学会年会) (2007年9月)
19. 機器中性子放射化分析法・即発ガンマ線分析法による環境試料・地球化学的試料の多元素分析、松尾基之・小豆川勝見・諸町大地、原子力機構施設利用一般共同研究成果報告会 (2008年8月)
20. 干潟および運河の底質・間隙水中の元素分析による環境評価、長谷川篤・田中美穂・松尾基

之、日本分析化学会第57年会 (2008年9月)

21. 干潟底質中の元素垂直分布への主成分分析の適応による環境変動の評価法の検討、諸町大地・松尾基之、日本地球化学会年会 (2008年9月)
22. 土壌の酸中和能へ影響を与える交換性Caイオンの化学形態、山ノ井俊・小豆川勝見・松尾基之、日本地球化学会年会 (2008年9月)
23. 酸性雨被害が見られる地域における土壌の元素分布と酸中和能との関連性、高橋麻子・小豆川勝見・松尾基之、日本地球化学会年会 (2008年9月)
24. 硫酸還元と栄養塩から見た都市河川の環境評価、原直樹・小豆川勝見・松尾基之、日本地球化学会年会 (2008年9月)
25. 過剰^{230}Thにより年代決定された遠洋性海洋堆積物表層におけるAragonite-Calcite相転移、小豆川勝見・金井　豊・佐野有司・松尾基之、第52回放射化学討論会 (2008 日本放射化学会年会) (2008年9月)
26. 放射化分析法を用いた干潟の変遷と底質中の元素垂直分布の関連性の検討、諸町大地・松尾基之、第52回放射化学討論会 (2008日本放射化学会年会) (2008年9月)
27. 酸中和能の観点から見た土壌におけるCaの吸着形態の分析、山ノ井俊・小豆川勝見・松尾基之、第52回放射化学討論会 (2008日本放射化学会年会) (2008年9月)
28. 底質・間隙水中の鉄の挙動による干潟の浄化機能に関する研究、長谷川篤・田中美穂・松尾基之、第5回茨城地区分析技術交流会 (2008年10月)
29. Monitoring of environmental contamination and environmental changes, M. Matsuo, FNCA 2008 Workshop on Research Reactor Utilization, Vietnam, (October 2008)
30. 干潟底質における酸化還元電位と元素の挙動に関する研究、原直樹・小豆川勝見・松尾基之、日本地球化学会年会 (2009年9月)
31. 還元的環境下における東京湾底質に含まれる元素の化学状態、原直樹・小豆川勝見・松尾基之、第53回放射化学討論会 (2009日本放射化学会年会) (2009年9月)
32. Neutron activation analysis of marine sediment samples for environmental monitoring, M. Matsuo, FNCA 2009 Workshop on Research Reactor Utilization, Hachinohe, (September 2009)

3-8

3-9

研究課題名：造山帯の熱年代学的研究Ⅱ　（課題番号：8136）

岡山理科大学自然科学研究所　兵藤　博信

岡山理科大学自然科学研究所　板谷　徹丸

岡山理科大学オープンリサーチセンター　郷津　知太郎*　　*現在の所属　蒜山地質年代研究所

Hironobu, Hyodo, Research Insititute of Natural Sciences, Okayama University of Science

Tetsumaru Itaya, Research Insititute of Natural Sciences, Okayama University of Science

Chitaro Gouzu*, Open Research Center, Okayama University of Science, *present address

*Hiruzen Institute for Geology and Chronology

目的と意義

造山帯はそれが形成される過程において複雑な地殻変動の歴史を経験する。その過程で形成された岩石や変成を受けた岩石にはその記録が同位体の拡散移動の結果、元素分布として残り、特に放射性崩壊をする同位体系ではそれを時計として活用し、形成年代や変動年代とともにそれらが起きた物理条件件を推定することができる。それらの核種の中で ^{40}K を用いた K-Ar 年代測定法は、熱的擾乱に対する鉱物中のアルゴン拡散に関する物理パラメータがよく研究されており造山帯の冷却過程で K-Ar 系が閉鎖されたと考えることができる温度を閉止温度と定義して測定から直接的に推定することが可能になっている。その半面、純粋な物理系では推定できないいろいろな地質学的要因から単純な解釈ができない事象が多数存在する。K-Ar 年代法を改良した原子炉での放射化を用いる ^{40}Ar/^{39}Ar 法はそのような場合に段階加熱法を用いることで一度閉鎖系になった岩石がその後、熱的・鉱物学的変化をうけているかを判断する基準を提供する。

この研究の目的は複数の事象が記録されていると予想される未知の岩石に対し ^{40}Ar/^{39}Ar 段階加熱法を適用することにより精細な熱的履歴の解析を行うことにある。それにより従来のように測定して得られた数値を単に年代とするのではなく、アルゴン同位体の拡散における特性を活用して岩体の削剥・上昇過程あるいは一度鉱物が形成された後でおきた事象のインジケータとして地質学的意味を明らかにする。

JRR-3、HR-2 パイプ、地球科学試料放射化分析

JRR-4、TB パイプ、地球科学試料放射化分析

実験

試料と照射実験

対象とした岩石はカナダ・グレンビル地質区のグレンビル岩脈の周辺の岩石（母岩）である。母岩の年代は変成年代がよく研究され、貫入年代は $^{40}\mathrm{Ar}/^{39}\mathrm{Ar}$ 法と U-Pb 法によって決定されており、その一致も良い。岩脈の熱的モデルは比較的分析しやすいので、貫入時にできた熱変成を経験した周辺の母岩片麻岩中の鉱物のアルゴン拡散を $^{40}\mathrm{Ar}/^{39}\mathrm{Ar}$ 法で解析することによりそれぞれの鉱物の特性を調べた。

試料をこぶし大の大きさで採取し、60 メッシュ程度の細粒に砕き、造岩鉱物である角閃石、黒雲母および長石をハンドピッキングにより分離した。対象とする鉱物を 2 ミリ径のドリル孔があいた高純度アルミトレイにのせ、4 - 5 段積みにしてボルトナットで固定する。この試料ホルダを JRR-3 は簡易アルミ容器、JRR-4 は石英管に真空封入した後 0.5 ミリ厚のカドミウムを巻いて、6 時間照射を 1 – 4 サイクル行った。各アルミトレイには未知試料の他に中性子照射量をモニターするための標準年代試料として hb-3gr を中性子束密度の偏りの有無をある程度評価できるようにトレイの外側対角に 2 個、中心に 1 個配置した。

年代測定実験

大きさ約 0.5 ミリの鉱物試料を赤外放射温度計

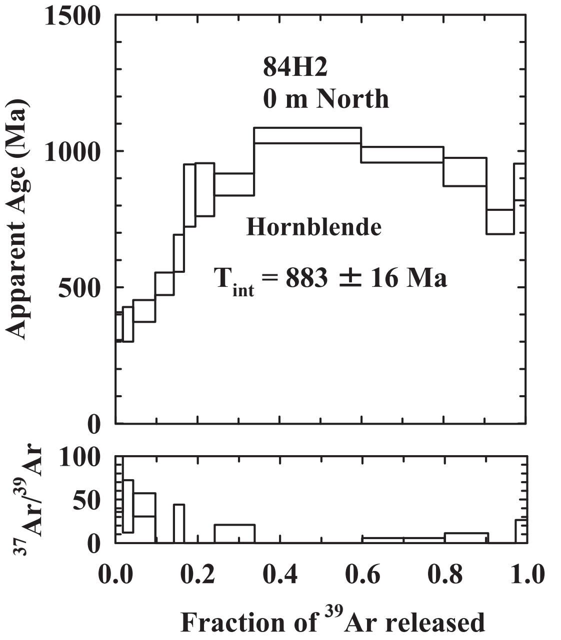

図 1　グレンビル岩脈に貫入された片麻岩中の熱変成を受けた角閃石試料（カナダ、オンタリオ）. コンタクトから 10cm 以内.

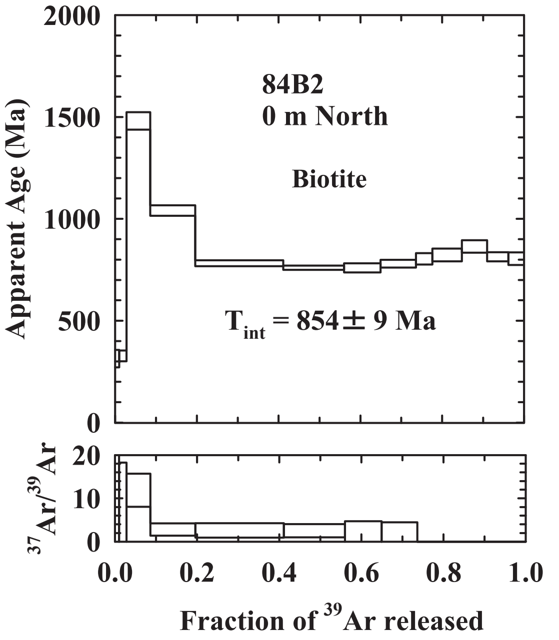

図 2　グレンビル岩脈に貫入された片麻岩中の熱変成を受けた黒雲母試料（カナダ、オンタリオ）. コンタクトから 10cm 以内.

によって温度をモニタしながら連続レーザーで段階的に温度を増加させながら30秒間加熱し、ゲッターによって反応性ガスを除去精製した後、希ガス質量分析計で各ステップごとの ^{40}Ar/^{39}Ar 年代測定を行った。

結果および成果

測定した角閃石および黒雲母は貫入岩脈の周りに図1および図2に示すような複雑な年代スペクトルを示す。これらは同じ熱履歴を経験しているのであるから閉止温度に対応した同じようなスペクトルを示すことが期待される。トータル年代だけに注目すれば必ずしもその開きは大きくなく整合的にみえる。しかし結果を見て明らかなようにそれらのスペクトル形状は低温部と高温部で全く異なる。この現象は接触部（コンタクト）から近いほど顕著である。また岩脈の走行は東西であり、平面が北に向かって垂直より約 20 度傾いているが、トータル年代だけでなく、同じ距離だけコンタクトから離れた北側と南側の試料で黒雲母、角閃石の年代スペクトル形状が全く異なる事が確認された。

ここにすべてのデータを示すことが出来ないので詳しい議論は別の機会とするが、岩脈をへだてた北と南の黒雲母の年代スペクトルの違いは岩脈の平面の両側に線対称を作り出す熱伝導プロセスだけで形成されたとは考えにくく、おそらくそれに伴う流体の移動が関与したと考える方が妥当であろう。その反面で流体による熱の移動は permeability の著しく低い結晶質岩石の中では量的な寄与はあまり大きくないと考えられるので、流体は主にアルゴンの移動に関与し、温度が支配する鉱物中のアルゴン拡散は、岩脈の両側でほぼ同等であると推測される。過剰アルゴンのソースはおそらく母岩自体であるので岩脈の両側での年代スペクトルの違いは、流体の経路の違いとその時間的変化であると推測される。

まとめと評価

この研究では ^{40}Ar/^{39}Ar 年代測定においてしばしば問題となる過剰アルゴンの原因が母岩に起因するものであることを示すことができた。またその蓄積のしかたで ^{40}Ar/^{39}Ar 年代スペクトルの形状が大きく異なる結果を示した。この原因として流体の関与が推論され、またその強度においても流体の経路が大きく影響していると思われる。

実施された JRR-3, JRR-4 での ^{40}Ar/^{39}Ar 年代測定では、干渉同位体の補正値は$(^{38}\mathrm{Ar}/^{39}\mathrm{Ar})_K$の値を除き前回の研究と同様まだ実験ごとに誤差が大きい。これが準備した標準試料に起因するものなのか、原子炉の立ち上げごとの中性子束密度のばらつきによるものかは判断がついていない。JRR-4 ではカドミウムを試料に巻いて熱中性子をある程度遮蔽することができる。試料の放射性強度はカ

ドミウムを巻いていないものと比べると著しく低く、また干渉同位体のへの影響も低減できる事がわかった。年代標準試料の J-値のばらつきから評価した中性子束の均質性では、同じ照射条件で水平および垂直分布はややばらつきが大きいがおおよそ数パーセントに収まっている。しかし個々の試料のばらつきで比較すると 10 パーセントを越えるものもあり、今後の検討課題である。

この報告での結果はまだ公の場で発表されていないものがほとんどである。それは照射後 3 ヶ月以上の冷却期間をおく必要性や、測定そのものに時間がかかること、マシンタイムなどによる。従って多くの測定は平成 19-20 年度の試料を 1 年後に測定するようなスケジュールとなり、発表の機会を得ていないものが多い。今後学会、論文誌などに発表していく予定である。

研究の性格上、同じ年度内に具体的業績を報告することは著しく困難である。今回の共同利用による照射実験の直接的結果とは無関係ではあるが、参考として 19-20 年度以前に京都大学原子炉で行った中性子照射による ^{40}Ar/^{39}Ar 年代測定の結果から発表された論文を以下に参考のために列挙する。このうち 4 と 5 のデータおよび解釈について原子力機構施設利用共同研究の結果を一部使用している。著者の不覚により謝辞に施設利用の件を記載していないことをお詫びいたします。

発表論文（^{40}Ar/^{39}Ar 法を用いたもの.

直接的関与は 4 と 5 のみ）

1) Itaya, T., Hyodo, H., Tsujimori, T., Wallis, S., Aoya, M., Kawakami, T., Gouzu, C. (2009) Regional-scale excess Ar wave in a Barrovian type metamorphic belt, eastern Tibetan Plateau, *Island Arc*, **18**, 293-305.
2) Miki, M., Taniguchi, A., Yokoyama, M., Gouzu, C., Hyodo, H., Zaman. H. and Otofuji, Y. (2009) Paleomagnetism and geochronology of the Proterozoic dolerite dyke from southwest Greenland: indication of low paleointensity, , *Geophysical Journal International*, **179**, 18-34.
3) Nuong, N.D., Itaya, T., Hyodo, H. and Yokoyama, K. (2009) K-Ar and ^{40}Ar/^{39}Ar phengite ages of Sanbagawa schist clasts from the Kuma Group, central Shikoku, SW Japan. *Island Arc*, **18**, 282-292.
4) Hyodo, H. (2008) Laser Probe ^{40}Ar/^{39}Ar dating: History and development from a technical perspective. *Gondwana Research* **14**, 609-616.
5) 兵藤博信 (2008) 研究炉JRR3で得られたJ値および干渉同位体補正値, *岡山理科大学自然科学研究所研究報告* 第34号, 39-42.
6) 内野隆之・川村信人・郷津知太郎・兵藤博信 (2008) 根田茂帯礫岩から得られた含ザクロ石泥質片岩礫の白雲母^{40}Ar/^{39}Ar年代. *地質学雑誌* **114** (6) 314-317.
6) Kawamura, M., Uchino, T., Gouzu, C. and Hyodo, H. (2007) 380 Ma ^{40}Ar/^{39}Ar ages of the high-P/T schists obtained from the Nedamo Terrane, Northeast Japan. *Journal of Geogical Society of Japan*, **113**, 492-499.
7) Nakatsukasa, M., Sawada, Y., Sakai, T., Hyodo, M., Hyodo, H., Itaya, T., Nakaya, H., Saegusa, H., Mazurier, A., Saneyoshi, M., Tsujikawa, H., Yamamoto, A., Mbua, E. (2007) A new Late Miocene great ape from Kenya and its implications for the origins of African great apes and humans. *Proceedings of National Academy of Science* USA, **104**, 19220-19225.

3-10

鉱石試料を含む日用品のSm/Gd比法による産地同定と鉱石の体系化

Production identification method of consumer products including ores as radiation sources and classification of ores by Sm/Gd ratios.

古田　悦子（お茶の水女子大学大学院）、箕輪はるか（東京慈恵会医科大学）
Etsuko Furuta; Ochanomizu University Graduate School
Haruka Minowa; The Jikei University School of Medicine

【研究目的、意義】

天然放射性同位元素を含む日用品は放射性コンシューマプロダクト(RCP)と呼ばれ、広く生活圏内に流通している。RCPは放射線を放出しており、放射線源の濃度の高いRCPは外部・内部被ばくの原因となる危険性がある。本研究は、鉱石由来成分を含むRCP（NORM）の原材料を、即発γ線放射化分析法（PGAA）により推定することを目的とする。

RCPの放射線源は、人工・天然の放射性同位元素のどちらも有りうるが、近年チタンなどの鉱石を用いた産業界における天然放射性同位元素の含有が作業者、廃棄物業者の被ばくにつながり、大きな社会問題となってきている。このような天然放射性同位元素を多く含む原材料（鉱石）、中間製品や一般消費財はNORM（Naturally Occurring Radioactive Materials)と呼ばれ、その健康影響は世界的な問題となってきている。IAEA,WHOなどがNORMの規制を検討しているところである。日本においても「ウラン又はトリウムを含む原材料、製品等の安全確保に関するガイドライン」が策定された。しかし、日本の「ガイドライン」はNORM原材料や一般消費財等の製造事業者を対象としたものであり、放射性物質が添加された一般消費財そのものの存在を否定するものではなく、この点がEUの「添加禁止」とは大きく異なっている。このため、今後も生活圏内には、放射線サーベイメータが大きく反応するような放射能の強い一般消費財が存在し続ける。

一般消費財の放射線源は、トリウム（Th），ウラン(U)がほとんどである。これら放射線源として、モナザイト鉱石、バストネサイトなど数種類が「ガイドライン」では、指定原材料として挙げられている。しかし、これは科学的根拠があるわけではない。

Th,Uを多く含む鉱石は、希土類元素を同時に多く含んでいることが多い。NORMのPGAによる非破壊分析により、Sm,Gdのみが測定出来ることから、一般消費財としてのNORMの原料鉱石の推定にはPGAAが有効であると考えられる。日本国内に入ってきている放射線源は、多岐にわたっているとは考えにくい。本法により原材料鉱石を特定することが可能と考えられる。原材料鉱石が特定された場合、輸入時の注意喚起につながり、不必要なRCPの生活圏への侵入を防ぐことが可能となると考えられ、この意義は大きい。

【計画と遂行方法】

（本研究計画は、平成19年度に古田が行った、PGAAトライアルユース時にNORMである「ホルミシス化粧品」から得られた結果に基づき、計画したものである。）

1. 脱臭材、燃費向上材、マイナスイオン製品などの多くの一般消費財及び産出国、地域の明らかな鉱石標本などのNORMを試料とし、半導体検出器によるγ線スペクトルの測定により、そのTh,U等の放射能濃度を求める。

JRR-3　PGAA　即発γ線放射化分析装置、放射化学、
PN-1　中性子放射化分析、放射化学

2. これら試料を3回のPGAAにより分析し､試料中のSm,Gdの放射能を求める。

3. １.及び２.の結果を図示することにより､Th/Uに対するGd/Smの関係を求める。

4. INAAを用いた放射化により、Sm,Gd以外の元素による体系化が可能であるか否かを探る。

【成果および今後の方針】

PGAA3回と、追加でお認めいただいたINAA1回を行った。しかし、鉱石等の標本試料は、結果として平成21年2月中旬に手元に届いたため、平成20年度内に遂行できた測定は以下の通りとなり、平成21年度以降に改めて実験計画を提出し､お認め頂いた。

１. 27種類の一般消費財NORMおよび鉱石試料の放射能測定（お茶大、HPGe）

２. 27種類の一般消費財NORMおよび一部鉱石試料の2～3回のPGAA測定

３. 一部の一般消費財と鉱石試料の1回のINAA測定

得られた放射能を表１；一般消費財(p３)、表２；鉱石試料として次ページ(p３～4)に記した｡さらに､PGAAから得られた一般消費財中のGdとSmの関係図1をｐ４に記した。

HPGeによるγ線測定により求めたThとUの関係からは、ThもしくはUが多いNORMの存在と、Th>UのNORMの存在が明らかとなった。しかし､鉱石試料との相関関係をTh,Uの関係のみから見出すことは､予想通り不可能であった。一方、一般消費財NORMに含まれるSm, Gdは､その多くが一直線上に集まり､特別な関係を示した。平成21年度以降、ここに鉱石試料を加え、何らかの傾向が得られるか、あるいは更なる元素による3次元グラフにより解析する必要があるかを見極めているところである。

【成果に対する評価】

H21年度、放射化学討論会において、口頭発表を行った。その結果、1. X線解析は行っているか、2. 試料としているNORMからの被ばく線量評価を行っているか否か、3.NORMに関する主張があったら聞かせてほしい、4.今後の方針の質問をいただいた。1.はいくつかの試料については行っており、今後も検討していること、2.は全てについて被ばく線量評価を行い、通常の使用形態では一般公衆に対する被ばく限度を超えることはない旨を報告、3.は「正当性」の話をさせて頂き、4.は産地の判明しているモナザイトに絞りPGAA, INAAを行う予定を述べた。

【今後の方針】

本課題は、遂行可能かも含め、単年度の申請としたが、可能であるとの感触を得て、H21-22年度の継続課題として申請し、継続している。

【成果の公表】

平成21年に開催されるAsia-Pacific Symposium on Radiochemistry’09において発表するとともに、そのProceedingsとしてJournal Radiochimica Actaに投稿予定である。

表 1　　22 種類の RCP(NORM)に含まれる放射能濃度

NORM			Effect clamed by maker	Concentration(Bq/g)		Ratio of Th/U	Additives specified in the label (Specification)
Code	Kinds:	Name		Th	U		
1	Toiletry	Jell-1	Hormesis	4.1×10^{1}	1.5×10^{1}	2.7×10^{0}	Zirconium Oxides
2		Liquid (red)		2.1×10^{1}	3.9×10^{0}	5.4×10^{0}	Tourmaline
3		Cream		2.1×10^{1}	7.1×10^{0}	2.9×10^{0}	Xenotime
4		Face powder		6.8×10^{1}	1.3×10^{1}	5.2×10^{0}	Dolomite, mica, Si and so on
5		Jell-2		4.1×10^{1}	1.5×10^{1}	2.7×10^{0}	(unknown)
6		Liquid	Minus-ion	3.0×10^{-2}	1.7×10^{-1}	1.7×10^{-1}	Tourmaline
7	Toothpaste		Healthy	3.4×10^{-3}	1.5×10^{-2}	2.2×10^{-1}	Tourmaline
8	Spring-bath powder	Bedrock-bath (red)	Relax and healthy	1.3×10^{3}	1.9×10^{2}	6.8×10^{0}	(Hearsay information: Monazite from China)
9		Bedrock-bath (white)		1.3×10^{3}	2.1×10^{2}	5.6×10^{0}	
10		Bakelite		5.4×10^{3}	8.6×10^{1}	6.3×10^{1}	(Rn spring)
11		Ra spring		2.6×10^{-1}	2.0×10^{-1}	1.3×10^{0}	(Ra powder)
12	Gas lantern mantle		Lightning	1.7×10^{2}	4.2×10^{0}	4.1×10^{1}	Th (Canada patent)
13				2.9×10^{2}	5.8×10^{0}	5.0×10^{1}	Th (China patent)
14	Car goods		Mileage improvement	2.0×10^{0}	4.6×10^{0}	4.3×10^{-1}	Mineral (unknown) (China patent ; brown)
15	Deodorant	Shoes-box	Deodorant	1.7×10^{2}	2.1×10^{1}	8.0×10^{0}	Monazite
16		Foot deodorant		1.6×10^{2}	1.6×10^{0}	9.9×10^{1}	Mineral (unknown)
17	Pillow		Relax and healthy	1.2×10^{2}	2.0×10^{1}	6.0×10^{0}	Mineral (unknown)
18	Wall-paper		Minus-ion	4.1×10^{0}	9.9×10^{-1}	4.2×10^{0}	Mineral (unknown)
19	Ornament	Bracelet	Hormesis	8.1×10^{2}	1.4×10^{2}	5.8×10^{0}	(The name is “monazu-bracelet”.)
20	Cloth	Under wear	Detoxification	1.1×10^{0}	1.1×10^{-1}	1.0×10^{1}	Ge
21		T-shirt	Minus-ion	1.0×10^{-2}	1.5×10^{-2}	7.2×10^{-1}	Mineral (unknown)
22		Wide stomach band	Minus-ion	1.5×10^{-2}	9.5×10^{-3}	1.5×10^{0}	Tourmaline

表 2-1　　50 種類の鉱石、鉱物、砂に含まれるトリウム、ウラン濃度

Ore				Concentration (Bq/g)		Ratio	Specification
Code	Kinds	Name	Producer and field	Th	U	Th/U	
1	Ore	Ti-ore*1	South Africa Richards Bay	1.6×10^{2}	5.4×10^{2}	3.0×10^{-1}	TiO_2 (Natural Rutile)
2			Australia Perth	2.8×10^{2}	2.2×10^{2}	1.3×10^{0}	$FeTiO_3$(Ilmenite)
3			South Africa Richards Bay	1.7×10^{2}	7.4×10^{1}	2.2×10^{0}	TiO_2 (Natural Rutile)
4			Vietnam	2.3×10^{2}	1.6×10^{2}	1.5×10^{0}	TiO_2 (Natural Rutile)
5			Australia Perth	2.3×10^{2}	5.3×10^{1}	4.4×10^{0}	$FeTiO_3$(Ilmenite)
6			Australia Perth	9.1×10^{3}	1.7×10^{3}	5.5×10^{0}	$FeTiO_3$(Ilmenite)
7			Canada	1.3×10^{3}	5.4×10^{2}	2.3×10^{0}	TiO_2 (Natural Rutile)
8			India	6.2×10^{4}	7.5×10^{3}	8.2×10^{0}	TiO_2, $FeTiO_3$
9			India	7.1×10^{4}	6.4×10^{3}	1.2×10^{1}	TiO_2, $FeTiO_3$
10	Sand	Zr-sand*1	Australia	5.9×10^{-1}	2.7×10^{0}	2.2×10^{-1}	ZrO_2・SiO_2 : $ZrSiO_4$
11			Australia (West coast)	5.5×10^{-1}	2.5×10^{0}	2.2×10^{-1}	ZrO_2・SiO_2 : $ZrSiO_4$
12	Mineral	Zircon	Pakistan	2.0×10^{0}	7.2×10^{0}	2.8×10^{-1}	ZrO_2・SiO_2 : $ZrSiO_4$
13			Pakistan	1.4×10^{1}	5.7×10^{1}	2.4×10^{-1}	$ZrSiO_4$ Red
14			Sri Lanka	1.7×10^{1}	7.1×10^{1}	2.4×10^{-1}	$ZrSiO_4$ Red
15			Australia Northern Territory	3.3×10^{-1}	3.5×10^{0}	9.4×10^{-2}	$ZrSiO_4$ Yellow
16			Malawi Rift Mineral Province	9.0×10^{0}	5.6×10^{1}	1.6×10^{-1}	$ZrSiO_4$ Red
17			Tanzania Mabumbi	8.0×10^{-1}	5.8×10^{0}	1.4×10^{-1}	$ZrSiO_4$ Red
18	Mineral	Bastnesite	Pakistan North West Province	9.5×10^{0}	-	-	(Ce):$Ce(CO_3)F$
19			Pakistan	4.8×10^{1}	6.7×10^{-1}	7.2×10^{1}	(Ce):$Ce(CO_3)F$
20			Pakistan	5.0×10^{1}	4.2×10^{-1}	1.2×10^{1}	(Ce):$Ce(CO_3)F$
21	Mineral	Monazite	America Colorado	2.7×10^{3}	2.9×10^{2}	9.4×10^{0}	ex.$(Ce,La,Nd,Th)PO_4$
22			Canada Ontario	2.5×10^{3}	3.5×10^{2}	7.2×10^{0}	ex.$(Ce,La,Nd,Th)PO_4$
23			Brazil Tocantis	4.0×10^{2}	4.2×10^{1}	9.5×10^{0}	ex.$(Ce,La,Nd,Th)PO_4$
24	Ore	Monazite	Unknown－1	6.1×10^{0}	9.7×10^{-1}	6.3×10^{0}	ex.$(Ce,La,Nd,Th)PO_4$
25			Unknown－2	2.9×10^{-1}	4.5×10^{-1}	6.5×10^{-1}	ex.$(Ce,La,Nd,Th)PO_4$
26			Unknown－3	3.6×10^{-1}	4.4×10^{-1}	8.3×10^{-1}	ex.$(Ce,La,Nd,Th)PO_4$
27			Unknown－4	2.8×10^{-1}	4.7×10^{-1}	5.9×10^{-1}	ex.$(Ce,La,Nd,Th)PO_4$
28*2		Monazite(+Xenotime)	Iran	6.5×10^{-1}	5.0×10^{-1}	1.3×10^{0}	Sold under the name of "Ra ore"

表 2-2

Ore				Concentration (Bq/g)		Ratio	Specification
Code	Kinds	Name	Producer and field	Th	U	Th/U	
29	(Beach) Sand	Monazite	India Thengapattanam-1	5.6×10^{1}	1.3×10^{1}	4.2×10^{0}	$(Ce,La,Nd,Th)PO_4$
30			India Thengapattanam-2	2.9×10^{2}	5.8×10^{1}	5.0×10^{0}	$(Ce,La,Nd,Th)PO_4$
31			India Thengapattanam-3	2.7×10^{2}	5.6×10^{1}	4.9×10^{0}	$(Ce,La,Nd,Th)PO_4$
32			India Thengapattanam-4	3.6×10^{2}	7.5×10^{1}	4.9×10^{0}	$(Ce,La,Nd,Th)PO_4$
33	Mineral	Xenotime	Brazil Bahia	6.8×10^{1}	1.8×10^{1}	3.9×10^{0}	YPO_4
34			Brazil	5.0×10^{1}	1.1×10^{1}	4.5×10^{0}	YPO_4
35			Pakistan North West Province	1.9×10^{1}	8.0×10^{1}	2.4×10^{-1}	YPO_4
36			Brazil	2.9×10^{4}	3.2×10^{3}	8.9×10^{0}	YPO_4
37	Ore	Tourmaline (powder)	China, South Africa and Brazil	1.3×10^{-1}	2.0×10^{0}	6.5×10^{-2}	$NaX_3Al_6(BO_3)_3Si_6O_{18}(OH)_4$, X=Al,Fe,M
38	Mineral	Aeschynite	Canada Bandcroft	1.6×10^{2}	1.5×10^{4}	1.1×10^{-2}	$(Y,Ca,Fe,Th)(Ti,Nb)_2(O,OH)_6$
39		Allanite	Brazil Minas Gerais	7.4×10^{3}	9.3×10^{1}	8.0×10^{0}	$Ca(Ce,La,Y,Th)(Al,Fe,Mg)_3OH(SiO_4)_3$
40[*2]		Allanite(+Zircon)	Korea	1.1×10^{-1}	8.6×10^{-2}	1.3×10^{0}	Sold under the name of "Ge ore"
41		Betafite	Madagascar Antsirabe	1.1×10^{4}	5.8×10^{-2}	1.5×10^{5}	$(Ca,Na,U)_2(Ti,Nb,Ta)_2O_6(OH)$
42		Davidite	Kazakhstan Qaraghandy Oblysy	2.2×10^{2}	5.5×10^{2}	4.0×10^{-1}	$(Ce,La)(Y,U,Fe^{2+})(Ti,Fe^{3+})_{20}(O,OH)_{38}$
43		Euxenite	Brazil Espirito Santo	8.0×10^{2}	1.9×10^{4}	4.3×10^{-2}	$(Y,Ca,Ce,U,Th)(Nb,Ta,Ti)_2O_6$
44		Euxenite	America Wyoming	1.0×10^{3}	2.2×10^{4}	4.7×10^{-2}	$(Y,Ca,Ce,U,Th)(Nb,Ta,Ti)_2O_6$
45		Samarskite	America Colorado	1.4×10^{3}	9.6×10^{3}	1.5×10^{-1}	$(Y,Fe^{3+},U)(Nb,Ta)_5O_4$
46		Samarskite	Rossiya South Ural	1.2×10^{2}	1.5×10^{3}	8.3×10^{-2}	$(Y,Fe,U)NbO_4$
47		Stillwellite	Tazhikistan Alayskiy	1.8×10^{0}	5.1×10^{1}	3.5×10^{-2}	$(Ce,La,Ca)BSiO_5$
48		Thorianite	Madagascar Taolanaro	2.3×10^{4}	8.6×10^{3}	2.6×10^{0}	ThO_2
49		Uraninite	Congo Katanga	1.1×10^{2}	8.6×10^{4}	1.2×10^{-3}	UO_2
50		Uraninite	America New Hampshire	6.9×10^{2}	6.7×10^{4}	1.0×10^{-2}	UO_2

*1; These ores and sand are used as industrial materials for paint, ink, plastic and so on. They are imported by some big companies and their radioactivities are controlled by the companies. They are called "industrial NORM".In the industrial NORM, 3 kinds of Ti-ores were not shown in

*2; The two ores of Code No. 24 and 36 were sold at a normal handcraft shop under the name of each ore shown in the Specification column. They were analyzed by Dr. Miyawaki like as each written in the Name column.

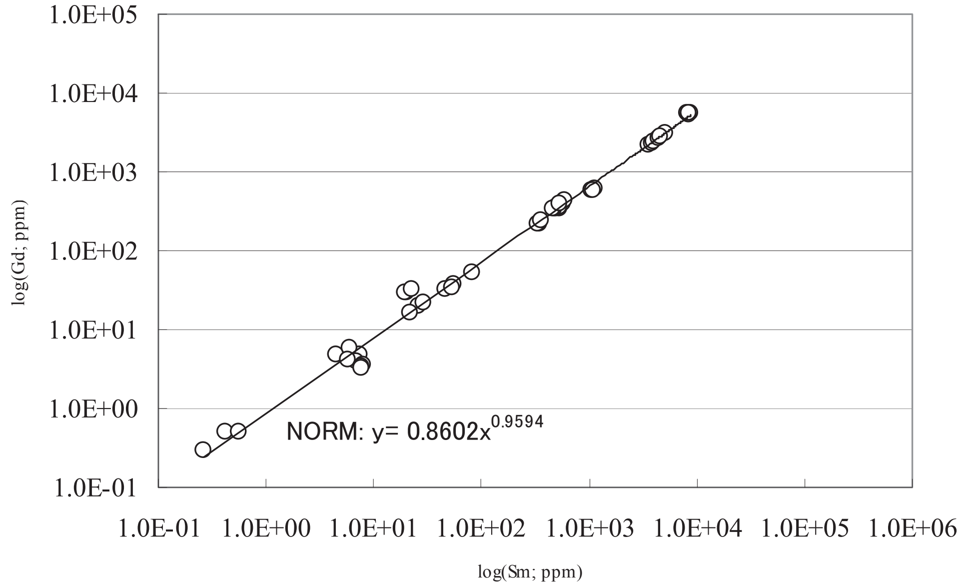

図 1　　　　PGAA により求めた NORM に含まれれる Sm と Gd の関係

3-10

3-11

大気環境試料における微量元素の定量とその挙動（Ⅱ）

Determination and behavior of trace elements in atmospheric samples (Ⅱ)

研究代表者：本多照幸（東京都市大学原子力研究所）
研究協力者：廣瀬勝己（気象研究所）
　　　　　　木川田喜一（上智大学理工学部）

Teruyuki HONDA (Atomic Energy Research Laboratory, Tokyo City University)
Katsumi HIROSE (Meteorological Research Institute)
Yoshikazu KIKAWADA (Faculty of Science and Technology, Sophia University)

Ⅰ．はじめに

大気環境を巡る状況は、18～19 世紀の産業革命以来著しく変動してきており、殊に二酸化炭素等の温室効果ガスの放出に伴う地球温暖化の問題は、地球規模の課題として提起されている。

しかしながら、大気環境の動態を正確に評価するには温室効果ガスの変動（濃度上昇）のみならず、微量元素や人工及び天然放射性核種等を用いた大気環境物質の起源並びに挙動を正確に把握し、評価する必要がある。

そこで本研究では、大気環境を探る上で重要となる降下物及び大気粒子状物質（Airborne Particulate Matters, APM）を試料として採取し、それらに含まれる微量元素並びに放射性核種を分析、解析し、その結果を用いて、大気降下物並びにPMの起源を解明し、さらに、検出、定量された放射性核種や微量元素の振舞いを通じて、大気環境物質がどのように挙動しているのかを明らかにすることを目的とした。

本研究に供する試料は、２種類ある。①降下物については、神奈川県川崎市の東京都市大（原子力研究所）で採取した全降下物（乾性＋湿性）月間試料であり、②APMについては、同じく東京都市大（原子力研究所）において、ハイボリウム・エアサンプラーにより採取した週間試料である。

なお、本研究では微量元素の定量に当該共同利用による中性子放射化分析を適用した。

Ⅱ．中性子放射化分析

本研究では、2種類の試料を用意した。

先ず、（1）全降下物については、①雨水を含む試料を蒸発乾固し、②専用の容器（V7）に封入した。（2）APMについては、①ハイボリウム・エアサンプラーにて石英フィルターに収集し、②一部をパンチで打ち抜き、放射化用試料とした。

それらの試料について、JRR-3 の P-3 並びに P-1 または P-2 気送管を用いて照射を行い、適当な冷却時間を経た後、アルミニウム (Al)、バナジウム (V)、マンガン（Mn）等の短寿命核種は、当日、原子力機構(JRR-3)にて測定し、他の中・長寿命核種については東京都市大原子力研究所に郵送した。然る後、東京都市大にてγ線スペクトロメトリを実行し、臭素（Br）、アンチモン（Sb）、ランタノイドおよびト

JRR-3　PN-1、PN-2、PN-3
地球科学試料放射化分析

表１　中性子照射及びガンマ線の測定条件

照射場所	最大熱中性子束[n/(cm²・s)]	照射時間	照射量(mg)	冷却時間	測定時間(sec)
PN-1	5.2×10^{13}	20(m)	30	1,4weeks	1500, 7000
PN-2	4.7×10^{13}	20(m)	30	1,4weeks	1500, 7000
PN-3	1.5×10^{13}	10(s)	5	7,40min	200, 300

リウム(Th)、ウラン（U）等の微量元素の分析・定量を行った。

照射及び測定条件を表１に記載する。

Ⅲ．成果の概要

１．大気降下物における微量元素等の挙動

1-1 元素濃度の季節変動

中性子放射化分析により、2007 年 9 月から 2008 年 9 月までの川崎試料から 27 元素（Na、Al、Sc、ランタノイド等）が定量された。定量された土壌起源元素 Al、Sc、Fe、La と海洋起源元素 Na の元素濃度（μg/g）の月別変化を図 1 に示す。図 1 より、土壌起源元素は春季にピークを持ち、海洋起源元素は春季と夏季～秋季にピークを持った。両起源元素とも春季のピークについては、偏西風の影響によりアジア大陸から粒子が飛来したため、ほかの月よりも多量に降下したと考えられる。海洋起源元素 Na については、トラジェクトリーの分析結果より、太平洋側からの海塩粒子が原因で夏季～秋季にピークを持ったと考えられる。また、2007 年 9 月に台風が 1 度上陸しているため、2007 年 9 月の Na のピークは台風が起因している可能性がある。

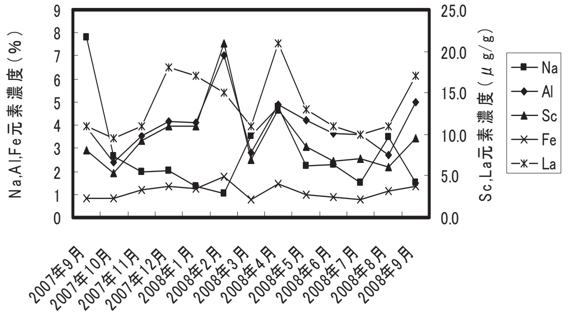

図１　元素濃度の月別変化

1-2 濃縮係数を用いた起源の検討

中性子放射化分析により定量された元素が自然発生的なものなのか、人為的なものなのか詳しく知るために、濃縮係数による検討を行った。濃縮係数とは定量された元素の起源を知る指標になるもので濃縮係数が 10 以上なら人為的で、10 より小さいなら自然発生的なものと考えられる。（１）式に濃縮係数（EF 値）の定義を示す。各元素に対する濃縮係数の最大値、最小値、平均値を図 2 に示す。図 2 より、ほとんどの元素は自然発生的なものであるが Zn、Sb は EF 値の平均値がそれぞれ 48、184 と 10 以上で、人為発生的と考えられる。

$$EFx=(C_x/C_{Al})_D/(C_x/C_{Al})_R \quad (1)$$

C_x：問題となる元素濃度

C_{Al}：Al濃度

添字D：降下物

添字R：地殻存在度

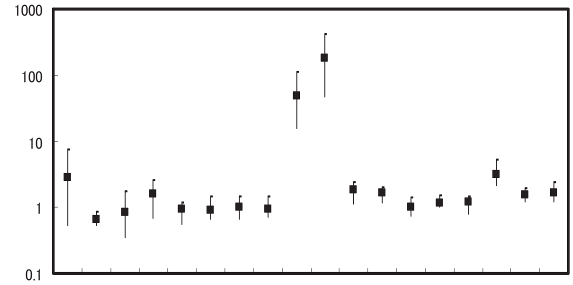

図２　濃縮係数（2007 年 9 月～2008 年 9 月）

1-3 統計学的主成分分析による検討

中性子放射化分析の結果を詳しく評価するために統計学的な主成分分析を行った。分析には海洋起源元素 Na、土壌起源元素 Al、Th、Sc、Fe、Ce、La、人為起源元素 Zn、Sb の元素濃度（μg/g）、気象因子、月間降下量を因子に用いた。

表 2 は主成分分析の結果である。第 1 主成分に対しては土壌起源元素が強い因子負荷量を持っている。

また気象因子が因子負荷量を持たないことを考慮すると、第1主成分は、土壌起源元素が自由落下により降下することを示していると考えられる。第2主成分に対しては、ZnとSbが強い因子負荷量を持っていることから、第2主成分はZnとSbの相関関係を示していると考えられる。第3主成分では海洋起源元素 Na、月間降水量及び月間平均気温が強い因子負荷量を持っていることから、第3主成分では海塩粒子に含まれている Na が月間降水量と相関を持つことを示していると考えられる。

次に、第4主成分の結果から海洋起源元素 Na と Zn が相関関係にある可能性が示唆されたので、Na、Zn 及び Sb の相関係数を算出した。表3は2008年6〜9月の海洋起源元素と人為起源元素の濃度の相関係数である。これより、夏季において各元素濃度がそれぞれの元素濃度に対して高い正の相関を示していることがわかる。1-1の検討から、Naは夏季において太平洋側から飛来すると考えられるので、相関係数から Zn、Sb も太平洋側から飛来すると考えられる。また、Znについては廃棄物の燃焼または自動車の排ガス、Sbについては廃棄物の燃焼または自動車のタイヤの摩耗により排出される。採取地点の南東約3㎞には東名高速道路や国道246号があるので、自動車が Zn、Sb の排出源になっている可能性がある。しかし、Zn、Sb は廃棄物の燃焼からも排出されるので、これらの元素の起源は別々の可能性もある。

表2　主成分分析

	第 1	第 2	第 3	第 4
Na	−0.26	−0.37	**0.57**	**0.62**
Al	**0.87**	−0.37	−0.05	−0.26
Th	**0.91**	−0.04	0.25	0.19
Sc	**0.89**	−0.21	−0.23	−0.05
Fe	**0.88**	0.20	0.05	−0.21
Ce	**0.92**	0.00	0.32	−0.02
La	**0.87**	0.20	0.34	0.08
Zn	−0.02	**0.76**	−0.05	**0.58**
Sb	0.16	**0.86**	0.37	0.08
風速	0.30	−0.76	0.08	0.29
降水量	−0.24	−0.03	**0.85**	−0.29
気温	−0.65	−0.21	**0.53**	−0.41
降下物量	−0.07	−0.94	0.01	0.24

表3　相関係数

	Na	Zn	Sb
Na		0.98	0.59
Zn			0.74
Sb			

1-4 Caとトラジェクトリーを用いた黄砂の飛来

中性子放射化分析で定量された Ca 濃度（%）とトラジェクトリーの分析結果を用いて黄砂の降下現象の月別変化について検討した。図3はCa濃度の月別変化を示したグラフである。図3より、Ca濃度は冬季から春先にかけて高い値を示すことがわかる。トラジェクトリーの分析結果より冬季から春先はアジア大陸から粒子が飛来していることがわかった。Caは黄砂に含まれる主な元素のひとつなので、少なくとも春季はアジア大陸から偏西風に乗って黄砂が飛来すると考えられる。

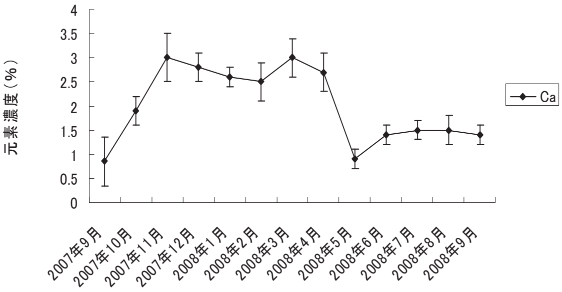

図3　Ca濃度の月別変化

2. 大気粒子状物質における微量元素等の挙動

2-1 ^{210}Pb放射能と^{7}Be放射能

まずAPM濃度と^{210}Pb放射能濃度の関係を調べるために、APM濃度と^{210}Pb放射能濃度の相関係数を求めたところ相関係数はR＝0.69であった。また、風速と降水量で規格化したところ、相関係数はそれぞれR=0.80、R=0.98となり、降水量で規格化した場合は非常に強い相関を示した。図4に降水量で規格化した場合のAPM濃度と^{210}Pb放射能濃度を示す。なお^{7}Beについても同様の傾向を示した。

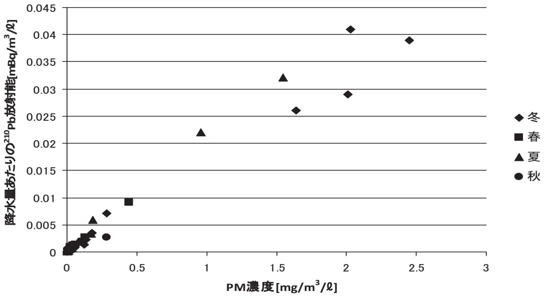

図4　降水量あたりのAPM濃度と^{210}Pb放射能

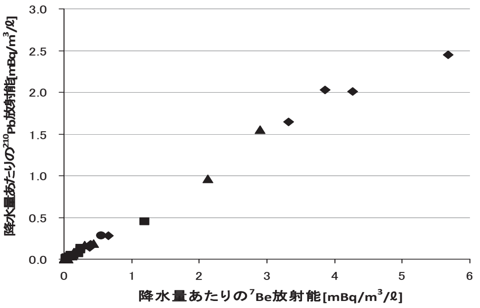

図 5　降水量あたりの^{210}Pbと^{7}Beの関係

次に^{210}Pbと^{7}Be両核種の関係を調べるために、同様に相関係数を求めたところR=0.84 と強い相関を示した。さらにAPM濃度と放射能濃度の関係と同様に、風速と降水量で規格化した上で相関係数を求めると、それぞれR=0.95、R=0.99 となり非常に強い相関を示した。このことからAPM濃度、^{210}Pb及び^{7}Be放射能濃度は降水現象と風速に支配されていることが分かる。図 5 に降水量あたりの^{210}Pb放射能濃度と^{7}Be放射能濃度を季節別に示す。

2-2 季節変動

^{210}Pbと^{7}Beの季節変動を調べるために、相関関係のある降水現象と風との関係を利用する。まず降水現象による季節変動を調べるために、図 6 に月間の降水量あたりの^{210}Pb放射能と降水量の関係を示す。図 6 より、放射能は冬に高くなり、その他の季節で低くなる傾向を示した。これは梅雨の時期や、夏から秋にかけて日本に接近してくる台風が雨を大量にもたらすことによってwash-out効果が起こり、APM濃度が低くなったことに起因していると考えられる。また図 6 において、夏に高い値を示している箇所があるが、これは 7 月のデータである。2008 年 7 月は例年と比較して降水量が大幅に少なかったため、冬の時期と似た傾向を示した。従って^{210}Pb放射能の季節変動は降水現象と密接に関係しており、APMと降水現象の密接な関係を裏付けている。なお^{7}Beについても同様の傾向を示した。

次に風との関係から季節変動を調べる。まず平均風速については、大きな季節変動を示さず、^{210}Pbと^{7}Beとの関係においても季節変動は見出せなかった。続いて風向との関係に着目してみると、北風が吹いた時は南風が吹いた時と比較して、放射能濃度が約 1.3 倍高い値を示した。そのため、南風が吹く 6 月から 8 月にかけて、放射能濃度が低くなる季節変動を示すことが分かった。このことは、^{210}Pbの起源が主に大陸の土壌であること、また^{7}Beの起源が主に高緯度地域であることに起因していると考えられる。このことは図 7 に示した 2008 年の冬(1 月～2 月)と夏(6 月～8 月)のトラジェクトリー分析の結果からも裏付けられている。

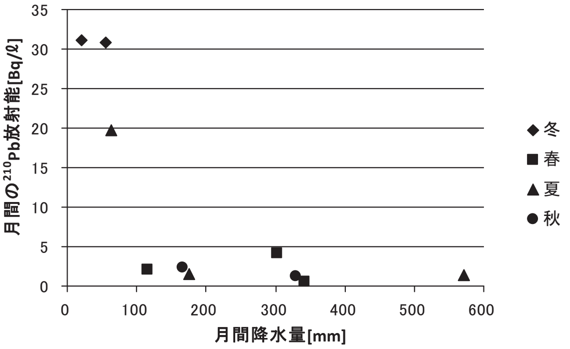

図 6　^{210}Pbの季節変動

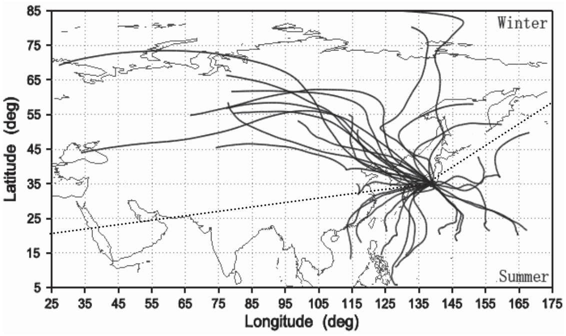

図 7　2008 年冬と夏のトラジェクトリー

2-3 放射化分析の定量結果と発生起源

2003 年 7 月から 9 月の 13 期間における APM において 19 種類の元素、2007 年及び 2008 年の 7 月から 9 月の 13 期間においては 26 種類の元素が定量できた。

定量できた元素の発生起源を推察するために濃縮係数(Enrichment Factor, E.F.)を求めた。E.F.値は以下の式で定義され、この値が 1 に近いほど自然起源の寄与が大きいことを意味する。

$$E.F.=\left[X/Al\right]_{APM}\Big/\left[X/Al\right]_{\text{地殻}}$$

X：注目する元素濃度

Al：Al の元素濃度

E.F.値を求めた結果を図 8 に示す。図 8 より、平均値からのずれ等を考慮して E.F.値 10 未満を自然起源元素、10 以上を人為起源元素とした。

また元素間の関係を調べるために、各元素間及び各元素と気象因子の相関係数を求めた。

まず自然起源の元素については、発生起源を土壌と海塩に分けることができる。土壌起源元素は Al, Sc, Ti やランタノイド等が挙げられ、Al, Sc, Ti が相互に強い相関(R=0.82～0.90)を示し、ランタノイドとも相関(R=0.35～0.61)を示した。また、これらの元素と Ca, Cr, Mn, Fe, Zn が比較的強い相関(R=0.55～0.81)を示したことから、Ca, Cr, Mn, Fe, Zn も土壌起源の影響を受けている元素と言える。海塩起源元素は Na, Cl, Ca, Br が挙げられる。Na は南風の風速と比較的強い相関(R=0.73)を示したことから海塩起源であると言え、Na と比較的強い相関(R=0.63)を示した Cl も海塩起源だと考えられる。Ca と Br は Na や Cl とは相関を示さなかったことから、Ca は土壌、Br は人為起源からの影響が大きいと考えられる。

次に人為起源の元素については、発生起源を主に石油燃焼系粒子、廃棄物焼却系粒子、自動車、鉄鋼、非鉄金属鉱業、肥料に分けることができる。石油燃焼系粒子起源の元素は、Mg, V, Mn, Fe,Cu, Zn, As などが挙げられる。この中で E.F.値から人為起源に分類されたのは Cu, Zn, As であり、これらは相互に相関(R=0.49～0.56)を示した。また Mn, Fe は Zn と相関(それぞれ R=0.74, R=0.70)を示しことから、少なからず影響を与えていると考えられる。廃棄物焼却系粒子起源の元素は Zn, Sb が挙げられ、Zn と Sb の相関を調べると、比較的強い相関(R=0.75)を示した。また風速との相関を調べたところ、南風に対して負の相関を示したことからサンプリング地点の北側からの運ばれてきた可能性が高い。自動車起源の元素は Zn, Cl, Br が挙げられるが、これらの元素は相関を示さなかった。そのため Zn と Cl は他の起源の影響が大きく、ガソリンの添加剤として用いられる Br が自動車起源の元素だと考えられる。サンプリング地点の南東約 3km に高速道路や幹線道路が通っているため、ここからの影響を受けている可能性がある。鉄鋼業・非鉄金属鉱業起源の元素は Cr, Mn, Fe, Cu, Zn, As, Sm が挙げられる。これらの元素はサンプリング地点南東の工業地帯からの排出が考えられるが、相互の相関が弱いため影響は非常に小さいものと考えられる。肥料起源の元素には U がある。E.F.値から U は人為起源元素であるので、畑などへの施肥の影響を受けたと考えられる。

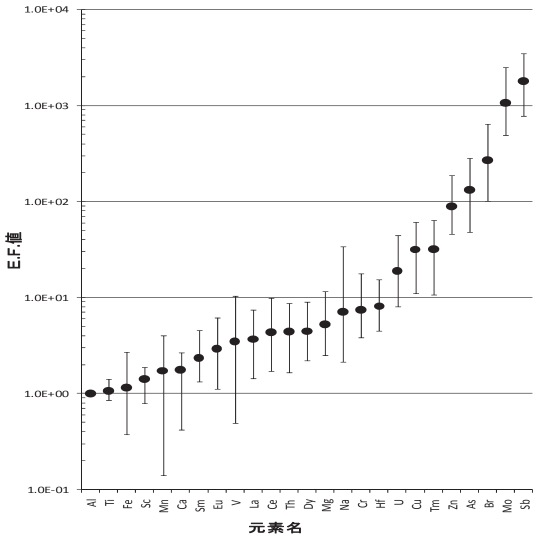

図 8　濃縮係数(2003、2007 及び 2008 年の 7 月から 9 月)

[成果の公表]

Ⅰ．学術誌

1．M. Suzuki and T. Honda；Investigation of the origin and sedimentary environment of marine sediments from coastal areas of western Japan by INAA, Journal of Radioanalytical and Nuclear Chemistry, vol.278 (No.2), 337-341(2008)

2．K. Oda, Y. Kikawada, T. Oi and T. Honda；Behaviors of chemical elements in the atmosphere, Kawasaki, Japan, Journal of Radioanalytical and Nuclear Chemistry, vol.278

(No.2), 475-478(2008)

3．T. Honda and H. Pettersson ; Determination of lanthanoids and uranium in groundwater from southeast Sweden by neutron activation analysis and their behavior including uranium series nuclides, RADIOISOTOPES, vol.57(No.1), 71-78 (2008)

4．T. Honda and Y. Satoh ; Sedimentary environment and origin of marine sediments collected from Kagoshima Bay and Shimabara Bay in Kyushu, Japan, Bulletin of the Society of Sea Water Science, Japan, vol.62 (No.1), 28-34(2008)

5. 木川田喜一，小田幸平，本多照幸，大井隆夫；放射性降下物標準試料のウラン同位体比，武蔵工業大学原子力研究所報，通巻 34 号，21-27(2008)

6．西田知広，木川田喜一，本多照幸，大井隆夫；神奈川県東部の大気粒子状物質に含まれる二次粒子の動態解析，武蔵工業大学原子力研究所報，通巻 34 号，28-39(2008)

7．嵯峨浩子，本多照幸；^{210}Pb並びに^{137}Csを用いた東京湾海底堆積物の堆積年代とインベントリー，フィッション・トラック　ニュースレター，第 21 号，28-30(2008)

8．永田寛，本多照幸，岩月輝希，水野崇；東濃ウラン鉱床周辺の瑞浪層群に産する堆積岩類中のウラン，トリウム及びランタノイドの分布と挙動，フィッション・トラック　ニュースレター，第 20 号，30-33(2007)

9．木川田喜一，早津岳宏，前川裕子，本多照幸，大井隆夫；逐次溶解法を用いた火山性海底堆積物の微量元素形態別分析，日本海水学会誌，第 61 巻（第 5 号），286-292(2007)

10. M. Suzuki and T. Honda ; Distribution and behavior of trace elements in marine sediments from coastal areas of western Japan, Bull. Atomic Energy Research laboratory, Musashi Institute of Technology, No. 34, 7-13(2007)

11. T. Honda and Y. Satoh ; Sedimentary environment in marine sediments from two coastal areas in the Kyushu district, Bull. Atomic Energy Research laboratory, Musashi Institute of Technology, No. 33, 7-15(2007)

12. 早津岳宏，木川田喜一，本多照幸，大井隆夫；火山性海底堆積物の微量元素形態別分析における逐次溶解法の適用，武蔵工業大学原子力研究所報，通巻 33 号，16-28(2007)

13. 本多照幸，後藤仁美，北原照央；2003-2004 年川崎大気環境中の^{210}Pbおよび^{7}Beの存在量と挙動，フィッション・トラック　ニュースレター，第 19 号，27-31(2006)

14. 鈴木美咲，本多照幸；伊勢湾並びに大阪湾海底堆積物中のウラン，トリウム及びランタノイドの分布と挙動，フィッション・トラック　ニュースレター，第 19 号，33-37(2006)

Ⅱ．口頭発表

1．Y. Kikawada, K. Oda, T. Oi, M. Nomura, T. Honda and K. Hirose; Uranium isotope ratios in atmospheric deposits in Japan, 18th Annual V. M. Goldschmidt Conference, Geochim. Cosmochim. Acta, 72, Suppl. 1, A469, 2008

2．木川田喜一，小田幸平，大井隆夫，野村雅夫，本多照幸，廣瀬勝巳；国内大気降下物試料の異常ウラン同位体比，2008 年度日本地球化学会第 55 回年会講演要旨集，p.345，2008

3．永田寛，本多照幸，岩月輝希，水野崇；地球化学的環境の相違に起因する堆積岩中の微量・主要元素の分布と挙動，第 45 回アイソトープ・放射線研究発表会要旨集，p.19，2008

4．M. Suzuki and T. Honda; Distribution and behavior of trace elements in marine sediments from coastal areas of western Japan, 12th International Conference on Modern Trends in Activation Analysis, pp. 92, 2007

5．K. Oda, Y. Kikawada, T. Oi, and T. Honda; Behavior of antimony in the atmosphere, Kawasaki, Japan, 12th International Conference on Modern Trends in Activation Analysis, pp. 104, 2007

６．鈴木美咲，本多照幸；紀伊水道，広島湾及び土佐湾海底堆積物における微量元素の分布と挙動，第 44 回アイソトープ･放射線研究発表会要旨集，p.98，2007

７．永田寛，本多照幸；瑞浪層群における地球化学的環境の変化に伴う微量元素の分布と挙動，2007 年度日本地球化学会第 54 回年会講演要旨集，p.181，2007

８．小田幸平，木川田喜一，大井隆夫，本多照幸，廣瀬勝巳；福岡における大気降下物中のウラン同位体比分析，2007 年度日本地球化学会第 54 回年会講演要旨集，p.247，2007

９．鈴木美咲，本多照幸；伊勢湾並びに大阪湾海底堆積物における微量元素の挙動と堆積環境，2006 年度日本地球化学会第 53 回年会講演要旨集，p.111，2006

3-11

3-12

「亜鉛欠乏状態における肝細胞および膵細胞中の可溶性タンパク質の構造変化」

Effects of Zn deficiency on metalloproteins in hepatic and pancreatic cells

矢永誠人、菅沼英夫、野口基子、上島淳慈、川島美智子、
村松　航、山野　喜、川口剛広、河村　昂、下山弘高、山本　督
静岡大学理学部
Makoto YANAGA, Hideo SUGANUMA, Motoko NOGUCHI, Junji KAMISHIMA,
Michiko KAWASHIMA, Wataru MURAMATSU, Yoshi YAMANO,
Takehiro KAWAGUCHI, Akira KAWAMURA, Hirotaka SHIMOYAMA, Osamu YAMAMOTO
Faculty of Science, Shizuoka University

（１）　はじめに

我々の体は、主として、炭素や酸素、水素など、有機物を構成する元素により構成されている。また、生命活動には、塩分、すなわちナトリウムやカリウム、塩素などの電解質も必要とされ、さらに、窒素やイオウ、リンなどは、タンパク質や核酸の構成成分となっている。我々の体には、これらの元素の他、その量は微量ではあるが、必須性の高い元素が多数含まれている。その中でも亜鉛は、存在量は鉄に次いで２番目であるが、その機能の多様性から、もっとも必須性の高い生体微量元素であると言えよう。

この亜鉛が欠乏すると味覚・嗅覚障害、性腺機能低下、皮膚障害、免疫機能低下、成長障害などの症状が現れることがある。亜鉛欠乏の原因の一つとして食餌中の亜鉛不足があげられるが、我々は、この食餌中の亜鉛不足に伴う亜鉛欠乏を対象とし、亜鉛欠乏が金属結合タンパク質、特に、亜鉛結合タンパク質を介して他の元素の挙動に与える影響について検討してきている。これまで、亜鉛欠乏餌および対照餌で飼育したマウスの各臓器および組織について、機器中性子放射化分析法により種々の微量元素の定量を行い、比較検討してきた。その結果、外観上および組織学的観察においても亜鉛欠乏による影響が認められない場合において、亜鉛濃度に関しては、亜鉛欠乏群の骨や膵臓では有意に低下していたが、その他の臓器では顕著な濃度低下は認められなかった。また、コバルト濃度に関しては、亜鉛欠乏マウスの全ての臓器・組織で増加していた。

これらことは、顕著な亜鉛欠乏症状が認められる以前の亜鉛結合タンパク質などの生体内金属結合物質の変化を示しているものと考えられる。そこで、本研究では、亜鉛欠乏症状が現れる以前に変化する生体物質、特に金属結合タンパク質が細胞内のどの部分にあるかを検索するために、肝細胞および膵細胞について遠心分離法による細胞分画を行い、各画分について、機器中性子放射化分析を行うこととした。

（２）　実験

２－１　供試動物および細胞分画

８週齢のＩＣＲ系オスマウスを、亜鉛欠乏群と対照群の２群に分け、亜鉛欠乏群には亜鉛欠乏餌および超純水を、また、対照群には対照餌（亜鉛欠乏餌に塩基性炭酸亜鉛を添加した飼料）および超純水を与えて飼育した。なお、各飼料は、（株）日本クレアに調製を依頼したものを使用した。各々のマウスについて、１週間の飼育の後、エーテル麻酔下において、臓器の摘出を行った。摘出した肝臓や膵臓を HEPES 緩衝液中にてホモジナイズし、その後、５回の遠心操作（50×g 7 分、1,000×g 10 分、9,000×g 10 分、30,000×g 30 分、105,000×g 65 分）により非破壊細胞、核画分、ミトコンドリア画分、リソソーム画分、ミクロソーム画分およびサイトゾル画分の６つの画分に分離した。分離した各画分は、秤量した後に凍結乾燥し、分析試料とした。なお、膵臓については、その大きさが小さいため、８個体分を合わせてホモジナイズおよび遠心操作を行って、分析試料とした。

２－２　照射および測定

凍結乾燥した各画分をポリエチレン袋で二重封入または三重封入し、照射試料とした。標準試料には、NIST SRM 1577b Bovine Liver および原子吸光分析用 Mg 標準溶液の一定量をろ紙上に滴下し乾燥さ

研究施設・装置
　JRR-3 気送照射設備(PN-1, PN-3)
　JRR-4 気送管および T パイプ

研究分野
　生体試料の放射化分析

せたもののそれぞれを、ポリエチレンで二重封入または三重封入したものを用いた。

熱中性子照射は、JRR-3M または JRR-4 において、目的元素に応じて２種類の照射を行った。すなわち、短寿命核種により定量する元素については、JRR-3M 放射化分析用照射設備（PN-3）または JRR-4 気送管にて１分間の照射を行った。まず、Mg、Cl および Cu の定量を目的として、照射２～10 分後に高純度 Ge 半導体検出器にて 120～300 秒間のγ線スペクトロメトリーを行い、次に、Na および Mn の定量のため、１回目の測定から 60～150 分後に、再度、250～600 秒間の測定を行った。

また、長寿命核種により定量する元素（Fe、Co、Zn、Se および Rb）の放射化のために、JRR-3M 気送照射設備（PN-1）にて 20 分間の照射または JRR-4 T-パイプにて 30～40 分間の照射を行い、10～60 日後に 3～48 時間のγ線測定を行った。

（３） 結果および考察

３－１ 肝臓

肝細胞の各細胞成分中の亜鉛濃度の分析結果を図１に示す。

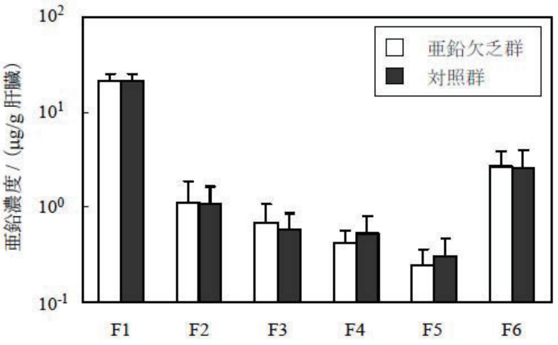

図１　８週齢から１週間飼育したマウス肝臓の各細胞成分中における亜鉛濃度；F1：非破壊細胞、F2：核画分、F3：ミトコンドリア画分、F4：リソソーム画分、F5：ミクロソーム画分、F6：サイトゾル画分

以前に行った、本研究と同条件で飼育したマウス肝臓中亜鉛濃度の分析結果では、８週齢から１週間飼育した場合において、亜鉛欠乏群の亜鉛濃度がわずかに低下していた。しかし、今回、分画していない肝臓と同様に考えることができる非破壊細胞の定量値について見ると、両群間に有意な差を認めることはできなかった。これは、複数の肝臓についての分画操作を完全に同じように行うことは困難であるため、もともとわずかであった差をとらえることができなかったためと考えている。

また、その他の細胞成分においても亜鉛欠乏群と対照群の間で亜鉛濃度に有意な差を認めることはできなかった。一方、過去に行った実験結果より、８週齢から３週間飼育したマウスの肝臓について、本研究と同様の実験を行ったとき、亜鉛欠乏群では対照群と比べて、ミトコンドリア、ミクロソーム、サイトゾルの３つの画分で亜鉛濃度の減少が見られることがわかっている。このことから、飼育１週間の時点では肝臓の各細胞成分中では、亜鉛濃度の変化は起こっていないか、または非常にわずかなものであるが、亜鉛欠乏状態の期間が長く続くにつれ、サイトゾル画分などで亜鉛濃度が減少していくと考えられる。

次に、肝細胞の各細胞成分中のコバルト濃度の分析結果を図２に示す。

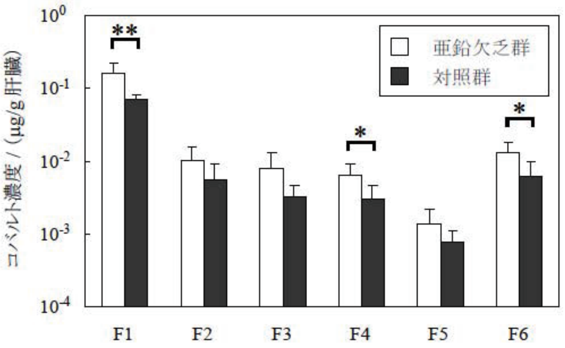

図２　８週齢から１週間飼育したマウス肝臓の各細胞成分中におけるコバルト濃度；F1：非破壊細胞、F2：核画分、F3：ミトコンドリア画分、F4：リソソーム画分、F5：ミクロソーム画分、F6：サイトゾル画分

コバルト濃度は、亜鉛欠乏群の非破壊細胞、リソソーム画分、サイトゾル画分において有意な濃度増加が見られた。また、その他の画分についても有意水準には達しなかったが、どの画分においても亜鉛欠乏群で濃度の増加傾向が見られた。以前に行った８週齢から３週間飼育したマウスの肝臓の分析においては、全ての画分で亜鉛欠乏群でのコバルト濃度の有意な増加が見られた。亜鉛欠乏群間および対照群間で、１週飼育時の定量値と３週飼育時の定量値とを比較したところ、飼育週によるコバルト濃度の変化は両群ともほとんど見られなかった。このことから、1 週飼育時にも全ての画分において亜鉛欠乏群でコバルト濃度の増加が起きていると考えられる。本実験において有意差の見られなかった核画分などについても、分析試料数をさらに増やすことにより、有意差が確認できると考えられる。また、肝臓の全分析においては、３週飼育した亜鉛欠乏群では１週飼育のものよりもわずかにコバルト濃度の増加が見

られていた。しかし、今回行った実験においては、どの画分においても１週飼育と３週飼育の間で濃度差を見出すことはできなかった。これは、分画操作を行ったことにより、分析試料として供することができる試料が少なくなったことや、試料間のばらつきが大きくなったためだと考えられる。

生体内に存在するコバルトの化学形としては、コバラミン等のビタミンB 群の形で存在するか、あるいは無機イオンとしてタンパク質と結合して存在していることが考えられる。コバルトを含む酵素としてはトランスカルボキシラーゼやアミノペプチダーゼなどがあるが、酵素活性に必要なのは他の金属であることから、今回の実験結果とこれら酵素との間の関係を議論することは難しいであろう。また、Zn^{2+}を Co^{2+}に置換した場合に、活性を保つあるいは活性を増大させる亜鉛酵素が数多く報告されている。さらに、微生物起源の亜鉛酵素の中には、添加したCo^{2+}が酵素中の Zn^{2+}と置換することなく取り込まれて、酵素を活性化させるものも知られている。このことから、食餌中の亜鉛が欠乏した場合には、コバラミンが食餌から積極的に取り込まれたり、体外への排出が抑制されたりするというよりは、亜鉛結合タンパク質中の亜鉛とコバルトが置換する、あるいはコバルトが付加することにより、その酵素活性を維持または上昇させるなどの働きをしている可能性が考えられる。亜鉛酵素中の亜鉛と置換が起きた場合には亜鉛濃度が減少することが考えられるが、肝臓中のコバルト濃度は亜鉛濃度の 100 分の 1 以下であるため、仮に増加したコバルトの全てが亜鉛と置換した場合においても、亜鉛濃度の減少を検出することは難しいと考えられる。また、亜鉛濃度が減少していない段階においてもコバルト濃度が増加していることから、細胞内の亜鉛濃度を保つための調節機能にコバルトが関与している可能性も考えられる。

３－２　膵臓

膵細胞の分析は、実験の章で記したように、その臓器の小ささのため、８個体分を１試料として分析を行った。再現性が得られた結果として、可溶性タンパク質が存在するサイトゾル画分では、亜鉛欠乏群の亜鉛濃度が低下し、コバルトの濃度が増加していた。可溶性画分以外の画分については、亜鉛濃度はミクロソーム画分を除く5画分において、亜鉛欠乏群で対照群のそれよりも減少していた。そのほかの元素については、有意な差を見ることができなかった。サイトゾル画分には多くのタンパク質が存在することから、サイトゾル画分中のタンパク質構造に何らかの構造変化が起こる可能性が示唆された。その考えられる可能性としては、亜鉛結合タンパク質の消失、亜鉛が遊離したアポタンパク質として存在、亜鉛と他の金属との置換がある。

そこで、サイトゾル画分中のタンパク質について、SDS-PAGE や２次元電気泳動の他、ゲルクロマトグラフィーによる分子サイズ別の分離と分離した各フラクションの分析等に着手した。今後は、これらの結果を踏まえて、食餌中の亜鉛不足と膵臓中の金属タンパク質の変化との関係を検討していく予定である。

（4）　研究成果

学会発表

1　川島美智子、上島淳慈、松下和馬、皆吉龍二、野口基子、菅沼英夫、矢永誠人、「亜鉛欠乏マウスすい臓細胞中の微量元素濃度の定量」、2006 日本放射化学会年会・第 50 回放射化学討論会（2006 年 10 月　水戸、東海）.

2　上島淳慈、小木貴憲、皆吉龍二、川島美智子、衣川信之、菅沼英夫、野口基子、石川勝利、世良耕一郎、矢永誠人、「亜鉛欠乏マウス肝細胞成分中における微量元素濃度および金属タンパク質の変化」、2006 日本放射化学会年会・第 50 回放射化学討論会（2006 年 10 月　水戸、東海）.

3　村松　航、上島淳慈、川島美智子、山野　喜、菅沼英夫、野口基子、矢永誠人、「亜鉛欠乏初期におけるマウス肝臓中の微量元素濃度の変化」、2007 日本放射化学会年会・第 51 回放射化学討論会（2007 年 9 月　静岡）.

4　村松　航、上島淳慈、川島美智子、山野　喜、菅沼英夫、野口基子、矢永誠人、「亜鉛欠乏初期におけるマウス肝臓中の微量元素濃度およびタンパク質の変化」、2008 日本放射化学会年会・第 52 回放射化学討論会（2008 年 9 月　広島）.

Publications

1　J. Kamishima, T. Ogi, R. Minayoshi, N. Kinugawa, H. Suganuma, M. Noguchi, K. Ishikawa, M. Yanaga, "Determination of trace elements in hepatocyte of zinc deficient mice by means of INAA", *J. Radioanal. Nucl. Chem.* , **272**, 419-422(2007).

3-12

3-13

放射化分析法を用いた樹木年輪解析による金属元素の環境動態

人間環境大学　片山幸士 、長井正博、青木　達
京都大学 大学院農学研究科　岡田直紀
東京農工大学 留学生センター　川端良子

Environmental Investigation of Metallic Elements by Dendrochronology with Activation Analysis

Yukio Katayama[1], Masahiro Nagai[1], Toru Aoki[1], Naoki Okada[2], Yoshiko Kawabata[3]
[1]The Division of Human Environment, University of Human Environments, [2]Graduate School of Agriculture, Kyoto University, [3]International Center, Tokyo University of Agriculture and Technology

愛知県北設楽郡の津具鉱山は金鉱山として知られ1600年ころから操業を始めた。金の副産物として出てくるSbの採掘と製錬も行われていた。鉱山は1930年代に活動が最も盛んで、1956年に閉山した[1)]。現在はスギとヒノキが植林され過去の姿を伺うことはできない。

Sbは毒性を持つ元素として知られており、石田と片山は滋賀県米原町にあるSbの製錬工場周辺のSb汚染を調査し周辺住民の健康被害について警告した[2)]。

津具鉱山周辺に現在どのくらい Sb が存在するか過去からの経過をふまえて明らかにすることは産業考古学的観点からも重要である。

樹木の年輪中に取り込まれた微量元素や放射性物質は周辺土壌の濃度を反映することから樹木年輪ごとの物質量を測定することで過去の環境の変遷を解明できる可能性を持つ。この樹木年輪解析法により鉱山周辺の Sb 濃度の変遷を調べた。Sb の定量には高感度で検出可能な中性子放射化分析法を用いた。

一部はすでに報告しているが[3)]、新しく測定結果も得られたので加えて報告する。

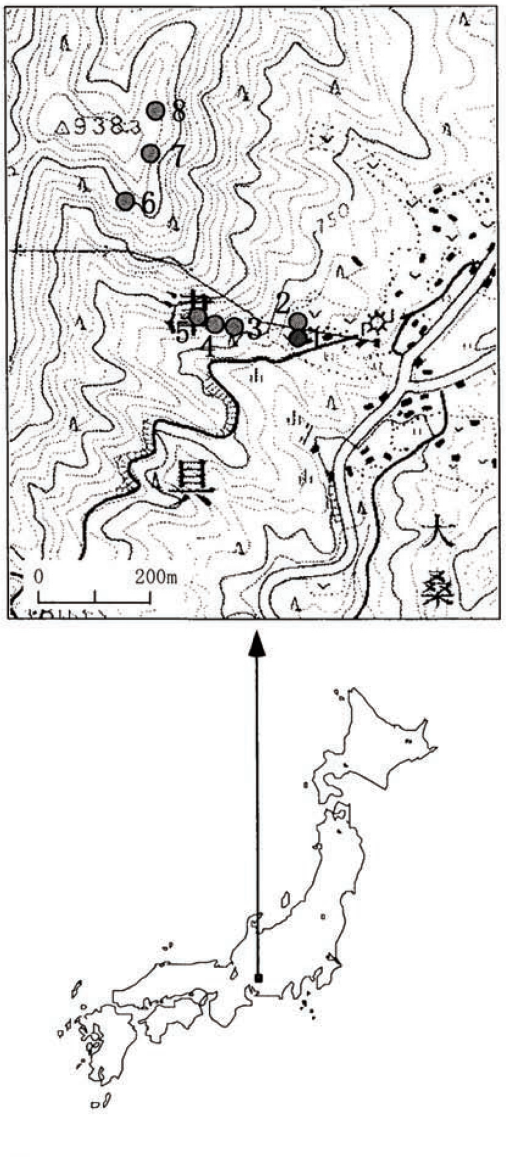

Fig. 1. Locations of sampling points.

実験

試料

津具鉱山の試料採取地点を Fig. 1 に示すとともに、Table 1 に各地点の目印等と標高を示した。土壌試料は2006年と2007年に地表から10 cmの深さから採取した。Sb の最大濃度が検出された地点で Sb の深度分布を見るため5cm間隔で深さ50cmまで土壌を採取した。予備実験と鉱山跡地の Sb 濃度を比較するため Sb の汚染は考えられない人間環境大学構内の演習林から2004と2005年に土壌を採取した。

JRR-4　TパイプA系統　　環境科学

Table 1. Sampling points

Point No.	Note	Altitude(m)
1	side of a woodland path	730
2	near wreckage of the structure	740
3	near wreckage of the structure	740
4	near the beginning of the second tunnel	750
5	near the beginning of the third tunnel	760
6	near the basset	885
7	near the small shrine	910
8	near the top of hill	930

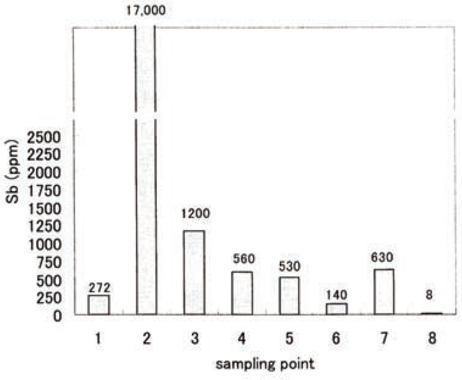

Fig.2. Concentrations of Sb in the soil.

土壌試料は 105℃で 24 時間乾燥した。荒く砕き、500μm メッシュのふるいを通した後、酸化アルミニウムの乳鉢で細かく砕いた。

樹木試料は成長錐(HagrofSweden AB 製、長さ 30cm、コア径 5.5mm)を使用し、ヒノキとスギ樹幹部から 2006 年と 2007 年に採取した。採取した試料は 105℃で 24 時間乾燥した後、辺材と心材に分け形成層側からそれぞれ約５年輪ごとに切り分けた。

樹皮試料は 105℃で 24 時間乾燥した後、細片化した。

Sb の定量

土壌試料は約 50mg 、樹木試料は 300-400mg 、樹皮は 200mg を精標しポリエチレンの袋に入れ密封し照射試料とした。中性子照射は、日本原子力研究開発機構の JRR-4 のＴパイプＡ系統（中性子束 5.3 x 10^{13} n cm^{-2})で 20 ないし 30 分間行った。^{122}Sb と ^{124}Sb のγ線測定は、照射約７日後から 7,000 秒間行った。

Sb の定量は、原子吸光分析用標準試料をろ紙上に一定量滴下し乾燥したのち、ポリエチレンシートで密封し試料と同じように照射して試料のγ線と比較した。

結果と考察

土壌中のＳｂ濃度

鉱山跡地のＳｂ濃度分布

津具鉱山跡地の土壌中の Sb 濃度を Fig. 2 に示す。Sb 濃度は採取場所により 8 ppm から 17,000ppm と大きく異なった。採取地点２で最大値を示し斜面の頂上に近づくにしたがい、その濃度は減少した。地点８の値を除き愛知県岡崎市本山町にある人間環境大学演習林の土壌中の Sb 濃度（1 – 2 ppm）より高い値となった。Sb で汚染されていない土壌の Sb 濃度は文献値で 0.2 – 2 ppm と報告されている [4)]。

地点２に近い地点１で Sb は 270 ppm となったがこの地点は森林の保守に利用する林道の傍である。従って鉱山閉山後撹乱されたため地点２の値に比べ低い濃度になったと考えられる。

Sb の深度分布

土壌中の Sb が最高濃度を示した地点２の周辺を詳細に調べた。地表より 50 cm の深さまで掘り下げ Sb の濃度変化を調べた。5 cm 刻みで測定した Sb 濃度を Fig. 3 に示す。地表近くで 300-390 ppm あった Sb が深度を増すにしたがいその濃度は減少した。この結果は過去になんらかの人工的影響があったことを示唆している。すなわち、製錬工場から Sb が飛散し地表に集積して現在もその影響が残っていると推測できる。

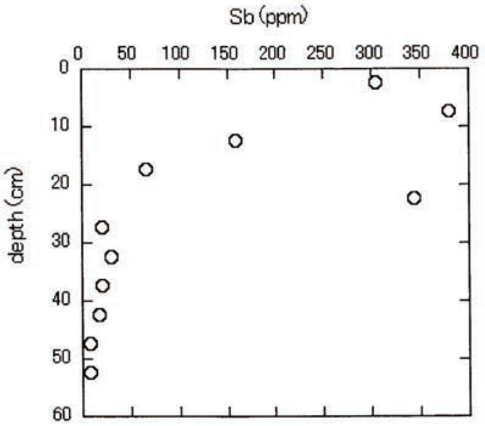

Fig. 3. Distribution of Sb in the soil at point 2.

採取地点２周辺のSb分布

採取地点２を中心にして西、北、南西方向に10 m間隔で土壌試料を採取した。結果をTable２に示す。

西側方向に沿ってSb濃度が高濃度になった。この測定地点の周辺には地点２と同様な工場の残骸が残っていた。この場所でも製錬の影響を受けたものと思われる。

Table 2. Concentrations of Sb in the soil around point 2 (ppm)

Distance from the center (m)	Westward	Northward	Northeastward
0		610 ± 5	
10	2920 ± 10	100 ± 2	860 ± 6
20	2290 ± 9	220 ± 3	1040 ± 6
30	5140 ± 14	9 ± 1	540 ± 4
40	90 ± 2	15 ± 1	19 ± 1
50	30 ± 1	12 ± 1	-

樹木年輪中のSb分布と樹皮のSb濃度

ヒノキ年輪中のSb分布

異なる５地点で生育したヒノキ年輪中の Sb 分布をFig. 4に示す。各番号は土壌を採取した地点の番号に対応している。Sb濃度は最も外側の年輪で最大値を示し、辺心材境界に向け減少したのち心材部でほぼ一定値となった。土壌試料のSb濃度が最も高かった地点２で生育したヒノキの Sb 分布は他の曲線と似たパターンが得られたが、Sb濃度は全体的に高く他の試料と比べ５倍程度の値となった。

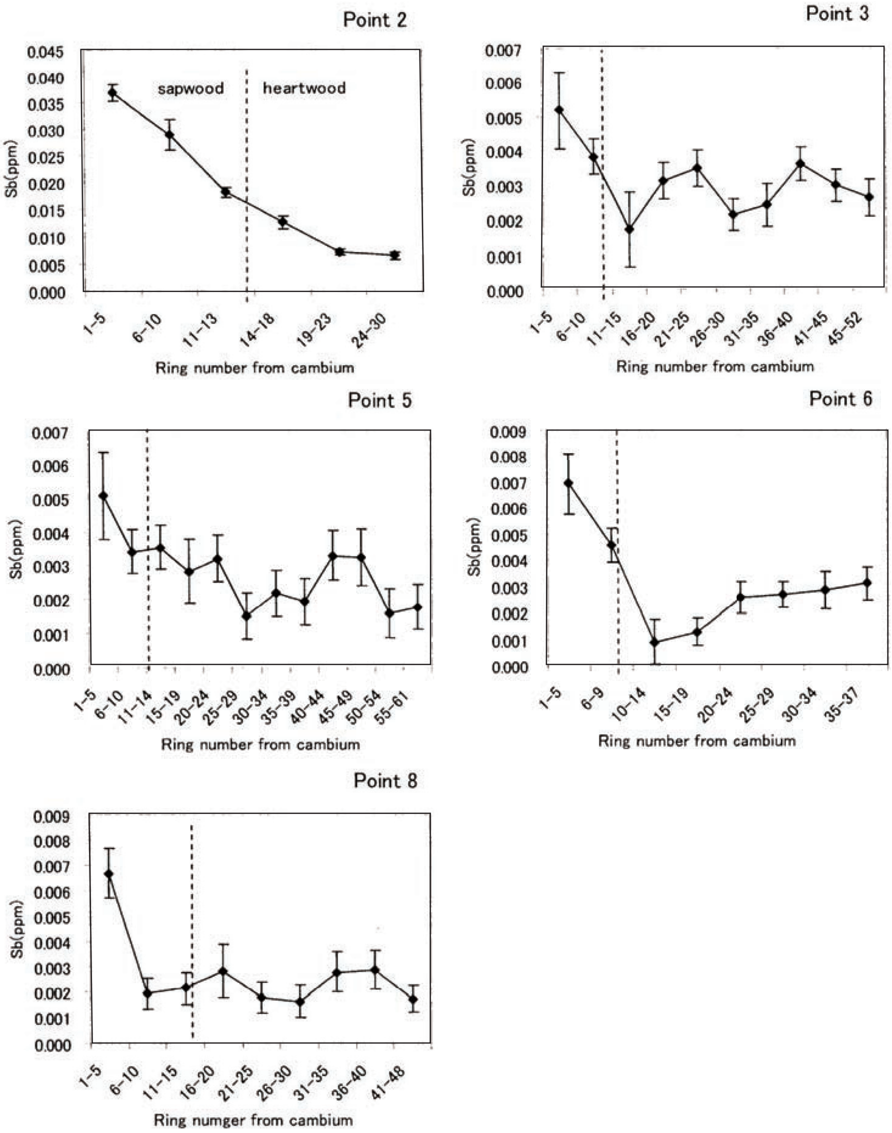

Fig. 4. Distribution of Sb concentrations in hinoki stems.

スギ年輪中の Sb 分布

Figure 5 に３本のスギ年輪中の Sb 分布を示す。番号はヒノキと同様土壌採取地点の番号に対応している。３樹木年輪の分布曲線のパターンはそれぞれ異なり、ヒノキのそれとも異なった。地点２の試料ではヒノキと同様 Sb 濃度が他の試料に比べ全体的に高い値となった。

これらの結果を総合すると、この年輪解析法で津具鉱山跡の過去の Sb 環境変動を評価することは困難であることが分かった。

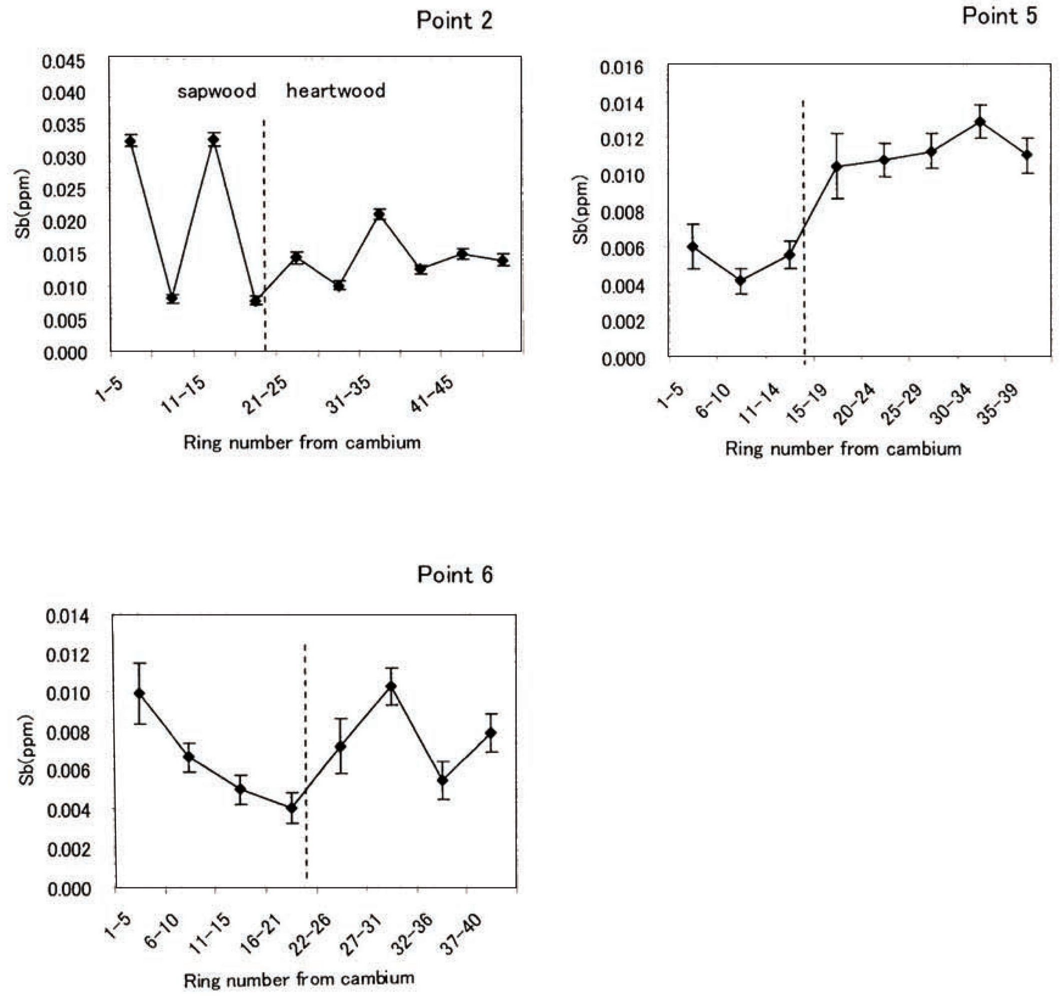

Fig. 5. Distribution of Sb concentrations in sugi stems.

3-13

ヒノキおよびスギ樹皮中の Sb

ヒノキおよびスギ樹皮中のSb濃度をTable 3に示す。地点２と地点３に生育する樹皮中の Sb 濃度は他の地点で得た樹皮中の濃度に比べ高い値を示した。この結果は樹木が生育する土壌環境を反映していると見なすことができる。すなわち樹皮はバイオモニターとしての可能性がある。

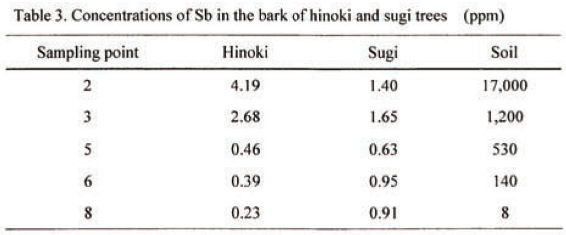

Table 3. Concentrations of Sb in the bark of hinoki and sugi trees (ppm)

Sampling point	Hinoki	Sugi	Soil
2	4.19	1.40	17,000
3	2.68	1.65	1,200
5	0.46	0.63	530
6	0.39	0.95	140
8	0.23	0.91	8

結論

津具鉱山跡地の８地点の土壌中 Sb 濃度は 8 - 17,000 ppm となった。製錬工場の基礎部分と思われる残骸が残っている地点２の表層土壌中の Sb は、17,000ppm と極めて高い値を示し深さとともに減少した。このことは過去に製錬工場が存在し操業していたことを明らかにするものである。このように製錬工場周辺土壌中の Sb濃度が高いことから操業当時製錬作業に従事した者のなかには多量の Sb にさらされた者がいたと推察される。現在も Sb の汚染に注意が必要である。

また、Sb はヒノキやスギに取り込まれにくく高感度の放射化分析法で定量したにもかかわらず検出限界に近く明瞭な傾向は得られなかった。この結果から年輪解析法で津具鉱山の Sb 環境を過去に遡って推定することは困難であることが分かった。

謝辞

放射化分析に関する指導助言を頂き、また測定にご助力いただいた東京大学大学院工学系研究科原子力専攻共同利用管理本部（大学開放研究室）のスタッフの方々に感謝の意を表します。

文献

1. 藤城豊： 津具金山、私本(1982)
2. 石田紀郎、片山幸士：アンチモンによる環境汚染、科学、**48** (1978) 509
3. Y. Katayama, A. Misawa, N. Yamada, S. Yachi, H. Muto, T. Aoki, Y. Kawabata, and M. Nagai: Analysis of Antimony Around the Abandoned Tsugu Mine in Aichi Prefecture by Neutron Activation Analysis, Journal of Radiochemical and Nuclear chemistry, **278** (2008) 283
4. 浅見輝夫：日本土壌の有害金属汚染、アグネ技術センター (2001)263.

成果の公表

Y. Katayama, A. Misawa, N. Yamada, S. Yachi, H. Muto, T. Aoki, Y. Kawabata, and M. Nagai, Analysis of Antimony Around the Abandoned Tsugu Mine in Aichi Prefecture by Neutron Activation Analysis, Journal of Radiochemical and Nuclear chemistry, **278** (2008) 283

3-13

3-14

サンゴ骨格中のハロゲン元素の放射化分析

Instrumental Neutron Activation Analysis of Halogen in Coral Skeletons

大出　茂、田中健太郎

S. Ohde, K. Tanaka

琉球大学理学部

Faculty of Science, University of the Ryukyus

1.　はじめに

サンゴ骨格（結晶形：アラゴナイト、主成分：$CaCO_3$）中のできるだけ多くの元素分析から、サンゴが生育していた環境水についての情報を得ることが本研究の目的である。サンゴ骨格への陰イオン共沈機構を解明することによって、サンゴが生育していた環境水の情報を得ることが可能である。1 価陰イオンの $CaCO_3$ への共沈が、つぎのイオン交換で起こると仮定すると、$CaCO_3 + 2A^- = CaA_2 + CO_3^{2-}$（$A^-$は１価陰イオン）、その平衡定数は、$K = [CaA_2][CO_3^{2-}]/[CaCO_3]/[A^-]^2$ と書ける。そして、$[CaA_2]/[CaCO_3]=K[A^-]^2/[CO_3^{2-}]$ と変形できる。したがって、サンゴ骨格中の陰イオン含量は、サンゴが生育した海水の炭酸イオンと陰イオンの比によって決定される可能性がある（サンゴの酸不溶解部は 0.1%以下であり、イオン交換を仮定することは可能である）。アラゴナイト結晶へフッ化物イオン（F^-）2 個が炭酸イオン 1 個のサイトへ置換する可能性はある。しかし、塩化物イオンより大きいハロゲンはフッ化物イオンよりイオン半径が大きいので、炭酸イオン 1 個に対して 2 個の置換はむずかしいかもしれない。そこで、サンゴ骨格中のハロゲン元素を定量する意義がある。平成１８年度から２０年度までの３年間、JRR-3 原子炉を使ってサンゴ試料中のハロゲンの放射化分析を PN-3 気送管照射、ガンマ線測定装置を使って行った。本研究では、試料としては、沖縄、和歌山、タイ、ポナペ、フィリピンのサンゴ礁で採取したサンゴ骨格のフッ素の放射化分析をおもに行った。

2.　サンゴ試料

炭酸塩標準として地質調査所が作成した JCp-1(サンゴ)、JDo-1(ドロマイト)を使用した。サンゴ骨格試料は沖縄（ルカン礁、水釜）、堺（和歌山）、タイ（カンカオ島）、フィリピン（セブ島）、ポナペのサンゴ礁から採取し、ミリキュウ水で数回、超音波洗浄し、乾燥して準備した。

3.　ハロゲンの放射化分析

サンゴは主成分が炭酸カルシウム(約 97%)であり、^{49}Ca および ^{47}Ca を内部標準としてして使用し、次の照射、測定条件によって非破壊放射化分析を行った。PN-3(JRR-3M)照射:サンゴ中のフッ素をおもに定量するために、サンゴ試料（粉末またはブロック状）30-50mg をポリ袋に封入、高純度ポリエチレン照射用キャプセルに 1 試料入れ、PN-3 気送管で 15 秒照射、6-7 秒間の冷却時間をおき、キャプセルを開封しないで、ガンマ線スペクトロメーターを用いて 15 秒間測定を行い、F　(^{20}F;

研究施設と装置

JRR-3(PN-3、気送管)

研究分野

環境化学、海洋地球化学

1633 keV)とAl(^{28}Al; 1779 keV)を定量した。標準はフッ化カルシウムを炭酸カルシウムに混合させて作成した。さらに、30-90分の冷却時間をおき、5分間測定を行い、Na、Cl、Mn、Sr、Iが分析可能であった。

4. 結果と考察

炭酸塩標準（JCp-1、JDo-1）をサンゴの放射化分析の比較標準として使用することが可能かを検討する目的で、標準試料の分析を表1に示すように10回以上繰り替えし放射化分析した。JCp-1、JDo-1のフッ素分析値はそれぞれ、764 ppm、279 ppmである（表1）。また、放射化分析の信頼性をチェックする目的で、試料を陽イオン交換樹脂を使って溶解し、フッ化物イオンをイオンクロマト法を使って分析した。さらに、試料を希塩酸に溶解後、アルフッソンをつかって発色させ、フッ素を比色分析法によって定量した。表1にその結果をまとめた。化学分離操作を伴う分析法を使ったフッ素の分析データは放射化分析によって得られたデータと比較して少し小さな値を示した。JCp-1は、石垣島から採取したハマサンゴから作成されているので、サンゴのフッ素分析用の標準物質として最適であると思われる。しかし、表1に示したように、JCp-1中のフッ素含量を正確に決定するまでには本研究では至らなかった。今後、分析回数を増やすなどして、信頼性の高いデータを得ることによって、JCp-1を放射化分析の標準試料とするようにしたい。

本研究では、特に、サンゴ中のフッ素含量から、サンゴが生息していた環境水の化学組成を推定することを試みた。海水からアラゴナイトへのフッ化物イオンの共沈は次のイオン交換反応式で起こることが知られている(Ichikuni 1979)。

$$CaCO_3(s) + 2F^-(aq) = CaF_2(s) + CO_3^{2-}(aq)$$

$$K_F=[CaF_2][CO_3^{2-}]/[CaCO_3][F^-]^2$$

上式は、海水のフッ化物イオンと炭酸イオンの比が、炭酸塩に共沈するフッ化物イオン量をコントロールすることを示している。さらに、海水の炭酸イオンは、pHと関係する。したがって、海水のpHおよび二酸化炭素に関する情報が得られる可能性がある。そこで、サンゴ殻のフッ素の正確な定量が重要である。そこで、和歌山（堺）沖縄（ルカン礁、水釜）、タイ（カンカオ島）、フィリピン（セブ島），ポナペ島のサンゴ礁から採取し、準備したサンゴ骨格試料の放射化分析を行った結果を表2に示す。

サンゴ骨格のフッ素含量とサンゴが成育した海域の炭酸イオン濃度の関係を考察するために、サンゴを採取した海域の炭酸イオン濃度を以下の方法で計算することが可能である。塩分、アルカリ度、pCO_2の値を一定（塩分 35psu, アルカリ度 2.3 mmol/kg, pCO_2 = 360 μatm）として、海水の温度を18 ℃から30 ℃まで1 ℃毎に変化させ、大気二酸化炭素（360 ppm）が1気圧下で海水と化学平衡にあると仮定し、海水中の炭酸イオン濃度が計算できる。海水中の炭酸イオン濃度は海水温の上昇とともに増加する傾向がある。海水中のフッ化物イオンは保存性成分であるので、その濃度は塩分35 psuに対し68 μMである。よって、$[F^-]^2{}_{(aq)}/[CO_3^{2-}]_{(aq)}$は温度の上昇に伴い減少する。生育海域の海水温が高いほど、海水中の炭酸イオンとフッ化物イオンの濃度比が小さくなる。したがって、上式からサンゴの生育海水の温度が高いほどサンゴ骨格中のフッ素含量が小さくなる傾向が予測される。サンゴ骨格の成長率はおよそ1 cm/yrなので，試料に用いた骨格が形成されたのは採取以前の約1年間である。採取地ごとにこの期間の1ヶ月毎の平均海水温をアメリカ海洋大気局(http://www.noaa.gov/wx.html)の人工衛星で観測した表面海水の温度のデータを用いて、生育期間の年平均海水温と海水の炭酸

イオン濃度を計算し、 表3及び図1に示す。サンゴが生育した海水の温度が低いほど骨格中のフッ素含量が大きい可能性があり，表3の温度データからポナペ，カンカオ，セブ，水釜，ルカン礁，堺港のサンゴ試料の順にフッ素含量が大きくなることが予想される．表3にまとめたフッ素含量の平均値は，ポナペとカンカオの順がいれかわっている以外は，セブ，水釜，ルカン礁，堺港の順に大きな値を示し，ほぼ予想どおりである．

サンゴ骨格に共沈したフッ素含量を測定し，フッ素含量とサンゴが生育した海域の炭酸イオン濃度の関係を考察した。その結果、サンゴ骨格のフッ素含量は海水中の炭酸イオン濃度に反比例する傾向を示した（図1）。また，海水と大気間の二酸化炭素平衡を仮定した計算の結果、海水中の炭酸イオン濃度は海水の温度の累乗に比例して変動すると計算できる。

5、今後の方針

本研究は、おもにフッ素の放射化分析について行われた。フッ素、塩素、臭素、ヨウ素などハロゲン元素の微量分析に関して実用的で最適な機器分析法は確立しているとは言えない。ここで示したように放射化分析はそれらの元素の便利な分析法の 1 つである。また、陽イオン元素や遷移元素に関しては、琉球大学に設置されているICP-MSを使って、放射化分析をおこなった同じサンゴ試料について、できるだけ多くの元素の定量を行う予定である。そして、データを比較検討し、サンゴが生息していた環境水の化学組成との関係を考察する予定である。

6、引用文献

(1) Aizawa S., AkaiwaH. Bull. Chem. Soc. Japan, 68(1995)825

(2) Ando A. et al., Bull. Geol. Surv. Japan,41(1990)27

(3) Ichikuni M. Chem. Geol. 27(1979)207.

(4) Ichikuni M., Tsurumi M., Anal. Sci., 6(1990) 111

(5) Ramos A. A. et al., J. Radioanal. Nucl. Chem., 257(2003)441

7、成果の公表

(1) 大出茂、吉村和久（2006）「炭酸塩の地球化学」によせて、地球化学、40，177-178

(2) 田中健太郎,大出茂（2007）サンゴ骨格中のフッ素含量と海水中の炭酸イオン濃度の関係，日本海水学会誌, 61, 118-122

(3) 大出茂（2007）サンゴの化学像を通してみる海洋環境の変遷，海洋化学研究, 20, 54-77

(4) Hossain, M. S., Ohde, S., Tanaka. K., Sirirattanachai, S., Snidvongs, A. (2008) Oxygen isotope composition in *Porites* coral from the Northern Gulf of Thailand: an implication for its skeletal growth. Bull. Soc. Sea Water Sci., Jpn., 62, 112-113

(5) Bogan, R. A. J., Ohde, S., Arakaki, T., Mori, I., McLeod, C. W. (2009) Changes in Rainwater pH associated with increasing atmospheric carbon dioxide after the industrial revolution. Water Air Soil Pollut., 196, 263-271

表1．炭酸塩標準のフッ素の分析結果（ppm）（括弧の数値は分析回数）

Code No. (Material)	INAA	IC	Spectrophotometry	Literature value
JCp-1 (coral)	764 ± 41 (18)	759 ± 7 (6)	699 ± 13 (3)	808 ± 67 (8)[5]
JDo-1 (dolomite)	279 ± 18 (11)	249 ± 6 (6)	186 ± 4 (2)	214-260[2]

表 2.　サンゴ試料のフッ素分析結果（ppm）

Sample[*1]	Location	Genus	F (ppm)
88031201	Pohnpei	*Porites*	758
88031202	Pohnpei	*Porites*	688
880313	Pohnpei	*Porites*	693
981101	Khang Khao	*Porites*	526
981102	Khang Khao	*Porites*	832
981103	Khang Khao	*Porites*	620
01031501	Khang Khao	*Porites*	667
01031502	Khang Khao	*Porites*	720
01031503	Khang Khao	*Porites*	698
03040406	Cebu	*Porites*	719
030405031	Cebu	*Pocillopora*	790
03040403	Cebu	*Pocillopora*	743
03040404	Cebu	*Porites*	677
03040405	Cebu	*Porites*	756
03040406	Cebu	*Porites*	552
03040407	Cebu	*Porites*	668
03040409	Cebu	*Porites*	864
03040410	Cebu	*Foliose*	636
03040501	Cebu	*Porites*	843
00070401	Mizugama	*Porites*	814
00070402	Mizugama	*Porites*	840
00070502	Mizugama	*Porites*	796
00071601	Mizugama	*Porites*	724
00071901	Mizugama	*Porites*	780
00071902	Mizugama	*Porites*	797
00071903	Mizugama	*Porites*	749
00071904	Mizugama	*Porites*	824
00081103	Mizugama	*Porites*	651
00081208	Mizugama	*Porites*	725
00081209	Mizugama	*Porites*	850
03073101	Rukan-sho	*Porites*	839
03073102	Rukan-sho	*Porites*	917
03073104	Rukan-sho	*Pocillopora*	896
03073105	Rukan-sho	*Porites*	896
03073106	Rukan-sho	*Pocillopora*	737
03073103	Rukan-sho	*Acropora*	826
83021621	Sakai port	*Fungia*	801
83021622	Sakai port	*Porites*	815
83021623	Sakai port	*Acropora*	1060
83021624	Sakai port	*Acropora*	1070
83021625	Sakai port	*Acropora*	1010
83021627	Sakai port	*Acropora*	974

[*1] : Sample code gives information on sampling data,
e.g. 88031201 was collected on 12 March 1988

3-14

表 3.　サンゴ骨格中のフッ素含量の平均値と CaF_2、および海水の温度と CO_3^{2-}（計算値）

Location	Number of samples	F (ppm)	CaF_2 (μmol/g)	Sea surface temprature (□)	CO_3^{2-} (μmol/kg)
Pohnpei	3	713±32	37.5	28.7(27.5-29.8)	248
Khang Khao	6	677±93	35.6	28.4(26.3-30.1)	246
Cebu	10	725±91	38.2	28.3(25.3-30.5)	246
Mizugama	11	777±57	40.9	23.1(19.5-28.9)	216
Rukan-sho	6	852±61	44.8	22.7(20.6-30.1)	213
Sakai	6	955±108	50.3	19.6(10.5-27.6)	194

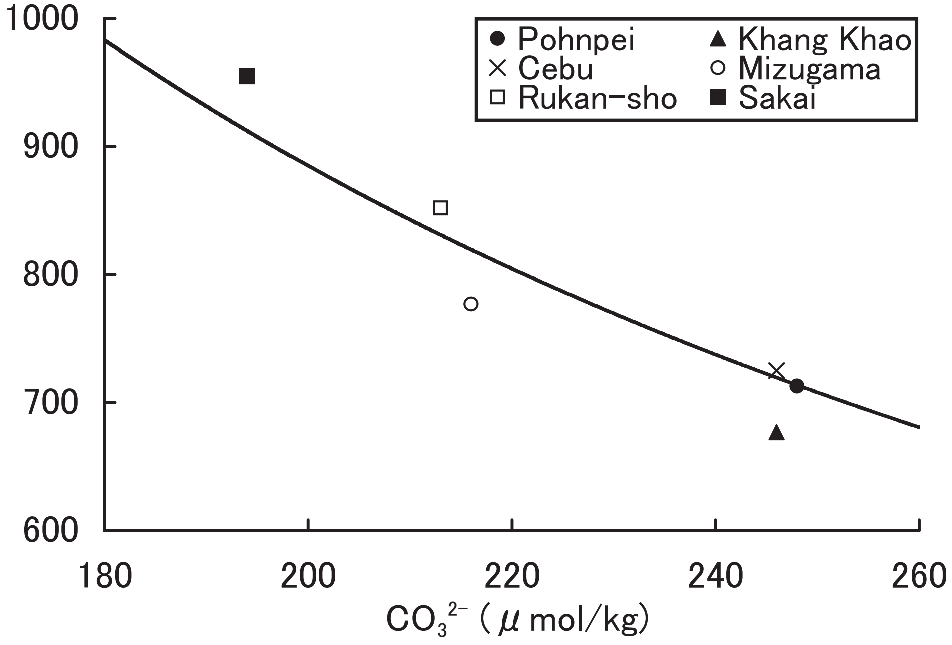

図 1.　サンゴ骨格中のフッ素含量（平均値）と海水の CO_3^{2-}濃度（計算値）の関係（$R^2 = 0.922$）

3-14

3-15

雌雄セレン欠乏における酸化ストレスと生体内微量元素動態

Dynamics of biotrace elements in selenium deficient female and male rats

遠藤和豊[1]、本田智香子[1]、松岡圭介[1]、塚田正道[2]
１昭和薬科大学薬学部、２明治大学農学部
Kazutoyo Endo[1], Chikako Honda[1], Keisuke Matsuoka[1], and Masamichi-Tsukada[2],
1 Showa Pharmacuetical University, Higashi-Tamagawagakuen, Machida, Tokyo, 194-8543,
2 School of Agriculture, Meiji University, Higashi-Mita, Tama-ku, Kawasaki 214-8581

生体の主要成分元素は酸素(O)、炭素(C)、水素(H)、窒素(N)、カルシウム(Ca)、リン(P)、硫黄(S)、カリウム(K)、ナトリウム(Na)、塩素(Cl)、及びマグネシウム(Mg)であり、それらを合わせると、体内に存在する全元素の99%以上になる。　一方、生体微量元素の体内存在量は全元素量の 1%未満であり、それらの殆どが蛋白質や酵素と結合して存在している。生体に存在する金属元素のうち、ヒトの必須微量元素として明らかにされているものはセレン(Se), 鉄(Fe), 亜鉛(Zn), 銅(Cu), マンガン(Mn), ヨウ素(I), モリブテン(Mo), クロム(Cr), 及びコバルト(Co)の 9 元素である。生体を取り巻く環境には多くの金属元素が存在し、生体にとって必須な金属元素だけでなく、有害な元素も共に、生体内へ取り込まれる可能性が極めて高い。また、たとえ、必須元素であっても、それらの元素を過剰に摂取した場合、生体に対して悪影響を与えることがある。一方、必須元素が欠乏すると生体に様々な障害を引き起こすことが知られている。このように生体微量金属元素は過剰摂取あるいは欠乏により様々な疾患の原因となることが明らかにされている。生体に存在する必須微量金属元素はその元素が単独で生体機能に関与しているだけでなく、他の元素と互いに作用し、その元素間相互作用が生理活性に影響を及ぼしている。特に Se, Fe, Zn, Cu, Mn, Co は酵素やビタミンの活性中心として存在し、生体内での酸化還元反応の調節に深く関わっている。Se は、生体内ではグルタチオンペルオキシダーゼ(GPX-Px)の活性中心で、過酸化水素(H_2O_2)の消去に関係している。GPX-Px おもに肝臓に多く存在しており、この酵素の活性が低下した状態では、肝臓は H_2O_2 を介した酸化的ストレスに曝されると考えられる。これまでの研究では、8 週齢雄性 Se-欠乏ラットの肝臓、およびその他の臓器の元素量を測定した。

本研究では、１）酸化ストレスのモデルとして雌性および雄性 Se 欠乏ラットをモデルに用いて、上記

研究施設と施設名：JRR-4　D パイプ　　　　研究分野：放射化分析、微量分析

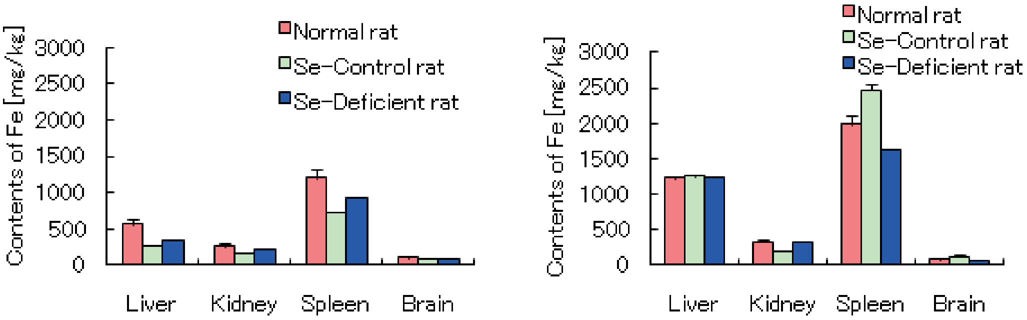

Fig. 1 肝臓、腎臓、脾臓、脳における Se 量の比較；　左）雄性ラット、右）雌性ラット

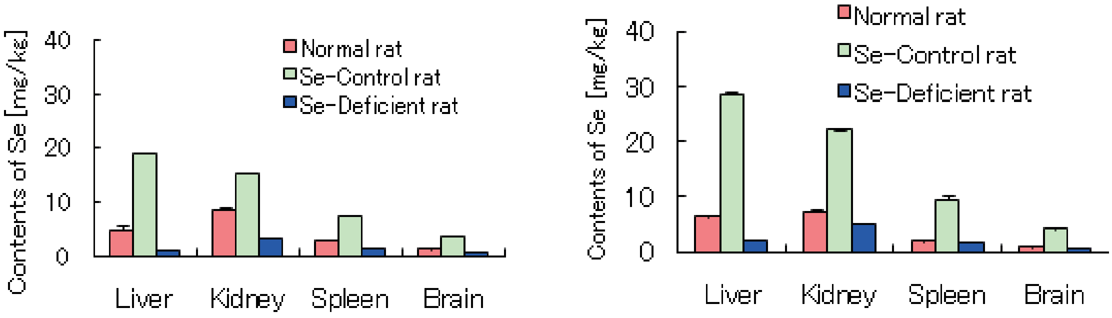

Fig. 2 肝臓、腎臓、脾臓、脳における Fe 量の比較；　左）雄性ラット、右）雌性ラット

微量元素の臓器分布と抗酸化酵素や抗酸化物質における雌雄の差異を比較検討すること、２）雄性 Se 欠乏ラットを用いて、長期間の Se 欠乏が及ぼす生体微量元素の臓器分布の変化を明らかにすることを目的にした。生体内での活性酸素の生成と消去に関わる抗酸化酵素・あるいは抗酸化物質である GPX 活性、GSH 量、SOD 活性、生体の酸化ストレスマーカーである TBARS 値、生体微量元素である Se, Fe, Co, Cu, Zn を放射化分析によって測定し、それぞれの量を比較した。

１）雌雄ラットの Se および Fe 量の取込み量

8 週齢の雌雄の正常(normal)群、Se コントロール(SeC)群、および Se 欠乏(SeD)群の肝臓、腎臓、脾臓、および脳中の Se 量を Fig.1 に示した。Se に関して雌雄を比較すると、Se 量の十分な SeC 群では各臓器とも雌性ラットのほうが、各臓器への取込みが多くなっている。これは、別に測定した GSH-Px 活性が雌性において有意に高いことに対応している。normal 群、SeC 群、および SeD 群の肝臓、腎臓、脾臓、および脳中の Fe 量を Fig.2 に示した。雌性と比較して雌性は、どの臓器も Fe 量が 1.5～2 倍程度多い。Fe 貯蔵と代謝に主要な役割をする脾臓において雌雄では異なっていた。8 週齢の雌雄ラット肝臓中の SOD 活性を測定した結果、SeC 群と SeD 群を

比較すると雄性においては両群とも有意な差はなかった。一方、雌性ではSeC群のほうが高い値が得られた。これは、雌性のほうがGSH-Px活性が高く、過酸化水素を還元するする能力が高くことと、それに伴いスーパーオキサイド（・O_2^-）から過酸化水素を生成するSOD活性が高くなっているとも考えられる。これまで、雄性について実験を続けてきて今回雌性について実験を行い、基礎データを得ることができた。雌性に関してはさらにデータの蓄積と比較が必要である。

２）長期間のSe-欠乏の影響

これまでにSe欠乏ラットの飼育開始週齢及びその飼育期間に伴い過酸化水素レベルなどの酸化ストレスに変化が生じることを明らかにしてきた。また、Se欠乏ラット及びビタミンE欠乏ラットでは共に肝臓でのFeの蓄積が観察されており、Se欠乏動物では週齢に伴うFeの動態変化も予想されている。Se欠乏の期間を延長させれば、生体に与えられる酸化ストレスに変化を生じ、それに伴い微量元素動態の変化も予想され、酸化ストレスの変化とそれに伴う微量元素動態を把握することで酸化ストレスと微量元素との関係がより明瞭になると思われる。また、長期間のSe-欠乏の影響については、これまで調べられていない。本研究では50週齢の期間に亘るSe欠乏ラット肝臓中の生体内酸化還元に関係のある微量元素（Mn, Fe, Co, Zn, Cu, Se）含量の変化を観察した。

Fig. 3には、臓器中のSe量の週齢依存性を示した。SeD群では4週齢で測定された（0.27±0.19 mg/kg, n=3）の少量を除いては、ほとんど検出限界に近い値を示した。しかし、SeはすべてのSeD群の腎臓で測定された。脾臓では、Seは4-,12-,16-, 20週齢においてはごく低いレベルで測定されたが、8-, 50-週齢では検出されなかった。正常群の臓器の中でSe量は、同じ週齢のSeD群よりもかなり高い。正常群ラットのSe量は、その速度は異なるものの、測定したすべての臓器で増加する傾向にあった。際立って高い値のSeが、50週齢正常群ラットの腎臓で測定された。Se量に密接に関連している肝臓のGSH-Pxの週齢依存（Fig.3A）と正常群ラットのGSH-Pxは相関している。

3-15

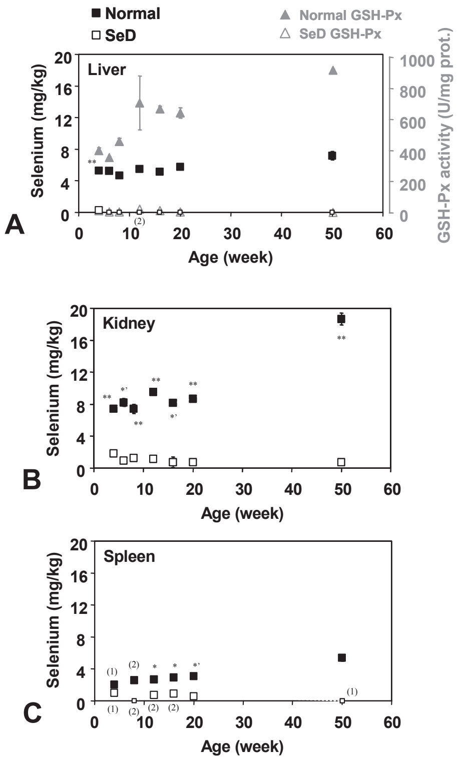

Fig.3 肝臓、腎臓、脾臓中の Se 量

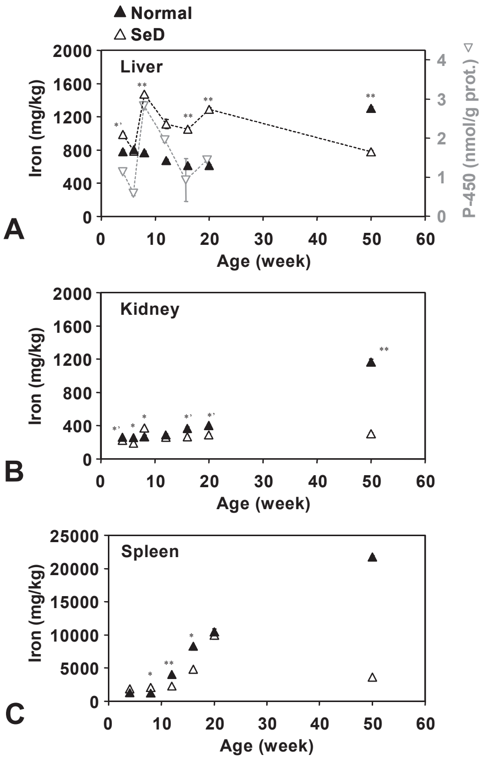

Fig. 4 肝臓、腎臓、脾臓中の Fe 量

Fig.4 にはいくつかの臓器中の Fe 量を示した。正常群ラット肝臓中の鉄量は、4 週齢で 800mg/kg から 20 週齢にかけては徐々に減少し、50 週齢では肝臓では 1300mg/kg をしめした。20 週齢よりも若い群では SeD ラット群の Fe 量は正常群よりも多いが、40 週齢の SeD ラット群では同じ週齢の正常群よりも Fe レベルは低かった。SeD 群のラット肝臓の Fe 量は週齢に依存して 780-1500mg/kg であり、その平均に依存していた。SeD ラット腎臓中の Fe 量は 190－370mg/kg であり、あまり変動は無い。一方、正常群ラット腎臓中 Fe 量は 4 週齢で 260mg/kg、50 週齢では 1160mg/kg であった。

脾臓中の Fe 量は、他の臓器よりも 1～2 桁高い値を示した。SeD 群と正常群の両方のラットの脾臓中の Fe 量は、8 週齢までは、比較的少なく、8 週齢以降に増加し始めた。正常ラット群の脾臓中の Fe は 50 週齢に至るまで増加した。20 週齢以降減少した。50 週齢の SeD 群は、正常群よりも際立って少ない量を示した。SeD ラットのシトクロム P-450 活性（Fig. 4 A）は SeD ラット脾臓の Fe 量に同期しているように見える。しかし、正常群ラット肝臓のシトクロム P-450 活性は Fe 量とは関連していないようである。

Zn は、Fe と異なり週齢に対して肝臓、腎臓、脾臓において 50 週齢に至るまで、変化が少なかった。また、正常群と SeD 群との間には著しい差はなかった。さらに臓器中の Zn 量は、生涯を通して変動は少なかった。なかでも脾臓中の Zn 量はもっとも差が少なかった。

【謝辞】　本研究を進めるにあたり、中性子照射にご協力を頂いた東京大学大学院工学研究科専門職大学院の澤畑浩之氏、川手　稔氏、石本　光憲氏に深く感謝いたします。本研究では科学研究費補助金基盤研究(C)(17590040)の一部を使用した。

【成果の公表】

学会発表等：

1)　セレン欠乏による酸化ストレスと生体内微量元素動態に関する研究　（昭和薬大）○遠藤和豊、佐久間泰亘、露木聡史、長山敦子、松岡圭介、本田智香子（放医研）松本謙一郎　第 127 回日本薬学会年会　（富山大 2007 年 3 月 28－30 日)。

2) Oxidative stress of selenium deficiency and mineral balance in rats, Y. Sakuma, K. Matsuoka, C. Honda, K. Matsumoto, K. Endo, *Int. Symp. Metallomics*, Nov.28 –Dec.1, Nagoya (2007).

国際会議 Proceeding：

１) Y. Sakuma, K. Matsuoka, C. Honda, K. Matsumoto, K. Endo: Dynamics of redox related elements (Fe, Co, Zn, and Se) and oxidative stress caused by Se-deficiency in rats. *J. Radioanal. Nucl. Chem.* **278**(2008)591-594.

論文：

1) Y. Sakuma, J. Sasaki, A. Futami, K. Yamasaki, K. Matsuoka, C. Honda, K. Endo, M. Tsukada, Changes in the components of biliary and plasma lipids in selenium-deficient rats, *Chem. Phys. Lipids* **148** (2007) 70-76.

2) K Matsumoto, S.Terada, M. Ariyosh, A. Okajo, A. Hisamatsu, I. Ui, K. Endo, The effect of long-running severe selenium-deficiency on the amount of iron and zinc in the organ of rats, *Molecules* **14** (2009) 4440-4453.

3-15

3-16

中性子放射化分析による生物試料中のアルミニウム分析

Aluminum Analysis in Biological Materials by Instrumental Neutron Activation Analysis

加藤洋（首都大学東京）
Y. Katoh (Tokyo Metropolitan University)
山本好男（三重大学社会連携研究センター）
Y. Yamamoto (Mie University Social Cooperation Research Center)

INTRODUCTION

The Al determination of various materials by this method has been employed. However, the application of INAA for biological materials has the following problems: 1) competing interference reactions from the elements Si and P, and 2) interference created by irradiation from impurities in wrapping material of the specimen material. INAA has contributed little to Al value certification for biological standard materials, etc, because the above factors prevent INAA from determining accurate Al concentrations. In this study, the concentrations of Si and P were determined by an alternative nuclear method, Particle Induced X-ray Emission (PIXE) for Si and P, and the β-ray measurement with Liquid Scintillation Counting (LSC) of ^{32}P produced by ^{31}P(n,γ)^{32}P in the specimens used for Al determination.

EXPERIMENTS AND MATERIALS

The Certified Reference Material (CRM) and Standard Reference Material (SRM) of the 6 botanical and 12 animal specimens used for Al determination are shown in Table 1. The samples that were irradiated were about 50 mg of CRM, SRM. The comparative standard for Al was prepared through deposition of an atomic absorption solution (Wako Pure Chemicals Co. Ltd.). The capsules were irradiated in the pneumatic tube of the JRR-4 reactor. The irradiation time was 40 seconds, and the irradiated samples with exchanged outer bags were immediately measured for 1779 keV γ-ray of ^{28}Al using a high pure Ge semiconductor detector coupled to a multi-channel pulse-height analyzer for 100 seconds.

Table 1　List of CRMs and SRMs

Material	Supplier	Abbreviation (in this report)
Algae	IAEA	Algae-391
Algae	IAEA	Algae-392
Algae	IAEA	Algae-393
Animal Bone	IAEA	AB
Animal Muscle	IAEA	AM
Bovine Liver	NBS	BL
Bovine Liver	NIST	BLa
Kale	BOWEN	BK
Dogfish Mussel	NRCC	DORM-2
Horse Kidney	IAEA	HK
Lobster Hepatopancreas	NRCC	TORT-1
Lobster Hepatopancreas	NRCC	TORT-2
Milk Powder	IAEA	MP
Mussel Tissue	BCR	MT
Orchard Leaves	NBS	OL
Pig Kidney	BCR	PK
Pine Needle	NIST	PNa
Whey Powder	IAEA	WP

IAEA : International Atomic Energy Agency24
NBS: National Bureau of Standard
NIST: National Institute of Standards and Technology
NRCC: National Research Council Canada
BCR: Community Bureau of Reference

For the determination of the interference factors from Si and P, SiO$_2$ and (NH$_4$)$_2$HPO$_4$ were also irradiated respectively. For the

JRR-4, PN 気送管照射設備，生物試料放射化分析

determination of P in specimens using the LSC method, the irradiated specimens after the γ-ray measurement were subjected to dissolution by the microwave-assisted high pressure digestion with the apparatus developed by Fuse Lim. Co.. These specimens and the $(NH_4)_2HPO_4$ powder were dissolved with 1 ml of concentrated HNO_3 (ultrapure general reagent; Wako Pure Chemical Inc. Ltd.). The activities of a 200 µl solution containing ^{32}P with a half-life (14.26 d) and a β-ray maximum energy (1.711 MeV) were measured following the decay. The counting of β-rays was conducted with the Packard Co. Ltd. LSC 2900TR using a cocktail (Soluscint XR, National Diagnostics, Inc.). The determination of ^{32}P activities were interfered by the β-rays from nuclides, ^{33}P, ^{35}S and ^{45}Ca due to S, Cl and Ca, respectively. The high purity of compounds containing S, Cl and Ca were used to obtain the quantitative interference factors from each element.

The specimen solutions dissolved by the above-mentioned method were also applied to the PIXE method by adding the atomic absorption solution of In (Wako Pure Chemical Inc. Ltd 1000 ppm.) as an internal standard. Five µl of the solution was dropped on a 4 µm thick backing film (polypropylene, Toray Ltd.) and dried. The polyethylene products could not been digested and directly were irradiated. The target films were bombarded by a proton beam at the Japan Radioisotope Association Nishina Memorial Cyclotron Center in Japan. The energy, flux, and diameter of the proton beam were 2.9 MeV, 50 nA and 6 mm, respectively. The induced X-rays were measured by two Si(Li) semiconductor detectors.

RESULTS AND DISCUSSION

The reliability for theP determination by PIXE, and the P determination by LSC was confirmed by comparisons with certified values for various biological CRMs and SRMs. The results are shown in Table 2. Except for P, the Si levels were almost below the detection limit. The contributions from Si to the Al values in the materials were neglected in spite of the larger interfering factor. The P values by both methods are consistent and either method is applicable for determination of P in materials. The value in AB could not be calculated due to the strong characteristic X-ray from the concentration of Ca (21.2 % *(2)*). In the exact determination of P, the PIXE is generally disadvantaged by spectral bremsstrahlung in the light elements region. However, the results can be obtained at a short experimental time.

Table 2 Concentrations of phosphorus in biological CRMs and SRMs

Materials	P (µg/g dry)		
	PIXE	LSC	Reference
Algae-391	12400	14900	14200** *(1)*
Algae -392	4500	5830	5490** *(1)*
Algae-393	17200	18100	15600** *(1)*
AB	NC	93900	100200* *(2)*
AM	6300	7000	6830* *(3)*
BL	13500	11800	10500* *(4)*
BLa	12500	11500	11100* *(5)*
BK	4200	5490	4880* *(6)*
DORM-2	9600	6390	
HK	11600	12800	11200* *(7)*
TORT-1	5700	8880	8790* *(6)*
TORT-2	11000	6390	
MP	7400	10100	9100** *(6)*
MT	5700	6930	6070** *(8)*
OL	1500	2300	2100* *(4)*
PK	12800	12800	12000** *(9)*
PNa	1100	1030	1070* *(10)*
WP	16200	16400	16210* *(11)*

* Certified value, ** Information value

In case of the LSC method, the measurement that follows the decay of the β-ray requires a long time. The LSC method of counting ^{32}P also has a additional disadvantage. The β-ray counting of biological specimens by LSC has interference from the characteristic elements in biological specimens. These elements are abundant in biological materials.

In LSC, activities were counted for the total β-rays over the 3 keV of energy due to the high degree of differential quenching with each specimen. These β-ray measurements were followed for six months and the decay curves were analyzed. The total β-rays contained, ^{32}P derived from P, ^{32}P from S, ^{33}P from Cl, ^{35}S from S and Cl, and ^{45}Ca derived from Ca respectively. The decay curve of WP, for example, is shown in Figure 1. In this figure, the dotted lines represent the theoretical decay curves of ^{32}P, ^{33}P and ^{35}S, respectively. The contribution from ^{33}P and ^{35}S is apparent. The contributions from ^{35}S derived from S and /or Cl were detected in all specimens, and the contribution from ^{33}P derived from Cl was also detected in the case of PK, DORM-2, TORT-2 and WP. The total ^{32}P count is influenced by the concentration of S and Cl in the specimens. The large contribution of the ^{35}S activities caused by S and Cl to the total counts could be avoided by carefully cutting the low energy β-rays in the LSC method, since the β-ray energy of ^{32}P and ^{35}S are largely different. The interference from ^{47}Ca could be avoided by counting after about two weeks except for the bone specimen. A careful analysis of the decay curves is required, in the case of HK (12600 μg/g), TORT-1 (55800), TORT-2 (17500), MT (27800) and WP (69200), which contain very high concentrations of Cl, respectively. The concentration of interfering elements in LSC can be determined by simultaneous γ-ray spectrometry in measurement of ^{28}Al in an objective specimen. The P values obtained by LSC, except for AB, were adopted in this study.

The Al concentrations corrected for P for botanical and animal CRMs and SRMs are shown in Table 3. The Contribution Rate (C.R. (%)), which refers to the degree of the interference is defined by following the equation,

$$\mathrm{C.R.} = \frac{(\text{non corrected Al value}) - (\text{corrected Al value})}{\text{corrected Al value}} \times 100$$

The non corrected values were the mean values of 6 replicate analyses with one standard deviation. The corrected P values were calculated using the mean P values. The corrected values are, in botanical CRMs and SRMs, lower than the reference values for the Algae series, although the

Table 3 Concentrations of Al in CRMs and SRMs

Materials	This study (μg/g dry)		C.R. (%)	References
	Non-corrected	Corrected		
Botanical tissues				
Algae-391	19.9±1.2	7.5	165	12.5** *(1)*, 4.5*** *(12)*
Algae-392	36.7±1.4	32.2	14	37.2** *(1)*, 30.3*** *(12)*
Algae-393	107±3	90	19	98.1** *(1)*, 71.6*** *(12)*
BK	44.0±2.5	39.8	11	39.9** *(6)*
OL	429±9	427	0.5	420*** *(4)*
PNa	587±13	586	0.2	580* *(10)*
Animal tissues				
AB	99.1±8.6	5.2	1800	101***(2)*
AM	12.4±2.0	6.1	103	10***(3)*
BL	13.4±0.8	NC		16** *(13)*
BLa	12.3±1.2	NC		2** *(13)*, 0.6***(15)*
DORM-2	21.2±3.6	11.6	83	10.9**(16)*
HK	11.4±1.3	NC		77.7*** *(7)*
TORT-1	39.4±5.7	33.7	17	43*** *(14)*
TORT-2	48.5±7.6	37.5	29	
MP	11.7±0.7	4.3	172	
MT	15.2±1.9	8.3	83	
PK	19.4±1.8	6.6	194	
WP	57.1±2.9	40.7	40	53***(11)*

* Certified value, ** Information value, *** Literature value, NC; Not detected

results of BK, OL and PNa are consistent with the certified or information values. Most of the botanical materials contained high levels of Al, and while the concentrations of the interference elements are lower in comparison with animal materials, the C.R. ratios varied from 0.2 % to about 11 %. The correction for P was in some cases necessary, even for the botanical material. The relatively higher C.R ratios were obtained for the Algae series and for BK.

Specifically, Algae-1 which has a lower Al value and a much higher P value, and this influence from P value should be re-examined to confirm the Al reference value *(1)*. The higher information values of Al for the Algae series may be influenced by INAA results. For this series, the results by Kawamoto et al. *(12)* by using ICP-MS were consistent with the corrected values obtained here. The results in this study also agreed with the reference value for BK. In comparing the present results with those of animal CRMs and SRMs, agreement is excellent for DORM-2.The reference value of DORM-2 was obtained by using the analytical methods except for those obtained by NAA. For WP, the difference between the information value and that in this study is significant. In a detailed examination of the IAEA values *(11)*, the IAEA mean value, 57.8 μg/g compiled by only the INAA method, was very consistent with the non-corrected value in this study.

The IAEA certified value for this material may be also influenced by the contribution of the non-corrected results obtained by INAA in the certification. This also applies to the case of BL, BLa and HK. The higher Al value of HK by IAEA was obtained from little study and the IAEA value (≒10 μg/g) by INAA agreed with the non-corrected value in this study *(7)*. The Al values in BL compiled by INAA varied in ranges of <3-65 μg/g *(2)*, the Al abundance in this material might be naturally inhomogeneous. For BL, Aluminum could not be detected by correction in this study (detection limit: 0.06 μg). The C.R. value for AB, derived from very the high P value in this material, is over the factor of 10^3; nevertheless, the Al concentration could be obtained.

The information of IAEA by INAA *(6)* also showed results comparable to the non- corrected value in this study. For TORT-1, the corrected value in this study seemed to be about 27% lower than that found by Kratochvil et al. *(14)* from INAA, and agreed with the value determined by Graphite Furnace Atomic Absorption Spectroscopy. For TORT-2, MP, PK and MT, no information for the Al levels could be found at all in the literatures and the results obtained in this study were novel findings for these materials. For animal materials, the correction for the concentration of Si may not be necessary. The contribution derived from Si is 0.9 %, for example, for a sample containing 10 μgAl/g and 30 μgSi/g. Due to its ease of use and high sensitivity, INAA has been applied to the determination of Al in SRMs and CRMs. Even thought animals have much lower levels of Al, because of the interference caused by P which is high animals, the concentration of Al appeared to be much higher in animals than it really has.

REFERENCES

1. Preliminary statistical evaluation of the intercomparison run IAEA-0390, Trace elements in three different level Algae IAEA-0391/IAEA-0392/IAEA-0393. IAEA/AL/101P (1998).
2. Intercomparison minor of trace elements in IAEA Animal Bone (H-5) IAEA. Progress report No.1 (1982).
3. Parr BM, Intercomparison of minor and trace elements in IAEA Animal Muscle (H-4). Report No.2, IAEA/RL/69, Vienna (1980).
4. Gladney ES, Elemental concentrations in NBS biological and environmental standard reference materials. *Anal. Chem. Acta* **118**, 385-396 (1980).
5. NBS Certificates of analysis for SRM-1577a Bovine Liver, National Bureau of Standards. Washington D.C. (1982).
6. Muramatsu Y and Parr RM, Survey of currently available reference materials for use in connection with the determination of trace elements in biological and environmental materials. IAEA/RL/128, Vienna (1985).

7. Intercomparison of Cadmium and other elements in IAEA Horse-Kidney (H-8) IAEA. Progress Report No.2 (1985).
8. Lamberty A and Huntau H, The certification of the mass fraction of As, Cd, Cr, Cu, Hg, Mn, Pb, Se and Zn in mussel tissue (mytilus edulis) CRM 278R. European Commission, Report EUR 18840 EN (1999).
9. Wagstaffe PJ and Griepink B, The certification of the contents (mass fraction) of Cd, Pb, As, Hg, Se Cu, Zn, Fe and Mn in three lyophilized animal tissue reference matelials (CRM No 186 Pig Kidney). European Commission, Report EUR 10618 EN (1986).
10. NIST Certificates of analysis for SRM- 1575a Trace Elements in Pine Needle, National Institute of Standards and Technology. Gaitherburg, MD (2002).
11. Zeiller E, Strachnov V and Dekner R, Report on the intercomparison run IAEA-155 trace elements in Whey Powder. IAEA/AL/034, Vienna (1990).
12. Kawamoto K, Sumino, T, Takada J, Tanaka Y and Akaboshi M, Determination of rare earth and other elements in algae by ICP-MS and neutron activation analysis. *J. Radioanal. Nucl. Chem.*, 236(1-2), 119-122 (1998).
13. Gladney ES, O'Mailey BT, Roelandts I and Gills TE, Compilation of elemental concentration data for NBS clinical, biological, geological and environmental Standard Reference Materials. NBS Special Publicatio 260-111 (1987).
14. Kratochvil B, Motkosky N, Duke MJM and Ng D, Determination of trace aluminum concentration and homogeneity in biological reference material TORT-1 by instrumental neutron activation analysis and graphic furnace atomic absorption spectroscopy. *Can. J. Chem.*, 65, 1047-1050 (1987).
15. Schmit JP, Youla M, and Gèlinas Y, Multi-element analysis of biological tissues by inductively coupled plasma mass spectrometry. *Anal Chem. Acta*, 249(2), 495-501 (1991).
16. Dogfish muscle certified reference material for trace metals and elemental species. National Research Council Canada (1999).

3-16

3-17

成長過程における葉の生体物質中の特定元素のとり込み
A growth depending uptake of some rare metal into Clethraceae leaves

笠原　茂、野矢　洋一、関　興一
Shigeru Kasahara, Youichi Noya, Koh-ichi seki

北海道大学アイソトープ総合センター
Central Institute of Isotope Science,Hokkaido University

１．はじめに

リョウブ科の植物は他の植物より一桁以上高いコバルト (Co) 含有を示す。他の植物は鉱化地帯と通常の土壌とでコバルト含量がほとんど変わらないのに対し、リョウブは土壌中にCoが多い場合、著しくこれを濃集する性質があることが知られている[1]。コバルトが生物界に普遍的に存在することは知られているが、その濃度は低く、陸上植物は通常、乾燥中0.1 ppmのオーダーである。リョウブがCoを濃集する特性は何らかの理由が考えられなくてはならない。動物体内にもコバルトが必要元素として含まれており、生体成分としてコバルトを含んでいるものとしてビタミンB_{12}が知られている。リョウブの抽出物について *Euglena* (ミドリムシの一種) および *Ochromonas* (黄金色藻の一種) を用いたバイオアッセイの結果と抽出物の吸収スペクトルから、ビタミンB_{12}ではないとしながらも、類縁体であるコバルト・ポルフィリン錯体として存在するものと推測されると報告されている。

しかしながらコバルトの植物体内における分布状態や集積の機序については、その後全く研究されていなかった。近年、放射線を二次元画像として検出するイメージングプレート (IP)が開発され、放射性物質の平面的分布の解析に極めて有効なものとして汎用されるようになってきた。コバルトは中性子により容易に放射化することができる。この性質を利用してコバルト(^{60}Co)のIPによる葉内の分布を明らかにし、リョウブの特異的集積機構に関する基礎的知見を得ることを目的に本研究を開始した。しかし、金属元素がどのようにリョウブに分布しているかは知られていない。近年イメージングプレート(IP)が開発され、放射性同位元素を用いるバイオサイエンスの研究分野で放射性同位元素の検出に使用されている。

我々は、平成７年度から、コバルトの植物体内における分布状態や集積の機序について明らかとすることを目的とする本研究を開始した。平成18年までには「植物の葉に含まれるコバルト分布図の作成」、「植物の葉等への特定元素の取り込み」について検討し、リョウブの葉、枝、さく果における種々の金属の分布を明らかにして来た。

しかし、この研究では、夾雑するそれぞれの金属固有の分布や集積機序について十分明らかにするには至っていなかった。

今回、

１）亜鉛(Zn)の影響を十分に取り除いたコバルトの選択的画像化
２）リョウブの成長に伴う各種金属イオン種の集積の経時的変化

について検討したので報告する。

本研究において、自然に生育しているリョウブから我々はリョウブの葉、総状花序を採取し、これを乾燥後または溶媒抽出法により試料を作成し、放射化に付した。それをガンマ線スペクトロメータで定量し、IPを用い画像化し、元素の定量、葉内分布を明らかに出来たので、それについて報告する。

２．実験

１）我々は、コバルトの選択的画像化のために、物理的前処理法（放射能の半減期を利用した減衰処理）と化学的前処理法を組み合わせることによる、選択的画像化に取り組んできた。

JRR-4 T-パイプ　放射化分析（環境）

その結果を平成１６年－平成１８年の成果報告書で報告している。

このときの測定は調整された葉を、放射化後５００日間冷却し、短半減期核種の放射能の減衰を待って、バイオイメージングアナライザーシステム（富士フィルムKK,BAS-5000）を用いて行った。得られた画像を図－１に示す。

図－１

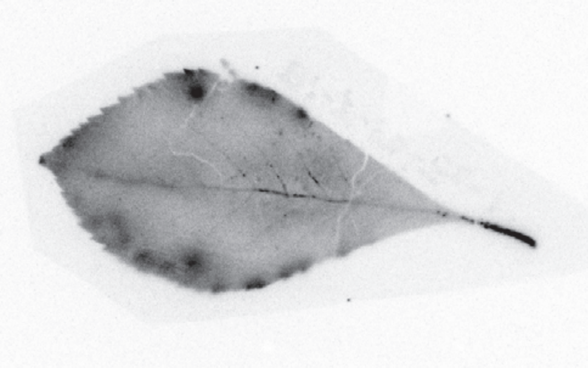

図－２

この場合、Ge半導体γ線検出装置では検出出来ない、β線のみを放出するカルシウム(^{45}Ca)によるＩＰへの影響を無視できないかもしれないと考え、アルミ箔を用いて、その影響を除去したものも併記した。図―２に示す。

これにより、葉柄における強い放射能はβ線放出核種によるものであることを明らかにすることができた。また、コバルトは葉の周辺に集積していることも示された。

しかし、５００日の冷却では、共存する亜鉛（^{65}Zn(T=244d) の減衰では十分でなく、その画像への影響が残存していることも考えられ、より長期間の放置によるその影響を除去した画像を得ることがコバルトの分布を正しく知る上で必須であった。このため、今回は前記の試料の^{65}Znが十分減衰したと考えられる、さらに１３３０日後（総計１８３０日後）に画像化した。結果を図－３、図－４に示す。

１）の結果

図から明らかなように、カルシウムは葉柄に多く、亜鉛は葉柄側の葉脈に多く、コバルトは葉の辺縁部に塊状に濃集されていることが明らかとなった。コバルトの濃集が塊状になっていることから、葉の中にはコバルトを集積する液胞のような組織（vacuole, spot, speckle, blob, mottle）が存在しているのではということを明らかにすることが出来たという点で興味深いと考えている。

図－３

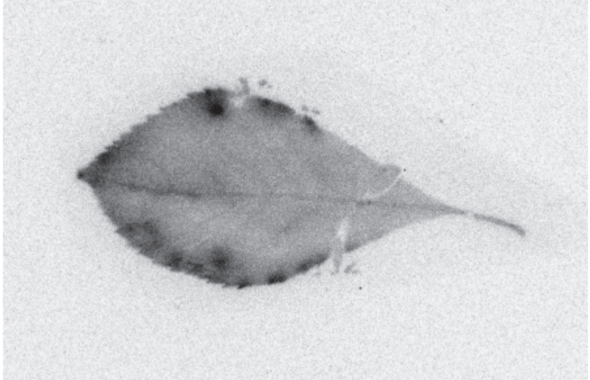

図－４

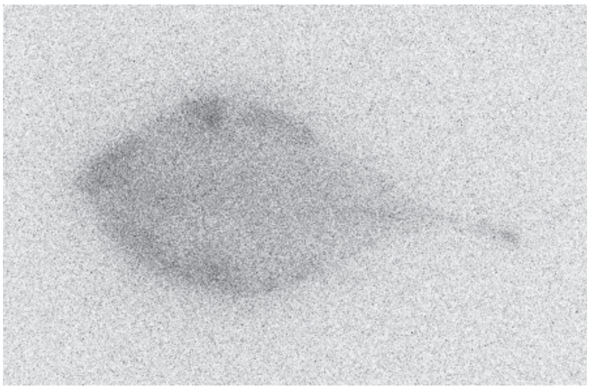

２）リョウブの成長に関わる元素の変化と葉、総状花序に含まれる主要金属である亜鉛(Zn)、コバルト(Co)、セシウム(Cs)、ルビジウム(Rb)について検討することとした。試料の葉、総状花序は採取後そのまま乾燥した。葉を採取する時

3-17

期は、総状花序に花が咲き始める、少し手前の７月から１１月までとした。放射化は日本原子力研究開発機構原子力科学研究所(日本原子力研究所)(JRR-３)Ｓパイプを用い、中性子束密度4.3×10^{13}n/cm^{2}s、照射時間２０分の条件で行った。試料の分析はGe半導体検出装置（SEIKO EG&G社製）を用いて行った。その結果をZn-65は図－５、60-Coは図－６、Cs-134は図－７、Rb-86は図－８に示す。

図－５

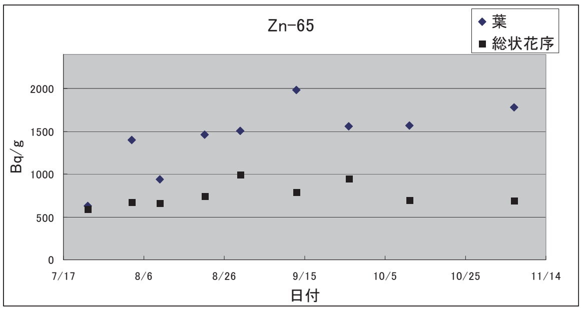

図－６

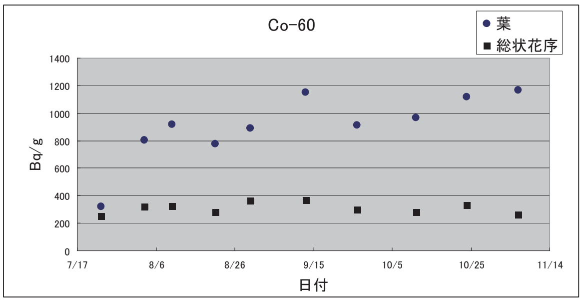

図－７

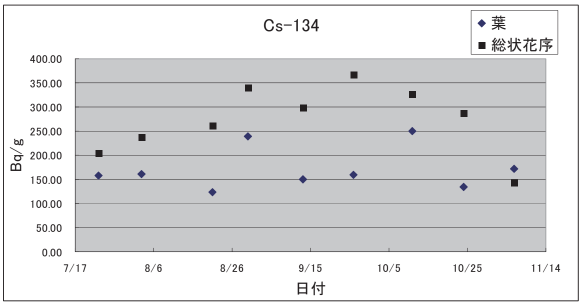

図－８

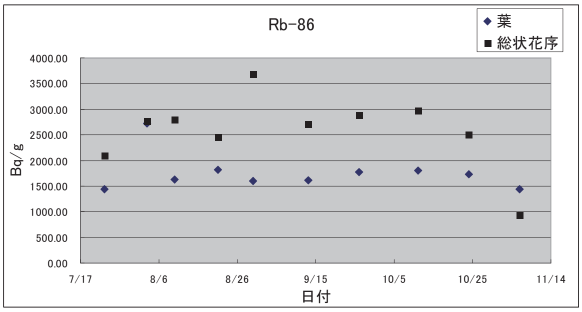

２）の結果

図－５，図－６の結果から、遷移金属である亜鉛（Zn-65）およびコバルト(Co-60)は葉に強い集積が認められ、季節の進行に伴い増加することがわかった。一方、アルカリ金属に属するセシウム(Cs-134)およびルビジウム(Rb-86)は総状花序に多く集まり、８月ないし９月までは集積していくが、それ以降は漸減する傾向が認められた（図－７、図－８）。

植物の生長の必須元素であるカリウムと同族のルビジウムおよびセシウムは土壌中において非常に低濃度で存在しているにもかかわらず、植物によって容易に吸収されていることが示された。亜鉛、コバルトの集積機序は明らかでないが季節の変化とともに葉に集積しているのに対し、ルビジウムおよびセシウムが植物の成長と関係して吸収されるという点で対称的であった。

参考文献

[1]Noboru Yamagata,Sadao Murata,Koshu EiseiinKenkyu Hokoku(1964)13(3)170-5.

謝辞

この実験にあたり、貴重な試料を提供して頂いた、北海道大学北方生物圏フィールド科学センター植物園大野　祥子技術専門職員および試料調整等の技術指導して頂いた、大学共同利用開放研究室の澤幡 浩之氏、川手 稔氏、石本 光憲氏に厚くお礼申しあげます。

3-18

PGA と INAA による微小大気浮遊粒子の元素組成(II)

Elemental Compositions of Atmospheric Suspended Particulate Matters
by PGA and INAA (II)

首都大学東京大学院理工学研究科分子物質化学専攻
Department of Chemistry, Graduate School of Science and Engneering,
Tokyo Metropolitan University
大浦泰嗣，海老原充
Yasuji Oura, Mitsuru Ebihara
首都大学東京都市教養学部理工学系化学コース
Division of Chemistry, School of Science and Engineering,
Faculty of Urban Liberal Arts, Tokyo Metropolitan University
富田智之，菅原慈，鈴木智誠
Toyoyuki Tomita, Shigeru Sugawara, Tomonori Suzuki
東北公益文科大学
Tohoku University of Community Service and Science
大歳恒彦
Tsunehiko Otoshi

---

1. はじめに

大気汚染は我々の健康に直接影響を及ぼすため，大きな関心事である．大気汚染物質の一つに大気浮遊粒子状物質(SPM)がある.粒径の小さな粒子は重力による沈降が遅く，しばらく大気中に漂い，呼吸により我々の肺の中にまで到達する． 1990 年代初頭，欧米で空気動力学的粒径 10 μm の粒子(PM10)の大気中濃度と心肺に疾患のある患者の日別死亡率に相関があるという疫学的データが報告され，PM10 粒子の性状・挙動が注目されてきた．さらに，粒径がもっと小さい PM2.5 粒子濃度は，死亡率との相関がより高いという報告もなされた．そのため，PM2.5 粒子に関する研究が世界的に盛んに行われるようになってきた.

SPM は自然活動や人間活動により様々な粒子が大気中に放出されている．これら粒子には多様な化学物質が含有あるいは吸着している．人体に影響を及ぼす化学物質も少なくなく，特に直接的な影響を与えると考えられる多環芳香族など有機物質の研究が精力的に行なわれている．また，有害な元素も数多く含まれており，粒子の元素組成を知ることも重要である．さらに，粒子の起源を解析する上でそれらの元素組成は重要な情報をもたらす.

そこで，2002 年から東京のベッドタウンの一つである多摩ニュータウンと山形県酒田市において，PM10 粒子の採集をおこない，元素組成を即発γ線分析法と中性子放射化分析法，ならびに光量子放射化分析法を用いて明らかにしてきた． 本研究では，ひきつづきこの 2 地点での PM10 採集を継続するとともに，都心部との大気環境を比較するために，八王子市と，東京都環境科学研究所の協力により東京都江東区において PM2.5 の採集を開始した．これらの大

JRR-3 即発ガンマ線分析装置，JRR-3 PN3，JRR-3 HR，JRR-4 PN，JRR-4 S パイプ，環境試料放射化分析

気環境試料の元素組成を放射化分析法にて調べた．

なお，本研究はアジア原子力協力フォーラム(FNCA)の研究炉利用グループ放射化分析サブグループで実施したINAAによるSPM分析プロジェクトの日本側実験をかねて行った．

2. 実験方法

PM10粒子は，東京都八王子市の首都大学東京南大沢キャンパス8号館の屋上，並びに山形県酒田市の東北公益大学教育研究棟の屋上にて粒径別に採取した．ポンプで大気を16.7L/mの流速で吸引し，NILUフィルタホルダーを用いて，インパクターを通過した粒径10μm以下のPM10粒子を孔径8μmと0.4μmのポリカーボネート製フィルタで分粒して1~数日間採集した．採集は，八王子では隔週で，酒田では毎月1回行った．なお，酒田での採集は2007年で中止し，2008年は行わなかった．

2006年4月より，東京都江東区の東京都環境科学研究所の屋上にてPM2.5粒子の採集を行った．サイクロン型サンプラーにより流速6.7 L/minにて大気を吸引し，孔径0.2μmのポリカーボネート製フィルタ上に，1日間採集した．また，八王子市においても，PM10粒子と同様に，PM2.5粒子の採集を行った．ただし，孔径0.2μmのフィルタを用いた．

採取後，フィルタを秤量し，半分に切断した．1/2片の一つを10×10mmの正方形状に折り畳み，FEPフィルムに熔封してJRR-3即発ガンマ線分析装置により熱中性子を6時間照射しながら，即発ガンマ線を測定した．その後，同試料をJRR-3 PN3またはJRR-4 PNにて5分間照射を行い，ただちに300秒間測定を行った．冷却後，同試料をポリイミド箔とAl箔で包み，20試料ほどをスタック上にして全体を石英管に熔封した．これをJRR-4 Sパイプまたは JRR-3 HR孔にて6時間照射した．冷却時間をかえて4~5回，3000~50000秒間測定を繰り返した．なお，PM10粒子はINAAのみ行い，PGAは行わなかった．

3. 結果と考察

まだ，採集した試料すべての分析は完了していない．5分間照射による分析は，すべての試料に対して行ったが，長時間照射については，測定に時間がかかるため，一部の試料についてしか行えなかった．また，データ解析もすべて終了していないため，ここでは，PM2.5粒子の短時間照射による定量結果を報告する．

PM2.5粒子の採集は，2006年から，八王子では流量16.7L/minでインパクター方式を用いて，江東では流量6.7 L/minでサイクロン方式を用いてはじめた．流量を自動調節できないため，八王子では，採集された粒子がフィルターの孔をふさいでいき，だんだん流量が減少していった．採集期間の平均流量

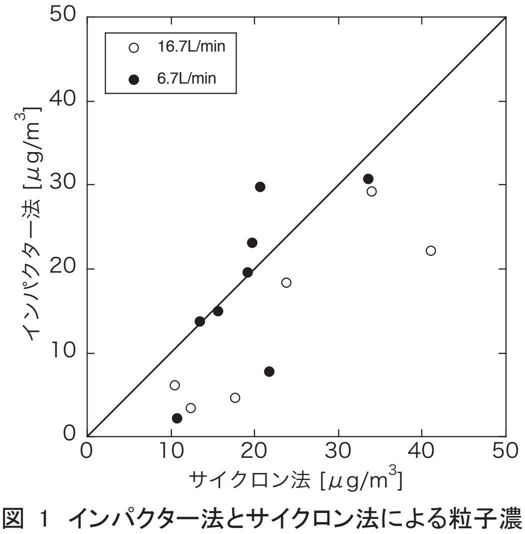

図 1 インパクター法とサイクロン法による粒子濃度の比較．サイクロン法は常に 6.7 L/min の流量で採集した．

が5.6L/minにまでなることもあった．一方，江東では，流量が八王子よりも少ないためか，顕著な流量の低下が観測されないことのほうが多かった．規定流量よりも低下すると，採集された粒子の粒径がPM2.5と異なってくる．そこで，江東にて，インパクタ方式とサイクロン方式の 2 つの方法で同時にPM2.5の採集を行い，粒子濃度を比較した．

図1に，両方式による粒子濃度を比較した．16.7 L/min でのインパクター方式による粒子濃度は系統的に，サイクロン方式よりも低くなった．つまり，同じ粒径の粒子が採集されなかったと判断できる．そこで,インパクター方式でも6.7 L/minの流量で採集を行ってみたところ，サイクロン方式による粒子濃度と，よく一致した．そこで，2008 年からは，八王子でも，6.7 L/min の流量による採集に変更した．

2008年に採集したPM2.5の粒子濃度を図2(a)に箱ヒゲ図で示した．参考として，2006 年から 2007 年に採集した PM2.5 の粒子濃度も図 2(b)に示した．2008年1年間での濃度分布の中心値は都心である江東よりも,郊外に位置する八王子の方が高かったが，分布を考慮すると八王子と江東の間での粒子濃度に，大きな差はみられなかった．2006~ 2007年は採取方法に問題があり，八王子のPM2.5粒子濃度は過小評価されていると思われるが,これを考慮に入れると，2006~ 2007年も2008年同様，八王子の方が粒子濃度中心値は高かったと推定される．

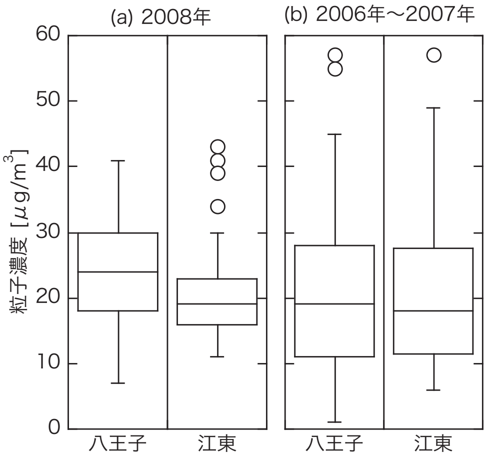

図 2 PM2.5 粒子濃度

16.7 L/minによるインパクター方式による粒子濃度は，6.7 L/min によるサイクロトロン方式と比較して，系統的に低くなったが，元素濃度では同様な傾向が観測されなかった．図 3 に例として Na と V の元素濃度の比較を示す．16.7 L/min と 6.7 L/min

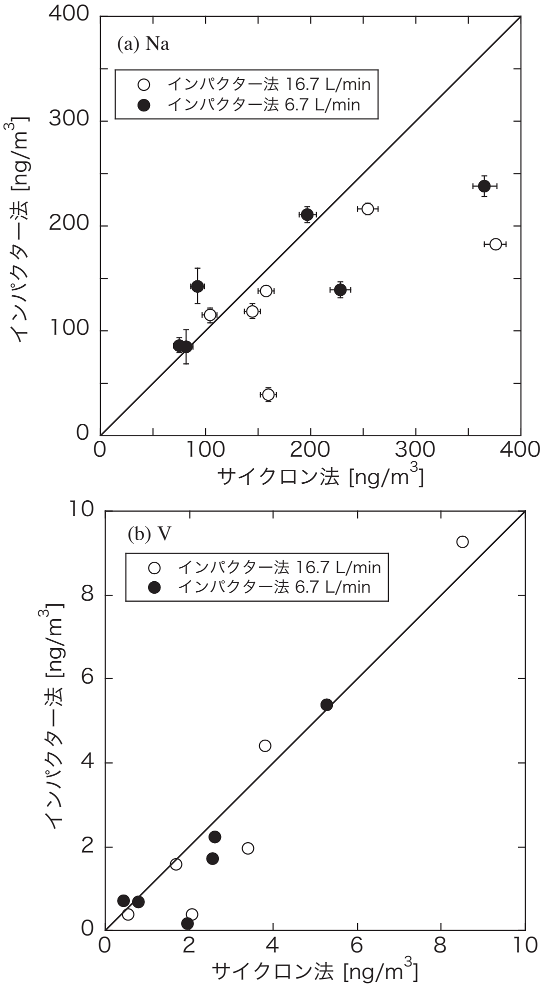

図 3 インパクター法とサイクロン法による元素濃度の比較．サイクロン法は常に 6.7 L/min の流量で採集した．(a) Na，(b)V.

のあいだに明瞭な違いは違いは見られず，V 濃度は，どちらの流量でも，サイクロン法とほぼ同じ濃度が得られた．粒子濃度の場合と矛盾するが，少なくとも本研究で定量した元素については，同等に採集されていたものと考えられる．粒子濃度減少の原因となり，これらの元素をあまり含まない粒子は何であるか興味がもたれる．

元素濃度は採取法による差がみられないため，

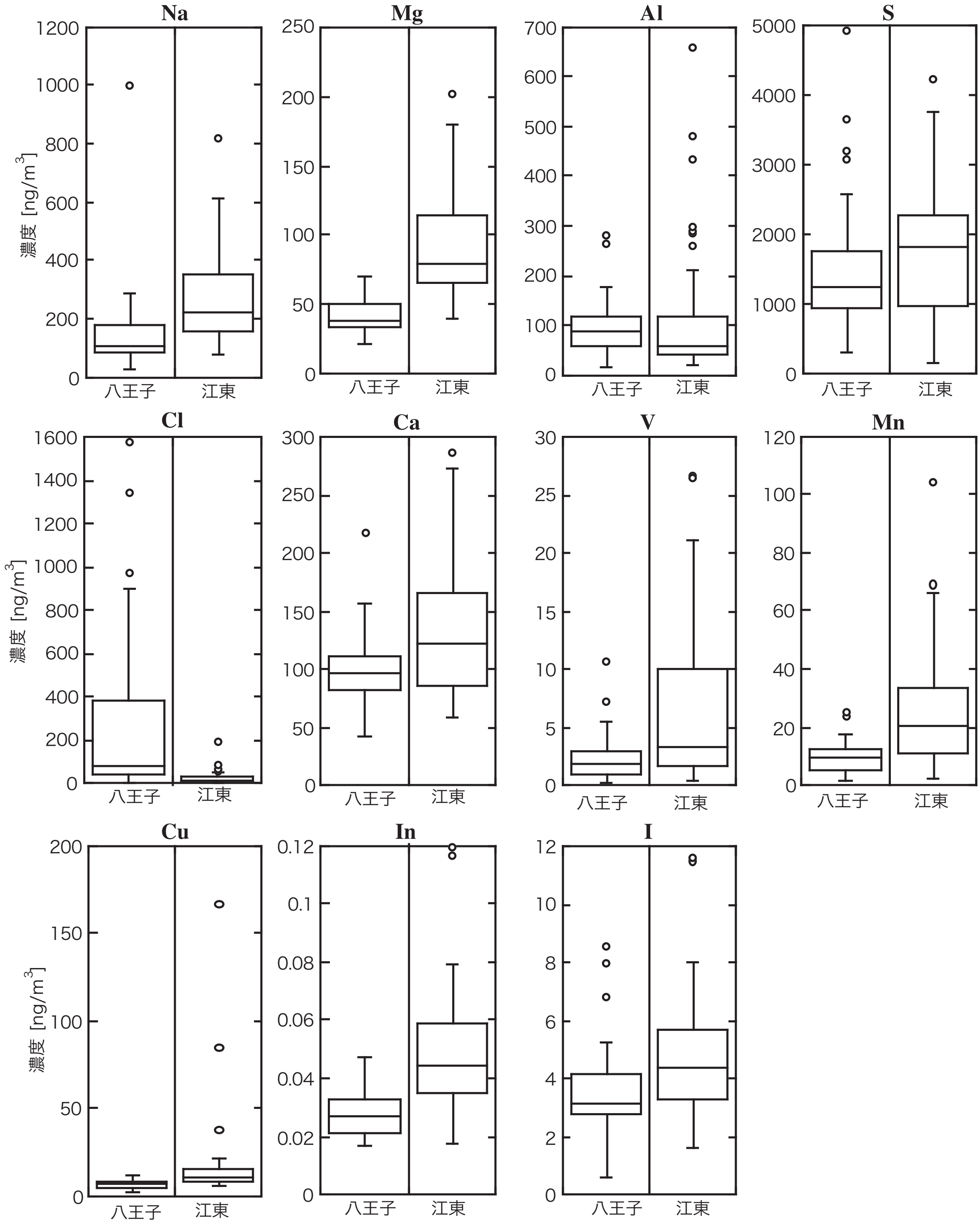

図 4. 2006 年から 2008 年に八王子市と江東区で採集した PM2.5 粒子の元素濃度.

2006 年から 2008 年に採集した PM2.5 の元素濃度分布を図 4 に示す.短時間照射により 11 元素の濃度を定量できた. 江東での粒子濃度は, 八王子よりも低かったが, Al と Cl を除く元素濃度は江東で高く, 特に, Na, Mg, V, Mn, Cu, In での中央値は, 江東が八王子よりも約 2 倍以上大きかった. 一方, Cl 濃度は, 八王子が江東よりも約 4 倍高かった. 日本海に面している酒田では,海塩の影響により Cl 濃度が大変高いが,ほとんどは PM10 の粗粒に含まれており, 細粒(PM2.5 にほぼ相当)での Cl 濃度は八王子の方が約 3 倍高いことがこれまでの研究よりわかっている. この高濃度は, 都市域で一般にみられるものではなく, 八王子に特有な特徴であるようである.

奥田ら(2007)は 2004 年に東京都目黒区で PM2.5 を採集し, その金属成分濃度を報告した. Al, V, Cu の冬季と夏季での平均濃度はそれぞれ, (399, 164), (8.68, 16.2), (46.0, －) ng/m^3(-:検出限界以下)であった. Al は冬季で, V は夏季で濃度が高いと報告された. 江東区でも同様な季節変動が観測された. 7 月~ 9 月に高い V 濃度が観測され, 12 月~ 1 月に Al 濃度が高かった.八王子でも V に同様な季節変動が観測された. また, 図 5 に示すように Cl に明瞭な季節変動が観測され, 12 月~ 1 月に高濃度となり, 7 月~ 8 月は低濃度であった. 夏季は気体状で多く存在し, 冬季になると低気温のため粒子上に凝縮するのであろう.

今後は, 長時間照射による元素の定量をすすめ, 都心部と郊外域における PM2.5 の元素組成の特徴を明らかにしていく.

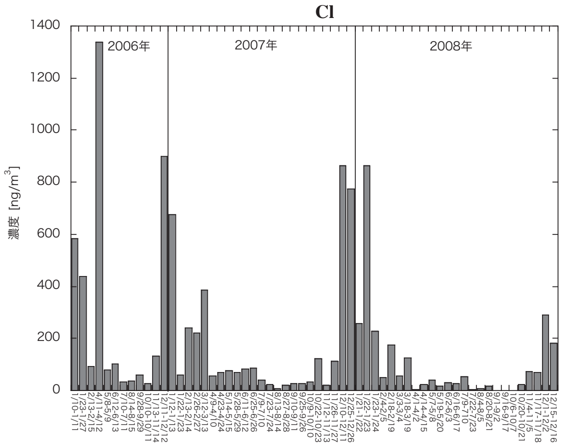

図 5. 八王子における PM2.5 粒子の Cl 濃度の経時変化

4. 成果の公表

1)"Collaborative Monitoring Study of Airbone Particulate Matters Among Seven Asian Countries", M. Ebihara, Y.S. Chung, W. Chueinta, B. F. Ni, T. Otoshi, Y. Oura, F. L. Santos, F. Sasajima, Sutisna, A. K. B. H. Wood, *J. Radioanal. Nucl. Chem.* **269**, 259-266 (2006).

2)" Progress of Atmospheric Suspended Particulate Matter Analysis in Japan" , Y. Oura, T. Otoshi, and M. Ebihara, The 2006 FNCA Workshop on the Utilization of Research Reactors (2006.8, Philippine).

3)"Elemental Compositions of Atmospheric Particulates Collected in Japan from 2002 to 2004", Y. Oura, H. Iguchi, T. Nagahata, H. Nakamatsu, T. Otoshi, M. Ebihara, *J. Radioanal. Nucl. Chem.* **272**, 381-385 (2007).

4)" NAA application to air particulate matter collected at thirteen sampling sites in eight Asian countries: A collaborative study" , M. Ebihara, Y. S. Chung, H. M. Dung, J. H. Moon, B.-F. Ni, T. Otoshi, Y. Oura, F. L. Santos, F. Sasajima, Sutisna, B. S. Wee, W. Wimolwattanapun and A. K. B. H. Wood, 12th International Conference on Modern Trends in Activation Analysis (2007.9, 八

王子).

5) “The Progress report of environmental sample analysis and its reflection to the environmental protection authority for the past one year in Japan”, Y. Oura, T. Tomita, T. Otoshi, and M. Ebihara, The 2007 FNCA Workshop on the Utilization of Research Reactors (2007.10, Indonesia).

6) “Application of NAA to air particulate matter collected at thirteen sampling sites in eight Asian countries: A collaborative study”, M. Ebihara, Y. S. Chung, H. M. Dung, J. H. Moon, B.-F. Ni, T. Otoshi, Y. Oura, F. L. Santos, F. Sasajima, Sutisna, B. S. Wee, W. Wimolwattanapun, A. K. B. H. Wood, *J. Radioanal. Nucl. Chem.* **278**, 463-467 (2008).

3-19

海成炭酸塩中のホウ素の即発ガンマ線分析

Prompt Gamma-ray Analysis of Boron in Marine Carbonates

大出　茂、田中健太郎

S. Ohde, K. Tanaka

琉球大学理学部

Faculty of Science, University of the Ryukyus

1、はじめに

本研究の目的は、炭酸塩殻（主成分：$CaCO_3$）中のできるだけ多くの元素分析から、その生物が生育していた環境水についての情報を得ることである。そこで、本研究と同時に、サンゴのハロゲン元素の放射化分析に関する研究をJRR-3M(PN-3)を使って行っている。

海水中のホウ素とその同位体については、大出、Zuleger(1999)に概説した。ホウ素同位体（$^{11}B/^{10}B$）の同位体交換を使って、paleo-pH と呼ばれるアイデアが、Spivack et al.(1993)によって提出された。すなわち、海成の化石炭酸塩（貝殻、サンゴなど）のホウ素同位体の分析から、それら生物が生息していた時の、海水の pH を推定できるというアイデアである。そのような、ホウ素同位体から古 pH を推定する研究の基礎として、サンゴ骨格中のホウ素含量を定量することが、本研究の目的である。

アラゴナイト（$CaCO_3$）中へのホウ素の共沈が、つぎのイオン交換で起こると仮定すると（$CaCO_3 + 2A^- = CaA_2 + CO_3^{2-}$）（$A^-$は、ホウ酸イオンとする）、サンゴのホウ素含量は、サンゴが生育した海水の炭酸イオンとホウ酸イオンの比によって決定される可能性がある。したがって、サンゴのホウ素を測定する意義がある。しかし、熱中性子放射化分析では、サンゴ骨格中のホウ素の定量ができない。現在、ICP-AES 法がサンゴのホウ素分析に使われている。その他ホウ素に関して最適な分析法があまりない。また、即発ガンマ線分析のように、非破壊での定量法はまったくみあたらないのが現状である。サンゴ骨格には、ホウ素が約 50ppm 存在するので、原研の装置(PGA)を使って正確かつ精度よい分析が可能である。本研究では、地質調査所のサンゴ標準試料（JCp-1）および沖縄、和歌山、タイ、フィリピンのサンゴのホウ素含量の定量を即発ガンマ線分析を使って行った。

2、サンゴ試料

炭酸塩標準として地質調査所が作成したJCp-1(サンゴ)を使用した。サンゴ骨格試料は沖縄（ルカン礁、水釜、南大東島）、和歌山（堺）タイ（カンカオ島）、フィリピン（セブ島）のサンゴ礁から採取し、ミリキュウ水で数回、超音波洗浄し、乾燥して準備した。

3、即発ガンマ線分析

サンゴ試料（粉末またはブロック状）50-150mg をポリ袋に封入後、テフロンシート（FEP）に再封入し、照射試料を作成した。ホウ素標準は、1000 および 2000 ppm ホウ素を含むホウ酸標準溶液をロ紙上に 10 μl 塗布し、乾燥させ、テフロンシー

研究施設と装置	研究分野
JRR-3M(PGA)	環境化学、海洋地球化学

ト中に封入して作成した。JRR-3M の熱中性子ビームを使って、試料にそれぞれ、3000 秒および 5000 秒中性子照射し、即発ガンマ線を測定した。即発ガンマ線スペクトルを解析した結果、サンゴ試料中の B、Ca、Na が定量可能であった。ホウ素の 478 keV 即発ガンマ線ピークを使ってサンゴ中のホウ素を定量した。472 keV のナトリウムピークとホウ素のピークが重なるので、放射化分析で定量したナトリウムのデータと炭酸ナトリウム標準(約 10mg)を同様に即発ガンマ線分析したデータを比較することによって、ナトリウムピークの補正を行った。サンゴのナトリウム含量は約 5000ppm であった。サンゴはホウ素を約 50ppm 含んでいるが、約 1ppm のナトリウムの寄与によるマイナス補正が必要であった。本研究で用いた即発ガンマ線分析の正確さ（再現性）を確かめるために、標準試料の分析をくり返し行った。この分析法の再現性は 2-3%である。

4、結果と考察

サンゴ標準試料（JCp-1；石垣島のサンゴ）をサンゴの即発ガンマ線分析の比較標準として使用することが可能かを検討する目的で、標準試料の分析を 10 回ほど繰り替えし即発ガンマ線分析した。JCp-1 の平均分析値は、48.0(±1.2) ppm であった。文献値(Okai et al. 2001)は、 47.7 ± 1.2ppm と報告されているので、非常によい一致を示す。JCp-1 は、石垣島から採取したハマサンゴから作成されているので、サンゴのホウ素分析用の標準物質として最適であると思われる。今後、分析回数を増やすなどして、信頼性の高いデータを得ることによって、JCp-1 を即発ガンマ線分析の標準試料として使用したい。

JRR-3 の熱中性子ビームを使い、沖縄のサンゴを分析した結果、ホウ素が 50 – 60 ppm 含まれることが明らかになった（表1）。サンゴ骨格中のホウ素含量は表1に示すように、どうも 50-60 ppm の狭い範囲の値を示すことが明らかになり、沖縄の同じサンゴ礁の試料間で約 20%の変動を示した。上記のイオン交換式がサンゴのホウ素の取り込みをコントロールしているのであれば、約 20%の変動は、サンゴが石灰化した時のサンゴ礁海水中の炭酸イオンとホウ酸イオンの活動度比（濃度比）と関係していると私は推定している。そこで、サンゴ礁で測定した pH とサンゴのホウ素量との関係について考察進めていく予定である。また、海外調査で採取したサンゴ中のホウ素の測定結果を表1にまとめた。

本研究では、特に、サンゴ中のホウ素含量から、サンゴが生息していた環境水の化学組成を推定することを試みた。ホウ素と同様に、1 価の陰イオンであるフッ素について、海水からアラゴナイトへのフッ化物イオンの共沈は次のイオン交換反応式に従うことが知られている(Ichikuni 1979)。

$$\mathrm{CaCO_3(s) + 2F^-(aq) = CaF_2(s) + CO_3^{2-}(aq)}$$

$$K_F=[\mathrm{CaF_2}][\mathrm{CO_3^{2-}}]/[\mathrm{CaCO_3}][\mathrm{F^-}]^2$$

上式は、海水のフッ化物イオンと炭酸イオンの比が、炭酸塩に共沈するフッ化物イオン量をコントロールすることを示している。さらに、海水の炭酸イオンは、pH と関係する。したがって、海水の pH および二酸化炭素に関する情報が得られる可能性がある。そこで、フッ素と同様にサンゴ殻のホウ素の正確な定量が重要である。そこで、沖縄（ルカン礁、水釜、南大東島）、タイ（カンカオ島）、フィリピン（セブ島）のサンゴ礁から採取し、準備したサンゴ骨格試料の即発ガンマ線分析を行った結果（平均値）を表1に示す。サンゴ骨格中の平均ホウ素含量はタイのサンゴが 48 ppm であり、フィリピンが 55 ppm であり、沖縄が 54 – 62 ppm、和歌山が 66 ppm であった。そこで、サンゴが生育していた海水温度（平均値）

とサンゴ骨格中のホウ素含量の関係を図 1 に示す。セブ（フィリピン）のデータを除くと、サンゴが生育していた海の平均水温はタイが一番高く、和歌山が低いので、サンゴが生育していた温度とホウ素含量の間に何か、間接的な関係があるものと推定される。

5、今後の方針

日本各地のサンゴの即発ガンマ線分析を行いデータを蓄積するとともに、実験室でのアラレ石合成実験を通して、ホウ素の炭酸カルシウムへの共沈条件を明らかにすることも重要と考える。また、琉球大学に設置されている ICP-MS を使って、分析をおこなった同じサンゴ試料について、ホウ素の定量を行う予定である。そして、データを比較検討する。そして、サンゴが生息していた環境水の化学組成との関係を考察する予定である。

6、引用文献

Ichikuni M. Chem. Geol. 27(1979)207.
Imai N. et al. Geostandard Newslett. 20(1996)165.
Ishikawa T., Nakamura E. EPSL 117(1993)567.
大出茂, Zuleger E. 地球化学, 33(1999)115
Okai T. et al. Geostandard Newslett. 26(2001)95.
Spivack A. J. et al. Nature 363(1993)149.
寺島滋ら, 分析化学 47(1998)451

7、成果の公表

(1) 大出茂、吉村和久（2006）「炭酸塩の地球化学」によせて、地球化学、40，177-178

(2) Hossain, M. M. M., Ohde, S. (2006) Calcification of cultured *Porites* and *Fungia* under differrent aragonite saturation state at 25℃. *Proceedings of the 10th Coral Reef Symposium,* pp. 597-606

(3) 田中健太郎,大出茂（2007）サンゴ骨格中のフッ素含量と海水中の炭酸イオン濃度の関係, 日本海水学会誌, 61, 118-122

(4)大出茂（2007）サンゴの化学像を通してみる海洋環境の変遷, 海洋化学研究, 20, 54-77

(5) Armid, A., Ohde, S. Shinjo, T., Toki, T. (2008) Determination of uranium in pore water from coastal sediment by standard addition ICP-MS analysis. Jour. Radioanal. Nuclear Chem., 275, 233-237

(6) Hossain, M. S., Ohde, S., Tanaka. K., Sirirattanachai, S., Snidvongs, A. (2008) Oxygen isotope composition in *Porites* coral from the Northern Gulf of Thailand: an implication for its skeletal growth. Bull. Soc. Sea Water Sci., Jpn., 62, 112-113

(7) Bogan, R. A. J., Ohde, S., Arakaki, T., Mori, I., McLeod, C. W. (2009) Changes in rainwater pH associated with increasing atmospheric carbon dioxide after the industrial revolution. Water Air Soil Pollut., 196, 263-271

(8) Ohde, S., Tanaka K. (in press) Anthropogenic surface ocean acidification with increasing atmospheric carbon dioxide and its impact on coral calcification. In Davin T. B. and Brannet A. P., Ed. Coral Reefs: Biology, Threats and Restoration, Nova Sci. Pub., NY

3-19

表１　図１中のサンプルのホウ素含有量の平均値と標準偏差

サンプル採取場所	サンプル数	B 平均値(ppm)	標準偏差(1σ)
カンカオ	7	47.9	3.83
水釜	22	57.0	3.83
セブ	19	55.3	5.39
南大東島	3	54.4	1.80
堺港	14	66.1	7.52
ルカン礁	7	62.8	5.33

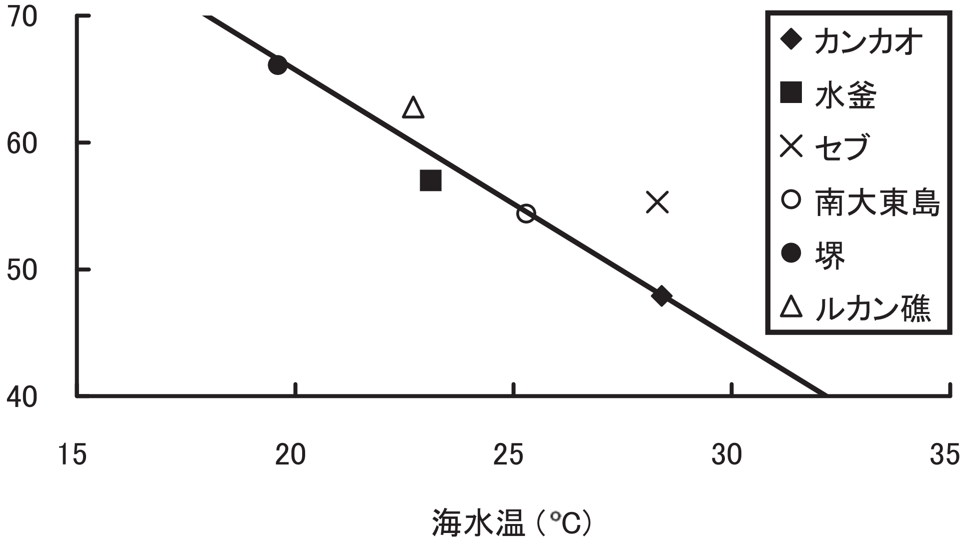

図１　サンゴ骨格中のホウ素含量（平均値）と海水温度の関係（$r^2 = 0.938$）

3-19

3-20

新奇な内包フラーレンの放射化学的手法による研究

Study on the new encapsulated-fullerenes using radiochemical method

筑波大学数理物質科学研究科 [1]・首都大学東京大学院理工学研究科 [2]

[1]Graduate School of Pure and Applied Sciences, University of Tsukuba

[2]Graduate School of Science and Engineering, Tokyo Metropolitan University

末木啓介 [1]・岩井雄 [1]・玉理美智子 [1]・秋山和彦 [2]

K. Sueki[1], Y. Iwai[1], M. Tamari[1], K. Akiyama[2]

近年、フラーレンは機能性物質の材料として様々な分野で用いられるようになってきている。このフラーレンに金属原子を内包している金属フラーレンはその特異な分子構造と電子状態から興味深い物質の一つでありながら、生成量が代表的なフラーレンである C_{60} に比べ 1/1000 以下と非常に少ないため、十分な研究が進展しているとは言えない状態にある。このような少量の物質の性質を調べる上で、試料から放出される放射線を検出手段とするラジオクロマトグラフィーは非常に有効な手段であると言える。また、γ 線をモニタに用いるラジオクロマトグラフィーでは他元素同時に分析が可能であり、金属フラーレンを分析対象とする場合は内包金属ごとの性質の違いを同時に調べることができる。また、放射性同位体を内包したフラーレンはそれ自体が新しい機能を有する物質であり、水溶性の分子を合成することによって新たな応用への発展性をもたらすと考えられる。

本研究ではランタノイド金属内包フラーレンの分子内の双極子モーメントの系統的研究と水酸基を導入する過程について原子炉で中性子放射化したトレーサーを用いて研究した。

1．ランタノイド金属フラーレンの双極子モーメントに関する研究について

La, Ce, Pr, Nd, Gd を内包した $M@C_{82}$ はケージを構成する C_{82} フラーレンの構造、内包金属原子からケージへの電荷移動数など電子状態が互いに非常に類似した化合物である。実際、化合物の電子状態を調べる手段の一つである紫外可視近赤外吸収スペクトル測定では、互いに非常に類似したスペクトルを示すことが知られている。[1] しかしながら一方でピレニル固定相を持つフラーレン分取用カラムである Buckyprep カラムにおけるこれら $M@C_{82}$ の保持時間は若干異なっており、内包された金属原子により、固定相と相互作用するフラーレンケージ表面の性質に若干の変化をもたらすことを示唆している。本研究では、金属内包フラーレン $M@C_{82}$（M = La、Ce、Pr、Nd、Gd）のピレニル固定相(Buckyprep カラム)における保持時間を精密に測定し、内包金属原子による $M@C_{82}$ の性質の違いを明らかにすることを目的とした。

実験は金属内包フラーレンの合成はアーク放電法を用いて行った。アーク放電に用いた炭素電極は 5 種類のランタノイドの金属酸化物（La_2O_3、CeO_2、Pr_6O_{11}、Nd_2O_3、Gd_2O_3）を混合した粉末とグラファイト粉末とを原子比にして金属：炭素=1:50 となるように混ぜ、10 ϕmm × 100 mm に形成し、1000 ℃にて焼結して作成した。この炭素棒を用いて He 雰囲気、圧力 500 Torr、直流電流 50 A の条件でアーク放電を行い、金属フラーレンを含むススを合成した。このススより 1,2,4-トリクロロベンゼンを用いた還流を 8 時間行い、フラーレン成分の抽出を行った。この抽出溶液からメンブレンフィルターを用いて不溶成分を除去し、溶液を乾固したものを熱中性子照射用の試料とした。この試料を高純度石英管中に封入し、日本原子力研究開発機構の JRR-3M 水力照射設備 HR-1 孔（flux: 9.6×10^{13} n/cm^2・sec）及び気送管照射設備 PN-1（flux: 5.2×10^{13} n/cm^2・sec）において熱中性子照射をそれぞれ 6 時間及び 20 分間行い、試料を放射化した。放射化した試料は開封後、すみやかに CS_2 に溶解し、メンブレンフィルターで熱中性子照射中に生じた不溶成分を除去した。このろ液を乾固した後、トルエン 1mL に再溶解して HPLC 展開用の試料とした。HPLC 分析には Agilent-1200LC システムを用い、固定相として Pyrenyl 固定相をもった Buckyprep カラムを用いた。試料は展開液としてトルエンを用い、flow rate: 3.2 mL/min、Sample Volume : 1 mL、温度：室温の条件で HPLC 展開し、溶出成分を 20

JRR-3M PN-1, JRR-4 T-パイプ, 放射化学

秒ごとに分画した。この分画した成分より放出されるγ線を高純度 Ge 半導体検出器にて測定し、各 $M@C_{82}$ 成分の保持時間を調べた。

結果は、図 1 に La, Ce, Pr, Nd, Gd を内包した $M@C_{82}$ の HPLC 溶離曲線を示している。La については PN-1 孔において照射した試料を、Ce、Pr、Nd、Gd については HR-1 孔において照射した試料から得られたデータを基に作成してある。PN-1、HR-1 各照射における保持時間は Ce の保持時間と UV によりモニタした空フラーレンの保持時間から補正した。得られた溶離曲線を次に示す Extreme モデルによりピークフィッティングを行い、各 $M@C_{82}$ の保持時間を求めた。

Extreme モデル： $y = y_0 + A e^{(1-e^{-\frac{x-x_c}{w}}-\frac{x-x_c}{w})}$

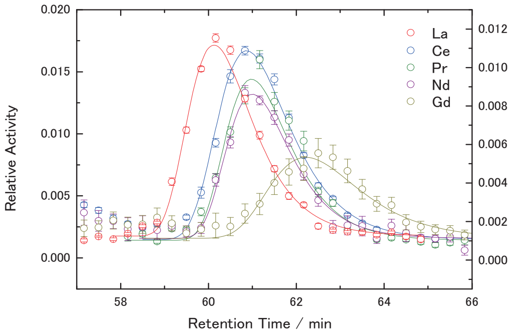

図 1. $M@C_{82}$ のピレニル固定相（Buckyprep カラム）における HPLC 溶離挙動：HPLC 展開条件は試料体積: 1 mL、流速: 3.2 mL/min、展開温度: 20℃であった。

表 1. $M@C_{82}$ の HPLC 保持時間

$M@C_{82}$	保持時間 / min
La	60.13 ± 0.03
Ce	60.88 ± 0.04
Pr	60.98 ± 0.05
Nd	61.00 ± 0.03
Gd	62.22 ± 0.07

詳細な双極子モーメントについての議論および分子構造については今後検討して行く予定である。

２．水溶性ランタノイド金属フラーレンの合成について

フラーレン類はそれだけでは水に不要であるが、誘導体を化学修飾することによって水溶性になり生体などへの取り込みが可能になる。また修飾する誘導体を変えることで、生体内の任意の臓器などに同フラーレンを誘導・凝縮することが可能になる。フラーレンケージには元素の内包が可能であり、内包される元素を放射性同位元素にすることで、高感度放射線測定を可能とする機能性物質の合成あるいは内包した放射性同位元素からの放射線を利用した診断薬などへの応用が期待できる。

そこで既存のランタノイド金属フラーレンを中性子放射化して得られた放射性同位元素内包フラーレン化学修飾する実験を検討した。

La および Sm 金属フラーレンを含む粗抽出物を原子炉で中性子照射した。CS_2 溶媒で溶解した後に 0.2μm のフィルターを用いてろ過し、溶媒をトルエンに置き換えた。Buckyprep 固定相を用いた HPLC 展開を行い $^{140}La@C_{82}$ および $^{153}Sm@C_{82}$ を分画した。この試料に C_{60} を 1 mg 加え、さらにトルエン溶液 2.5ml した。ここに飽和 KOH 水溶液 1ml と TBAH10%溶液 3 滴を加えて激しく振とうさせて化学反応を起こさせた。振とう時間の違いによるトルエン溶液及びアルカリ溶液さらに不溶性成分における ^{140}La および ^{153}Sm の放射能分布、不溶性成分を蒸留水で溶解したのちにサイズ排除ゲルクロマトカラムを用いてアルカリイオンなどから分離し、放射性同位体内包フラレノールの収率などを調べた。

C_{60} にTBAH を触媒にしてKOH を反応させると $C_{60}(OH)_X$ が合成される[2]。同様の手法により $^{140}La@C_{82}$ および $^{153}Sm@C_{82}$ から $RI@C_{82}(OH)_X$ を合成させた。それぞれのRIからのガンマ線を用いて反応させるための振とう時間を変化させた時の水溶性生成物の収率を求めた。当初、トルエン相に存在していたRIは飽和KOH 水溶液とTBAH を反応させるとすぐに水相側とトルエンと水溶液の間に茶色の不溶性成分へと移動する。この変化はトルエン相に溶けている紫色の C_{60} が反応により水相に移動して茶色になるのと同時に大部分は茶色の難溶成分に変化することと一致している。これらの相への移動量を図２ に示す。振とう時間10 分では難溶物に８０%存在しているが振とう時間を8 時間にするとその成分は６０%程度になり、KOH 水溶液相に溶解する割合が上昇した。また、難溶物に蒸留水を加えると溶解するが、この溶液をサイズ排除ゲルクロマトカラムに通してアルカリイオンなどから分離する。これについても RI からのガンマ線によって収率を求めた。振とう時間による変化を図３に示す。溶出位置２１-６０滴は分子サイズが大きな $RI@C_{82}(OH)_X$ が溶出している、これに対して６１-１００滴は分子サイズの小さなイオンなどが溶出している。２１-６０滴のフラクショ

ンでは振とう時間１０分では収率が４０％であるが振とう時間８時間になると６０％まで上昇している。また、６１−１００滴のフラクションには放射線はほとんど観測されていない。今回振とう時間を１０分から８時間まで変化させて生成物の収率変化などを調べたが反応時間が短い場合に３相に分離するうちの難溶成分に８０％存在し、その成分を蒸留水で溶かしてカラム分離するとカラムの固定相に吸着する成分が存在することがわかった。これらの成分は OH が十分に付加していないだけではなくゲルに対して吸着するような反応性を持っていることが推定される。これらのことから反応時間は１時間以上が必要であることがわかった。

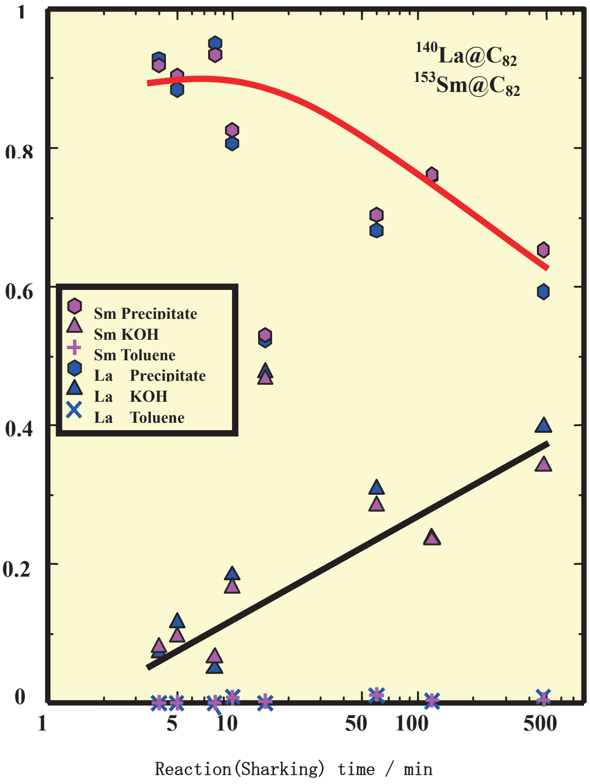

Fig.2. The activity ratios of ^{140}La and ^{153}Sm in three phases as function of reaction time.

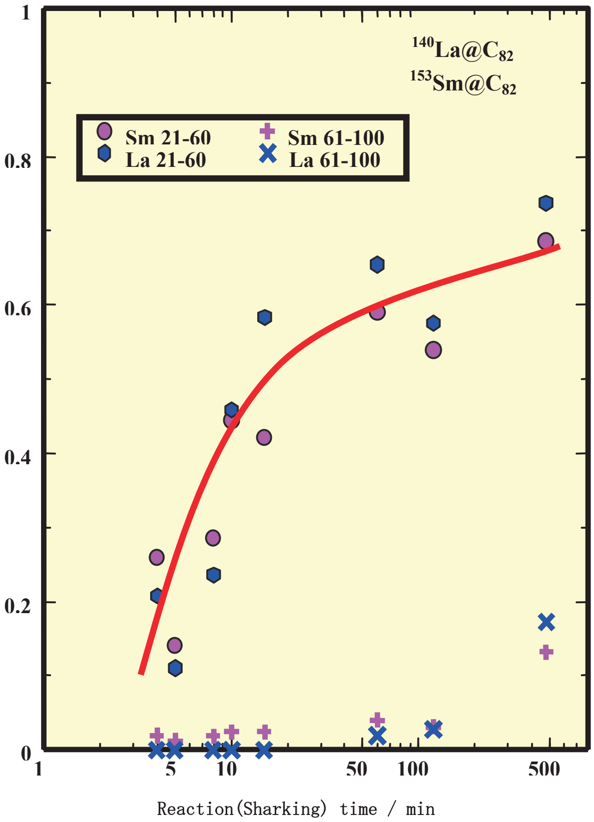

Fig. 3. The fraction yields of ^{140}La and ^{153}Sm in dissolved precipitate through a Sephadex G25 as function time of reaction time.

References

1. K. Akiyama et al., *J. Phys. Chem. A*, 104, 7224 (2000).
2. J. Li et al., *J. Chem. Soc. Chem. Commun.*, 1993, 1784 (1993).

成果の公表

学術誌

1. K. Sueki and Y. Iwai, “Synthesis of radio-metallofullerenols” *J. Radioanal. Nucl. Chem.*, 272 (2007) 505-509.

学会発表

1. 秋山和彦、古川英典、齋藤陽博、濱野達行、末木啓介、片田元己、ピレニル固定相を用いたランタノイド金属フラーレンの HPLC 溶離挙動に関する研究，第 53 回放射化学討論会，2009 年 9 月，東京
2. 末木啓介、長崎芳紀、上司智義、秋山和彦、塚田和明、浅井雅人、豊嶋厚史、永目諭一郎、水

溶性放射性同位体内包フラーレンの合成，第53回放射化学討論会，2009年9月，東京

3. K. SUEKI, Y. Nagasaki, T. Kamitsukasa, K. AKIYAMA, K. TSUKADA, M. ASAI, A. TOYOSHIMA, Y. NAGAME, “Synthesis of water-soluble encapsulated-radioisotope fullerenes” APSORC09, Dec. 2009, Napa.

3-20

3-21

文化財鉄関連資料および環境試料中の微量元素の挙動に関する研究

Determination of trace elements in old iron and tea leaves as environmental standard candidate by neutron activation analysis

平井昭司、加藤将彦、岡田往子：Shoji Hirai、Msahiko Kato、Yukiko Okada
東京都市大学(旧　武蔵工業大学)　工学部：Faculty of Engineering、Tokyo City University
(Musashi Institute of Technology)

１．はじめに

約 4000 年前に人類が始めて鉄を使用して以来永遠と現代まで鉄は国家形成の礎となり、使用されている。鉄鉱石あるいは砂鉄を原料として鉄作りの技術は、発祥を西アジア地方であり、ヒッタイト帝国の基盤として鉄生産技術は確固としたものとして東アジア、南アジア、ヨーロッパと経済と勢力の拡大とともに世界中に広まってきた。わが国においては、弥生末期(3～4 世紀頃)には中国あるいは韓国から青銅器とともに鉄器も流入していた。その後、6 世紀から 7 世紀にかけて鉄作りもわが国独特なたたら製鉄法により鉄作りが行われてきた。

現在、土地の開発や建造物の修復に伴って古代も含めて古い鉄が出土している。このような鉄は、文化財資料として貴重なものとして取り上げられ、各地の博物館や埋蔵文化財センター等に収蔵されている。しかし、鉄の生産技術、鉄の流通過程、鉄作りのための鉄原料の種類・産地や鉄の材質等の知見を得るためには、収蔵だけでは何もわからず、自然科学的な調査と文化財・工学的な調査ではじめて当時作られた鉄の姿の一面を捉えることができる。

本研究はこのような背景の下、鉄材・鉄器に含有する微量元素の着目し、鉄の材質、鉄原料の推定および鉄原料の産地推定を行うなうことを目的とし、中性子放射化分析を行った。また、中性子放射化分析法の選択の理由は、文化財資料である鉄材・鉄器は貴重なため多くの試料を分析に供することができないことと合わせて、鉄の化学的性質で時代とともに錆びて朽ちてなくなることが多いので、多量の試料を得ることが困難なことが挙げられ、少量の試料で多元素を高感度で真度高く定量できる本法は、最適な方法である。

従来のわれわれの研究成果によると、鉄材あるいは鉄器中のヒ素(As)とアンチモン(Sb)の濃度比から鉄材あるいは鉄器を生産した鉄原料の産地推定を可能にすることができた。また、鉄生産に関連して排出される鉄滓においては、鉄滓に含有されているチタン(Ti)とバナジウム(V)の濃度比から鉄生産に関係する鉄原料の産地推定を可能にしている。さらに、遺跡の性質、すなわち、当時操業されていた鉄作りのプロセスを鉄滓の成分から推定することも可能にすることができる。

それゆえ、本研究では、様々な遺跡から出土した鉄材あるいは鉄器を中性子放射化分析し、前述した特質を解明することを目的とした。さらに、文化財鉄関連資料とは異なるが、中性子放射化分析の特徴の一つである真度の高さを生かした環境標準物質候補となる試料の値付けの共同分析に参画した。各種分析法による値付けが終了した後には、認証値として公表され、本標準物質を利用して多くの環境試料の分析値の信頼性確保の一助として貢献することが期待されている。

２．復元たたらによる生産される鉄および鉄滓中の微量元素の挙動

2005 年 11 月 5 日～6 日に福島県文化財センター白河館『まほろん』において、「鉄作り」イベントが行われた。ここでは、砂鉄を原料として平安時代の炉形の大きさを復元したたたら炉が操業され、鉄作りが行われた。

（研究施設、装置、研究分野）：JRR-4　気送管（Pn）　T-パイプ、γ線波高分析器システム、文化財鉄関連試料放射化分析、環境標準物質候補試料放射化分析

本研究では、この鉄製錬過程において生産された鉄塊及びスラグ（鉄滓）中の含有元素濃度から製錬過程によりどのような元素がどのような挙動をするかを評価することを目的としている。

2-1　分析試料

分析試料は、手動ダイヤモンドカッターを使用して鉄塊の金属部を切削した。砂鉄及びスラグ試料は約数ｇの試料をメノウ製乳鉢により粉砕（100μm以下）・均質化したものを採取した。いずれの試料も約 50mg を放射化分析用の試料とした。

2-2　分析条件

中性子照射の条件は、日本原子力研究開発機構の JRR-4 原子炉(熱出力 100kW)を利用した。中性子照射条件およびγ線測定条件を表 1 に示す。なお、Mn の定量では、^{56}Fe（n ， p）^{56}Mn 反応により ^{56}Mn が生成するので、高純度鉄（Mn 極微量）を用いて Fe からの寄与（Mn 28.5μg/Fe 1g）を計算し、補正を行った。また、Cr の定量においては、^{54}Fe（n ， α）^{51}Cr 反応により ^{51}Cr が生成するので、高純度鉄（Cr 極微量）を用いて Fe からの寄与（Cr 8.32μg/Fe 1g）を計算し、補正を行った。

表 1　中性子照射条件およびγ線測定条件

熱中性子束密度 (n·cm^{-2}·s^{-1}) 照射場所		照射時間	冷却時間	測定時間	測定位置 Ge検出器からの距離	分析元素
9.1×10^{11} 気送管	S1 （短寿命核種）	60 sec	3〜6 min	7 min	100 mm	Na Mg Al Cl Ca Ti V Mn
1.5×10^{12} Tパイプ（水力）	L1 （中寿命核種）	6 hr	2 days	60 min	150 mm	K Ga As Br Mo Sb La Sm W U
	L2 （長寿命核種）	6 hr	7 days	120 min	2 mm	Sc Cr Fe Co Ni Zr Sb Cs Ba Ce Yb Lu Hf Au Th

2-3　結果及び考察

表 2 に中性子放射化分析した結果を示す。これらの元素の分析結果のうち、Ti と V との濃度比および As と Sb との濃度比をみると、砂鉄の Ti/V 濃度比：28 であり、排出されたスラグでは約 30 であった。このときの鉄塊でも約 30 であった。また、砂鉄の As/Sb 濃度比：7 であり、生産された鉄塊では約 8 であった。Ti/V 濃度比および As/Sb 濃度比に関しては、原料である砂鉄と生産された鉄塊とそのとき排出されたスラグの間で、同一の値を得ることができた。すなわち、これらの濃度比が鉄原料の産地推定を行う上で、指標となる重要な数値であることが判明した。

表 2　製鉄関連試料の中性子放射化分析の結果

（ppm）

	鉄塊1	鉄塊2	鉄塊3	鉄塊4	鉄塊（卸し）	スラグ4	鍛冶滓
Na	4400	2050	270	2020	51.9	3800	11900
Mg	9100	<4700	< 2700	10000	< 630	17000	<13000
Al	24000	9900	3800	19000	150	38000	48000
Cl	<160	<100	< 54	<140	< 45	<170	<150
K	9600	4500	650	4250	106	9200	19600
Ca	9000	3000	790	8300	< 690	11000	4100
Sc	40.8	21.3	3.24 *	20.4	0.62 *	47.6	15.0
Ti	41000	23000	6100	29000	170	50000	1400
V	1500	970	230	640	11	2500	34
Cr	89.6	61.6	48.0 *	58.1	36.5 *	150	4.36
Mn	3200	1400	530	2500	29	3400	100
Fe	675000	866000	1000000 *	929000	1000000 *	452000	24100
Co	341	382	908 *	292	581 *	15.3	3.44
Ni	<116	<113	< 117 *	109	213 *	<92.5	<61.8
Cu	<270	<200	< 110	<220	93.3	<410	<240
Zn	<69.1	<46.8	< 39.8 *	<37.2	< 33.5 *	<66.1	<54.4
Ga	50.3	58.2	67.8 *	58.1	67.0 *	46.8	22.3
As	39.4	19.4	35.8 *	31.7	29.3 *	<1.07	15.5
Br	<2.04	<1.42	< 0.83 *	<1.30	< 0.70 *	<0.70	<2.90
Zr	<71.3	<68.1	< 68.7 *	62.8	< 61.1 *	<58.8	<30.6
Mo	<44.0	<30.6	21.1 *	<27.7	25.5 *	<35.4	<57.8
In	<0.65	<0.52	< 0.31	<0.62	< 0.07	<0.80	<0.74
Sb	4.82	2.88	1.99 *	2.82	2.38 *	0.15	1.34
I	<29	<22	< 13	<27	< 3.2	<37	<26
Cs	<0.760	<0.712	< 0.692 *	<0.647	< 0.623 *	<0.628	2.74
Ba	118	106	< 113 *	81.2	< 107 *	156	246
La	8.79	4.52	0.88 *	4.42	0.56 *	11.9	11.5
Ce	27.0	<6.47	< 5.81 *	<9.17	< 5.24 *	36.9	42.8
Sm	3.33	1.61	0.25 *	1.59	< 0.07 *	4.33	4.02
Dy	5	<3.3	< 0.88	<2.0	< 0.21	7.4	<1.9
Yb	2.81	1.21	< 0.32 *	1.69	< 0.29 *	3.04	3.32
Lu	0.53	<0.09	< 0.09 *	<0.08	< 0.08 *	<0.09	<0.07
Hf	5.12	2.04	< 0.09 *	2.28	< 0.83 *	5.41	5.34
W	0.75	<1.10	< 0.64 *	<1.04	< 0.90 *	<0.73	<2.40
Au	<0.0067	<0.0065	< 0.0067 *	<0.0063	< 0.0063 *	<0.0061	<0.0036
Th	3.87	2.41	< 0.50 *	2.17	< 0.44 *	4.81	10.8
U	<2.28	<1.56	< 0.85 *	<1.42	< 0.67 *	<1.41	<2.09

<：検出下限値以下の値
＊Feを100%として補正した値

３．佐賀藩反射炉跡から出土した鉄関連資料

江戸幕末期の嘉永 3 年(1850)年、佐賀藩(現　佐賀県)の築地にわが国最初の反射炉が建設され、次いで嘉永 6 年(1853 年)に多布施にも建設された。反射炉においては、大砲つくりに鉄が溶解されるが、その鉄原料がわが国のものか、外国から輸入されたものか、あるいは砂鉄原料としたものか、鉄鉱石原料としたものか未だ解明されていないことが多い。本研究ではこれらのことを解明するため、中性子放射化分析を行った。

分析試料のための前処理や中性子照射条件およびγ線測定条件は、2-1 および 2-2 に示した条件とほぼ同様なので省略する。

3-1　結果及び考察

分析した試料は、鉄滓（SN-3)、鉄棒片（SN-5)、大砲鉄錆片（SN-10、SN-11)、鉄滓（小さな鉄粒を含む)(SN-14m、SN-14ｓ)5 点である。SN-14m と SN-14s との違いは、同一遺物試料の金属部と滓部あるいは錆部である。これらを分析した結果を表 3 に示す。

表 3　佐賀藩反射炉跡から出土した鉄遺物
および大砲鉄錆の分析結果

（μg/g ： ppm）

	SN-3	SN-5	SN-10	SN-11	SN-14m	SN-14s
Na	110	5.2	840	190	9.3	8900
Mg	<630	<1200	<1600	<2300	<5600	<12000
Al	430	15	18	72	150	51000
Cl	420	2200	2200	1800	640	<270
K	270	—	360	170	—	15000
Ca	<990	<810	<770	1100	<1200	6.6
Sc	—	—	0.04	—	0.043	6.6
Ti	<79	<110	<240	<350	570	4400
V	12	49	64	150	1600	530
Cr	67	69	78	120	570	180
Mn	27	120	1600	2900	3900	7200
Fe	830000	1000000	700000	700000	990000	92000
Ni	310	—	360	150	680	—
Co	220	200	110	100	240	15
Cu	230	610	260	110	590	<340
Ga	4.8	52	15	53	75	-
As	26	36	310	22	410	14
Br	5.2	2.0	6.6	3.7	1.1	—
Sb	2.0	3.4	17	3.6	12	0.44
Cs	—	—	—	—	—	1.9
Hf	—	—	—	0.71	0.26	3.9
Ce	—	—	—	—	—	32
Yb	—	—	—	—	—	1.5
La	0.50	0.36	—	0.34	—	12
Sm	-	-	-	0.71	0.15	2.5
W	7.8	9.2	110	2.3	4.9	2.0
Th	—	—	—	—	—	4.6
U	0.43	0.50	0.49	0.42	0.72	1.3
As/Sb	13	11	18	6	34	32

ー:検出されず　　＜:定量下限値以下の値

錆びているか滓部の試料は、Fe 濃度が 100%以下となるが、健全な鉄金属部を残しているところは 100%近くの値になる。それゆえ、Fe 濃度から錆の進行度合いや滓の混入割合を推測できる。また、錆の度合いは、Cl 濃度からも推測でき、これらの試料は滓も含まれるが、Fe が錆びたものであることがわかる。

また、砂鉄原料の指標となる Ti や V 濃度が検出されないあるいは小さいことと、鉄鉱石に比較的特徴な Cu 濃度が高いことからこれらの鉄原料物質は、鉄鉱石であることが推察できた。

分析した試料の鉄原料の同一性をみるために、As/Sb 濃度比を表 3 に示した。表から明らかなように SN-3 と SN-5 の同一性を除けば、全て異なっていた。なお、同一試料である SN-14m と SN-14 s の値は、当然ながら同一の値になっている。

放射化分析を行わなかったが、大きな同一遺物試料の別な箇所の試料 SN-15 の鉄金属部が残存する SN-15m の金属組織を EPMA で観察した図を図 1 に示す。全体が Fe であることがわかるが、図中央部には S が存在していることがわかる。恐らく CuS の形で存在しているものと思われ、表 3 における高濃度な Cu の存在を裏付けるものと推察でき、鉄原料中にこのような化合物が存在していることを示唆する。また、C 濃度が線状に高濃度でみられるのは、Fe 中にセメンタイト（Fe_3C）が多く存在し、鉄自体が鋳鉄の状態にあることを示すものである。

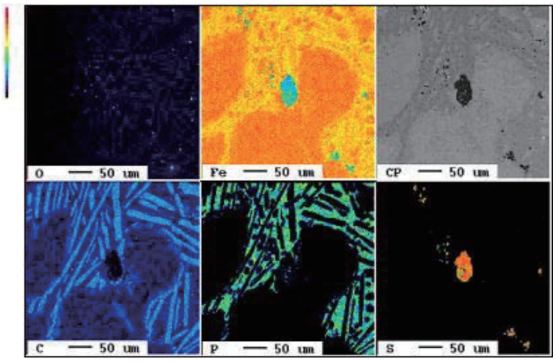

図 1　鉄滓中に含有する Fe 金属部の EPMA 解析像

４．豊島区巣鴨遺跡から出土した鉄釘

豊島区巣鴨遺跡・ハーモニーハイツ地区の遺構は、調査面積 151.4 ㎡で、1999 年４月～６月に調査された遺構である。中山道の街道沿いの町場で鍛冶屋であったと思われる遺構であり、江戸時代の幕末から明治にかけての時期のものである。本遺構のうち 20 号遺構では、ほぼ同じ鉄釘が多量に出土し、釘のリサイクルが行われていたことが推定できる。本研究では、これらの釘がどのような特質を持っているかを調査するため、中性子放射化分析を行った。

分析試料のための前処理や中性子照射条件および γ 線測定条件は、2-1 および 2-2 に示した条件とほぼ同様なので省略する。

4-1　結果及び考察

分析した鉄釘は、長さ 3～6cm、重さ 1～6g の四角い皆折釘で、表面は錆びているが内部は健全な金属部が残っている。炭素濃度が 0.004～0.008%と軟鉄に属するものから、0.02～0.06%の低炭素鋼に属するものである。

表 4 には 6 本の鉄釘を中性子放射化分析した結果を示す。Fe 濃度がほぼ 100%であることからも健全な金属部が残存していることがわかる。本試料中には鉄中に濃集しやすい Co、Ni、As、Sb が高濃度で存在していた。特に、鉄原料の指標となる As/Sb 濃度比は、SG-6 を除いてほぼ 2～4 の値であり、これらの鉄釘は同一の鉄原料により作られたものであることが推察できる。なお、元素濃度だけの情報では、鉄原料の種類を特定できないが、EPMA の解析像で確認すると P が高濃度で検出されていることから鉄鉱石由来であることが推定できた。

表 4　巣鴨遺跡から出土した鉄釘の分析結果

	定量値(ppm)					
	SG-1	SG-2	SG-3	SG-4	SG-5	SG-6
元素	巣鴨遺跡 鉄釘	巣鴨遺跡 鉄釘	巣鴨遺跡 鉄釘	巣鴨遺跡 鉄釘	巣鴨遺跡 鉄釘	巣鴨遺跡 鉄釘
Na	100	34	53	26	140	95
Mg	<360	<320	<290	<310	<290	350
Al	120	120	240	150	130	390
Cl	260	120	<13	<28	25	210
K	200	40	44	<36	57	350
Ca	530	<160	<200	<200	<200	<420
Sc	0.12	0.41	0.36	0.48	0.45	0.36
Ti	<70	<66	<57	<68	<58	<29
V	33	53	32	27	37	10
Cr	43	42	35	33	41	69
Mn	450	570	270	570	380	40
Fe	1030000	980000	1000000	970000	960000	1010000
Co	78	89	110	110	64	150
Ni	190	160	240	240	180	470
Zn	<25	<18	15	<21	<20	<20
Ga	-	25	20	20	17	-
As	130	120	450	130	470	46
Se	-	<1.7	<2.5	<2.1	<2.3	-
Br	1.1	0.61	<0.60	<0.50	<0.57	0.96
Rb	17	<13	43	<16	<15	18
Zr	<210	<230	<290	<270	<260	<170
Ag	23	13	45	<13	41	7.1
Sb	40	27	220	63	220	2.7
Te	<61	<62	<100	<78	<92	<43
I	<3.6	<3.1	<2.8	<3.4	<2.8	<1.3
Cs	<0.38	15	130	39	130	<0.68
Ba	<93	<67	<91	<81	<83	<72
La	0.25	0.28	0.35	0.17	0.13	0.18
Ce	<2.4	<2.1	<2.5	<2.5	<2.5	<1.8
Sm	<0.081	<0.049	<0.097	<0.058	<0.089	<0.024
Tb	<0.42	<0.22	<0.27	<0.26	<0.24	<0.33
Yb	<0.21	<0.14	<0.23	<0.18	<0.21	<0.15
Lu	<0.041	<0.025	<0..038	<0.031	<0.035	<0.030
Hf	<0.47	<0.31	<0.42	<0.37	<0.38	<0.36
Ta	-	<0.33	<0.52	<0.38	<0.41	-
Au	0.008	0.022	0.13	<0.0042	0.22	<0.0040
Hg	<0.42	-	-	-	-	<0.27
Th	<0.30	<0.20	<0.31	<0.25	<0.28	<0.22
U	<1.0	-	-	-	-	<0.65
As/Sb	3.2	4.3	2.1	2.1	2.1	16.6

５．鏡鉄鉱を原料とした模擬たたら製鉄による各元素の挙動

鳥取県日南町と島根県奥出雲町の県境にある船通山は、「八岐大蛇」の神話になった舞台で、船通山からは赤鉄鉱の一種である鏡鉄鉱が産することが知られている。古代にいて鳥取県や島根県で数多くのたたら製鉄が行われてきたが、一般にはこの地方で産する砂鉄が利用されて鉄作りが行われてきた。しかし、船通山で鏡鉄鉱が産するとなると、この鉄鉱石を利用してどのような鉄ができるかは、非常に興味あることである。本研究では、この地方で産した鏡鉄鉱を利用した模擬たたら実験と、他地域の品質のよい鏡鉄鉱を用いて模擬たたら実験を行った。この実験を通しての各元素がどのような共同をするかを調査の目的とした。

分析試料のための前処理や中性子照射条件および γ 線測定条件は、2-1 および 2-2 に示した条件とほぼ同様なので省略する。

5-1　結果及び考察

各種鏡鉄鉱を分析した結果を表 5 に示す。表中の Fe 濃度をみると、20～60%と幅広くばらついている。Fe 濃度が高ければそれだけ鏡鉄鉱の品位が高く、逆に低ければ品は悪くなる。すなわち、品位が悪いということは、それだけ脈石成分が多いということに

なり、それだけ不純物元素が多いということになる。このような観点からすると、脈石成分の多くは長石類や石英となる。長石は K_2O が多く含有され、石英は SiO_2 が成分となるが、放射化分析では、K しか定量できないが、Fe 濃度と逆相関がみられる。また、相関性は必ずしもないが、Ti、Mn、Co、As の間にも大きな濃度のばらつきがみえてくる。特に、同一地域の鏡鉄鉱となると As/Sb 濃度比が興味深い。2 点の試料については、As あるいは Sb が定量下限値以下の値であったので比較をすることができないが、KN1-4A の試料を除いてほぼ同一の値であった。KN1-4A の試料は谷川の中で採取した試料であることから、他の地域から川の流れによって運ばれたものと推定でき、値が異なったものと思われる。

模擬たたら実験ではこれら鏡鉄鉱を混ぜて使用したので、たたら実験により生産された鉄塊の各元素濃度を比較しようとしたとき、混入割合を知ることができなかったので、今回はその評価を行うことができなかった。しかし、鉄塊と鉄滓(スラグ)との間で、特定の元素がどちらかに濃集する傾向をみることができた。細かい数値はここでは省略する。

表 5　船通山地域からの鏡鉄鉱の分析結果

(ppm)

Element	KN1-1	KN1-2	KN1-3A	KN1-3B	KN1-3C	KN1-3D	KN1-4A
Na	56	360	760	170	270	300	520
Mg	2100	7800	<3000	5800	7000	9900	5100
Al	2600	51000	35000	44000	42000	61000	36000
Cl	<36	110	<140	<130	<180	<160	<110
K	3200	30000	<11000	12000	19000	22000	840
Ca	<180	<1600	21000	<1800	<4800	<2300	<1900
Sc	7.6	31	4.3	4.6	16	2.9	3.0
Ti	1500	2400	1000	1100	3700	790	<340
V	<0.64	260	29	43	220	31	33
Cr	46	<3.4	31	19	53	25	24
Mn	710	710	620	2500	14000	1300	1300
Fe (%)	59	41	42	36	21	32	38
Co	8.7	13	250	150	13	730	480
Ni	<58	<58	<80	<61	<62	<88	<78
Zn	<16	31	<20	130	75	110	130
As	<0.82	2.3	11	2.5	1.1	22	16
Se	<2.0	<1.4	<2.3	<1.8	<1.9	2.5	<1.5
Br	<1.3	<2.5	<3.8	0.74	<0.88	<1.6	1.1
Rb	55	240	65	100	140	190	62
Zr	<220	100	<170	92	<140	<190	<170
Ag	<0.89	2.3	<2.7	<2.1	<2.4	<3.0	<2.6
Sb	1.1	2.3	7.4	1.2	1.8	<0.83	1.0
Te	<76	<49	<97	<73	<80	<110	<100
I	<4.6	<24	<17	<17	<21	<20	<18
Cs	1.2	6.9	2.4	2.6	4.1	4.6	<0.55
Ba	<90	310	<100	250	490	560	190
La	1.4	2.0	28	22	2.6	5.2	6.9
Ce	<2.2	<1.7	70	48	6.5	12	16
Sm	<0.19	0.71	4.9	3.5	0.75	0.8	1.1
Tb	<0.19	<0.23.	0.22	<0.16	<0.21	<0.37	<0.31
Yb	0.41	<0.18	1.6	1.8	<0.40	<0.54	0.94
Lu	<0.034	<0.038	0.28	0.25	0.099	0.078	0.15
Hf	<0.44	<0.43	3.2	4.2	1.5	2.7	3.6
Ta	0.24	ND	0.49	0.41	<0.21	0.92	<0.16
Au	<0.0044	0.0038	<0.017	<0.013	<0.015	<0.020	<0.019
Th	<0.26	<0.25	5.3	7.6	2.9	7.4	10
U	0.64	3.3	4.5	2.8	0.62	2.1	2.0
As/Sb *	—	1.0	1.5	2.1	0.6	—	16.0

６．　舞崎遺跡出土の鉄材の材質

舞崎遺跡は、福井県敦賀市に位置し、弥生時代から古墳時代前期にかけて多くの住居跡や古墳からなる遺跡である。今回、このうちの 1 号古墳と 3 号古墳の中から不明板状鉄製品が出土した。図 2 は 3 号古墳から出土した不明板状鉄製品 (TM-1) (長さ 18.0cm×幅 5.4～6.9cm×厚さ 1.0～1.3cm、重さ 649g) の概観である。分析は、図中右下にあるようなところから試料を切り出した。1 号古墳からも同様な試料(TM-2m)を切り出した。TM-2m は明らかに金属部が見えたが、TM-1 は全て錆びていた。

分析試料のための前処理や中性子照射条件およびγ線測定条件は、2-1 および 2-2 に示した条件とほぼ同様なので省略する。

図 2　舞崎遺跡 3 号古墳から出土の不明板状鉄製品 ((TM-1)

6-1　結果及び考察

これら不明板状鉄製品の C 濃度は、0.09％と 0.55％であり、現代で言う低炭素鋼と中炭素鋼に属していた。中性子放射化分析をした結果を表 6 に示す。TM-1 は錆びていたが、黒錆の状態であり、Fe 濃度は 69％であった。一方、金属部を残した TM-2m は 100％であった。錆びた TM-1 では、Na、Al、Cl、K の濃度が高かった。金属が残存する TM-2m では、金属部に濃集しやすい Co や As が低濃度であったが、Mo や Sb が高濃度であった。また、両試料に共通して Zr が高濃度であった。

鉄原料の産地推定の指標となる As/Sb 濃度比を

みると、TM-1 が 0.033、TM-2m が 0.037 と両試料とも 1.0 以下の値となっていた。過去のわれわれの分析結果から推測すると、本鉄原料は日本産の鉄原料を使用して作った鉄ではなく、韓半島産の鉄原料を使用したものと思われる。また、砂鉄特有の Ti や V 濃度が非常に低濃度であったことから鉄鉱石であることも推察できた。

以上の結果により、本試料は韓半島からの舶載品であることが判明した。

表 6　舞崎遺跡出土の不明板状鉄製品の

(ppm)

elements	TM-1	TM-2m
Na	750	< 100
Mg	< 900	< 580
Al	1200	78
Cl	8500	100
K	180	< 34
Ca	< 1200	< 980
Sc	0.70	< 0.084
Ti	< 140	< 56
V	1.5	< 0.4
Cr	26	24
Mn	4	ND
Fe	690000	1000000
Co	6.4	9.3
Ni	< 91	< 120
Cu	< 67	< 25
Zn	< 27	< 34
Ga	6.6	8.8
As	2.7	11
Br	1.7	< 0.67
Zr	450	1600
Mo	22	28
In	< 0.23	< 0.072
Sb	81	290
I	< 6.9	< 3.3
Cs	< 0.49	< 0.80
Ba	< 100	< 150
La	1.3	< 0.063
Yb	< 0.29	< 0.46
Lu	< 0.082	< 0.18
Ce	< 5.4	< 7.6
Sm	0.14	< 0.10
Hf	< 0.71	< 1.0
W	< 0.85	0.40
Dy	< 0.56	< 0.19
Au	< 0.006	< 0.0093
Th	0.75	< 0.19
U	< 1.3	< 1.1
As/Sb*	0.033	0.037

*：Ratio of As concentration to Sb concent
＜：Lower limit of determination
ND：No detected

7．本願寺境内から出土した鉄滓と鉄塊の関係

京都の西本願寺は、浄土真宗の宗祖親鸞聖人を祀った本願寺派の本山である。境内には、寛永 13 年(1636 年)に建立された御影堂があり、平成 10 年(1998 年)から平成 21 年(2009 年)にかけて大規模な修復工事が行われてきた。その工事の一環では、屋根瓦の吹き替えも行われ、長さ約 40cm、重さ 300～400g の瓦用鉄釘や裏甲に留める裏甲用鉄釘が抜き取られた。これらの鉄釘は、すでに分析され、全てが同一地域(奥出雲地方)の砂鉄を原料とした鉄材から加工したものであることが明らかとなっている。

今回、西本願寺境内の防災設備工事による掘削を行ったところ、鉄鍛冶に関連する羽口や鉄滓が出土した。鉄滓の一つには、大部分が鉄塊である試料も出土した。これらの試料が、どのような性格の試料であるかを調査するため、中性子放射化分析を行った。

分析試料のための前処理や中性子照射条件およびγ線測定条件は、2-1 および 2-2 に示した条件とほぼ同様なので省略する。

7-1　結果及び考察

鉄滓 5 点および鉄塊 1 点と鉄塊に隣接する滓部あるいは錆部 1 点を分析した。全ての分析結果は省略するが、鉄原料の産地推定の指標となる As/Sb 濃度比は、先に分析した瓦用鉄釘および裏甲用鉄釘の値 11±2 の値とほぼ一致していた。図 3 は従来分析した瓦用鉄釘と裏甲用鉄釘（◆）の結果と、今回分析した鉄滓（□）と鉄塊(○)の結果を基に、縦軸を Sb/Fe 濃度比、横軸を As/Fe 濃度比の図にプロットしたものである。図中の 45 度の点線は、As/Sb=11 の直線で、この点線上にある試料は、As/Sb 濃度比が全て一定の 11 であることを意味する。

すなわち、西本願寺境内から出土した鉄鍛冶に関連する遺物は、全て鉄釘の成分と関連していた。御影堂に使用されていた瓦用鉄釘の総本数が、およそ 3500 本であることを考えると総重量で約 1 トン近くになる。これに裏甲用鉄釘や他の建築用の鉄釘を考えると合わせて数トンの鉄釘が使用されていたと思われる。それゆえ、当時(寛永 16 年)の建立に際して

は、多くの鉄材が境内に持ち込まれ、そこに設置された鍛冶工房により、鉄釘の加工がなされていたことが伺える。今回出土した鉄鍛冶に関係する羽口や鉄滓はそのとき破棄されたものの一部と思われる。今回の分析の成果により、当時の材料の調達等の様子を新たに知ることができ、貴重な発見と思われる。

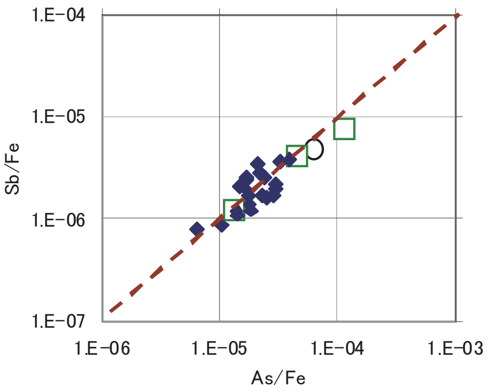

図 3　西本願寺御影堂に使用された瓦用鉄釘と裏甲用鉄釘および境内から発掘された鉄滓と鉄塊の As/Fe 濃度比－Sb/Fe 濃度比の相関関係

表7　分析試料の重量

	短時間照射	試料重量(mg)		長時間照射	試料重量(mg)
茶葉NIES-23	T-23	182.7	茶葉NIES-23	T-1	317.0
	T-4	119.4		T-2	743.9
	T-5	209.7		T-7	194.3
	T-6	523.6		T-8	462.8
				T-9	221.4
類似物質	R-1	99.5	類似物質	R-4	141.8
	R-2	201.8			
	R-3	301.9			
比較標準試料 NIES-7	T7-2	107.6	比較標準試料 NIES-7	T7-4	332.7
	T7-3	330		T7-5	159.1
NIST1573a	TL-1	104.4	NIST1573a	TL-4	163.6
	TL-2	195.7			
	TL-3	347.4			

表８　照射・測定条件と分析元素

Irradiation facility, Thermal neutron flux ($n\cdot m^{-2}\cdot sec^{-1}$)	Irradiation time	Cooling time	Counting time	Anlyzed elements
JRR-3				
PN-3 1.5 × 10^{17}	0.5 sec	3 min～4 min	400 sec	(Na) Mg Al Cl Ca Ti V Mn Cu I Dy (K)
PN-1 5.2 × 10^{17}	10 min	4～5 d	2.7 hr	Na K (As) Br (Mo) (Sb) La Sm (Yb) (U) Rb
		20 d～21 d	2.7 hr	Sc Cr Fe Co (Ni) Zn Sb Ba La Cs Sm (Yb) (Se) (Hf) Ta Th (Sb) (Ba) Rb

８．環境標準物質候補試料（茶葉Ⅱ）の値付け

（独）国立環境研究所（NIES）は、多元素分析を行う際の精度管理や分析機器の校正のために、認証標準物質を従来から開発してきた。今回、環境標準物質の一つとなる茶葉標準物質候補試料（NIES CRM No.23）を中性子放射化分析した。

8-1　分析試料

分析試料は、表 7 に示す重量をポリエチレン袋に二重封入した。比較標準物質は、NIES CRM No.7（茶葉）と送付されてきた類似物質と NIST SRM 1573a（トマト）を用いた。

8-2　中性子照射およびγ線測定

試料の中性子照射は、JRR-3M の PN-3 の気送管（短寿命用）と PN-1 の気送管（中・超寿命用）を使用し、詳細を表８に示す。また、照射後のγ線測定は生成する核種の半減期に合わせて、表８に示す条件で行った。

8-3　結果および考察

分析した結果をまとめたのが表 9 である。表では複数の試料（n=4～5）のデータの平均値と標準偏差を示している。Cr については試料名を書くマジックインクの影響が出てばらつきが多かった。

表9　環境標準物質候補　NIES CRM No.23の分析結果

元素	平均値 (mg/kg)	標準偏差 (mg/kg)	CV (%)	分析数 n	認証値（参考値） (mg/kg)
Mg	1770	± 85	4.8	4	1690 ± 120
Al	569	± 22	3.9	4	(540)
Cl	904	± 14	1.6	4	
Ca	2830	± 373	13	4	2490 ± 210
Mn	699	± 27	3.8	4	704 52
Na	9.27	± 0.44	4.8	5	(21.6)
K	20650	± 370	1.8	5	20300 ± 1100
Sc	0.0164	± 0.0003	2.0	5	
Cr	0.170	± 0.087	51	5	
Fe	102	± 5	4.6	5	
Co	0.221	± 0.010	4.6	4	
Zn	32.7	± 1.0	3.1	5	31.9 ± 2.2
Br	4.73	± 0.11	2.4	5	
Rb	15.1	± 0.1	0.8	5	
Cs	0.115	± 0.016	14	4	(0.0932)
La	0.168	± 0.020	12	5	
Sm	0.0274	± 0.0017	6.3	4	
Ta	1.72	± 0.10	5.9	5	

定量できた多くの元素は CV 値も数%でよい精度で分析が行えた。認証値の決定については、各種分析法による共同分析で行われた。表 9 には参考のため、国立環境研究所から報告された認証値および参考値も掲載した。認証値に付けられた不確かさは、包含係数 k ＝2 の値である。参考値の Na を除いていずれも認証値あるいは参考値と等しかった。また、数値のないものは、他の方法で値付けがされなかったものである。

９．おわりに

文化財関連資料特に鉄に関しては、鉄原料の種類の同定や産地の推定が非常に重要なこととなる。中性子放射化分析による微量な As、Sb、Ti、V の濃度を知ることにより、これらの問題解決に有効になりうる。そのため、今回報告した成果は、文化財科学の分野で大いに役立つものと確信している。

また、環境標準物質候補の値付けに関しても中性子放射化分析は真度が高いことから、欠かせない分析法であることも実証できたと思われる。

１０．成果の公表

10-1 論文等

1) まほろん２号炉における復元たたら製鉄からの製鉄関連資料中の元素濃度及び金属学的組織の調査；平井昭司、加藤将彦、小椋幸司、鈴木章悟、岡田往子、福島県文化財センター白河館研究紀要 **2006**、63-80（2007）
2) 佐賀藩反射炉由来の鉄鋼の分析；加藤将彦、平井昭司、鈴木章悟、岡田往子、幕末佐賀科学技術史研究　第 3 号、1-48（2008）
3) 佐賀築地及び多布施反射炉跡地から発掘された鉄及びスラグの分析；加藤将彦、平井昭司、岡田往子、鈴木章悟、長野暹、考古学と自然科学、**58**、13-24（2009）
4) 豊島区巣鴨遺跡及び染井遺跡出土の鉄釘の自然科学的分析；加藤将彦、平井昭司、豊島区埋蔵文化財調査報告 **26**　巣鴨町 XII、293-303、写真図版 137-写真図版 145（2009）
5) 鏡鉄鉱を原料とした模擬たたら製鉄からの製鉄関連試料の科学的調査；加藤将彦、平井昭司、鈴木章悟、鉄と鋼、**95**、No. 6、473-482（2009）
6) 理科学的分析法による舞崎遺跡出土の古代鉄材の材質調査；加藤将彦、平井昭司、鈴木章悟、岡田往子、鉄と鋼、**95**、No. 7、550-556（2009）
7) 自然科学的分析法による本願寺境内より出土した鉄滓の科学的調査；加藤将彦、平井昭司、本願寺防災施設工事・発掘調査報告書、189-210（2009）
8) 西本願寺境内より出土した鉄滓及び鉄塊の金属学的分析；加藤将彦、平井昭司、鉄と鋼、**95**、No. 10、682-689（2009）

10-2 発表

1) 佐賀県反射炉由来の鉄鋼分析；加藤将彦、小椋幸司、平井昭司、岡田往子、鈴木章悟、長野暹、日本文化財科学会第 24 大会、2007 年 6 月
2) 鏡鉄鉱を原料としたせい鉄関連資料の科学的調査；加藤将彦、平井昭司、鈴木章悟、岡田往子、日本鉄鋼協会「鉄の歴史フォーラム」第 9 回公開研究発表会、2007 年 7 月
3) たたら製鉄を解明するための分析技術；加藤将彦、平井昭司、日本学術振興会製鋼第 19 委員会、2007 年 11 月
4) 燃焼赤外線吸収法及び機器中性子放射化分析法による日本刀中の微量元素の定量、岡田往子、平井昭司、大谷眞一、日本鉄鋼協会第 155 回春季講演大会、2008 年 3 月
5) 微量元素からみた弥生の鉄；平井昭司、日本鉄鋼協会「鉄の歴史フォーラム」第 18 回フォーラム講演会
6) 西本願寺境内から出土した鉄滓と御影堂の鉄釘との関係；平井昭司、加藤将彦、岡田往子、日本文化財科学会第 25 回大会、2008 年 6 月
7) As/Sb 濃度比を指標とした西本願寺の鉄釘及び鉄滓の原材料の産地推定；加藤将彦、平井昭司、日本文化財科学会第 26 回大会、2009 年 7 月

4.　その他

4. Others

4-1

研究テーマ：フィッショントラック法による環境試料中の核物質検出
表　　　題：フィッショントラック法の保障措置環境試料パーティクル分析への応用

保障措置環境試料のための高濃縮ウランを含む粒子の選択的選出

李 致圭、鈴木大輔、江坂文孝、間柄正明、木村貴海、篠原伸夫
日本原子力研究開発機構　原子力基礎工学研究部門　環境・原子力微量分析研究グループ

保障措置環境資料法は、原子力関連施設から採集したスワイプ試料中に含まれる核分裂性物質の同位体比を測定することにより未申告原子力活動の検知を目的とした、IAEAの保障措置の強化策として導入されたものである。スワイプ試料から回収した個々の粒子の同位体比を測定するパーティクル分析では回収された無数の粒子の中で疑いのある粒子が僅かに存在する場合でも、それを確実に検出する必要がある。FT-TIMS法によるパーティクル分析では、サブミクロンサイズの粒子に対しても高感度な検出と分析が可能である。1) 本研究では保障措置上重要な高い濃縮度のウラン粒子を、FTを検出するためのエッチング時間等の制御により、質量分析の前に検出できる方法を開発した。2)

FTは熱中性子照射によりウラン粒子の一部が核分裂した際生成する核分裂片の飛跡であり，ウラン粒子を構成しているウラン同位体の中で核分裂が起きやすいのは^{235}Uのみであるので，^{235}Uの含有量が多い高濃縮度粒子ほどFTが多くなる。FTのエッチング速度は粒子の濃縮度の増加と共に速くなる。3) これは，高濃縮度の粒子ほど短いエッチング時間で検出されることを意味し，エッチング時間を制御することによりウラン粒子の濃縮度別検出が可能であること示唆する。ウラン粒子をFT検出器のエッチング時間の制御により濃縮度別に検出するためには，まず各濃縮度の粒子が検出されるエッチング時間を決める必要がある。図 1 は，種々の濃縮度のウラン粒子に対して，45℃の 1M NaOH のエッチング条件で，FTを検出するために必要なエッチング時間のウラン粒子の濃縮度依存性を示す。濃縮度の増加と共にそのエッチング時間が短くなることが分かる。図 1 の関係に基づいて，粒径分布が 0.8～3 μmの 10%濃縮ウランと天然組成のウラン粒子を混合した試料を調製し，10%濃縮ウランを優先的に検出する実験を行った。検出器のエッチング法は 2 段階エッチング法を用い，エッチングー1 で粒径の大きい 10%濃縮ウランを検出し，エッチングー2 で粒径の小さい 10%濃縮ウランを検出する。エッチングー1 でのエッチング時間は，10%濃縮ウランのみが検出される 100 分を用いた。図 2 に 100 分のエ

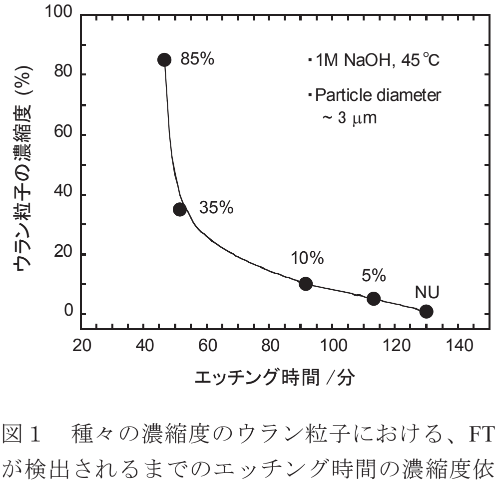

図１　種々の濃縮度のウラン粒子における、FT が検出されるまでのエッチング時間の濃縮度依存性。

原子炉：JRR-3　　　　装置：気送管　　　　分野：その他（フィッショントラック）

ッチングにより検出されたFT形状の例と，それに対応するウラン粒子の同位体比測定結果を示す。図に示したように，エッチングー1 により検出されたウラン粒子はすべて10%濃縮ウランであることが確認された。続いてのエッチングー2 では，すべてのウラン粒子が検出される条件であるので，FT形状だけでは両者区別は困難である。即ち，粒径の小さい 10%濃縮ウランと粒径の大きい天然ウランの場合，双方のFT形状は類似する場合があるので区別できない。このような場合は，FTに対応する粒子の大きさを比較する。一般に，FTの数が同程度であれば，粒径が小さい方が高濃縮である。その例を図 3 に示した。FT形状が同程度でれば，粒径の小さい粒子は 10%濃縮ウラン, 粒径の大きい粒子は天然ウランであることが確認できる。

このように, 高い濃縮度のウラン粒子を粒径毎に 2 回にわたって検出するので, 検出効率は高くなる。特に，スワイプ試料から回収した無数のウラン粒子の中に高濃縮度ウランがわずかに存在する場合でも, それを見逃さず見つけ出すことができる。

参考文献

1) C. G. LEE *et al.*, Jan. J. Appl. Phys. 42 (2006) L1121-L1123.
2) C. G. LEE *et al.*, J. Nucl. Sci. Techol., 46 (2009) 809-813.
3) C. G. LEE *et al.*, NIMB 245 (2006) 440-444.

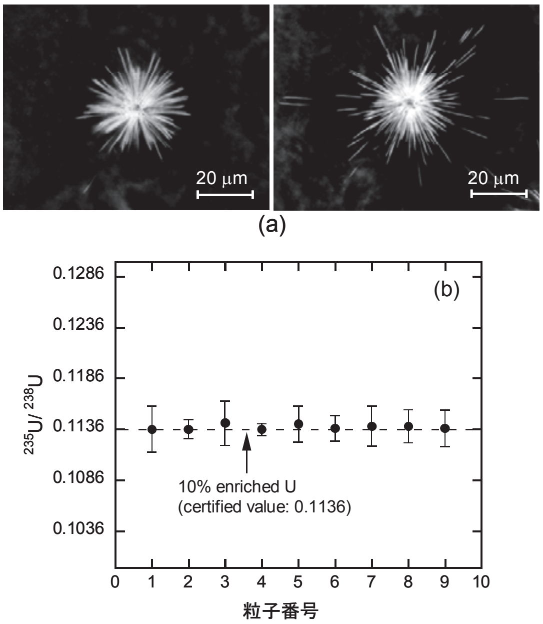

図 2　エッチングー 1 により検出された FT（a）とそれに対応するウラン粒子の同位体比測定結果（b）

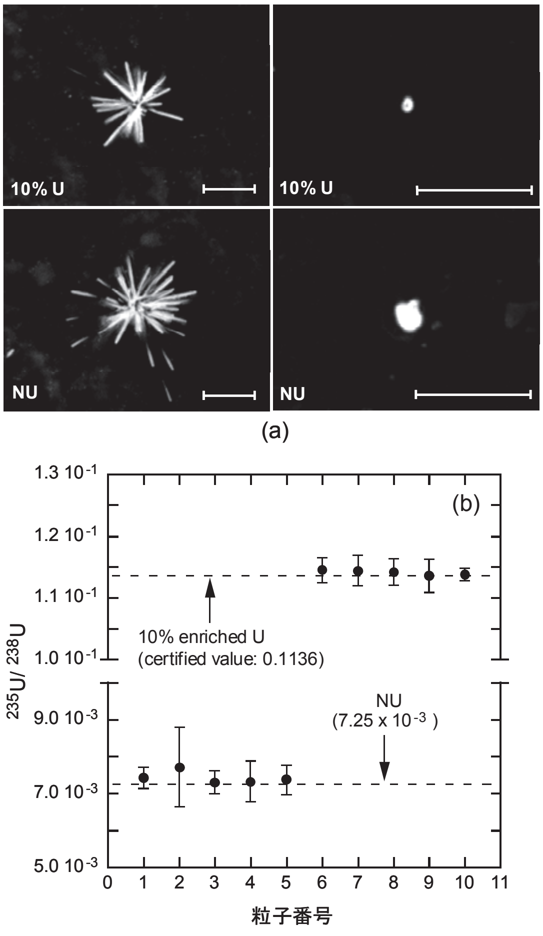

図 3　エッチングー2 により検出された FT（a）とそれに対応するウラン粒子の同位体比測定結果（b）。図(a)中のスケールは 10 µm である。

お わ り に

本報告書は、研究炉（JRR-3、JRR-4）を利用した利用者の協力を基に、研究炉の成果を提出して頂き、研究炉利用課で編集したものであります。この成果を公表する事で、研究炉の今後の有効利用並びに利用拡大に役立つ事を期待します。

編集委員

編集委員メンバー	
笹島　文雄	（研究炉利用課長）
高橋　広幸	（研究炉利用課）
大和田博之	（研究炉利用課）

謝　辞

本報告書の発刊にあたり、多くの皆様から多大なご協力を頂きました。

原稿を提出して頂いた利用者の皆様のご協力に感謝するとともに、今後も研究炉が有効に利用され、種々の研究がさらに進展されることを期待します。

編集に際し、ご協力頂いた、研究炉加速器管理部長 丸尾毅氏、研究炉加速器管理部 JRR-4管理課課長 木名瀬政美氏に深く感謝致します。

付　録

Appendixes

付 録

原科研研究炉の利用設備一覧

１．ＪＲＲ－３

１）実験設備

実験孔	実験装置
１Ｇ	高分解能粉末中性子回折装置（ＨＲＰＤ）
１Ｇ－Ａ	生体高分子用中性子解析装置（ＢＩＸ－Ⅲ）
１Ｇ－Ｂ	生体高分子用中性子解析装置（ＢＩＸ―Ⅳ）
２Ｇ	三軸型中性子分光器（ＴＡＳ－１）
３Ｇ	中性子トポグラフィ及び精密光学実験装置（ＰＮＯ）
４Ｇ	汎用三軸型中性子分光器（ＧＰＴＡＳ）
５Ｇ	偏極中性子散乱装置（ＰＯＮＴＡ）
６Ｇ	東北大学中性子散乱分光器（ＴＯＰＡＮ）
７Ｒ	中性子ラジオグラフィ装置（ＴＮＲＦ）
Ｔ１－１	中性子偏極回折装置（ＨＱＲ）
Ｔ１－２	単結晶中性子回折装置（ＫＳＤ）
Ｔ１－３	粉末中性子回折装置（ＫＰＤ）
Ｔ１－４－１	即発ガンマ線分析装置（ＰＧＡ）
Ｔ１－４－２	多重即発ガンマ線分析装置（ＭＰＧＡ）
Ｔ１－４－３	ＴＯＦ型中性子反射率計（ＴＯＦ）
Ｔ１－４－４	中性子ラウエ回折装置（ＬＡＵＥ）
Ｔ１－４－５	中性子ベータ崩壊基礎測定装置
Ｔ２－１	残留応力測定中性子回折装置（ＲＥＳＡ）
Ｔ２－２	中性子４軸回折装置（ＦＯＮＤＥＲ）
Ｔ２－３	多目的単色熱中性子ビームポート（ＭＵＳＡＳＨＩ）
Ｔ２－４	高分解能三軸型中性子分光器（ＴＡＳ－２）
Ｃ１－１	高エネルギー分解能三軸型中性子分光器（ＨＥＲ）
Ｃ１－２	二次元位置測定小角散乱装置（ＳＡＮＳ－Ｕ）
Ｃ１－３	超高分解能後方散乱装置（ＵＬＳ）
Ｃ２－１	冷中性子散乱実験デバイス開発装置（ＬＴＡＳ）
Ｃ２－２	高Ｑ領域対応中性子反射率計（ＳＵＩＲＥＮ）
Ｃ２－３－１	中性子スピンエコー分光器（ＮＳＥ）
Ｃ２－３－２－１	多重即発ガンマ線分析装置（ＭＰＧＡ）
Ｃ２－３－２－２	即発ガンマ線分析装置（ＰＧＡ）
Ｃ２－３－３－１	冷中性子ラジオグラフィ（ＣＮＲＦ）
Ｃ２－３－３－２	パルス中性子機器開発装置（ＣＨＯＰ）
Ｃ２－３－３－３	ＴＯＦ型中性子反射率計（ＴＯＦ）
Ｃ２－３－３－４	中性子ラウエ回折装置(ＬＡＵＥ)
Ｃ３－１－１	高分解能パルス冷中性子分光器（ＡＧＮＥＳ）
Ｃ３－１－２－１	中性子光学システム評価装置（ＮＯＰ）
Ｃ３－１－２－２	多層膜中性子干渉計／反射率計（ＭＩＮＥ）
Ｃ３－２	中性子小角散乱装置（ＳＡＮＳ－Ｊ）

２）照射設備

水力照射設備	ＨＲ－１，２
気送照射設備	ＰＮ－１，２
放射化分析用照射設備	ＰＮ－３
均一照射設備	ＳＩ－１
回転照射設備	ＤＲ－１
垂直照射設備	ＶＴ－１，ＲＧ－１～４ ＢＲ－１～４，ＳＨ－１

２．ＪＲＲ－４

１）実験設備

プール
中性子ビーム設備
散乱実験設備
冷却水循環ループ
医療照射設備（ＢＮＣＴ）
即発ガンマ線分析装置

２）照射設備

簡易照射筒	Ｔパイプ（水力）
	Ｓパイプ
	Ｄパイプ
	Ｎパイプ
気送管照射設備	ＰＮ

国際単位系（SI）

表１．SI 基本単位

基本量	SI 基本単位	
	名称	記号
長さ	メートル	m
質量	キログラム	kg
時間	秒	s
電流	アンペア	A
熱力学温度	ケルビン	K
物質量	モル	mol
光度	カンデラ	cd

表２．基本単位を用いて表されるSI組立単位の例

組立量	SI 基本単位	
	名称	記号
面積	平方メートル	m^2
体積	立法メートル	m^3
速さ，速度	メートル毎秒	m/s
加速度	メートル毎秒毎秒	m/s^2
波数	毎メートル	m^{-1}
密度，質量密度	キログラム毎立方メートル	kg/m^3
面積密度	キログラム毎平方メートル	kg/m^2
比体積	立方メートル毎キログラム	m^3/kg
電流密度	アンペア毎平方メートル	A/m^2
磁界の強さ	アンペア毎メートル	A/m
量濃度 (a)，濃度	モル毎立方メートル	mol/m^3
質量濃度	キログラム毎立法メートル	kg/m^3
輝度	カンデラ毎平方メートル	cd/m^2
屈折率 (b)	（数字の） 1	1
比透磁率 (b)	（数字の） 1	1

(a) 量濃度（amount concentration）は臨床化学の分野では物質濃度（substance concentration）ともよばれる。

(b) これらは無次元量あるいは次元１をもつ量であるが、そのことを表す単位記号である数字の１は通常は表記しない。

表３．固有の名称と記号で表されるSI組立単位

組立量	SI 組立単位			
	名称	記号	他のSI単位による表し方	SI基本単位による表し方
平面角	ラジアン(b)	rad	1 (b)	m/m
立体角	ステラジアン(b)	sr(c)	1 (b)	$m^{2/}m^2$
周波数	ヘルツ (d)	Hz		s^{-1}
力	ニュートン	N		$m\ kg\ s^{-2}$
圧力，応力	パスカル	Pa	N/m^2	$m^{-1}\ kg\ s^{-2}$
エネルギー，仕事，熱量	ジュール	J	N m	$m^2\ kg\ s^{-2}$
仕事率，工率，放射束	ワット	W	J/s	$m^2\ kg\ s^{-3}$
電荷，電気量	クーロン	C		s A
電位差（電圧），起電力	ボルト	V	W/A	$m^2\ kg\ s^{-3}\ A^{-1}$
静電容量	ファラド	F	C/V	$m^{-2}\ kg^{-1}\ s^4\ A^2$
電気抵抗	オーム	Ω	V/A	$m^2\ kg\ s^{-3}\ A^{-2}$
コンダクタンス	ジーメンス	S	A/V	$m^{-2}\ kg^{-1}\ s^3\ A^2$
磁束	ウエーバ	Wb	Vs	$m^2\ kg\ s^{-2}\ A^{-1}$
磁束密度	テスラ	T	Wb/m^2	$kg\ s^{-2}\ A^{-1}$
インダクタンス	ヘンリー	H	Wb/A	$m^2\ kg\ s^{-2}\ A^{-2}$
セルシウス温度	セルシウス度(e)	℃		K
光束	ルーメン	lm	cd sr(c)	cd
照度	ルクス	lx	lm/m^2	$m^{-2}\ cd$
放射性核種の放射能 (f)	ベクレル (d)	Bq		s^{-1}
吸収線量, 比エネルギー分与, カーマ	グレイ	Gy	J/kg	$m^2\ s^{-2}$
線量当量, 周辺線量当量, 方向性線量当量, 個人線量当量	シーベルト (g)	Sv	J/kg	$m^2\ s^{-2}$
酸素活性	カタール	kat		$s^{-1}\ mol$

(a)SI接頭語は固有の名称と記号を持つ組立単位と組み合わせても使用できる。しかし接頭語を付した単位はもはやコヒーレントではない。

(b)ラジアンとステラジアンは数字の１に対する単位の特別な名称で、量についての情報をつたえるために使われる。実際には、使用する時には記号rad及びsrが用いられるが、習慣として組立単位としての記号である数字の１は明示されない。

(c)測光学ではステラジアンという名称と記号srを単位の表し方の中に、そのまま維持している。

(d)ヘルツは周期現象についてのみ、ベクレルは放射性核種の統計的過程についてのみ使用される。

(e)セルシウス度はケルビンの特別な名称で、セルシウス温度を表すために使用される。セルシウス度とケルビンの単位の大きさは同一である。したがって、温度差や温度間隔を表す数値はどちらの単位で表しても同じである。

(f)放射性核種の放射能（activity referred to a radionuclide）は、しばしば誤った用語で”radioactivity”と記される。

(g)単位シーベルト（PV,2002,70,205）についてはCIPM勧告2（CI-2002）を参照。

表４．単位の中に固有の名称と記号を含むSI組立単位の例

組立量	SI 組立単位		
	名称	記号	SI 基本単位による表し方
粘度	パスカル秒	Pa s	$m^{-1}\ kg\ s^{-1}$
力のモーメント	ニュートンメートル	N m	$m^2\ kg\ s^{-2}$
表面張力	ニュートン毎メートル	N/m	$kg\ s^{-2}$
角速度	ラジアン毎秒	rad/s	$m\ m^{-1}\ s^{-1}=s^{-1}$
角加速度	ラジアン毎秒毎秒	rad/s^2	$m\ m^{-1}\ s^{-2}=s^{-2}$
熱流密度，放射照度	ワット毎平方メートル	W/m^2	$kg\ s^{-3}$
熱容量，エントロピー	ジュール毎ケルビン	J/K	$m^2\ kg\ s^{-2}\ K^{-1}$
比熱容量，比エントロピー	ジュール毎キログラム毎ケルビン	J/(kg K)	$m^2\ s^{-2}\ K^{-1}$
比エネルギー	ジュール毎キログラム	J/kg	$m^2\ s^{-2}$
熱伝導率	ワット毎メートル毎ケルビン	W/(m K)	$m\ kg\ s^{-3}\ K^{-1}$
体積エネルギー	ジュール毎立方メートル	J/m^3	$m^{-1}\ kg\ s^{-2}$
電界の強さ	ボルト毎メートル	V/m	$m\ kg\ s^{-3}\ A^{-1}$
電荷密度	クーロン毎立方メートル	C/m^3	$m^{-3}\ sA$
表面電荷	クーロン毎平方メートル	C/m^2	$m^{-2}\ sA$
電束密度，電気変位	クーロン毎平方メートル	C/m^2	$m^{-2}\ sA$
誘電率	ファラド毎メートル	F/m	$m^{-3}\ kg^{-1}\ s^4\ A^2$
透磁率	ヘンリー毎メートル	H/m	$m\ kg\ s^{-2}\ A^{-2}$
モルエネルギー	ジュール毎モル	J/mol	$m^2\ kg\ s^{-2}\ mol^{-1}$
モルエントロピー, モル熱容量	ジュール毎モル毎ケルビン	J/(mol K)	$m^2\ kg\ s^{-2}\ K^{-1}\ mol^{-1}$
照射線量（X線及びγ線）	クーロン毎キログラム	C/kg	$kg^{-1}\ sA$
吸収線量率	グレイ毎秒	Gy/s	$m^2\ s^{-3}$
放射強度	ワット毎ステラジアン	W/sr	$m^4\ m^{-2}\ kg\ s^{-3}=m^2\ kg\ s^{-3}$
放射輝度	ワット毎平方メートル毎ステラジアン	$W/(m^2\ sr)$	$m^2\ m^{-2}\ kg\ s^{-3}=kg\ s^{-3}$
酵素活性濃度	カタール毎立方メートル	kat/m^3	$m^{-3}\ s^{-1}\ mol$

表５．SI 接頭語

乗数	接頭語	記号	乗数	接頭語	記号
10^{24}	ヨタ	Y	10^{-1}	デシ	d
10^{21}	ゼタ	Z	10^{-2}	センチ	c
10^{18}	エクサ	E	10^{-3}	ミリ	m
10^{15}	ペタ	P	10^{-6}	マイクロ	µ
10^{12}	テラ	T	10^{-9}	ナノ	n
10^9	ギガ	G	10^{-12}	ピコ	p
10^6	メガ	M	10^{-15}	フェムト	f
10^3	キロ	k	10^{-18}	アト	a
10^2	ヘクト	h	10^{-21}	ゼプト	z
10^1	デカ	da	10^{-24}	ヨクト	y

表６．SIに属さないが、SIと併用される単位

名称	記号	SI 単位による値
分	min	1 min=60s
時	h	1h =60 min=3600 s
日	d	1 d=24 h=86 400 s
度	°	1°=(π/180) rad
分	’	1’=(1/60)°=(π/10800) rad
秒	”	1”=(1/60)’=(π/648000) rad
ヘクタール	ha	$1ha=1hm^2=10^4m^2$
リットル	L，l	$1L=11=1dm^3=10^3cm^3=10^{-3}m^3$
トン	t	$1t=10^3$ kg

表７．SIに属さないが、SIと併用される単位で、SI単位で表される数値が実験的に得られるもの

名称	記号	SI 単位で表される数値
電子ボルト	eV	$1eV=1.602\ 176\ 53(14)\times10^{-19}J$
ダルトン	Da	$1Da=1.660\ 538\ 86(28)\times10^{-27}kg$
統一原子質量単位	u	1u=1 Da
天文単位	ua	$1ua=1.495\ 978\ 706\ 91(6)\times10^{11}m$

表８．SIに属さないが、SIと併用されるその他の単位

名称	記号	SI 単位で表される数値
バール	bar	$1\ bar=0.1MPa=100kPa=10^5Pa$
水銀柱ミリメートル	mmHg	1mmHg=133.322Pa
オングストローム	Å	$1\ Å=0.1nm=100pm=10^{-10}m$
海里	M	1 M=1852m
バーン	b	$1\ b=100fm^2=(10^{-12}cm)2=10^{-28}m^2$
ノット	kn	1 kn=(1852/3600)m/s
ネーパ	Np	SI単位との数値的な関係は、対数量の定義に依存。
ベル	B	
デジベル	dB	

表９．固有の名称をもつCGS組立単位

名称	記号	SI 単位で表される数値
エルグ	erg	$1\ erg=10^{-7}\ J$
ダイン	dyn	$1\ dyn=10^{-5}N$
ポアズ	P	$1\ P=1\ dyn\ s\ cm^{-2}=0.1Pa\ s$
ストークス	St	$1\ St=1cm^2\ s^{-1}=10^{-4}m^2\ s^{-1}$
スチルブ	sb	$1\ sb=1cd\ cm^{-2}=10^4cd\ m^{-2}$
フォト	ph	$1\ ph=1cd\ sr\ cm^{-2}\ 10^4lx$
ガル	Gal	$1\ Gal=1cm\ s^{-2}=10^{-2}ms^{-2}$
マクスウェル	Mx	$1\ Mx=1G\ cm^2=10^{-8}Wb$
ガウス	G	$1\ G=1Mx\ cm^{-2}=10^{-4}T$
エルステッド (c)	Oe	$1\ Oe \triangleq (10^3/4\pi)A\ m^{-1}$

(c) ３元系のCGS単位系とSIでは直接比較できないため、等号「 ≙ 」は対応関係を示すものである。

表10．SIに属さないその他の単位の例

名称	記号	SI 単位で表される数値
キュリー	Ci	$1\ Ci=3.7\times10^{10}Bq$
レントゲン	R	$1\ R=2.58\times10^{-4}C/kg$
ラド	rad	$1\ rad=1cGy=10^{-2}Gy$
レム	rem	$1\ rem=1\ cSv=10^{-2}Sv$
ガンマ	γ	1 γ =1 nT=10-9T
フェルミ		1フェルミ=1 fm=10-15m
メートル系カラット		1メートル系カラット = 200 mg = 2×10-4kg
トル	Torr	1 Torr = (101 325/760) Pa
標準大気圧	atm	1 atm = 101 325 Pa
カロリー	cal	1cal=4.1858J（「15℃」カロリー），4.1868J（「IT」カロリー）4.184J（「熱化学」カロリー）
ミクロン	µ	$1\ \mu=1\mu m=10^{-6}m$

（第8版，2006年改訂）